CONF-801022

1980 FLYWHEEL TECHNOLOGY SYMPOSIUM

October, 1980
Scottsdale, Arizona

DISTRIBUTION STATEMENT A
Approved for public release;
Distribution Unlimited

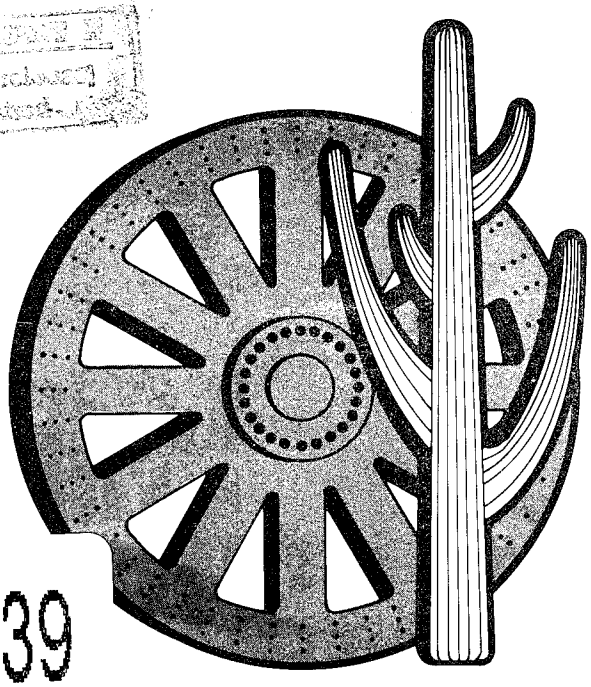

19960322 139

Co-sponsored by
The U.S. Department of Energy

The American Society
of Mechanical Engineers (ASME)

The Lawrence Livermore
National Laboratory

DEPARTMENT OF ENERGY
PLASTICS TECHNICAL EVALUATION CENTER
MIRADCOM, DOVER, N.J. 07801

This report was prepared as an account of work sponsored by the United States Government. Neither the United States nor the United States Department of Energy, nor any of their employees, nor any of their contractors, subcontractors, or their employees, makes any warranty, express or implied, or assumes any legal liability or responsibility for the accuracy, completeness or usefulness of any information, apparatus, product or process disclosed, or represents that its use would not infringe privately owned rights.

Reference to a company or product name does not imply approval or recommendation of the product by the University of California or the U.S. Department of Energy to the exclusion of others that may be suitable.

Printed in the United States of America
Available from
National Technical Information Service
U.S. Department of Commerce
5285 Port Royal Road
Springfield, VA 22161
Price: Printed Copy $;Microfiche $3.50

Page Range	Domestic Price	Page Range	Domestic Price
001-025	$ 5.00	326-250	$18.00
026-050	6.00	351-375	19.00
051-075	7.00	376-400	20.00
076-100	8.00	401-425	21.00
101-125	9.00	426-450	22.00
126-150	10.00	451-475	23.00
151-175	11.00	476-500	24.00
176-200	12.00	501-525	25.00
201-225	13.00	526-550	26.00
226-250	14.00	551-575	27.00
251-275	15.00	576-600	28.00
276-300	16.00	601-up [1]	
301-325	17.00		

[1] Add 2.00 for each additional 25 page increment from 601 pages up.

Work performed under the auspices of the U.S. Department of Energy by the Lawrence Livermore Laboratory under Contract W-7405-Eng-48.

Ad-A134750
434765

CONF-801022

1980 FLYWHEEL TECHNOLOGY SYMPOSIUM

October, 1980
Scottsdale, Arizona

DISTRIBUTION STATEMENT A
Approved for public release
Distribution Unlimited

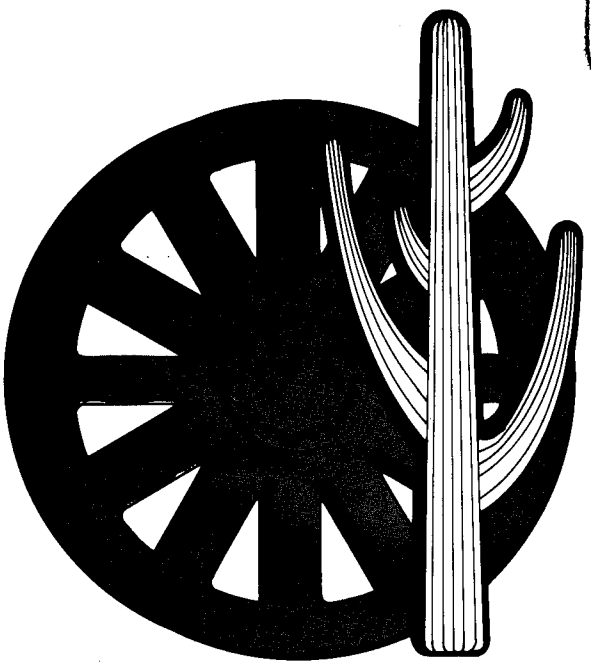

Co-sponsored by
The U.S. Department of Energy

The American Society
of Mechanical Engineers (ASME)

The Lawrence Livermore
National Laboratory

DTIC QUALITY INSPECTED 1

1980
FLYWHEEL TECHNOLOGY SYMPOSIUM

Thomas M. Barlow	Chairman
Paul Zygielbaum	Vice Chairman
Shelley Rose	Administrator

STEERING COMMITTEE

T. Barlow*
A. Cambel
L. Conta
H. Hurwicz
W. Jackson
E. Reimers
P. Zygielbaum*

PROGRAM COMMITTEE

K. Barber
T. Barlow*
N. Beachley
C. Bert
J. Campbell
T. Chiao
E. Cornell
H. Decker
D. Eisenhaure
W. Jackson
S. Kulkarni
A. McDonald
R. Stone
D. Towgood
D. Ullman
J. Vance
C. Wyman
P. Zygielbaum*

*Committee Co-chairmen

SPONSORING ORGANIZATIONS

THE UNITED STATES DEPARTMENT OF ENERGY

Charles Duncan	Secretary
Thomas E. Stelson	Assistant Secretary, Conservation and Solar
Maxine Savitz	Deputy Energy Assistant Secretary for Conservation
John J. Brogan	Acting Director, Office of Advanced Conservation Technologies
James H. Swisher	Director, Division of Thermal
Saul Strauch	Chief, Advanced Physical Methods Branch and Magnetic Energy

THE LAWRENCE LIVERMORE NATIONAL LABORATORY

Roger E. Batzel	Director
Richard L. Wagner Jr.	Executive Associate Director
Kenneth Street	Associate Director, Energy and Resource Program
Henry C. McDonald	Associate Director for Engineering

AMERICAN SOCIETY OF MECHANICAL ENGINEERS

Charles E. Jones	President
James R. Jones	Vice President, Power Dept.
Rogers B. Finch	Executive Director
Walter B. Moen	Managing Director

ENERGETICS DIVISION
Executive Committee

Joseph W. Pepper	Chairman
Jack S. Snell	Vice Chairman
James C. Corman	Secretary
Finn A. Hals	Program
John W. Larson	Paper Review Chairman
Dennis O. Blackletter	Past Chairman

DIESEL & GAS ENGINE POWER DIVISION
Executive Committee

Frank J. Pekar	Chairman
Edwin C. Younghouse	Vice Chairman
Walter R. Taber, Jr.	Vice Chairman & Program Committee Chairman
Douglas Exline	Member
Karl T. Geoca	Member
Lewis D. Conta	Secretary (Ex-Officio)
William W. Nugent	Treasurer (Ex-Officio)

AEROSPACE DIVISION
Executive Committee

Holt Ashley	Chairman
R. F. Hartung	Vice Chairman
J. W. Robinson	Secretary
J. R. Vinson	Member
R. M. Laurenson	Member
A. V. Srinivasan	Member
Walter Glowski	Member

FOREWORD

The 1980 Flywheel Technology Symposium provides a measure of the maturity of this important energy storage technology. As in the previous symposia of 1975 and 1977, new ideas are presented and progress is reported on concepts that have been investigated. More importantly, perhaps, the Symposium emphasizes the realization that cooperation and communication are important factors in the success of our work.

This year, for the first time, the American Society of Mechanical Engineers (ASME) has joined with the United States Department of Energy (DOE) and the Lawrence Livermore National Laboratory (LLNL) in the co-sponsorship of the Symposium. The ASME's Energetics, Diesel and Gas Engine Power, and Aerospace Divisions have actively participated in the planning and conduct of the Symposium, with the lead role for ASME being carried by the Energetics Division. We view the ASME's contribution as a significant step in the transition of flywheel technology from DOE and LLNL to the private sector.

Our objectives for the 1980 Symposium are similar to those of the two previous meetings:

- To provide a forum for the exchange of information and the stimulation of new ideas concerned with the development of the technology and its application in the commercial sector.

- To offer an opportunity for interested persons to become familiar with the technology and its potential for facilitating energy substitution and conservation.

In this context, several papers present the basics of flywheel technology and its implementation, while others describe the progress and status of technical programs. Still others present new topics for possible future development. Together, these provide a basis for further discussion, both formal and informal. The symposium affords us the opportunity to begin and to continue those discussions. We welcome your participation and we look forward to a most successful meeting.

Thomas M. Barlow
Paul Zygielbaum

TABLE OF CONTENTS

	Page
COMMITTEES	ii
SPONSORING ORGANIZATIONS	iii
FOREWORD	v
Overview of the Flywheel Technology Programme in the Netherlands G. J. van Mourik, ECN Netherlands Energy Research Foundation	1
The Flywheel Rotor and Containment Technology Development Program of the U. S. Department of Energy S. V. Kulkarni, Lawrence Livermore National Laboratory	3
Flywheel Energy Accumulators for City Buses--Steel and Composite Design Günter Besel, Erich Hau, Maschinenfabrik Augsburg Nürnberg	4
The UMTA Flywheel Trolley Coach Program--An Overview Harold D. Decker, Transportation Systems Center	13
Flywheel Automotive Marketability--An Overview William F. Adolfson, Advanced Technology, Inc.	20
Fiber Composite Materials Development for Flywheel Applications T. T. Chiao, Lawrence Livermore National Laboratory	22
Flywheel-Powered Shuttle Car for Mine Haulage Tom Zemo, U. S. Department of Energy, and Don Christofferson, FMC Corporation	33
Flywheel Delivers Precise 60 Hz Over Wide Speed Range Richard T. Morash, Richard Morash & Associates	45
Flywheel Energy Storage Systems Operating on Magnetic Bearings Pierre C. Poubeau, Société Nationale Industrielle Aerospatiale	55
Development of a Flywheel Storage System for Electrical Energy Applications G. J. W. van Altena and W. A. van Kampen, Delft University of Technology	68
Inertial Energy Storage for Home or Farm Use Based on a Flexible Flywheel J. M. Vance and B. T. Murphy, Texas A&M University	75

41928

Flywheel Motor/Generator for the Control of Hydraulic Surge or Water Hammer in Pumped Pipeline Systems 88
Wilhelm S. Everett, Everett Associates

Maximum Energy Densities for Composite Flywheels 93
Donald E. Johnson, Avco Systems Division, and
James J. Gorman, U. S. Department of Transportation

Torque Transfer in Composite Flywheels 101
Dr. K. R. Berg, Riggs Engineering Corporation

On the Performance of Hoop Wound Composite Flywheel Rotors . . . 121
Ralph F. Foral, University of Nebraska-Lincoln, and
Norman L. Newhouse, Brunswick Corporation

An Analog Simulation of a Flywheel Propulsion System for Buses 131
C. M. Ong, Purdue University

A Flywheel Energy Storage Propulsion System for Intra Urban Buses 145
R. E. Rinehart, General Electric Company

Flywheel Trolley Coach Propulsion with a High-Capacity Composite Flywheel 153
Louis J. Lawson, Garrett-AiResearch

Achieving Desirable Stress States in Thick Rim Rotating Disks by Variation of Properties 159
Gerard C. Pardoen, University of California at Irvine, and
Rod D. Nudenberg and Bruce E. Swartout, U. S. Flywheels

Design and Fabrication of a Flywheel Rotor for Automotive Use . . . 168
Stephen F. Post and Francis C. Younger,
William M. Brobeck & Associates

Composite Material Flywheel for UMTA Flywheel Trolley Coach 175
Theodore W. Place, AiResearch Manufacturing
Company of California

Elastomeric Regenerative Braking Systems 181
L. O. Hoppie, Eaton Corporation

The Fuel Economy Potential of Heat Engine/Flywheel Hybrid Automobiles 187
Steve M. Rohde and Neil A. Schilke, General Motors
Research Laboratories

Control Considerations for a Flywheel Hybrid Automobile with a Mechanical Continuously-Variable Transmission 188
Norman H. Beachley and Andrew A. Frank, University of
Wisconsin-Madison

Evaluation of a Hybrid Flywheel/Battery Propulsion System for Electric Vehicles 198
E. P. Cornell and F. G. Turnbull, General Electric Company,
and T. M. Barlow, Lawrence Livermore National Laboratory

Feedback Control Systems for Flywheel Radial Instabilities 209
Mont Hubbard and Paul McDonald, University of California at Davis

Dynamic Analysis of a Magnetically Suspended Energy Storage Wheel 218
Prof. L. L. Bucciarelli and Dr. A. Rangarajan, Massachusetts Institute of Technology

Forced Whirling Response of a Pendulously Supported Flywheel with Nonlinear Oil-Type Damping 225
C. A. Kocay and C. W. Bert, University of Oklahoma

Simplified Gyrodynamics of Road Vehicles with High-Energy Flywheels 240
Prof. Alan T. McDonald, Purdue University

Performance Testing and Economic Analysis of a Photovoltaic Flywheel Energy Storage and Conversion System 259
R. D. Hay, A. R. Millner, and P. O. Jarvinen, Massachusetts Institute of Technology

The Accelerating Flywheel 268
Dr. David G. Ullman, Union College, and John Corey, Mechanical Technology Incorporated

Conceptual Design of a Flywheel Energy Storage System 287
William H. Bauer and Francis C. Younger, William M. Brobeck & Associates

Composite Failure Analysis for Flywheel Design Applications . . 41936. . (296)
P. V. McLaughlin, Jr., A. Dasgupta, and Y. W. Chun, Villanova University

Material Design Properties of Cellulosic Flywheel Rotor Cores 41937. . (316)
David L. Hagen, Scott A. Gaff, and Arthur G. Erdman, University of Minnesota

Remarks on the Stress State in Rotating Orthotropic Disks . . . 41938. (330)
G. Genta, M. M. Gola, and A. Gugliotta, Istituto della Motorizzazione

Hybrid Power Systems Using Flywheels 339
Eberhart Reimers, U. S. Department of Energy, and Thomas M. Barlow, Lawrence Livermore National Laboratory

Utilization of Field-Modulated Machines for Flywheel Applications 353
David Eisenhaure, William Stanton, Emery St. George, and Tim Bliamptis, The Charles Stark Draper Laboratory, Inc.

Mosfet Based Power Converters for High-Speed Flywheels 363
David Eisenhaure, William Stanton, Richard Hockney, and Tim Bliamptis, The Charles Stark Draper Laboratory, Inc.

Flywheel Bearing Design for Automotive Applications 371
William H. Bauer and William M. Brobeck, William M. Brobeck & Associates

Factors Affecting the Control of a Magnetically Suspended Flywheel 380
David Eisenhaure, James Downer, and Richard Hockney, The Charles Stark Draper Laboratory, Inc.

Magnetic Bearing Support of a 10 KW HR Energy Storage Flywheel 392
Martin W. Eusepi, Mechanical Technology Incorporated

Hydraulic Accumulators as Energy Buffers; Thermodynamic Modeling and Thermal Losses 393
David R. Otis, University of Wisconsin-Madison

High Performance Dual Mode Car 403
D. W. Rabenhorst, The Johns Hopkins University Applied Physics Laboratory

Influence of Constant Power Start/Stop and Regenerative Braking Regimes on EV Batteries 405
E. J. Dowgiallo, U. S. Army Mobility Equipment Research and Development Command, and S. M. Caulder and A. C. Simon, Naval Research Laboratory

Combined Energy Storage (Flywheel/Battery Hybrid) 413
Edward Kuznetsov, Battelle's Columbus Laboratories, and Gary Kinzel, The Ohio State University

Nondestructive Evaluation of Fiber Reinforced Flywheels . . . 41939 . . . 421
B. W. Maxfield, D. M. Boyd, A. J. Schwarber, and S. Kulkarni, Lawrence Livermore National Laboratory

Data Analysis Techniques Used at the Oak Ridge Y-12 Plant Flywheel Evaluation Laboratory 423
R. S. Steele, Jr. and E. F. Babelay, Jr., Union Carbide Corporation

Moire' Strain Analysis of Composite Flywheels . . . . . 41940 . . . 435
G. Cuccuru and B. Picasso, Universita Di Cagliari

Experimental Investigation on the Vibratory Behaviour of Filament Wound Composite Material Discs . . . . . 41941 . . . 437
G. Cuccuru, B. Picasso, and P. Priolo, Universita Di Cagliari

From Vehicles to Satellites: The Technology Revolution of High Performance Flywheels 444
Dr. D. Davis, A. Csomar and B. Ginsburg, Rockwell International/Rocketdyne Division

Laminated, Composite Flywheel Failure Analysis 445
R. P. Nimmer, General Electric Company

Rotor Testing and Diagnostics 458
Alan D. Sapowith, AVCO Systems Division

Evaluation of Flywheel Containment . . . . . 41942 . . . 459
D. L. Kerr and J. Hickey, General Electric Company

OVERVIEW OF THE FLYWHEEL TECHNOLOGY PROGRAMME IN THE NETHERLANDS

G. J. van Mourik
ECN Netherlands Energy Research Foundation
Research Centre
3 Westerduinweg
Pettern (NH), The Netherlands

ABSTRACT

The Netherlands Energy Research Foundation ECN has developed a national flywheel technology research and development programme in cooperation with industry, research institutes, universities and utilities. The programme started in 1978 and will be terminated in September 1980.

The programme concerns a feasibility study of the applications of flywheels in hospitals and offices, in electric utilities, in the industry and in the transportation field. Furthermore it concerns the development of rotor design, bearing and damper system, housing requirements, motor/generator and converter system. Afterwards a hybrid flywheel-unit of 0,7 to 1 KWh will be developed for a bus used in urban transport.

Large scale use of flywheel-units in hospitals and offices with a total capacity of 400 MW will give an improvement of the output of the existing equipment for electricity supply of 0,2%, presupposing that the output for the flywheel-unit is about 90%.

The interest in the application of flywheels in the Dutch industry is still small, although some interested applications are considered.

Recent studies have shown that application of a hybrid flywheel system in a bus for urban transport in the Netherlands may result in a fuel saving of about 26% if the transmission output is about 60%. The energy capacity of such a flywheel system lies between 0,7 and 1 KWh.

Two types of rotor design will be tested; namely a flat disk shaped composite flywheel and a filament wound flywheel. At the Netherlands Energy Research Foundation and the Technical University of Delft testing facilities are being built.

Motor/generator and converter systems are in study at this moment. In the next four years there can possibly be built a prototype of a hybrid flywheel driven bus.

The full text of this paper was not available for inclusion in this volume of the Proceedings. It will be published later in a separate volume.

THE FLYWHEEL ROTOR AND CONTAINMENT TECHNOLOGY DEVELOPMENT PROGRAM OF THE U.S. DEPARTMENT OF ENERGY*

Satish V. Kulkarni
University of California, Lawrence Livermore National Laboratory
Livermore, California 94550

ABSTRACT

The status of the flywheel rotor and containment technology development program in the United states, sponsored by the Department of Energy, is reviewed in this paper. The specific objectives of the effort are delineated, and prototype composite rotor designs are described. These prototypes are being evaluated to identify promising designs for future development and enduse applications. The composite-laminated-rotor development effort at Lawrence Livermore National Laboratory (LLNL) and General Electric are also discussed, including design modifications to improve energy density, fabrication of thick composite laminates and filament-wound rings, low-cost manufacturing processes, generation of rotor-design data, nondestructive inspection, and spin testing of rotors. Finally, an assessment is made of the current rotor-burst-containment design philosophy and of the applicability of jet-engine fan-blade containment technology to flywheel systems. Based on this assessment, preliminary design criteria for containment are evolved.

---

*This work was performed under the auspices of the U. S. Department of Energy by Lawrence Livermore National Laboratory under contract No. W-7405-Eng-48.

The full text of this paper was not available for inclusion in this volume of the Proceedings. It will be published later in a separate volume.

FLYWHEEL ENERGY ACCUMULATORS FOR CITY BUSES
- STEEL AND COMPOSITE DESIGN -

Günter Besel, Erich Hau
MAN-Neue Technologie *
Abt. ERS
Postfach 50 06 20
8000 München 50

ABSTRACT

This paper deals with the design and the development of different types of flywheel energy accumulators for city buses. The test results of a flywheel unit consisting of a steel rotor, a cast steel housing and a reduction gear are discussed. Current efforts include the development of a fibre compound rotor with a maximum energy capacity of 750 Wh. This program is carried out in the framework of a working group "Gyrobus" comprising MAN, Daimler Benz, Bosch and the Technical Universities of Aachen and Berlin. With the support of the German Ministry of Research and Technology three experimental buses will be equipped with hybrid drive systems consisting of a diesel engine and a flywheel energy accumulator.

INTRODUCTION

Professor Helling of the Technical University of Aachen presented an experimental vehicle with a flywheel component to the German public for the first time in 1973. The concept of this hybrid drive system with a combustion engine and brake-energy storage was realized in a small bus, and the basic advantages of such a drive system were demonstrated. Stimulated by this project, M.A.N. began work on a drive system for city buses using a diesel-engine and a flywheel.

This preliminary work was extended in 1975 in the framework of a working group "Gyrobus", comprising MAN, Daimler Benz, Bosch, and the Technical Universities of Aachen and Berlin partially funded by the German Ministry of Research and Technology.

A comprehensive study worked out by this group on the technical and economical feasibility of brake-energy recovery in road vehicles by means of a hybrid drive system led to the following findings:

- The most suitable vehicle for economical application of a flywheel brake-energy storage system is the city bus, a fuel saving of up to 20% being expected.
- The flywheel energy storage unit should be constructed in conventional steel design for the first experimental vehicles and should have an energy storage capacity of 750-1500 Wh.
- Energy transfer through a hydromechanical continuously variable transmission represents the most economical solution for the 16-ton city bus. For smaller vehicles (3.7-ton bus) electric power transmission would also be of interest.

On the basis of these findings a program for the development of 3 experimental vehicles was started in 1976 under the the auspices of the Ministry of Research and Technology.

These vehicles are:

- A 16-ton city bus with a 100 kW diesel engine, a 750 Wh flywheel, and a hydrostatic transmission system (MAN design)
- A 16-ton city bus with a 100 kW diesel engine, a 1500 Wh flywheel, and a hydrostatic transmission (Daimler Benz design).
- A 3.7-ton city bus with a 48 kW diesel engine, a 750 Wh flywheel, and electrical power transmission (Daimler Benz design).

* MAN = Maschinenfabrik Augsburg Nürnberg

The flywheel energy-storage units for the first vehicles were constructed in steel by MAN-Neue Technologie. At the same time a program for the developement of flywheels in fiber-composite design was initiated. The first experimental vehicles were completed in May, 1980; road tests were commenced in June 1980.

FLYWHEEL BRAKE-ENERGY STORAGE SYSTEMS IN STEEL DESIGN

In the first generation of flywheel brake-energy storage systems conventional designs were deliberately used in order to keep developement risks and costs to a minimum. Corresponding to the design goals of the three experimental vehicles two models were developed with different storage capacities. The smaller flywheel with an energy capacity of 750 Wh is able to store twice the kinetic energy generated in braking a 16-ton city bus from a speed of 50 km/h.

For the second experimental vehicle a storage capacity of 1500 Wh was selected to allow the vehicle to operate over short distances (1-2 km) driven only by the flywheel unit for emission-free driving.

The construction of both models is fundamentally the same. Only the geometry of the flywheel disk and bearing support are slightly modified.

DESIGN

Rotor. The centrifugal mass consists of a forged steel disk of a high-grade material. The geometry corresponds to a disk of equal stress with rim. The rotor mass of the 750 Wh model is 115 kg and of the 1500 Wh model 226 kg. The outside diameter of both models is 520 mm the maximum rotational speed 12.000 rpm i.e. 200 rps (Fig. 1). The maximum material stress was calculated at σ = 360 N/mm². The allowable stress for this material is 1000 N/mm². The safety factors were calculated on the basis of a measured load collective for a service life of 10 years. The stress safety factor is between 1.60 and 1.95, depending on the type of loading. In this design the specific maximum energy density is 6.5 Wh/kg.

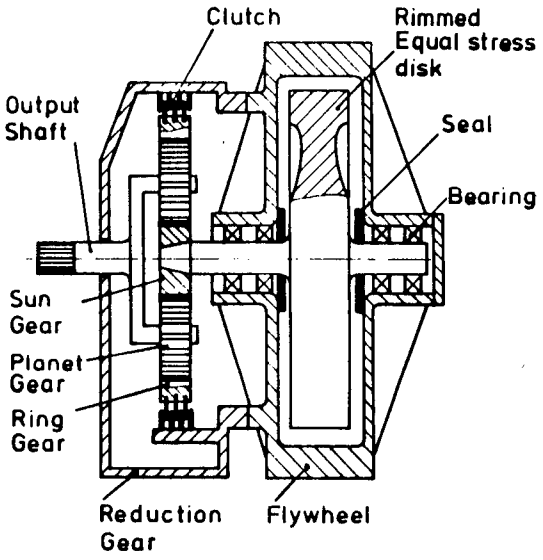

Fig. 1 Flywheel System Assembly Cross Section

Housing. The rotor spins in an evacuated housing. The two cast housing halves are of cast steel.

Due to weight and space considerations a full burst containment ring was not installed in the first experimental units. In view of the low internal stress level chosen this appeared justified.

Bearing supports and seals. The rotor is mounted on conventional ball bearings. The housing is sealed with axial face seals. The bearings were dimensioned to ensure maximum safety under the dynamic loads of vehicle operation.

Vacuum and oil supply. The housing is evacuated to 5 mbar by means of a 110 W vacuum pump. The lubricating oil is injected with a pressure of 1.5 mbar through nozzles directly onto the bearings. The oil and bearings temperatures are monitored.

Reduction gear. A reduction gear with a gear ratio of 4 : 1 is flangemounted on the flywheel assembly (Fig. 2).

The single-stage planetary gearbox is provided with a clutch that can release the ring gear, thus disengaging the flywheel from the rest of the drive train.

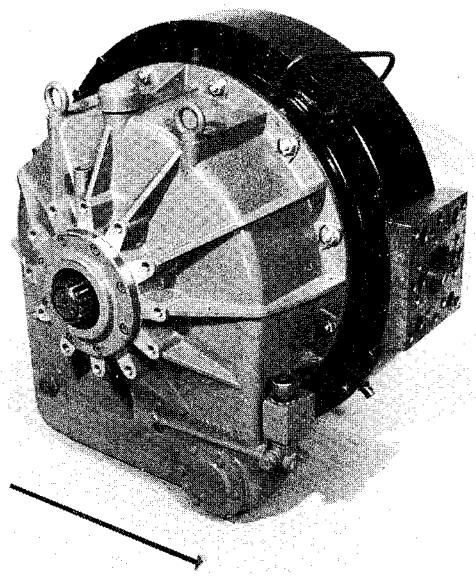

Fig. 2 Flywheel Unit directly mounted to Reduction Gearing

Safety system. The flywheel unit is equipped with a monitoring and safety system. In the event of excessive pressure in the housing, excessive bearing or oil temperature or insufficient oil pressure a valve in the housing opens to destroy the vacuum and the clutch disengages the flywheel from the drive train.

TESTS AND RESULTS

Before being installed in the test vehicles the flywheel assemblies were subjected to comprehensive tests.

These tests included:

- Ultrasonic testing of the rotor
- Overspeed tests at 14,000 rpm (Fig. 3)
- Long-time test with simulation of dynamic and gyroscopic loads
- Measurement of power losses
- Tests to optimize the lubricating oil flow rate with regard to power losses, oil temperature, and bearing temperature
- Functional tests in the full drive system (diesel engine + flywheel) on the test bed (Fig. 4)

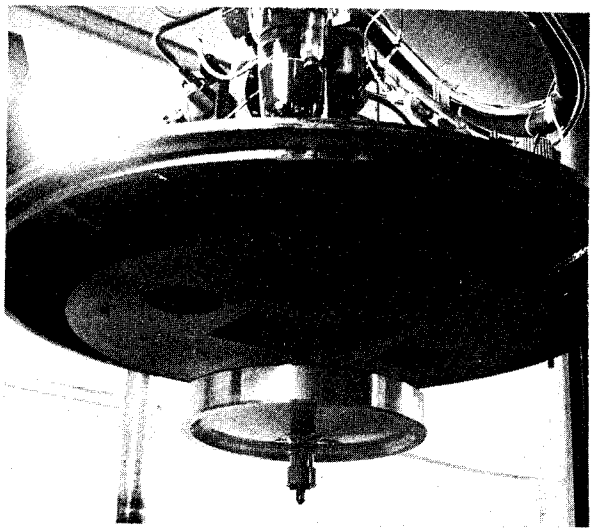

Fig. 3 Flywheel in spin test facility

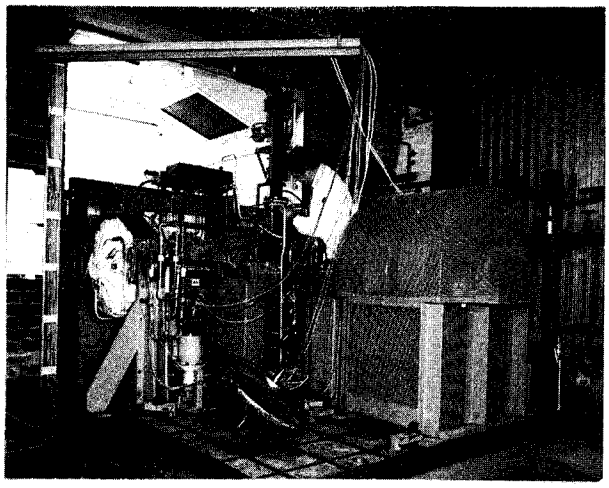

Fig. 4 Test Bench with Drive Train 100 kW Diesel engine, 750 Wh flywheel and hydromechanical continuously variable transmission. (The vehicle mass is simulated by the two momentum wheels in the foreground).

The power loss of the flywheel storage unit is a function of the partial pressure in the housing (air friction) and the frictional losses in the bearings and seals. It increases approximately as the square of the rotational speed.

Whereas at the rated speed of 12,000 rpm the power loss is 11 kW at atmospheric pressure, it drops to 1.9 kW at an internal pressure of 0.1 mbar. In the trade-off between the vacuum pump power and power losses from air friction the optimal solution for the design chosen was an internal pressure of 5 mbar with a pump power of 110 W.

Figure 5 plots the power loss from air and bearing friction as a function of speed with an internal pressure in the housing of 0.1 mbar.

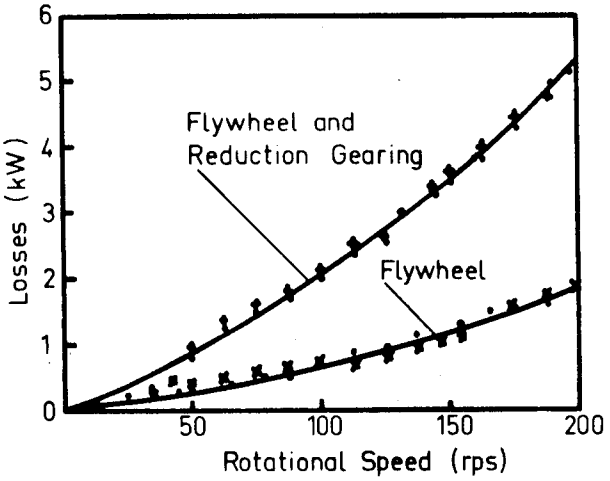

Fig. 5 Measured losses of the 750 Wh flywheel with and without reduction gear.
Vacuum 0.1 mbar.
Lubricant flow rate 1.0 liter/min

The lubricant flow rate proved to have a unnegligible effect on the power loss of the flywheel (Fig. 6). Optimal conditions were achieved with a flow rate of 1.0 liter/min on each pair of bearings, the oil and bearing temperature being about 80 degrees Centigrade.

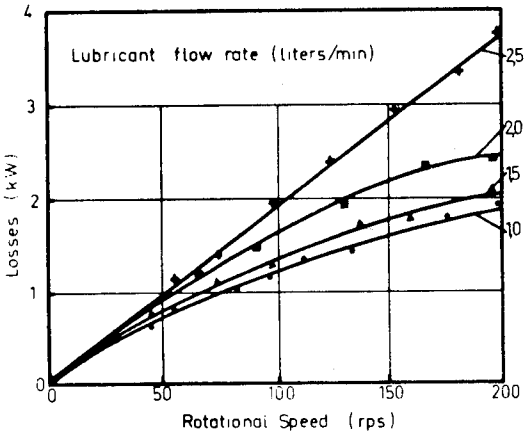

Fig. 6 Losses of the 750 Wh flywheel as a function of the lubricant flow rate
Vacuum 0.1 mbar

INSTALLATION OF FLYWHEEL ASSEMBLY IN VEHICLE

The flywheel storage unit is installed as a component of a hybrid drive system, diesel engine + flywheel, in a standard city bus. The dimensions and installation location were selected so that the entire drive system can be accomodated without major modifications of the vehicle structure especially without raising the vehicle floor. Figure 7 shows the installation in a standard city bus.

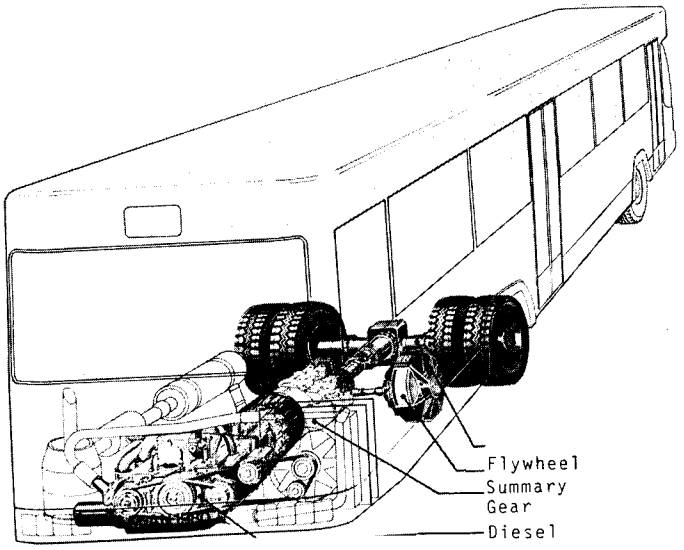

Fig. 7 Hybrid Drive System "Diesel Engine + Flywheel" in a MAN City Bus

FLYWHEELS IN FIBER-COMPOUND DESIGN

The long-term objectives in the development of flywheel energy storage systems will be characterized by the use of fiber -compound materials. There are two essential reasons for this:

- The higher strength of the fibers permits substantially greater energy-storage densities.
- The bursting behavior of a composite flywheel is less problematic than that of a steel flywheel, so that full burst protection can be incorporated in the vehicle without involving serious weight problems.

On the basis of model experiments with small flywheels and theoretical studies a basic design was developed whose suitability for use in vehicles will be examined. The design and first test results will be descibed.

SELECTION OF MATERIAL

The following fiber materials were considered for use in flywheel energy storage systems:

- glass fiber (E or S type)
- polyamide fiber Kevlar 49 and 49 FK
- carbon fiber in various grades

Owing to its outstanding load-cycle characteristics, which in view of the design load cycle of 10^7 is of decisive importance, carbon fiber were selected - at least for the first experimental units - despite their higher costs. This decision is also justified by the considerabe cost reduction of carbon fiber anticipated by the time series production of the flywheels can be expected.
Epoxy resin is used as matrix material.

	Theorectical max. energy density Wh/kg	Energy densitiy realizable with today's technology in short-duration tests Wh/kg	After 10^7 load-cycles (10 years lifetime) Wh/kg	After 10^7 load cycles with 50% safety Wh/kg
Glas-fiber	222	132	37	24
Carbon-fiber	247	134	107	71
Kevlar FK	306	150	50	33
Steel (σ_B 2600 N/mm², disk of equal stress)	90	90	36	24

DESIGN

The main dimensions of the basic design were determined by the goal of replacing the existing steelrotor by the composit-rotor. The outside diameter and maximum energy content were therefore retained. Figure 8 shows the construction of the composite flywheel rotor.

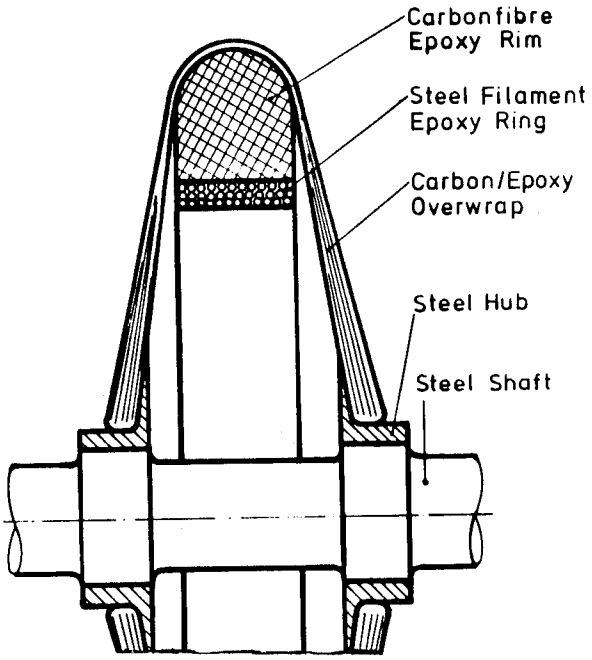

Fig. 8 Composite Flywheel Cross Section

The centrifugal mass is formed mainly of an outer rim consisting of wound circumferencially wound layers. This rim is wound with a closed overwrap that assumes the function of spokes. The overwrap is bonded to the metal hub.

A special feature of this design is an inner ring of circumferentially wound high-strength steel filement/epoxy. This ring, which expands more than the composite ring, reduces through "internal pressure" the radial stress in the outer composite ring arising from centrifugal forces (Fig. 9).

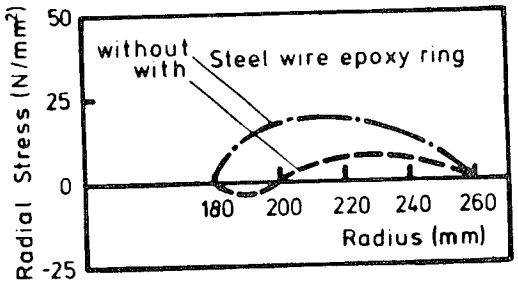

Fig. 9 Calculated radial Stresses in the Composite Rim with and without Steel Filement Epoxy Ring

STRESS ANALYSIS

Stress calculations were based on two load cases:

- static load at max. speed
- acceleration and braking of the flywheel with a max. torque of 250 Nm on the hub

The calculation of dynamic load was based on a load cycle total of 10^7 to ensure a service life of 10 years.

In calculating and designing the composite flywheel various finite element model idealizations were set up.

Among others, the following parameters were subjected to close examination:

- stress in the composite rim and the influence of the steel filement/epoxy ring
- optimization of the overwrap contour and the winding geometry
- interface of composite rim to overwrap
- interface of overwrap to hub (bonding)

The calculations yielded to the following results:

- Radial stress in the opposite ring was substantially reduced by the steel filement inner ring (Fig. 9)
- Variation of the overwrap contour within the framework of the basic design has virtually no influence on the magnitude of the tensile stress in the carbon fiber/epoxy circumferencial layers. This result is slso clearly demonstrated in the deformation behavior of the overwrap (Fig. 10).

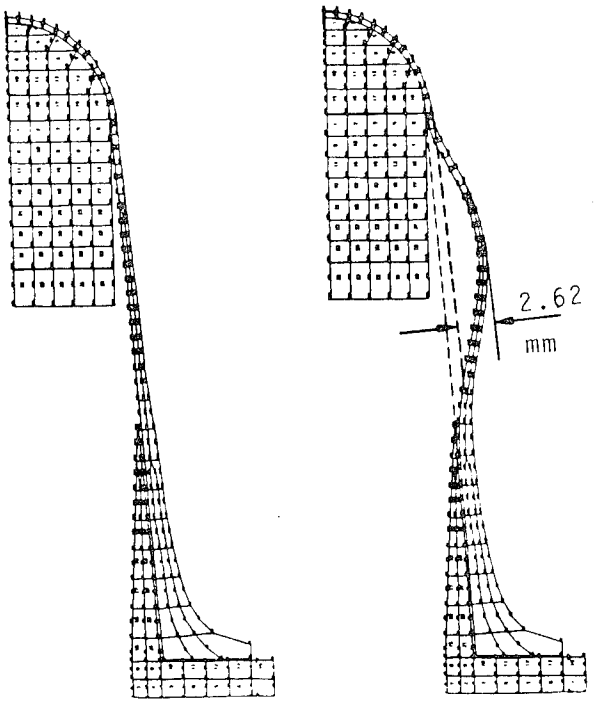

Fig. 10 Deformation of Overwrap at Design Speed 28 500 rpm

- Bending stresses occur in the transition from the overwrap to the composite ring, which can be reduced to acceptable levels by decreasing the inclination angle between overwrap and the plane of the flywheel (Fig. 11). Stresses in the bonded joint between the overwrap and the hub are kept to a minimum by the use of elastomer bonding Fig. 12).

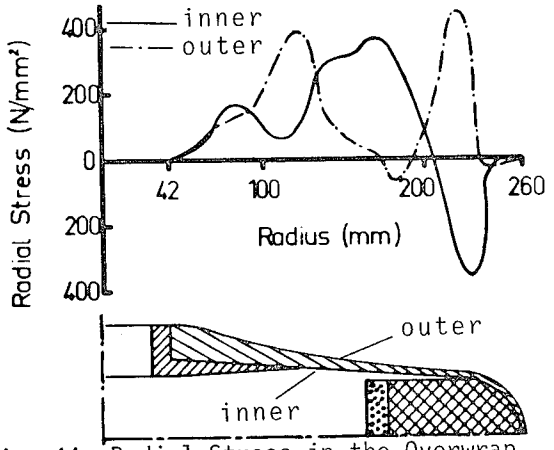

Fig. 11 Radial Stress in the Overwrap

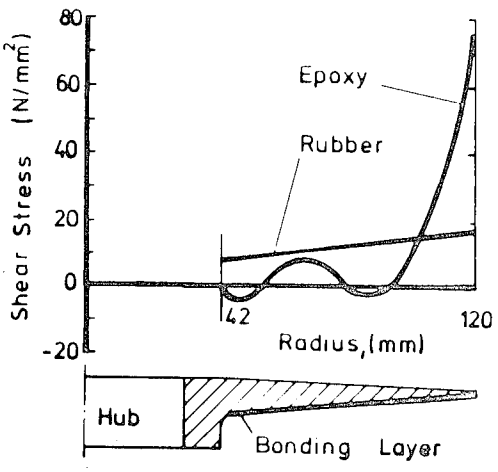

Fig. 12 Calculated Shear Stress in the Overwrap/Hub Bonding Layer

MANUFACTURING

the carbon fiber ring is produced by winding 7 mm thick circumferential layers, each cured separately. In this way stresses arising in the curing process can be kept small and flaws in the composite material avoided. The steel filement/epoxy ring is produced by winding. The carbon fiber/epoxy ring is mashined to the desired cross-sectional shape. The carbon fiber/epoxy ring and the steel filement ring are press-fitted together and bonded (Fig. 13).

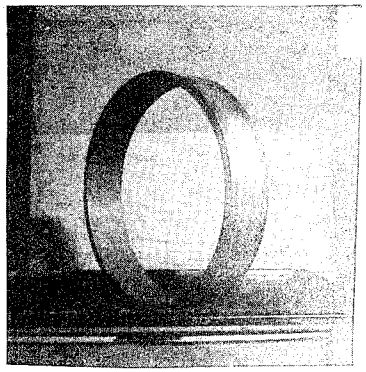

a

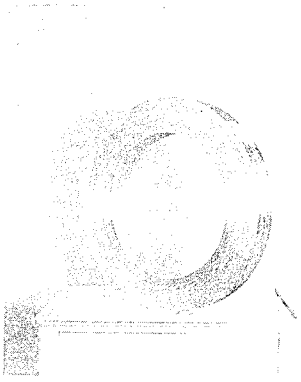

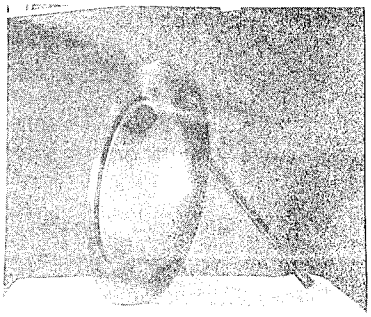

c

Fig. 13 Composite Flywheel Manufacturing Steps

a Inner Steel Filement/Epoxy Ring

b Carbon Fiber/Epoxy Rim as wound

c Machined Carbon/Epoxy Rim with pressfitted Steel Filement/Epoxy Ring

The overwrap is wound with the aid of a numerically coded machine (Fig. 14). To fix the carbon fiber/epoxy steel ring to the hub during winding a jig is used which can be dismantled after completion. The individual parts can then be removed through the bore in the hub.

The winding is built up in three layers, each layer being cured separately.

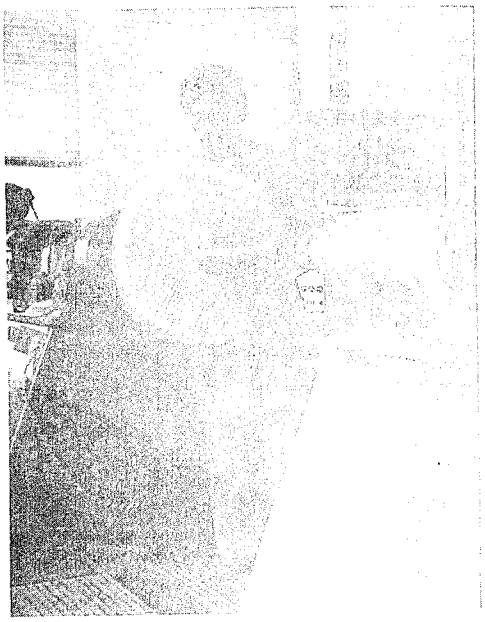

Fig. 14 Flywheel on Winding Machine

TEST RESULTS

The testing program will first comprise operational tests up to the rated speed of 28,500 rpm and overspeed tests up to the calculated bursting speed of 35,000 rpm.

So far three units have been tested. All the tests have had to be interrupted due to increasing imballance with increasing speed. The highest speed attained has been 22,000 rpm. A deformation of the composite structure has not been observed. The imbalance may result from tolerance errors between the shaft and the hub. In the forthcoming tests these errors will be rectified and balancing improved. Until now the balancing masses were fixed in the interior of the flywheel rim and were sometimes lost during the spin test. It is hoped that this situation can be remedied by rigidly mounted steel balancing disks from which material can be removed.

COMPARISON OF THE STEEL AND THE COMPOSITE DESIGN

A comparison of steel and composite flywheels on the basis of the test units described cannot, of course, have general validity in every aspect. Both the steel design as a forged disk and the relatively complex composite form with carbon fibers represent to a certain extent extreme solutions. Nevertheless, the results show the order of magnitude of the differences (Fig. 15).

	Steel flywheel	Composite flywheel
Rotor Material	Refined steel 34 Cr Ni Mo 6	Carbon fiber/epoxy rim steel filament/epoxy ring steel hub
Outer diameter	520 mm	520 mm
Mass	115 kg	32 kg
Moment of inertia	3.42 kgm²	0.73 kgm²
Max. rotational speed	12,000 rpm	28,500 rpm
Max. energy content	750 Wh	750 Wh
Design life time	10 years	10 years
Operating cycles	10^7	10^7
HOUSING Material Mass Vacuum	 cast steel 105 kg 5 mbar	 cast aluminium 45 kg 0,1 mbar
REDUCTION GEAR Gear ratio Mass	 single stage planetary gear 1 : 4 72 kg	 single stage planetary gear 1 : 9.5 70 kg

Fig. 15 Comparison of steel and composite flywheel design

A comparison of technical data is less difficult than a comparison of costs, because only experimental units have been constructed so far. Production costs of DM 3,500 have been calculated for the steel flywheel storage system without step-down gearing, based on an annual production of 100 units.

The production costs for the composite design are largely determined by material costs. Whereas nowadays the production costs of the design described before are prohibitively high, about DM 6,000. Based on series production, a dramatic cost reduction is anticipated in the future for carbon fibers, so that series production of composite flywheels will certainly be economically feasible.

SUMMARY AND PERSPECTIVES FOR THE FUTURE

Two approaches have been followed in the development of flywheel brake energy storage systems for city buses.

The first approach employs units of relatively conventional design with steel rotors in order to realize functional hybrid drive systems with brake energy recovery for the first generation of experimental vehicles without great development risks.

At the same time an appraoch has been pursued to develop flywheels in composite fiber design.

For the conventional steel flywheels the safety question remains a problem, at least with regard to large-scale application. Composite flywheels, which do not present a problem in this regard entail difficult technical problems, for example balancing and deformation of the structure under load.

The future design objective will therefore be the attempt to combine the virtues of both designs. A conceivable design may incorporate metal and composite materials. The metal parts should be so thin-walled that they do not constitute a hazard in the event of failure, and the composite material, supported by metal, will still form the centrifugal mass, but will be greatly simplified in design and manufacturing.

THE UMTA FLYWHEEL TROLLEY COACH PROGRAM - AN OVERVIEW

Harold D. Decker
Transportation Systems Center
Kendall Square
Cambridge, MA 02142

ABSTRACT

Based on the favorable results of recent parallel studies by General Electric and Garrett/AiResearch, UMTA has proceeded to implement the development of engineering prototype flywheel propulsion systems for urban transit coaches. Parallel contracts for the development of competitive prototypes have been awarded, with General Electric using a steel flywheel and Garrett a flywheel of composite material. System design and fabrication will be followed by comprehensive laboratory tests, and each prototype will subsequently be installed in an urban transit coach for field test and evaluation in both a pure flywheel and a flywheel/trolley coach hybrid mode. When operating off the flywheel, the coach will have a range of 3.5 miles between flywheel charges with all auxiliary systems operating, and 6 miles with minimum auxiliary loads. Flywheel charging is accomplished though automatic power collectors that engage a wayside DC source at terminal and transfer points or under wire when operating as a trolley coach. Advantages of the system include reduced energy consumption through recuperation of braking energy, independence from petroleum fuels, and minimized noise and pollution. Satisfactory demonstration of performance by the prototypes would be followed by deployment of several vehicles of each type in revenue service.

BACKGROUND

Although several early attempts were made to utilize flywheels as a stored energy device in transportation, none were successful until the Oerlikon Engineering Company of Switzerland used a small railway locomotive powered by flywheels to switch rail cars in it yards. The flywheels were recharged or brought up to maximum speed periodically from an electric power surce. In 1950, Oerlikon demonstrated its similarly powered "Gyrobus" under service conditions. Subsequently, these Oerlikon vehicles were built and placed in service in Yverdon, Switzerland; Leopoldville, Zaire (formerly the Belgian Congo); and in Gand, Belgium. These vehicles employed a 3300 lb steel flywheel 5 feet 4 inches in diameter, with a maximum speed of 3000 rpm. A squirrel cage induction machine was used to put power drawn from an overhead three-phase ac source into the flywheel during charging and to extract power from the flywheel and apply it to the traction motor during vehicle operation. The traction motor was a similar induction machine; the vehicle operator controlled the speed by manually changing the number of poles. Regenerative braking was employed to recover braking energy and return it to the flywheel. These vehicles performed satisfactorily for many years. They were gradually replaced by the more economical diesel buses; the last one was removed from service in 1969. Although their service record was excellent, the relatively short distance traveled (about 1 mile) between flywheel charges, the length of time (1 - 2 minutes) required to charge the flywheel, and the complexity of their controls hastened their demise.

Subsequently, a study[1] prepared for the San Francisco Municipal Railway Improvement Corporation (MUNI) and the Urban Mass Transportation Administration (UMTA) of the U.S. Department of Transportation (DOT) showed that flywheel propulsion with 2 miles between flywheel recharges was suitable and practicable for bus type transit vehicles on many routes, although a greater range was desirable. This effort was not carried beyond the study stage.

In 1972, the New York State Metropolitan Transportation Authority (MTA) awarded a contract to the Garrett/AiResearch Manufacturing Company of California for the modification of the propulsion

systems of two type R-32 subway cars of the New York City Transit Authority (NYCTA) to provide on-board energy storage, and recuperation of braking energy.[2,3] These objectives were achieved through the use of two flywheel energy storage units on each car and chopper controls. Each flywheel unit had an energy storage capacity of 3.2 KWHR, and the flywheel rotor comprised four steel disks bolted together rather than a single large disk. In service, these Energy Storage Cars showed a saving of about 31 percent of the propulsion energy that is normally consumed; the saving is achieved by regenerative braking and the use of chopper controls. Installation of flywheel energy storage units of improved design in 22 of NYCTA's newest cars, the type R-46, to obtain operational, performance and maintenance data is being held in abeyance pending the availability of funds.

Other applications of flywheels pertinent to transportation include a similar flywheel installation in UMTA's Advanced Concept Train (ACT),[4] and Department of Energy (DOE) work on flywheels for smaller, personal-sized vehicles.[5]

UMTA FLYWHEEL/TROLLEY COACH PROGRAM

These successful applications of flywheel energy storage techniques have led UMTA to formulate a program to consider them as potential solutions to the problems of responding to national priorities and meeting the transportation needs of the nation's many urban areas. Specifically, the program is designed to accomplish the following objectives:

- Minimize dependence on petroleum fuels.
- Minimize environmental impacts (noise and pollution).
- Maintain or improve vehicle performance.
- Maintain or decrease life cycle costs with respect to the conventional urban diesel bus.

The program, as developed, comprises four discrete phases, which are briefly described below and are considered in detail in subsequent paragraphs:

Phase I - Conduct technical and economic feasibility studies on the applicability of flywheel energy storage techniques to urban transit motor vehicles and prepare preliminary designs for recommended systems.

Phase II - Design, develop, fabricate, test, and evaluate engineering prototypes of the recommended system(s) in urban transit motor vehicles.

Phase III - Demonstrate in limited revenue service a number of preproduction prototypes installed in urban transit motor vehicles.

Phase IV - Demonstrate in full revenue service a larger number of production prototypes installed in urban transit motor vehicles.

Progression from phase to phase is not automatic but requires specific government approval. Such approval depends upon the degree of success achieved in the preceding phase, the continuing need for the program, and the availability of funds. A summary schedule for the program is shown in Figure 1.

The program is supported by funding from DOE, and is being handled by DOT's Transportation Systems Center (TSC) as Systems Manager.

PHASE I - FEASIBILITY STUDIES

This phase, initiated in 1975 and completed in 1977, had as its objectives the determination of propulsion system requirements, the analysis of several configurations of propulsion systems employing flywheel energy storage techniques to fulfill them, a determination of their technical and economic viability, the preparation of preliminary designs for viable systems, and the preparation of recommendations for candidate vehicles and the prototype development work to be carried out under Phase II.

The Phase I work was carried out under two parallel study contracts, awarded on a competitive basis to the General Electric Company, Corporate Re-

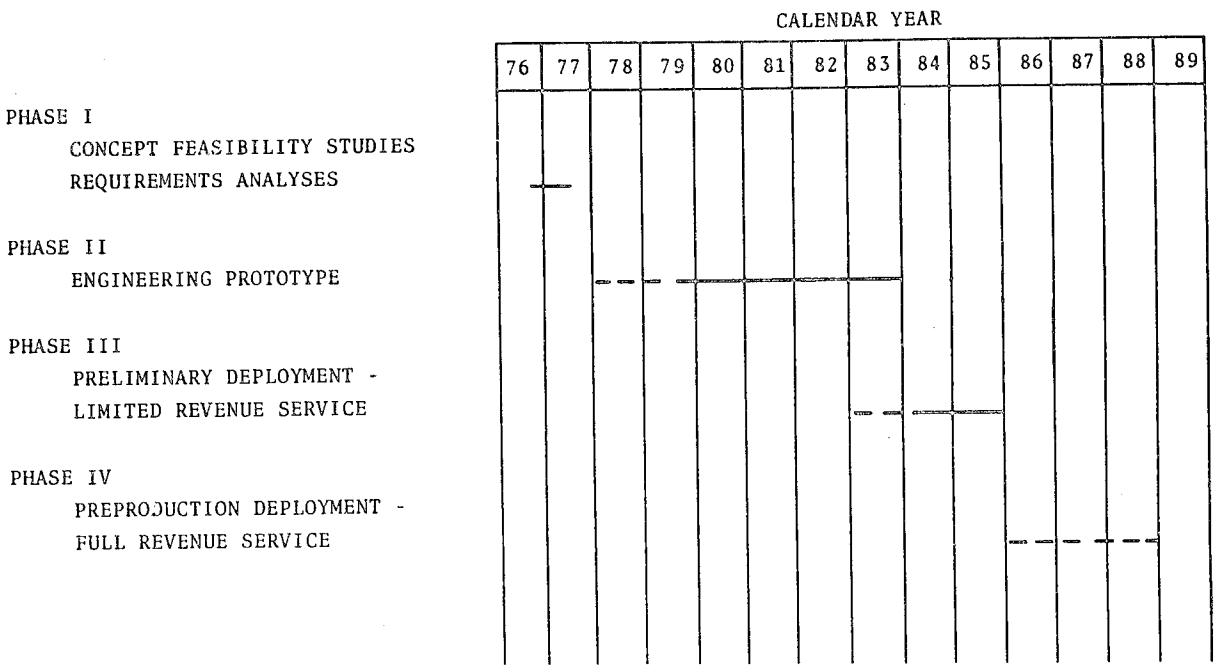

Fig. 1. UMTA flywheel/trolley coach - summary schedule.

search and Development, and to AiResearch Manufacturing Company of California, a division of the Garrett Corporation.[6,7] Typical system configurations considered by both contractors include pure flywheel, flywheel/trolley coach hybrid and flywheel/battery hybrid. These were compared to the baseline diesel bus, battery bus, and trolley coach. In addition, Garrett addressed the flyhweel/diesel hybrid and referenced it to the diesel bus. Various sizes of urban transit vehicles were considered.

Both contractors arrived at essentially the same conclusions. The vehicle recommended for consideration was the 40-foot urban transit bus or trolley coach; this is the most prevalent size in use in urban areas. The propulsion systems considered were evaluated and analyzed in terms of applicability to this vehicle.

The propuslion system configurations studied were found to be tecnically feasible and realizable within the present state of the art. All of the configurations, with the exception of the battery bus and flywheel/battery bus, were found to be within a cost-competitive range on a life cycle cost basis with the conventional diesel bus when the shorter life of the diesel bus (14 years) is compared to the expected life of a trolley coach (23 years). The flywheel/battery bus showed a cost advantage over the battery bus because of the extended life of the battery installation, but it was much more costly than the diesel bus. The homopolar inductor motor alternator, recommended as the electrical power input-output device for the flywheel by both contractors, presents a major technical challenge since a homopolar machine of this small size and high rating has never been built before.

Both contractors recommended that Phase II of the program be undertaken with a pure flywheel propulsion system having a total energy storage capacity of 12 to 20 KWHR installed in a 40-foot urban transit vehicle. Both contractors recognized that the equipment components should be designed on a modular basis so that they may readily be adapted to other vehicles and propulsion system configurations.

PHASE II - ENGINEERING PROTOTYPES

In January, 1978, UMTA decided to proceed into Phase II and designated TSC as its systems manager. The specific objectives of Phase II are:

- Design, development, fabrication, and comprehensive laboratory test of two competitive engineering prototype flywheel propulsion systems, one from each Phase I contractor in accordance with his recommendations.

- Field Test and evaluation of the performance of the prototypes installed in a 40-foot urban transit vehicle in simulated revenue service.
- Development of a solid base for the preparation of production costs.
- Collection of data pertinent to propulsion system and vehicle operation and maintenance.

Parallel contracts were negotiated with, and awarded to, each of the Phase I contractors by TSC for the design, development, fabrication, test and evaluation of an engineering prototype of a pure flywheel propulsion system installed in a 40-foot urban transit vehicle. The prototypes are to be consistent with the respective preliminary designs as established in Phase I. It was subsequently decided to add automatic power collection equipment to each prototype system so that each system would have the capability of operating as a flywheel/trolley coach under a pair of conventional trolley wires. Each test vehicle will then be demonstrated and evaluated in a pure flywheel mode and/or in a flywheel/trolley coach mode with the capability of running under trolley wires or running off wire for distances of up to 3.5 miles with full auxiliary loads. The specified performance characteristics of the vehicle are presented in Table I. A simplified block diagram of the planned propulsion system is shown in Figure 2. A schedule of the Phase II activities is shown in Figure 3.

Both contractors are proceeding along parallel paths in development. A major difference exists in the area of materials shown for the flywheel rotor. General Electric has selected a high strength steel, and Garrett is proceeding with the use of composite material. Other differences are minor and reflect the detailed design approaches of the two contractors.

Table 1. Performance characteristics - flywheel/trolley coach.

Acceleration	
Maximum	3.5 mph/sec
Initial	3.0 mph/sec
Deceleration	
Normal	3.0 mph/sec
Emergency	4.5 mph/sec (minimum)
Jerk	0.1 g/sec (max)
Maximum speed	
General Electric	40 mph
Garrett	55 mph
Range, UMTA Drive Cycle C	3.5 miles with maximum hotel loads
	6.5 miles with minimum hotel loads
Gradability, 20% grade	
In pure flywheel mode	15 mph for 1000 feet
In flywheel trolley coach mode	15 mph minimum
Flywheel charging time	
Full recharge (50-100% speed)	90 seconds
Standstill to full speed	180 seconds

Performance based on gross vehicle weight of 30,000 pounds on a level road at sea level on a calm day.

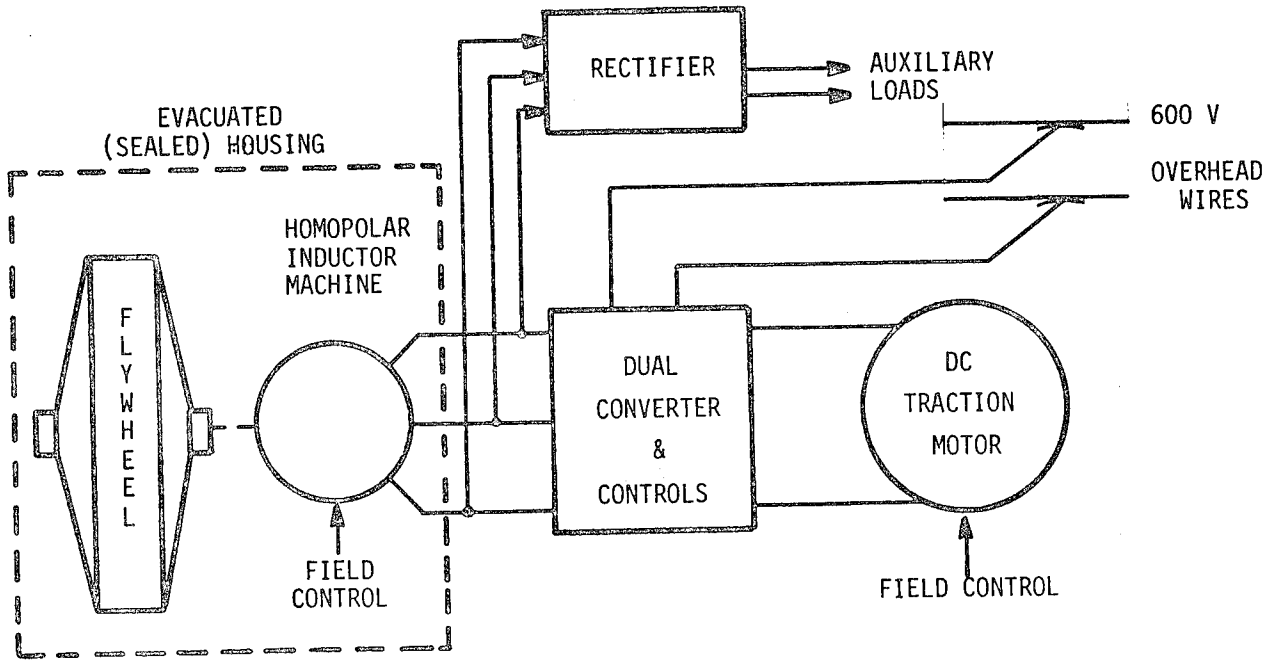

Fig. 2. Flywheel/trolley coach-schematic diagram.

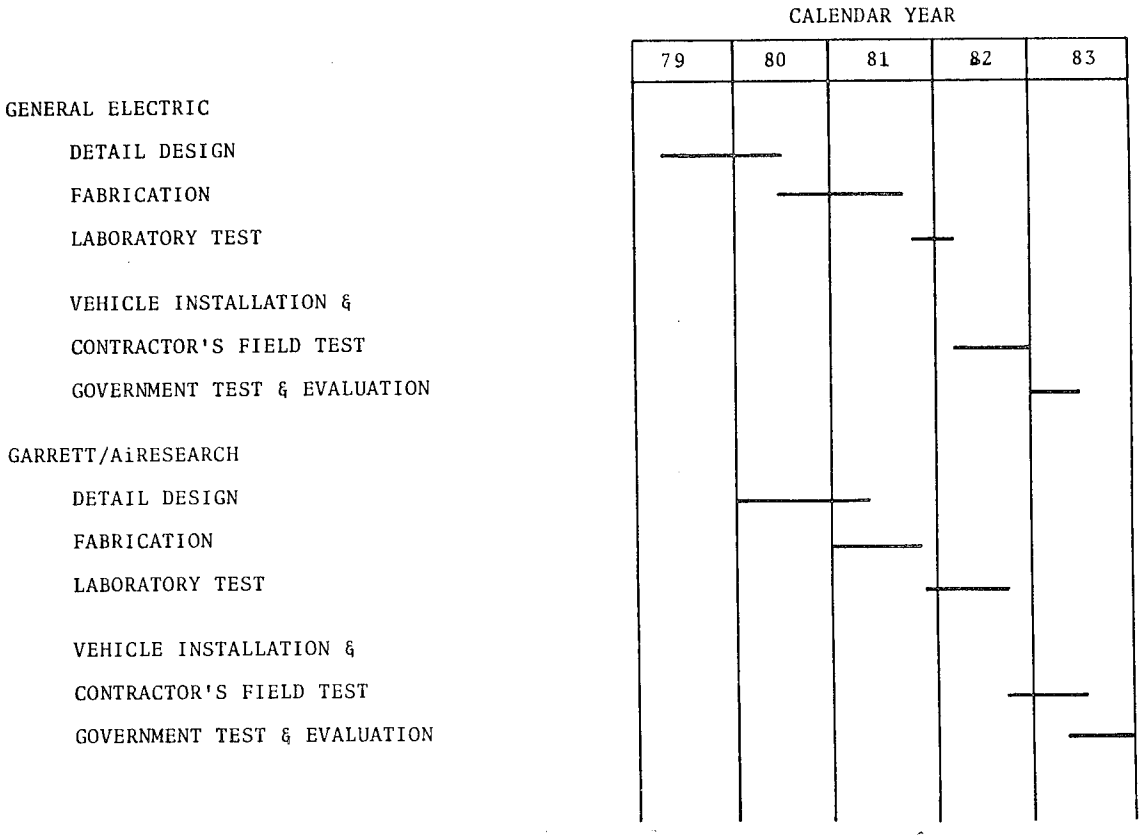

Fig. 3. UMTA flywheel/trolley coach - Phase II schedule.

General Electric has completed its flywheel rotor design and analysis, and is proceeding with the containment system design. Scale model flywheel burst tests have confirmed the flywheel rotor design and established the basis for the containment system design. The design of the flywheel homopolar motor-alternator and of the power and control electronics is complete. The traction motor, a modification of the proven GE type 1213 design, is being fabricated. Acquisition of the test vehicle is being pursued. No major technical problems have been encountered. Completion of the contractor's 6-month test and evaluation program is expected to occur in December, 1982, at which time the vehicle will be delivered to TSC for the Government's test and evaluation program under simulated revenue service conditions.

Garrett is proceeding with the design of its system. It is completing the design of its flywheel and inductor motor alternator, and has completed the design of the power and control electronics. The traction motor is being processed, and vehicle acquisition is being negotiated. Completion of the 6-month contractor's test and evaluation program is expected to occur in June, 1983, following which the vehicle will be delivered to TSC for the Government's test and evaluation program under simulated revenue service conditions.

Based on progress made to date, it is anticipated that the Phase II efforts will be completed on schedule and that the specific objectives of this phase will have been met. Accordingly, in the near future, plans and funding requirements for Phases III and IV will be prepared and submitted so that the necessary approvals can be obtained.

PHASE III - DEPLOYMENT IN LIMITED REVENUE SERVICE

Assuming that Phase II is satisfactorily completed by GE and Garrett, it is planned to award parallel contracts for the building of 5 to 10 preproduction prototypes of the flywheel/trolley coach system of each design, their installation in 40-foot urban transit buses, and their deployment in limited revenue service with cooperating properties. The objectives of this phase are the collection and evaluation of data and experience relevant to the operation and maintenance of the vehicles and their propulsion systems, and to determine their suitability for more widespread deployment. In addition, this effort will provide a basis for subsequent manufacture of the units, and a firm basis for estimating production costs. Any design deficiencies found in Phase II will be corrected in the Phase III installations.

PHASE IV - DEPLOYMENT IN FULL REVENUE SERVICE

Upon the satisfactory completion of the Phase III work, parallel contracts may be awarded for building 10 to 25 systems of each type and their deployment in full revenue service with cooperating transit properties. These equipments will be designed for quantity production. The objectives of this phase include the collection and evaluation of data and experience relevant to the operation and maintenance of the vehicles, and the demonstration of the vehicles in full revenue service. Information gathered in this phase will then be used in the preparation of plans for large-scale deployment of the vehicles.

CONCLUSION

The UMTA flywheel/trolley coach Program has been laid out as described in order to proceed expeditiously from system studies to production prototypes of a flywheel propulsion system at minimum cost and minimum risk. Continuing participation by bus and trolley coach operators is being obtained to ensure that the planned systems will satisfy real needs of the transit industry. Active cooperation has indeed been promised by several transit operators in the test, evaluation, and demonstration phases. At the conclusion of the program, it is expected that two competitive production designs of bus/trolley coach propulsion systems employing flywheel energy storage techniques will have been established, demonstrated, and made available to the transit industry.

REFERENCES

1) Woods, J.M. and Lawson, L.J., "Energy Storage Propelled Transit Vehicle Application Study," prepared for U.S. Department of Transportation, Urban Mass Transportation Administration, Washington DC, April 30, 1975.

2) New York Metropolitan Transportation Authority, "Energy Storage Propulsion System for Rapid Transit Cars: System Design and Equipment Description," U.S. Department of Transportation, Urban Mass Transportation Administration, Washington DC, September 1975, UMTA-NY-06-0006-75-1.

3) Raskin, D., "Energy Storage Propulsion System for Rapid Transit Cars: Test Results and System Evaluation," U.S. Department of Transportation, Urban Mass Transportation Administration, Washington DC, October 1978, UMTA-NY-06-0006-78-1.

4) Boeing-Vertol, "Act-1 Advanced Concept Train Development Program, Simulated Demonstration Test Report," U.S. Department of Transportation, Urban Mass Transportation Administration, Washington DC, July 1979, UMTA-IT-06-0026-79-7.

5) Towgood, D.A., "An Advanced Vehicular Flywheel System for the ERDA Electric Powered Passenger Vehicle," 1977 Flywheel Technology Symposium Proceedings, pp. 63-68, October 1977, PC A22/MF A01.

6) Fleck, J.J. et al., "A Study of Flywheel Energy Storage for Urban Transit Vehicles," U.S. Department of Transportation, Urban Mass Transportation Administration, Washington DC, September 16, 1977, PB-282 929.

7) Lawson, L.J. et al., "Study of Flywheel Energy Storage," prepared by AiResearch Manufacturing Co. for the U.S. Department of Transportation, Urban Mass Transportation Administration, Washington DC, September 1, 1977, UMTA-CA-06-0106-77-1:
   Volume 1. Executive Summary
   Volume 2. System Analysis
   Volume 3. System Mechanization
   Volume 4. Life Cycle Costs
   Volume 5. Vehicle Tests

FLYWHEEL AUTOMOTIVE MARKETABILITY - AN OVERVIEW

William F. Adolfson
Advanced Technology, Inc.
7923 Jones Branch Drive, Suite 500
McLean, Virginia 22102

ABSTRACT

Significant reduction in domestic consumption of liquid petroleum fuels in the automobile transportation sector is possible by applying flywheel energy storage (FES) technology to conventional gasoline-powered vehicles or integrating an FES system with an electric vehicle to enhance performance. While the DOE estimates that annual fuel savings from using flywheel hybrid vehicles could be about 20 MBOE by the year 2000, the U.S. automobile manufacturers, however, believe they can meet Federal requirements for more efficient cars with downsized fleets, weight reduction, improved engines and more efficient transmissions. These measures are regarded as more cost effective than developing FES technology, whose future in automotive applications is perceived very pessimistically.

Changing this perception requires an aggressive program to develop and demonstrate FES technology compatible with marketable electric/flywheel hybrid vehicle or gasoline-engine/flywheel hybrid vehicle. While the technical feasibility of FES is generally accepted, the technology needs to be developed for specific end-use applications by:

- Determining the specific performance and cost characteristics of a marketable vehicle.
- Determining the performance and cost characteristics of the FES unit proposed for a marketable vehicle.
- Establishing design specifications and allocating costs among components of FES units.
- Developing and testing the FES technology that meets these specifications and cost requirements.

These steps will help to ensure that the efforts of government research facilities, private industry and universities will be coordinated and supportive. The result will be the development of a vehicle that from its initial design is acceptable from the customer's perspective.

The full text of this paper was not available for inclusion in this volume of the Proceedings. It will be published later in a separate volume.

FIBER COMPOSITE MATERIALS DEVELOPMENT FOR FLYWHEEL APPLICATIONS*

T. T. Chiao
Lawrence Livermore National Laboratory, University of California
Livermore, California 94550

February 1980

ABSTRACT

The fiber composite materials program was formulated to support the development of various flywheel rotor designs for energy storage. Our areas of activity include matrix and fiber evaluations, static properties of composites for engineering design, and lifetime data to predict the long-term performance of composites. In this article, we summarize the highlights of our technical accomplishments to date, and describe our overall program and the key technical issues involved for future activities.

INTRODUCTION

Because of the importance of composite materials to flywheel applications, the fiber composite materials program was started at the beginning of the national flywheel program for energy storage in 1975. The objectives of the materials program are to:

- Develop an engineering data base on the static properties of composite materials for flywheel rotor designs.
- Study the time-dependent behavior of composites in order to predict the long-term performance of a flywheel rotor.
- Screen and develop new materials, fibers, and matrices for potential flywheel applications.
- Disseminate information to the industry.

The criteria for planning our program can be summarized as follows:

- Selection of materials for evaluation in this program should be based on both performance and cost.
- Materials work should be commonly applicable to several flywheel rotor designs, such as rings, molded short-fiber plates, and laminated plates.
- Environmental conditions should cover two temperatures (75° and 150°C) in vacuum. However, the reference point in air is 23°C.
- Data generated in this program should be basic and longlasting in value. This program is not intended to replace a company's routine short-term materials activities, but to complement them and answer questions which are either extensive in scope or difficult.

Our effort covers the specific areas listed below. Names of the principal investigators are given in parentheses.

- Matrix evaluation and formulation (J. Kolb, LLL)
- Fibers other special topics (T. T. Chiao, R. Sherry, LLL)

*This work was performed under the auspices of the U. S. Department of Energy by the Lawrence Livermore Laboratory under Contract No. W-7405-ENG.

- Engineering data on composite materials for flywheel design (H. T. Hahn, Washington University)
- Time-dependent behavior of composites (E. M. Wu, LLL)
- Information dissemination to industry (T. T. Chiao, LLL)

In this article we summarize highlights of progress made in several technical areas and briefly review our future plans. Detailed technical information in specific areas has been published as topical reports and articles. We have also published many timely short subjects in Composites Technology Review.

MATRIX MATERIALS

Both performance and cost must be considered when selecting materials for composite flywheels. To date, effort in the matrix area has been concentrated on epoxies, particularly on formulations for wet filament winding.

Criteria for evaluating matrix formulations include processability, commercial availability, physical and mechanical properties, degree of toxicity, and cost. Many epoxy systems have been characterized in our program[1-5]; few can meet all the expectations. Table 1, summarizes the most promising epoxy systems for flywheel applications based on our selection criteria at different use temperatures. To avoid confusion several other well-characterized systems were not included. Table 2, lists the chemical names and the sources of supply, and Table 3 summarizes key properties of these resin systems.

FIBER MATERIALS

Our effort on fiber evaluations for flywheel applications has been concentrated on continuous filament bundles. Following the criteria of commercial availability, mechanical properties in terms of the ratio of tensile strength to density, number of filaments per bundle, and cost, we selected four fibers for evaluation: S-2 glass, Kevlar 49 and 29, and E-glass (Table 4).

Because performance was compared by using epoxy-impregnated strands, the effect of the matrix on the fiber properties is included to give realistic results. Figure 1 shows the ranking order of the four fibers in epoxy "A" (described in Table 1) in terms of fiber strength (calculation based on

TABLE 1. Recommended epoxy systems for flywheel applications based on use temperature.

Service temp. °C	Formulation ratio by wt.	Recommended practical cure cycle*	Key advantages	Key drawbacks	Refs.
23 to 50	A. DER332/Jeffamine T-403 (100/45)	Gel at 60o C or below; Cure for 1 h @ 100oC	1. Low toxicity 2. Acceptable prop. 3. Low cure temp.	Low service temp.	1 and 2
75 to 100	B. DER332/RD-2/Tonox 60-40 (100/25/29)	Gel @ 80o C or below; cure for 1-1/2 h @ 120oC	Balanced prop.	High toxicity	3
	C. DER 332/Kelpoxy G293/Heloxy 68/ Tonox 6040 (77/23/65/34)	Gel at 90oC or below; Cure for 2 h @ 130oC	1. Tough system 2. Acceptable prop.	1. High toxicity 2. Complex system	4
100 to 150	D. CY-179/CTBN/MTHPA/ 1 MI (100/5/100/1)	Gel at 90oC cure for 2 h @ 150oC	1. High temp. svs. 2. Low toxicity	1. Low tensile and shear 2. Long cure cycle	5

*Recommended cycle is from structure processing point of view. Time required to heat structure to temperature should be added to the cure cycle.

TABLE 2. Chemical name of resins and sources of supply.

Trade name	Chemical name	Sources of supply
DER 332	Pure Diglycidyl Ether of Bisphenol-A Epoxy	Dow Chemical Co. Shell Chemical Equiv., Epon 825
Jeffamine T-403	Aliphatic Polyether Triamine	Jefferson Chem. Co.
RD-2	Diglycidyl Ether of 1,4 Butanediol	Ciba-Geigy Corp.
Tonox 60-40	Eutectic mixture of crude Methylene Dianiline (60%) and m-Phylene Diamine (40%)	Uniroyal
Kelpoxy G-293	Rubberized Diglycidyl Ether of Bis-phenol-A	Spencer Kellog Division of Textron
Heloxy 68	Diglycidyl Ether of Neopentyl Glycol	Wilmington Chem. Co.
CY-179	Cycloaliphatic Epoxy	Ciba Geigy Corp.
CTBN	Hycar 1300 X 8 Rubber	B. F. Goodrich Chem. Co.
MTHPA	Methyl Tetrahydroph-thalic Anhydride	Archem Co.
1 MI	1 Methylimidazol	Aldrich Chem. Co.

fiber cross-sectional area only) vs fiber volume in a composite strand. Designers often prefer to use composite strength in structural calculations. For this purpose, Fig. 2 can be plotted using the same values for as Fig. 1 with corrections for the matrix contribution in terms of the cross-sectional area of a strand. The ranking order of the four fibers remains unchanged. Two important points are evident:

- Optimum fiber content for a composite structure should be selected by balancing the fiber efficiency as well as the composite efficiency.
- Optimum fiber content for these fibers seem to be between 60% and 70% by volume. Although the higher fiber content shows high static properties, the lower fiber content is preferred for long-term performance of a flywheel.

Since a flywheel is a tensile-critical application, tensile testing of the composite strands represents realistic upper bound values of material capabilities. When strength, density, and cost of the fiber/epoxy strands are considered together, as shown in Table 5, two interesting points become evident:

TABLE 3. Comparison of key properties of the recommended epoxy systems.

	Epoxy A*	Epoxy B*	Epoxy C*	Epoxy D*
Cure cycle	7 h @ 60oC 1 h @ 100oC	3 h @ 60oC 2 h @ 120oC	1.5 h @ 90oC 2 h @ 130oC	2 h @ 90oC 4 h @ 150oC
Viscosity, Pa•s @ 25oC	1	1	0.95	0.38
Gel time for 30-g mass @ 25oC, h	18.5+	24+	29.3	43.7
Tensile properties				
Modulus, GPa	1.6	2.7	2.43	2.4
Max. stress, MPa	66.5	89	72.5	58.1
Failure strain %	7.7	7.7	8.4	2.8
Shear properties				
Modulus, GPa	1.3	-	1.59	.47
Failure stress, MPa	52	52	54.9	27.5
Water absorption %, 24 h	0.75 @ 23oC	0.93 @ 23oC	3.1 @ 100oC	2.1 @ 100oC
Glass transition temp., oC	72	126	104	210
Toxicity	Low	High	High	Low

*Formulations defined in Table 1.

TABLE 4 Fiber information

Fiber	Density, Mg/m^3	Filaments/ Strand	Current Cost $/lb.
Kevlar 49 (DuPont)	1.45	1000	9.75
Kevlar 29 (DuPont)	1.44	1000	9.75
E-glass, Type 30 (Owens-Corning Fiberglas)	2.57	2052	0.65
S2-glass, 20-end roving (Owens-Corning Fiberglas)	2.43	4080	2.70

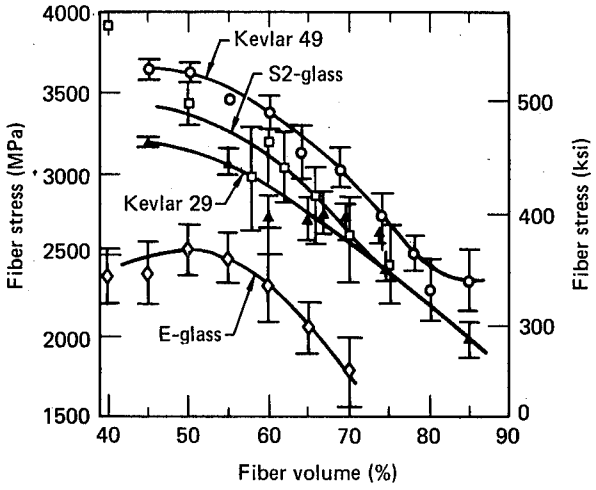

Fig. 1. Strand test results plotted as fiber failure stress

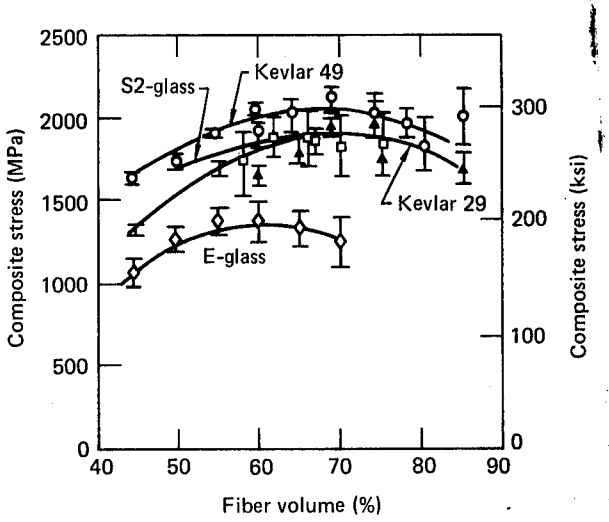

Fig. 2. Strand test results plotted as composite failure stress.

- When tensile strength is the only consideration, Kevlar 49/epoxy material ranks the best for flywheel applications.
- When both the cost of raw materials and the tensile strength are both considered, E-glass/epoxy material is the best.

It should be pointed out that values in Table 5 have been verified by experiments with idealistic thin-rim composite rotors.[6] Other factors, such as design variations, processes of rotor fabrication, and failure modes, can contribute significantly toward lowering the energy density of a flywheel. In order to focus on material capabilities, these factors are not considered in this comparison

STATIC MECHANICAL PROPERTIES OF COMPOSITES FOR FLYWHEEL DESIGN

Materials activities have been limited to continuous fiber reinforced composites with emphasis on filament-wound rings of various size and thickness and quasi-isotropic layups of molded or machined plates. To avoid confusion in final specimens used to generate design data should closely simulate both the flywheel design and

TABLE 5. Comparison of several composite materials for flywheel applications.

Composite strand	Density, Mg/m^3	[a] Cost, $/kg	[b] Composite/failure stress of strand M Pa	[c] Failure/stress To density ratio kJ/kg	[d] Max. energy density of flywheel kJ/kg	Energy density per $, kJ/$
Kevlar 49/Epoxy A	1.36	15	2145	1577	789	53
Kevlar 29/Epoxy A	1.36	15	1755	1290	645	43
S-2 Glass/Epoxy A	2.03	5	1885	929	465	93
E-Glass/Epoxy A	2.07	2.0	1500	725	368	184

[a] 1980 Prices: Kevlars, $9.75 per lb.; S-2 glass, $2.70 per lb.; E-glass, $0.65 per lb.; and Epoxy "A", $1.50 per lb.

[b] Composite stresses are based on a nominal 65% fiber volume.

[c] Stress/density = $\frac{(MPa)(m^3)}{Mg} = \frac{Pa\ m}{g} = \frac{N\ m}{g} = \frac{kJ}{kg}$.

[d] For a simple rim flywheel, the maximum energy density is approximately one-half of the stress to density ratio. To convert kilojoule per kilogram to watt-hours per pound multiply by 0.126.

the process of fabrication. In this section, we emphasize the material characterization of flat laminates.

Ten composite material systems have been characterized, mainly for use at 23-50°C. The key properties of three important systems[8-11] are summarized in Tables 6, 7, and 8.

Work is continuing on composite systems which can be used at 75°-100°C. Incomplete data[12] on a Kevlar 49/epoxy C composite system are shown in Table 9. The effect on the lamina properties of this system is surprisingly small except on the shear and transverse tensile moduli, .

LONG-TERM PERFORMANCE OF COMPOSITE MATERIALS

Reliable long-term use of composite flywheels requires lifetime data for both sustained loading (stress-rupture) and cyclic loading (fatigue). Figure 3 summarizes the data from several years of stress-rupture studies on composite materials relevant to flywheel applications. Large sample sizes of various fiber/epoxy composite strands (45 to 100 in most cases) were used for these

TABLE 6. Lamina Properties of Kevlar 49/Epoxy A.

Mechanical properties

Elastic constants (tensile and compressive)	
Longitudinal Young's modulus (E_{11}), GPa	81.1 ± 1.5
Transverse Young's modulus (E_{22}), GPa	5.10 ± 0.10
Shear modulus (G_{12}), GPa	1.82 ± 0.09
Major Poisson's ratio (μ_{21})	0.310 ± 0.035
Minor Poisson's ratio (μ_{21})	0.0193 ± 0.0014

Ultimates	Tension	Compression	Shear
Longitudinal strength, MPa	1850 ± 50	235 ± 3	-
Longitudinal ultimate strain %	2.23 ± 0.06	0.48 ± 0.3	-
Transverse strength, MPa	7.9 ± 1.1	53 ± 3[b]	-
Transverse ultimate strain, %	0.161 ± 0.023	1.41 ± 0.12	-
Shear stress at 0.2% offset, MPa	-	-	24.4 ± 2.4
Shear strain at 0.2% offset, %	-	-	1.55 ± 0.16

Thermal propertiesc

	-50	-25	0	25	50	75	100	125
Linear coefficient of thermal expansion, (10-6/°C)								
Longitudinal	-3.8	-3.8	-3.8	-4.0	-4.7	-6.0	-	-
Transverse	61	66	72	79	87	150	214	214
Thermal conductivity (W/m·°C)								
Longitudinal	2.62	2.84	3.05	3.22	3.31	3.34	-	-
Transverse	-	0.27	0.33	0.35	0.37	0.39	-	-
Heat capacity, (J/kg·°C)	840	930	1020	1120	1190	1300	-	-

NOTES: The Kevlar 49/Epoxy A is at 60% fiber volume.

Fiber: Kevlar 49, 1420 denier.

Matrix: 100 parts Dow Chemical DER 332
45 parts Jefferson Chemical Jeffamine T-403.

Cure: 1 d at room temperature and 16 h at 85°C.

studies.[13-20] S-glass/epoxy had the most, E-glass/epoxy less, and Kevlar/epoxy the least stress-rupture problems.

When analyzed using a two-parameter Weibull distribution,[21] these lifetime data show the following trend:

- For simple Kevlar/epoxy composites, the lifetime distribution shape parameter changes with the applied stress level from less than unity at stress levels above 80% of the ultimate to more than unity at lower stress levels. This indicates that there is an increasing rate of failure and a reduction of scatter in the data at lower stress levels. A strength degradation or "wear-out" type of failure process is often associated with this phenomenon. This stress-dependency of the Weibull shape parameter makes life predications at low stress levels both difficult and hazardous.

- For the simple S-glass composite, the lifetime distribution shape parameter remains approximately constant at close to unity for all stress levels tested. This indicates that the failure rate is constant, the scatter of data is the same, and a random failure process is operating with this composite. The nearly constant shape parameter simplifies the analysis and makes life prediction possible provided that the environmental effect on the composite is accounted for.

TABLE 7. Lamina properties of S-2 glass/epoxy A.

Mechanical properties

Elastic constant (tensile and compressive)	
Longitudinal Young's modulus (E_{11}), GPa	58.80 ± 1.16
Transverse Young's modulus (E_{22}), GPa	17.46 ± 0.24
Shear modulus (G_{12}), GPa	7.28 ± 0.19
Major Poisson's ratio (μ_{12})	0.2651 ± 0.0057
Minor Poisson's ratio (μ_{21})	0.0789 ± 0.0023

Ultimates	Tension	Compression	Shear
Longitudinal strength, MPa	1749 ± 67	500 ± 60	
Longitudinal ultimate strain, %	2.87 ± 0.27	0.93 ± 0.07	
Transverse strength, MPa	41.81 ± 0.95	111.6 ± 2.3	-
Transverse ultimate strain, %	0.263 ± 0.010	3.89 ± 0.47	-
Shear stress at 0.2% offset, MPa	-	-	-
Shear strain at 0.2% offset, %	-	-	30.12 ± 0.39
			0.620 ± 0.014

Thermal properties

	-50	-25	0	25	50	75
Linear coefficient of thermal expansion, ($10^{-6}/^{o}C$)						
Longitudinal	3.523 ± 0.038	3.523 ± 0.038	3.523 ± 0.038	3.523 ± 0.038	3.523 ± 0.038	3.523 ± 0.038
Transverse	19.9 ± 0.8	21.3 ± 0.8	23.2 ± 0.8	25.1 ± 0.8	27.6 ± 3.4	77 ± 21
Thermal conductivity, ($W/m \cdot {}^{o}C$)						
Longitudinal	-	-	1.62 ± 0.26	1.70 ± 0.26	1.80 ± 0.26	1.88 ± 0.26
Transverse	-	-	-	-	-	-
Heat capacity, ($J/kg \cdot {}^{o}C$)	-	-	-	-	-	-

NOTES: The S-2 glass/Epoxy A is at 65% fiber volume.

Fiber: S-2 glass: Owens Corning Fiberglas grade P263A-750[a]

Matrix: 100 parts Dow Chemical DER 332
45 parts Jefferson Chemical Jeffamine 7403

Cure: 16 h at 60°C

TABLE 8. Lamina Properties of E-glass/Epoxy A

Mechanical Properties

Elastic constants (tensile and compressive)	
Longitudinal Young's modulus (E_{11}), GPa	52.15 ± 0.89
Transverse Young's modulus ($_{22}$), GPa	14.03 ± 0.61
Shear modulus (G_{12}), GPa	6.3 ± 0.5
Major Poisson's ratio, (μ_{12})	0.207 ± 0.016
Minor Poisson's ratio, (μ_{21})	0.056 ± 0.011

Ultimates	Tension	Compression	Shear
Longitudinal	1108 ± 25	530 ± 110	-
Longitudinal ultimate strain, %	2.16 ± 0.11	1.11 ± 0.27	-
Transverse strength, MPa	7.5 ± 1.1	(78 ± 4)[b]	-
Transverse ultimate strain, %	0.054 ± 0.009	(0.68 ± 0.10)	-
Shear stress at 0.2% offset, MPa	-	-	22.4 ± 1.7
Shear strain at 0.2% offset, %	-	-	0.546 ± 0.045

Thermal properties

	Temperature°C				
	-60	-20	20	50	80
Linear coefficient of thermal expansion, (10-6/°C)					
Longitudinal	6.31 ± 0.51	6.31 ± 0.51	6.31 ± 0.51	6.31 ± 0.51	6.31 ± 0.51
Transverse	20.2	22.4	25.6	30.5	90
Thermal conductivity, (W/m·°C)					
Longitudinal	-	1.14	1.26	1.35	1.44
Transverse	-	0.53	0.59	0.63	0.68
Heat capacity, (J/kg·°C)	640	750	850	900	950

NOTES: The E-glass/Epoxy A is at 65% fiber volume.

Fiber: E-glass: Owens-Corning Fiberglas Type 30, grade 410AA-450

Matrix: 100 parts Dow Chemical DER 332
45 parts Jefferson Chemical Jeffamine T-403

Cure: 16 h at 60°C

- In the case of simple E-glass composites, the lifetime distribution shape parameter for the three high-stress-level studies is much lower than unity, indicating a large lifetime data scatter and a decreasing rate of failure with time. At the lower stress levels, (60% of ultimate or below) as shown in Fig. 1, E-glass seems to have a longer lifetime than the corresponding S-glass composite.

There are limited fatigue data on Kevlar 49/epoxy composites. Results to date of square-wave loading at 1 Hz of Kevlar 49/epoxy "A"-strands are summarized in Fig. 4.[22] For comparison, stress-rupture data from the same batch of Kevlar composite strands used for the fatigue tests are also plotted in Fig. 2. Clearly, at the same stress level, fatigue loads are much more damaging than static sustained loads to the Kevlar composite.. This means that both cycle frequency and the time under stress affect the lifetime of the simple Kevlar 49 composite.

DISSEMINATION OF INFORMATION TO THE INDUSTRY

We have used several means of disseminating information on composite

TABLE 9. Lamina properties of Kevlar 49/Epoxy C.

	Room Temp.	No of specimens	75oC	No of specimens
Mechanical properties a				
Elastic modulus				
Longitudinal (E_{11}), GPa	79.82 ± 4.73a	8	82.03 ± 4.00a	10
Transverse (E_{22}), GPa	4.79	2	3.168 ± 0.276	11
Shear (G_{12}), GPa	1.77 ± 0.11	4	1.458 ± 0.112	5
Poisson's ratio (ν_{12})	0.393 ± 0.012	8	0.426 ± 0.024	10
Strength				
Longitudinal tension, MPa	1590 ± 79	14	1563 ± 70	23
Transverse tension, MPa	7.395 ± 0.450	10	7.125 ± 0.877	10
Shear, MPa	26.47 ± 0.89	8	27.15 ± 0.61	17

NOTE: The Kevlar 49/Epoxy C is at nominal 65% fiber volume.

a95% confidence limits

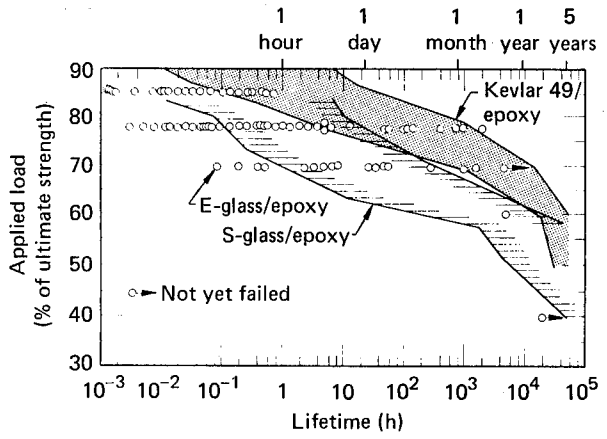

Fig. 3. Comparison of lifetime stress-rupture for composite strands.

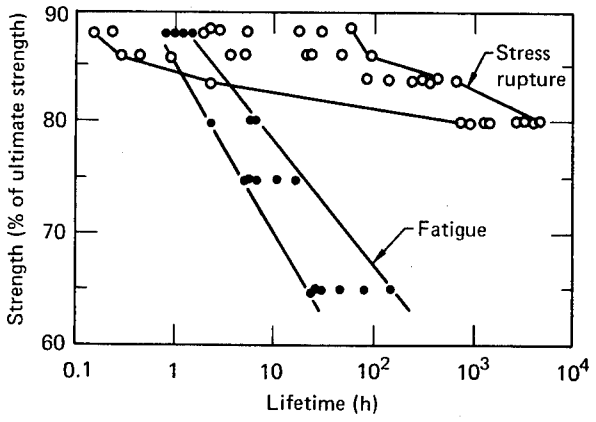

Fig. 4 Stress-rupture and fatigue life of Kevlar 49 composite.

materials to the industry. These include Lawrence Livermore Laboratory reports, published journal articles, and presentations at conferences. Short subjects and timely information have often been reported in Composites Technology Review, which is edited at LLL. Other very effective but informal means include visits to LLL by enginers working in the industry and consultation of LLL personnel to the industry.

FUTURE PLAN

EFFORT ON MATERIALS WILL BE STEADY AND CONTINUOUS

The concept of flywheel energy storage had been rather unattractive until recent years when high-performance composites became available as the baseline materials. Composites, which potentially offer the highest strength to density ratio compared to other materials, will continue to be the key for any significant improvement in energy density of flywheels. We are maintaining a steady effort on materials, because:

- New materials are being introduced continuously, and their potential should be established.
- The requirements for flywheels are sufficiently different than

those for aerospace and commercial applications that a reliable data base on composites for flywheel designs is needed

- Some of the high-performance epoxies being used need to be replaced because of their toxicity. Other well-characterized epoxies are being discontinued because of changing market conditions.

- The technical issues involved, such as fatigue, creep, and stress-rupture are inherently difficult and time consuming to study.

KEY TECHNICAL ISSUES FOR FUTURE EFFORT

In the recent assessment of the materials program, we have identified key technical issues for concerted effort in the future.

(1) Raw Materials

- Epoxies will be the baseline matrix materials. A major effort will concentrate on high-temperature systems (glass temperature of 100° - 150°C). Two kinds of formulations are being considered: a) liquid resins for the wet filament winding process---and b) a single-component fast-cure prepreg system for laminating. The number of formulations will be carefully limited in order to achieve an in-depth evaluation of these resin systems.

- Graphite fibers, and possibly short-fiber reinforced materials, will be examined because of their improved properties and cost attractiveness.

- Ultra-high-strength fibers may be included for a future generation of flywheels.

(2) Engineering Data

- Composite flat panels of 65% ± 2% fiber volume made from the combination of approximately four fibers and four matrix formulations will be characterized for minimum static thermal mechanical properties and dynamic fatigue properties. Tests will be conducted in air at room temperature and at 75°C, and in vacuum at 75°C only.

- For thermal-mechanical properties, test specimens will be 0°, 90°, and ± 45° laminates; for fatigue, we will use only 0° and quasi-isotropic specimens. The material data base will be computerized.

(3) Special Topics

Many important topics such as time dependent behavior of composites and matrix-controlled properties like transverse strength, and interfacial bonding considerations between fiber and matrix, require an understanding of the basic materials behavior. These topics are generally a complex and time-consuming study. Nevertheless, they are critical in controlling the long-term performance of the composite flywheel and the mode of failure in certain designs.

For these studies, we use simple specimens and limit the work to a minimum number of materials. Work on fatigue, stress rupture, and creep of composites is continuing, we plan to start a program on the transverse properties of composites.

INTERACTION WITH INDUSTRY

We plan to strengthen ties with the industry by:

- Continuing to solicit industry needs and problems associated with composite materials.

- Offering consulting services in the broad area of composites.

References

1. T. T. Chiao, and R. L. Moore, "A Room-Temperature-Curable Epoxy for Advanced Fiber Composites," in Proc. 29th Ann. Conf., SPI Reinforced Plastics/Composites Inst., Washington, D. C. Section 16-B (1974).

2. unpublished data Lawrence Livermore Laboratory, Livermore, Calif. ( ).

3. T. T. Chiao, E. S. Jessop and H. A. Newey, SAMPE Qu. 6, (1), (1974).

4. J. A. Rinde, E. T. Mones, R. L. Moore, and H. A. Newey, "An Epoxy Resin-Elastomer System For Filament Winding," in Proc. 34th Ann. Conf., Reinforced Plastics/Composites Inst., New Orleans, LA, Section 17-A, 1979.

5. J. A. Rinde, H. A. Newey, and I. L. Chiu, "A Cycloaliphatic Epoxy Resin/ Anhydride System Usable Up to 150°C," Compos. Tech. R. 2 (2), (1980).

6. L. S. Penn, "Comparative Properties of Fiber Composites For Energy Storage Flywheels," in Proc. 1977 Flywheel Technology Symp., San Francisco, CA. (1977).

7. L. L. Clements, Fiber Composite Flywheel Program: Filament-Wound Composite Data Sheets, Lawrence Livermore Laboratory, Livermore, Calif., UCID -17874, (1978).

8. L. L. Clements, and T. T. Chiao, "Engineering Design Data For An Organic Fibre/Epoxy Composite," Composites 8, 87 (1977).

9. L. L. Clements, and R.L. Moore, "Composite Properties of An Aramid Fiber in A Room-Temperature-Curable Epoxy Resin Matrix," SAMPE Q. 9, 6 (1977).

10. L. L. Clements, and R.L. Moore, "Composite Properties For S-2 Glass in A Room-Temperature-Curable Epoxy Matrix," SAMPE Q. 10, (2), (1979).

11. L. L. Clements, and R.L. Moore, "Composite Properties For E-Glass Fibre in a Room-Temperature-Curable Epoxy Matrix," Composites 9, 93 (1978).

12. H. T. Hahn, private communication (March 18, 1980).

13. T. T. Chiao, J. K. Lepper, N. W. Heterhington, and R. L. Moore, Compos. Mater. 6, 358 (1972).

14. T. T. Chiao, Hamstad, M. A., and E. S. Jessop, Compos. Mater. 8, pp. 405 (1974).

15. T. T. Chiao, J. E. Wells, R. L. Moore, and M. A. Hamstad, Compos. Materials: Testing and Design (Third Conf.), ASTM STP 546, 1974, pp. 209-224.

16. H. T. Hahn, I. L. Chiu, and Gates, T. L., in Proc. 35th Ann. Conf., SPI Reinforced Plastics/ Composites Inst., 1980, 17-D.

17. R. L., Moore, M.A. Hamstad, and T.T. Chiao, Fukugo Zairyo (Composite Materials and Structures) 3, (1974) 19.

18. T.T. Chiao, C.C. Chiao, and R.J. Sherry, in Fracture Mechanics and Technology, G. C. Sih and C. L. Chow, Eds. (Sijthoff and Noordhoff Int. Publ, City, 1977), pp. 257-269.

19. C.C. Chiao, R. J. Sherry, and N. W. Hetherington, J. Composite Materials 11, 1977, pp. 79-91.

20. J. A. Rinde, Lawrence Livermore Laboratory UCRL Report-83043, July 26, 1979.

21. H. T. Hahn, and T. T. Chiao, "Long-Term Behavior of Composite Materials," to be presented at the 3rd International Conference on Composite Material, Paris, August 25-29, 1980.

22. E. M. Wu, Private Communication, May 1980, LLL report in progress.

Reference to a company or product name does not imply approval or recommendation of the product by the University of California or the U.S. Department of Energy to the exclusion of others that may be suitable.

FLYWHEEL-POWERED SHUTTLE CAR FOR MINE HAULAGE

Tom Zemo
U.S. Department of Energy
Pittsburgh Mining Technology Center
P.O. Box 10940
Pittsburgh, PA 15236

Don Christofferson
FMC Corporation
Engineered Systems Division
328 Brokaw Road
Santa Clara, CA 95052

ABSTRACT

The practicality of utilizing the flywheel energy storage device to propel shuttle cars in underground coal mining has been studied in the Department of Energy contract, "Evaluation of a Flywheel-Powered Shuttle Car."[1] This study, funded by the Department of Energy and conducted by the General Electric Company, concluded that the shuttle car is a feasible application for a flywheel from technical, economic, and safety standpoints. It was also concluded that a viable system can be constructed, capable of charging the flywheel car in the underground coal mine environment, in times that are compatible with current and future face haulage cycle time constraints. A follow-on contract has been awarded to FMC Corporation, Engineered Systems Division, Santa Clara, California. Under this contract, a flywheel of optimum shape and size and the best concepts of a flywheel on a vehicle with spin-up and power transmission systems will be specified, designed, fabricated, and tested. The flywheel package will be installed in a standard FMC shuttle car which will be tested aboveground and later in an underground coal mine to demonstrate the practical application of this concept. The contract is presently in the design phase. Work to date and future plans for project completion will be discussed, along with the detailed conclusions and requirements generated by the GE study.

INTRODUCTION

With the growing awareness and concern for safety, coupled with the desire to increase productivity in underground mines, FMC Corporation, Engineered Systems Division, has teamed with Rockwell International, Canoga Park, California, under Department of Energy contract to design, develop, and demonstrate a practical flywheel energy storage system for a shuttle car.

The shuttle car (Fig. 1) is a vehicle on rubber tires used in underground mines to transport material from a mining machine (Fig. 2) to a haulage system. About 85 percent of the coal in U.S. underground mines is now transported by various types of shuttle cars from the continuous miner at the working face (Fig. 3) to a secondary haulage system, usually a conveyor belt. More than 70 percent of these units are electric powered and use a trailing cable from the reel on the shuttle car to a stationary tie-off point to transmit power to the vehicle.[2] There are close to 7,000 of these vehicles in use today. They are compact, low-profile vehicles featuring a relatively high ratio of payload capacity-to-vehicle weight and exhibit good traction, power, and maneuverability. However, the electrical trailing cable imperative to this system presents a major drawback to the machine.

A typical underground mine system is shown in Fig. 3. It shows a four-entry system with the continuous miner operating at one face, and the shuttle car paths to the belt feeder. Each shuttle car has a dedicated haulage route to avoid entangled or damaged cables. A crosscut near the miner is designated as the changeout point. One shuttle car waits at this point until the other car is loaded and out of the way. Lack of available haulage routes and a fixed operating path imposed by the trailing cable are two major restrictions of this system.

Another restriction caused by the cable is travel distance. The cable storage and retrieval system limits travel distance to

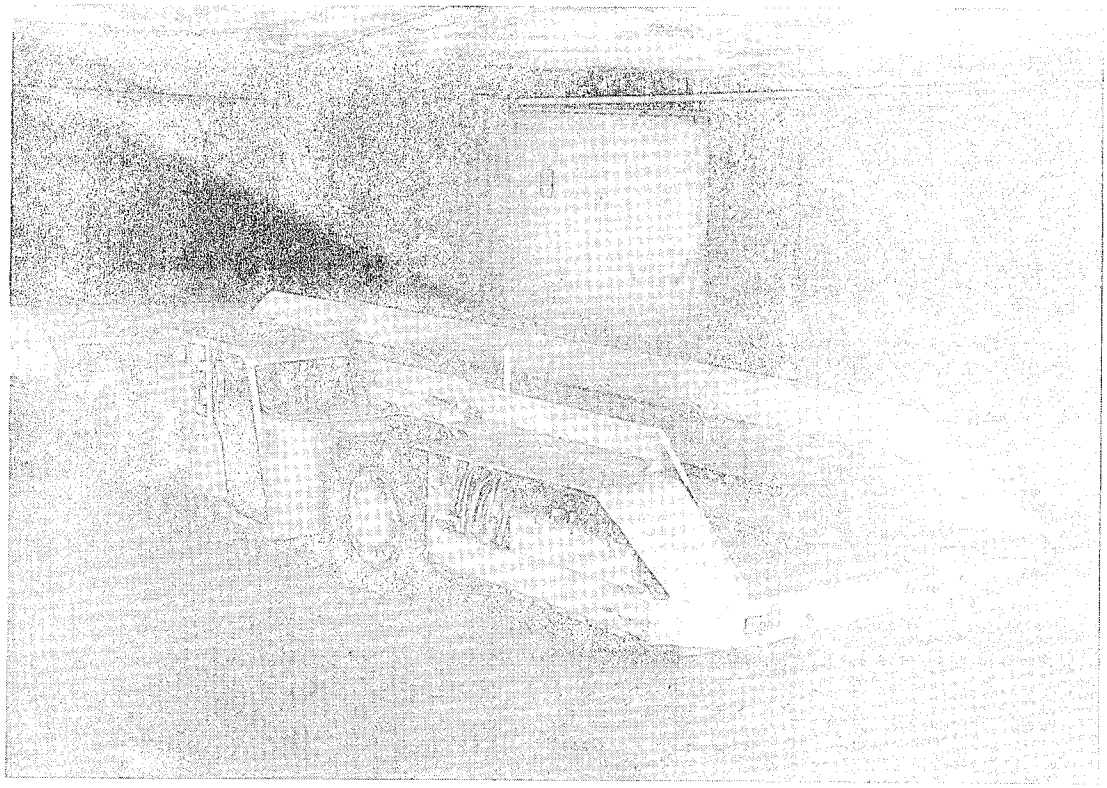

Fig. 1 SHUTTLE CAR

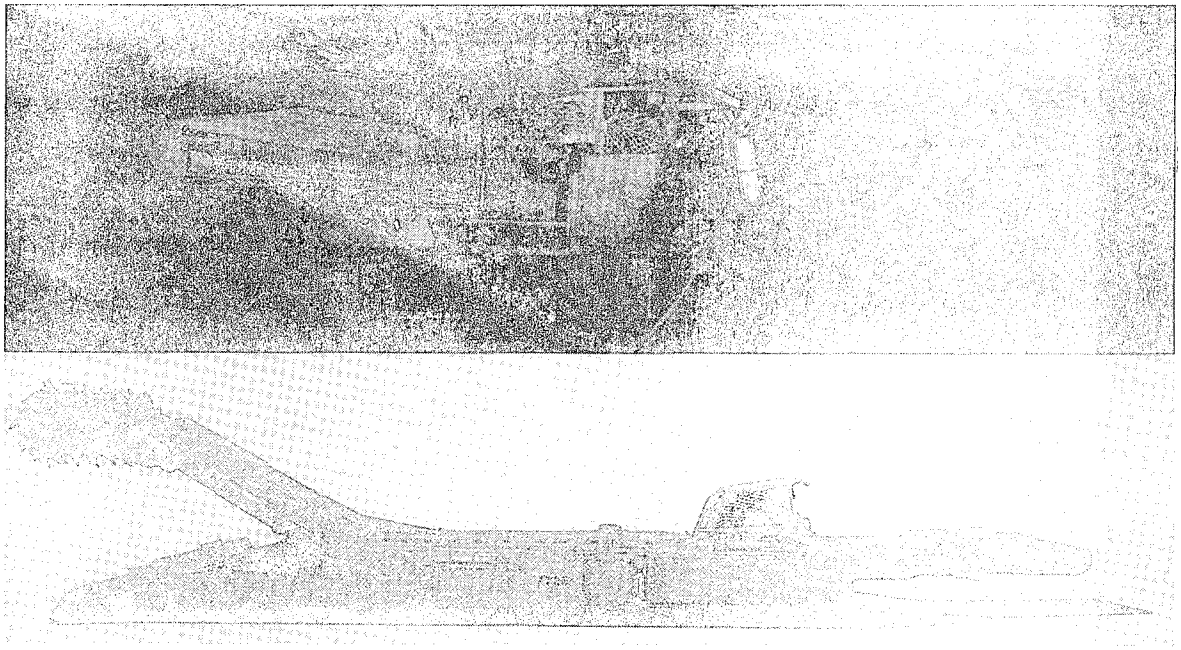

Fig. 2 MINING MACHINE

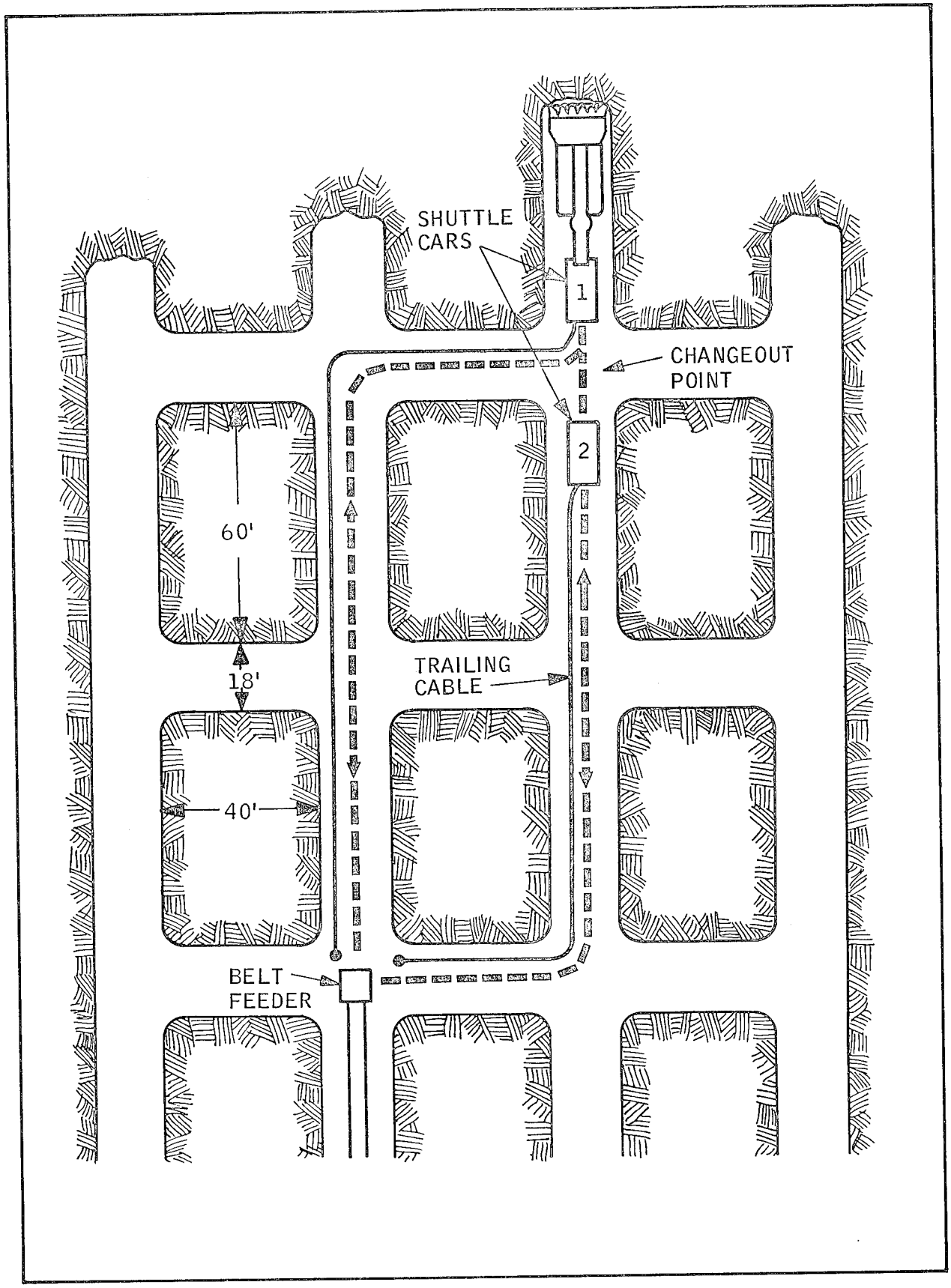

Fig. 3 TYPICAL UNDERGROUND MINE SYSTEM

500 feet, causing frequent production delays to extend the belt haulage system. The General Electric study shows that in moderate mining conditions, productivity can be increased by extending tram distances to as much as 1,100 feet. Of utmost concern is the safety hazard connected with a trailing cable, as it is often a source of electrical accidents and injuries. Other problems are the delays in production caused by frequent maintenance requirements and cable rerouting and handling.

Elimination of the trailing cable restriction with application of a self-contained power source like the flywheel would add immense flexibility to mining operations, enhancing the safety of the miner. Toward this objective, battery and diesel-powered shuttle cars have been developed and used to a limited extent. The primary limitation of the battery-powered car is that the battery energy capacity is often insufficient to propel the car for a full shift when conditions are adverse or the batteries are old. The diesel-powered car has not found general acceptance in U.S. underground coal mines, and no change in this appears to be forthcoming at this time. Development and testing of a low-emission steam engine for underground coal haulage has been conducted under funding by the U.S. Bureau of Mines and Department of Energy, but further development of the engine is needed before an underground demonstration is attempted.

The extensive development activity in flywheel technology offers a more promising alternative for eliminating the trailing cable. Since the flywheel has the ability to absorb energy at a very high rate, a charging station can spin up the flywheel to store energy for one cycle of operation and quickly recharge each time the shuttle car unloads at the conveyor belt.

If a flywheel propulsion system proves practical for shuttle cars, the trailing cable can be eliminated, safety can be enhanced, increased flexibility in routing can be achieved, including longer tram distances, and more shuttle cars can be used on each production section to increase productivity.

GENERAL ELECTRIC COMPANY STUDY

The study conducted by the General Electric Company was concluded August 1978 with the publication of the final technical report.[1] Technical, economic, and safety aspects were considerations in determining the feasibility of utilizing advanced flywheel technology to develop a practical shuttle car propulsion system. These key areas of consideration are discussed below.

TECHNICAL FEASIBILITY

The General Electric study concluded that (a) a steel flywheel should be used, rather than composite, to enhance the probability of a successful near-term demonstration in the mine vehicle, and (b) at least 4.5 kilowatt-hour usable energy storage capacity is needed for the nominal duty cycle. This was based on results of computations using Penn State University's mine simulator with duty cycle conditions that would cover 90 percent of U.S. underground coal mines.

COST EFFECTIVENESS

The productivity and cost effectiveness study indicated that cost per ton and rate of return for the flywheel-powered vehicle system would be superior to the conventional system when used as follows:

- With equal capacities in a two-car system with average charge times of 60 seconds or less
- With equal capacities in a three-car system with average charge times of 90 seconds or less.

SAFETY IMPACT

The very important safety impact study indicated that 50 percent of the 90 to 120 annual electrical accidents and injuries caused by electrical cables in the face area of underground coal mines is attributed to shuttle car cables. Therefore, it was concluded that the introduction of the flywheel-powered shuttle car holds the promise of eliminating at least 45 to 60 electrical accidents and injuries per year in these mines. The fatality data reveal that three out of eight of the cable-related fatalities were due to shuttle car operations and at least two of these were the direct result of splicing activities.

FOLLOW-ON HARDWARE CONTRACT, FMC CORPORATION

After thorough evaluation of results

of the feasibility study, an RFP was prepared, and the contract was awarded to FMC in September 1979. Objectives of this three-phase contract are to (a) specify, design, fabricate, and test a flywheel of optimum shape and size, and a flywheel vehicle with spinup and power transmission systems, (b) install the flywheel in a functional underground coal shuttle car, and (c) conduct aboveground and underground demonstrations of the flywheel-powered shuttle car.

FLYWHEEL POWER PACK

The Rocketdyne Division of Rockwell International, recognized specialists in the analysis, design, fabrication, and testing of both metal and composite rotor flywheels, agrees with the conclusions of the General Electric report that, at the present time, a steel rotor should be used for the flywheel-powered shuttle car feasibility study. Rotors from the Rocketdyne patented, fail-safe 30-kilowatt-hour flywheel, Fig. 4, developed under Army contract, were scaled down to meet the requirements of this program. A modified constant-stress disk is enclosed within a braking ring in which clearances and tolerances are maintained to protect against overspeed or overtemperature. The design permits assembling several rotors without either the potential of undetected flaws caused by welding or the stress-doubling effect of through holes.

FLYWHEEL SYSTEM DESIGN

The baseline design (Fig. 5) consists of an assembly of seven steel rotors with 6 kilowatt-hour total capacity. Power is extracted by a variable-speed constant-voltage DC generator. The rotors are energized by means of an AC motor, a spinup shaft, and a gearbox that applies power through an overrunning clutch. The clutch automatically disconnects the spinup system when the charge motor is de-energized to reduce windage and friction losses.

The flywheel module is a 28-inch-square, 42-inch-long assembly consisting of an outer protective cover (not shown in the diagram) and a cylindrical inner case with end plates and load-bearing subassemblies at each end. A 23-inch-diameter, seven-disk flywheel rotor and braking ring are mounted within the case. To reduce windage losses, the chamber is evacuated to approximately 1mm of mercury absolute (1 TORR). The rotor disks are scaled from the U.S. Army MERADCOM flywheel that was a result of extensive optimization studies.[3] The material used for the flywheel is HP-9-4-30 steel, identified as the optimum

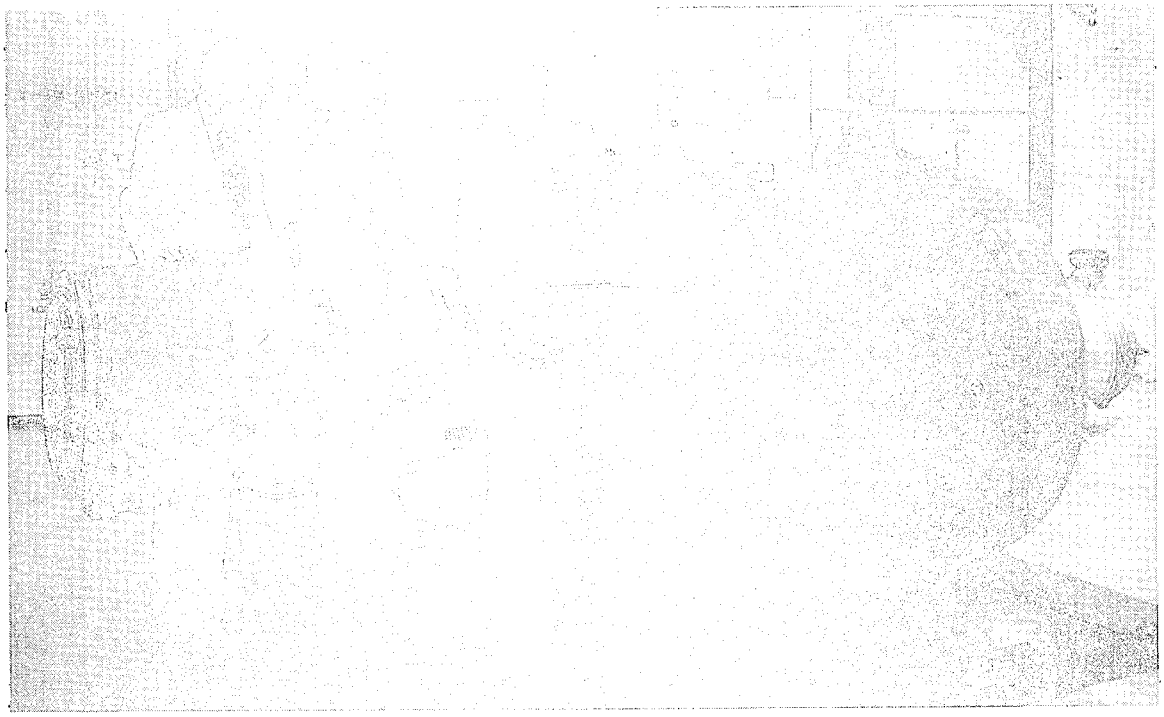

Fig. 4 ROCKETDYNE'S MERADCOM UNIT

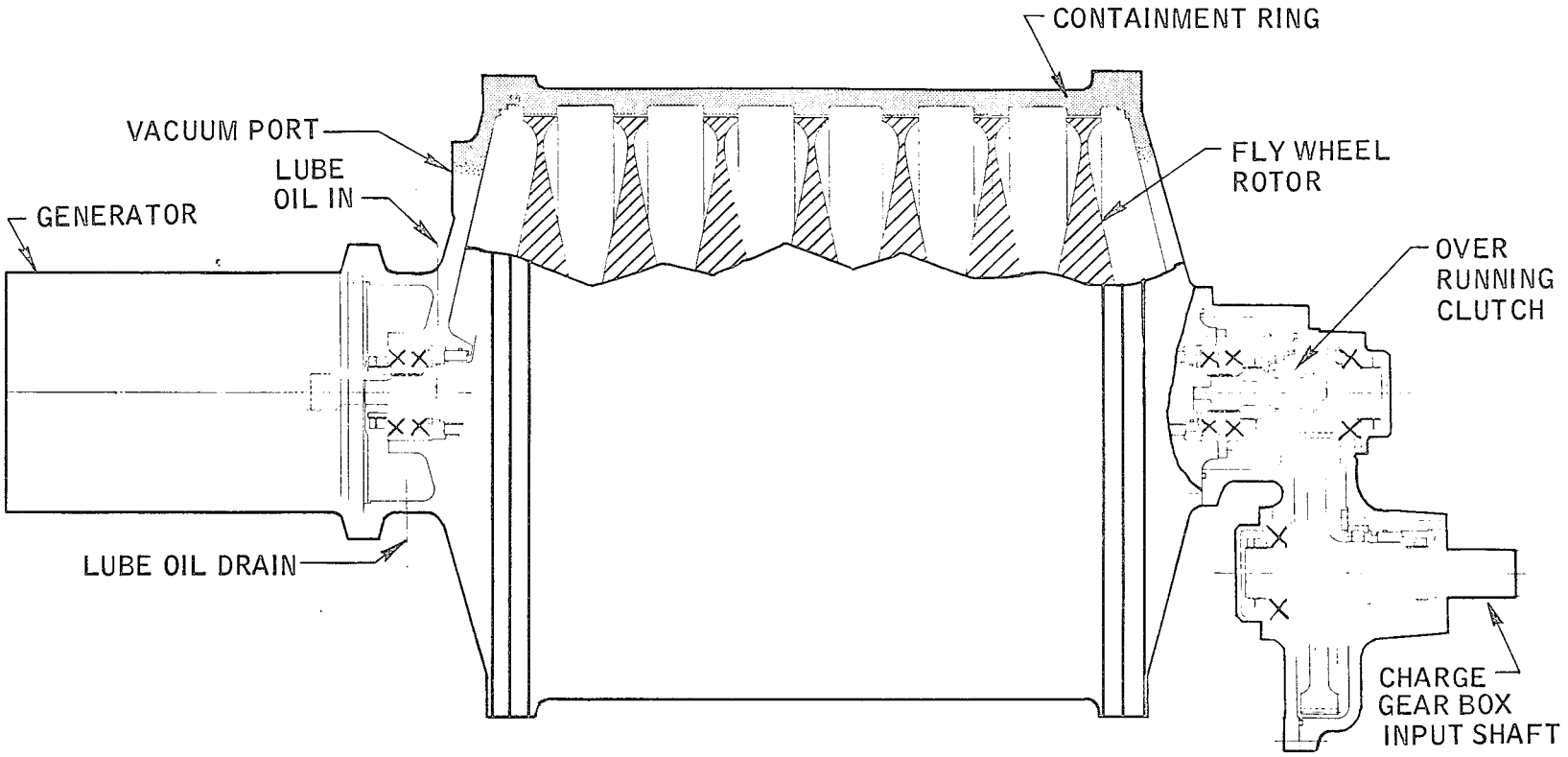

Proprietary Information. Not to be copied, used, or disclosed
without prior written permission from Rockwell International.

isotropic flywheel material because of its high ductility and endurance limit. Maintaining a very conservative fatigue factor of safety of two, the rotor assembly is rated at 6 kilowatt hours at 17,000 rpm and will supply 4.5 kilowatt hours of energy over the speed range of 17,000 to 8,500 rpm. The power transmission system operates with 88- to 90-percent efficiency and over a broad range of required output levels.

The total flywheel package consists of the flywheel module, the gearbox and overrunning clutch, the constant voltage generator, and a system-supporting accessory package. The accessories include a vacuum pump to evacuate the chamber, an air-to-oil heat exchanger, and a self-contained hydraulic system that provides lubrication and cooling fluid and power to drive the vacuum pump and cooling fan. The schematic diagram, Fig. 6, shows the function of the accessory package.

Central to the productivity and economic feasibility of a flywheel-powered shuttle car for use in an underground mine, is the capability to recharge the flywheel in a timely manner consistent with production cycle needs. This requires a power source which can transfer a large amount of energy in a short period of time. At the end of each duty cycle, charging will be accomplished with a mine-permissible 300-horsepower AC motor, returning the flywheel to its high energy condition for the next trip. This procedure can be accomplished during the dumping operation (60 to 90 seconds), eliminating any production delay.

Once the flywheel is energized, a DC-to-DC solid-state control unit on the car interfaces directly with the constant-voltage generator output to provide infinitely variable speed control to the traction motors at high efficiency.

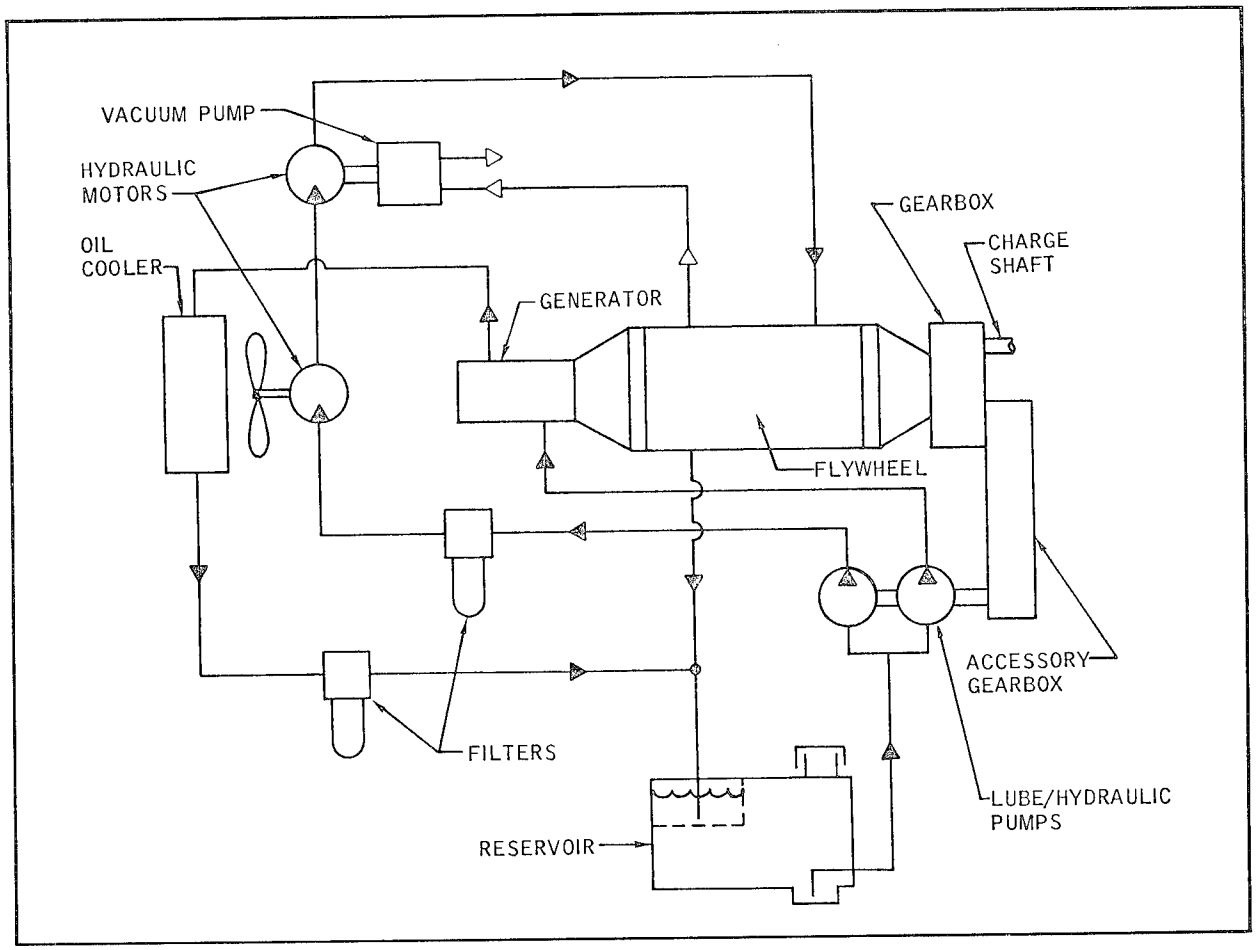

Fig. 6 HYDRAULIC SYSTEM ACCESSORY PACKAGE

GENERAL ARRANGEMENT

The general arrangement of the 6L shuttle car will be modified, Fig. 7, to replace the trailing cable and reel with the flywheel package in an area located opposite the operator's compartment. The low profile configuration of the flywheel power pack will be compatible with a great many types and sizes of equipment.

The charging motor is placed between the wheels in the space previously occupied by the hydraulic system. A revised hydraulic system, smaller because of decreased requirements and higher efficiency, is relocated at the other side of the vehicle.

The overall unit is well balanced and unencumbered by the addition of the flywheel power pack. All components have been placed in locations where they are readily accessible for maintenance or service, an important consideration for use in the confined spaces of an underground coal mine.

MISSION DUTY CYCLE

A major prerequisite for successfully sizing and integrating a flywheel power module into a production shuttle car is determining the energy requirements involved in a typical load-haul-dump cycle. This energy demand will vary with bottom conditions, travel distance, grade, changeout times, and overall cycle time. For this program a duty cycle was specified that is representative of a "near worst case" condition that will operate in over 90 percent of the operating coal mines.

The theoretical energy required to complete one round trip from the belt feeder to the miner and back was calculated by using the assumed duty cycle of 550 feet each way, with a 3-percent grade, going uphill loaded and downhill unloaded. Rolling resistance was assumed to be 200 pounds per ton for a vehicle of 40,000 pounds loaded and 28,000 pounds unloaded. Provision was also made for the estimated energy requirements of the conveyor, hydraulic system, lighting system, lube systems, windage, and losses due to mechanical friction and electrical efficiency.

A schematic of the system power train is shown in Fig. 8. This schematic shows the minimum efficiencies anticipated from each major component in the system and identifies both operational and time-related losses.

Time-related losses include 3,900 watts for flywheel windage friction and accessories, 150 watts for generator windage, 300 watts for lights, and 1,100 watts for the vehicle hydraulic system. This ammounted to a continuous 5.5 kilowatt drain on the system.

Most power-related losses relate to vehicle mobilization. Efficiency of the system from the flywheel output through the alternator, controls, motor, and drive train is estimated to be 60 percent.

In order to define the power requirement associated with each of these losses, a complete shuttle car cycle is described and the times associated with each step are defined. Based on these values and the theoretical power levels required, Table 1 was generated. The shuttle car operating cycle starts at the belt feeder which is also the charging station. The empty car will accelerate to the changeout point, where a 60-second delay is anticipated. (This assumes that the flywheel shuttle car will be tested in conjunction with a trailing cable shuttle car that must clear the changeout point.)

At the belt feeder, a self-aligning contactor connects the power lines to the shuttle car. The operator activates power to the charging motor and belt feeder, then activates the conveyor to discharge the coal into the belt tachometer charge-indicator until fully charged. He then deactivates the power to the charge motor, disconnects the power source, and returns the empty shuttle car to the face to begin the cycle again.

It is calculated that the trip described will take 333 seconds, and the total flywheel energy required is 3.25 kilowatt hours. The flywheel will have an estimated 1.29 kilowatt hours of usable energy remaining at the end of the cycle, for unscheduled delays and problems.

Based on the results of this analysis, a 6-kilowatt-hour flywheel, which has 4.5 kilowatt hours of usable energy, should be sufficient to satisfy the specified conditions.

SUMMARY

With these calculations in mind, the flywheel system was developed for the

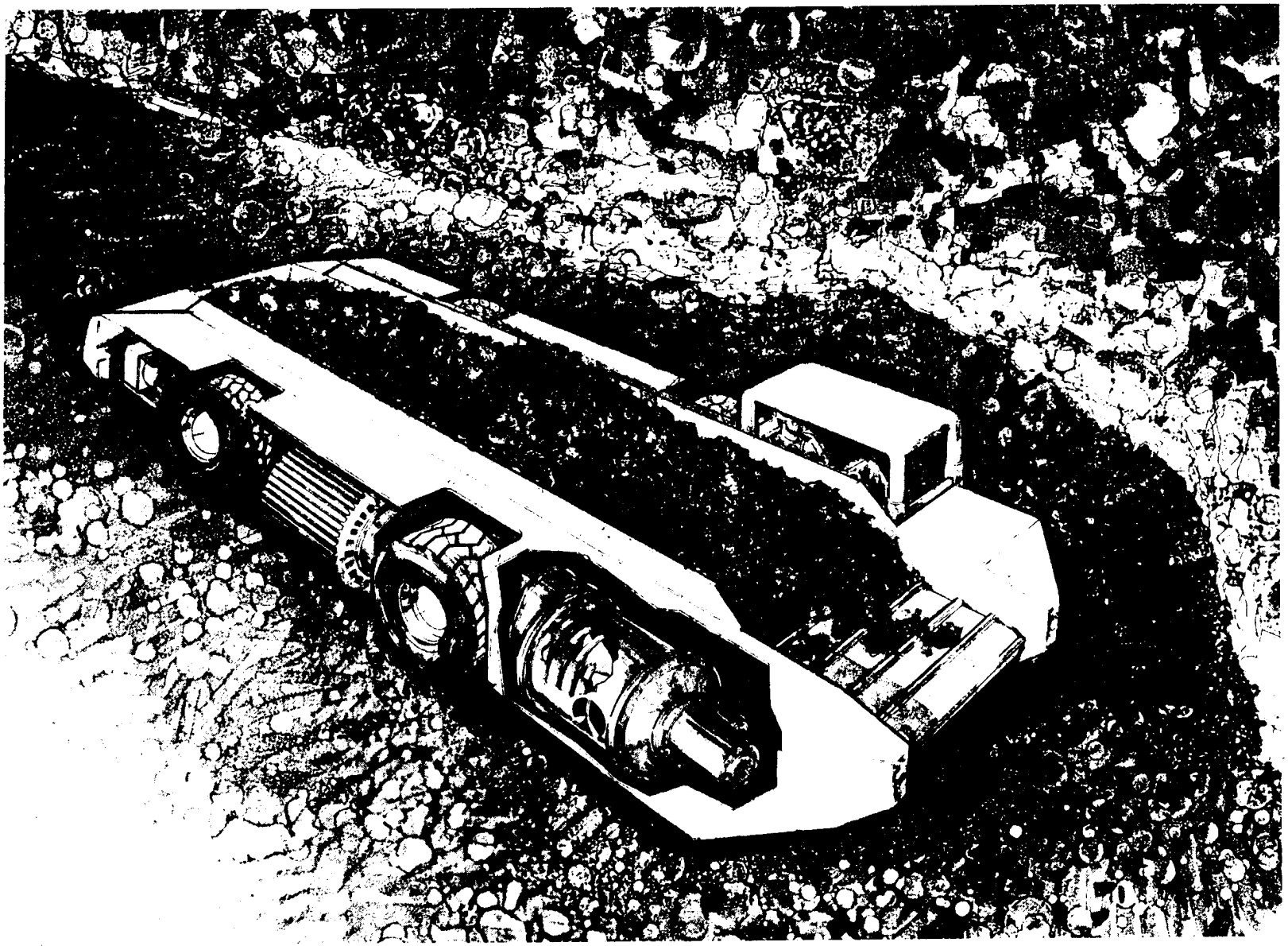

Fig. 7 FLYWHEEL-POWERED SHUTTLE CAR, ARTIST'S CONCEPT

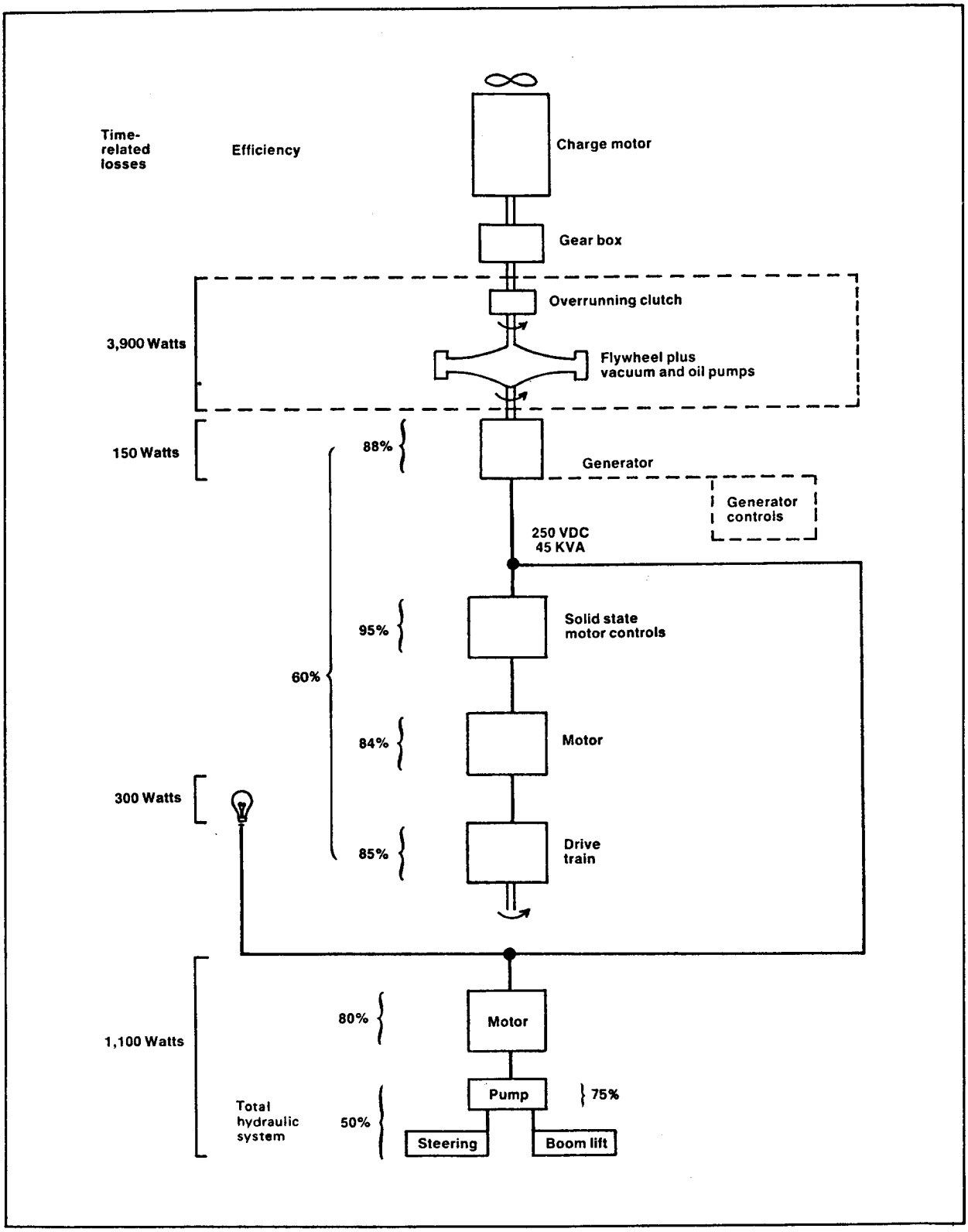

Fig. 8 POWER TRAIN SYSTEM

Table 1 MISSION DUTY CYCLE

	Time, seconds	Cumulative time, seconds	Energy, kilowatt-hours	Cumulative energy, kilowatt-hours	Remaining usable energy, kilowatt-hours	Power level, kilowatts
Accelerate to 4.2 mph	2	2	0.02	0.02	4.48	32.3
Tram to changeout station (350 feet)	55	57	0.4	0.43	4.07	27.2
One 90-degree turn (8 seconds)	—	—	0.01	0.44	4.06	6.2
Decelerate to stop	2	59	—	—	—	—
Wait at changeout	60	119	—	—	—	—
Accelerate to 4.2 mph	2	121	0.02	0.46	4.04	32.3
Tram at 4.2 mph to miner (200 feet)	31	152	0.23	0.69	3.81	27.2
Two 90-degree turns	—	—	0.03	0.72	3.78	6.2 each
Decelerate to stop	2	154	—	—	—	—
Load coal, four-second bursts	60	214	0.02	0.74	3.76	18.6 each
Accelerate to 3.5 mph	1.67	216	0.04	0.77	3.73	75.5
Tram at 3.5 mph to unloading station (550 feet)	105	321	1.76	2.53	1.97	60.3
Three 90-degree turns (8 seconds)	—	—	0.04	2.57	1.79	6.2 each
Decelerate to stop	2	323	—	—	—	—
Connect power	10	333	—	—	—	—
Parasitic loss	333	—	0.36	3.07	1.43	3.9
Lights (300 watts)	333	—	0.03	3.09	1.41	0.3
Generator windage loss	333	—	0.01	3.11	1.39	0.2
Hydraulic system loss	333	—	0.10	3.21	1.29	1.1
Total		333	3.25		1.29	

shuttle car. It is a completely integrated power delivery package sized to fit within a 28- by 28-inch cross-section compartment of the FMC Model 6L shuttle car. It is designed to deliver 4.5 kilowatt hours of usable energy. The power system consists of a flywheel energy storage module, clutch, gearbox, charging motor, lube oil reservoirs, and various accessory valves, filters, and sensors.

The flywheel concept offers compactness and the necessary high energy-per-unit volume required for integration with the shuttle car. The particular advantages are listed below:

- Elimination of Trailing Cable
  The flywheel shuttle car is freed of a tethered cable and the associated production and safety problems posed by a damaged cable. Mobility is improved because the haulage route is not predetermined by power center location and cable routing. High cable-maintenance costs are also eliminated.

- High Charge and Discharge Rate
  The flywheel has the capability of storing energy at high-input power levels and of releasing the energy as the load demands at virtually any rate the output drive system can accept. Conventional lead-acid batteries are limited to a discharge rate of about 15 watts per pound and require several hours for recharging.

- Low Emissions
  The flywheel represents a safe, nonpolluting alternative to diesel power.

- Long Cycle Life
  A flywheel-power storage system can be designed to have a minimum life which is higher than the expected life of the vehicle.

FMC believes the demonstration will confirm the flywheel-powered shuttle car's capability to operate within the cycle expected of a cable-powered or battery-powered shuttle car.

The concept has generated considerable interest in the mining industry as a viable means to eliminate haulage and safety problems associated with shuttle car trailing cables. The potential of arriving at an efficient alternative to conventional systems has been established with this program to design and develop a flywheel-powered shuttle car.

REFERENCES

1. General Electric Company. 1978. Evaluation of a Flywheel-Powered Shuttle Car, Final Technical Report. U.S. Department of Energy Contract #ET-77-C-01-8890, U.S. Department of Energy.

2. U.S. Department of Energy. Coal, Bituminous and Lignite. Energy Data Report.

3. Davis, Dr. D., D. Hodson, and C. Heise. Rocketdyne's High Energy-Storage Flywheel Module for the U.S. Army. Presented at the 1977 Flywheel Technology Symposium, San Francisco Bay Area, California.

"Permission to present and publish Fig. 5 was provided by Robert M. Sperry, Patent Counsel for Rockwell International in a letter to T. Barlow dated July 17, 1980".

FLYWHEEL DELIVERS PRECISE 60 Hz OVER WIDE SPEED RANGE

Richard T. Morash
Richard Morash & Associates
P.O. Box 1243, Anna Maria, Fl. 33501

ABSTRACT

This paper describes one of the first commercial applications of the Roesel Generator. It is a flywheel energy storage system which delivers exactly 60 Hz to critical applications such as computers. A number of the units have been operating for over two years in a variety of installations. These are on-line in customer facilities. They all serve the same basic function -- which is, to continue to deliver correct power to a computer even when the prime power source is erratic or temporarily interrupted. The Roesel Generator is a variable-speed constant-frequency generator. Through the means of instantaneous or continuous remagnitization of the rotor field poles, it provides exactly the correct number of poles at any instant to accommodate the speed and hold the output frequency constant. A 900 pound flywheel, 15 inches diameter and 3 feet long is actually the rotating portion of the generator and the inner periphery is a layer of "permanent" magnets. Rotation is normally 3580 rpm, driven by a 2 pole induction motor. Speed varies with load, but frequency is a constant 60 Hz. When power to the motor is interrupted, flywheel energy continues to deliver generated power from the machine to the load. Speed can drop to 3050 rpm before the machine is unable to deliver full load at the rated voltage. There is no change in output frequency beyond the accuracy of the crystal oscillator frequency source. Present units in service deliver 7 1/2 KVA for 10 to 25 seconds after input power is interrupted. Larger designs are anticipated for the future. Two units running in parallel deliver 15 KVA at one installation, and since they are controlled by a single crystal, speed differences do not affect the operation. Other installations have unique problems with erratic power. The discussion shows how these have been solved by use of the flywheel generator. Also discussed is how the system delivers constant frequency over speed ranges of 2:1 and 4:1.

INTRODUCTION

The matter of transferring energy from a flywheel to an output device has always been an interesting problem. This paper shows an application of a combination flywheel and Roesel Generator which produces a constant frequency output over a wide speed range. Roesel Generators were developed and manufactured and sold commercially by Roesel Laboratories in Bradenton, Florida, since 1973. Flywheel generators were first sold in 1978.

HOW THE ROESEL GENERATOR WORKS

A block diagram of the Roesel Generator is shown in figure 1. The stator frame is similar to that of a conventional inverted construction generator, with the addition of an exciter, or write "head". The rotor is the outside shell and can be designed with flywheel characteristics, for energy storage. It is constructed of high permeability steel lined by a layer of magnetizable material on its inside periphery.

The electronic section consists of a voltage regulator and a standard oscillator/exciter circuit. The oscillator synchronizes a low power inverter which drives an exciter coil and capacitor in a resonant circuit. This exciter power is typically less than 5% of the power produced in the generator.

The Exciter Head induces a series of alternating polarity (North and South) field poles on the rotor magnetizable material. These field poles couple to the Stator Windings for the generation of output power. As the flywheel speed varies, the length of the field poles vary. However, as the speed varies the number of poles induced per unit time

is constant. Hence the frequency of the output power remains constant.

FREQUENCY CONTROL

Output frequency does not require feedback or speed control. The exact frequency of the oscillator is the only input which determines output frequency. With a quartz crystal output remains within 0.02% at nominal value, whether it be 50, 60 or 400 Hertz. More accurate oscillators are available if desired.

No matter what speed the flywheel-rotor turns output frequency is constant. As the flywheel speed changes it has no effect on the frequency because it has no effect on the poles per second on the rotor.

VOLTAGE REGULATION

The pole writing technique also provides a simple and effective means for voltage regulation. It is easy to control the magnitude of the writing process and thus the output voltage. This provides a simple reliable voltage regulating loop. Precise voltage regulation is achieved from the inherent characteristics of the generator augmented by an electronic regulator controlling the current in the exciter coil. Voltage regulation is typically better than $\pm 5\%$ and the sine wave contains less than 5% total harmonic distortion under all load conditions within specifications.

FLYWHEEL ENERGY STORAGE

The fact that high quality power can be generated with variable shaft speed opens the door to flywheel energy storage for electric power. A flywheel stores energy by virtue of its inertia. Once it is spinning at its rated speed, the only energy required to keep the speed is to supply the Generator Load, Excitation, Heat Losses, Windage and Friction. The energy of acceleration is stored in the rotating mass, and can be recovered when the mass slows down.

Conventional Generators change frequency as RPM drops. However, the Roesel Generator-flywheel allows the speed to drop considerably while it continues to deliver precise 60 Hertz.

UNINTERRUPTIBLE POWER SYSTEM (UPS)

The flywheel-generator is of particular importance to users of critical equipment such as computers, process control equipment, etc. The flywheel-generator is designed to provide as much energy as needed to maintain critical load power. In a motor-generator set, utility power feeds the induction motor which drives the generator-flywheel. The generator provides 100% isolated power to the load (such as a computer). When utility power is interrupted, the flywheel delivers its energy, without interruption, to the system. The generator slows down, but frequency and voltage remains precisely within specification. If utility power is restored within a few seconds (which is true in 95% to 98% of cases), the flywheel accelerates to operating speed, without output interruption and the system stays on line.

If the utility power remains off, there is sufficient flywheel energy to allow time to bring up auxilliary engine-generators, or to allow orderly shutdown of the computer or other load.

AN ON-LINE SYSTEM

One of the first commercial applications of the Roesel generator is as a flywheel energy storage uninterruptible power system (UPS) for critical loads such as computers. Present units in the field deliver 7 1/2 kilo-volt-amperes (KVA), for 10 to 25 seconds after loss of input power. This design is depicted in Figures 2, 3 and 4. Figure 2 shows the cutaway assembly with the principal operating components. Figure 3 shows the stationary (internal) generator components, and Figure 4 shows the rotating components which are in reality the flywheel.

The basic flywheel assembly is 36 inches long and 15.5 inches outside diameter. It weighs 900 pounds and delivers 7 1/2 KVA power output (plus losses) for at least 10 seconds while speed changes from about 3580 rpm to 3150 rpm. Energy storage is increased to 25 seconds by affixing an additional cylinder (1" thick) to the OD, yielding a 17.5 inch OD.

FIELD INSTALLATION RESULTS

Small generators were delivered to customers and have operated continuously since 1973. These are frequency converter units, which have 60 Hz input and 400 Hz output. They produce 1 or 3 KVA, and were not designed for flywheel energy storage.

The 7 1/2 KVA flywheel generators were installed in customer facilities, starting in March 1978. Several units will be described for the type of use to which they have been subjected; commonly, all are for keeping computers on-line when power problems occur.

BROWARD COUNTY, FLORIDA, DEPT. OF TRANSPORTATION

A computer in the Fort Lauderdale Traffic Engineering Division controls traffic systems throughout the City. The manufacturer of the computer had experienced outages caused by power line fluctuations in other installations, and specified an uninterruptible power system (UPS) for the application. Power consumption is about 6 KVA, single phase. The Roesel Flywheel Generator is free standing in a storage area just outside the Computer Room. Figure 5 shows a photograph. The unit operates on-line continuously. A few minor electronic problems and bearing noise in the starter motor were the only problems encountered in 2 years.

The problems were corrected on site within a few days of being reported. Computer downs due to power failures are minimal. If power input is out for more than 10 seconds, the system shuts down. This has only happened about 4 or 5 times since installation.

MONTGOMERY WARD, ORLANDO, FLORIDA

A central processor in Montgomery Ward's Orlando facility receives data transmitted continuously from all stores in the Southeast States. If the Central Processor goes down, on line information is lost, and a large staff of people is idled. Orlando is in an area where line transients are frequent. A power interruption normally shuts down the system which requires 15 minutes to power up again. Therefore, UPS is necessary.

Two flywheel generators operate in parallel to provide 15 KVA to the system, (3 phase, 208/120). They are installed in a paper Storage Room next to the computer. Batteries were impractical due to lack of space and the requirements of hydrogen venting in this office building. There have been a few problems, as could be anticipated with a new development, but they were minor and fixed on site. The ones of interest to flywheel design are redesign of the mechanical coupling, and the necessity to isolate vibrations in the building structure.

The original drive design was a hard coupling between the motor and generator shaft. Design tolerances were held very tightly, and the shaft design provided a long cantilever to provide sufficient flexibility to smooth out any small misalignment. One unit was apparently out of tolerance, resulting in imperceptible relative motion at the key and generator shaft. The motion resulted in fretting corrosion at the key after 10 months of operation. The permanent solution was to add a bearing to the generator shaft, next to the coupling, and use a standard flexible coupling to accommodate misalignment. This is being up-graded in the units in production.

The units are vertically mounted, and hard rubber mounts suspend the rotating unit within a steel sleeve. Dynamic balancing generally provides such smooth running at 3600 rpm that vibration is not a problem. However, in the Montgomery Ward installation, the building was designed as a lightweight office structure, with a 4 inch floor slab. Half inch anchor bolts tie the unit to this floor.

The floor with its reinforcing rods, acted as an amplifier for the nominal vibration that did transmit to it. Since a staff of CRT operators was sitting at desks within 15 feet of the unit, the vibrations were noticable. The solution was to provide rubber mounting pads between the generator housing and the concrete floor.

The customer in this installation is very satisfied with the units. They operate 24 hours/day, either 6 or 7 days per week,

depending on workload. They have data to show such a remarkable improvement in up-time on the computers that payback was very short.

THE ESTEE CORPORATION, PARSIPPANY, NEW JERSEY

This factory in New Jersey has a computer installation which shut-down frequently because of voltage dips when heavy machinery was starting or operating in the facility. Inventory and Accounting Departments were constantly interrupted by computer outages. Installation of the flywheel-generator solved the problem. It is placed in a corner of a warehouse area, outside the Computer Room.

This unit operates 8 hours a day, 5 days a week. It is started up every morning, and shut off every night. After about 16 months of operation, a key between the starter motor and main drive motor sheared. On-site repair was accomplished in a few hours. New units do not use this drive key design. The customer is very happy with his installation, and computer power downs due to electrical power are no longer a problem.

U.S. NAVY

A small shipboard installation with a computer on board was having continuous problems with erratic power from an engine-generator. This is natural with these type units, but the computer needs very steady power. Use of the flywheel generator provides precise 60 Hz within the operating range of the engine generator.

The customer is satisfied with this unit, but there is not very much information about its use characteristics. The information we received during the first month it was operated is that the system performed well for their application and, for the first time in the program (which was several years along) they could operate a normal mission. Prior to putting the flywheel in use, whenever they wanted to use the computer, almost all other electrical devices on board needed to be shut-down, and a crew was required to stand-by the engine to monitor the governor.

A GEOPHYSICAL APPLICATION

In Caracus, Venezuela, utility power is subject to much more variation than most U.S. cities. A computer to process geological data was attempted to be put into service, but power interruptions made the use nearly impossible. A 25 second, 7 1/2 KVA flywheel generator was shipped, completely assembled and ready to operate. After several installation delays, (which are apparently normal in this area) the unit was finally put on line. It is installed in a shed at ground level and power is wired directly to the computer on the 10th floor. The 25 second flywheel provides enough energy to keep the computer operating through most of the power dips, and the computer is operating satisfactorily.

SPEED RANGES POSSIBLE

The frequency of a Roesel generator is constant from almost zero speed to any practical upper limit of rotating machinery. However, there are design parameters to be considered in any device, and this machine is no exception.

Some of the practical limitations on speed are discussed in a paper, reference 1. This discusses the concepts of agreement speed, synchronous speeds, magnetics and voltage regulation, among other things.

Output voltage is a function of field strength and generator shaft speed. The magnetic materials we currently use restrict the field strength control to a limited range. To achieve voltage regulation of $\pm 2\%$ (400 Hz) or $\pm 5\%$ (60 Hz) using a single set of stack windings, the speed must stay within about $\pm 30\%$ of a nominal value. Thus, for a 2 pole machine driven by an induction motor at 3580 rpm, good voltage regulation can be maintained down to about 2700 rpm and is a speed range more than adequate for UPS applications.

In addition, providing a cost effective machine requires practical size for the main drive motor. This motor is used to drive the generator at full load, and while delivering this full load after a power interruption it must accelerate the flywheel to 3580 rpm. To meet this

requirement, the motor we use has a speed torque curve which limits our operation to a low speed of about 3000 rpm. In the UPS application, not much stored energy is sacrificed for this compromise, as the stored energy is proportional to the square of the speed.

There are potential applications for the Roesel machine that would require a speed range greater than that which is satisfactory for the UPS design. In the straight-forward design, it is believed that a practical (economical) limit is about 2:1 speed variation. This is accomplished by proper use of different magnetics and winding designs. There are also design variations which will allow as much as 4:1 speed range for special applications. Optimization studies are required for any designs to determine cost-effectiveness of integrated systems.

CONCLUSION

Flywheels operating in conjunction with the Roesel Variable-Speed, Constant-Frequency Generator provide precise 60 Hz over a wide speed range.

Units have been operating continuously in commercial sites for more than 2 years with flywheel energy storage. The basic generators (without flywheel utilization) have been operating for more than 6 years.

Although the commercial applications have been for frequency converters and uninterruptible power systems until now, future systems will be the key to cogeneration in small installations, using flywheels to store peak energy requirements and to store energy from alternative sources, such as windmills.

The UPS machines were designed for cost effective operation at a speed range of 3600 down to 3000 or 2700 rpm. Ranges of 2:1 or 4:1 are practical for design if applications show them to be cost effective.

Numerous flywheel applications are available and with a practical means now proven to allow them to deliver precise a.c. power over wide speed ranges, they should become commercially acceptable.

ABOUT THE AUTHOR

The author is a professional engineer, member ASME and ASHRAE. He is one of the 5 man Roesel Laboratory team which developed the generator in Bradenton, Florida. He participated in installations and field engineering and evaluation.

REFERENCE

1. Ott, Barber and Roesel, "The Roesel Generator, A Unique VSCF Generator", IEEE Applied Magnetics Workshop, Marquette University, June 1975.

ACKNOWLEDGEMENTS

The author appreciates permission from Roesel Laboratory, Montgomery-Ward, The Estee Corporation and Broward County Department of Transportation to use information cited in this paper.

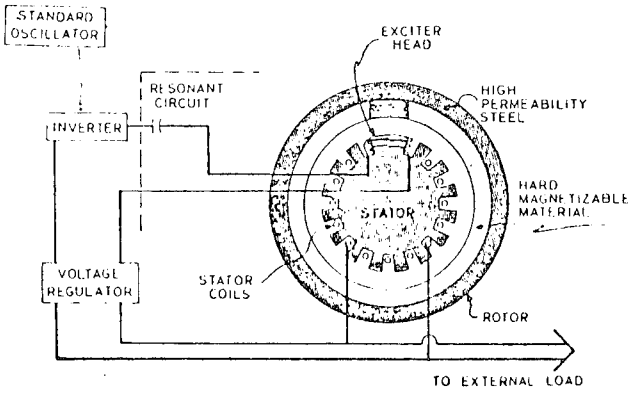

GENERATOR BLOCK DIAGRAM
FIGURE 1

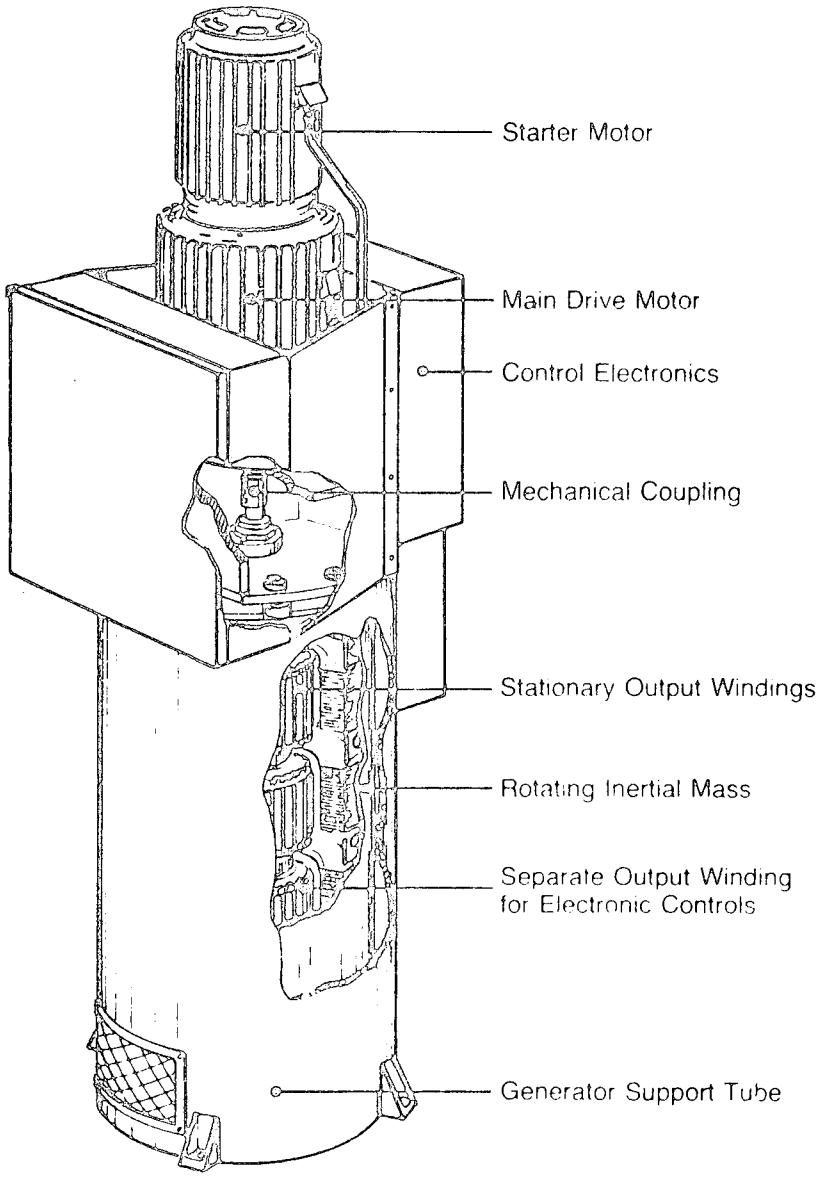

7-60 NON-INTERRUPTIVE POWER SYSTEM
7.5 KVA 10 SECOND 60 HZ
MECHANICAL ASSEMBLY

FIGURE 2

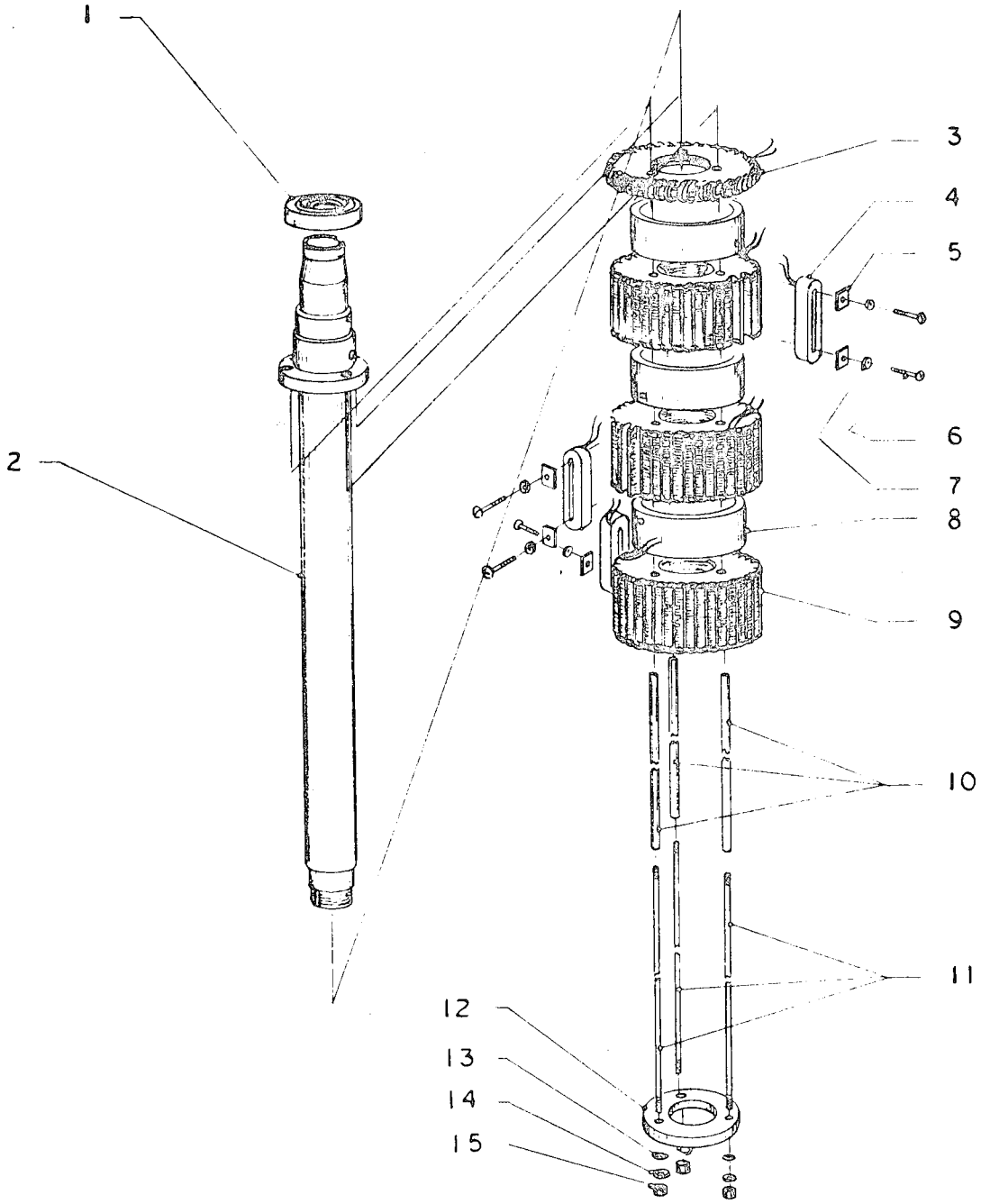

STATOR ASSEMBLY

FIGURE 3

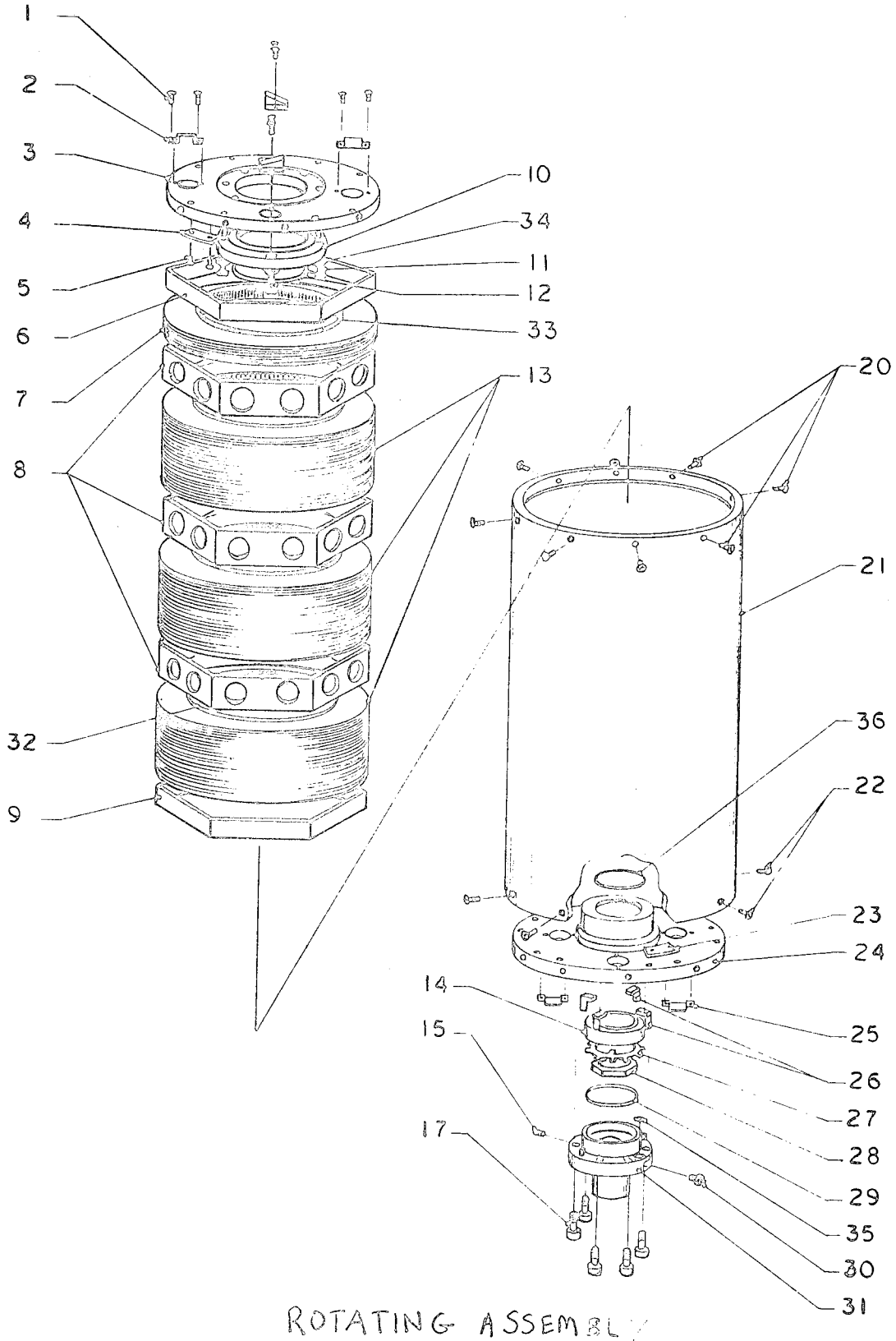

ROTATING ASSEMBLY

FIGURE 4

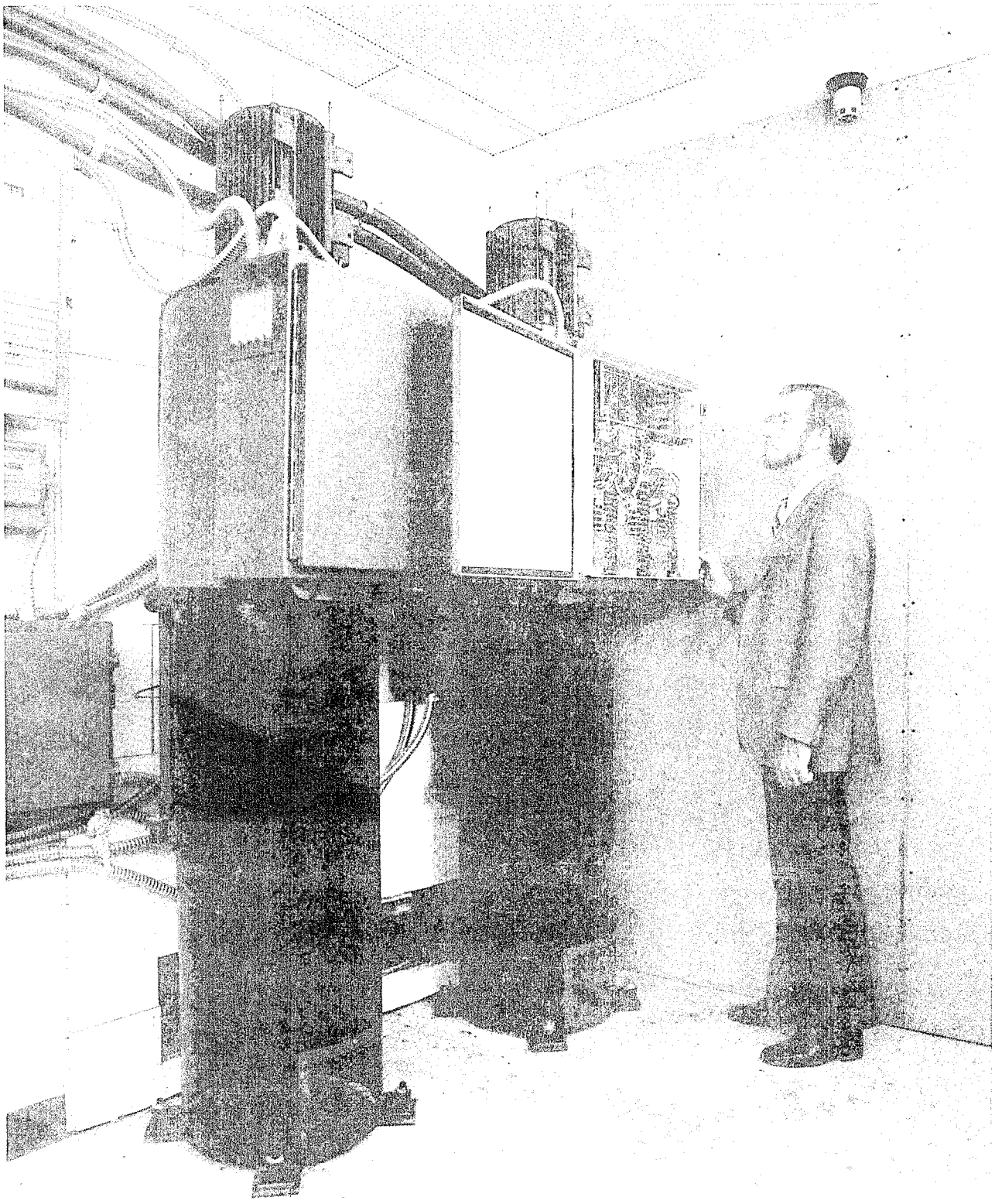

Figure -5-
Roesel Flywheel-Generators; Installed at Montgomery-Ward, Orlando. Two Units Operate in Parallel, Deliver 15 KVA for 10 Second Power-Outs.

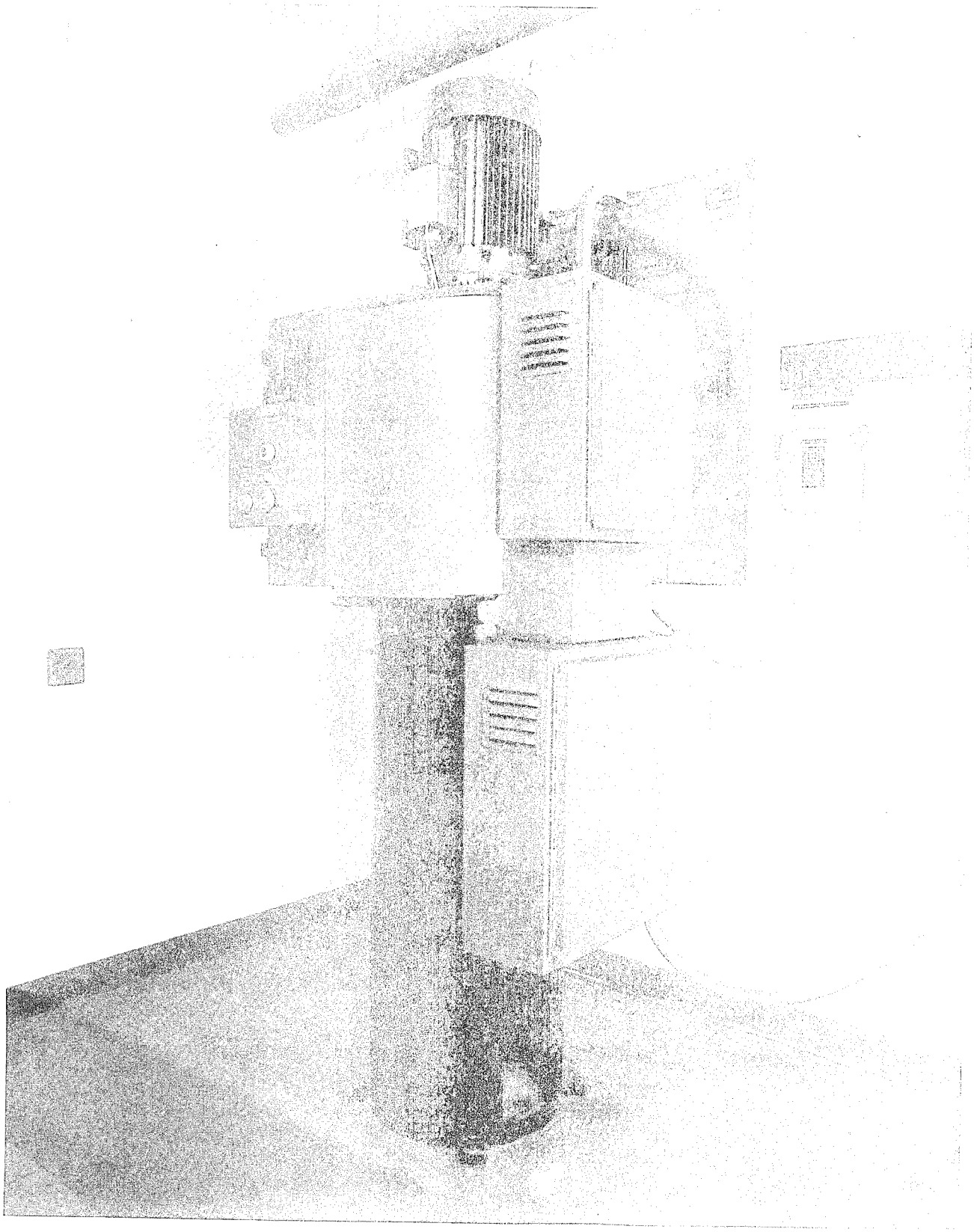

7 1/2 KVA Flywheel/Generator, 10 Sec. Energy Storage Installed at Broward County, FL., Dept. of Transportation.

FLYWHEEL ENERGY STORAGE SYSTEMS OPERATING ON MAGNETIC BEARINGS

Pierre C. POUBEAU

Société Nationale Industrielle Aerospatiale

B.P. 2

78130 - Les Mureaux - France

ABSTRACT

The lecture describes the technical progress in the field of magnetic bearing flywheels. Initially, this work was oriented towards flywheels for satellite attitude control without friction and without wear at the level of the bearings.After the successful development of medium and high speed magnetic bearing flywheels for satellites, the concept of these systems was applied to the development of flywheels utilized as back-up energy sources. This industrial development was initiated at the energy and power level of 1 kilowatt-hour, 3 kilowatts with a steel rotor for providing back-up energy in telephone centers and is being extended in the range of energy and power with a next step at 10 kilowatt.hours - 10 kilowatts with a composite rotor. The key points of these systems are described here.

INTRODUCTION

Flywheels have played a significant role in human activities.Throughout history,such systems which were unearthed are probably about 4000 years old. In the industrial age, flywheels were associated practically to each steam or internal combustion engine. In the recent times,the main part of the satellites which had to be accuretaly oriented in space in a three axes stabilized concept were equiped with one or several flywheels utilizing the gyroscopic stiffness,or action reaction torques which appear between rotor and stator when the rotor is accelerated or decelerated, or both gyroscopic stiffness and torques.

With the increase of satellite pointing accuracy and life-time, the operation of ball-bearings became a difficult problem concerning wear, friction and stiction torques, life-time and reliability. This problem led to the development of a magnetic suspension flywheel concept which presents some specific aspects compared to other systems and which will be described in its main lines since the key aspects were presented and described in some details at the 1977 Flywheel Technology Symposium. Consequently, the emphasis will be on the application of the satellite magnetic bearing flywheel concept to the kinetic storage system for ground applications.

GENERAL CONCEPT OF THE FLYWHEELS

This concept initially developed for satellite flywheels is presented on Fig. 1, and comprises several subsystems : the centering magnetic suspension, the motor-generator, the rotor.

CONCEPTS OF THE MAGNETIC BEARINGS

For the fixed kinetic energy storage systems, the magnetic bearings which are now mature,in the one active axis concept described here,with a great simplicity and a high reliability will take an important place. For a general understanding of the problem, it is useful to review different concepts utilized for magnetic bearings.

During the last ten years several types of rotor magnetic suspensions were developed according to the following principles concerning the position control and the angular control of the rotor along the different degrees of freedom except the rotation axis. The main ones are the following :

- the "five active axes" concept : the position of the rotor is maintained by five servoloops controlled by five position sensors

- the "two active axes" concept : the axial position of the rotor and its angular position along axes orthogonal to the rotation axis and passing through the gravity center are controlled passively by magnet rings face to face on rotor and stator ; the possible radial excursions of the rotor are controlled by two servoloops operating in two orthogonal directions and controlled by two position sensors
- the "one active axis" magnetic suspensions ; in this concept the rotor axis is aligned along the stator axis by magnetic rings placed at the two ends of the rotor and facing magnetic rings on the stator ; two modes of operation were utilized till now : the magnetic rings provide the position control of the rotor along two axes of freedom and its angular control along two axes of freedom. One servoloop is necessary to control the axial rotor position with or without position sensor.

Another type of magnetic suspension has to be mentioned for its scientific interest : the suspension by eddy currents. However it cannot be utilized in the near term because it involves a wide amount of dissipated power assuming that it is not utilized in cryogenic conditions. The magnetic suspension which is described here is based on the "one active axis" concept with attractively operated magnetic rings.

RADIAL AND AXIAL MAGNETIC CENTERING

The radial centering of the rotor is performed by pairs of magnetic rings equiped with permanent magnets. The rings are placed at the two extremities of the rotor and stator ; one ring on the rotor faces one ring on the stator. In such conditions, statically, the axis passing through the centers of the upper and lower rings of the rotor is constrained to remain aligned with the axis passing through the centers of the corresponding rings placed on the stator. For a flywheel which has to operate in no gravity as a satellite flywheel the axial forces created by the upper and lower rings have to be in opposition.

In gravity, such a system has an axial position of equilibrium slightly different from the equilibrium position in no gravity. For equipment which has to operate only under gravity, the axial forces created by the upper and lower bearings are in the same direction, opposite to the gravity force on the rotor. The equilibrium position is determined from the gap at which the axial magnetic forces of the magnetic rings are equal and opposite to the weight of the rotor.
This equilibrium position is unstable. A servoloop stablizes the position by utilizing as input signal the axial rate of the rotor delivered by an electro-magnetic sensor and a signal proportional to the current in an axial actuator which is a double biased electromagnet.

The particularities of this magnetic suspension are :
- the magnetic centering rings are separated from the axial actuator
- the axial servoloop is operated from the signal of an axial rate sensor without any position sensor. The lift-off operation is provided by a logic electronics without any position reference.

MOTOR

The motor is an ironless brushless DC motor-generator. It has high efficiency and does not introduce any negative radial stiffness. In the motor configuration, the electronic commutation is performed either by an electro-optical device or by an electromagnetic sensor.

TOUCH DOWN BEARINGS

When the axial suspension of the magnetic bearings is not activated the rotor goes down (or up) to a "touch-down" ball bearings which is dry lubricated. In case of an anormal operation of the system these ball bearings allow operation down to zero speed preventing any contact between rotor and stator parts.

ROTORS

For light and small satelliteflywheel rotors, a special technique called clyclo-profile was utilized. Cycloprofile is directly issued from the fabrication of composite wound pressure-vessels for satellite launchers. For energy storage application another type of rotor is utilized ; the subcircular rotor it was introduced about ten years ago for ultracentrifuge applications and was tested in a flywheel configuration in 1973 and 1974. It operates according to the following picture. (Fig.1)

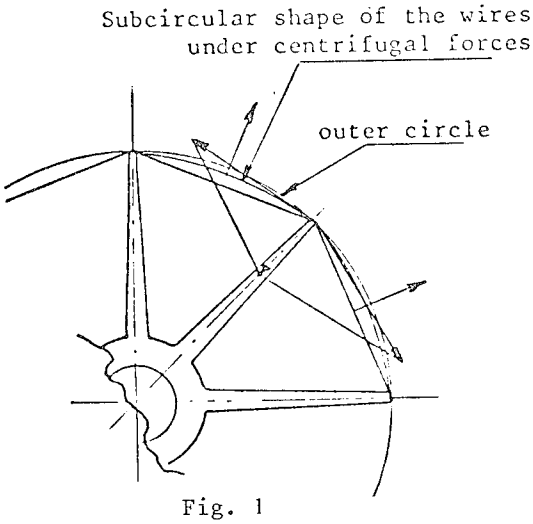

Fig. 1

The filamentary material constituting the rim is placed on several spokes along a polygonal shape or along a shape which is between the polygone and the circle defined by the extremities of the spokes. Under the elongation due to centrifugal forces the rim elongates but remains subcircular. Consequently, the resulting forces applied from the rim to the spokes are compressive forces.

THE KEY POINTS IN ENERGY STORAGE FLYWHEELS

It is well known now that the break-through of flywheels as industrial energy storage systems is correlated to the utilization of composite materials incor-porating high performance fiber such as glass or polyamide fiber.

The amount of kinetic energy stored by mass unit is proportional to the ratio $\frac{\sigma}{\rho}$, σ is the stress at which the compo-site operates, ρ is the specific mass of the composite. This ratio $\frac{\sigma}{\rho}$ is several times higher with composites than with metals (steel, titanium, aluminium).
But to store a reasonable amount of energy, the stress has to be sufficiently high and the elongation of the rim is much higher than the elongations to which engineers are accustomed with metals.
An exemple :
In a thin rim of glass fiber composite rotating at a peripheral speed of 700m/sec the specific kinetic energy storage will be in round figure 70 watt-hours per Kg for a stress of 1000 MPa and relative elongation of 2 % for a longitudinal elasticity modulus of 50 000 MPa.
The interest in the subcircular concept appears here because the elongation is "absorbed" mainly by a change in the shape of the rim instead of a diameter increase which would be 2 centimeters for a 1 meter diameter. Nevertheless one other problem arises from this situation : the rotor has to keep the accurate balancing (static and dynamic) through the whole speed range in spite of the fact that non homogeneous composite materials have varia-tions in modulus of elasticity from one point to the other. It is observed that a rotor which was well balanced a 3000 RPM with an accuracy of 10^{-7} meter will present a much larger unbalance when the speed increases. This is a key point of the composite rotors. In addition to this first key point, a second one is as important as the first. The technical compatibility of the balancing has to be achieved with an economical concept .Two aspects have to be taken into consideration :
- the cost of the material
- the cost of the fabrication

Good balancing conditions (materials and technics) are not necessarily those which give economical compatibility. The trade-offs are not easy, but appear possible.

A large part of the development work concerned the concept and design of a composite flywheel. To help solving these problems the magnetic suspension can improve the situation in accepting much higher unbalances than conventional bearings can do.

For example, an unbalance of 10^{-4} meter (i.e. 0.1 mm between the gravity center and the axis of rotation), unacceptable with conventional bearings for high rotation speeds because of radial loads, wear and disspated power, can become acceptable with a magnetic suspension with proper design.

INDUSTRIAL DEVELOPMENT IN PROGRESS

The present development involves two first steps :

- a 1 kilowatt-hour, 3 kilowatts model
- a 10 kilowatt-hours, 10 kilowatts model.

1 KILOWATT-HOUR, 3 KILOWATTS MODEL

This model was developed under a contract from the French Administration : Direction Generale des Telecommunications. Such a model was produced for the back-up supply of small telephone centers. In the event of a break in the distribution of electric power from the utility network it provides the electric power to the telephone circuit for 20 minutes, allowing the starting of an I C E electrogen group. What are the particularities of such model ? It is constituted with :

- a steel rotor operating up to 12000 RPM
- a magnetic suspension of the rotor as described above
- one motor and one generator, electromechanically identical, capable of producing 3 KW of power
- one of the key advantages of the magnetic suspension is that in addition to the absence of wear, the energy losses are very low : no power is needed for the radial centering;5 watts are needed for the operation of the axial servoloop, which stablizes the unstable equilibrium position of the rotor.

10 KILOWATT-HOURS, 10 KILOWATTS MODEL

This model is under development and will benefit from the development of the magnetic suspension of the one kilowatt-hour model. The glass fiber subcircular rim will be able to store 70 watt-hours per kilogram for an useful energy at the output of the generator of 50 watt-hours per kilogram taking into account the depth of discharge, 75 % for a speed ratio of 1 to 0.5, and the generator efficiency 95 %.

This involves a rotor rim between 200 and 250 kilograms according to the processing of the output power, which introduces some additional losses. The magnetic suspension developed for the 1 kilowatt-hour model will be adapted. It will be a small technical step since the 1 kilowatt-hour model has a magnetic suspension for a steel rotor of nearly 400 kilograms, and the rotor of 10 kilowatt-hours with a composite rim will have a mass of the same order of magnitude.

APPLICATIONS

Many applications appear for the kinetic energy storage systems.
For space utilization : kinetic energy storage for satellites.
For ground utilization two general types of applications can be foreseen in a near future for :

- the smoothing of the "soft energy" solar and wind systems
- the back-up power supplies

These two applications will involved more and more demand.

After the development of the 10 kilowatt-hours model the growth capabilities in energy and power will be a matter of advanced design rather than research and development because the key problems will have been solved. Kinetic energy storage of up to 100 kilowatt-hours and later 1 to several megawatt-hours can be envisioned.

It is not unrealistic to foresee the application of flywheel storage to higher level soft energy production (solar, wind and sea) and to large safety systems, such a blocks of buildings or towns.

The introduction into the utility networks can optimize the electrical distribution during peakhour, and give a delay to unload a network when there is danger of total disjunction by overloading. It is possible to eliminate low frequency oscillations on long distribution line by the addition of some local energy sinks.

KEY CHARACTERISTICS OF KINETIC ENERGY STORAGE

Exact level of energy storage is indicated by speed measurement. Energy and power level are independant. The energy is correlated to the flywheel and mainly to its rim ; the charge and discharge power involves the time of charge and the time during which the energy is utilized and are correlated to the motor-generator. It is possible to design a flywheel energy storage system either for high energy and low power or for low energy and high power, or for any other combination.

Concerning reliability and life time, such systems can be designed for twenty years life and, if necessary with redundant electronics.

Insensitive to natural environment, the system can be adapted for low or high temperatures.

Another important feature should be mentioned. One of the basic materials for large fixed flywheels is glass fiber. Glass is produced from sand wich is a raw material abundant everywhere, and the amount of energy necessary to process this raw material is small compared to other materials.

These characteristics added to the fact that flywheel technology is progressing rapidly indicate a large industrial development of flywheel energy storage systems.

REFERENCES AND BIBLIOGRAPHY

1. ERDA 76-GS-UC-94B. Economic and Technical Feasibility Study for Energy Storage Flywheels ; prepared by Rockwell International Space Division.

2. C.J. PENTLICKI and P.C. POUBEAU Magnetic Bearing Momentum Wheel AIAA/CASI 6th Communications Satellite Systems Conference - Montreal, Canada April 1976.

3. P.C. POUBEAU High Speed Flywheels Operating on "One Active Axis" Magnetic Bearings - 1977 Flywheel Technology Symposium - San Francisco, California U.S.A. - October 1977.

4. C.H. HENRIKSON, J. LYMAN and P.A.STUDER - Magnetically Suspended Momentum Wheels for Spacecraft Stabilization - AIAA Conference 1974.

5. D.W.RABENHORST , P.C. POUBEAU and Al- First European Symposium on Flywheels - Neufchatel, Switzerland - Septembre 1976.

6. Lynn S. PENN and Linda L. CLEMENTS - Comparative Properties of Fiber Composite for Energy Storage Flywheels - 1977. Flywheel Technology Symposium - October 1977.

7. D.A. TOWGOOD - An Advanced Vehicular Flywheel System for the ERDA Electric Powered Passenger Vehicle - 1977. Flywheel Technology Symposium - October 1977.

PLATES

Plate 1 - Principle of a magnetic bearing flywheel ("one active axis" concept)

Plate 2 - Magnetic bearing medium speed flywheel developed under European Space Agency Contract (9000 RPM)

Plate 3 - Magnetic bearing high speed flywheel developed under Intelsat contract (24000 RPM)

Plate 4 - Composite rotors - Feasibility models

Plate 5 - 1 KW.H Steel rotor magnetically suspended (mass : 370 Kg)

Plate 6 - Adaptation of a 1 KW.H - 3 KW energy storage system as a back-up power supply

Plate 7 - Overall view of a 1 KW.H - 3 KW energy storage system

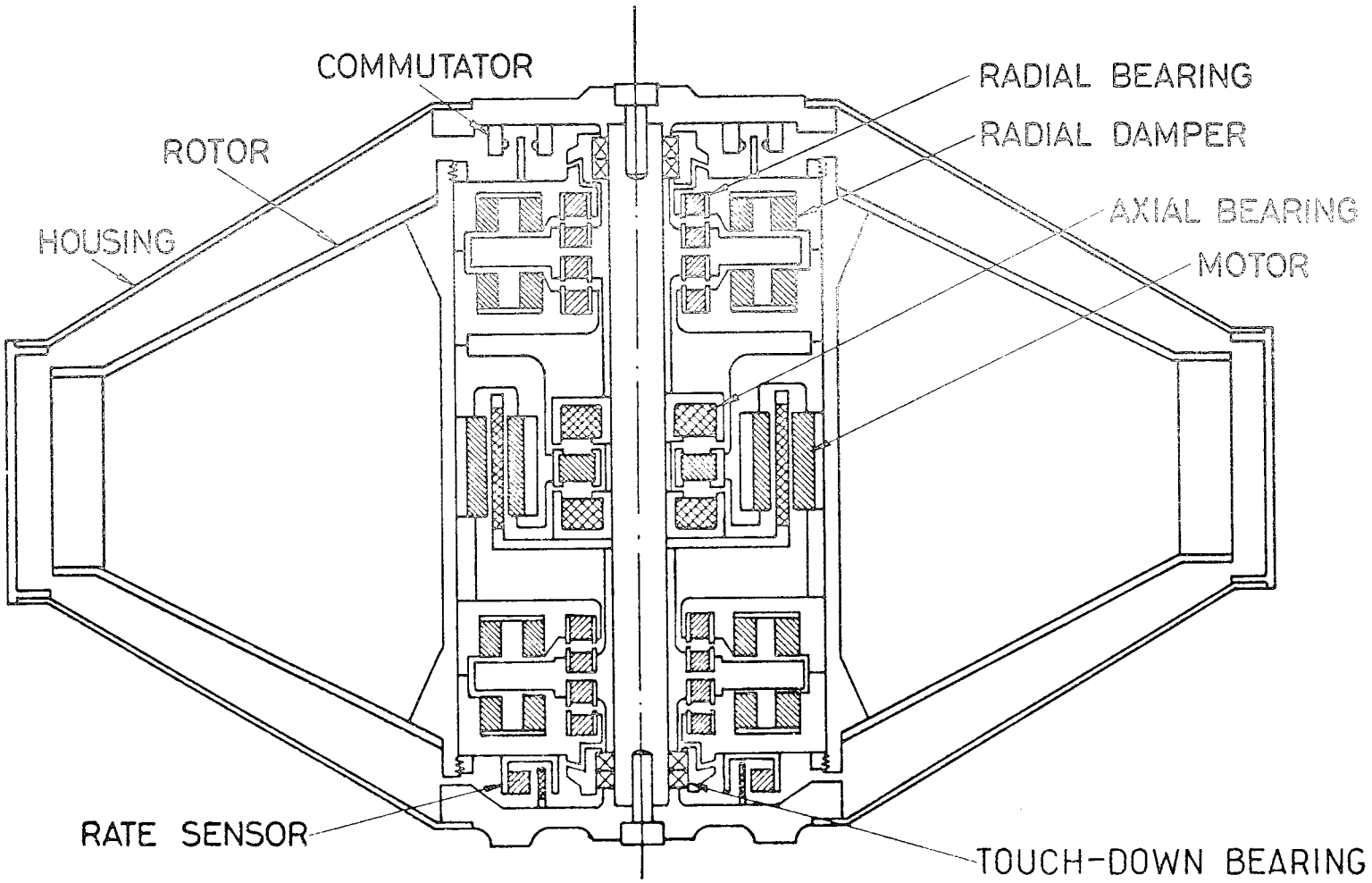

MAGNETIC BEARING MOMENTUM WHEEL

PLATE I

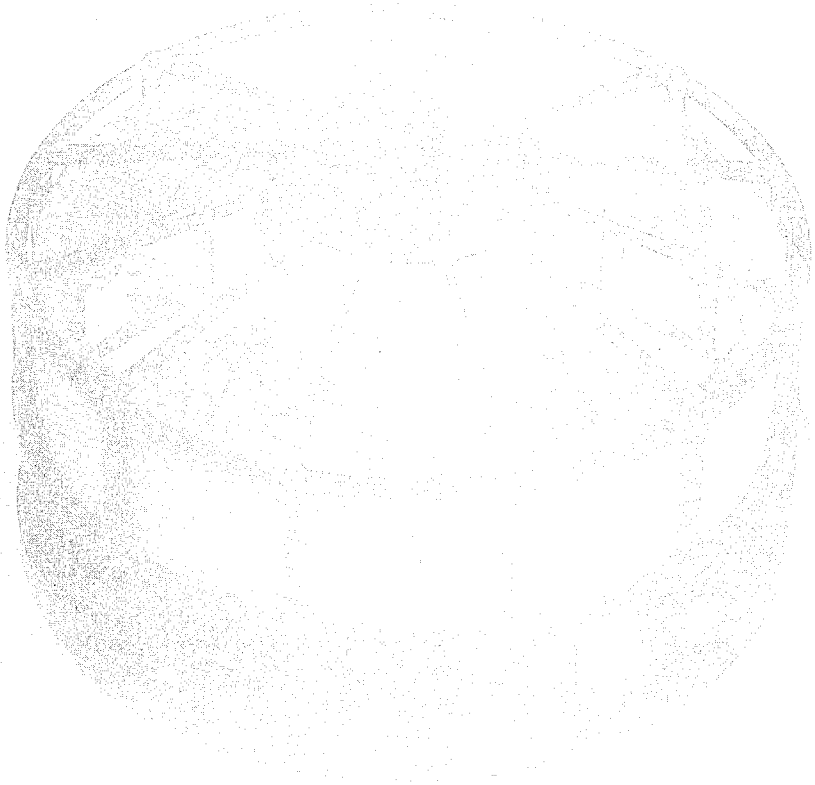

Magnetic bearing medium speed flywheel

PLATE II

I-AXE MAGNETICALLY SUSPENDED MOMENTUM WHEEL

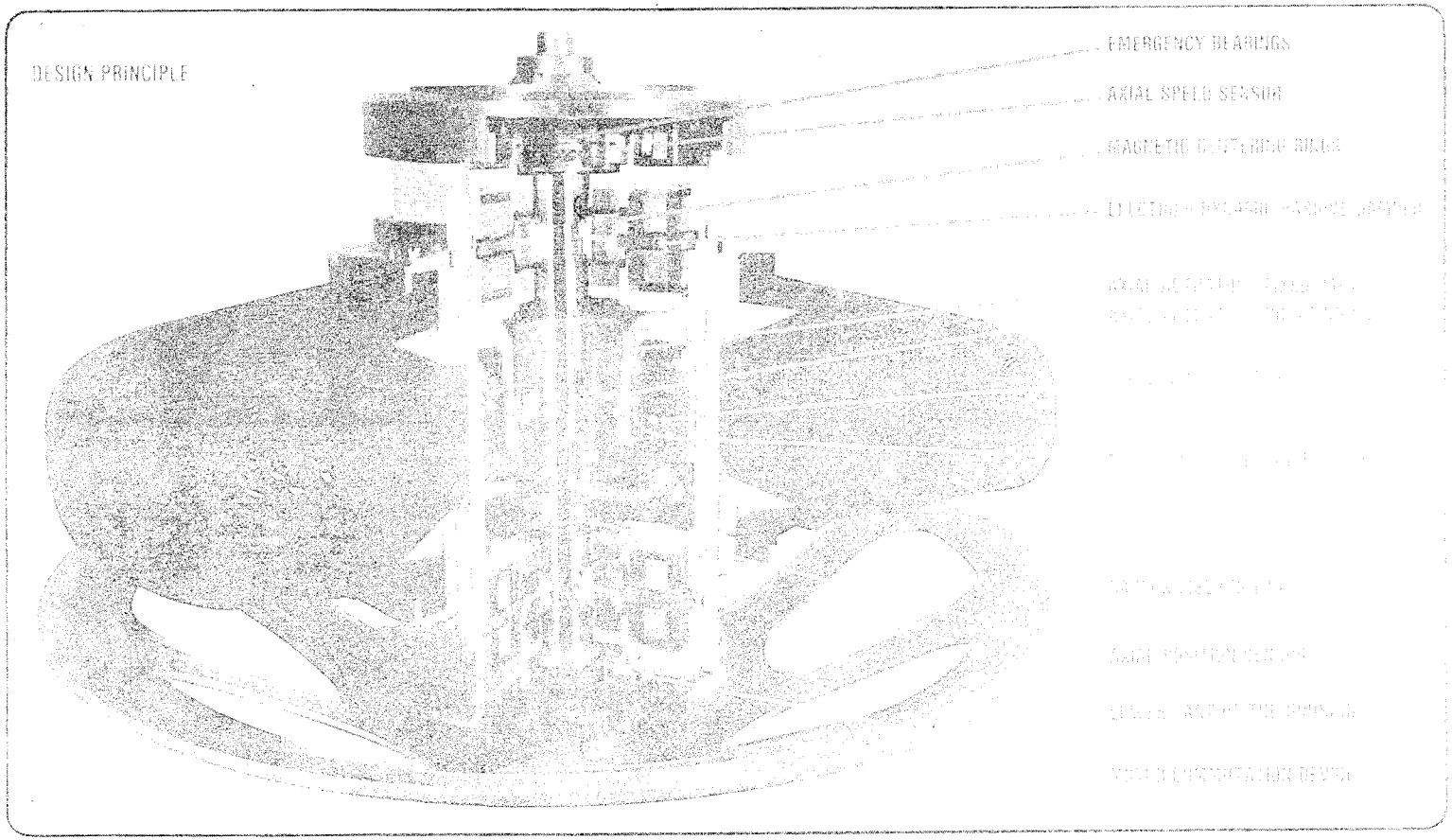

Magnetic bearing high speed flywheel (24.000 RPM)

PLATE III

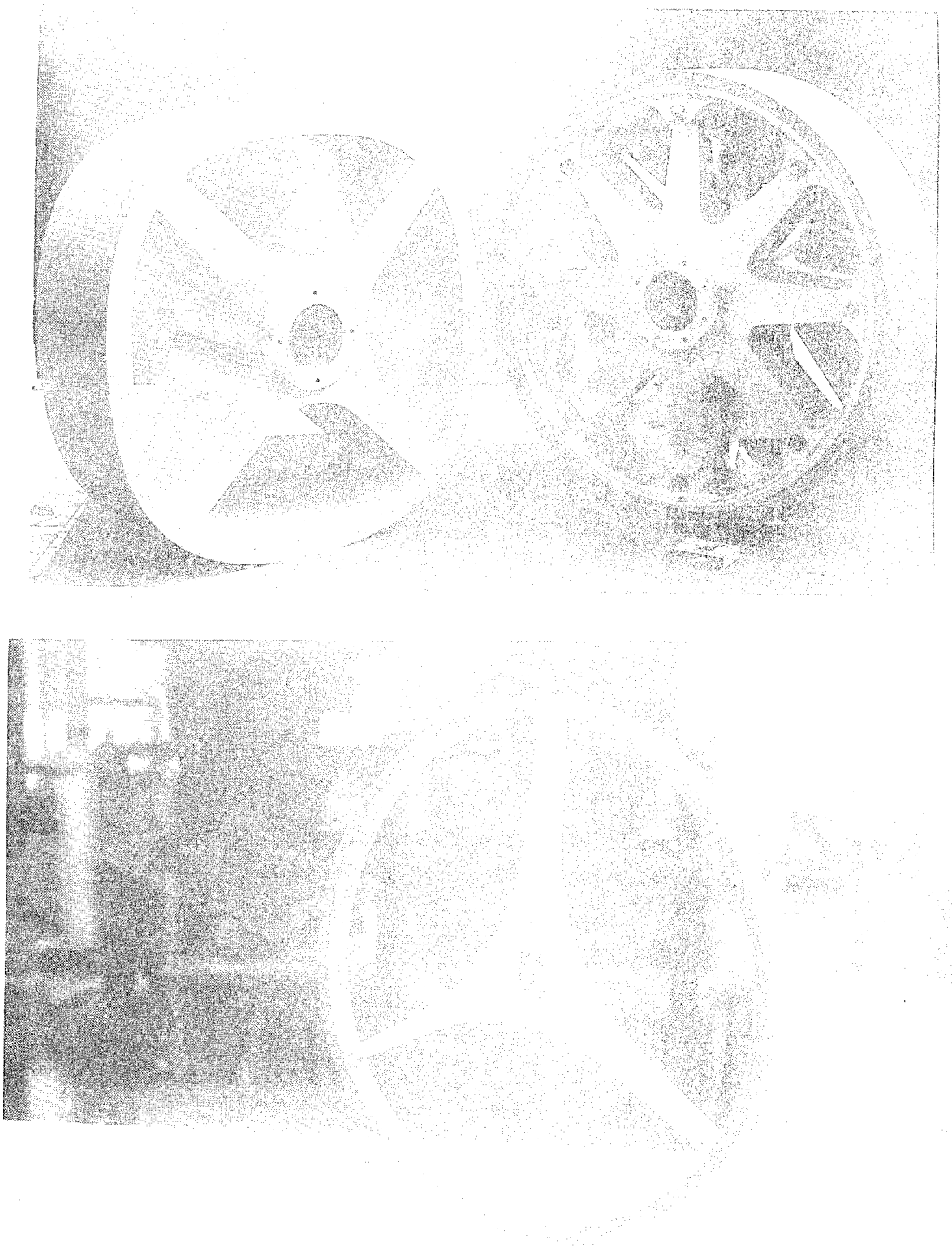

Composite rotors - Feasibility models

PLATE IV

1 KW.H Steel rotor, magnetically suspended

PLATE V

Ground energy storage flywheels 1 kWh/3 kW

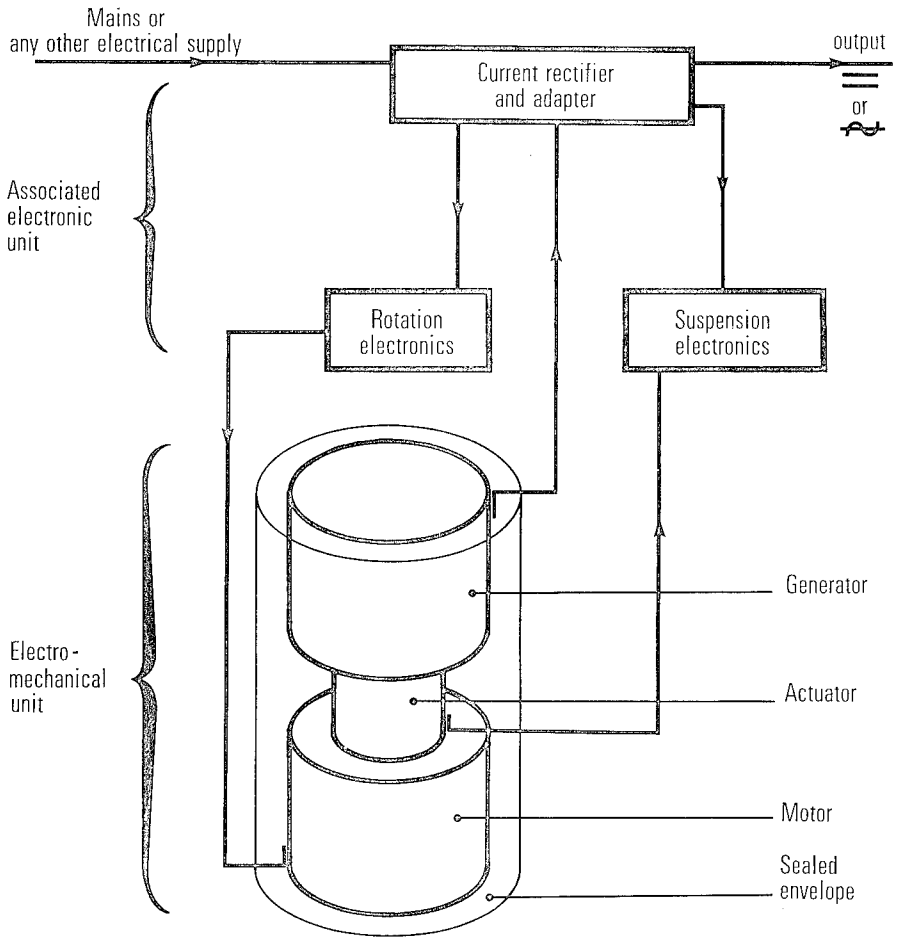

Functional bloch diagram

The energy storage flywheel readily replaces the electrical power supply whenever inoperative (voltage variations or supply failure).
The system stores energy under the form of kinetic energy with a very high efficiency, during mains normal operation.

Adaptation of a 1 KW.H - 3 KW energy storage system as a back-up power supply

PLATE VI

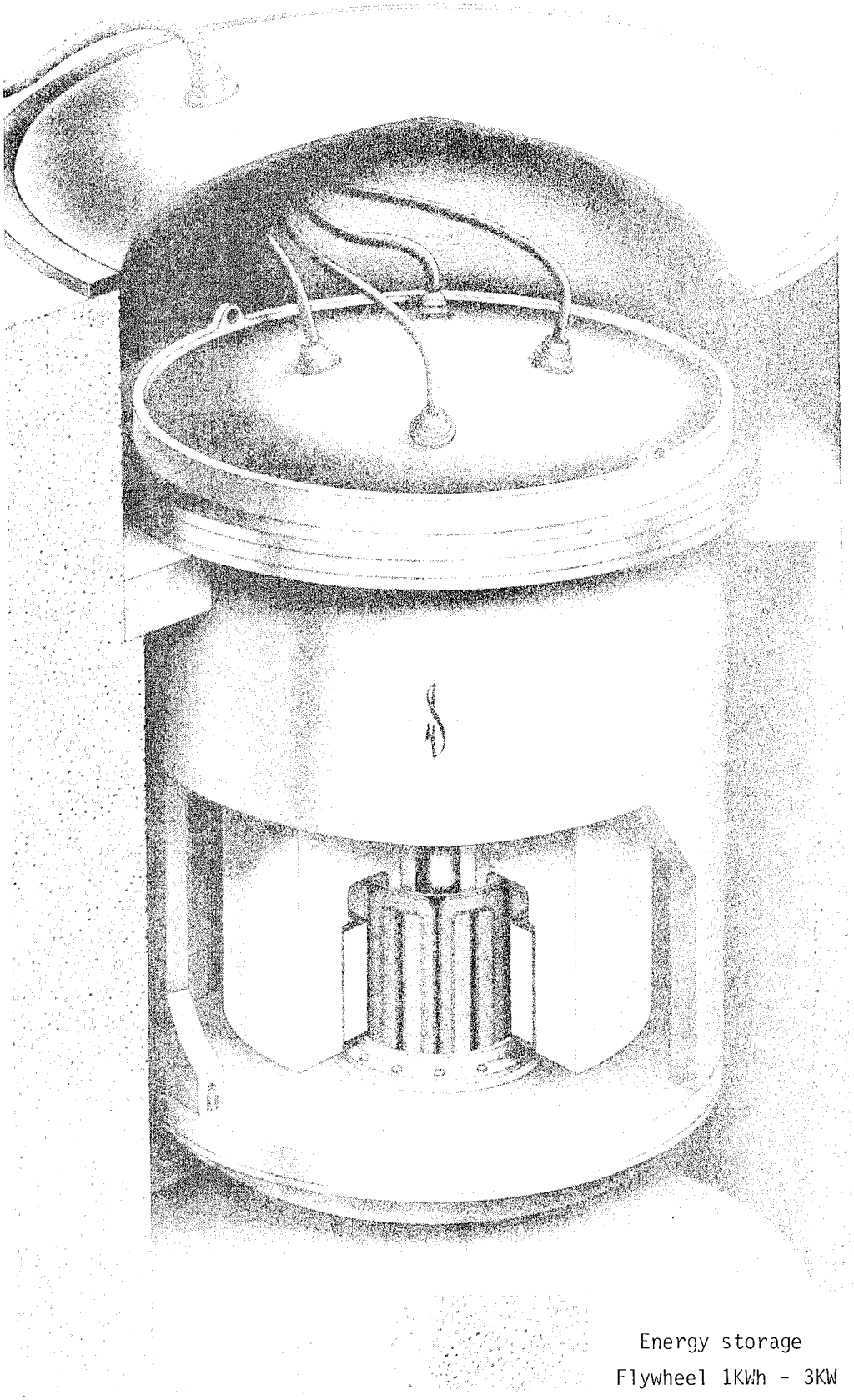

Energy storage
Flywheel 1KWh - 3KW

DEVELOPMENT OF A FLYWHEEL STORAGE SYSTEM FOR ELECTRICAL ENERGY APPLICATIONS

G.J.W.van Altena,
and
W.A.van Kampen,
Lab.of Magnet Technology,
Dpt.of Electrical Engineering,
Delft University of Technology,
The Netherlands.

ABSTRACT

A status report is given of a program to develop a flywheel energy storage system at the Delft University of Technology. The aim is to assess the feasibility of a flywheel system for (quasi)stationary applications. A test facility has been constructed for testing flywheel systems up to energies of 10 kWh under vacuum. Several types of flywheels will be tested, i.e. laminated fibre wheels, wound fibre wheels, and isotropic laval discs. A switch mode convertor is applied to transfer energy to and from the user. Rotating parts are in vacuum. Active magnetic bearings are used with permanent magnets incorporated, forming virtually a zero power system in the equilibrium position. A complet energy storage system with an energy content of 10 kWh and a power of 10 kW is due late 1980.

INTRODUCTION

At the Delft University of Technology a program is carried out to develop flywheel energy storage systems in cooperation with laboratories outside the University. The major object of the program is to demonstrate the feasibility by building and testing a complete system. The system will have an energy content of 10 kWh, and a life-time in the order of 10^5 charge-discharge cycles. The system should supply an electric load with power, receiving its energy from intermittent primary energy sources such as photovoltaic cells or a windturbine. High reliability is necessary with applications in remote areas where maintenance is difficult or expensive.

GENERAL

For storage periods of about one day or more low losses are necessary.Windage losses will be reduced in a vacuum environment, which makes it possible to apply velocities well above the speed of sound in air at normal pressure. To obtain a high energy density, flywheels constructed from materials with a high ratio of tensile strength to specific mass are favoured. A flywheel directly coupled to the rotor of an electric machine, with magnetic bearings in a vacuum environment is attractive because it offers a solution to the problem of high speed, will give good reliability and extremely low wear. It narrows the field of applicable motor-generator types, as no mechanical contact with the surroundings occurs. The heat dissipation of the rotor of the electric machine has to be low.

STATUS OF THE PROGRAM

A complete 10 kWh, 10 kW system is expected to be ready for tests at the end of 1980.

FLYWHEEL

Several types of flywheels, constructed in such a way that they can be put into the main system, are developed at various laboratories.

Laminated Fibre Wheel. In cooperation with the Netherlands Aircraft Factories Fokker a prototype of a laminated fibre wheel has been developed. Constructed in E-glass a single disc has an energy content of 440Wh

at 26,200 rev/min. This wheel has a diameter of 46 cm, a height of 5 cm and a mass of 17 kg, see Fig.1. The ratio of the maximum allowable working stress to tensile strength of the composite is 1:1.5, by reason of the uncertainty of the fatigue strength. In carbon fibre the energy content will be 1.25 kWh, so that 8 discs will give the 10 kWh we aim for.

Wound Fibre Wheel. Three types of flywheels wound of fibres are under development at the Laboratory of Fibre Technology of the University.

a. A wheel wound circumferentially of E-glass fibre around a modified laval disc of aluminum 6061. There are interlayer spokes of E-glass, see Fig.2. The fibres are impregnated with an epoxy resin before being wound. The dimensions are a diameter of 46.5 cm and an axial height of 12 cm. Mass moment of inertia 0.478 kgm^2.

b. A wheel wound circumferentially of E-glass fibre around an aluminum hub, optimized for energy in a given volume, see Fig.3. Six spokes of E-glass will give the wheel sufficient stiffness. After being wound, the wheel will be vacuum impregnated with an epoxy resin. The dimensions are a diameter of 50 cm and an axial height of 9 cm. Mass 32.3 kg. Energy content 1.16 kWh.

c. A wheel as under b, but wound with a high strength steel fibre.

Laval Disc. Two Laval discs are under construction at the central workshop of the University, see Fig.4. Selected materials are maraging steel and tool steel. Design values: diameter 47.4 cm, height 9.6 cm, mass 25.9 kg. Design stress of 780 N/mm^2 at 33,000 rev/min and an energy content of 600 Wh.

MOTOR-GENERATOR

The heat dissipation of the rotor has to be low. The high centrifugal stress in the rotor makes a rotor construction necessary with a high inherent strength. These requirements can be met by using synchronous machines in which a field coil for generating the pole flux of the rotor is mounted in the stator.

Homopolar Machine, Statexyn® type. The rotor of the machine consists of one piece of ferromagnetic material.[1] This machine has been designed for the first test runs of bearings and flywheels in a range of 10,000-25,000 rev/min. Nominal torque 1 Nm, rotor mass 6 kg, gap 2 mm, number of poles 4, see Fig.8.

Salient Pole Machine, Nadyne® type. The magnetic field of the machine is generated by two watercooled coils in the stator. The magnetic flux is transported by means of magnetic brushes to the poles.[2] The flux generates in the induction windings of the laminated stator part an alternating voltage, see Fig.5. The design values are 10 kW at 20,000 rev/min. Number of poles 2, gap 2 mm.

BEARINGS

Active magnetic bearings are used. Position transducers are of the h.f. type in which the quality of a resonant electric circuit is a measure of the distance. The advantage of magnetic bearings is the fact that the flywheel can choose its natural axis of rotation. In this way an unbalance may be accepted one order of magnitude higher than in the case of stiff mechanical bearings. Specifically, the unbalance of the rotor may change due to centrifugal loading during speeding up. The bearings are divided in an axial bearing and a radial bearing system, which operate independently at the moment. The bearings are designed such as to be fast reacting. In this way one is free to choose the dynamic properties such that the bearings can be adapted to the motor properties and the dynamic unbalance of the rotor unit.

Axial Bearing System. We have opted for a vertical axis of rotation, to get minimum power consumption in the bearings. The axial bearing system consists of two magnet systems, one at each end of the rotor shaft, see Fig.8. In the upper system a permanent magnet and an electromagnet are combined. It is designed such that at the nominal gap distance the permanent magnet field precisely lifts the rotor. The lower system has a single electromagnet. Upper and lower system are combined in one control loop, with position transducers for determining the vertical position of the shaft. Automatic gap control will be applied to set the magnet currents to zero for minimum power consumption.

® Statexyn registered trade name of Holec Machines and System Group of Holland.

® Nadyne registered trade name of Rockwell International Space Division.

Radial Bearing System. Two radial bearings are used with its own position transducers. Each bearing has four poles and a set of ball bearings for emergencies, see Fig.6. The complete radial bearing system should continuously correct the Coriolis force and the motion of the housing. The radial stiffness should be greater than the radial stiffness of the electric machine. The control circuitry of the system should give the right correction signal for the gyroscopic motion of the rotor.

ELECTRONIC POWER CONVERTER

The power converter for the electric machine consists of a bidirectional DC to AC convertor and a DC to DC convertor for the field current control, see Fig. 7. The motor currents are regulated electronically by pulse width modulation. MOS-FET power transistors are used. Infrared detectors measure the angular position of the rotor by means of a disc with a mirror Gray code giving an angular resolution of 3 degrees. Random access memories are used for generating a reference signal determining the shape of the motor currents. The power convertor has a power of 10 kW for a 3 phase machine. The system is self-starting.

CONTAINMENT

Tests will be carried out in a concrete vessel developed in cooperation with the Royal Military Academy, see Fig. 9. The vessel is made of a concrete bound with high aluminum cement and reinforced with steel fibres. The cylindrical part has a split wall construction. The top and bottom lids are pre-stressed with steel cables. The interior walls have been coated with an epoxy resin so that the vessel can be evacuated for lowering the windage losses of the flywheel. Vessel dimensions: internal diameter 1.5 m, height 1.2 m. Total mass 9,000 kg. Maximum energy content for steel discs 10 kWh. One of the questions to be answered is how the containment structure has to be designed. For example, a fibre flywheel desintegrating in small parts requires another containment structure then a metal flywheel coming apart in lumps. The development of a low weight containment structure has been started, in which a multi-layer technique will be used.

VACUUM SYSTEM

For pumping the test vessel, a vacuum pump with a capacity of 50 m^3/h is used. Vacuum end pressure 1.3 Pa (10 μmHg). For a vacuum of about 10 mPa (76.10^{-3} μmHg) a second pump of the Rootes type will be mounted in series. Water vapour is frozen out by liquid nitrogen at the top of the vessel, see Fig. 9. The vacuum pressure in the vessel is important, because in air a minimum breakdown voltage of 350 V is reach when the product of pressure and distance of the electrodes is equal to 0.57 mmHg.cm. Both lower and higher values of the product give a higher breakdown voltage.[3] A stainless steel vessel for a vacuum of 0.1 mPa ($0.76 .10^{-3}$ μmHg) is available for tests. This vessel can be mounted inside the concrete test vessel. Internal diameter 1.4 m, height 1.2 m, maximum load on mounting studs 40,000 N.

SYSTEM MONITORING, DATA ASSEMBLING, SYSTEM ANALYSIS

Measurement of the critical frequencies and the damping of the rotor assembly, are carried out separately with an excitator, with the rotor in a stationary position. During test runs a number of system parameters are measured. The data will be assembled by a small data processor and a 15 track analog recorder. The diameter and the temperature of the flywheel will be measured contact free. The temperature of the electromagnets of the bearings and the windings of the electric machine are measured as well. The motion of the frame will be measured in three directions with accelerometers. The radial and axial position of the rotor are measured directly with the analog sensors of the bearings, the angular position with the code disc of the motor control system. A system will be developed for the registration of a flywheel crash. Waterflow for cooling is measured by rotating flowmeters. The different components of the storage system, like bearings, flywheels and power convertors will be tested separately, see Fig. 8. Automated test series will be carried out with the processor. For analysis of measured data the central computer facility of the Delft University is used.

CONCLUSION

In the near future tests will be carried out in the described facility. The tests will provide pertinent information about the feasibility of flywheel energy storage systems.

REFERENCES

1 Richter,E.,"New Developments in Very High Speed Alternators," Proceedings of the Intersociety Energy Conversion Engineering Conference, Boston 1971, No. 719019, pp. 132-139.

2 Final Report to the Energy Research & Development Administration Division of Conservation Research and Technology, "Economic and Technical Feasibility Study for Energy Storage Flywheels," ERDA 76-65 UC-94B, Dec. 1975, pp. (2-6), (2-7),(5-24)-(5-29).

3 Von Ardenne, M., "Durchbruch in Gasen," Tabellen zur Angewandten Physik,Vol.III, VEB Deutscher Verlag der Wissenschaften, Berlin, 1973, pp. 416-426.

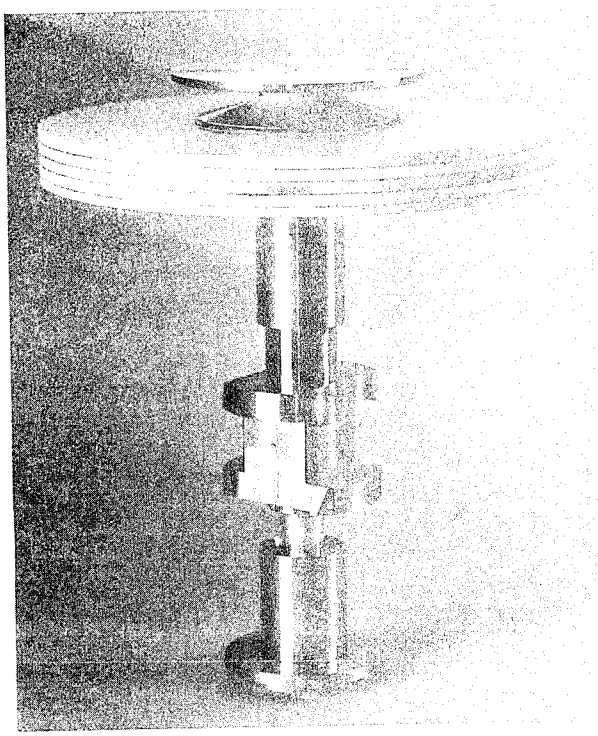

Fig.1
laminated fibre wheel,
E-glass Ø 46 cm, hg. 5 cm excl. taps.

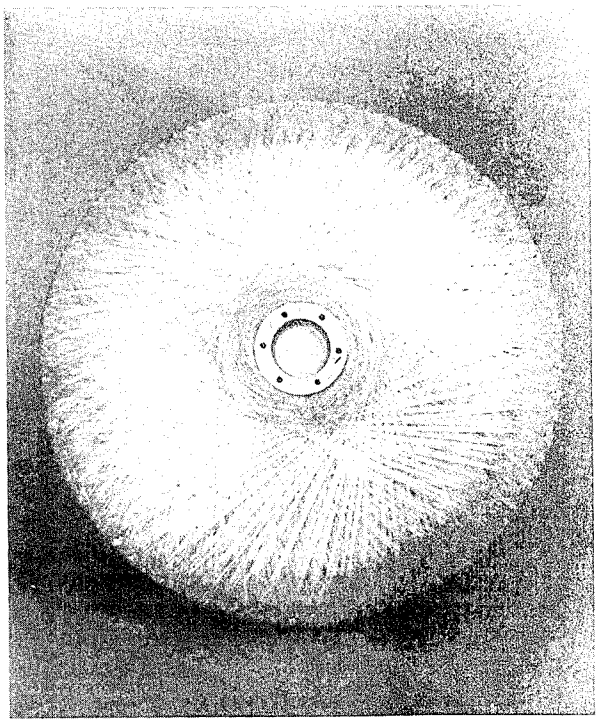

Fig.2
wound fibre wheel,
Aluminum 6061 modified Laval disc and E-glass,Ø 46.5 cm, hg. 12 cm.

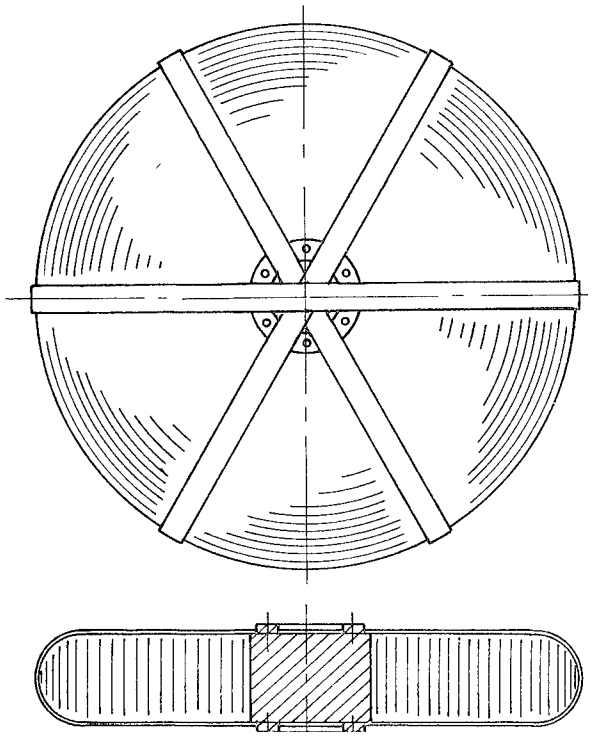

Fig.3
wound fibre wheel,
Aluminum hub and E-glass, Ø 50 cm, hg. 9 cm.

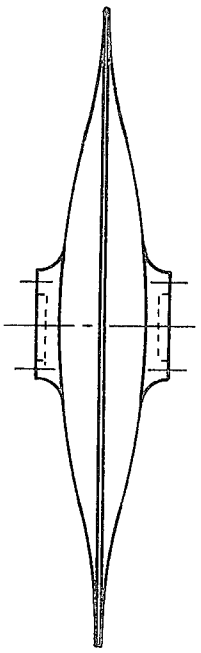

Fig. 4
Laval disc, Ø 47.4 cm, hg. 9.6 cm.
incl. taps.

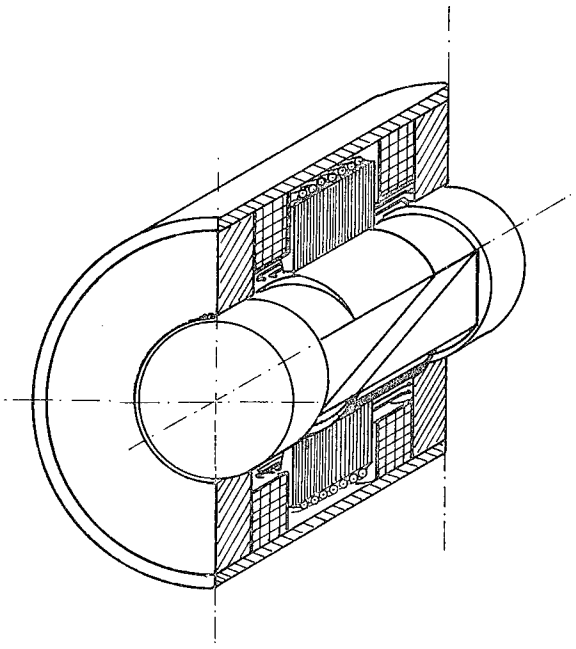

Fig. 5
salient pole machine

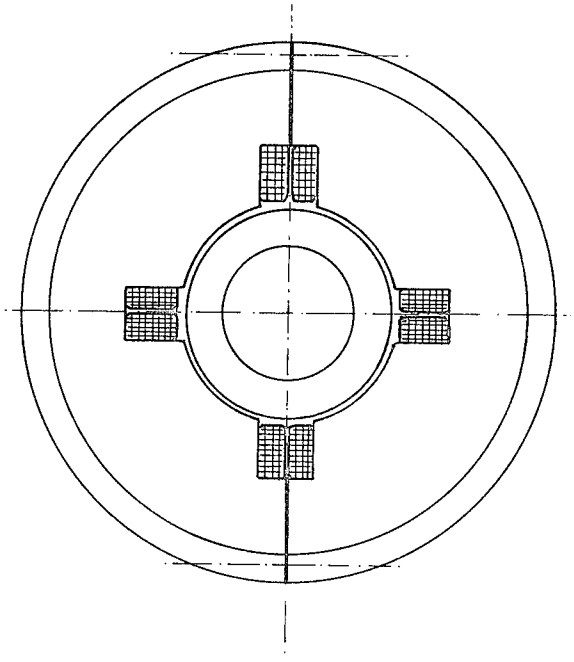

Fig. 6
radial bearing, four poles configuration.

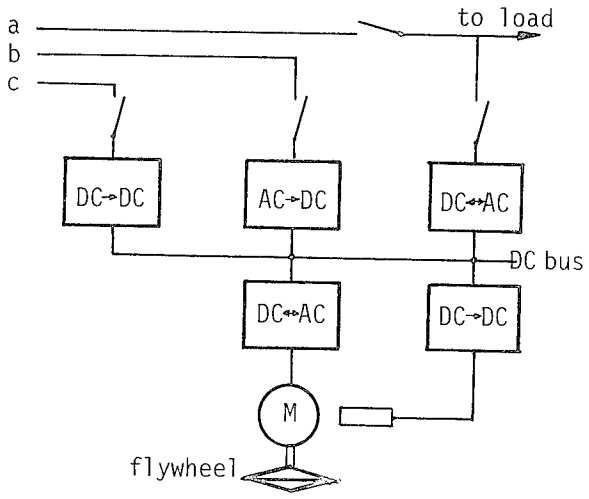

Fig. 7
electric scheme,
a - AC line 50 Hz,
b - AC line variable frequency,
e.g. windturbine,
c - DC line from solar panel.

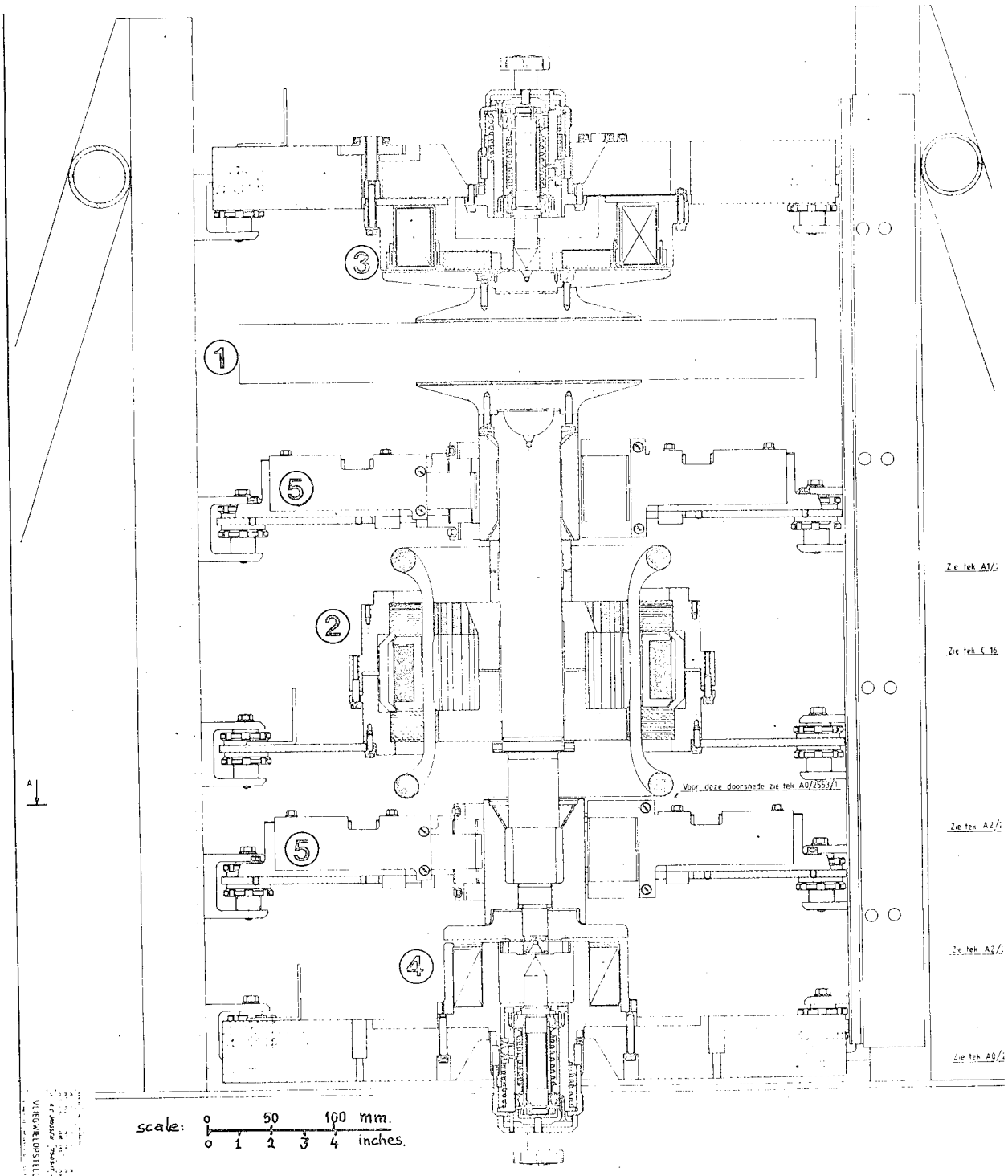

Fig. 8
test frame,
1 - flywheel, laminated fibre wheel,
2 - homopolar machine,
3 - upper axial bearing,
4 - lower axial bearing,
5 - radial bearing, 3 electromagnets configuration.

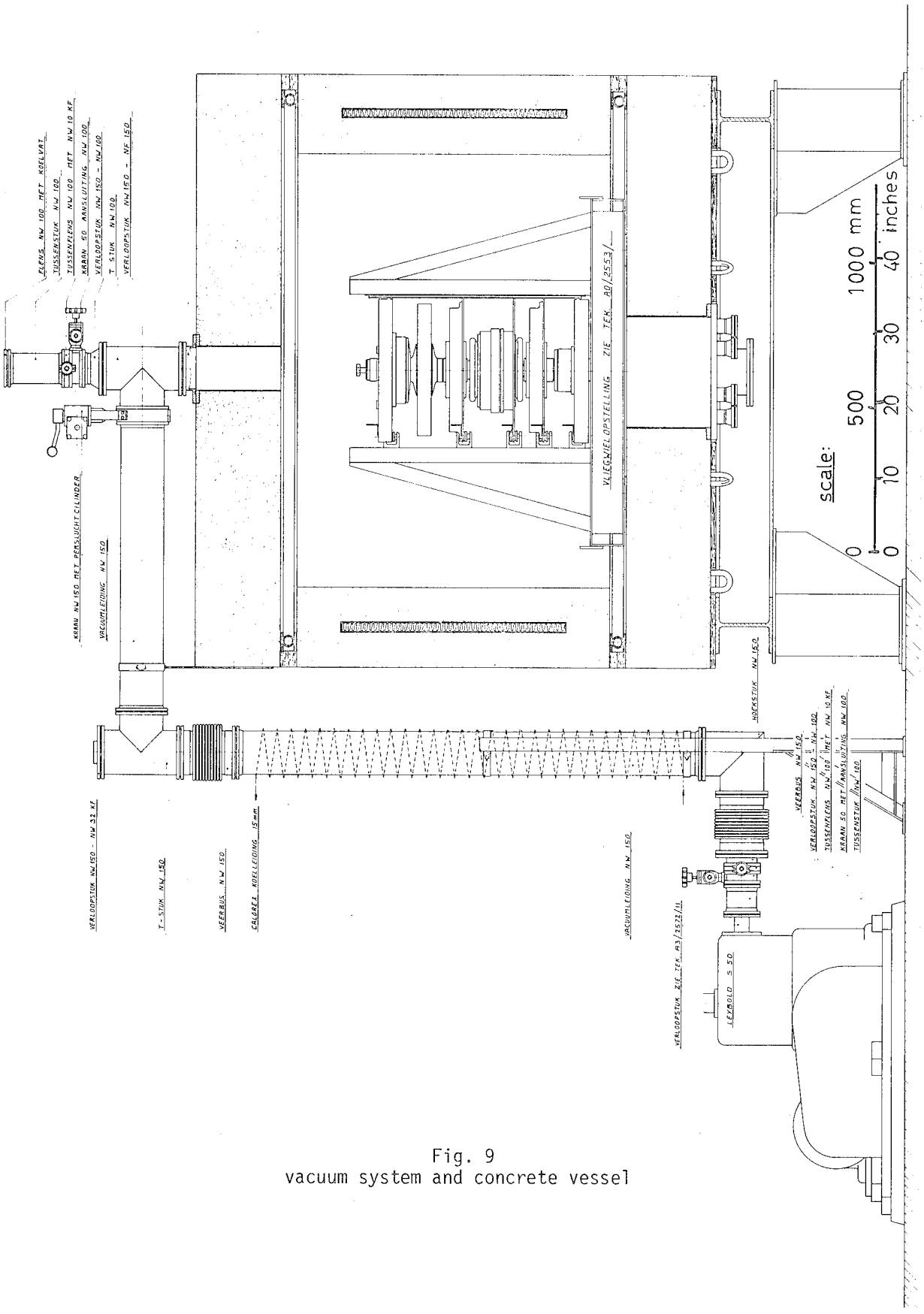

Fig. 9
vacuum system and concrete vessel

INERTIAL ENERGY STORAGE FOR HOME OR FARM USE BASED ON A FLEXIBLE FLYWHEEL

J. M. Vance
Dresser Industries Associate Professor
B. T. Murphy
Research Associate
Department of Mechanical Engineering
Texas A&M University
College Station, Texas 77843

ABSTRACT

An attractive design concept for an energy-storage flywheel suitable for home or farm use has been investigated at Texas A&M University. A unique feature of the "flexible flywheel" is its construction from high strength fibers (such as synthetic rope) with no bonding agent. Advantages which have been indicated by the work done to date are low cost, self-balancing, safe failure modes, and the possibility of a very high energy density (60 watt-hrs./lb.).

A major thrust of the research to date has been to find a solution to the subsynchronous whirling instability, a problem common to all high speed flywheels, which is especially severe in the flexible flywheel due to the high supercritical speed ratio and the large amount of internal friction. A unique gimbal support system has been designed, analyzed, and tested which stabilizes the flywheel without the need for a squeeze film damper.

A computer program to predict the effect of design parameters on whirl stability has been developed.

The conceptual design was developed for a flexible flywheel energy storage system suitable for interfacing with a small-scale solar energy source. Cost estimates were prepared for a 50 KWh flexible flywheel system.

INTRODUCTION

In 1975, Dr. R.T. Schneider at the University of Florida conceived the idea of a flexible flywheel made of rope for energy storage. The idea was to develop a cheap, safe, self-balancing energy storage device to make solar or wind-generated electricity practical for home or farm use.

Beginning in 1976, a flywheel test facility was constructed and the first rope flywheels were spun up. It soon became evident that one of the advantages of the flexible flywheel, its self-balancing feature, had been bought at the price of a subsynchronous whirling instability caused by internal friction, since the whirl critical speed is well below operating speed.

After the major technical problem of the flexible flywheel was found to be one of rotor dynamics, the first author (who is active in this field) joined work on the project while in the Department of Mechanical Engineering at the University of Florida. The project was subsequently moved to Texas A&M University in 1978 when the authors moved there, and all experiments and analyses described in this paper were performed there.

CONFIGURATION AND ADVANTAGES OF THE FLEXIBLE FLYWHEEL

Figure 1 shows a photograph of an experimental flexible flywheel. Notice that the support ropes carry only the weight of the flywheel, and that there is no hub or spoke array as in a conventional solid or composite flywheel.

The flywheel is a simple hoop, constructed by coiling ropes or fibers in a circle of the desired radius until the

design mass is achieved. At speed, centrifugal force maintains the circular configuration. For the sake of shape integrity when not spinning, one layer of rope is wound around the cross section of the hoop. (Early models were of macrame' construction, but this was found to sacrifice strength with no apparent advantage). The loose ends of the coiled hoop are joined by tying or splicing.

From the standpoint of energy density, this fiber/hoop configuration is the optimum attainable. It is obviously cheap to manufacture, and newly developed high strength fibers will be easy to incorporate into the design without the need to develop new bonding techniques.

The advantages claimed for this configuration are:

1. High strength fibers in pure tension with no bonding materials to create mismatch in elasticity or strength.
2. Self-balancing, due to a highly flexible rotor operating at supercritical speeds.
3. Simple construction is cheap to manufacture. Newly developed fibers can be easily incorporated without expensive redevelopment of manufacturing techniques.
4. Less destructive, safer, failure mode due to fiber construction.
5. Large hoop diameters made possible by the simple construction allows lower operating speeds and lower power losses than conventional high-performance flywheels.

These advantages mean that the flexble flywheel should be safer and less costly than conventional solid or composite flywheels.

FLEXIBLE FLYWHEEL DESIGN EQUATIONS AND CONSTRAINTS

Analysis has shown that to optimize energy density, a flywheel should be

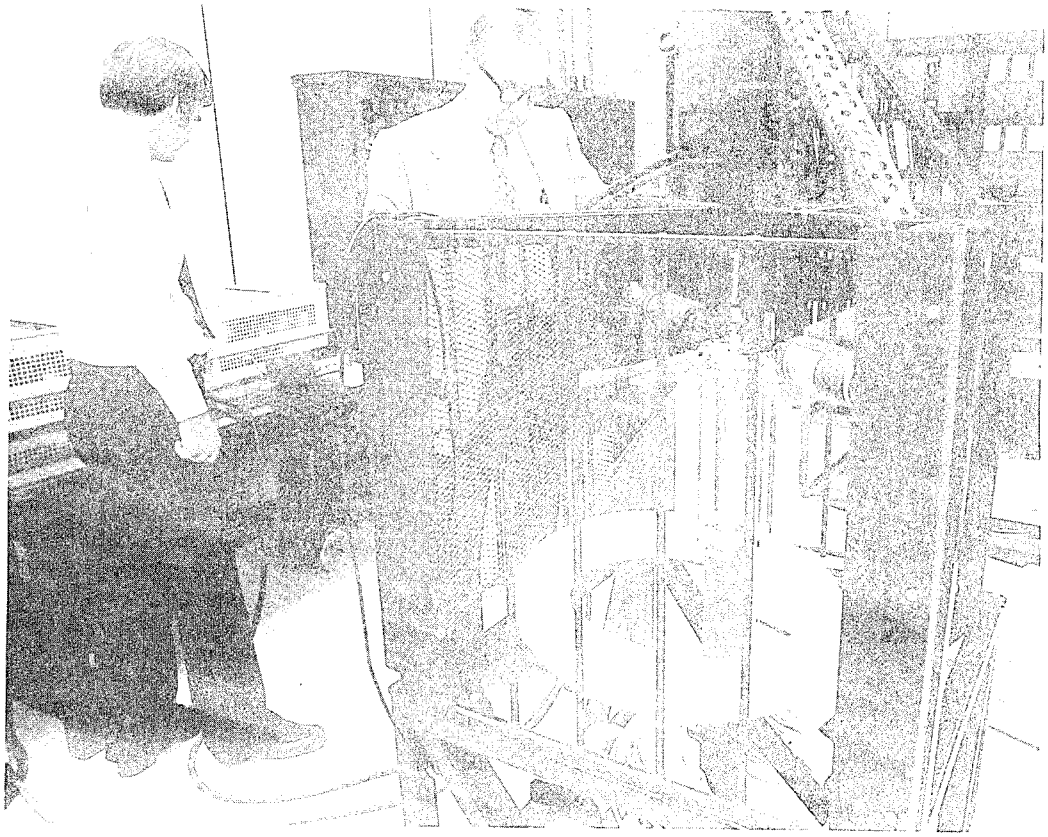

Figure 1: Experimental Flexible Flywheel Executing Nonsynchronous Whirl

constructed of high strength materials to operate at high speeds. The maximum storable energy in a hoop flywheel is (See Appendix A)

$$E = \pi RP \text{ ft-lb}$$

$$\bar{E} = (.3768)\ (10^{-6})\ \pi RP \text{ KW-hrs} \qquad (1)$$

where R = hoop mean radius, ft.
P = cummulative strength of all hoop fibers, lb.

Notice that the material mass density does not appear in the equation. Materials with high mass density (heavy materials) do not optimize energy density, which is contrary to popular intuition.

The mass density does, however, affect the speed at which the maximum energy is stored. This speed is given by (See Appendix A).

$$N_E = \frac{60}{2\pi}\sqrt{\frac{Pg}{\bar{w}R^2}} \text{ rpm} \qquad (2)$$

where $\bar{w}$ = hoop specific weight, lb/ft.
g = 32.2 ft/sec^2.

Although there are many advantages to using super-strong fibers to take advantage of equation (1), the resulting high rotational speeds (most high-strength fibers are not heavy) pose rotor dynamics and bearings problems which must be properly appreciated in the preliminary design phases of any modern flywheel. For example, contemporary electrical motors and generators are designed to operate well below the speed dictated by equation (2) for Kevlar^R wheel.

There are also practical constraints on the dimensions of the flywheel to be used in the home or on a small farm. Figure 2 gives dimension limits for a fiber hoop flywheel to be a practical size for home or farm installation (R), to remain a hoop (r), and to avoid flexural bending modes of whirling (L).

Applying the above equations and constraints to the design of a flexible flywheel allows the calculation of hoop sizes, weights and costs for various choices of material. Comparative results for Dacron^R, steel, and Kevlar^R are shown in Table 1, for a 10 KWh flywheel.

For successful energy storage, the most important parameter is the cost. Table 1 shows that the high strength of Kevlar^R pays off in a lower total material cost for the flywheel. The technical price, however, is high operating speeds. As shown below, the speed can be brought down by the use of a larger hoop diameter. There are many applications, however, where space is limited and Figure 2 or similar constraints sill govern the design.

Table 1. Comparative Parametric Values for a 10 KW-hr Flexible (Safety Factor = 2)

MATERIAL-HOOP	WEIGHT-LBS.	MAX.RPM	LENGTH FT.	L-MAT'L COST$
Dacron (1/4")	1298	5,167	1.74	2954
Steel (1/2" IRWC)	2123	4,039	.642	1938
Kevlar (1500 Den.-"29")	162	14,606	.287	1280

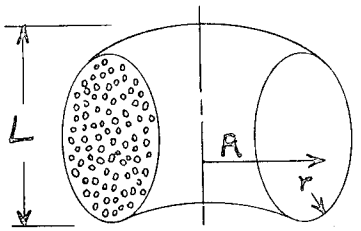

R = 3 ft.
r = 4 in.
L = 4 ft.

Figure 2. Dimension Constraints

THE EFFECT OF SIZE

There are significant advantages to increasing the hoop diameter of a flexible flywheel.

The values in Table 1 were calculated under the constraints of Figure 2. If we choose Kevlar^R as the material, remove the constraint on the hoop radius "R", and use a safety factor of 2, equations (1) and (2) can be written as

$$E = (10.97)R \text{ KW-hrs.} \qquad (1)'$$

and

$$N_E = 31{,}005/R \text{ rpm.} \qquad (2)'$$

These equations show that the energy stored is increased and operating speed is decreased by making the hoop diameter larger (with fixed circular cross section). Reference [1] shows that the latter effect (lower speed) reduces power losses.

As an example, a 10' diameter Kevlar^R flexible flywheel could store 50 KW-hrs. at a speed of only 6200 rpm, and have

bearing power losses of only 178 watts.

Futhermore, a flexible flywheel of large diameter can be constructed without the problems of inhomogeneous curing, uncertain balance retention, and high cost of manufacture, which are associated with composite construction.

ROTOR DYNAMICS

It was recognized early that the significant technical problems associated with the flexible flywheel would be in the area of rotor dynamics, specifically the problem of subsynchronous whirling due to internal friction. The advantage of self-balanced operation at supercritical speeds must be purchased with the price of suppressing or avoiding a self-excited dynamic instability.

The flexible flywheel, by virtue of its low stiffness rotor, always operates at speeds which are highly supercritical, where synchronous whirl (due to unbalance) amplitudes are minimized. Experiments to date have verified that the flexible flywheel produces extremely low levels of synchronous vibration, with no precision balancing required.

Early tests also showed subsynchronous whirling which tended to grow with speed and/or time. Figure 3 illustrates the mechanism of the internal friction excitation. For subsynchronous whirl the spin speed Ω is faster than the whirl speed $\dot{\phi}$. As support rope 3 moves around to position 1, its rate of strain is a maximum at position 2, thus generating the friction force F on the hoop which is tangential to the whirl orbit in the forward direction.

Rotor dynamics theory and analysis has identified several ways of suppressing self-excited subsynchronous whirl. They are:

1. Flexible bearing supports.
2. Asymmetric bearing support stiffness.
3. Bearing support damping.
4. Bearing support mass (dynamic absorber effect).

For a cost effective design, these methods of suppressing whirl must be applied in conjunction with the overall system design constraints, as follows.

SYSTEM DESIGN CONSIDERATIONS

1. A shaft seal through the vacuum chamber wall is expensive.
2. A disconnect clutch also increases the total system cost.
3. A new motor/generator must be developed to match flywheel torque-speed characteristics.
4. Low friction bearings must be designed for the application, to operate in a vacuum environment.
5. The total number of bearings should be minimized, for lowest cost, and for lowest power loss.

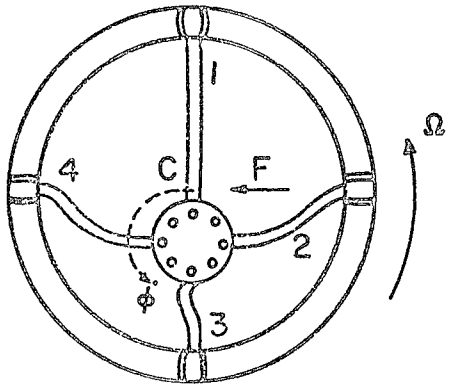

Figure 3. Instantaneous Configuration of Rope Ring

When these design considerations are coupled with the design requirements to suppress the subsynchronous whirl, a design philosophy for the flexible flywheel emerges. The basic elements of this philosophy are shown in Table 2.

Table 2. Flexible Flywheel Design Philosophy

Design Factors or Constraints	Solution or Conclusion
*Shaft seal is expensive *New motor/generator required	Put motor inside vacuum chamber.
*Clutch increases cost *New bearing required *Minimize no. of bearings	Support flywheel directly from motor shaft.
*Need low support stiffness *Need asymmetric support stiffness *Need support damping and mass	Gimbal motor/generator on nonintersecting axes.

Figure 4 shows how the motor/generator can be gimballed on nonintersecting axes to provide the low support stiffness, stiffness asymmetry, and bearing support mass (the motor itself), which are the parameters important to whirl stability.

The motor bearings are designed to support the flywheel, thus minimizing the number of bearings and eliminating the necessity for a clutch, since the motor armature becomes effectively a part of the flywheel inertia.

Work to date has been aimed at verifying whirl stability for this concept, both experimentally and analytically, and at estimating the system cost.

EXPERIMENTAL RESULTS

A small scale model was constructed for preliminary evaluation of whirl stability characteristics. The distance from the y axis down to the motor center of mass was made adjustable, so as to vary the stiffness asymmetry produced by the gimbals. The flywheel used in this model is 10-1/2" diameter and is made from a continuous coil of Nylon rope. The weight of the flywheel hoop alone is 2.7 lb. Figures 5 and 6 are photographs of the small model, which show the support ropes "untwisted" and "twisted" (wound up), respectively.

Tests were made with the gimbals locked (rigid), and with the gimbals free, to evaluate the effect on whirl stability.

With locked gimbals, the small flywheel is violently unstable in subsynchronous whirl at all speeds above 100 rpm, for all support rope configurations.

With the gimbals free, and twisted support ropes, the flywheel is stable and

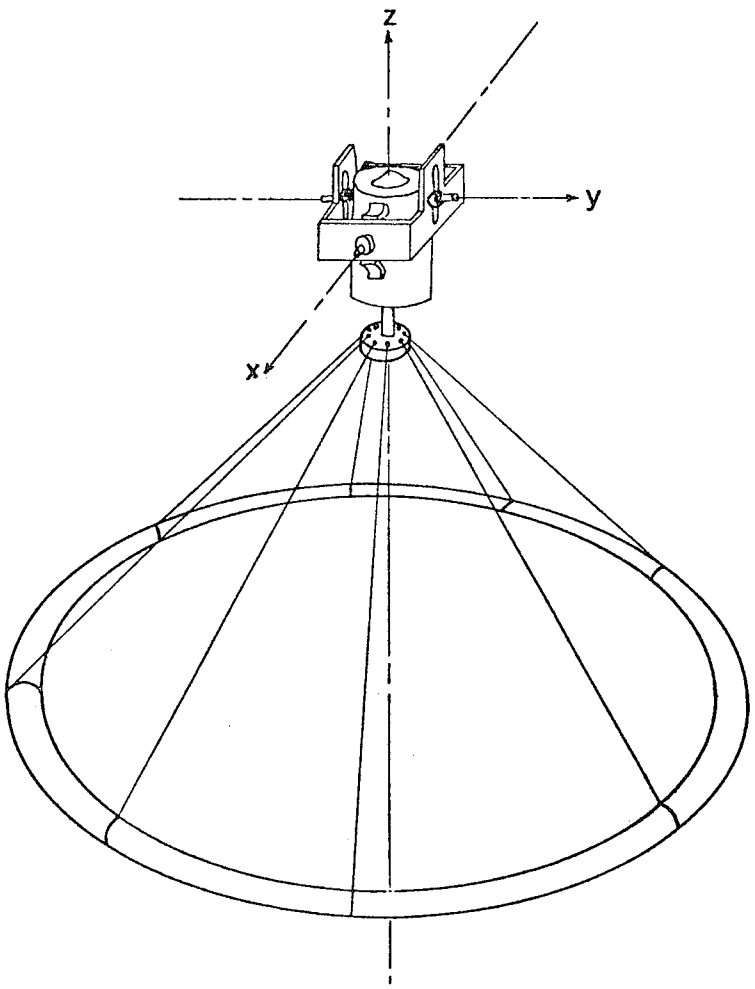

Figure 4. Flexible Flywheel On Gimballed Support

runs smoothly up to the maximum speed allowed by available motor power to overcome air drag (about 2600 rpm). With the gimbals free, and untwisted support ropes, the threshold speed of instability is between 600-750 rpm, depending on the length of the support ropes. In this configuration, asymmetry of the gimbal supports (one gimbal axis free, one locked) produces a slightly higher threshold speed than with both gimbals free.

No effort has ever been made to balance this flywheel, and at one time small unbalance weights were added at random to the twisted rope configuration to demostrate its insensitivity to unbalance. The smooth and stable operation was not impaired.

A larger gimbal-supported motor/generator system was used to test a 22-1/2" diameter Dacron flywheel weighing 19 lb. Its 15 HP motor allowed speeds in the atmosphere up to 2000 rpm before air drag caused power supply circuit breakers to trip.

Figure 7 shows the 22-1/2" wheel with its motor/generator, gimbal support system, and protective cage.

The major shortcoming of the 22-1/2" wheel was its relatively low weight (19 lb.) compared to the motor/generator weight (90 lb.). It was felt that this impeded the stabilizing influence of the gimbals, an intuition which was later verified by results from a computer stability analysis. Experiments with the 22-1/2" wheel showed an even stronger sensitivity to the method of support rope attachment, both at the flywheel and at the motor hub. The 2,000 rpm speed was achieved with untwisted steel cable supports attached to the flywheel with rope bridles. As mentioned above, the speed limitation in this case was imposed by excessive current demand tripping circuit breakers in the power supply. Shortly after this test, the 22-1/2" wheel was removed so that the motor/generator and gimbal supports could be installed in a

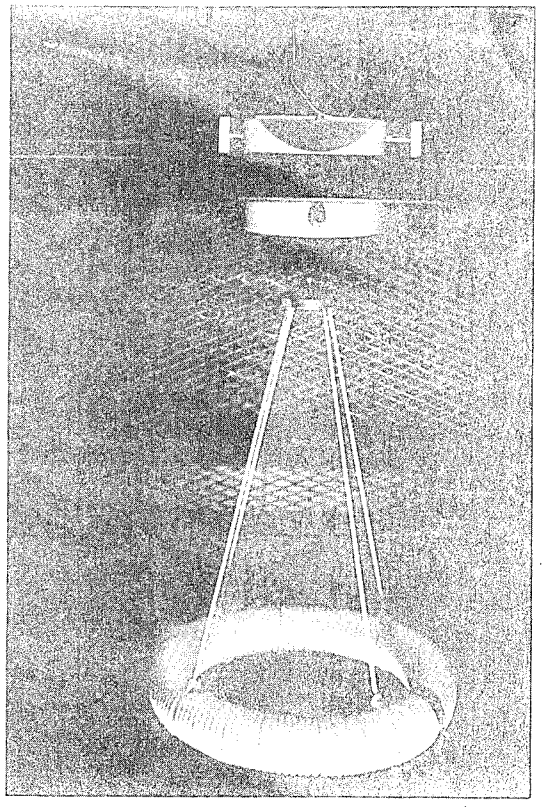

Figure 5. 10 1/2" Flywheel With Untwisted Support Ropes

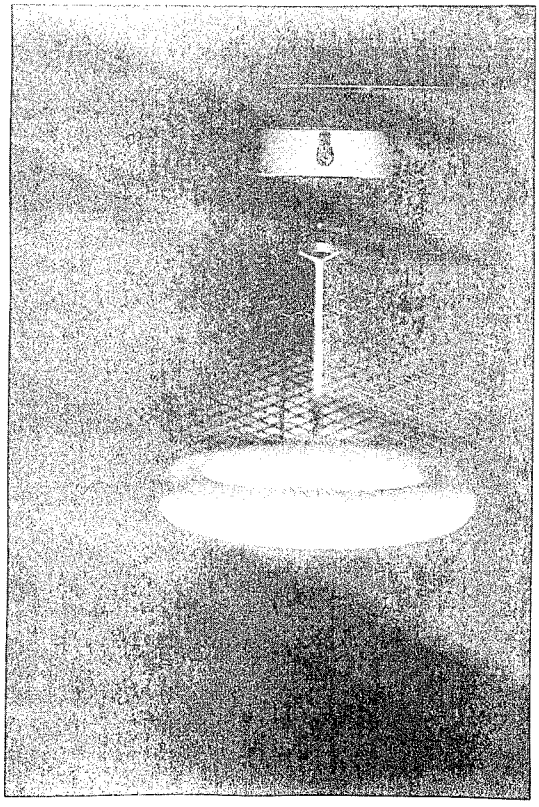

Figure 6. 10 1/2" Flywheel With Twisted Support Ropes (At Speed)

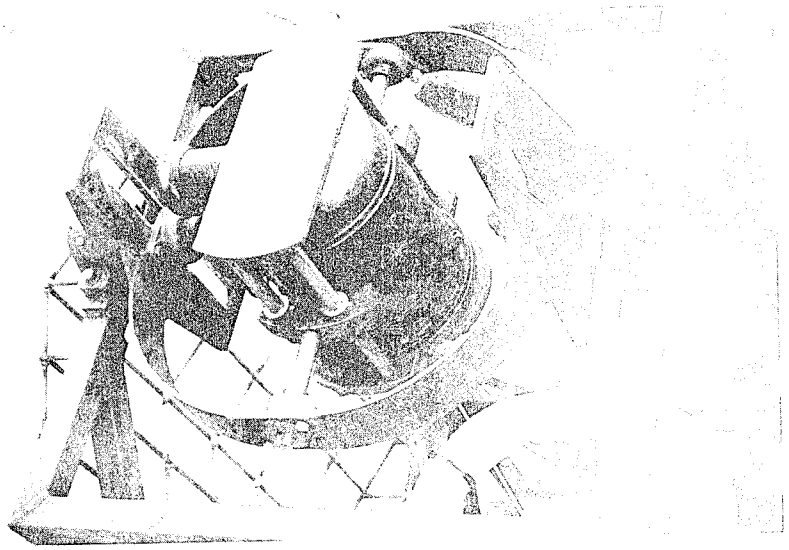

Figure 7. 22 1/2" Flywheel Suspended From Gimballed Motor

vacuum chamber (as a safety measure, and for possible pump-down at a later date). After this was done, the 22-1/2" wheel was reinstalled, but the 2,000 rpm speed could not be repeated with untwisted support ropes. Since a considerable volume of air blows out of one of the chamber ports when the flywheel runs, it was hypothesized that aerodynamic pressure may produce an additional destabilizing force in the chamber. This has since been verified by model tests of a wheel rotating with and without a chamber enclosure. This excitation would not be present in a vacuum.

Finally, a 30" diameter Nylon wheel weighing 88 lb. was constructed and tested in the vacuum chamber, using the same 15 HP motor/gimbal assembly as used with the 22-1/2" flywheel. This flywheel can store 1 KW-hr at 10,650 rpm, and has a breaking speed of 14,548 rpm. Figure 8 shows the vacuum chamber, and Figure 9 is a photograph of the 30" flywheel in the vacuum chamber, (looking down from the top). With the flywheel supported by untwisted support ropes made from monofilament Nylon, the threshold speed of instability was 1,000 rpm. To simulate the twisted support ropes which had proved stable in the smaller models, and yet retain torque capability in both directions, a four-strand bridle was braided into a square cross section. With this support rope configuration, no instability was encountered up to the maximum speed of 1500 rpm which was limited only by the power supply overload due to air drag.

To answer questions about the capability of the support ropes to transmit enough torque to generate useful magnitudes of electrical power, the torque actually transmitted in overcoming air drag was measured on both the 22-1/2" and 30" flywheels.

Fig. 8. Flywheel Vacuum Chamber Facility

Figure 9. 30" Flywheel Installation in Vacuum Chamber

For the 22-1/2" flywheel, this was accomplished by measuring the rope angles in photographs and movies, and relating these angles to static torque measurements. Figure 10 shows the results for both the untwisted steel cable supports and twisted 1/4" rope supports.

For the 30" flywheel, the electrical power supplied to the drive motor was computed from the measured voltage and current. Using an efficiency factor of 0.9, this turned out to be 6 KW at 1500 rpm, which represents enough torque to generate 42 KW at the design speed of 10,650 rpm. The support rope configuration used for this measurement was the four-strand bridle described earlier. The larger cross section of the braid, as compared to a simple twist, together with the larger wheel diameter explain the much greater torque transmitted to the 30" flywheel. On several occasions during the experiments, the electrical current demand due to air drag caused circuit breakers to trip in the power supply, thus subjecting the flywheel to a severe transient decelerating torque (reversing). It was found that the flywheel could handle these transients with no unfavorable effects.

INSTRUMENTATION AND MEASUREMENTS

Flywheel speed of the small (10-1/2") model was measured with a photocell reflective tachometer. The reflective tape was installed on the flywheel hoop itself. Natural frequencies were measured with a SELSPOT optical tracking instrument, tracking the motion of LED's installed on the flywheel. The signal was captured on a storage oscilloscope, so that the logarithmic decrement (damping) could be determined as well as the natural frequency.

Flywheel speeds of the larger (22-1/2" and 30") flywheels were measured with a pulse tachometer, consisting of a magnetic transducer excited once per revolution by a projection from the steel hub of the motor shaft, with the period between pulses measured by an H-P electronic timer. (An electronic tachometer reading in rpm was also used in the early stages of the project).

Whirling frequencies of instability were so low (typically 1-2 Hz) that it was found possible to measure them visually, using a stopwatch, and by movies, placing a clock with a sweep second hand in the camera field of view.

Due to the flexible support with no hub or spokes, the flywheel hoop whirled as a rigid body. No flexural vibrations of the hoop were ever observed.

STABILITY ANALYSIS

A computerized stability analysis was also developed to guide the design, improve understanding of the destabilizing mechanism, and ultimately to optimize the design parameters for dynamic stability. Details of the method and results will be forthcoming in a subsequent technical paper.

All of the predicted critical speeds and mode shapes agreed closely with experimental measurements, and the thresholds of stability could be accurately simulated by adjusting the (unknown) values of internal hysteresis in the mathematical model.

One of the most difficult tasks of the analysis was to rationally explain why the twisted ropes configuration is more stable than the untwisted support rope

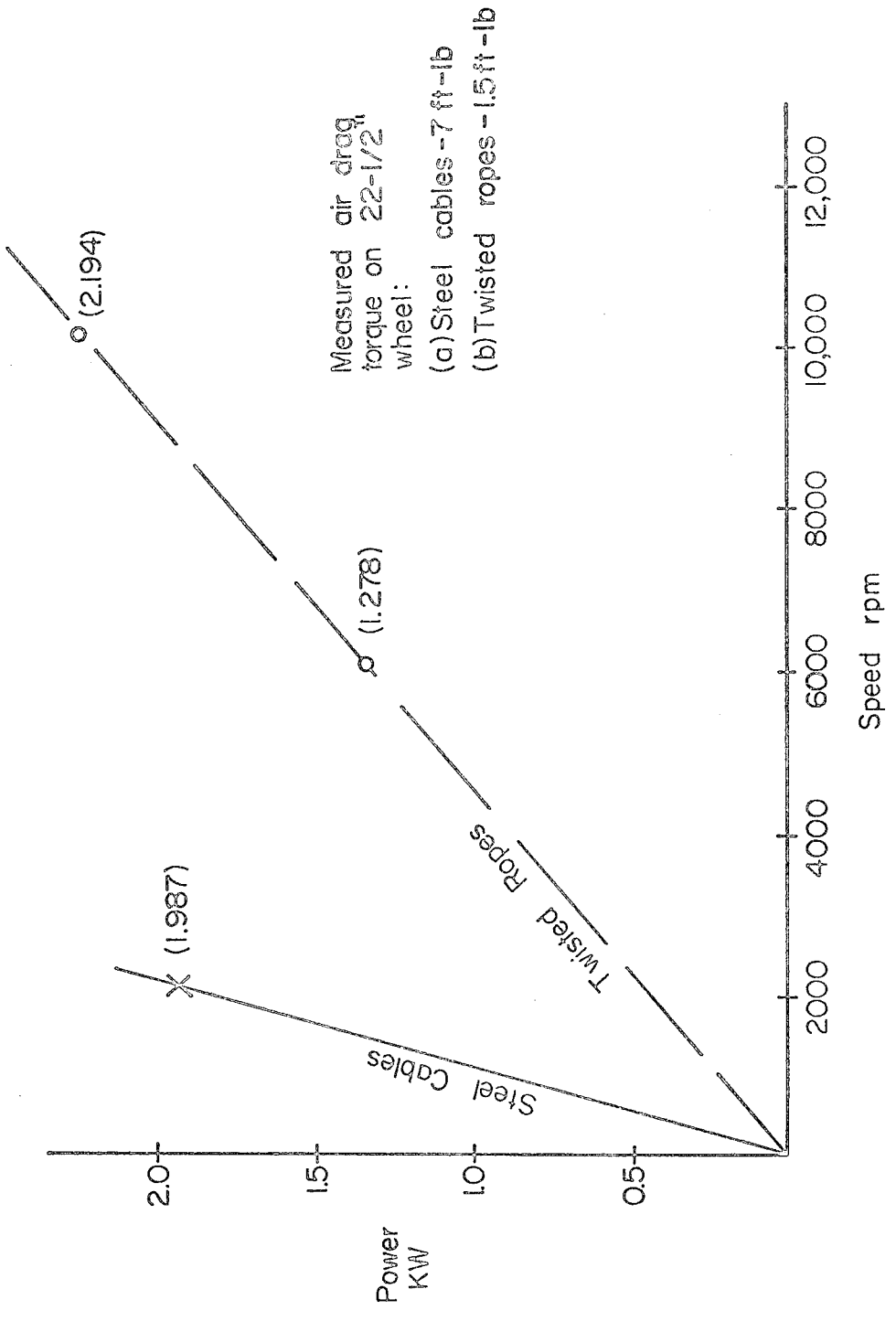

Figure 10. Electrical Power Capability of Flexible Flywheel from Measured Torque

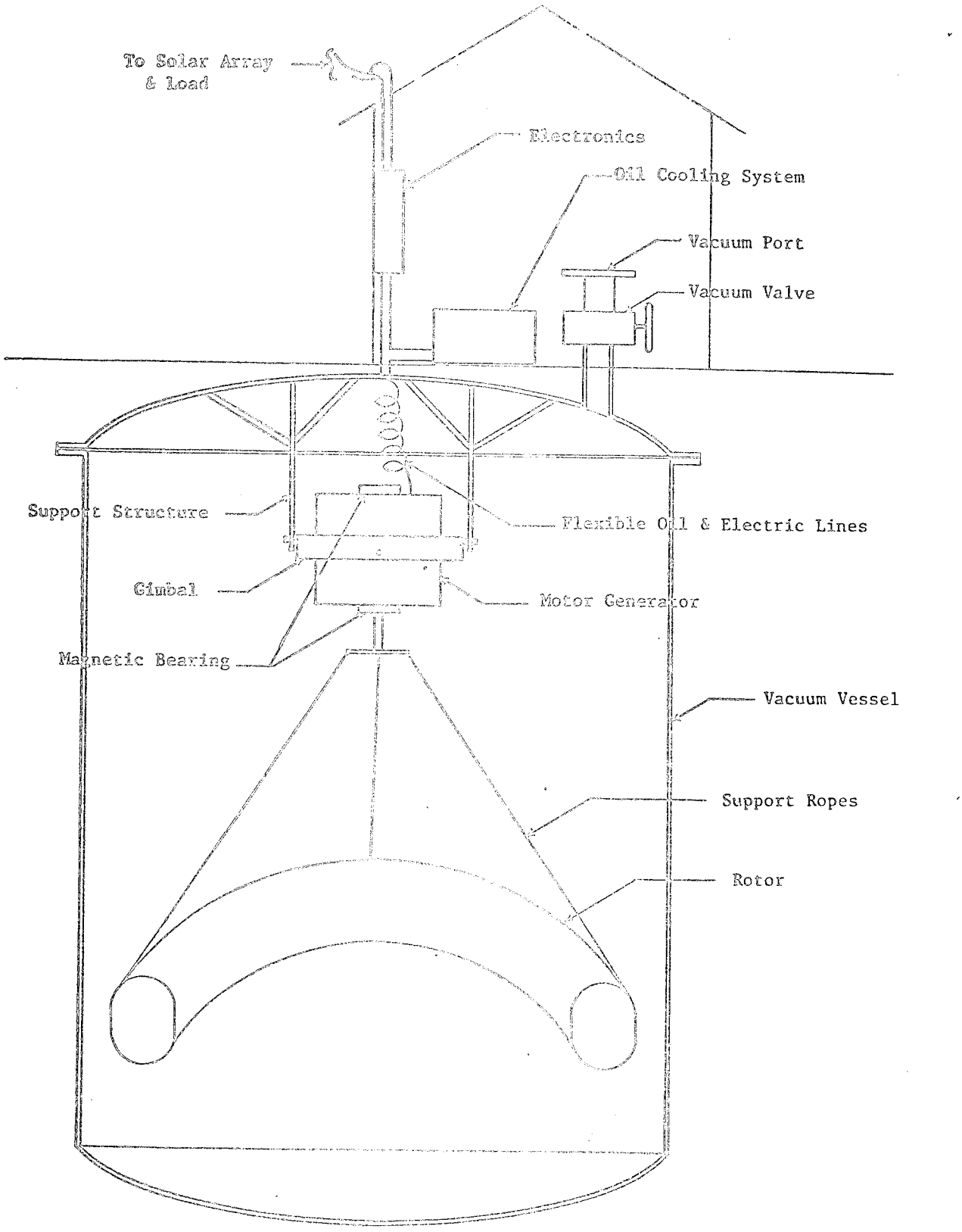

Figure 11. Conceptual Design of a 50 KWh Flexible Flywheel Energy Storage System.

configuration. This was done on the basis of the different magnitudes and directions of internal friction torques generated by the different support rope geometries.

FLYWHEEL SYSTEM COST ANALYSIS

An economic analysis of a 50 KWh residential flexible flywheel energy storage system was performed, based on a life cycle cost methodology developed for solar energy systems.

The conceptual design of the proposed 50 KWh Flexible Flywheel Energy Storage System is shown in Figure 11. The system is design for below ground installation although above ground or partially below ground installation would represent only minor changes and not greatly affect the cost of the system. The system stores a nominal 50 KWh with an input of 10 KW DC and a peak output of 10 KW AC.

The major components of the system are: 1) the rotor; 2) the gimbal mounted motor/generator, magnetic bearing and electronics; 3) the oil cooling system; and 4) the vacuum vessel.

The rotor is a simple hoop constructed by coiling Kevlar fibers into a circle 6' in diameter with a minor radius of 4". The overall hoop assembly weighs 850 pounds and stores a nominal 50 KWh at 14,000 rpm. Maximum rpm is 14,600 with a safety factor of 2. Four flexible ropes attach the hoop to the motor/generator shaft.

The oil cooling system consists of a radiator, oil pump and flexible lines to the motor/generator. The radiator is an oil-to-air cooling unit similar to those found in large cars and trucks. A small oil pump is included to provide flow in the systems. Because the pressures involved would be low, the pump would only have to overcome small head losses and only require 50 to 100 watts of power. The flexible lines are needed to allow free movement of the motor generator in its gimbal mounts. The system uses insulating transformer oil to eliminate the possibility of shorting out the armature stator.

The vacuum vessel is designed to provide ease in final assembly and installation of the system. The vessel is comprised of two sections. The lower section consists of 1/4" thick steel cylinder with a semihemispherical bottom. The upper section, also semihemispheric, contains all necessary feedthroughs for the electric oil lines and the support structure for the motor generator and rotor assembly. Also provided is a pump-down port and vacuum valve. This arrangement allows the entire system to be assembled on the upper head then lowered into the rest of the vacuum vessel. The two sections are then welded together at the mating flanges either at the manufacturing plant or at the installation site. This design also has the advantage, should the motor-generator or rotor fail, that only the upper section need be removed, by cutting the weld, for unit repair or replacement instead of removing the entire vacuum vessel from its below ground installation.

A motor/generator similar to the one being developed at MIT/Lincoln Laboratory (Reference [2]) will be used. A significant departure from the referenced design is to "can" the stator armature to enable cooling of the windings with transformer oil. The MIT motor/generator is being developed under the sponsorship of the U.S. Department of Energy (DOE), specifically for flywheel applications interfaced with solar phovoltaic systems. It is of a brushless-DC, permanent magnet design offering the advantages of high-efficiency and relatively simple power conditioning electronics for high speed applications. Oil cooling of the stator armature was added to the design because it is believed that conduction through the frame and gimbal support structure would provide insufficient cooling.

Magnetic bearings were chosen over ball bearings in this economic study. It was felt that maintenance cost increases would more than offset, over the life of the system, the higher cost of the magnetic bearing (based on the life-cycle costing methodology used in the cost analysis). The bearings can be powered by auxiliary windings on the motor allowing fail-safe spin-down operation. Mechanical touchdown bearings are included for cold start/stop situations.

The electronics interface between the DC solar array and the PM motor/generator provides high quality 60 Hz AC for residential power consumption. All solar/electric power would go into the motor/generator to spin up the rotor.

The motor/generator would be electronically controlled to serve as a maximum power tracker. This is important because the varying electrical output of solar arrays is generally mismatched to the characteristics of the storage system and load, causing inefficient operation. The generator output is fed into a silicon controlled rectifier (SCR) cycloconverter which, with a transformer, provides 220V/60 Hz output to the load.

Table 3 gives a comparative cost breakdown, in 1979 dollars, of the 50 KWh Flexible Flywheel system. Major cost items are: 1) the rotor; 2) the motor/generator; 3) the magnetic bearings; 4) the electronics and 5) the vacuum vessel. The rotor is constructed of 1500 den Kevlar at a cost of $8.00 per pound. This results in a cost of $6800 (*850 lbs.). Rotor construction costs are estimated to be $0.10 per pound or $85 per unit for a large number of units. The total cost is then $6885, which appears to be much less than the cost of a comparably sized composite wheel. It should also be noted that a large savings can be realized if the cost of Kevlar decreases in the future.

TABLE 3. Cost Breakdown (1979 Dollars) for 50 KWh System

Rotor	$ 6,885
Motor/Generator	1,000*
Electronics	1,600*
Bearings	3,750*
Vacuum Vessel	5,150
Gimbal	2,125
Support Structure	1,400
Installation & Assembly	2,000
Oil Cooler	200
Backup Power Switchover	50
	$24,160

Maintenance $500/yr based on 2 pumpdowns per year

*A.R. Millner, "A Flywheel Energy Storage and Conversion System for Solar Photovoltaic Applications," ASME, 79-501-1, March 1979.

The cost of the vacuum vessel is determined based on 1979 costs of steel vessels of similar dimensions. This cost is $5,150 and quite subject to fluctuations in the price of steel.

The cost analysis based on the life-cycle cost methodology seems quite reasonable for analysis of energy storage devices even though it was developed for solar energy systems [3]. Using that methodology, the annual residential cost for a 50 KWh flexible flywheel is $4,086.26. Details of the life-cycle cost calculations can be found in references [3] and [4].

CONCLUSIONS

The principal conclusions from this research can be summarized as follows:

(1) Subsynchronous whirl instability of a flexible flywheel at supercritical speeds, due to internal friction, is strongly suppressed by a gimballed motor/generator support system. (This finding is applicable to more conventional flywheels as well.)

(2) A flexible flywheel made from synthetic rope or fiber with no bonding agent is relatively inexpensive, easy to construct and can be made self-balancing by a properly designed support system.

(3) Based on 1979 technology, a flexible flywheel energy storage system is seen as being cost competitive with other storage systems for home or farm use.

ACKNOWLEDGEMENTS

The authors wish to acknowledge the major contributions to this work by the following people:

Dr. Richard T. Schneider invented the flexible flywheel, did much of the setup and construction work for the vacuum chamber (not yet pumped down), and guided the economic analysis.

Mr. Wallace Ables performed many of the experimental measurements and constructed most of the experimental apparatus.

Mr. B. Dudley Carter helped with the study of costs and economic factors for a flexible flywheel storage system.

REFERENCES

1. Eisenhaure, D.B., and Kingsbury, E.P., Final Report on the Development of an Advanced Flywheel Bearing Performance Model, Sandia Laboratories, SAND 79-7003, March 1979.

2. Millner, A.R., "A Flywheel Energy Storage and Conversion System for Solar Photovoltaic Application," ASME Paper

79-Sol-1, Gas Turbine and Solar Energy Conference, San Diego, California, March 12-15, 1979.

3. Perino, A.M., A Methodology for Determining the Economic Feasibility of Residential or Commercial Solar Energy Systems, Sandia Laboratories Report SAND 78-0931, January 1979.

4. Vance, J.M., Research and Development for Inertial Energy Storage Based on a Flexible Flywheel, Final Report for Sandia Contract No. 07-3693. June 1980.

5. Timoshenko, S., MacCullough, G.H., Elements of Strength of Materials, Third Edition, D. Van Nostrand Company, Inc., Princeton, New Jersey.

APPENDIX A

The energy stored in a rotating hoop flywheel is proportional to the mass of the flywheel and to the square of the speed.

$$E = \frac{1}{2}mv^2 = \frac{1}{2}m(\omega R)^2$$

where m = flywheel mass
ω = flywheel speed
R = mean hoop radius

Since the centrifugal forces acting on the flywheel increase with the speed there is a limit to how fast the flywheel can go before failure. If one assumes constant stress over the hoop cross section then Timoshenko (Ref. 5) gives a relation for the tensile force in the flywheel as

$$P = \frac{\bar{w}}{g}(\omega R)^2$$

where $\bar{w}$ = the weight per unit length
$(m = 2\pi R\bar{w}/g)$

g = gravity, 32.2 ft/s^2

Let P become the maximum safe load for the flywheel. This now allows one to specify the maximum safe speed.

$$\omega = \sqrt{\frac{Pg}{\bar{w}R^2}}$$

or

$$N_E = \frac{60}{2\pi}\sqrt{\frac{Pg}{\bar{w}R^2}} \text{ rpm}$$

This speed can be substituted into the above energy expression to obtain the maximum storable energy $E = \pi RP$.

FLYWHEEL MOTOR/GENERATOR FOR THE CONTROL OF HYDRAULIC SURGE OR WATER HAMMER IN PUMPED PIPELINE SYSTEMS

Wilhelm S. Everett
EVERETT ASSOCIATES
P. O. Box 1535
Ventura, California 93002

ABSTRACT

This paper presents an alternate viable method of controlling surge and water hammer in pipeline systems by using a flywheel motor/generator which essentially electricially connects flywheel inertia to pumps. The flywheel motor/generator can also be used in other centrifugal equipment such as blowers, fans, and centrifugal compressors where continuity of flow is required but where the power declines by the cube of the rotative speed. Various methods used for the solution of problems in pipelines are reviewed including the procedure for sizing the flywheel inertia. Also included is a comparison of a flywheel motor/generator to a surge tank.

NOMENCLATURE

WR^2	Inertia of rotating elements which includes flywheel motor/generator (FM/G), pumps, drivers, and couplings.
N	Rated rotational speed - $min.^{-1}$
V	Rated velocity in pipeline
L	Pipeline length
A	Pipeline liquid cross sectional area
BHP	Actual brake horsepower of pumps: (KW)
a	Speed of sound of liquid in pipeline
h_s	Static head of pipeline system
h_f	Friction head of pipeline system
h_p	Total pump head - $(h_s + h_f)$
h_d	Down surge head
s	Slope of surge line $\frac{a\ V}{g.h_p}$
g	Gravitation constant
α	Rotational speed ratio
β	Rotational torque ratio
t	Time constant of pipeline system 2.L/a
K	Inertia factor during the decelerated pumping
FM/G	Flywheel motor/generator

SUBSCRIPTS

p	Pump
s	Static
f	Friction
g	FM/G

SURGE SOLUTIONS FOR PIPELINE SYSTEMS

Power outages in pump stations for pipeline systems, including sewage force mains, produce surge and water hammer pressures of sufficient magnitude to cause failures in not only the pump stations but also at high points in the pipeline profile. Fig. 1 is a typical pipeline schematic showing the pipeline system and pump station. The inertia of the pump, motors, and coupling are generally insufficient to continue the flow of water during the deceleration phase and as a result the water column separates. The rejoining impact developes water hammer which is expressed as a product of the rejoining velocity, the speed of sound in the conduit divided by the gravitational constant. For a pipeline fluid velocity of 5'/sec. (1.52 m/sec.) this would amount to a surge head of liquid superimposed on the pipeline static head of 528' (161 m). There are several means of surge control, the most commom of which is the surge tank shown in Fig. 1 serving as a standby source of water to the pipeline at a decelerating rate to prevent column separation.

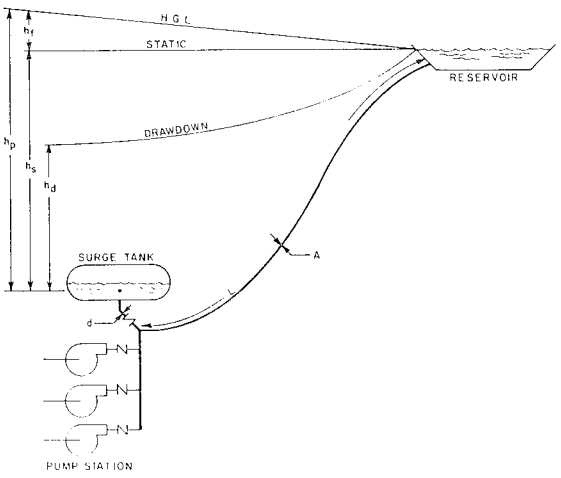

Fig. 1. Surge tank - Pipeline schematic

Another method is a surge control valve with air release and vacuum valves at high points. The later is generally rejected, particularly by the Bureau of Reclamation, because air drawn into the pipeline system causes other problems. Using inertia or flywheels imposes mechanical problems in the fastening of the flywheel to production pumps and motors. Moreover, electrically it is difficult to start because the large inertia mass fastened to the pump shaft must be quickly accelerated to rated speed and the keyways are overstressed.

An unique method to add inertia to the system is to use an independent flywheel motor/generator shown in Fig. 2. To start the FM/G a small induction turning motor is used to bring the unit up to slip speed where upon the unit is put on the line with reduced field excitation. Subsequently excitation is governed by the voltage regulator.

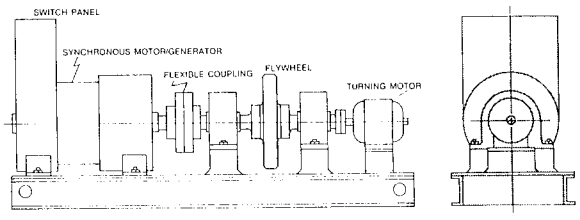

Fig. 2. Outline of flywheel (motor/generator)

The flywheel motor/generator acts as a synchronous condenser improving power factor and reducing voltage blinks during the normal operation of the pump station. Upon power failure the flywheel drives the generator at a decreasing rate and the pumps continue to pump at a reduced rate, thereby preventing column separation in the pipeline. A synchronous motor and a synchronous generator are identical with the exception that the generator is generally provided with damper windings. During normal operation the synchronous motor drives the flywheel, overcoming windage and friction, but during the power outage phase the flywheel drives the generator which supplies reduced electrical power at diminishing frequency to the pump motors.

The method of wiring into the electrical power system is illustrated by the block diagram of Fig. 3. A reverse current switch (common in pumping plants) must be used to prevent the FM/G from powering the utility.

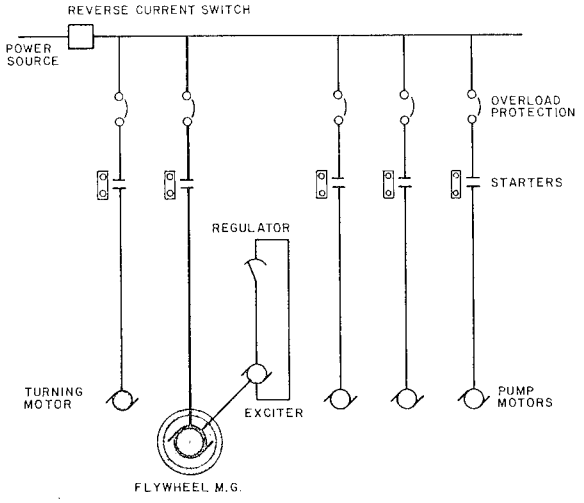

Fig. 3. Electrical block diagram

A typical pumping plant would consist of one or several pumps, either horizontal or vertical, a switch board for pump control, and the FM/G, all as illustrated in Fig. 4.

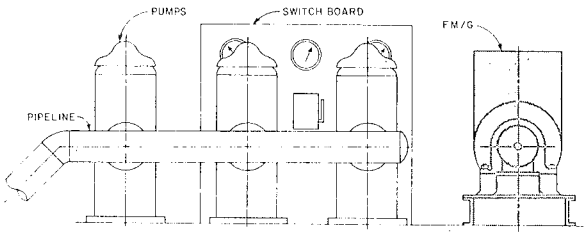

Fig. 4. Typical pump station installation

SIZE OF THE FLYWHEEL INERTIA

The needed flywheel inertia can be sized using the Parmakian method, Ref. 1. After the size has been selected a characteristic computer program may be used to verify the downsurge ratio, h_d/h_p. If however, the results from the characteristic (Streeter) method, Ref. 2, differ, a second approximation may be made and the computer program rerun.

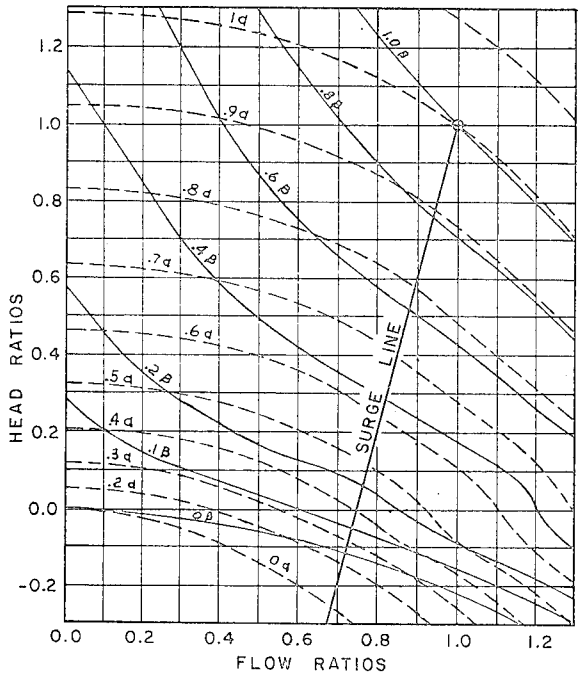

Fig. 5. Pump Characteristics Diagram N_S = 1800 (GPM Units) (34.8 S.I.)

To understand the sizing of the flywheel element the surge characteristics of the pipeline system must be determined. This is expressed in a non-dimensional term "s"; the surge head divided by the system head, and is plotted on the pump characteristic diagram. A typical pump characteristic diagram is presented for specific speed (N_S) of 1800 (34.8 S.I.), Fig. 5. The pump characteristics are plotted in non-dimensional head ratios for the ordinance and flow ratios for the abscissa. A head ratio value can be chosen, h_d/h_p, for a minimum allowable downsurge. Where this value intersects "s" the torque and speed ratios "α" and "β" can be determined as well as the dimensioned flow ratio.

The expression K, the inertia factor which prolongs pumping at a diminished rate, is expressed (Ref. 1) as:

$$K = \frac{BHP(Kw)\cdot C}{\Sigma N^2 \cdot WR^2} \qquad (1)$$

$$C = 8.067\cdot 10^5 (447 \text{ S.I.})$$

The time for the pressure to drop to a chosen stabilized minimum may be expressed as follows:

$$t = 2\,L/a \qquad (2)$$

The inertia factor can now be determined, Ref. 1, as follows by inserting values of α, β, K, and t from Eq. (1) and (2)

$$1 - \alpha = (1 + \beta)\cdot K\cdot t \qquad (3)$$

The initial rotative speed, N_g, of the FM/G for a 60 cycle, 4-pole unit is 1800. Using the values of α, β, t, and the pump rated BHP (KW) and rearranging Eq. (3), the value of WR^2 can be determined, Eq. (4). It is increased by 25% due to pump motor and generator losses in transfering power from the flywheel to pump shafts.

$$WR^2 = \frac{1.25}{N_g^2}\left\{\frac{1+\beta}{1-\alpha}\cdot BPH(Kw)\cdot C\cdot t - N_p^2\cdot WR_p^2\right\} \qquad (4)$$

EXAMPLE OF FLYWHEEL MOTOR/GENERATOR COMPARED TO SURGE TANK

A typical example of the application of a FM/G compared to a surge tank is a sewage force main installed at the Los Angeles County Sanitation District, Long Beach, California Water Reclaimation and Interceptor Sewer Pumping Plant.

The surge tank was selected even though the FM/G was seriously considered. The plant was designed using variable frequency pump drives and there was some skepticism of the effect of variable voltage and frequency on the transistors in the variable frequency control system.

Digital models were prepared for each system. The surge tank did produce surge waves during the "downsurge" process due to switching from pumping by pump to pumping by surge tank. The FM/G however, would have provided a smooth downsurge transition.

The conditions are shown in Table 1. below.

Table 1. Design Conditions - Los Angeles County Sanitation District Project.

L = 7,950 ft. (2,423 m)
A = 4.91 ft.^{2} (5.69 m^2)
a = 3,255 fps (992 m/s)
h_f = 36 ft. (11 m)
h_s = 13 ft. (3.96 m)
h_p = 49 ft. (14.93 m)
h_d = 1.37 ft. (.4176 m)
h_d/h_p = .0279 α = .52 β = 0.2
s = 10.097
t = 4.885 sec.
Pump specific speed = 3,467 (67.1 S.I.)

BHP = 167 (125 KW)
N_p = 875 Min.$^{-1}$
WR^2_p = 274 lb. ft.^{2} (11.5 K_g m^2)

N_g = 1800 Min.$^{-1}$
WR^2_g = 528 lb. ft.^{2} (22.2 K_g m^2)
Gen. WR^2 = 106 lb. ft.^{2} (4.46 K_g m^2)
Flywheel WR^2 = 422 lb. ft.^{2} (17.7 K_g m^2)
Flywheel size = 24 in. dia. (731.5 mm)
x 7 in. (213.4 mm) thick cast iron
Flywheel weight - 806 lb. (365.6 K_g)

The pipeline is constructed of reinforced concrete 7,950 ft. (2,423 m) long with a diameter of 30 in. (914 mm). The buried surge tank is 8 ft. diameter (2.44 m) by 24½ ft. (7.47 m)long. An 18 in. diameter (457 mm) line connects the vessel to the pipeline.

Table 2 details the size, weight, and estimated installed cost of the flywheel motor/generator to the surge tank.

Table 2. Surge Tank Flywheel Motor/ Generator Comparison.

	Surge Tank	Flywheel M/G
Size	8' dia. (2.44 m) x 24½ l_g (7.47 m)	10' L_g (3.05 m) x 2' W (.61 m) x 59" high (1.4 m)
Weight	11,600 lbs. (5,262 kg)	3,600 lbs. (1,633 kg)
Installed Cost-1980 dollars	$61,000	$50,000

The estimated cost of the flywheel generator includes electrical panels as follows:

Table 3. Free Standing Control Panel, Nema I Construction.

Motor Section

1 - across the line motor starter with overload and undervoltage protection for the turning motor
1 - main run contactor for motor/generator
1 - control transformer with fuse
1 - set start/stop pushbuttons
1 - ammeter
1 - metering current transformer
1 - time delay relay for motor starter

Generator Section

1 - voltmeter
1 - ammeter
3 - metering current transformers
1 - voltmeter/ammeter selector switch, combined
1 - voltage regulator with volts per Hertz assembly

1 - power factor controller
1 - reverse power relay to switch the controls from the motor circuit to the generator circuit
1 - set of auxiliary control relays as required

The return surge is regulated by the air trapped in the tank which acts as a pneumatic spring, while in the case of the FM/G, slow closing check valves are used to regulate the return surge.

CONCLUSIONS

Some of the drawbacks to the surge tank are size, location, aesthetics, and the problem of cleaning sewage filled surge tanks. In addition, surge tanks do require, if they are hydropneumatic, special level controls, compressors, and high and low alarms. If they are vented tanks, where air is drawn in and slowly released, fresh water purge systems are required to prevent valve fouling. The connecting line from surge tank to main line is sometimes a problem. Too long a line complicates the surge analysis because it introduces additional inertia.

With a flywheel motor/generator there are none of the problems enumerated above. The system is all electric and the installation costs are generally less. Each time there is a power outage it is necessary for an attendant to restart the FM/G. It must be on the line before individual pumps are started. Starting can be automated but this is an additional cost. However, for pumping plants power outage restarting is generally not automated. The FM/G also corrects power factor since it is a synchronous motor operating at a very low load and replaces static condensers. Voltage blinks and small variations in the voltage supply to the pumping plant are also corrected by the FM/G. Computer systems, flow indicators, etc. in the pumping plant requires steady voltage.

REFERENCES

1 Parmakian, John, "Waterhammer Analysis", Dover Publications, Inc., New York, 1963.

2 Streeter, Victor L. and Wylie, E. Benjamin, "Hydraulic Transients", McGraw-Hill, 1962.

3 Bergeron, L., "Water Hammer in Hydraulics and Wave Surges in Electricity" John Wiley and Sons, New York, 1961.

4 Everett, Wm. S., "A Simplified Method for Sizing of Hydropneumatic Surge Chambers", ASME Fluid Transients and Acoustics in the Power Industry, Winter Annual Meeting, San Francisco, 1978.

MAXIMUM ENERGY DENSITIES FOR COMPOSITE FLYWHEELS

Donald E. Johnson
Avco Systems Division
Wilmington, Massachusetts 01887

and

James J. Gorman
U. S. Department of Transportation
Cambridge, Massachusetts 02142

ABSTRACT

A theoretical derivation of the maximum energy densities for composite flywheels is presented. The formulation is based on the Virial Theorem and is sufficiently general to include composite wheels, isotropic wheels, and hybrid wheels composed of several different materials either orthotropic or isotropic. The results provide simple rules for computing the maximum possible energy density without recourse to the usual parametric computer stress analyses. Of particular interest are the rules presented for hybrid rotors. In addition, the theoretical approach is used to develop a shell rotor design which appears to have a number of practical advantages.

INTRODUCTION

A primary goal of flywheel rotor design is to achieve the maximum possible energy density, i.e., the maximum stored kinetic energy per unit rotor weight. The maximum energy density depends on the overall rotor geometry and on the geometry and properties of each constituent material making up the rotor. Although it would seem that the wide choice of geometries and material properties could be combined to achieve very high energy densities, it is well known that there are theoretical limits on the maximum energy densities beyond which the designer cannot penetrate. These limits are known for a small number of cases, such as for the isotropic (Stodola) disc.[1] For hybrid and composite rotors, the evidence of limits is less complete, and is often deduced from stress analysis on narrowly defined geometries and material properties. The purpose of this paper is to present a general method for determining the maximum energy densities for these more complex rotors and to give specific rules for a variety of cases.

The development presented here begins with the Virial Theorem and then applies it to the set of general continuum problems listed below.

1. Isotropic disc (Stodola)
2. Composite disc
3. Hybrid disc
4. Shell rotor

In each case, the appropriate maximum stress failure theories are used, and analytical assumptions are presented.

VIRIAL THEOREM

We consider the Virial Theorem[2,3] as it applies to the case of a rotor undergoing constant spin. The rotor is treated as an isolated system of N interacting particles. Let a scalar function X be defined by the following sum of scalar products.

$$\chi = \sum_{a=1}^{N} \bar{p}_a \cdot \bar{r}_a \qquad (1)$$

Where $\bar{p}_a$ and $\bar{r}_a$ are the momentum and position vectors of the particles. For the constant spin rotor, the momentum vector $\bar{p}_a$ is in the tangential (hoop) direction. If the origin of the position vector is taken on the axis of spin, then the vector $\bar{r}_a$ remains perpendicular to $\bar{p}_a$ as they both rotate. Consequently,

$$\chi = \sum_{a=1}^{N} \bar{P}_a \cdot \bar{r}_a = 0 \qquad (2)$$

Differentiation with respect to time gives

$$\sum_{a=1}^{N} \dot{\bar{P}}_a \cdot \bar{r}_a = -\sum_{a=1}^{N} \bar{P}_a \cdot \dot{\bar{r}}_a = -\sum_{a=1}^{N} m_a V_a^2 = -2T \qquad (3)$$

Where T is the kinetic energy of the system.

The derivative of the momentum $\dot{\bar{P}}_a$ equals $\bar{F}_a$ is the force on the particle due to all the other particles in the system. Thus Eq. (3) becomes

$$T = -\frac{1}{2} \sum_{a=1}^{N} \bar{F}_a \cdot \bar{r}_a \qquad (4)$$

which is the virial theorem.

APPLICATION TO CONTINUUM

For the constant spin rotor, the vectors $\bar{r}_a$ and $\dot{\bar{r}}_a$ remain perpendicular to the axis of spin. Hence, Eq. (2-4) are unchanged if $\bar{r}_a$ is replaced by its radial component $r_a \bar{e}_r$, where r_a is the local rotor radius and $\bar{e}_r$ is a unit vector in the radial direction. Noting that $V_a = \Omega r_a$, Eq. (4) can be put in the form

$$\sum_{a=1}^{N} (\bar{F}_a \cdot r_a \bar{e}_r) + \sum_{a=1}^{N} m_a \Omega^2 r_a^2 = 0 \qquad (5)$$

The continuum equivalent of Eq. (5) can also be obtained by writing the equilibrium in the radial direction, multiplying it by $r dV$, and then integrating it over the volume of the rotor. This then is the procedure used in this paper.

APPLICATION TO SPINNING DISK

We assume that the stresses σ_r , σ_θ , and $\sigma_{r\theta}$ do not vary through the thickness of the disk. The equation of equilibrium for a differential element of thickness h and unit area then becomes:

$$\frac{\partial h\sigma_r}{\partial r} + \frac{1}{r} \frac{\partial h\sigma_{r\theta}}{\partial \theta} + \frac{h(\sigma_r - \sigma_\theta)}{r} + \rho \Omega^2 r h = 0 \qquad (6)$$

According to the procedure established in the preceding section, we next multiply this equation by r and convert it into the appropriate volume integral. This gives,

$$\int_{r_i}^{r_o} \int_{\theta_1}^{\theta_2} r \left[\frac{\partial h\sigma_r}{\partial r} + \frac{1}{r} \frac{\partial h\sigma_{r\theta}}{\partial \theta} + \frac{h(\sigma_r - \sigma_\theta)}{r} + \rho \Omega^2 r h \right] r\, d\theta\, dr = 0 \qquad (7)$$

In Eq. (7), r_i - the inside radius, r_o = the outside radius, and $\theta_2 - \theta_1 = 2\pi^o$.

A key relation used to change (7) is:

$$\frac{\partial}{\partial r}(r^2 h \sigma_r) = r h \sigma_r + r \frac{\partial}{\partial r}(r h \sigma_r) \qquad (8)$$

using (8), Eq. (7) becomes:

$$\int_{r_i}^{r_o} \int_{\theta_1}^{\theta_2} \left[\frac{\partial}{\partial r}(r^2 h \sigma_r) + r \frac{\partial h\sigma_{r\theta}}{\partial \theta} - r h (\sigma_\theta + \sigma_r) + \rho \Omega^2 r^3 h \right] d\theta\, dr = 0 \qquad (9)$$

The next step is to introduce the maximum stress allowable σ as follows:

$$\sigma_\theta = \sigma + (\sigma_\theta - \sigma) \,, \quad \sigma_r = \sigma + (\sigma_r - \sigma) \qquad (10)$$

Substituting (10) into (9) and integrating gives:

$$I_1 + I_2 - 2\sigma V + I_3 + I_4 + 2T = 0 \qquad (11)$$

where

$$I_1 = \int_{\theta_1}^{\theta_2} r^2 h \sigma_r \Big|_{r_i}^{r_o} d\theta \qquad (12)$$

$$I_2 = \int_{r_i}^{r_o} r h \sigma_{r\theta} \Big|_{\theta_1}^{\theta_2} dr \qquad (13)$$

$$I_3 = \int_{r_i}^{r_o}\int_{\theta_1}^{\theta_2} (\sigma - \sigma_\theta)\, r h \, d\theta\, dr \qquad (14)$$

$$I_4 = \int_{r_i}^{r_o}\int_{\theta_1}^{\theta_2} (\sigma - \sigma_r)\, r h \, d\theta\, dr \qquad (15)$$

$$V = \int_{r_i}^{r_o}\int_{\theta_1}^{\theta_2} r h \, d\theta\, dr \qquad (16)$$

$$T = \int_{r_i}^{r_o}\int_{\theta_1}^{\theta_2} \rho \Omega^2 r^3 h \, d\theta\, dr \qquad (17)$$

Explanation of I_1, I_2, I_3, I_4 is as follows. Because the radial stress equals 0 at the inside or outside edge, $I_1 = 0$ for a hollow or solid wheel. Even if the wheel is not axisymmetric, periodicity in θ gives $I_2 = 0$. And since $\sigma_\theta \leq \sigma$, $\sigma_r \leq \sigma$, we have $I_3 \geq 0$, $I_4 \geq 0$.

Solving Eq. (11) for the energy density gives

$$\frac{\text{Kinetic Energy}}{\text{Weight}} = \frac{T}{\rho g V} = \frac{\sigma}{\rho g} - \frac{I_3 + I_4}{2W} \qquad (18)$$

by virtue of $I_3 \geq 0$, $I_4 \geq 0$, Eq. (18) becomes:

$$\frac{T}{W} \leq \frac{\sigma}{\rho g} \qquad (19)$$

It is customary to define the shape factor K_s by:

$$\frac{T}{W} = K_s \cdot \frac{\sigma}{\rho g} \qquad (20)$$

Hence:

$$K_s \leq 1 \qquad (21)$$

Implications. Equation (21) confirms the well-known Stodola wheel result. However, the theoretical development is not strictly limited to isotropic wheels and in subsequent sections will be generalized to composite and hybrid wheels. Other characteristics of this derivation are: (1) It is not limited to axisymmetric wheels, (2) Material constitutive equations are not involved, (3) The density is assumed constant throughout, and (4) It utilizes the same stress allowable, σ, in each of the r and θ directions.

Examination of Eq. (14), (15) and (18) shows that the maximum energy density is reached when there is a state of constant stress. ($\sigma_r = \sigma_\theta = \sigma$, $I_3 = I_4 = 0$). This agrees with the intuitive design strategy seeking to approach a uniform stress wheel.

APPLICATION TO COMPOSITE DISK

We next extend the previous derivation to include a wheel composed of layers alternately reinforced in the hoop and radial directions. This is sometimes referred to as bidirectional[4] wheel. We consider the special case in which the same material is used in each layer (same relative volume fraction of fibers) and the anisotropy is obtained from the differing fiber directions and by using different thicknesses for the hoop versus radial layers. The approach is then to modify the derivation (Eq. 9 and 21) to accommodate this configuration. This is done by recognizing that the stresses (σ_r, σ_θ) are average stresses through the thickness and by replacing the $h(\sigma_\theta + \sigma_r)$ term in Eq. (9) as follows:

$$h(\sigma_\theta + \sigma_r) = h_\theta \sigma_{\theta_L} + h_r \sigma_{r_T} + h_r \sigma_{r_L} + h_\theta \sigma_{\theta_T} \qquad (22)$$

in which:

h_θ = thickness in hoop (reinforced) layer

h_r = thickness of radial (reinforced) layer

σ_{θ_L} = longitudinal stress in hoop layer (23)

σ_{θ_T} = transverse stress in hoop layer

σ_{r_L} = longitudinal stress in radial layer

σ_{r_T} = transverse stress in radial layer

Next, the analogous relations in terms of stress allowables:

$$\begin{aligned} \sigma_{\theta_L} &= \sigma_L + (\sigma_{\theta_L} - \sigma_L) \\ \sigma_{r_L} &= \sigma_L + (\sigma_{r_L} - \sigma_L) \\ \sigma_{\theta_T} &= \sigma_T + (\sigma_{\theta_T} - \sigma_T) \\ \sigma_{r_T} &= \sigma_T + (\sigma_{r_T} - \sigma_T) \end{aligned} \tag{24}$$

Where σ_L = the longitudinal stress allowable

σ_T = the transverse stress allowable

The result of these substitutions is:

$$I_3 + I_4 = \int_{r_i}^{r_o}\int_{\theta_1}^{\theta_2} h_\theta\left[(\sigma_L - \sigma_{\theta_L}) + (\sigma_T - \sigma_{\theta_T})\right] + h_r\left[(\sigma_L - \sigma_{r_L}) + (\sigma_T - \sigma_{r_T})\right] r\, d\theta\, dr \tag{25}$$

and

$$\frac{T}{W} = \frac{(\sigma_L + \sigma_T)}{2\rho g} - \frac{(I_3 + I_4)}{W} \tag{26}$$

Because the various stresses are assumed to be less than or equal to their respective allowables, Eq. (25) gives $I_3 + I_4 \geq 0$, and

$$\frac{T}{W} \leq \frac{\sigma_L + \sigma_T}{2\rho g} \qquad K_s = \frac{1 + \frac{\sigma_L}{\sigma_T}}{2} \tag{27}$$

Here the K_s is defined in terms of σ_L. For most high strength laminated composites σ_T is much less than σ_L, and $K_s \approx .5$, the value commonly understood to be the maximum K_s for this type of layup.[5]

APPLICATION TO HYBRID DISK

Consider the hybrid disk made up of N rings of different materials. We denote a given ring by the index of j.

Define:

h_j = thickness of j^{th} ring

σ_{r_j} = radial stress in j^{th} ring

σ_{θ_j} = hoop stress in j^{th} ring

σ_j = stress allowable in j^{th} ring*

r_j, r_{j+1} = inner, outer radii of j^{th} ring

The integral I_1 in Eq. (12) then becomes:

$$I_1 = \sum_{j=1}^{N} \int_{\theta_1}^{\theta_2} r^2 h_j \sigma_{r_j} \Big|_{r_j}^{r_{j+1}} d\theta \tag{29}$$

It can be shown that, to satisfy equilibrium across the boundary between two rings

$$h_{j+1}\, \sigma_{r_{j+1}}\Big|_{r_j} = h_j\, \sigma_{r_j}\Big|_{r_j} \tag{30}$$

Using (30), one can show that $I_1 = 0$.

For this problem, I_3 is of the form

$$I_3 = \sum_{j=1}^{N} \int_{r_j}^{r_{j+1}}\int_{\theta_1}^{\theta_2} (\sigma_j - \sigma_{\theta_j})\, r\, h_j\, d\theta\, dr \tag{31}$$

and because the stresses do not exceed the allowables in each ring, we have $I_3 \geq 0$.

In a similar fashion, one can show that $I_4 \geq 0$. The analogue of Eq. (16) gives the volume V as follows:

$$V = \sum_{j=1}^{N} \delta V_j \;, \quad \delta V_j = \int_{r_j}^{r_{j+1}}\int_{\theta_1}^{\theta_2} r\, h_j\, d\theta\, dr \tag{32,33}$$

Working through the analogous derivation, one obtains in place of Eq. (19), the following:

$$\frac{T}{W} \leq \frac{\sum_{j=1}^{N} \frac{\sigma_j}{\rho_j g}\, \delta W_j}{W} \tag{34}$$

Where $\delta W_j = \rho_j g\, \delta V_j$ = the weight of the j^{th} ring.

Implications. This result (34) indicates that the energy density of the multi-ring hybrid configuration will not exceed the weighted average of the maximum energy

*Note that the present derivation is limited to equal allowable stresses in the hoop and radial directions.

densities achievable in wheels composed of one of the constituent materials alone. The weighting in this average is the weight of each material. For example, consider a wheel made up of two different materials, (Material #1 and Material #2), i.e., a two-ring wheel. If the maximum energy density for a flywheel of Material #1 is 50 watt-hours/pound and for a flywheel of Material #2 is 30 watt-hours/pound, and if a ring-type hybrid wheel is fabricated with 70% (by weight) of Material #1 and 30% of Material #2, then the maximum possible energy density for the hybrid wheel is given by:

.7 x 50 + .3 x 30 = 44 watt-hours/pound.

This kind of information is useful in setting design strategies and goals at the onset of a project.

APPLICATION TO SHELL ROTOR

A somewhat different rotor application of the Virial Theorem approach is the spinning shell structure shown in Fig. 1.

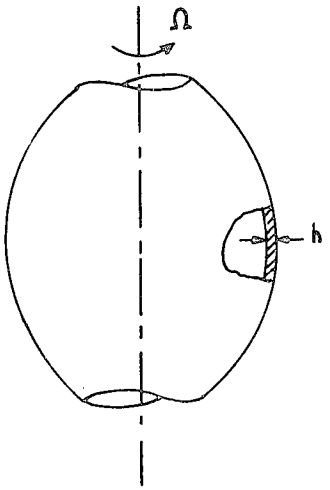

FIGURE 1: SCHEMATIC OF SPINNING SHELL FLYWHEEL

Several potential advantages could result from the use of spinning shell structures (1) The attachment could be made an integral part of the structure, thus reducing the attachment problems typical of flat disks, (2) Two separate attachment points should improve structural dynamics, (3) A sphere-like shape would result in more efficient vacuum chamber design, (4) The shell structure might be more easily contained at failure, and (5) If a laminated composite is used, the plys would be continuous in the region of maximum radius, thus avoiding edge effect problems that are typical in quasi-isotropic and other wheels.

To apply the theoretical approach to this problem, we use membrane shell theory and neglect bending. For the current application, we also assume a shell of constant thickness and with equal allowable stresses in the longitudinal (φ) and circumferential directions (θ). Starting with Timoshenko's[6] membrane equations, summing forces in the radial direction gives the following equation of equilibrium.

$$\frac{d}{d\varphi}(\cos\varphi\ \sigma_\varphi r_o) - \sigma_\theta r_1 + r_1 r_o^2 \Omega^2 \rho = 0 \qquad (35)$$

The geometric variables φ, r_o, r_1 are shown in Fig. 2.

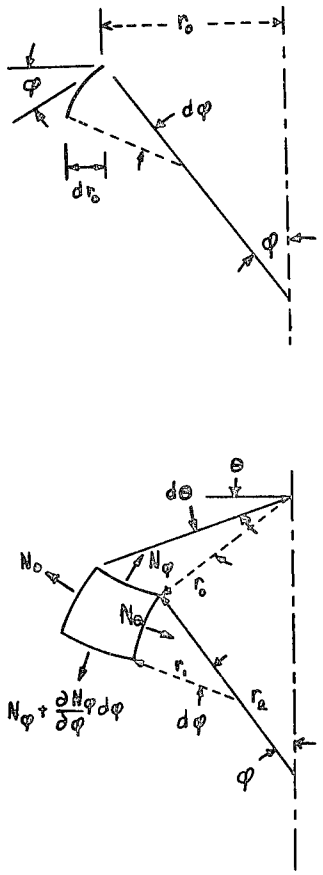

FIGURE 2: SHELL ELEMENT GEOMETRY

The elemental volume dV is given by $h r_1 r_0 \, d\varphi \, d\theta$, where h is the thickness of the shell. Following the Virial Theorem approach, we multiply Eq. (35) by the local radius r_0 and integrate over the surface. The result is:

$$\frac{T}{W} = \frac{1}{2}\frac{\sigma}{\rho g}\left[1 + \frac{\int_{\varphi_1}^{\varphi_2} r_0 r_1 \cos^2\varphi \, h \, d\varphi}{\int_{\varphi_1}^{\varphi_2} r_0 r_1 \, h \, d\varphi}\right] - \frac{I_A + I_B}{2W} - \frac{I_C}{W} \qquad (36)$$

Where:

$$I_A = \int_{\varphi_1}^{\varphi_2}\int_{\theta_1}^{\theta_2} r_0 r_1 \cos^2\varphi \; h(\sigma - \sigma_\varphi) \, d\varphi \, d\theta \qquad (37)$$

$$I_B = \int_{\varphi_1}^{\varphi_2}\int_{\theta_1}^{\theta_2} r_0 r_1 \, h(\sigma - \sigma_\theta) \, d\varphi \, d\theta \qquad (38)$$

$$I_c = \pi\left(\cos\varphi \, h \sigma_\varphi \, r_0^2\right)\Big|_{\varphi_1}^{\varphi_2} \qquad (39)$$

The terms I_A and I_B are analogs of I_4 and I_3 (Eq. 14-15) and can likewise be shown to satisfy $I_A \geq 0$, $I_B \geq 0$. If the shell extends to $r_o = 0$, then $I_c = 0$. In such a case:

$$K_s \leq \frac{1}{2}\left[1 + \frac{\int_{\varphi_1}^{\varphi_2} r_0 r_1 \cos^2\varphi \, h \, d\varphi}{\int_{\varphi_1}^{\varphi_2} r_0 r_1 \, h \, d\varphi}\right] \qquad (40)$$

From Eq. (40) we can expect the maximum possible value of K_s to be between 1/2 and 1. The derivation is based on use of the same stress allowable, σ , in both the φ and θ directions. Hence, it would apply directly to a material with isotropic strength properties for which, by comparison, the spinning disc can have a shape factor of up to 1.0. The value of $K_s = 1.0$ is only obtainable with infinite radius Stodola shapes: practical optimal isotropic discs achieve shape factors up to approximately .93. Hence, it is of great interest to examine promising shell shapes and determine the values of K_s obtained.

Constant Stress Shell Rotors. From Eq. (37), (38) and (36), it can be seen that the energy density is greatest when $I_A = I_B = 0$, i.e., for the constant stress wheel. A series of constant stress shell shapes were obtained by setting $\sigma_\varphi = \sigma_\theta = \sigma$ in Eq. (35), transforming the resulting differential equation into r, θ, z cylindrical coordinates, and solving the equations numerically. Unlike the constant stress Stodola disc, there is a whole family of constant stress shell shapes which are functions of the parameter r_1/R, the ratio of the two radii of curvature at the location of maximum radius. These shapes are shown in Fig. 3 as functions of the parameter λ , given by:

$$\lambda = \frac{R^2 \Omega^2 \rho}{\sigma} = 1 + \frac{R}{r_1}$$

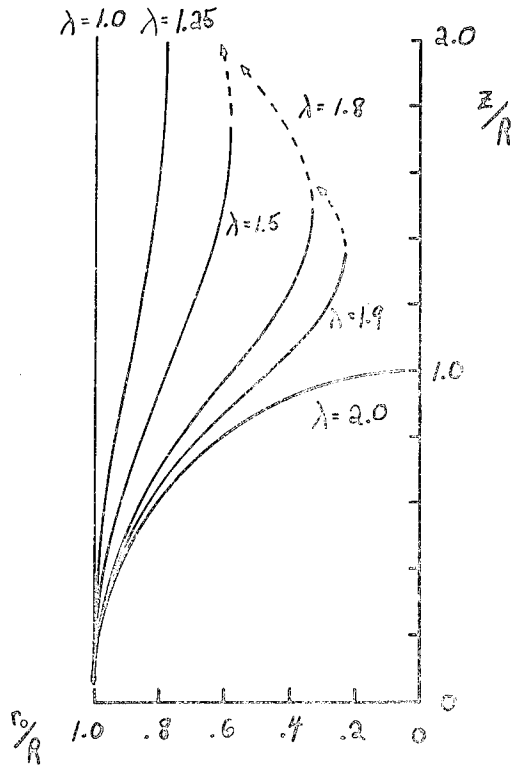

FIGURE 3: CONSTANT STRESS SHELL GEOMETRIES AS A FUNCTION OF λ

The shape factors associated with these shapes are shown in Fig. 4 as a function of λ.

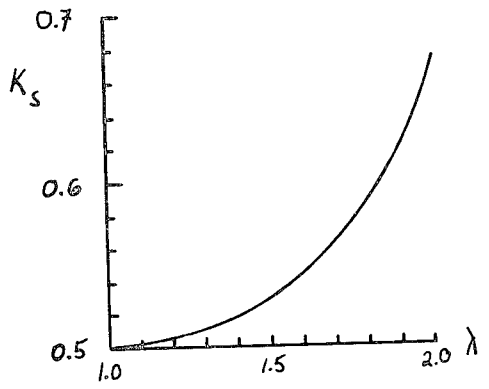

FIGURE 4: K_s vs. λ FOR CONSTANT STRESS SHELLS

For $\lambda = 2$, the equations are integrable in closed form and give a spherical shape with a shape factor K_s of 2/3. As the parameter λ is decreased to 1, the shape factors decrease to .50 as shown in the figure. The limiting case of $\lambda = 1$ represents a spinning cylinder (or ring) for which the shape factor of .5 is well-known.

The shapes shown in Fig. 3 appear to have practical value. A curve such as that shown for $\lambda = 1.9$ could be attached to a small support wheel at its minimum radius.

For $\lambda > 2$ it can be shown analytically that constant stress solutions do not exist for the isotropic strength case for:

$$r_o < \left(1 - \frac{2}{\lambda}\right)^{1/4} R$$

Where R equals the maximum radius. Potential use of cases for $\lambda > 2$ is unclear at the present time.

The family of shapes shown in Fig. 3 do not give shape factors as high as the Stodola wheel ($K_s = 1.0$) but may have advantages that more than offset this disadvantage. If one includes the weights of attachment, vacuum chamber, and containment structure, it is possible that the shell shapes will give a higher overall energy density.

It should also be pointed out that advantages might accrue in more general shell shapes than those given here for the constant thickness, isotropic strength shells. Tapered thicknesses and orthotropic strengths associated with the shell analogs of the bidirectionally reinforced composite layups might lead to greater energy densities.

CONCLUSIONS

A general theoretical method for predicting the maximum possible energy densities of flywheel rotors has been presented. The method, based on the Virial Theorem, is used to give results for various types of rotors including isotropic disks, laminated composite disks, hybrid disks, and shell rotors. The results contained check with the few cases where results were previously known. The often used intuitive approach of designing for constant stress is shown mathematically to lead to optimal energy densities.

The results provide simple rules for computing maximum possible energy densities for various material combinations and/or wheel configurations before stress analysis is undertaken. This can be of great value in setting realistic design goals during preliminary design. In addition, the method can be rather easily extended to a number of promising cases such as hybrid laminated composite disks and laminated shell rotors.

REFERENCES

1. Stodola, A., Steam and Gas Turbines, Vols. I and II, McGraw-Hill, New York, 1927.

2. Ter Haar, D., Elements of Hamiltonian Mechanics, North-Holland Publishing Co., Amsterdam, 1964.

3. Bradbury, T.C., Theoretical Mechanics, John Wiley & Sons, Inc., New York, 1968.

4. Johnson, D., and Gorman, J., "The Effect of Interlaminar Stresses in Composite Flywheel Design", Fibrous Composites in Structural Design. Proceedings of 4th Conference of Fibrous Composites in Structural Design, Nov. 14-17, 1978.

5. Christensen, R.M., and Wu, E.M., "Optimal Design of Anisotropic (Fiber-Reinforced) Flywheels", University of

California, Lawrence Livermore Laboratory Report, UCRL-52169, November 2, 1976.

6. Timoshenko, S., and Woinowsky-Krieger, S., Theory of Plates and Shells, McGraw-Hill, New York, 1959.

TORQUE TRANSFER IN COMPOSITE FLYWHEELS

Dr. K. R. Berg
Riggs Engineering Corporation
8245A Ronson Road, San Diego, CA 92111

ABSTRACT

The primary interest in composite flywheels centers around the weight efficiency in energy storage achieved by high strength fibrous materials. An important secondary factor that is often overlooked is the transfer of torque into and out of the flywheel through shear forces. Although fibrous materials oriented properly have excellent shear properties inplane, these materials exhibit relatively poor shear properties transverse to the plane for any orientation. The fibrous orientation best for shear is also relatively poor for tension.

For relatively low power input/output systems the inplane shear loading is also low. But as demands for a greater power exchange increases, so do the shear requirements.

In this paper the shear transfer requirements versus power requirements are discussed. An analysis of the effects of the hoop plus radial biaxial stress in the web of a rotating flywheel, in combination with input/output torque shear stress, is discussed. A discussion of the failure criteria under these combined loads indicates the differences compared to a shear only analysis. This state of combined stress reduces the allowable torque transfer capability.

For relatively shallow ring designs the web to ring shear transfer may not be a problem. As the ring depth increases however there may be an interlaminate shear transfer problem. However this problem will not be discussed in this paper.

INTRODUCTION

The primary interest in composite flywheels centers around the weight efficiency in energy storage achieved by high strength fibrous materials. An important secondary factor that is often overlooked is the transfer of torque into and out of the flywheel through shear forces. This paper discusses the shear transfer in a particular flywheel design, a filament wound "delta" type. This type of flywheel consists of a circumferentially wound rim (or rims) and a web. The web connects the rim to the input/output shaft. Since the web is an integral part of the flywheel it is subjected to rotational stresses combined with the input/output torque.

Thus this paper considers two aspects of the web design,

1. Effects of shear stress on the power transfer requirements.
2. Effects of combined loading on the shear transfer capability.

INPUT/OUTPUT POWER

For a flywheel spinning without friction (bearing or air friction) no torque or shear transfer to the energy storage ring is required. However all practical flywheels require energy input and output. The rate at which energy is input or output then determines the shear forces which must be considered in the design.

Consider a flywheel design based on tape wrapping as shown on Fig. 1 and Fig. 2. This type of flywheel has been referred to as "Bandwrap" or "Deltawrap Overwrapped Rim".[1] This type of flywheel has been stress analyzed.[2] The torque is transmitted from the shaft through the web to the flywheel ring. Although the attachment of the web to the ring is an important consideration, it will not be discussed at this time.

Due to the method of winding, the thickness of the web varies parabolically, with the maximum thickness occuring at the shaft radius. The thickness of the web varies as shown on Fig. 3. Due to the winding pattern, the fiber orientation also varies with radius. This variation in orientation is shown on Fig. 4.

The torque requirements vary not only with power requirements but also with the ring mass (geometry). Neglecting the mass of the web (not a good assumption in some cases) would result in the following analysis of torque versus power.

Consider a Kevlar ring of inside radius R1 and outside radius R2. The mode of failure versus radius ratio R1/R2 = B2 is shown on Fig. 5 for various rotational speeds. The energy per unit width is shown on Fig. 6 for the radius at which failure occurs. The crossover point is where the radial and circumferential failure stresses occur simultaneously.

The torque requirements are based on the rate of change of energy, input or output.

For a ring of thickness t_1, (R2 - R1) the energy at a rotational velocity of ω is,

$$E = \frac{\pi}{4} \omega^2 \rho R_2^4 (1 - B_2^4) b \qquad (1)$$

b - ring width

The power input/output is the time rate of change of the energy,

$$P = \frac{dE}{dt} = \frac{\pi}{2} \omega a \rho R_2^4 (1 - B_2^4) b \qquad (2)$$

where a is the rotational acceleration.

The torque is,

$$T = P/\omega \qquad (3)$$

Thus the torque requirements of the web are a function of the power requirements and the rotational speed. For a vehicle, the torque requirements are perhaps the more important. On that basis a curve of torque versus power can be plotted for various rotational speeds utilizing the parameters shown on Fig. 6.

Shown on Fig. 7 is the relation between the torque required to be transmitted through the web and the power demand.

SHEAR STRESSES IN WEB DUE TO TORQUE

The torque, T, that can be carried by the web at Radius R is,

$$T = 2 \pi A_1 R_2^2 t_2 F_s \qquad (4)$$

Where F_s is the allowable shear strength for the angle α, Fig. 8, to correspond with position A_1 of Fig. 4.

Define a shear coefficient K8,

$$K8 = T/(R_2^2 t_2) = 2 \pi A_1 F_s \qquad (5)$$

The values of K8 versus the position A1 can be plotted for each of the materials. The plot for graphite/epoxy is shown on Fig. 9.

For a given torque and outside diameter, the web thickness t_2 at R_2 ($A_1 = 1$) becomes proportional to:

$$t_2 \approx 1/K8 \qquad (6)$$

Introducing the material density $\gamma(g/cm^3)$ one can estimate the relative weight efficiency of the web:

$$t_2 \gamma \approx \gamma/K8 \text{ at } A_1 = 1 \qquad (7)$$

The parameters K8 and $\gamma/K8$ were plotted as functions of B_1 in Fig. 10. This figure shows that the graphite fiber composite is the most efficient material for the web. That is a graphite composite web can transmit a greater torque and at a lower weight than Kevlar or glass. This is true for all values of B_1.

As previously stated, the factor K8 represents the capability of the web to carry shear loads along the shear web radius and is based on the shear ultimate stress at the appropriate ± alpha angle. The web has the highest shear efficiency at a radius where the fiber crossing angle is ±45°. The radial location of this point shifts depending on B_1. The resistance to torque decreases from a maximum near mid web to a minimum value at $A_1 = B_1$ at the shaft. At this point the allowable shear strength is a minimum. Therefore, the critical design point for

shear transfer is at the shaft. The K8 values at this radius are plotted in Fig. 11. This diagram illustrates that K8 increases linearly with B_2, that the values for graphite and glass are identical, and that Kevlar is capable of only 71% of their value.

EFFECTS OF COMBINED LOADING ON SHEAR TRANSFER CAPABILITY

The above analysis for torque capability in the web is based on the allowables shown on Fig. 8. However due to the centrifugal field that exists in the web, the allowable ultimate shear strength of the web is not as shown on Fig. 8.

Consider the laminate of Fig. 12, loaded in shear and biaxial tension due to torque loading and a centrifugal field. As shown on Fig. 12 this loading represents a similar loading on each lamina.

A further transformation of axes will result in the loading along and perpendicular to the fiber direction as shown on Fig. 13.

For shear, the addition of biaxial loading in all cases reduces the shear stress capability of the laminate. For biaxial tension the allowable for axial tension increases at certain angles when transverse loading is applied. This can be seen on Fig. 14 where the axial allowable is presented for several cases of biaxial stress ratios. As discussed in Reference 3, the maximum stress theory versus maximum strain was considered. The Hashin and Rotem failure criteria,[4] is shown on Fig. 15.

The results of applying the failure criteria to the shear stresses of a laminate with a $\pm\alpha$ fiber orientation are shown on Fig. 16. Included for reference is the Hoffman failure criteria.[5] The maximum stress and maximum strain curves are taken from Reference 6. A more detailed discussion of failure criteria is available in Reference 7.

Utilizing the failure criteria of Hashin and Rotem the allowable shear stresses of a flywheel web are shown on Fig. 17. Also shown are the effects of a zero centrifugal field and two biaxial tension stress fields of 35 N/mm^2 and 70 N/mm^2. These curves are based on a maximum strain criterion.

FLYWHEEL DESIGN EXAMPLE

Consider a flywheel with a ring of width b = 10 cm and an inside radius R1 = 22 cm and an outside radius of R2 = 28 cm. The failure of the ring circumferentially and radially will occur simultaneously at 40,000 RPM.

Consider a hub diameter of 5.6 cm. The value of F1 = S1/R2 (See Fig. 4) is 0.1. For a graphite/epoxy web the stress coefficient K8 is shown on Fig. 9 for all values of B_1. K8 is the torque capability of the web divided by the outer radius squared and the web thickness at the outer rim, equation (5). Since the web is considered integral with the ring the displacement must be equal at the ring/web interface. The web thickness is a fixed ratio of the ring width, for this example 0.1 of the ring width (b = 10). Also for this example the web is in tension and the ring is in com compression at the rim. Thus the thickness of the web is t_2 = 1 cm at the rim.

The torque capability therefore is,

$$T = K8\ R2^2\ t2 = (420)(28)^2(1)$$

T = 329 KNm Maximum @ A1 = .15

T = 196 KNm Minimum @ A1 = .30

Near the shaft additional reinforcement is necessary as the coefficient drops rapidly (See Fig. 9).

Calculation of the radial and circumferential stresses in the web result in biaxial tension stresses which reduce the allowable shear stress as shown on Fig. 17. Thus the torque transfer capability is reduced accordingly.

SUMMARY

The allowable flywheel torque not only varies due to the changing filament orientation, and changing web thickness, but also varies with the rotational speed. Since the web biaxial tension stress varies with radius, the allowable torque then becomes a function of this biaxial stress at each radius.

REFERENCES

1. Knight, C. E. Jr., Kelly, J. J., Huddleston, R. L. and Pollard, R. E., "Development of the 'Bandwrap' Flywheel", 1977 Flywheel Technology Symposium Proceedings, Oct. 5, 1977, San Francisco, CA

2. Berg, K. R., Flywheel Parametric Analysis, Final Report, REC No. R-7731 Volume I, 1 Feb. 1977, CEA, Paris, France

3. Naar, R. Z., Panora, R. A., Jr. and Halpin, B. M., "Constant Radial Displacement, Thick Wall, Filament Wound Flywheels", 1977 Flywheel Technology Symposium Proceedings, Oct. 5-7, 1977, San Francisco, CA

4. Hashin, Z., Rotem, A., "Failure Modes of Angle Ply Laminates", J. Composite Materials, Vol. 9 (1975) P. 191

5. Hoffman, O., "The Brittle Strength of Orthotropic Materials", J. Composite Materials, Volume 1 (1967) P. 200

6. Berg, K. R., "STR 8", Computer Program Riggs Engineering Corp., May 1980

7. Berg, K. R., "A Discussion of Anisotropic Failure Theories", A technical seminar presented to CASA, 21 April 1980, Madrid, Spain. REC Report No. R-0168

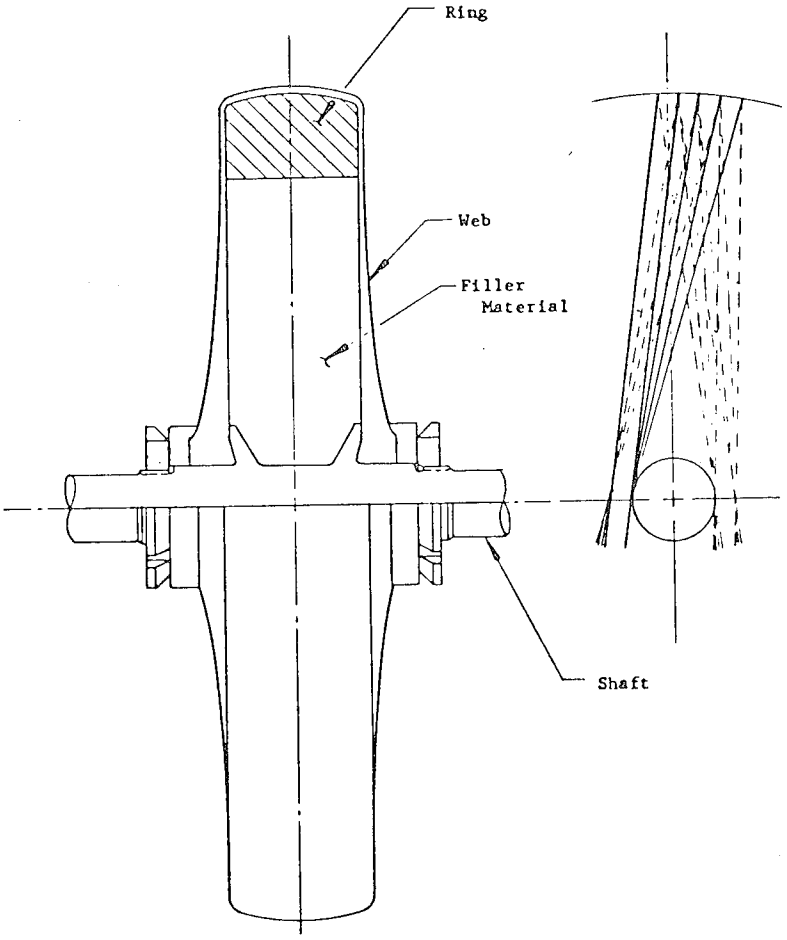

Figure 1 Flywheel Concept

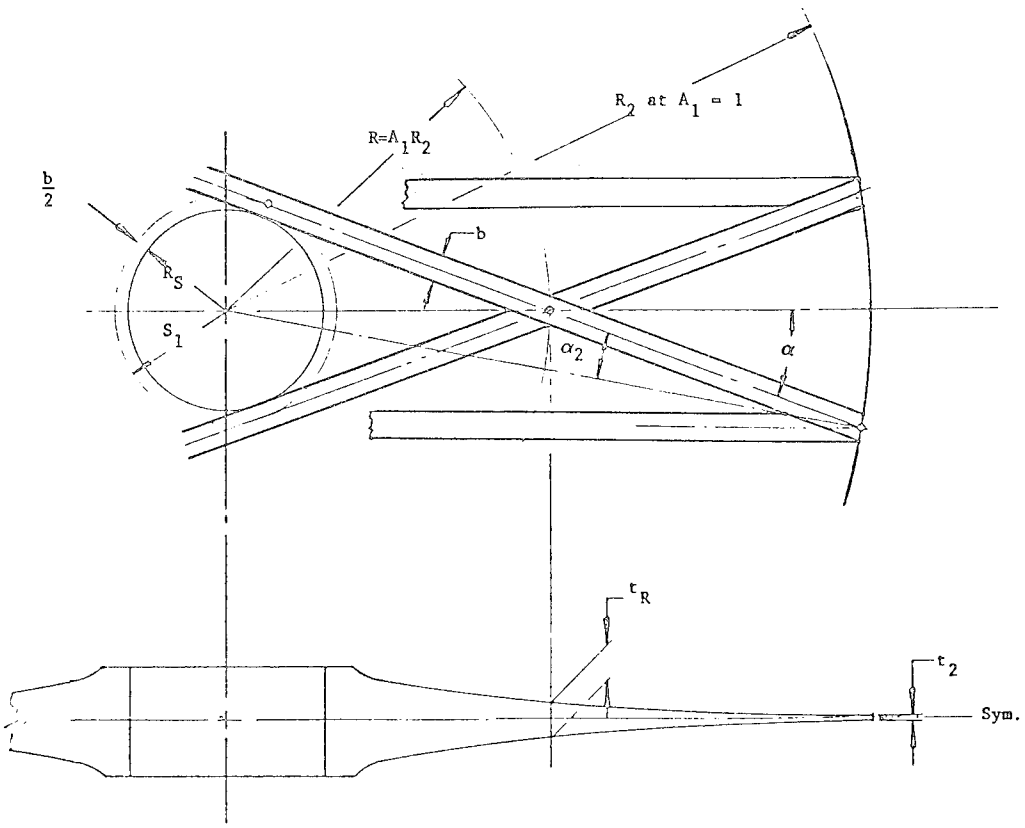

Figure 2 Web Disc Geometry

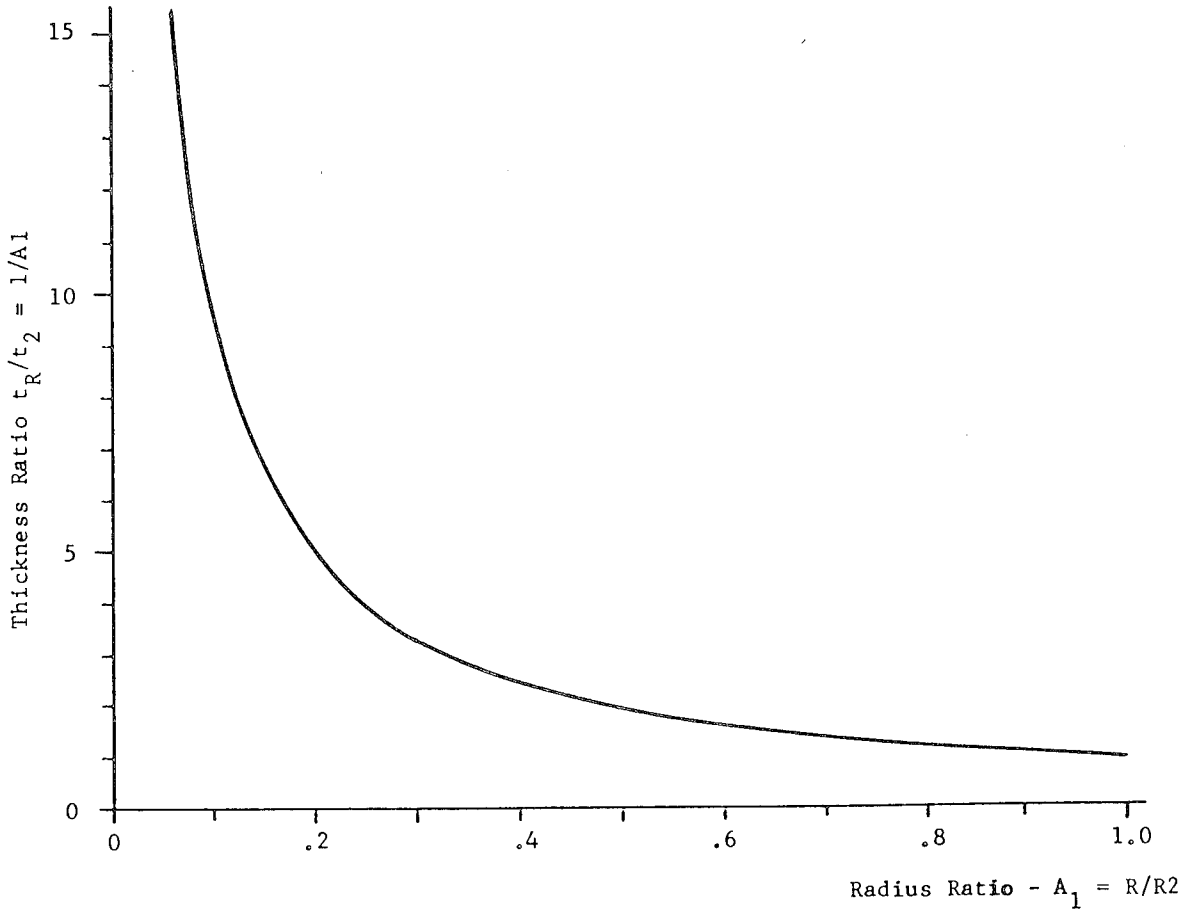

Figure 3 Web Thickness Distribution

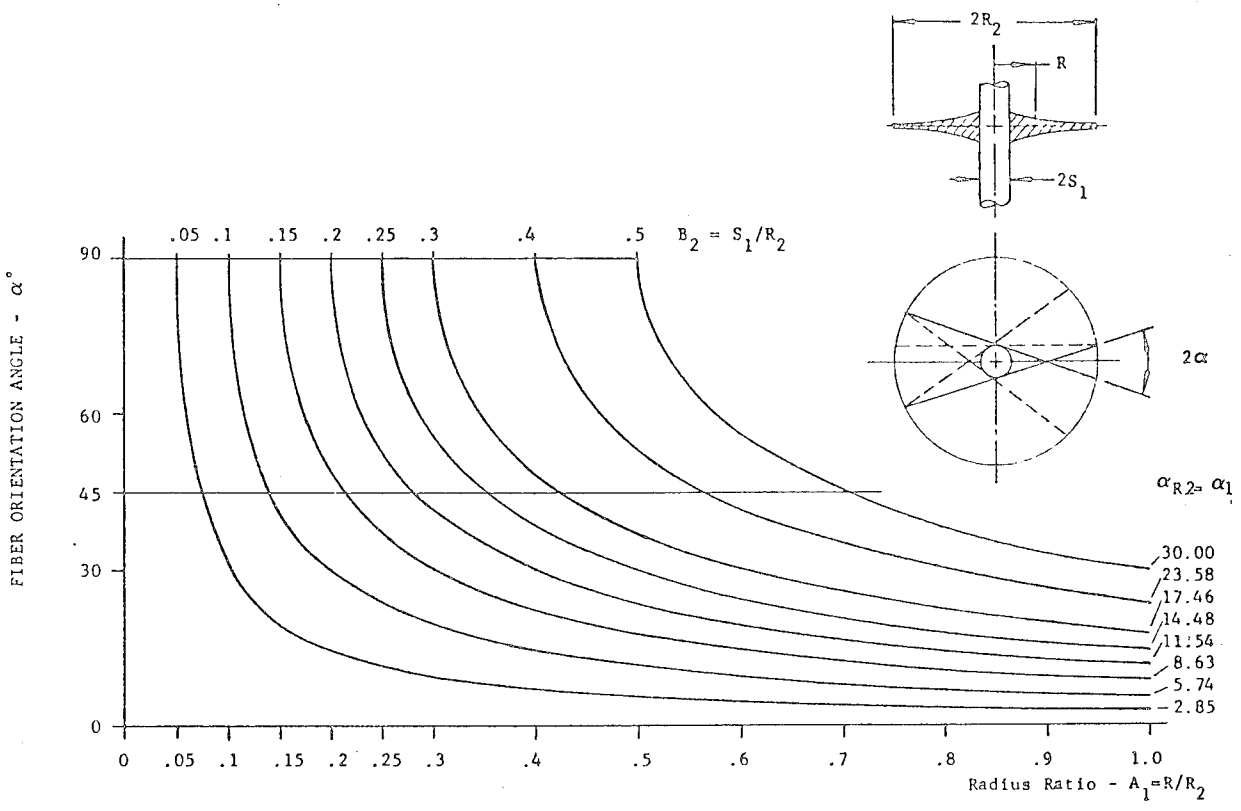

Figure 4 Web Fiber Orientation Versus Radius

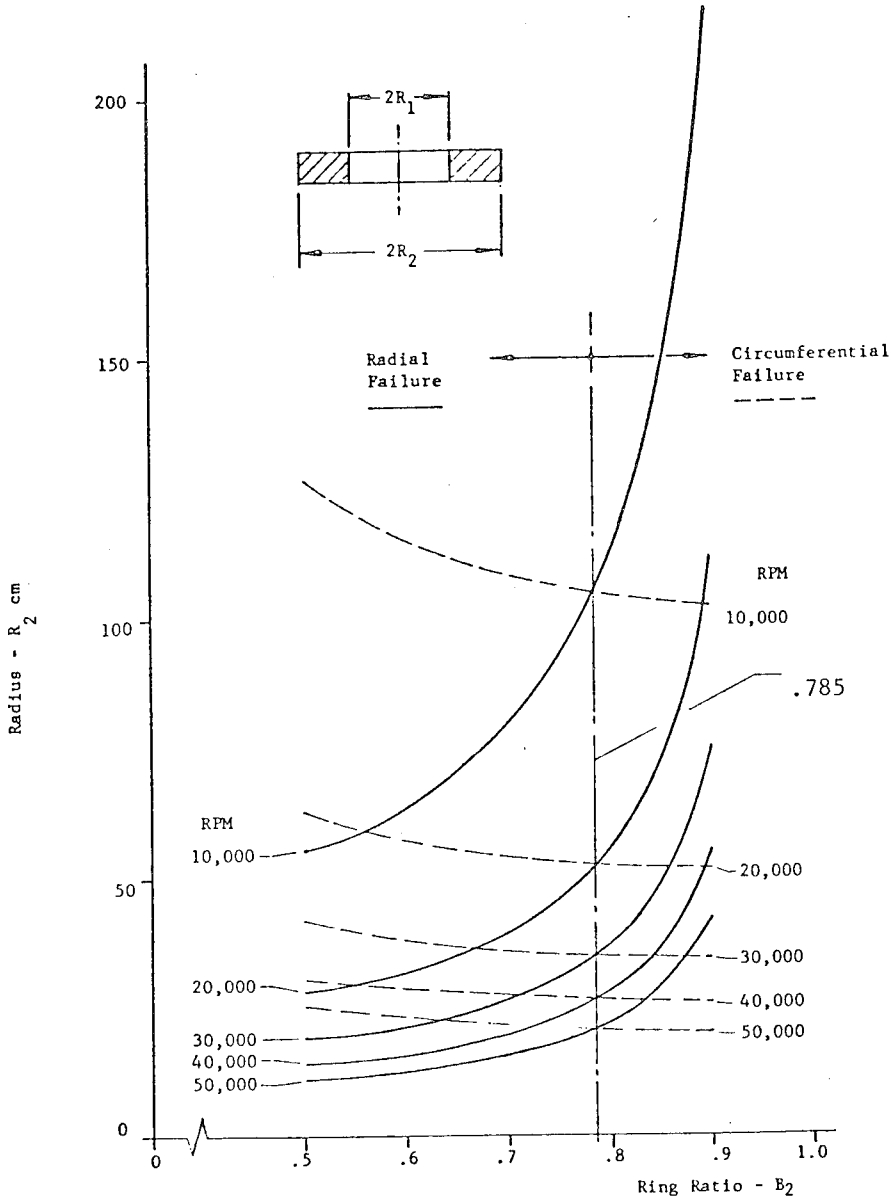

Figure 5 Kevlar Ring - Mode of Failure

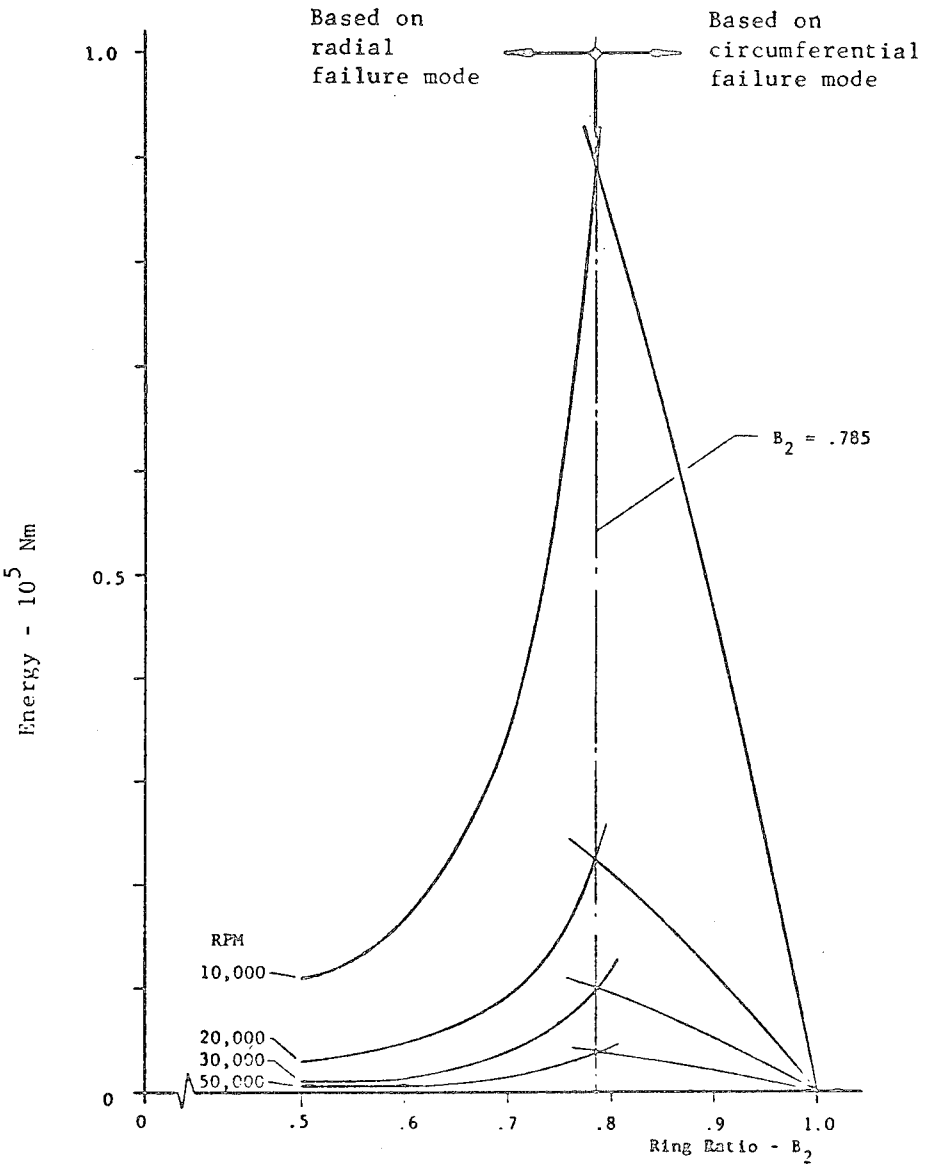

Figure 6 Energy Per Unit Width - Kevlar Ring

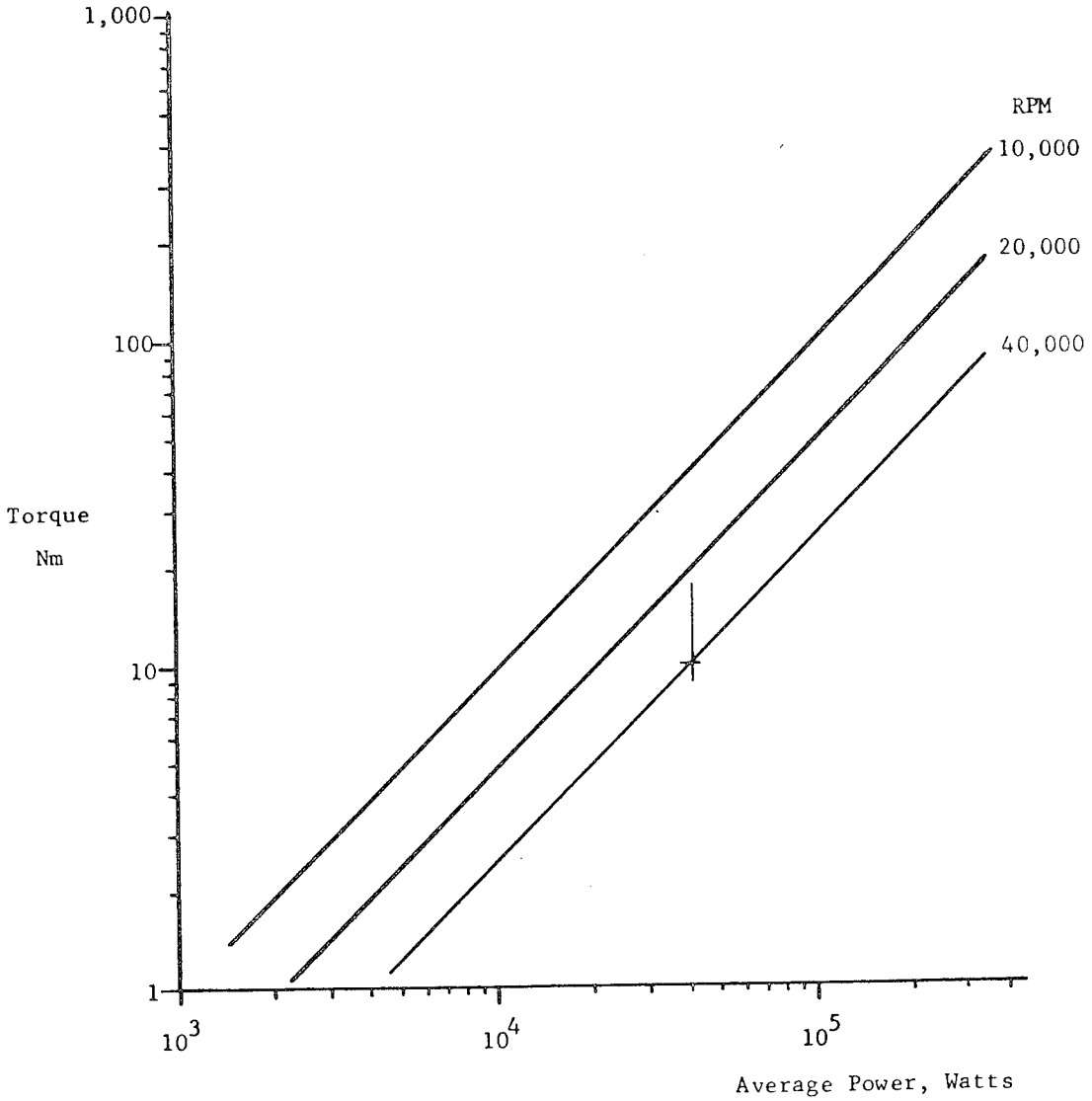

Figure 7 Torque vs Power

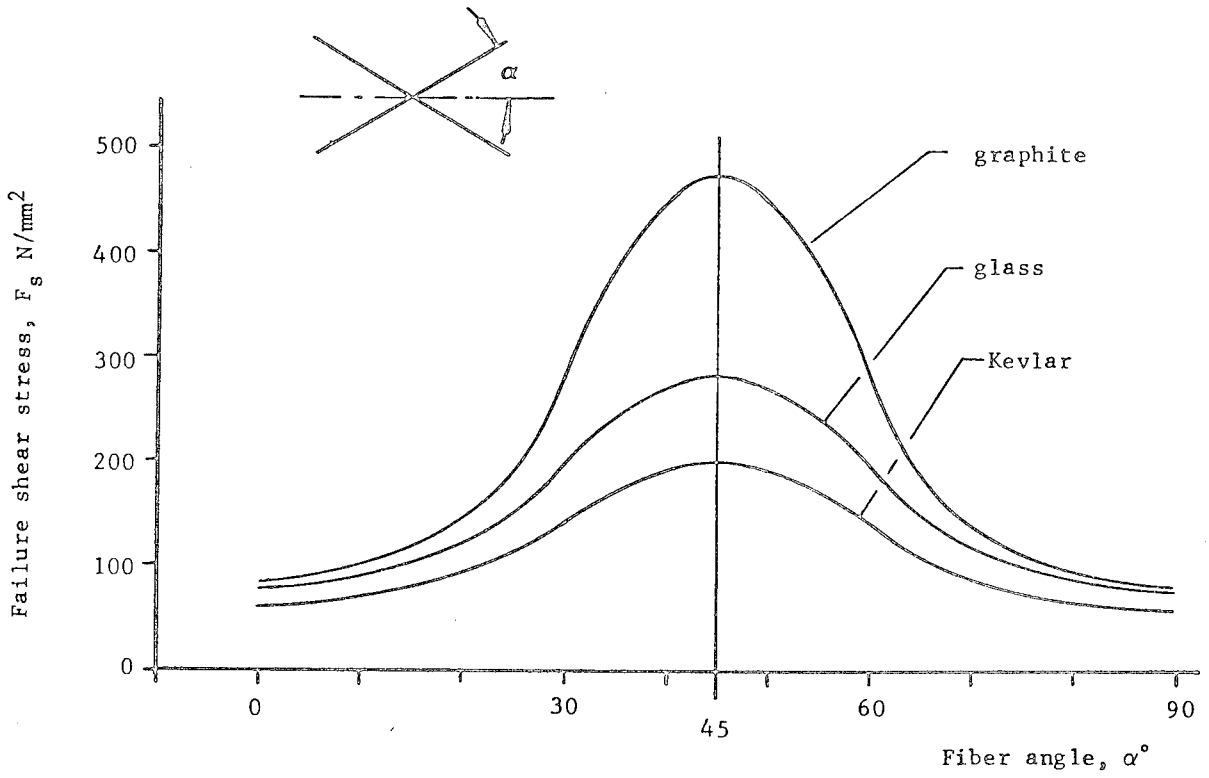

Figure 8 Failure Shear Stress as Function of Fiber Angle

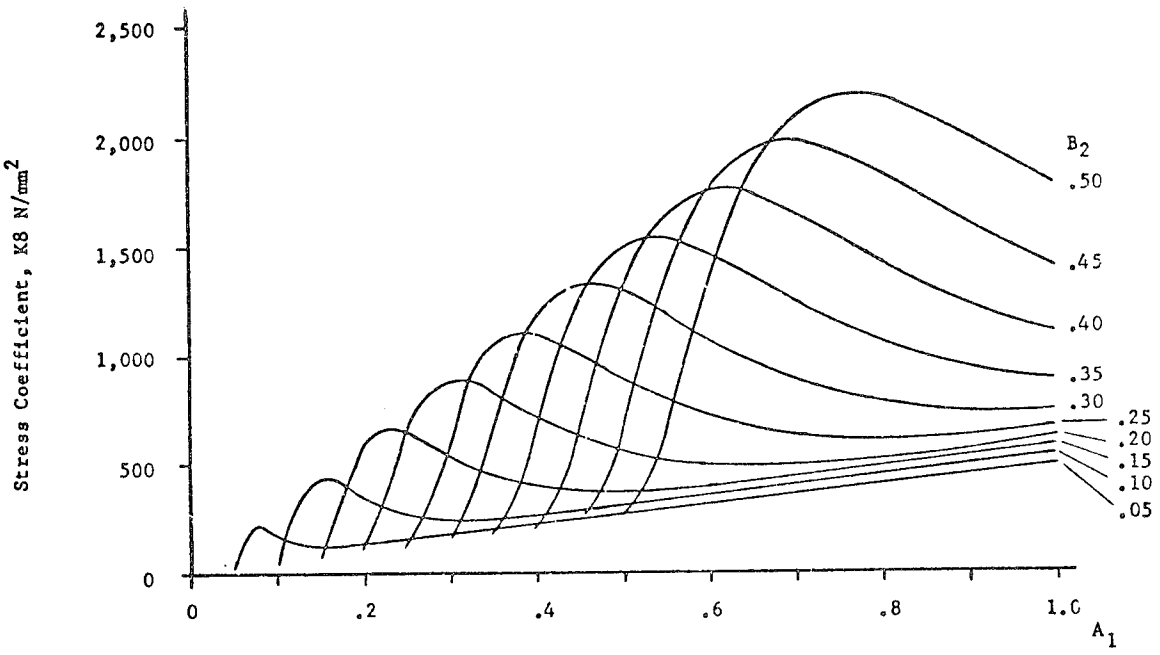

Figure 9 K8 - Web Torque Coefficient - Graphite

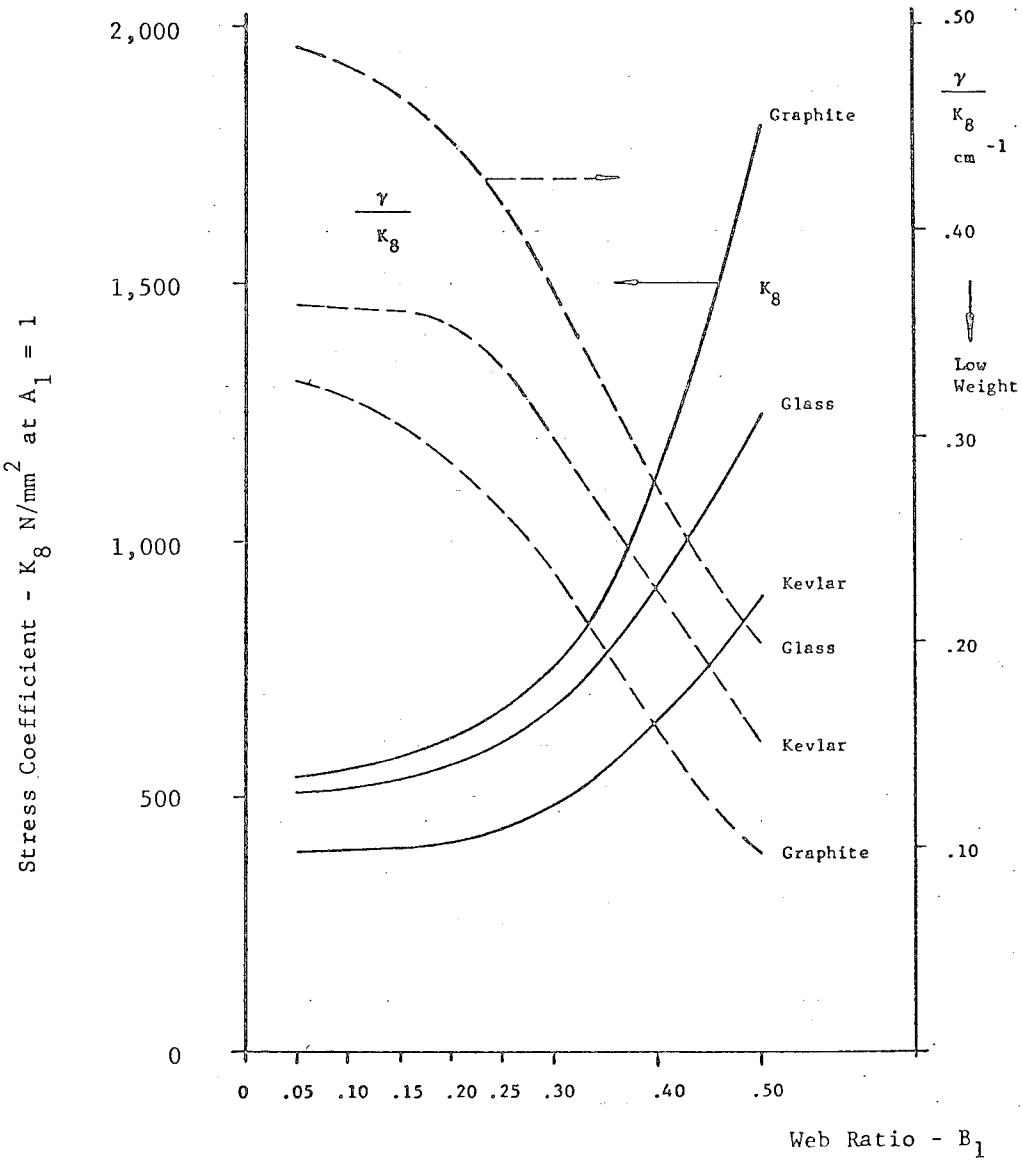

Figure 10 Shear Web Material Efficiency

T/R_2^2 = Const.

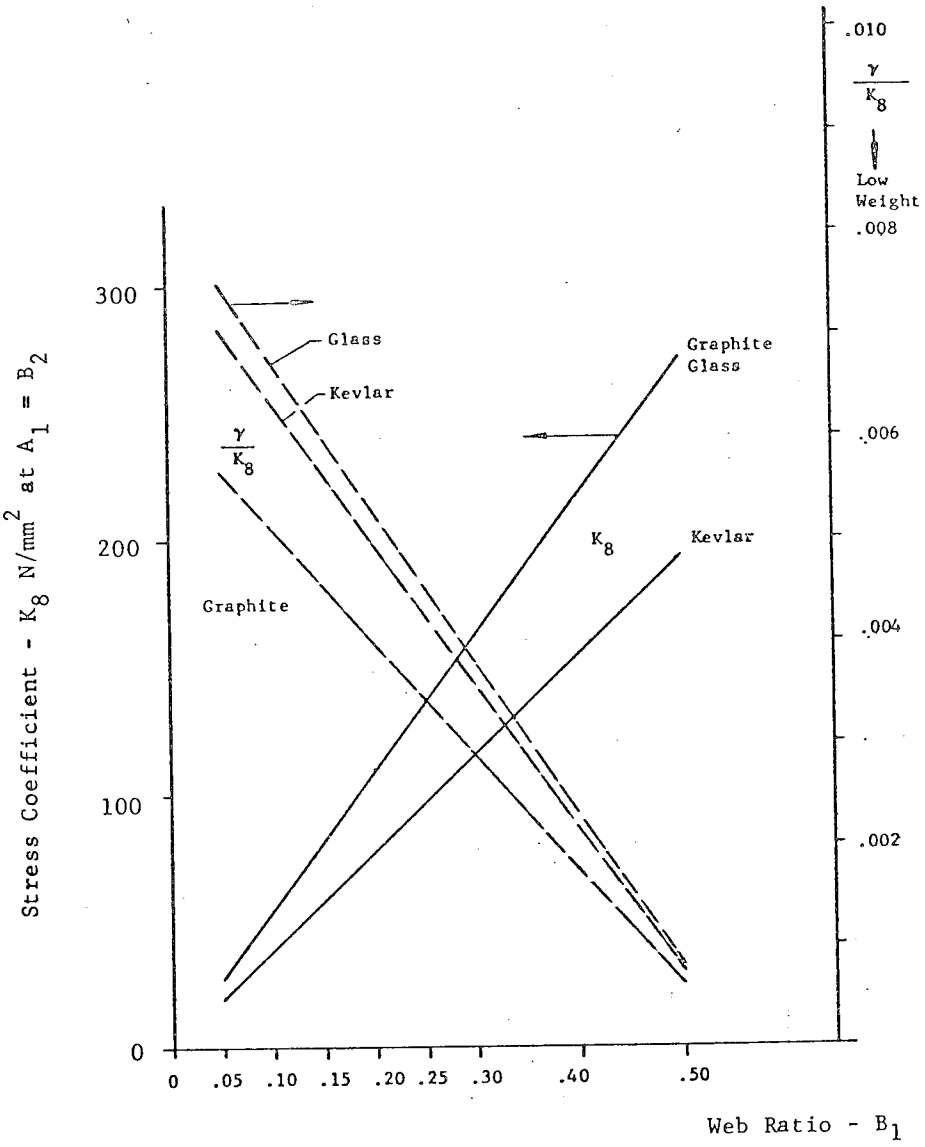

Figure 11 Shear Capacity at $A_1 = B_1$

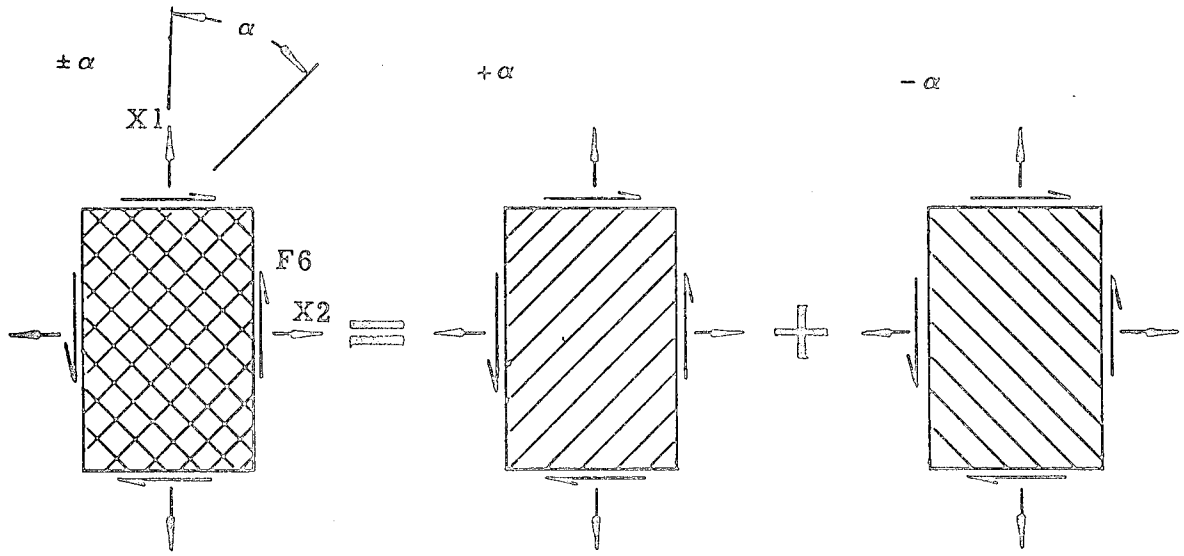

Figure 12 Laminate Analysis

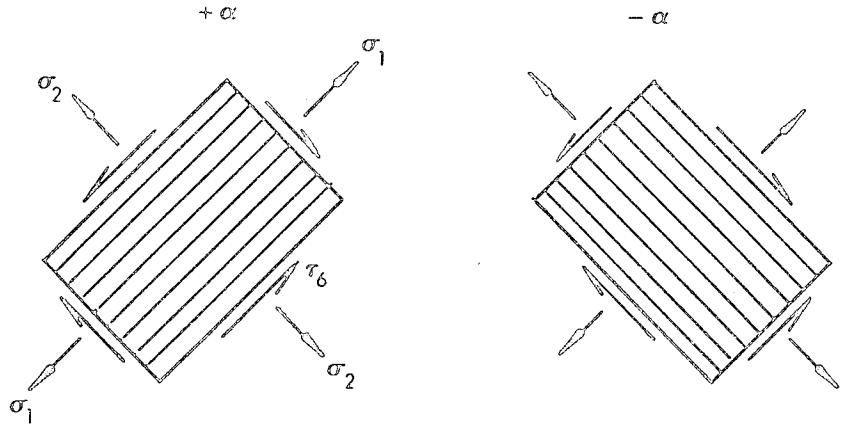

Figure 13 Lamina Analysis

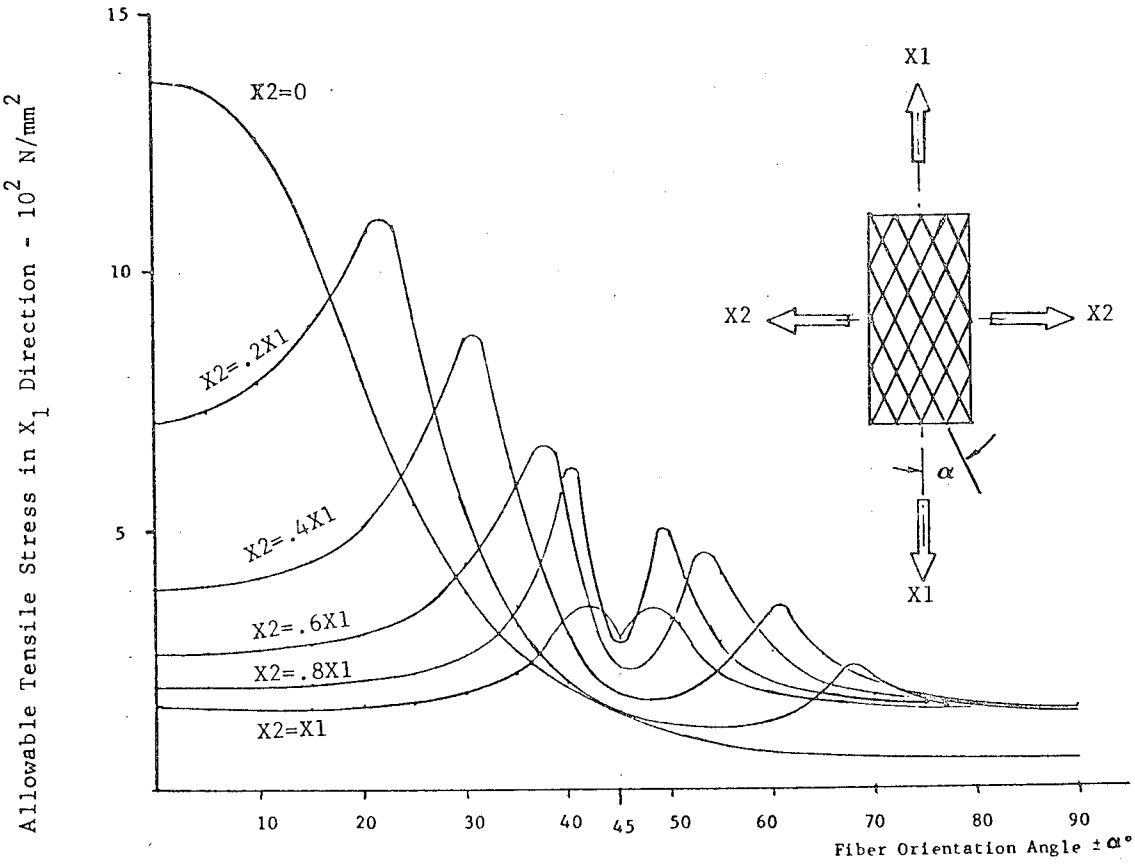

Figure 14 Allowable Axial Tension with Biaxial Loading

$$\sigma_z = 0 \quad , \quad \tau_{yz} = 0 \quad , \quad \tau_{zx} = 0$$

$$\frac{\sigma_1}{T_{1t}} = 1 \qquad \sigma_1 > 0$$

$$\frac{\sigma_1}{T_{1c}} = 1 \qquad \sigma_1 < 0$$

$$\left(\frac{\sigma_2}{T_{2t}}\right)^2 + \left(\frac{\tau}{T_{12}}\right)^2 = 1 \qquad \sigma_2 > 0$$

$$\left(\frac{\sigma_2}{T_{2c}}\right)^2 + \left(\frac{\tau}{T_{12}}\right)^2 = 1 \qquad \sigma_2 < 0$$

Where σ's are applied stresses and T's are allowable stresses

Figure 15 Failure Criteria of Hashin and Rotem

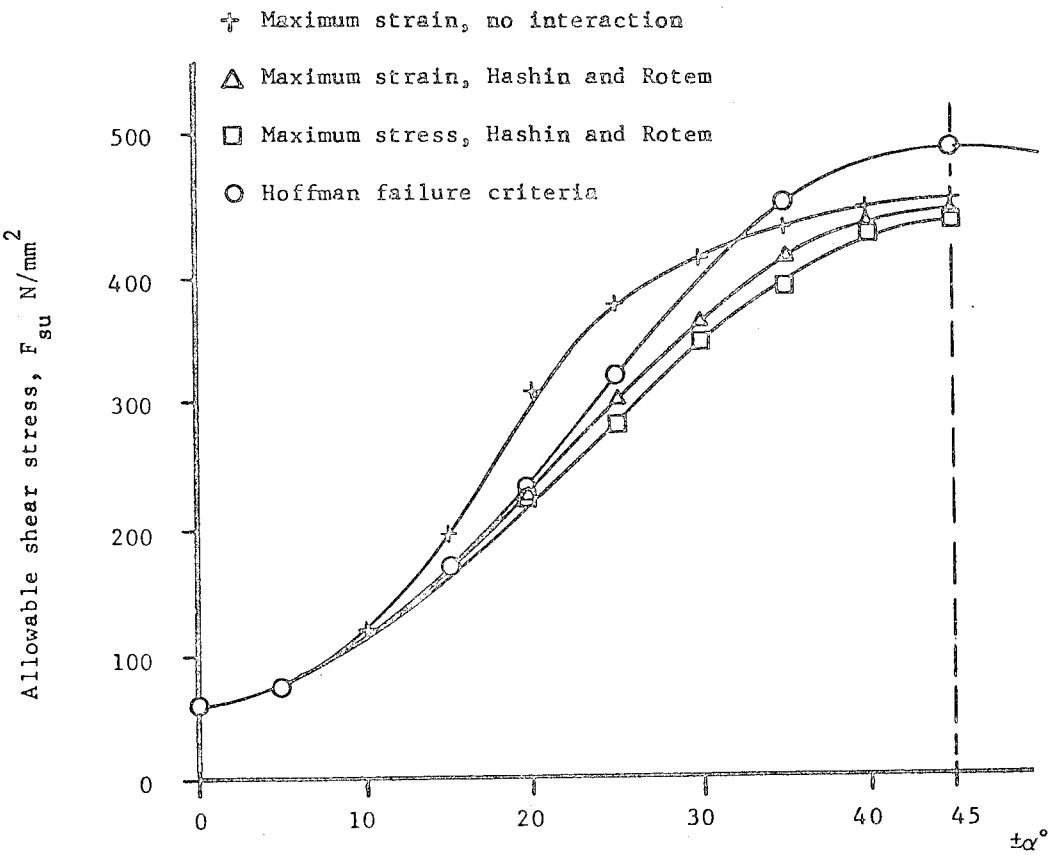

Figure 16 Allowable Shear Stress vs Orientation Graphite/Epoxy

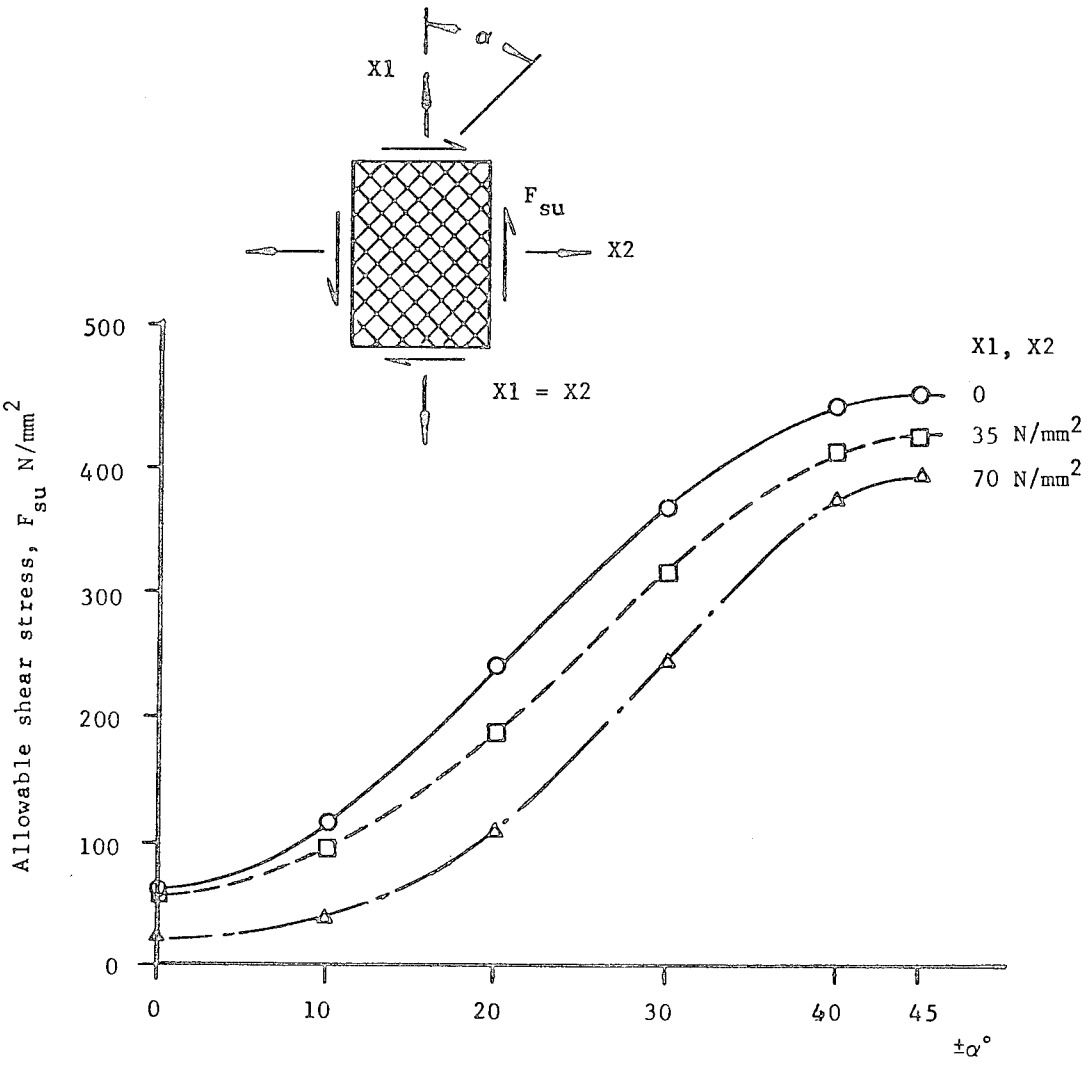

Figure 17 Effect of Centrifugal Field on the Allowable Shear Stress

ON THE PERFORMANCE OF HOOP WOUND COMPOSITE FLYWHEEL ROTORS

Ralph F. Foral
Department of Engineering Mechanics
University of Nebraska-Lincoln
Lincoln, Nebraska 68588

Norman L. Newhouse
Brunswick Corporation
Lincoln, Nebraska 68504

ABSTRACT

This paper investigates the performance of hoop wound composite flywheel rotors. Performance measurements used in the study are energy stored per unit swept volume, per unit rotor weight, and per unit material cost. Emphasis is placed on showing the interaction between these performance parameters in design selection. Rotors of single material construction are compared with rotors having two materials in a nested ring, hybrid construction. Numerical results are presented for epoxy matrix composites with E-Glass, S-Glass, Kevlar 49, and Thornel 300 fibers. Effects of temperature increase on performance are demonstrated and failure modes are noted. Design charts illustrating performance interactions are presented.

NOMENCLATURE

a,b	inner and outer radius of flywheel rotor.
A,B	parameters defined in Eqs. (A4) and (A5).
I	mass moment of inertia of rotor about rotational axis.
m	$= (Q_{\theta\theta}/Q_{rr})^{1/2}$.
Q	material constant defined in Eq. (3).
r,θ	radial and circumferential polar coordinates.
s	parameter defined in Eq. (A2).
S	allowable stress.
t	radial thickness
U	stored energy.
V	swept volume, $= \pi b^2 w$.
v_f	fiber volume percentage.
W	weight.
w	axial thickness.
α	linear coefficient of thermal expansion.
ΔT	temperature change.
ε	linear strain.
ρ	mass density.
σ	normal stress.
ω	rotational speed.
$	cost, dollars.

Subscripts

i,o	inner, outer.
M	maximum.
r,θ	radial, circumferential.
S	S-Glass.
49	Kevlar 49.

INTRODUCTION

Energy storage systems using flywheels show considerable promise for continued development and application[1]. Contributing to this is the availability of high strength fiber reinforced plastics for use in the flywheel rotor. These materials are light and strong, and thus, at high rotational speeds, allow efficient energy storage capacity.

Considerable effort has been expended towards optimizing composite rotor design and performance[2,3,4]. Several measures of flywheel performance can be used, including total energy storage capacity, as well as energy stored within a swept volume envelope, a weight restriction, and/or a cost limitation. Important constraints include fabrication capability and bearing design, among others. Selection of an optimum configuration involves trade-offs, comparing appropriate performance parameters within

the imposed design constraints.

Of the many configurations available in composite rotor design, a very attractive, easily fabricated one is the simple hoop wound rotor, with continuous filaments circumferentially wound in an epoxy matrix. The resultant composite has high circumferential strength, in the direction of the fibers, and relatively low radial strength, transverse to the fibers. Developmental work to date has shown composite transverse strength to be an important consideration in rotor design. This can be addressed by working to improve the transverse strength itself[4] or by inducing suitable prestresses during fabrication[5]. An additional approach uses a multiple material design where the rotor is constructed with nested circumferential rings, each with a different structural material. The materials are chosen and positioned radially so that the resultant properties distribution prevents excessive tensile radial stress build-up in any one ring. Properly selected material combinations can produce significantly increased energy storage capacity[4,6,7].

During operation of high speed flywheels, aerodynamic heating can cause significant increase in temperature of the material[8]. This temperature increase can be controlled to some extent by inducing low environmental pressures around the rotor and by maintaining an aerodynamically smooth rotor design. The thermal stresses caused by such temperature increases have potentially significant effect on rotor performance, but little has been reported in the literature on this.

The purpose of this paper is to investigate the performance of hoop wound composite flywheel rotors. Performance measurements used in the study are energy stored per unit swept volume, per unit rotor weight, and per unit material cost. Emphasis is placed on showing the interaction between these performance parameters in design selection. Rotors of single material construction are compared with rotors having two materials in a nested ring, hybrid construction. Numerical results are presented for epoxy matrix composites with E-Glass, S-Glass, Kevlar 49, and Thornel 300 fibers. Effects of temperature increase on rotor performance are demonstrated and failure modes are noted. Design charts illustrating performance interactions are presented.

The stress analysis of the rotor assumes a constant width disk rotating at constant speed under plane stress conditions. Although the plane stress assumption implies thin disks, other investigators[2] have reported slight effect on stresses in comparing plane stress with plane strain solutions for hoop wound rotors. The analysis uses stress free boundary conditions at the inner and outer edges. These conditions are considered to provide a conservative estimate of actual conditions for rotors supported at the outer edge, a highly attractive support condition for hoop wound rotors[9]. Several of the support methods used are designed so that the rotor is free to dilate radially, allowing the rotor analysis to be essentially independent of the attachment, with stress free boundaries.

BASIC EQUATIONS

Consider a constant width flywheel rotor with inner and outer radii a and b rotating at constant speed ω. The rotor is made up of n discrete, nested rings, each with inner and outer radii r_i and r_o, respectively, and of a single specified material of mass density ρ. In each ring, the radial and circumferential stresses σ_r and σ_θ must satisfy

$$\frac{d\sigma_r}{dr} + \frac{\sigma_r - \sigma_\theta}{r} + \rho\omega^2 r = 0, \qquad (1)$$

and the corresponding strains are given by

$$\varepsilon_r = \frac{du}{dr}, \qquad \varepsilon_\theta = \frac{u}{r}, \qquad (2)$$

in terms of the radial displacement u. The composite is assumed to be linear elastic with stresses related to strains by

$$\begin{Bmatrix} \sigma_r \\ \sigma_\theta \end{Bmatrix} = \begin{bmatrix} Q_{rr} & Q_{r\theta} \\ Q_{r\theta} & Q_{\theta\theta} \end{bmatrix} \begin{Bmatrix} \varepsilon_r - \alpha_r \Delta T \\ \varepsilon_\theta - \alpha_\theta \Delta T \end{Bmatrix}, \qquad (3)$$

where Q_{rr}, $Q_{\theta\theta}$, $Q_{r\theta}$ are material constants, and α_r and α_θ are the radial and circumferential linear coefficient of thermal expansion during temperature change ΔT.

The solution for radial displacement

u_o satisfying Eqs. (1) through (3) over a single discrete ring, is written in Appendix I, Eqs. (A1) through (A5). The result is expressed in terms of the radial displacement at the inside and outside of the ring, u_i and u_o. These are found by imposing continuity conditions between the discrete rings, and boundary conditions for the overall rotor, as follows. With n discrete rings, there are 2n total unknowns u_i and u_o. At each of the (n-1) interfaces between rings, continuity of radial displacement and of radial stress is required, producing 2(n-1) continuity equations. The assumed stress free rotor boundary conditions require zero radial stress at the inner and outer edges, a and b. This completes the required 2n equations, which may be solved simultaneously[10]. Once u_i and u_o are known, stresses and strains can be found by using Eq. (A1) in Eqs. (2) and (3).

COMPUTATIONAL PROCEDURES

The above equations have been programmed for digital computer solution. For given material properties, the program sequences rotor geometries, calculating the performance for each. Rotor geometry is described by the radius ratio a/b and the layer thickness ratio if a layered construction is used. Rotational stresses vary as the square of rotational speed. The radial and hoop stresses are first calculated point-by-point through the rotor for unit rotational speed. The maximum rotational speed ω_M produces the allowable radial and/or hoop stress at some point or points; ω_M is calculated as the minimum value of the square root of allowable stress divided by unit-speed stress. Once ω_M is known, all quantities of interest can be found. In particular, the stored energy U is the kinetic energy

$$U = \frac{1}{2} I\omega_M^2, \qquad (4)$$

where I is the mass moment of inertia of the rotor about the rotational axis.

Stresses due to temperature change are treated as prestresses. The thermal stresses are first calculated for $\omega = 0$, then used to modify the allowable stresses; the modified allowable is the original allowable minus the thermal stress. These modified allowables are used in the above procedure to find maximum rotational speed. This same procedure can be used to include the effect of prestresses due to fabrication.

The program is designed to automatically seek maximum values of a prespecified performance parameter. The equations are simple enough that multiple cases can be calculated with little cost, and the desired maximum value obtained directly. Then, the mesh of solutions can be displayed graphically to provide insight into design trade-offs. This will be demonstrated in the numerical results to follow.

Table 1. Material Properties - Unidirectional Fiber-Epoxy Composites.

Fiber	v_f	Q_{rr}	$Q_{r\theta}$	$Q_{\theta\theta}$	ρ	Cost	S_θ	S_r	α_θ	α_r
Units[a]	%	10^6 Psi			$\frac{lb}{in^3}$	$\frac{Dollars}{lb}$	10^3 Psi		$10^{-6}/°F$	
S-Glass	67	2.04	0.637	8.74	0.075	2.30	240.	6.0	3.5	13.5
Kevlar 49	62	0.883	0.281	12.1	0.049	6.49	225.	2.28	-0.70	31.0
E-Glass	67	1.87	0.613	7.34	0.076	1.02	180.	6.0	3.3	13.5
Thornel 300	59	1.28	0.406	20.3	0.055	18.00	200.	4.8	-0.54	17.4

[a] 1 psi = $6.89 \cdot 10^3$ Pa; 1 lb/in^3 = $2.77 \cdot 10^4$ kg/m^3; 1 Dollar/lb = 2.20 Dollar/kg; $10^{-6}/°F = 1.8 \cdot 10^{-6}/°C$.

Performance parameters chosen for this study are:

- U/V stored energy per unit swept volume,
- U/W stored energy per unit weight of the rotor,
- U/$ stored energy per unit cost of rotor materials.

The calculations are conducted for constant outer radius b. Sequencing the radius ratio a/b then varies the inner radius a at constant swept volume. At a given a/b, the above performance values are independent of b. The maximum speed, however, depends on b, and is expressed in terms of b.

NUMERICAL RESULTS AND DISCUSSION

To study performance of hoop wound composite flywheel rotors, four relatively common reinforcement fibers - E-Glass, S-Glass, Kevlar 49, and Thornel 300 - are selected. Representative properties of unidirectional epoxy matrix composites utilizing these fibers are listed in Table 1. These properties are typical for (unidirectional) hoop wound composites; with other methods of fabrication or under severe service conditions, the values will change. Of the four materials listed in Table 1, S-Glass and Kevlar 49 are selected to demonstrate a detailed performance investigation. Final results only will be presented for the other materials.

Consider a two material hybrid flywheel rotor constructed with a Kevlar 49 epoxy ring nested over one of S-Glass epoxy (denoted as Kevlar 49/S-Glass).

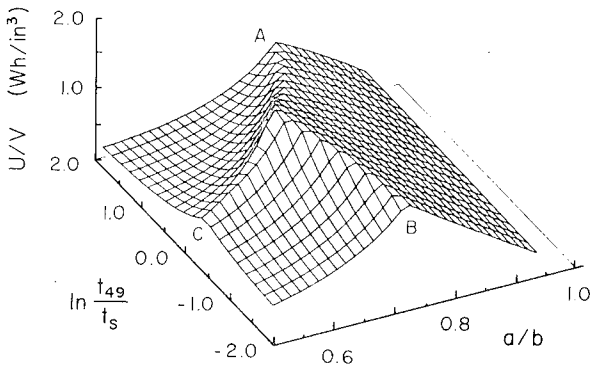

Fig. 1. Performance Surface - Energy per Unit Swept Volume - Kevlar 49/S-Glass Hybrid Rotors (1 Wh/in^3 = 2.20·10^{8}J/m^3).

Figure 1 shows the performance surface of energy stored per unit swept volume (U/V) plotted versus the rotor radius ratio (a/b) and the natural logarithm of the layer thickness ratio ($\ell n\ t_{49}/t_S$). Although the mesh in Fig. 1 is coarse, a distinct U/V peak is apparent. An iterative numerical analysis shows the peak value to be 1.88 Wh/in^3(4.14·10^{8}J/m^3) occurring at a/b = 0.628 and t_{49}/t_S=0.772 ($\ell n t_{49}/t_S$ = -0.259). The corresponding maximum rotational speed times b (ω_Mb) is 0.411·10^6 rpm-in. (1.04·10^4 rpm-m.) i.e., a rotor with a 10 in. (0.254 m.) outer radius would rotate at 41,100 revolutions per minute.

The ridges in Fig. 1 divide regions of specific failure modes. The uniformly sloped region to the right of ridge AB defines rotors with a hoop stress failure mode in the Kevlar 49. Rotors in the region to the left of AB (lower a/b values) fail radially. The ridge beginning at C divides the radial failure region; the region to the right of this ridge (lower t_{49}/t_S values) defines radial stress failure in the S-Glass, and to the left (higher t_{49}/t_S values) in the Kevlar 49. The peak, where the ridges intersect, defines a rotor in which the failures occur simultaneously. This is demonstrated in Fig. 2 where the actual rotor stresses are plotted, and the allowables indicated as horizontal dashes. With the Kevlar 49/S-Glass materials used here, failure occurs

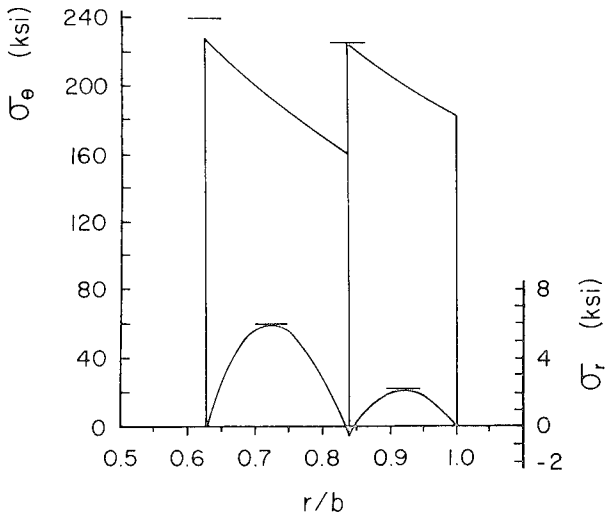

Fig. 2. Stress Distribution at Maximum Energy per Unit Swept Volume - Kevlar 49/S-Glass Hybrid Rotor (1 ksi = 6.89MPa).

simultaneously in three of the four possible failure modes; the hoop stress in the inner S-Glass ring does not quite attain its allowable value. The radial stress at the interface between rings is compressive, indicating no tendency for separation. This is a typical, but not necessary, condition when synergism occurs.

Behavior of single material rotors is demonstrated by the plots for extreme t_{49}/t_S values in Fig. 1. The single material rotors exhibit radial failure for thick rings (low a/b ratios) and hoop failure for thin rings (high a/b ratios). Best performance is attained at the a/b ratio for which simultaneous radial and hoop failure is accomplished (demonstrated by points A and B in Fig. 1).

Several sources[2,3,10] detail rotational stress distributions in hoop wound composite flywheel rotors; Newhouse[10] plots stresses due to temperature change. Here, the effects of temperature change

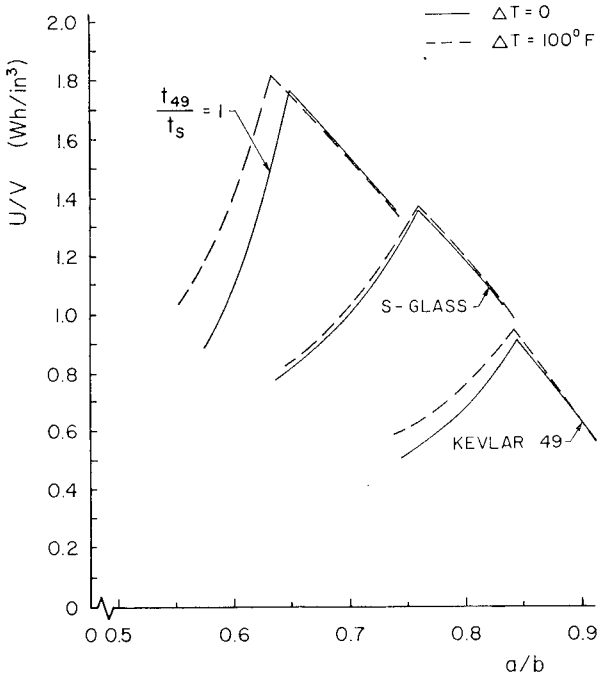

Fig. 3. Effects of Temperature Increase on Energy per Unit Swept Volume Performance - Kevlar 49, S-Glass, and Kevlar 49/S-Glass Rotors (1 Wh/in^3 = 2.20·10^{8}J/m ; 100°F = 55.6°CΔT.)

on performance are demonstrated. In Fig. 3, stored energy per unit swept volume (U/V) is plotted versus a/b for single material rotors of Kevlar 49 and S-Glass, and for a sample two material rotor of Kevlar 49/S-Glass with t_{49}/t_S = 1. The solid lines show results with no temperature change and the dashed lines represent results with a temperature increase of 100°F (55.6°C). Material properties were assumed to be unaffected by the temperature increase. With proper resin systems and processing, this is a valid assumption. With other materials or processing, or at extreme temperatures, a significant effect may be produced on material properties, which effect must be taken into account.

Analytically, stresses due to temperature change are treated as prestresses to be superposed with the rotational stresses. Favorable thermal stresses allow higher rotational speeds and improved performance. This is the case in Fig. 3 for both single material rotors over the range of a/b considered. The two material wheel in Fig. 3 demonstrates a condition of mixed effects. On most of the low a/b portion of the curve, representing radial failure, significant improvement in performance is noted with a temperature increase; on the high a/b portion, representing hoop failure in the outer (Kevlar 49) ring, temperature increase produces a reduction in performance. Figure 3 demonstrates that stresses due to temperature change can have potentially significant effect on rotor performance. This effect should be investigated as part of the design process.

The plot of Fig. 3 can be used to judge the effects of fabrication prestresses on performance. For the single material rotors at the radius ratios considered, a temperature increase causes compressive radial stress throughout the rotor, and monotonically increasing hoop stresses from compressive at the inside to tensile at the outside[10]. These are the same as the ideal prestresses which could be induced by fabrication control[5]. When the tensile stress field due to rotation[10] is superposed, performance improvements such as are shown in Fig. 3 are produced. Similar comments apply to fabrication prestresses in two material wheels. With suitable selection of the prestresses, potentially significant effects on performance can be produced.

Figure 4 shows the energy stored per unit weight (U/W) performance surface for the same Kevlar 49/S-Glass materials and geometry considered in Fig. 1. The largest U/W value for this surface, 62.2 Wh/lb. ($4.94 \cdot 10^5$J/kg), occurs for the thinnest wheel (a/b = 0.935) and the most Kevlar 49 ($\ell n t_{49}/t_S$ = 1.8) of all the configurations analyzed. The surface maintains a fairly high level over a wide range of configurations up to the ridge AB; in particular, where the energy per unit swept volume is a maximum (a/b = 0.628, t_{49}/t_S = 0.772), the energy stored per unit weight is 50.0 Wh/lb. ($3.97 \cdot 10^5$J/kg).

Figure 5 plots the interaction between U/V and U/W for single material rotors and for Kevlar 49/S-Glass rotors with selected t_{49}/t_S values. The dashed line in Fig. 5 shows the envelope enclosing other two material configurations. Proceeding from left to right on any one of the solid line plots traces behavior as the a/b ratio increases. Past the peak, there is a significant drop in U/V for little change in U/W. Taking a slight penalty in energy per unit weight performance allows significant increase in total energy stored within the volume envelope. This should be a factor considered in the design selection process.

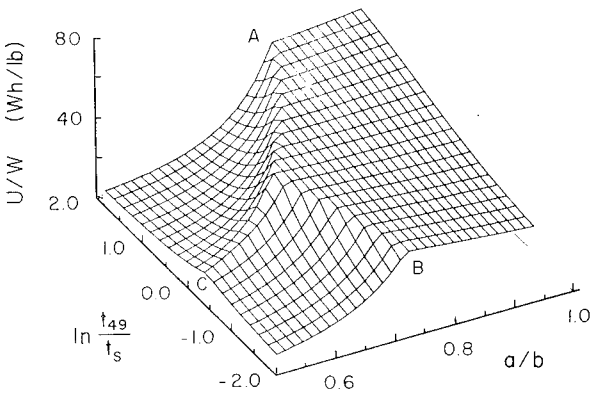

Fig. 4. Performance Surface - Energy per Unit Weight - Kevlar 49/S-Glass Hybrid Rotors (1 Wh/lb = $7.94 \cdot 10^3$J/kg).

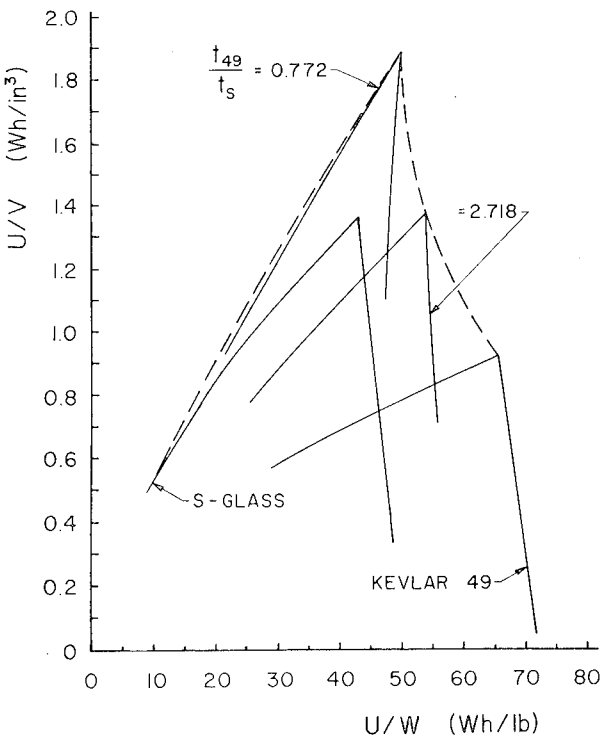

Fig. 5. Performance Interaction - Energy per Unit Swept Volume vs. Energy per Unit Weight - Kevlar 49, S-Glass, and Kevlar 49/S-Glass Hybrid Rotors (1 Wh/in^3 = $2.20 \cdot 10^8$J/m^3; 1 Wh/lb = $7.94 \cdot 10^3$J/kg).

Economic success of any energy storage system depends upon the energy stored per unit cost. Including all costs is outside the scope of this paper; only rotor material costs, using the values given in Table 1, are considered here. Figure 6 shows the performance surface of energy stored per unit rotor material cost (U/$) for the same Kevlar 49/S-Glass materials and geometry analyzed in Figs. 1 and 4. The largest U/$ value for this surface, 16.1 Wh ($5.80 \cdot 10^4$J) per dollar, occurs at point B in Fig. 6, the peak on the curve for rotors with the most S-Glass of those analyzed. But, as with the U/W plot, the U/$ surface maintains a fairly high level over a wide range of configurations up to the ridge AB. In particular, where the energy per unit swept volume is a maximum (a/b = 0.628, t_{49}/t_S = 0.772), the energy stored per unit material cost is 12.75 Wh ($4.59 \cdot 10^4$J) per dollar.

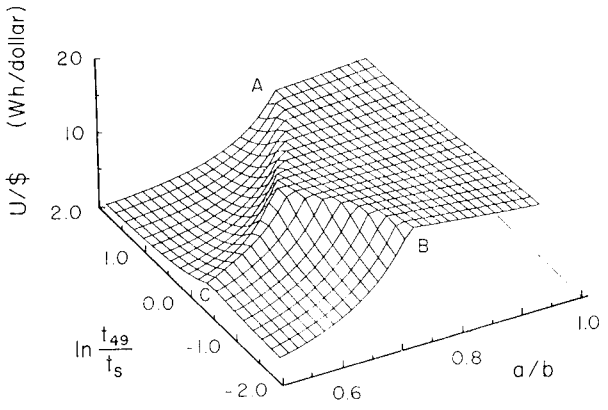

Fig. 6. Performance Surface - Energy per Unit Material Cost - Kevlar 49/S-Glass Hybrid Rotors (1 Wh/dollar = $3.60 \cdot 10^3$J/dollar).

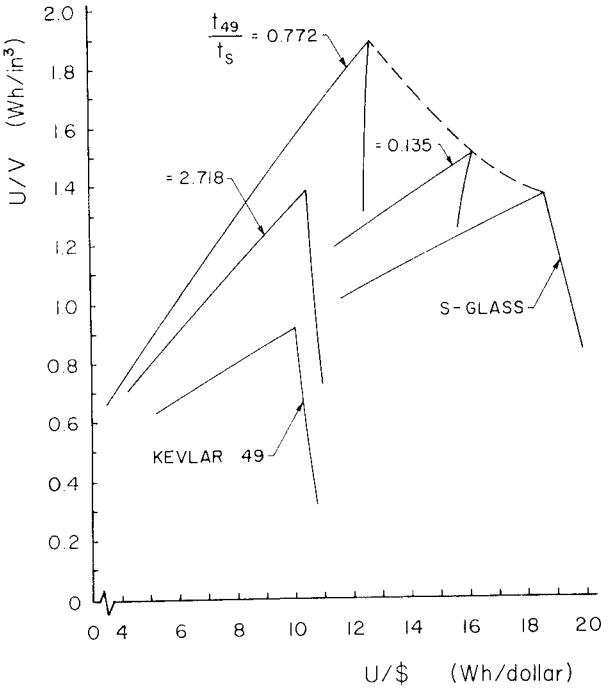

Fig. 7. Performance Interaction - Energy per Unit Swept Volume vs. Energy per Unit Material Cost - Kevlar 49, S-Glass, and Kevlar 49/S-Glass Rotors (1 Wh/in³ = $2.20 \cdot 10^8$J/m³; 1 Wh/dollar = $3.60 \cdot 10^3$J/dollar).

Figure 7 plots the interaction between U/V and U/$ for single material rotors and for Kevlar 49/S-Glass rotors with selected $t_{49}t_S$ values. The dashed line in Fig. 7 shows the envelope

Table 2. Single Material Rotor Performance[a].

Fiber	a/b	$\omega_M b$	U/V	U/W	U/$
Units[b]		10^6 rpm-in.	Wh/in³	Wh/lb	Wh/dollar
S-Glass	0.761	0.350	1.36	43.1	18.7
ΔT = 100°F	0.761	0.351	1.37	43.3	18.9
Kevlar 49	0.845	0.414	0.916	65.4	10.1
ΔT = 100°F	0.842	0.417	0.947	66.3	10.2
E-Glass	0.726	0.303	1.12	31.2	30.5
ΔT = 100°F	0.726	0.304	1.13	31.4	30.7
Thornel 300	0.760	0.378	1.17	50.2	2.79
ΔT = 100°F	0.752	0.382	1.21	50.8	2.82

[a]Values given are for rotors with maximum energy per unit swept volume.

[b]1 rpm-in = $2.54 \cdot 10^{-2}$rpm-m; 1 Wh/in³ = $2.20 \cdot 10^8$J/m³; 1 Wh/lb = $7.94 \cdot 10^3$J/kg; 1 Wh/dollar = $3.60 \cdot 10^3$J/dollar; 100°F = 55.6°CΔT.

Table 3. Two Material Rotor Performance[a].

Fibers	a/b	t_o/t_i	ω_M[b]	U/V	U/W	U/$
Units[b]			10^6 rpm-in.	Wh/in^3	Wh/lb	Wh/dollar
Kevlar 49/S-Glass	0.628	0.772	0.411	1.88	50.0	12.8
ΔT = 100°F	0.616	0.797	0.413	1.92	49.9	12.6
Thornel 300/Kevlar 49	0.686	2.04	0.385	1.38	48.9	3.27
ΔT = 100°F	0.673	1.95	0.389	1.44	49.4	3.32
Thornel 300/S-Glass	0.493	1.09	0.373	1.75	36.8	3.46
ΔT = 100°F	0.472	1.09	0.378	1.81	37.0	3.45

[a]Values given are for rotors with maximum energy per unit swept volume.

[b]1 rpm-in. = $2.54 \cdot 10^{-2}$ rpm-m; 1 Wh/in^3 = $2.20 \cdot 10^8$ J/m^3; 1 Wh/lb = $7.94 \cdot 10^3$ J/kg; 1 Wh/dollar = $3.60 \cdot 10^3$ J/dollar; 100°F = 55.6°CΔT.

enclosing the other two material configurations. Proceeding from left to right on any one of the solid line plots traces behavior as the a/b ratio increases. Interestingly, the position of the Kevlar 49 and the S-Glass single material rotors are interchanged on the U/$ plot of Fig. 7 as compared with the U/W plot of Fig. 5. The plot of Fig. 7 facilitates trade-offs involving materials cost and performance.

The foregoing plots have considered rotors of two materials, Kevlar 49 and S-Glass. Tables 2 and 3 summarize final results for rotors of these materials and of E-Glass and Thornel 300 as well; Table 2 gives results for single material rotors and Table 3 for two material rotors. Performance values are given for no temperature change and for a temperature increase of 100°F (55.6°C). The values for energy stored per unit weight (U/W) and for energy stored per unit material cost (U/$) are for the rotor producing maximum energy per swept volume (U/V), with the corresponding geometric proportions and maximum rotational speed indicated. Study of the values in Tables 2 and 3 provides an interesting contrast in performance on a volume, weight, and cost basis for the materials considered. No one material or material combination appears best on all counts.

CONCLUSIONS

A performance study of hoop wound composite flywheel rotors has been conducted using three measures of performance; stored energy per unit swept volume, stored energy per unit weight, and stored energy per unit material cost. Single material construction and two material nested ring construction are considered. Numerical results are presented for epoxy matrix composites with E-Glass, S-Glass, Kevlar 49, and Thornel 300 fibers. The principal conclusions of this investigation are:

The computer generated three dimensional displays showing energy surfaces are useful for understanding rotor performance. Relating failure modes to easily recognized regions of the energy surface provides added insight in design selection.

With proper choice of materials in the nested ring hybrid construction, a cooperative action between the discrete material layers occurs, so that the total stored energy is greater than for either material acting independently.

Study of the interaction between performance parameters in design selection shows that important trade-offs are involved. Taking a slight penalty in one

parameter may produce a design with significantly improved performance in another. In general, no one optimum exists for all performance parameters.

Temperature change has potentially significant effect on rotor performance, and may be beneficial or harmful. The analytical technique used to account for temperature change can be used to account for prestresses due to fabrication.

For the examples considered here, the maximum energy stored within a volume envelope occurs when the largest number of failure modes that can occur, do occur, simultaneously. This observation may conceivably be extended to "n" material configurations, with resulting improved efficiency. Effective material properties can be more finely tailored in composite materials to approximate the desired distribution. Techniques for doing this include controls on fiber volume percentage and fabrication prestresses, for example, as well as by fiber selection, as was used here.

ACKNOWLEDGMENT

This investigation has been supported in part by the University of Nebraska-Lincoln and by the Brunswick Corporation. Use was made of PLOT3D, a three dimensional computer plotting routine written by R. F. Schwartz and L. G. Weikes at the University of Nebraska-Lincoln.

REFERENCES

1. Chang, G. C. and Hirschfeld, F., For the Latest in Energy Storage, Try the Flywheel, Mech. Engng., 100, 38-45 (Feb. 1978).

2. Portnov, G. G. and Kulakov, V. L., Investigation of Energy Storage Capacity of Wound Composite Flywheels, Polymer Mechanics, 14, 1, 61-68 (Sep. 1978). Translated from Mekhanika Polimerov, No. 1, 73-81 (Jan.-Feb. 1978).

3. Danfelt, E. L., Hewes, S. A., and Chou, T. W., Optimization of Composite Flywheel Design, Int. J. Mech. Sci., 19, 69-78 (1977).

4. Allred, R. E., Foral, R. F., and Dick, W. E., Improved Performance for Hoop Wound Composite Flywheel Rotors, 1977 Flywheel Technology Symposium Proc., U. S. Dept. of Energy, 377-392 (Mar. 1978).

5. Knight, C. E., Jr., and Pillard, R. E., Prestressed Thick Flywheel Rims, 1977 Flywheel Technology Symposium Proc., U. S. Dept. of Energy, 183-192 (Mar. 1978).

6. Dick, W. E., and Foral, R. F., Design and Material Considerations in the Fabrication of an Optimized Fiber Composite Flywheel, Proc. 23rd National SAMPE Symposium, 675-702 (May 1978).

7. Reedy, E. D., Jr., and Gerstle, F. P., Jr., Design of Spoked-Rim Composite Flywheels, 1977 Flywheel Technology Symposium Proc., U. S. Dept. of Energy, 99-110 (Mar. 1978).

8. Baer, M. R., Aerodynamic Heating of High-Speed Flywheels in Low-Density Environments, Proc. 1978 Mechanical and Magnetic Energy Storage Contractor's Review Meeting, U. S. Dept. of Energy, 99-107 (Oct. 1978).

9. Knight, C. E., Jr., et. al., Development of the Bandwrap Flywheel, 1977 Flywheel Technology Symposium Proc., U. S. Dept. of Energy, 137-154 (Mar. 1978).

10. Newhouse, N. L., A Computerized Analysis of Axisymmetric Flywheels, 1977 Flywheel Technology Symposium Proc., U. S. Dept. of Energy, 89-98 (Mar. 1978).

APPENDIX I - ALGEBRAIC SOLUTION

The solution for radial displacement u, satisfying Eqs. (1) through (3) over a single discrete ring, is[10]

$$u = \frac{1}{s}\{(u_o r_i^{-m} - u_i r_o^{-m})r^m + (u_i r_o^m - u_o r_i^m)r^{-m} + A\frac{\rho\omega^2}{Q_{rr}} + B\Delta T[\alpha_r(1 - \frac{Q_{r\theta}}{Q_{rr}}) - \alpha_\theta(m^2 - \frac{Q_{r\theta}}{Q_{rr}})]\} \quad \text{(A1)}$$

where

$$s = (\frac{r_o}{r_i})^m - (\frac{r_i}{r_o})^m \quad , \quad \text{(A2)}$$

$$m = (Q_{\theta\theta}/Q_{rr})^{1/2} \quad . \quad \text{(A3)}$$

$$A = [(r_i^3 r_o^{-m} - r_o^3 r_i^{-m})r^m - (r_i^3 r_o^m - r_o^3 r_i^m)r^{-m} + (r_i^{-m} r_o^m - r_i^m r_o^{-m})r^3] / (m^2 - 9) \quad \text{(A4a)}$$

if $m \neq 3$, and

$$A = \frac{1}{6}[(\frac{r_i}{r_o})^3 r^3 \ell n \frac{r}{r_i} + (\frac{r_o}{r_i})^3 r^3 \ell n \frac{r_o}{r} - \frac{r_o^3 r_i^3}{r^3} \ell n \frac{r_o}{r_i}] \quad \text{(A4b)}$$

if $m = 3$.

$$B = [(r_o r_i^{-m} - r_i r_o^{-m})r^m + (r_i r_o^m - r_o r_i^m)r^{-m} + (r_o^{-m} r_i^m - r_i^{-m} r_o^m)r] / (m^2 - 1) \quad \text{(A5a)}$$

if $m \neq 1$, and

$$B = \frac{1}{2}(\frac{r_o r_i}{r} \ell n \frac{r_o}{r_i} - \frac{r_o}{r_i} r \ell n \frac{r_o}{r} - \frac{r_i}{r_o} r \ell n \frac{r}{r_i}) \quad \text{(A5b)}$$

if $m = 1$.

AN ANALOG SIMULATION OF A FLYWHEEL PROPULSION SYSTEM FOR BUSES

C. M. Ong
School of Electrical Engineering
Purdue University
West Lafayette, IN 47907

ABSTRACT

Simulation plays an important role in the design and performance evaluation studies of most new system. Analog and digital techniques may be used in a simulation, each has its own advantages and disadvantages. For thyristor drive systems, an analog simulation is generally considered more efficient. This paper presents the techniques used in an analog simulation of a flywheel energy storage drive system, in which the electrical components, such as the thyristors of the converter, the controller, and the electrical machines are simulated in detail. Such a simulation is extremely useful for purposes of gathering design information on the voltage stresses on the various components, especially the semiconductor devices, in evaluating the dynamic performances of the system under different types of control, and in investigating the effects of changes in system parameters.

INTRODUCTION

Recent advances in material processing technology have made available materials of high energy storage per pound for flywheel rotors. Compact, lightweight flywheel energy storage units are especially attractive in transportation applications. As with many of such applications which involves storing energy in one form and using it in another, the converter is an essential component of the system.

As part of a larger research program funded by the Department of Transportation, the work described in this paper was carried out in the Energy Systems Simulation Laboratory at Purdue University. The purpose of it was to develop a simulation of the load-commutated flywheel propulsion system studied earlier by General Electric, with particular emphasis on the electrical components. Of special interest are the techniques used in the analog simulation, with the ultimate intention of adapting some of these techniques to a digital simulation, which would then be of use to a wider group of users with access to digital computers. As designed[1,2], the model bus propulsion system consisted of

- an inductor machine mechanically coupled to the energy storage flywheel,
- a thyristor controlled dual converter with an auxiliary commutation circuit for forced-commutation operation during startup,
- a dc traction motor, and
- the vehicle transmission system.

The simulation developed consisted of simulation of individual components in each of the above subsystems, appropriately interfaced with one another, and interacting as they would in an actual system. The detailed simulation, which readily yields information on the instantaneous behavior of physical variables of each and every component when these are operating as a whole, would be invaluable for design and performance studies. As in most other simulation techniques, changes in system parameters can easily be implemented.

DESCRIPTION OF THE SYSTEM

The configuration of the pure flywheel vehicle drive system[3,4] is shown in Figure 1. The flywheel and the solid-iron

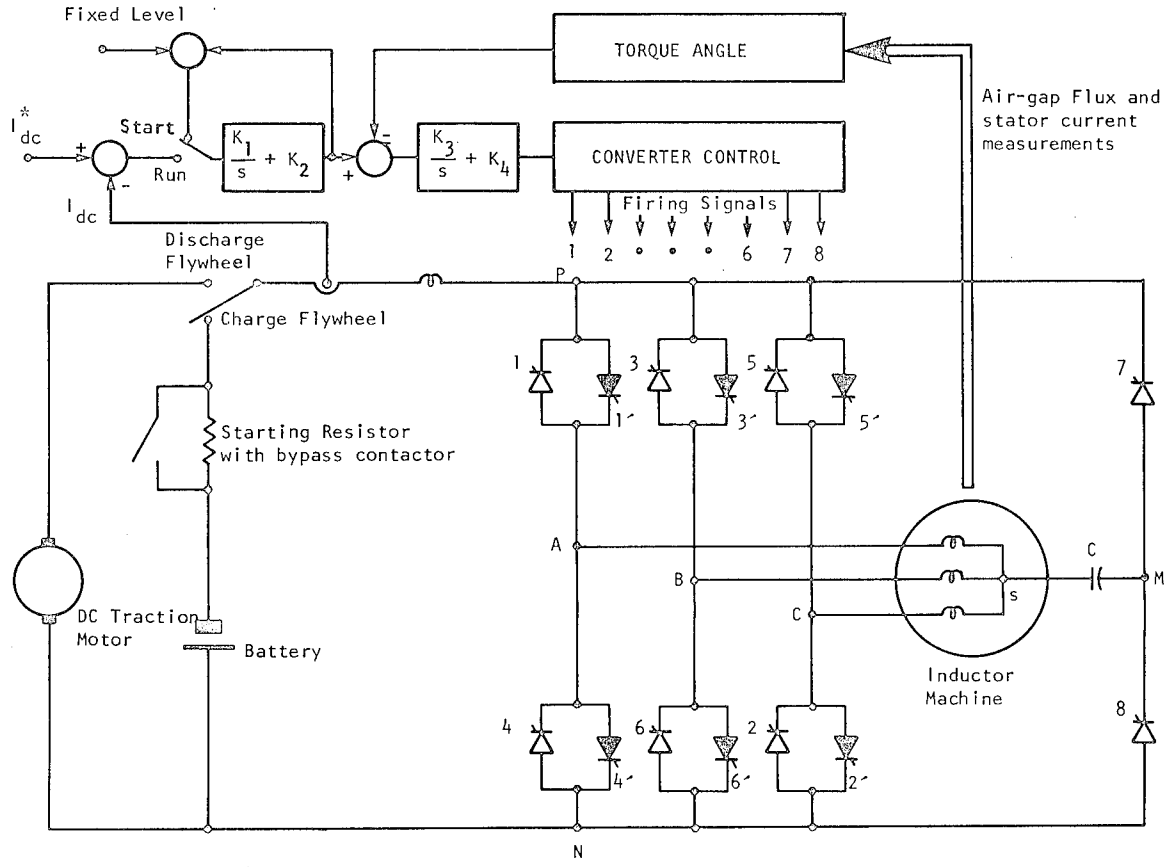

Fig. 1. Circuit diagram of flywheel propulsion system.

rotor inductor machine are housed in a low pressure unit to reduce windage loss at high operating speed. The inductor machine, shown in Figure 2, is of the Lorentz-type with its dc field coil wound between two stacks of stator laminations. Since this machine has no rotor field winding, its robust rotor construction is ideally suited for high speed operation in combination with an energy storage flywheel.

The dual converter, which consisted of two 3-phase bridges connected in antiparallel, serves as an interface between the variable frequency ac voltages of the inductor machine and the dc system. This converter configuration affords a swift and smooth changeover in the direction of flow of power without requiring a reversal of dc voltage polarity. Power flowing into or out of the inductor machine is controlled by adjusting the converter firing control. The two thyristors forming an antiparallel pair share a common gating signal source. For a given mode of operation, whether it be inverting or rectifying, the gating signal is applied only to the appropriate thyristor in the pair. Initially, when the flywheel and the rotor of the inductor machine are at rest, no voltage is induced in the stator windings of the inductor machine with dc field excitation.

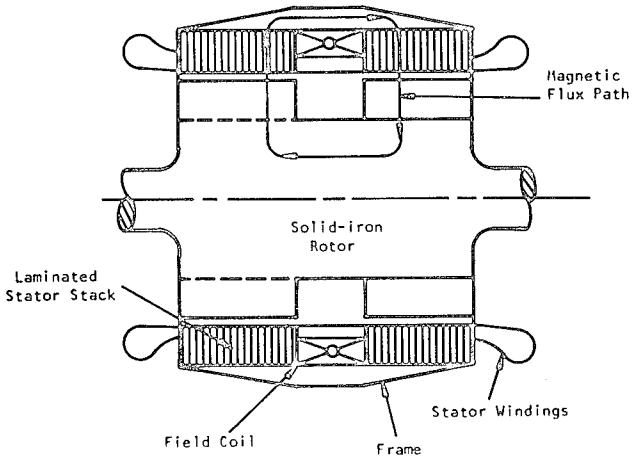

Fig. 2. Cross-sectional view of an inductor motor.

The rotor of the machine is set in motion by electronically switching, using forced commutation, the dc supply current into the appropriate sets of stator phase windings, generating a switching m.m.f in the airgap to accelerate the rotor along. The back e.m.f. of the inductor machine builds up with rotor speed, and until this is of sufficient magnitude to load-commutate the converter operating in the inverting mode, the converter has to be forced-commutated. Thus during startup, the auxiliary commutation circuit has to maintain the necessary conditions to forced-commutate the converter. At every sixth of a cycle, a firing of the main thyristor in the bridge is momentarily delayed; this enables the capacitor C connected to the neutral of the machine to charge up to a predetermined magnitude of voltage that will successfully commutate the main thyristor at low machine speeds.[5,6,7]

As the rotor/flywheel speeds up, at some stage forced-commutation can be dispensed with and the motor continues to accelerate under load-commutation operation. To load-commutate the current successfully, the back e.m.f. of the motor has to be not only above a certain magnitude but also be at a proper phase relationship to the current. Proper phase relation between voltage and current is obtained when the motor is overexcited, operating as a leading power factor load. Also, as the motor speed increases, its back e.m.f. rises beyond some value that would load-commutate the current by a safe margin. When the above conditions are fulfilled, a change over from forced to load-commutation of the converter is effected simply by turning off the firing control to the auxiliary thyristors of the commutation circuit. Power flow to the flywheel may then be adjusted by changing the reference value of the dc current regulator which in turn alters the timing at which the main thyristors of the bridge converter are triggered to give the required dc voltage. The output voltages of the bridge converter are synchronized with the machine's internal voltages by triggering the main thyristors at appropriate instants relative to the machine's rotor position. Information on the rotor position could be obtained directly from a mechanical shaft position sensor[6] or derived from terminal measurements giving the angular displacement between the machine's air-gap flux and the stator m.m.f.[3] When sufficient kinetic energy is stored in the flywheel, the dc source may be disconnected.

The kinetic energy stored in the flywheel could later be extracted to power the vehicle. This reverse flow of power from the flywheel to the dc system is effected by operating the inductor machine as a generator, which is underexcited so as to provide reactive power to the bridge converter. The dc output from the bridge converter is applied to a dc traction motor which is coupled by transmission gears to the drive wheels of the vehicle. If the drawdown is limited to one half rated flywheel speed, as much as three quarters of its kinetic energy stored at rated speed is available for driving the vehicle between charging stops. Moreover, at subsequent charging stops, when the converter is connected to an external dc voltage source for recharging the flywheel up to speed again, the internal voltage of the machine at about one half rated speed is ample to load-commutate the converter; hence there is no further need for forced-commutation.

MODELING

In modeling, it is essential to represent adequately the pertinent characteristics of the device. An exact representation is seldom accomplished. The question of adequacy is dependent on the use to which the model is applied.

The models presented here are intended for use in design and performance assessment studies. An attempt has been made to model the system components to a degree of accuracy and detail adequate for such studies.

INDUCTOR MACHINE

The solid-iron inductor machine may be represented as a synchronous machine with one field winding. The damping effects of the solid-iron rotor may be approximated by two equivalent rotor circuits, one on the d-axis and the other on the q-axis. It should be pointed out that the solid-iron rotor does have significant effects on the damping of the machine and on the commutation performance of the converter, and there are circuit models[8,9] of the solid-iron rotor which

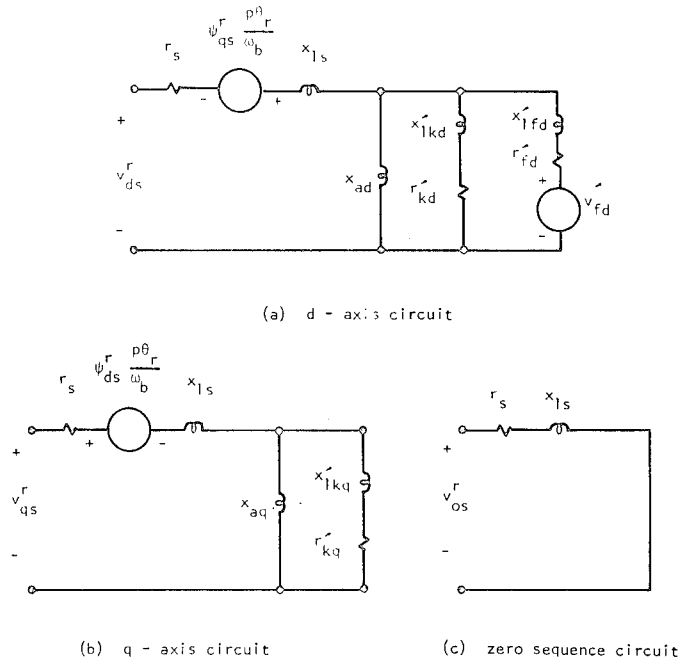

Fig. 3. Equivalent circuits of a synchronous machine with reference frame fixed onto the rotor.

are of greater detail than what is used in this paper. However, these models are complex, costly to implement, and require additional test data which are not generally available.

The synchronous machine model used to represent the inductor machine is derived from the analysis by Park.[10] The direct (d-) and quadrature (q-) axis equivalent circuits in the rotor reference frame are shown in Figure 3. The superscripts r and s attached to the variables indicate that these variables are on the reference frame attached to the rotor and on a stationary reference frame, respectively

The electromagnetic torque developed by the machine is given by

$$T_{em} = \frac{3P}{4\omega_b} (\psi^r_{ds} i^r_{qs} - \psi^r_{qs} i^r_{ds}) \quad \text{N.m.}$$

where

P is the number of poles

ω_b is the base angular frequency

ψ^r_{ds}, ψ^r_{qs} are the d- and q-axis stator flux linkages in the rotor reference frame, respectively

i^r_{ds}, i^r_{qs} are the d- and q-axis stator currents in the rotor reference frame, respectively.

With analog computation, it has been found convenient to arrange the voltage and flux linkage equations into the following form.[11] Using a generator notation:

Stator d-q flux linkages

$$\psi^r_{qs} = \int \omega_b \{v^r_{qs} - \psi^r_{ds} \frac{\omega_r}{\omega_b} + \frac{r_s}{x_{ls}} (\psi^r_{aq} - \psi^r_{qs})\} \, dt$$

$$\psi^r_{ds} = \int \omega_b \{v^r_{ds} + \psi^r_{qs} \frac{\omega_r}{\omega_b} + \frac{r_s}{x_{ls}} (\psi^r_{ad} - \psi^r_{ds})\} \, d$$

where ω_r is the rotor speed (or $p\theta_r$)

Field flux linkage

$$\psi'_{fd} = \int \{v'_{fd} + \frac{r'_{fd}\omega_b}{x'_{lfd}} (\psi^r_{ad} - \psi'_{fd})\} \, dt$$

where

$$v'_{fd} = \frac{\omega_b r'_{fd}}{x_{ad}} E_x$$

E_x is the exciter voltage.

Damper d-q flux linkages

$$\psi^r_{kq} = \frac{\omega_b r'_{kq}}{x'_{lkq}} \int (\psi^r_{aq} - \psi^r_{kq}) \, dt$$

$$\psi^r_{kd} = \frac{\omega_b r'_{kd}}{x'_{lkd}} \int (\psi^r_{ad} - \psi^r_{kd}) \, dt$$

Mutual flux linkages on the d- and q- axes

$$\psi^r_{aq} = x_{mq} \left(\frac{\psi^r_{qs}}{x_{ls}} + \frac{\psi^r_{kq}}{x'_{lkq}}\right)$$

$$\psi^r_{ad} = x_{md} \left(\frac{\psi^r_{ds}}{x_{ls}} + \frac{\psi^r_{fd}}{x'_{lfd}} + \frac{\psi^r_{kd}}{x'_{lkd}}\right)$$

where

$$\frac{1}{x_{mq}} = \frac{1}{x_{aq}} + \frac{1}{x_{ls}} + \frac{1}{x'_{lkq}}$$

$$\frac{1}{x_{md}} = \frac{1}{x_{ad}} + \frac{1}{x_{ls}} + \frac{1}{x'_{lfd}}$$

Also,

$$\psi^r_{qs} = \psi^r_{aq} - x_{ls}\, i^r_{qs}$$

$$\psi^r_{ds} = \psi^r_{ad} - x_{ls}\, i^r_{ds}$$

$$\psi'_{fd} = \psi^r_{ad} + x'_{lfd}\, i'_{fd}$$

Changing the stator d-q variables from the reference frame attached to the rotor to a similar d-q stationary reference frame, or vice-versa, is effected by the transformation $[T_1]$, given in matrix form as:

$$[T_1] = \begin{bmatrix} \cos\theta_r & -\sin\theta_r & 0 \\ \sin\theta_r & \cos\theta_r & 0 \\ 0 & 0 & 1 \end{bmatrix}$$

Figure 4 shows the axes of the above-mentioned reference frames relative to the coil axes of the stator phase windings.

For example, the transformation of dqo stator voltages from stationary to the rotor reference frame is given by

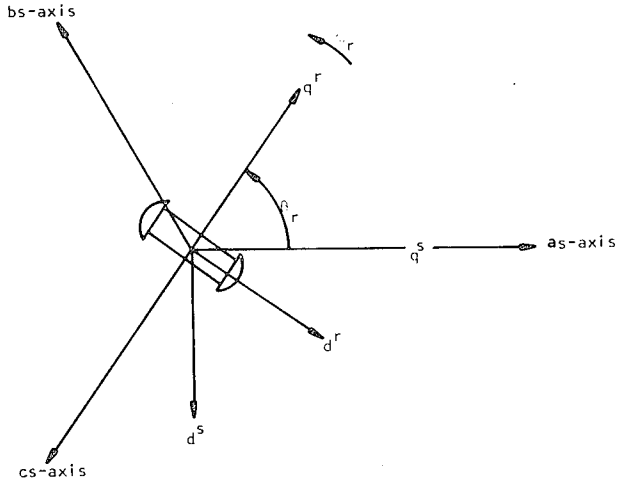

Fig. 4. Axes of reference.

$$\begin{bmatrix} v^r_{qs} \\ v^r_{ds} \\ v^r_{os} \end{bmatrix} = [T_1] \begin{bmatrix} v^s_{qs} \\ v^s_{ds} \\ v^s_{os} \end{bmatrix}$$

Transformation of dqo stator currents from rotor to stationary reference frame is

$$\begin{bmatrix} i^s_{qs} \\ i^s_{ds} \\ i^s_{os} \end{bmatrix} = [T_1]^{-1} \begin{bmatrix} i^r_{qs} \\ i^r_{ds} \\ i^r_{os} \end{bmatrix}$$

Similarly, the relationships between the stationary reference frame dqo variables and the abc phase variables are given by

$$\begin{bmatrix} v^s_{qs} \\ v^s_{ds} \\ v^s_{os} \end{bmatrix} = [T_2] \begin{bmatrix} v_{as} \\ v_{bs} \\ v_{cs} \end{bmatrix}$$

$$\begin{bmatrix} i_{as} \\ i_{bs} \\ i_{cs} \end{bmatrix} = [T_2]^{-1} \begin{bmatrix} i^s_{qs} \\ i^s_{ds} \\ i^s_{os} \end{bmatrix}$$

where

$$[T_2] = \begin{bmatrix} \frac{2}{3} & -\frac{1}{3} & -\frac{1}{3} \\ 0 & -\frac{1}{\sqrt{3}} & \frac{1}{\sqrt{3}} \\ \frac{1}{3} & \frac{1}{3} & \frac{1}{3} \end{bmatrix}$$

ROTOR/FLYWHEEL ASSEMBLY

The electromagnetic torque developed by the inductor machine acts on the rotor/flywheel assembly; when motoring, it accelerates the flywheel. In the generating mode, the momentum of the flywheel overcomes the counter elec-

tromagnetic torque developed by the machine. The equation of motion of the rotor/flywheel assembly is given by:

$$J \frac{d\omega_r}{dt} + T_{em} = T_f$$

where

J is the combined inertia of the rotor/flywheel assembly

T_f is the rotational friction torque

BRIDGE CONVERTER AND AUXILIARY COMMUTATION CIRCUIT

The simulation of the dual converter and its auxiliary commutation circuit is built upon simulated thyristor modules. The thyristor is represented as an ideal switch with negligible forward voltage drop, infinite reverse-voltage resistance and negligible turn-on and turn-off time. Each thyristor module consisted of an ideal thyristor device and a small $\frac{di}{dt}$ limiting inductor in series.

Conduction through the thyristor is unidirectional. It is triggered on by a gating signal when the device is forward bias, and it remains in conduction until the current falls below a threshold value, in this case zero. The following equations describe the operation of the thyristor T_1 in the upper half and thyristor T_2 of the lower half of the bridge converter:

$$i_1 = \frac{1}{L_\ell} \int (v_{as} - v_{ps})\, dt$$

when $\int (v_{as} - v_{ps})\, dt > 0$ and $v_{g1} > 0$

otherwise $i_1 = 0$

$$i_2 = \frac{1}{L_\ell} \int (v_{ns} - v_{cs})\, dt$$

when $\int (v_{ns} - v_{cs})\, dt > 0$ and $v_{g2} > 0$

otherwise $i_2 = 0$

where

v_{g1} and v_{g2} are the gating signals to T_1 and T_2, respectively

L_ℓ is the series di/dt limiting inductance

Similar equations can be written for the other thyristors in the circuit by substituting in the appropriate forward bias voltages.

Gating signals for the main thyristors are obtained from a 6-stage ring counter which is shifted around by pulses from a pulse generator triggered by a level comparator. The inputs to the level comparator are the output from a triangular wave generator, which is driven by the phase angle regulator, and a synchronous square wave of fixed magnitude. The rate of switching is thus proportional to the output from the phase angle regulator. With forced-commutation, the top and bottom auxiliary thyristor is delayed until the commutating capacitor in the neutral connection charges to a predetermined voltage level.[6] The voltage across the capacitor C can be expressed in terms of the currents flowing through the auxiliary thyristors:

$$v_{ms} = \frac{1}{C} \int (i_8 - i_7)\, dt$$

With analog computation, it is at times advantageous if not essential to assign as output of integrators such state variables as current flowing through an inductor or voltage across a capacitor. Such an approach, however, could bring about problems in interfacing elemental simulations to satisfy connections constraints. Figure 5 shows the equivalent circuit used to simulate one

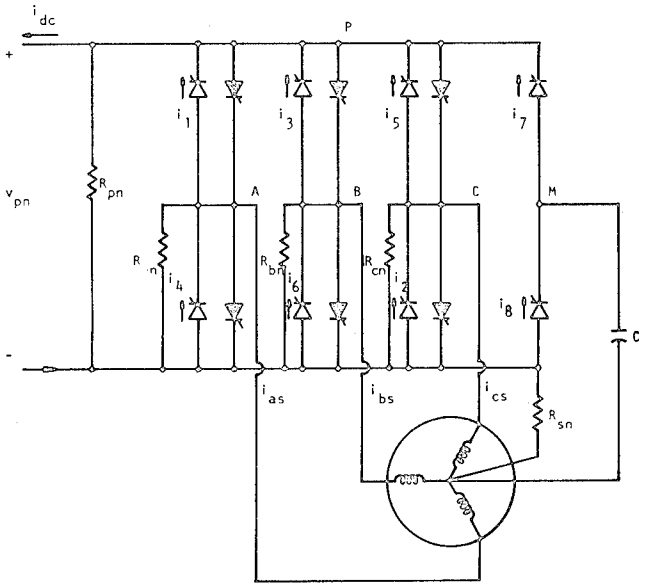

Fig. 5. Simulation of converter bridge circuit.

bridge of the dual converter, the auxiliary commutation circuit and the stator windings of the inductor machine. Resistors R_{pn}, R_{sn}, R_{an}, R_{bn} and R_{cn} are introduced in between points across which voltages are required. These resistors in the simulation are necessarily large so as to minimize any unwanted effects not inherent in the actual system. With the introduction of these resistors, the equations for the following voltages can be written in terms of available current variables:

$$v_{pn} = R_{pn}(i_1 + i_3 + i_5 + i_7 - i_{dc})$$

$$v_{ns} = R_{ns}(i_{as} + i_{bs} + i_{cs} - i_{ms})$$

$$v_{ps} = v_{pn} + v_{ns}$$

$$v_{an} = R_{an}(i_{as} - i_1 + i_4)$$

$$v_{bn} = R_{bn}(i_{bs} - i_3 + i_6)$$

$$v_{cn} = R_{cn}(i_{cs} - i_5 + i_2)$$

$$v_{as} = v_{an} + v_{ns}$$

$$v_{bs} = v_{bn} + v_{ns}$$

$$v_{cs} = v_{cn} + v_{ns}$$

DC LINK

In the flywheel charging mode, the dc terminals of the converter are connected to a dc voltage source. The dc link between converter terminals and dc source has a small inductance and negligible resistance. However, during the initial charging operation, when the flywheel has to be accelerated from rest, a starting resistor is inserted in the dc link to limit the starting current. The starting resistor is shorted out when the inductor machine builds up sufficient voltage with increase in rotor speed. The dc link current during the flywheel charging operation is given by:

$$i_{dc} = \frac{1}{L_{dc}} \int (V_{dc} - v_{np} - i_{dc} R_{dc})\, dt$$

where

V_{dc} is the battery or external dc source voltage

L_{dc} is the inductance of the dc link

R_{dc} is the resistance of the dc link

In the discharging mode, the inductor machine operates as a generator drawing on the kinetic energy stored in the flywheel. The controlled rectifier section of the inverse-parallel converter arrangement rectifies the machine's ac voltages. The dc voltage output is applied to the armature winding of the dc traction motor, which drives the vehicle. The dc link current during the flywheel discharge mode is given by:

$$i_{dc} = \frac{1}{(L_{dc} + L_{aq})} \int (v_{pn} - e_a - i_{dc} R_a)\, dt$$

where

L_{aq} is the armature inductance

R_a is the armature circuit resistance including that of the dc link

e_a is the back e.m.f of the traction motor

DC TRACTION MOTOR AND VEHICLE LOADING

Assuming the bipolar field-excited traction motor is a shunt-excited machine, the currents in the armature and field windings are given by:

$$i_a = i_{dc}$$

$$i_f = \frac{1}{L_{ff}} \int (v_f - i_f R_f)\, dt$$

where

v_f is the dc field voltage

L_{ff} is the inductance of the field winding

The induced e.m.f of the armature winding e_a can be expressed in terms of the field excitation and speed of the machine ω_m:

$$e_a = K_f i_f \omega_m$$

where K_f is a machine constant that can be obtained from the no-load magnetization curve of the dc traction motor.

The electromagnetic power output of the traction motor is given by

$$P_{em} = e_a i_a$$

Main components of vehicle loading[12] on the traction motor are

- air resistance or drag, P_D
- rolling and bearing friction, P_F
- gravitational force, P_G

In kilowatts; P_D, P_F and P_G are given by

$$P_D = 5.089 \times 10^{-6} C_D S V^3$$

$$P_F = (11.215 \times 10^{-6} V + 5.926 \times 10^{-8} + 3.76 \times 10^{-1} V^3) W$$

$$P_G = 1.99 \times 10^{-3} WV \sin (\tan^{-1} \frac{\gamma}{100})$$

where

C_D = air drag coefficient
S = vehicle frontal area; sq. ft.
V = vehicle velocity; mph
W = gross weight of vehicle; lbs.
γ = slope; percent

The combined inertia power in kilowatts, assuming that the rotational component is 10 percent of the translational component, is given by

$$P_A = 9.977 \times 10^{-2} W V \frac{dV}{dt}$$

If the relation between linear velocity of the vehicle and the rotational speed of the dc machine is given by

$$V = k \omega_m$$

The equation of motion of the rotor of the traction motor can be expressed in terms of the mechanical power developed by the motor, the equivalent loading, and inertia power at the shaft of the machine:

$$P_{em} - P_D - P_F - P_G = \frac{1}{2} J_e p\omega_m^2$$

where

$$J_e = 9.977 \times 10^{-2} Wk^2$$

SAMPLE RESULT

Following the approach described, an analog simulation of the flywheel energy storage vehicle drive system was implemented on two EAI 680 analog computers. Figure 6 shows the interconnections between the major components in the simulation. A sample run showing the start-up, with the flywheel initially at a standstill, is presented in Figures 7a and 7b. Transitions from forced- to load-commutation and from fixed torque angle reference to current control are indicated by the event markers A and B, respectively. The transients caused by shorting out the starting resistor at about one half rated speed (point C) and that due to reinserting the same resistor a short time thereafter (point D) are shown in Figures 8a and 8b.

These results obtained from the simulation compared favorably with those published by Plunkett and Turnbull.[3,4] A typical set of results shown in Figs. 7 and 8 yields considerable information, such as the instantaneous torque pulsations, voltage and current levels of various components under steady-state and transient operations. Readily observable from these traces are the presence of voltage and current spikes during the period when the converter is forced-commutated, and the large overshoot of current following the shorting of the starting resistor. Examples of some observations which are not apparent from the figures shown, but are noted when operating the simulation, are: (i) a knowledge of the position of the rotor when it is at rest is helpful in determining the initial pattern of thyristor firing of the converter bridge for a smoother startup, and (ii) a good proportion of the total input energy during the initial startup period is dissipated in the starting resistor when a simple unregulated voltage source supply is used.

CONCLUSION

A method of simulation of the flywheel propulsion system for buses has been presented. This simulation is sufficiently detailed and flexible to be of use in performance evaluation and design studies of the system. Although an analog simulation of the system has been implemented, this same techniques may be adapted to a digital simulation.

ACKNOWLEDGEMENT

The work reported in this paper was supported by the U.S. Department of Transportation under contract DCT-RC-92004.

APPENDIX

The parameters of the system for the sample run were taken from References 2 and 4.

base frequency	f_{base}	= 500 Hz
base voltage (peak phase value)	V_{base}	= 71.8 V
base power	P_{base}	= 20 kVA
number of poles	P	= 8 poles
field to stator winding turns ratio	$\frac{n_f}{n_a}$	= 52.6
stator resistance	r_s	= 0.0139Ω
stator leakage reactance at base frequency	x_{ls}	= 0.07228Ω
d-axis magnetizing reactance at base frequency	x_{ad}	= 0.215Ω
q-axis magnetizing reactance at base frequency	x_{aq}	= 0.1197Ω
field leakage reactance referred to stator	x'_{lfd}	= 0.7458Ω
field resistance referred to stator	r'_{fd}	= 0.00309Ω
d-axis damper circuit resistance referred to stator	r'_{kd}	= 0.02Ω
q-axis damper circuit resistance referred to stator	r'_{kq}	= 0.04Ω
d-axis damper circuit leakage reactance referred to stator	x'_{lkd}	= 0.1401Ω
q-axis damper circuit leakage reactance referred to stator	x'_{lkq}	= 0.6283Ω
commutation capacitor	C	= 300 μF
thyristor series inductance	L_ℓ	= 10 μH
starting resistor	R_s	= 1 Ω
dc source voltage	V_{dc}	= 100 V

REFERENCES

1. "A Study of Flywheel Energy Storage for Urban Transit Vehicles," Phase 1 - Preliminary Conceptual Design Studies, Final Report, Contract No. DOT-UT-60096T, September 16, 1977, General Electric Co.

2. "Demonstration of an Inductor Motor/Alternator/Flywheel Energy Storage System," Phase 1, Final Report, Contract No. EY76-C-02-4010, January 2, 1978.

3. A. B. Plunkett and F. G. Turnbull, "Load Commutated Inverter/Synchronous Motor Drive Without a Shaft Position Sensor," 1977 IEEE/IAS Annual Meeting, Conference Record, pp. 748-757.

4. A. B. Plunkett and F. G. Turnbull, "System Design Method for a Load Commutated Inverter-Synchronous Motor Drive," 1978 IEEE/IAS Annual Meeting, Conference Record, pp. 812-819.

5. C. Adamson and N. G. Hingorani, High Voltage Direct Current Power Transmission, Garraway Ltd., London (1960), pp. 121-124.

6. R. L. Steigerwald and T. A. Lipo, "Analysis of a Novel Forced-Commutation Starting Scheme for a Load Commutated Synchronous Motor Drive," 1977 IEEE/IAS Annual Meeting, Conference Record, pp. 739-747.

7. R. L. Steigerwald, "Characteristics of a Current-Fed Inverter with Commutation Applied Through Load Neutral Point," 1978 IEEE/IAS Annual Meeting, Conference Record, pp. 502-516.

8. W. B. Jackson and R. L. Winchester, "Direct and Quadrature Axis Equivalent Circuits for Solid-Rotor Turbine Generators," IEEE Trans., Vol. PAS-88, July 1969, pp. 1121-1136.

9. I. M. Canay, "Causes of Discrepancies on Calculation of Rotor Quantities and Exact Equivalent Diagrams of the Synchronous Machine," IEEE Trans., Vol. PAS-88, July 1969, pp. 1114-1120

10. R. H. Park, "Two-Reaction Theory of Synchronous Machines," Generalized Method of Analysis - Part I, AIEE Trans., Vol. 45, July 1929, pp. 716-730.

11. C. H. Thomas, discussion of "Analogue Computer Representations of Synchronous Generators in Voltage-Regulation Studies," by M. Riaz, AIEE Trans., Vol. 75, Dec. 1956, pp. 1178-1184.

12. G. S. Larson and H. Zuckerberg, "Flywheel/Diesel Hybrid Power Drive: Urban Bus Vehicle Simulation," Final Report, UMTA-MA-06-0044-78-1, May 1978, U.S. Department of Transportation.

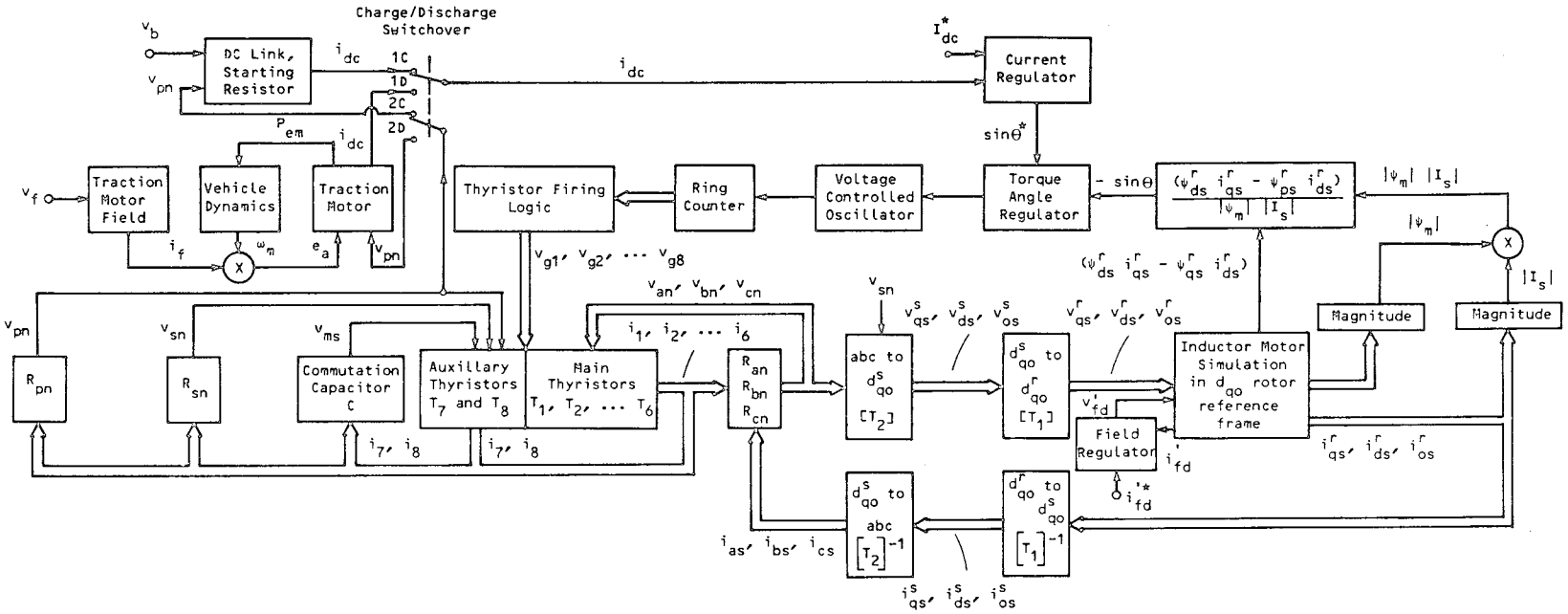

Fig. 6. Analog simulation of a flywheel energy storage propulsion system.

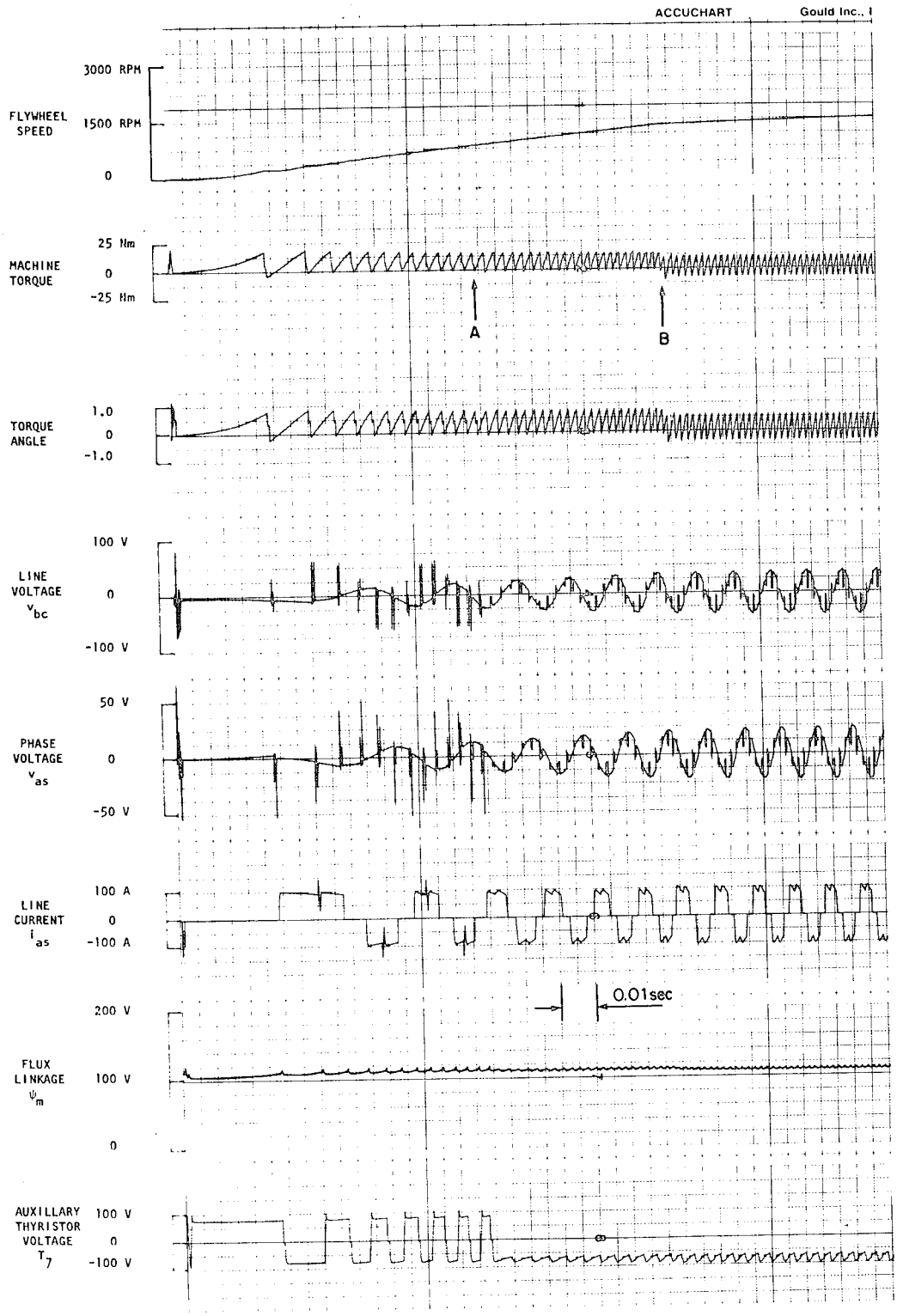

Fig. 7a. Startup from Standstill:
Point A - forced to load-commutation,
Point B - torque angle control to current control.

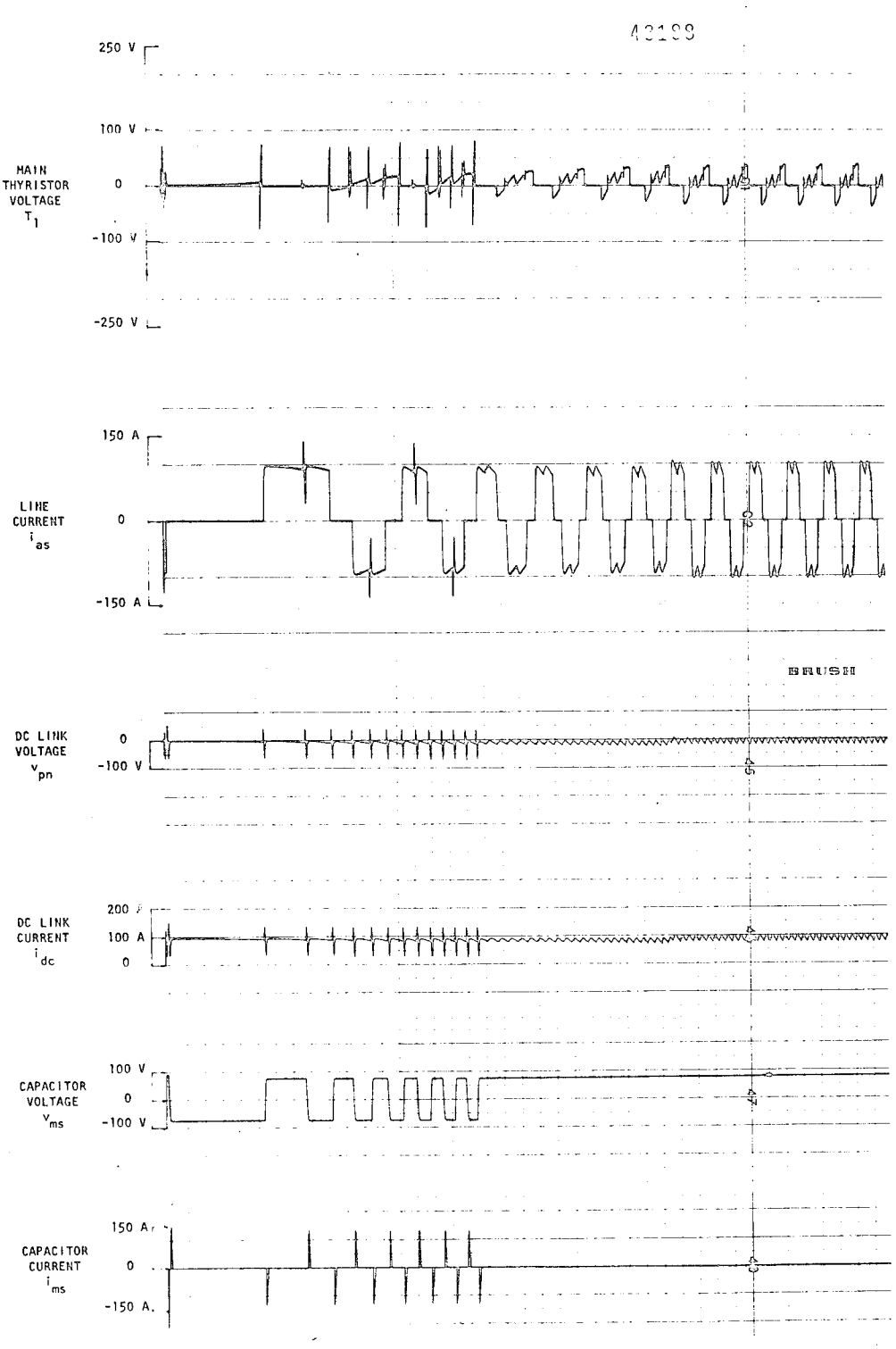

Fig. 7b. Startup from standstill.

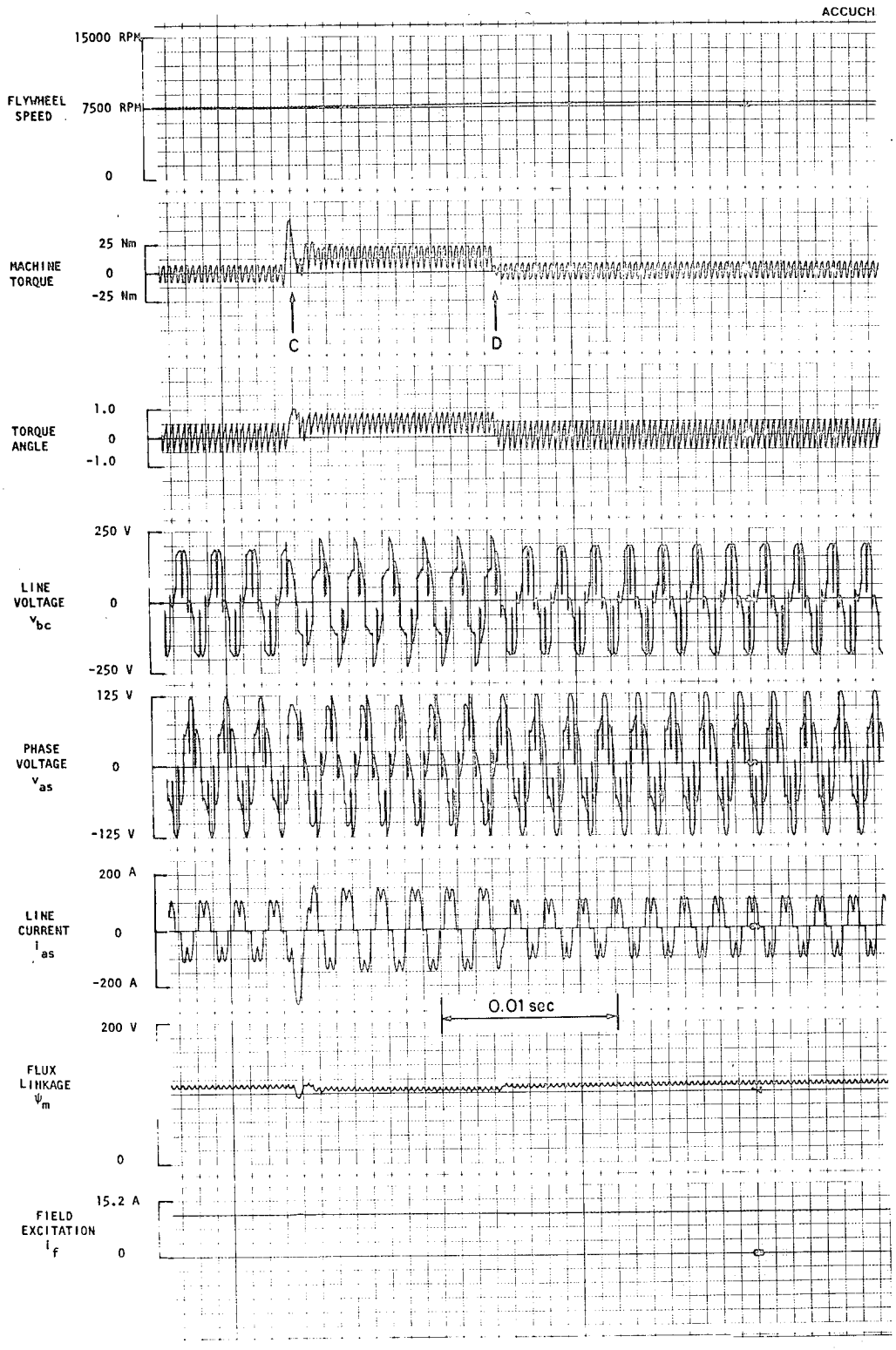

Fig. 8a. Shorting of starting resistor:
Point C - resistor shorted,
Point D - resistor reinserted.

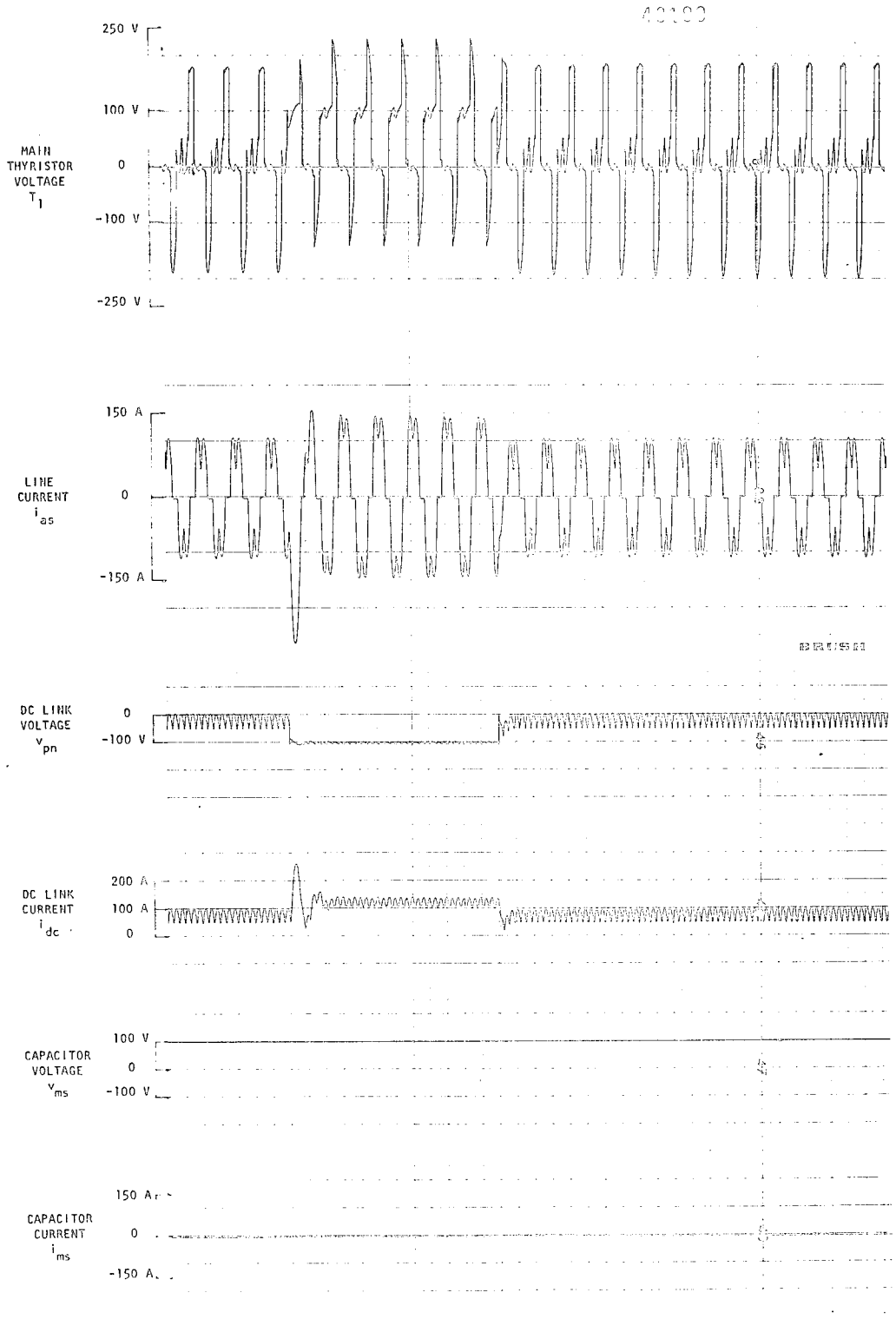

Fig. 8b. Shorting of starting resistor.

A FLYWHEEL ENERGY STORAGE PROPULSION SYSTEM FOR INTRA URBAN BUSES

By R. E. Rinehart
FESS Program Manager
Transportation Systems Business Division
General Electric Company
Erie, Pennsylvania 16531

ABSTRACT

The development of a flywheel energy storage propulsion system for an urban transit coach is described. This project is being carried out under government contract, and is a major element in an energy conservation and propulsion technology program that is jointly sponsored by the U.S. Departments of Energy (DOE) and Transportation (DOT). Within DOT, responsibility for this program rests with the Urban Mass Transportation Administration (UMTA), and UMTA has designated DOT's Transportation Systems Center (TSC) in Cambridge, Mass., as its systems manager.

The designs of the key system elements - the flywheel machine package, the power conditioning subsystem, and the DC traction motor - are briefly described at their present stage of development, together with the installation proposed for mounting the system in the coach.

Operation of the flywheel powered coach is described as it executes a typical urban transit mission. Projected performance of the flywheel powered coach is then presented, and the estimated life cycle costs compared with those of diesel and electric trolley coach systems.

INTRODUCTION

IMPETUS

Present urban transit coaches waste a substantial portion of their propulsion energy, energy derived largely from petroleum based fuels which are becoming increasingly more costly. An on-board flywheel offers a way to store the energy normally wasted in braking in the form of rotational kinetic energy. If the on-board flywheel can be periodically recharged from a wayside source, the vehicle need not require petroleum based fuels for its propulsion energy.

Unlike conventional batteries, a Flywheel Energy Storage System (FESS) can receive regenerated energy during vehicle braking at a very high rate, and can supply propulsion energy during vehicle acceleration at the same high rate. To recharge it, the FESS can accept energy at this high rate from wayside electric power sources. Since it does not use an on-board combustion engine, FESS can help reduce dependence on petroleum based fuels and also reduce noise and air pollution in urban areas.

For the preceding reasons, the U.S. Departments of Energy (DOE) and Transportation (DOT) decided to jointly sponsor a FESS development program. Within DOT, responsibility for this program rests with the Urban Mass Transportation Administration (UMTA), and UMTA has designated DOT's Transportation Systems Center (TSC) in Cambridge, Mass., as its systems manager. In April, 1979 TSC awarded General Electric a contract for the design, development, fabrication, test and evaluation of an engineering prototype FESS. This paper describes the progress made during the first eighteen months of this contract.

GENERAL ELECTRIC FESS PROPULSION CONCEPT

Figure 1 shows the main elements comprising the General Electric FESS propulsion concept.

- A flywheel machine, consisting of a multi-disk flywheel rotor, directly coupled to the shaft of an inductor

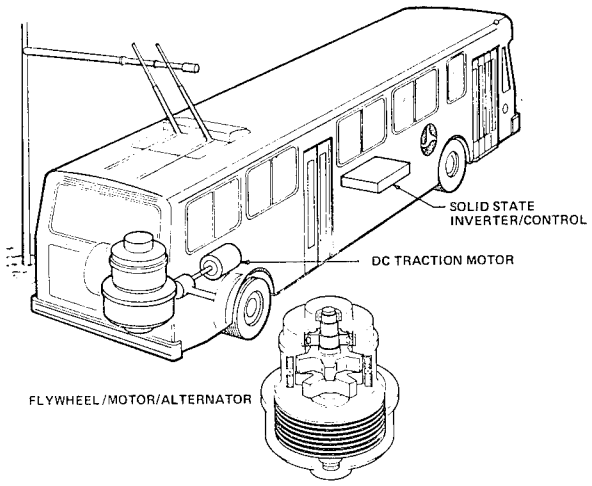

Fig.1 FESS Vehicle System

motor/alternator, which transfers power into or out of the flywheel rotor. It is mounted vertically to avoid generating gyroscopic forces when the coach executes a turn.

- A solid state inverter/rectifier to control the electrical power to and from the flywheel machine.

- A DC traction motor which provides the final drive to propel the coach, and, acting as a generator, brakes the vehicle regeneratively, providing electrical energy to the flywheel machine via the inverter.

Succeeding sections of this paper describe the design of each of the major components and auxiliary subsystems, as well as performance predictions for the FESS installed in a typical urban transit coach.

EQUIPMENT DESCRIPTION

This section describes the flywheel machine and its major components:

- The flywheel rotor which stores the energy
- The inductor motor alternator which effects the transfer of energy to and from the flywheel.

The power conditioning system is briefly described, and the installation of all the components in a typical coach is then shown.

FLYWHEEL MACHINE

The flywheel machine, Figure 2, stands 4 ft. (1.22m) high, and is 4 ft. (1.22m) in diameter. The rotor assembly consists of three pieces:

- The multi-disk, high strength steel, flywheel rotor, bolted to
- A non-magnetic coupler ring, in turn bolted to
- The solid steel rotor of the inductor motor/alternator.

It is designed to cycle between 5750 and 11,500 rpm during operation, providing 12.0 Kw-hr (43 MJ) of useful energy with 16Kw-hr (51 MJ) stored at top speed. The tapered roller bearing at the bottom supports the weight of the rotor, while the top bearing serves only to guide the shaft. Stiffness of the rotor and its

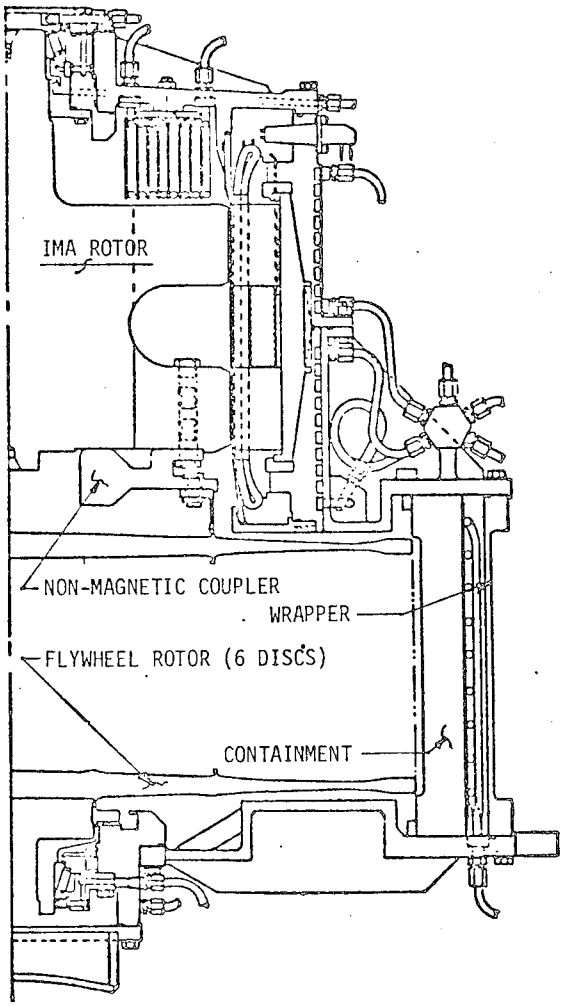

Fig.2. Flywheel Machine

bearings have been selected to avoid critical speeds during operation. An internal, integral lubrication system supplies oil to the bearings at all speeds.

To reduce windage losses the rotor assembly fits inside an evacuated chamber containing helium at 0.01 atmospheres. To avoid corona problems, the motor/alternator stator is at atmospheric pressure, isolated from the low pressure chamber by a cylindrical non-metallic liner. O-rings are used throughout the machine to seal the low pressure chamber. Surrounding the flywheel rotor is a 1.7 in. (4.32cm) thick high strength steel containment cylinder, designed to withstand the forces developed by the failure of any individual disk. Ample space is provided between the containment and the outer wrapper to permit the containment to distort without causing a failure of the structure which holds the machine together. To conserve weight, the frame heads and connecting pieces which form the shell of the machine are welded aluminum structures. The stator of the motor alternator is liquid cooled via passages in the outer shell. An external heat exchanger dissipates the heat from both the motor coolant and the lubricating oil.

Flywheel Rotor. Figure 3 shows the flywheel rotor, consisting of six 40" (1.02m) diameter solid disks inertia welded together. A flange is welded to one of the end disks, to permit the flywheel rotor to be bolted to the rotor of the inductor motor/alternator. A stub shaft is welded to the other end disk to provide a bearing spindle. Each disk weighs 230 pounds (104 Kg) and the total weight of the flywheel rotor assembly is 1440 pounds (654 kg).

The disks are made from a special low alloy, high strength steel which has been triply refined to remove gaseous and solid impurities. After heat treating, the material has a minimum ultimate strength of 220,000 psi (1517 MPa). The material undergoes extensive non-destructive testing to inspect for any serious material flaws.

The specific energy of a rotating disk, in Kwhr/#(J/g) is given by the

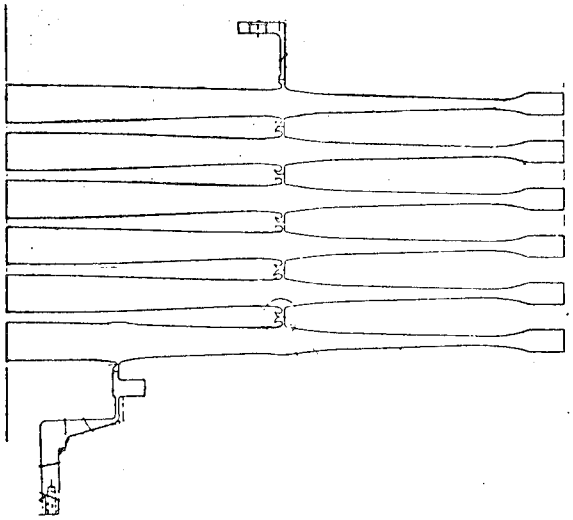

Fig. 3 Inertia Welded Flywheel Rotor

equation

$$\frac{E}{W} = K \frac{\sigma}{\rho}$$

and is a measure of how well the material is being utilized for energy storage. The stress level σ, and the density ρ, are functions of the material itself, but the constant, K, is determined by the shape of the disk. It may vary from 0.61 for a constant thickness disk, to a theoretical maximum of 1.0 for a constant stress disk of infinite diameter. The disk profile shown in Figure 3 is essentially a constant stress design of a finite diameter, with a ring added to form a rim at the periphery. The shape factor for the resultant profile is 0.87. At a speed of 11,500 rpm the combined von Mises stress is 105,000 psi (725 MPa) resulting in a peak energy density of 9.8 watt-hr/#(7.7 J/g).

Since the speed of the flywheel varies as the bus performs its mission, the design of the rotor must insure an adequate fatigue life. Calculations indicate that a flywheel powered bus would experience about 240,000 cycles of 50%-100% speed changes during its 23 year life.

Inertia welding is used to join the flywheel disks to each other, and to the stub shaft and coupler flange as well. The inertia welding machine has a flywheel of its own. One of the

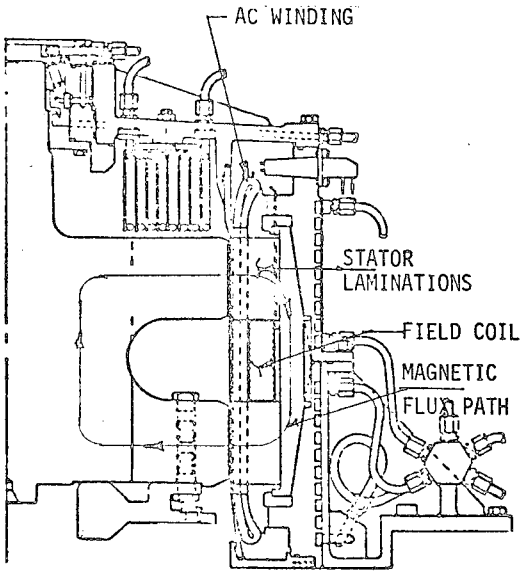

Fig.4 Inductor Motor Alternator Crossectional View

pieces to be welded is coupled to this flywheel, and the assembly spun up to a predetermined speed. The mating piece is stationary, and is thrust against the rotating piece. The heat generated raises the contacting material to plastic temperature and the applied pressure forges the two pieces together. The resultant joint has excellent strength and avoids the stress concentrations present in a bolted assembly.

Inductor Motor/Alternator. The inductor motor/alternator design is shown in Figure 4. The stator is 22 in. (0.56 m) long overall and has a 34 in. (0.86 m) outside diameter. The rotor diameter is 22 in. (.56 m) in diameter across the lobes and 12 in. (.30 m) in diameter for its cylindrical portion. The rotor weighs 760 lbs. (345 kg) and stores 1.4 Kw-hrs (5.0 MJ) of useful kinetic energy. The entire motor/alternator has 1620 lbs. (736 kg) electromagnetic weight.

The inductor motor/alternator has been selected as the interface between the flywheel and the electrical portion of the propulsion system because it can be directly coupled with the flywheel and can be operated within an hermetically sealed environment. This is made possible because of its solid rotor construction, low rotor electrical losses, and relatively high rotor-temperature capability.

Fundamentally, it is a ten pole synchronous-type machine whose magnetic circuit configuration has been modified in such a fashion as to allow the DC excitation winding to be placed in the stator. As with most rotating electrical machines, it performs equally well as a motor or as an alternator. Since the basic AC machine is to be operated in a DC system, a DC-AC inverter is required as an interface. If the frequency output of the inverter in the motoring mode is controlled by the rotating velocity of the rotor, this system represents what is commonly known as a brushless DC motor system.

The operation of an inductor machine can best be explained by means of Figures 4 and 5. Figure 4 shows a DC field coil between two stacks of stator laminations. A DC current in the field coil drives a magnetic flux, as indicated, through one stack of laminations, into the rotor, through the rotor center axially, and through the frame to close the loop. Large magnetic slots (Figure 5) in the rotor interrupt the flux at the air gap and cause the flux through the AC winding to pulsate., This, in turn, generates an AC voltage in these winding. The windings are located in slots in the laminated stator stacks close to the airgap.

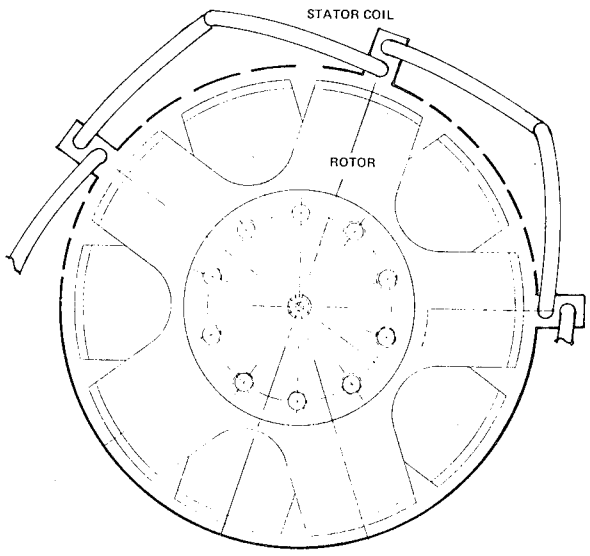

Fig.5 Inductor Motor Alternator End View

In order to make the induced voltage in both stator stacks add properly, the magnetic rotor slots in both rotor halves are offset by one-half pole pitch.

POWER CONDITIONING

Figure 6 is a schematic of the entire FESS, including the power conditioning. The power from the 600 VDC supply must be properly conditioned to supply the synchronous motor/alternator for flywheel acceleration. The conditioning consists of a synchronous motor commutated inverter which is simply a phase-controlled rectifier operating in the inversion mode. The requirement of a full useful energy recharge in 90 seconds establishes the power conditioner rating. Special equipment located in selected substations is required to accelerate the flywheel from 0 to 50% speed, but any source of 600 VDC power can be used to charge the flywheel within its normal operating range of 50% to 100% Flywheel speed. During normal coach operation the power conditioner controls energy transfer between the DC traction motor and the inductor motor/alternator for coach acceleration, cruise, and deceleration. This completely electronic energy control system provides the ultimate in smoothness of coach operation.

An onboard auxiliary power conditioner, identified as "SCR Rectifier" in Figure 6, provides a regulated 600 VDC for hotel loads, battery charging, motor fields, power conditioning blower, flywheel machine ancillary loads, and electronic control power. Three transistorized DC-DC converters provide isolation and convert the regulated 600 volts to appropriate levels.

The system is controlled by a microcomputer subsystem. Operator requests are compared to operating conditions such as flywheel and vehicle speed to determine appropriate field and armature currents. All feedbacks are

FLYWHEEL ENERGY STORAGE SYSTEM

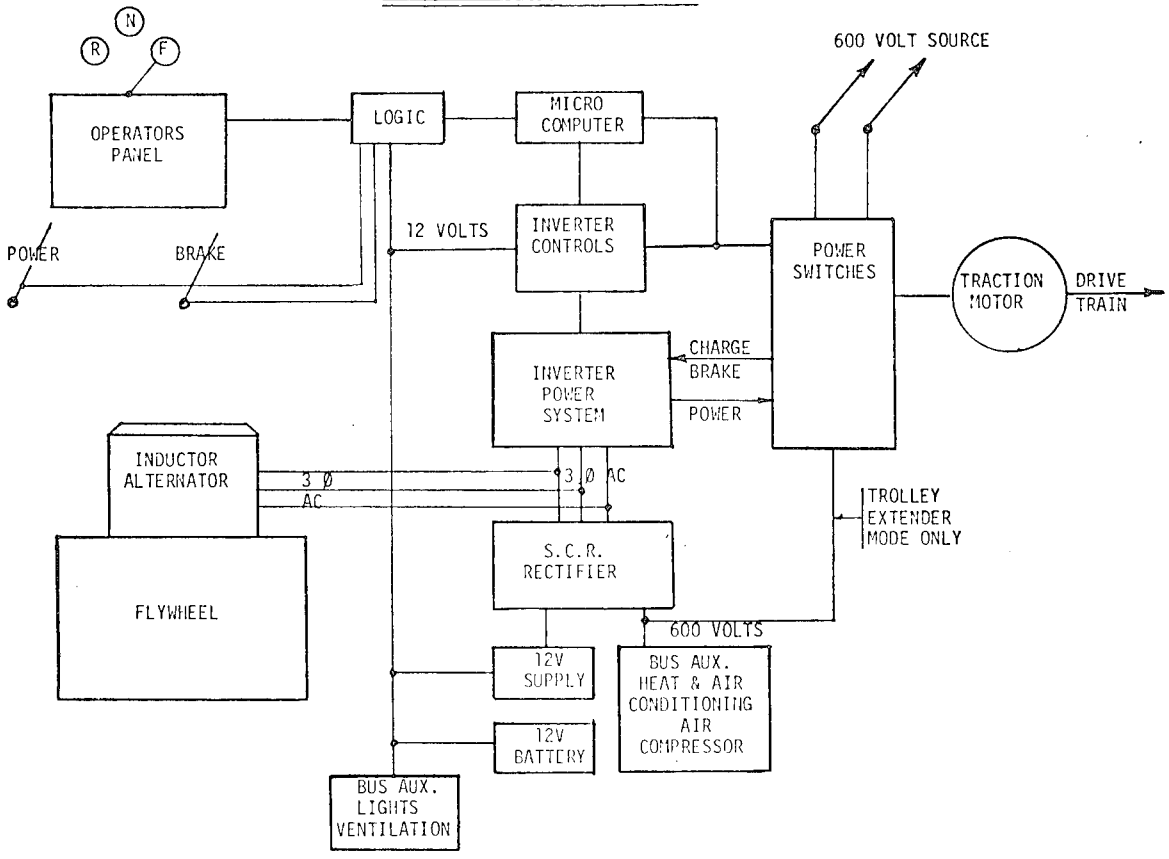

Fig.6 FESS Electrical Schematic

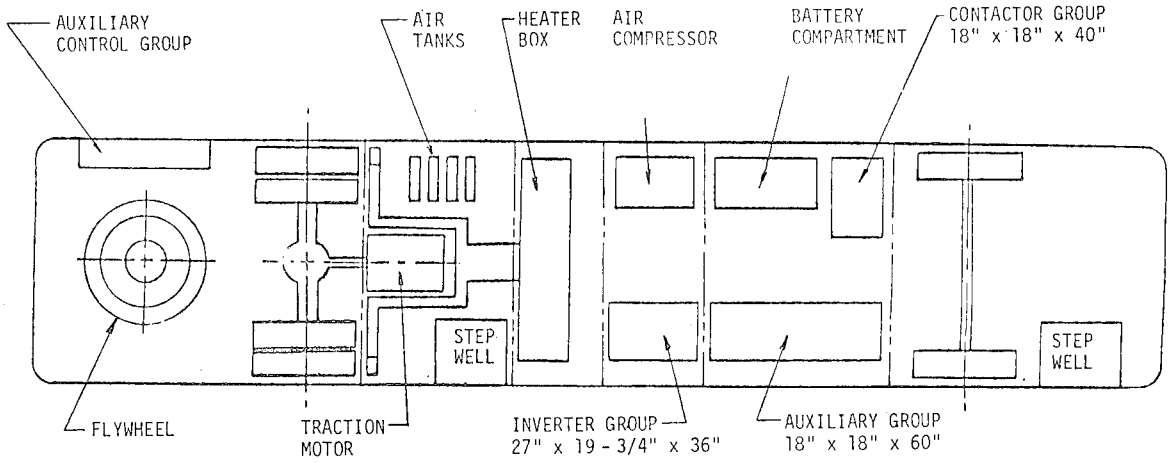

Fig.7 FESS Equipment Location

monitored to determine operating errors, and if a fault is observed, all conditions existing at that time are stored for later retrieval.

VEHICLE INSTALLATION

The prototype system is designed to be installed in a 40 foot (12 m) long by 102 inch (2.6 m) wide trolley coach, as shown in Figure 7. Because of its size, the flywheel machine will be installed aft of the rear axle to prevent intrusion into the passenger space. The traction motor, a separately excited standard GE1213M trolley coach motor, will be located forward of the rear axle. A heavier duty new axle is required to accommodate the added weight of the FESS machine and an additional estimated 1200 pounds (545 Kg) of structure which is added to the rear of the bus. This additional structure is needed to support and protect the flywheel machine package, as well as to gimbal it to prevent large gyroscopic forces from being developed during typical bus maneuvers.

The batteries, air compressor and power conditioning devices will be mounted underfloor, directly behind the front axle. This is the area normally occupied by the fuel tank on a diesel coach. This equipment is located as far forward as possible to help improve the weight distribution between the axles.

SYSTEM OPERATION AND PERFORMANCE

Figure 6 depicts the schematic of the total flywheel propulsion system, while Table I lists the anticipated performance.

Operator controls for the FESS vehicle are similar to a standard diesel or trolley coach. Depression of the accelerator pedal by the operator will translate into an armature current command for the traction motor. The further the pedal is depressed, the greater the current and the greater the torque for a given motor field. Full depression of the pedal will correspond to a maximum allowable current command, considering limitations due to the motor and/or to a maximum desirable acceleration with a light passenger load.

The brake pedal will perform a number of functions. Initial depression will establish connections to the armature of the traction motor so as to provide regenerative braking. Further depression of the brake pedal will command increasing amounts of traction motor armature current. At a point of intermediate pedal depression, a maximum allowable armature current will be commanded, and further depression will not increase this command. Further depression will, however, gradually increase the air-brake pressure from zero to a maximum value. At full pedal depression, both regenerative

Table I. Flywheel Bus Performance

Capability	Average Operation	Prototype Performance
Vehicle Load + driver	8 passengers + driver	47 seated/24 standees
Acceleration Rate	2.5 mph/sec (4.0 km/hr/sec)	3.5mph/sec (5.6Km/hr/sec)
Acceleration Time to Cruise Speed	10 sec.	
Cruise Speed	25 mph (40 Km/hr)	40 mph (60 Km/hr)
Cruise Time	18.8 sec.	
Decelerantion Rate	2.5 mph/sec (4.0 Km/hr/sec)	
Deceleration Time from Cruise Speed	10 sec.	
Dwell	20.4 sec.	
Stops per Mile	5	8
Turn Around Time, Every 6 Miles	330 sec.	
Average Speed	10.3 mph (16.5 Km/hr)	
Useable Energy Stpraoge	12.0 Kw hrs (43.2 MJ)	
Flywheel Speed Range	5750-11,500 rpm	
Charge Times	90 sec/50%-100% speed	40 sec/50% energy recharge
Range for Average Duty Cycle	3.4 miles (5.5 km)	
Grade	0%	20% @ 15 mph

and air-brake torques will be at their maximum. Except where very heavy braking is required, regenerative braking returns the coach kinetic energy to the flywheel. The system is programmed to use the traction motor to its maximum regeneration capability.

Actuation of a reversing switch by the operator will reverse the normal traction-motor armature connection. Acceleration and braking in reverse will then follow the same sequence as though the coach were operating in the forward direction.

Charging of the flywheel system will be accomplished by the trolley poles on the roof of the coach contacting a suitable 600 VDC overhead supply. In a pure flywheel application, the vehicle will go 3.4 miles (5.5 km) of stop-and-start driving with full auxiliary loads before requiring a recharge. If auxiliary heating and air conditioning loads are reduced, the range between recharges could be almost doubled.

LIFE CYCLE COSTS

Studies have been made to compare the life cycle costs of an all flywheel system to conventional diesel and trolley systems.

In these studies, costs were treated as being either capital costs (vehicle purchased cost, initial spare parts, garage facilities, and wayside facilities) or recurring costs (fuel or power cost, garage maintenance cost, wayside maintenance cost, and fixed cost). Adjustments were made for economic life, salvage, and vehicle reliability. For uniformity of comparison with results of other investigators, the following ground rules have been utilized in presenting life cycle costs for all of the systems:

- o 3.5% discount with constant 1980 dollars
- o Based on net present value, expressed in cents per coach mile.
- o Fuel costs based on average duty cycle (Table I)
  - Diesel fuel @ 89¢/gal
  - Electrical energy @ 4¢/kwhr

The results of these studies are summarized in Table II, where all the tangible cost elements are tabulated. An allowance is also included for the social benefits of electric propulsion systems: reduced air and noise

TABLE II Life Cycle Cost Comparison

	Diesel	Trolley	Flywheel
Vehicle Capital Cost	22.7	20.7	32.2
Less - Salvage Credit	-0.1	-0.0	-0.0
Spare Parts Capital Cost	1.9	2.1	3.3
Garage Facilities Capital Cost	8.0	7.3	5.7
Wayside Facilities Capital Cost	0.0	19.5	8.6
Reliability Adjustment	3.6	1.5	2.1
Total Capital Cost	36.1	51.1	51.9
Fuel Cost	17.5	11.2*-12.2**	13.5
Garage Maintenance Cost	30.4	21.2	23.7
Wayside Maintenance cost	0.0	8.0	2.1
Total Recurring Cost	47.9	40.4*-41.4**	39.3
Fixed Cost	150.7	150.7	150.7
Total Tangible Costs	234.7	242.2*-243.2**	241.9
Less Social Benefits	0.0	-2.7	-5.4
Net Life Cycle Cost	234.7	239.5*-240.5**	236.5

* Assumes energy regeneration capability as long as the traction motor, acting as a generator, develops a voltage equal to or greater than the line voltage.

**Without regeneration

pollution (flywheel and trolley) and elimination of overhead wire (flywheel only). The diesel coach is seen to be the lowest in life cycle cost, but the cost of the flywheel coach is only 1% higher if social benefits are included, or 3% higher without the social benefit allowance. The trolley coach system has the highest life cycle cost.

SUMMARY AND CONCLUSIONS

A new flywheel propulsion for urban transit coaches has been described and shown to provide the performance required in service and to have life cycle costs comparable to those of a diesel powered coach. Increases in diesel fuel costs are expected to result in a clear life cycle cost advantage for an all flywheel coach, except in areas where the cost of electrical energy is significantly above the national average. Flywheel propulsion thus offers a way to provide the public transportation the nation requires in its urban areas, while reducing exhaust emissions, the use of petroleum based fuels, and the expense of the extensive overhead wire network required for a trolley coach system.

ACKNOWLEDGEMENTS

The author wishes to acknowledge the contributions of several members of the General Electric FESS design team who provided the following inputs to this paper:

R. E. Birkett	Flywheel
J. P. Franz	Motor/Alternator
J. A. Nelson	Flywheel Machine
R. B. Bailey	Power Conditioning
D. L. Curtis	Vehicle Installation
I. W. Lichtenfels	System Design and Performance

and personnel of the General Electric Corporate Research and Development Center.

FLYWHEEL TROLLEY COACH PROPULSION WITH A HIGH-CAPACITY COMPOSITE FLYWHEEL

Louis J. Lawson
Program Manager
Garrett-AiResearch
2525 West 190th Street
Torrance, California 90509

ABSTRACT

The development of a flywheel propulsion system for a full-size transit bus is currently in progress at Garrett under a U.S. Department of Transportation contracted program sponsored by the Urban Mass Transportation Administration (UMTA) and managed by the Transportation Systems Center (TSC). A determination of requirements for the flywheel coach based on contacts with the transit industry has shown that the maximum possible range between recharges is desired. Thus, consideration has been directed toward a composite flywheel rotor since this technology can provide a high-capacity flywheel package (including containment) which has an energy density which is several times that of a metallic flywheel unit. The composite flywheel under development will provide more than 12 kwh of usable energy which will provide an urban operating range for the bus of nearly six kilometers between charges. The demonstration of flywheel propulsion in transit buses is expected to establish new alternatives in energy-efficient, ecologically acceptable urban transit vehicles.

INTRODUCTION

During the past 18 months, the application of flywheel propulsion to urban transit buses has received increased impetus with the decision by the Urban Mass Transportation Administration (UMTA) of DOT to proceed with the development, test, and evaluation of full-size prototype systems in such vehicles. Under UMTA sponsorship, the Transportation Systems Center (TSC) as systems manager has awarded parallel contracts to Garrett and General Electric for such systems. Garrett and General Electric are currently involved in the detail design of the propulsion components, principally the flywheel units.

The Garrett study of flywheel propulsion[1] for transit buses, which preceeded the present contract, identified the predominant requirements which the ultimate users (the U.S. transit properties) desire from the flywheel coach. These requirements are as follows:

- Maximum range between recharges
- Minimum recharge time
- Equivalent performance to Diesel bus
- Lower life cycle cost than Diesel bus

The first two requirements, which are clearly not mutually compatible, appear to require primary attention since no difficulty is foreseen in matching or surpassing the performance of a Diesel bus; and the life cycle costs of a flywheel coach, which are presently in the competitive range with the Diesel bus, are expected to become more favorable as fuel costs continue to escalate. Recharge time will ultimately be determined as a compromise between charging component ratings, peak power demand, and flywheel capacity. In contrast, vehicle range (or flywheel capacity) is a more independent variable which is largely constrained by axle load and volumetric limitations of the vehicle. This paper describes the tradeoff analysis which has been used to establish the maximum practical vehicle range between recharges.

PROPULSION SYSTEM DESCRIPTION

The block diagram of the flywheel propulsion system being developed by Garrett is shown in Fig. 1. During

flywheel charging operations, as shown in Fig. 1, the Automatic Collector System[2] is in contact with either stationary 600-volt dc charging terminals or the coach is operated under a short section of conventional trolley wires. For the stationary case, dc power is switched to the Dual Converter (with the Traction Motor disconnected). The Dual Converter is a three-phase full-wave phase delay rectifier which operates as an inverter during charging with load commutation provided by the overexcited synchronous homopolar inductor-type Flywheel Motor. In this mode of operation, the Flywheel Motor and Flywheel are accelerated until the fully charged condition is reached. Enroute charging of the flywheel is accomplished by engaging the trolley wires at a stop with the Automatic Collector and then operating the coach over its route while charging is accomplished. Power from the trolley wires is coupled to both the Traction Motor and Dual Converter to provide for normal vehicle performance while Flywheel charging is being accomplished. When the Flywheel is fully charged, the Automatic Collector poles may be stowed without stopping the vehicle.

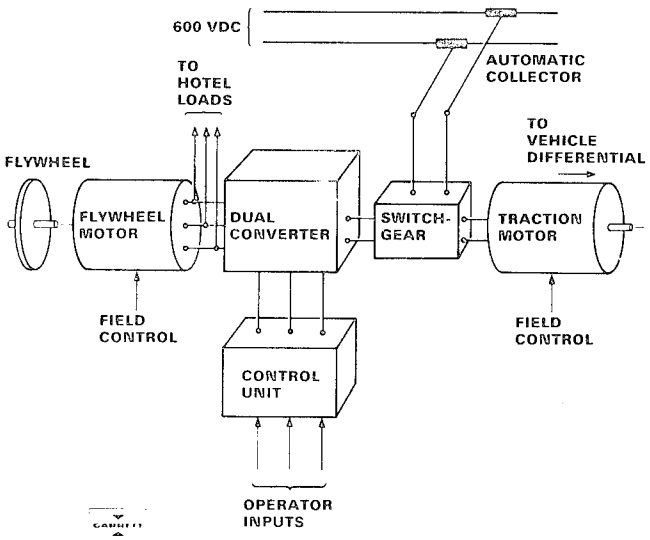

Fig. 1. Block Diagram of Flywheel Propulsion System

The startup of the Flywheel from standstill is accomplished by the use of a solid-state commutator in conjunction with the Dual Converter. This circuit controllably interrupts the dc current into the Dual Converter to provide for variable frequency Flywheel Motor voltage to accelerate the Flywheel. When the Flywheel reaches about 10 percent of full speed, the overexcited Flywheel Motor will naturally commutate the Dual Converter, and the solid-state commutator can be disabled.

The normal route operation of the flywheel propulsion system of Fig. 1 on Flywheel energy is accomplished by extracting energy from the Flywheel by field control of the Flywheel Motor. This three-phase ac power is rectified by the Dual Converter and fed to the armature of the Traction Motor. During initial acceleration, the Traction Motor armature voltage is varied in proportion to vehicle speed up to the Traction Motor speed at which full armature voltage can be applied (base speed). At that point, constant armature voltage is applied, and the tractive effort is controlled by varying the field excitation of the Traction Motor. The control of the two motor fields and the conducting angles of the Dual Converter thyristors is coordinated by the Control Unit in response to the operator inputs.

Essentially all vehicle braking is done electrically by the use of the Traction Motor as a generator which converts vehicle kinetic energy to dc power. The Traction Motor output is then coupled to the Dual Converter which acts to accelerate the Flywheel in the same manner as during charging. Recuperative electric braking is continued until near-zero speed at which point the normal bus service brake system is used to stop and hold the vehicle.

The operation of the flywheel coach may be continued with full route freedom until the flywheel is discharged. Trade-off studies have determined that the optimum flywheel speed range is about two to one, which makes available 75 percent of the stored energy for propulsion. Thus, when the flywheel slows to half speed, the vehicle is recharged at a charging station or under enroute trolley wires.

FLYWHEEL BACKGROUND

The broad Garrett experience with flywheels of various designs and materials was reviewed in order to determine the optimum configuration and capacity for the flywheel coach. The early Garrett flywheel experience was with steel flywheels used for rail car braking energy recuperation.

The joint UMTA/New York Metropolitan Transportation Authority program, which equipped two type R-32 subway cars[3] with flywheels, made use of a four steel disc configuration shown in Fig. 2. In this design, the 75-kg individual discs of AISI 4340 steel were bolted together and held in concentricity by the use of curvic couplings between discs. One disadvantage with this design is the heavy containment ring which was required to guard against the spectre of catastrophic disc failure. This ring, which has a radial thickness of 7.6 cm, is heavier than the flywheel rotor.

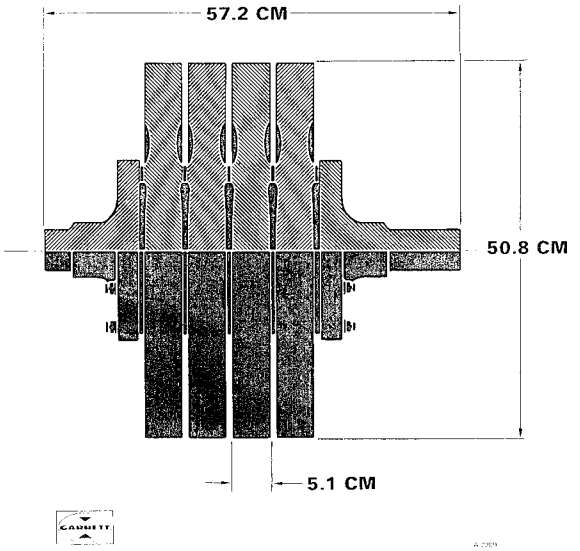

Fig. 2. R-32 Rotor Assembly

An improved steel flywheel was developed for the Advanced Concept Train (ACT-1)[4] in which the containment requirement was reduced by increasing the axial segmentation of the rotor. This flywheel assembly, which is shown in Fig. 3, is comprised of 27 individual 1-cm thick steel discs which are shrink-fitted onto a central hub. As a result of the greater rotor segmentation, the containment ring capable of full containment of two simultaneously bursting flywheel segments need only be 3.8 cm thick. A similar flywheel assembly design was used for the 0.5-kwh flywheel which was supplied to the University of Wisconsin for the hybrid vehicle[5].

Recent flywheel activities at Garrett have been directed toward the development of practical composite flywheels for various vehicular and stationary applications. The description of this experience and the resulting hardware is presented in another paper at this conference[6].

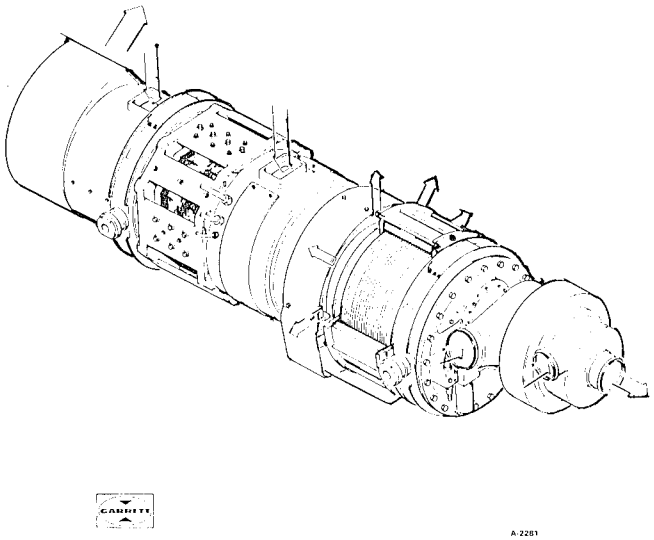

Fig. 3. ACT-1 Energy Storage Unit

A summary of representative Garrett flywheel experience is shown in Table 1 where various flywheel hardware is listed along with the energy storage capacities and rotor energy densities. Representative composite flywheels are shown in Fig. 4 (1.0-kwh Near-Term Electric Car flywheel[7]) and Fig. 5 (Sandia 1.4-kwh high-energy density flywheel[8]).

Table 1. Representative Garrett flywheel experience.

Material	Application	Flywheel Capacity	Rotor Energy Density
Steel:	R-32 car	3.2 kwh	9 wh/kg
	ACT-1	4.5 kwh	8 wh/kg
	U of W car	0.5 kwh	7 wh/kg
Composite:	IR&D	0.2 kwh	19 wh/kg
	MERADCOM	2.4 kwh	53 wh/kg
	Near-Term Electric Vehicle (NTEV)	1 kwh	44 wh/kg
	Lawrence Livermore	0.25 kwh	39 wh/kg
	Sandia	1.4 kwh	80 wh/kg

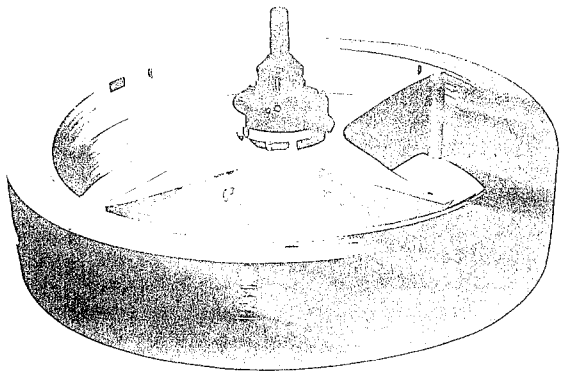

Fig. 4. 1.0-KWH Near-Term Electric Vehicle Composite Flywheel

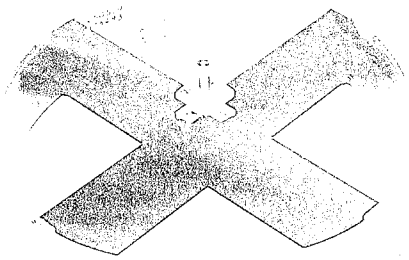

Fig. 5. Sandia 1.4-KWH High-Energy Density Composite Flywheel

Flywheel failure tests[9] have shown that composite flywheels require only about 15 percent of the containment weight needed for metallic flywheels. On this basis, the five-fold improvement in flywheel rotor energy density shown in Table 1 for composites over steel flywheels in Table 1 may be multiplied by a factor of two. Thus, the possible energy density of a composite flywheel assembly can be as much as 10 times that of a metallic flywheel unit when containment is included.

The composite flywheel, when compared to metallic flywheels, offers other advantages which must be considered, particularly for vehicle applications. For example, flywheel overspeed leading to catastrophic failure is always a dreaded possibility with metallic rotors but is not a serious problem with the composite flywheel in which the rim is designed to lift off the hub at 110 percent rated speed. In addition, unpredicted structural failure of a composite flywheel results in microfractures of the matrix and unraveling of the fiber which fills the housing with a fluff-like material which transfers rotor momentum to the housing at a relatively low rate. In contrast, the momentum transfer from a metallic flywheel following catastrophic failure is nearly instantaneous which requires that the flywheel assembly mounting be capable of allowing the entire flywheel unit to rotate.

FLYWHEEL MATERIAL SELECTION

On the basis of the Garrett flywheel background, a tradeoff study was made to determine the capacity and material selection for the coach flywheel. The constraint on axle weight was first considered since the permissible limit for this weight is 11,340 kg. Since the most likely location for the flywheel appears to be in the propulsion compartment at the rear of the bus, the weight of the flywheel unit will be cantilevered from the rear axle. The present propulsion system in a typical Diesel bus like the Grumman-Flxible Model 870 Advanced Design Bus (ADB) weighs about 2720 kg with the engine and transmission located in the bus propulsion compartment. This weight could be increased to 2900 kg without exceeding the rear axle load limit when the bus is fully loaded with 48 seated passengers and 44 standees. This limiting propulsion system weight for the flywheel system permits the flywheel with its containment and housing to weigh 680 kg. The resulting flywheel capacities based on previous Garrett experience with various proven design approaches are shown below:

Flywheel Design Type	Total Capacity
R-32	2.7 kwh
ACT-1	3.4 kwh
NTEV	16.0 kwh
Sandia	27.0 kwh

Clearly the two steel flywheel designs will not provide sufficient vehicle range to be attractive to transit properties since the flywheel coach requires about 2.06 kwh/km for average transit service making three stops per kilometer. In contrast, the range available

(with the flywheel operated from full to half speed) for the NTEV-type flywheel is 5.8 km, while that for the Sandia-type design is 9.8 km. These range capabilities appear to be suitable for widespread deployment of the flywheel coach in place of the present Diesel bus. A recent survey which was made of 10 transit properties operating 15,000 buses has shown that the use of the NTEV-type flywheel in flywheel coaches would provide service over 60 percent of routes with no more than one enroute recharge.

The 5.8-km range capability which can be provided by the NTEV-type flywheel has been selected as adequate for the DOT program at this time with the future potential of obtaining the higher range which can be provided by the Sandia-type unit. This decision was primarily based on the much higher experience level with the NTEV construction.

The selected 16-kwh composite flywheel package is compatible with installation in the propulsion compartment of the selected transit bus, even though the volumetric energy density of the composite rotor is somewhat lower than that for a steel flywheel. A pictorial view of the installation of the flywheel unit and other system components in the coach is shown in Fig. 6.

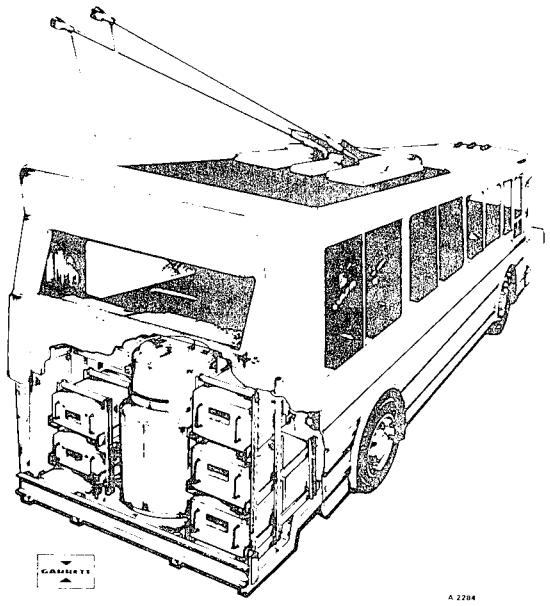

Fig. 6. Installed Flywheel Propulsion System in Transit Coach

CONCLUSIONS

The selection of a composite flywheel for the DOT flywheel coach program was made by Garrett for the following reasons:

- Composite flywheels have lower technical risk than metallic flywheels in large capacities having high-energy density
- Composite flywheels can be modular in design which can make a single rotor module design suitable for a wide range of applications
- Lower development cost for a composite flywheel than a metallic flywheel
- Greater system safety due to inherent safe failure modes of composite flywheels
- Reduced flywheel assembly weight and, therefore, greater vehicle range without exceeding permissible axle loading
- Greater growth potential of composite flywheels to nearly twice the energy density of the selected design

REFERENCES

1. Lawson, L. J., "Flywheel Propulsion for Urban Transit Buses," 1977 Flywheel Technology Symposium Proceedings, pp. 193-200, October 1977.
2. Dietrich, E., "The Duo-Bus, An Evolutionary Contribution to an Ecologically Acceptable Local Traffic System," Proceedings of the 57th Annual Meeting of the Transportation Research Board of the National Research Council, Washington, DC, January 1978.
3. Raskin, D., "Energy Storage Propulsion System for Rapid Transit Cars, Test Results, and System Evaluation," prepared for UMTA by Metropolitan Transportation Authority under Contract No. UMTA-NY-06-0006-75, October 1978.
4. "ACT-1 Advanced Concept Train Development Program, Final Report," prepared for UMTA under Contract No.

DOT-UT-10007, July 1979.

5. Beachley, N. H., et al., "Experimental Evaluation of Flywheel Energy Management Automobile," Proc. 4th International Symposium on Automotive Propulsion Systems, April 1977.

6. Place, T. W., "Composite Material Flywheel for Department of Transportation Coach," Proceedings of 1980 Flywheel Technology Symposium.

7. Rowlett, B. H., "Battery-Flywheel Power System for an Urban Automobile," NATO Proceedings of the 4th International Symposium on Automotive Propulsion Systems, Vol. 2, pp. 902-913, February 1978.

8. Satchwell, D. L. and Towgood, D. A., "High-Energy Density Composite Flywheel," Final Report prepared for Sandia Laboratories under Contract No. AT/29-1/789, February 1980.

9. Towgood, D. A., "An Advanced Vehicular Flywheel System for the ERDA Electric-Powered Passenger Vehicle," 1977 Flywheel Technology Symposium Proceedings, pp. 63-68, October 1977.

ACHIEVING DESIRABLE STRESS STATES IN THICK RIM ROTATING DISKS BY VARIATION OF PROPERTIES

Gerard C. Pardoen, Asst. Prof., Civil Engineering
University of California, Irvine, California

Rod D. Nudenberg, Proj. Manager, U.S. Flywheels,
Irvine, California

Bruce E. Swartout, President, U.S. Flywheels,
Irvine, California

ABSTRACT

The advantage of thin rim flywheels over conventional heavy metallic circular devices is that composites, in general, can store more energy per unit mass than metallic alloys. This is due, in part, to the high tensile strengths that are achievable in composites in order to resist the hoop stresses. In order to increase the kinetic energy storage for a given swept volume, an obvious extension to the thin rim composite flywheel is the thick rim composite flywheel. Unfortunately the advantage of composite flywheels, in general, diminishes with rim thickness due to the resulting increase in radial stress. Although the radial stress is one to two orders of magnitude lower than the hoop stress the low interlaminar strength of conventional composites restricts the inner radius to outer radius ratio to values of 0.9 or greater.

This paper considers the variation of mass and stiffness properties in order to achieve desirable stress states in thick rims with an inner radius to outer radius ratio of 0.6 or lower. In fact one thick rim concept of variable mass density and stiffness exhibits the stress characteristics of the thin rim concept, namely, the radial stress is zero throughout whereas the hoop stress is constant and equal to the product of a mass density term times the peripheral speed squared.

INTRODUCTION

Flywheels are usually thought of as heavy metallic circular devices for storing kinetic energy, whereas advanced design concepts have considered thin rim flywheels of composite materials. The limit to the amount of kinetic emergy stored in a flywheel is, among other things, ultimately related to the tensile strength of the constituent materials. For a thin rim flywheel of an isotropic or orthotropic material, such as in Fig. 1, the tensile strength must be sufficient to withstand the hoop stress resulting from the centrifugal forces. The radial stress for such a thin rim configuration is of little or no significance upon the structural integrity of the rim.

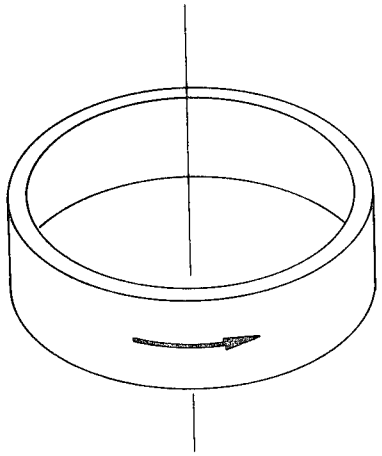

Fig. 1. Thin hoop spinning about a central axis

The advantage of thin rim flywheels over conventional heavy metallic circular devices is that composites, in general, can store more energy per unit mass than metallic alloys. This is due, in part, to the high tensile strengths that are achievable in composites in order to resist the hoop stresses. In order to increase the kinetic energy storage for a given swept volume, an obvious extension to the thin rim composite flywheel is the thick rim composite flywheel. Unfortunately

the advantage of composite flywheels, in general, diminishes with rim thickness due to the resulting increase in radial stress. Although the radial stress is one to two orders of magnitude lower than the hoop stress the low interlaminar strength of conventional composites restricts the inner to outer radius ratio to values of 0.9 or greater.

This paper is devoted to investigating the theoretical implications of varying the mass and stiffness properties in order to achieve desirable stress states in thick rim flywheels. The theoretical investigations include

a) Thick rim with a quadratic variation of mass density

b) Thick rim with a quadratic variation of mass density an exponential variaof stiffness

The objectives of considering the thick rim concept include its ability to store more kinetic energy per swept volume while eliminating the need for the concepts with inherent high parts count. In the cases considered, the appropriate stress and deformation equations are derived from anisotropic elasticity and are given in closed-form expressions as well as graphical form. Degenerate cases of these closed-form expressions include, as one should expect, the stress and deformation expressions for a rotating orthotropic disk with a constant mass density.

In some cases, the variation of mass and stiffness properties in order to achieve desirable stress enables one to consider thick rims with an inner radius to outer radius ratio of 0.6 or lower. In fact the thick rim concept of variable mass density and stiffness exhibits the stress characteristics of the thin rim concept, namely, the radial stress is close to zero throughout whereas the hoop stress is constant and equal to the product of a mass density term times the peripheral speed squared.

THICK RIM WITH A QUADRATIC VARIATION OF MASS DENSITY

The stress and deformation equations for a quadratically varying mass density, polar orthotropic composite rim are presented in this section. In developing the appropriate equilibrium and compatibility equations, certain fundamental assumptions are made:

- the mass density of the composite may vary quadratically with respect to the radial coordinate,
- the material's constitutive relations can be characterized by the moduli and Poisson's ratios of a polar orthotropic material,
- the elastic properties, the rim's geometry, and the inertia loading are axisymmetric, and
- the elastic properties are assumed to be constant.

The fundamental strain-displacement and stress-strain relations for a axisymetric rim are

$$\varepsilon_r = \frac{\sigma_r}{E_r} - \frac{\nu_{\theta r}\sigma_\theta}{E_\theta} = \frac{du}{dr} \qquad (1)$$

$$\varepsilon_\theta = \frac{\sigma_\theta}{E_\theta} - \frac{\nu_{r\theta}\sigma_r}{E_r} = \frac{u}{r}$$

When an axisymmetric disk of variable mass density rotates at a constant angular speed ω, the force equilibrium equation in the radial direction is given by

$$\frac{d}{dr}(r\sigma_r) - \sigma_\theta + \rho(r)\omega^2 r^2 = 0 \qquad (2)$$

The equilibrium equation can be expressed in terms of the radial displacement u as

$$E_r r^2 \frac{d^2u}{dr^2} + E_r r \frac{du}{dr} - E_\theta u + \rho(r)\omega^2(1-\nu_{\theta r}\nu_{r\theta})r^3 = 0 \qquad (3)$$

In the deriving Eq. (3) it was assumed that the material parameters satisfied the symmetry of stiffness coefficients of the stress-strain relations such that $E_r\nu_{\theta r} = E_\theta\nu_{r\theta}$. In addition, it was assumed that the material properties such as the elastic moduli and Poisson ratios do not vary

with respect to the radial coordinate. This condition will be relaxed in a later part of this paper.

Assume that the mass density of the composite material varies quadratically with respect to the radius such that

$$\rho_{(r)} = \rho_b (r/b)^{-2} \qquad (4)$$

which, in words, defines a quadratic variation of mass density that is maximum at the inner radius and has a nominal value of ρ_b at the outer radius. The quadratic variation of the mass density could be achieved, for instance, by combining modest amounts of lead or tungsten powder to the epoxy matrix material. The general solution to the differential Eq. (3), subject to the mass variation given in Eq. (4), is

$$u = c_1 (1+k)(k-\nu_{\theta r})(r/b)^k - c_2 (1-k)(k+\nu_{\theta r})(r/b)^{-k} + \frac{\rho_b \omega^2 b^3 (k^2-\nu_{\theta r}^2)}{E_\theta (k^2-1)} (r/b) \qquad (5)$$

The constants c_1 and c_2 can be determined from the radial stress boundary conditions of an ideal rim with stress free edges

$$\sigma_r(a) = 0 \qquad \sigma_r(b) = 0 \qquad (6)$$

By solving the appropriate equilibrium differential equation subject to the zero radial stress boundary conditions at the inner and outer radii, it can be shown that the radial displacement becomes

Equation (7)

Furthermore, the radial and hoop stress expressions can be shown to be

Equation (8)

Equation (9)

Figs. 2, 3, and 4 depict, respectively, the analytical expressions for radial displacement, radial stress and hoop stress for a moderately thick rim (inner radius/ outer radius = 2/3).

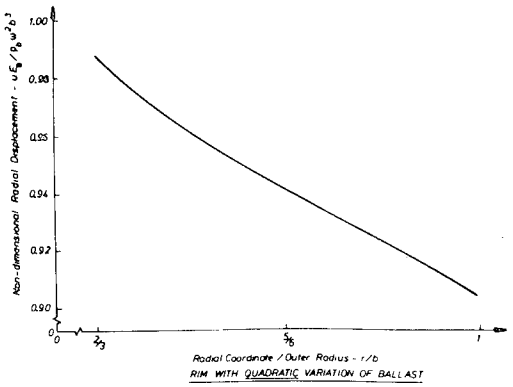

Fig. 2. Rim with quadratic variation of ballast

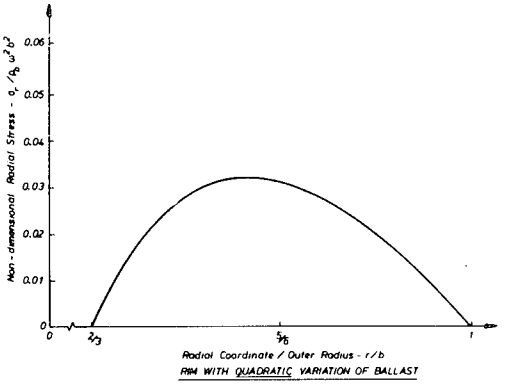

Fig. 3. Rim with quadratic variation of ballast

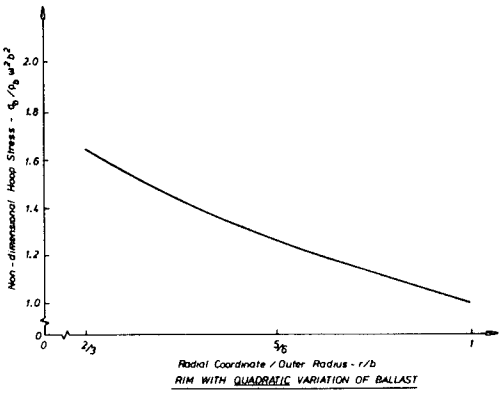

Fig. 4. Rim with quadratic variation of ballast

If one compares the deformation and stress quantities for a thick rim with a quadratic variation of mass density with the same deformation and stress quantities of a thick rim with a uniform mass density[1] then the following characteristics appear:

a) the radial displacement is roughly 59% higher for the quadratic variation of mass density,

b) the radial stress is roughly 36% lower for the quadratic variation of mass density,

c) the hoop stress is roughly 59% higher for the quadratic variation of mass density.

Although the radial stress distribution is significantly reduced (which is very desirable), it is at the expense of the increased radial displacement and hoop stress (undesirable features). Based upon these conclusions, it would appear that the quadratic variation of mass density does not offer any significant advantages for a thick rim. However, as will be shown in the next section, a quadratic variation of mass density coupled with a realistic variation of hoop modulus does provide a very attractive stress and deformation state for a thick rim.

THICK RIM WITH A QUADRATIC VARIATION OF MASS DENSITY AND AN EXPONENTIAL VARIATION OF STIFFNESS

In a previous section, the appropriate stress and deformation equations were derived for an orthotropic rim with a quadaratic variation of mass density. A fundamental assumption of Eqs. (7), (8), and (9) is that the elastic properties did not vary radially. Although this assumption is convenient mathematically, it is unrealistic when one considers the possible variation of elastic properties by just adding a ballast material to the composite's epoxy. If the concept of a quadratic variation of mass density is retained, then a zeroth order approximation to the hoop modulus would be to increase in radius. Specifically, the radial variations of the mass and hoop elastic modulus will be assumed to be characterized by

$$\rho(r) = \rho_b (r/b)^{-2}$$

$$E_\theta = E^*_\theta (r/b)^{1+\nu_\theta r} \qquad (10)$$

Although these properties are hypothetical, they do lead to some very significant stress results that cannot be overlooked. Figure 5 depicts the radial variation of mass density and hoop elastic modulus. As an example, the curves indicate that the mass density at r/b = .7 should be approximately 2.04 times as dense as that of the unballasted material and that the hoop elastic modulus should be approximately 63% of the value at the outer radius. Figure 6 depicts the mass density versus radius whereas Fig. 7 depicts the hoop elastic modulus versus radius for various values of Poisson's ratio.

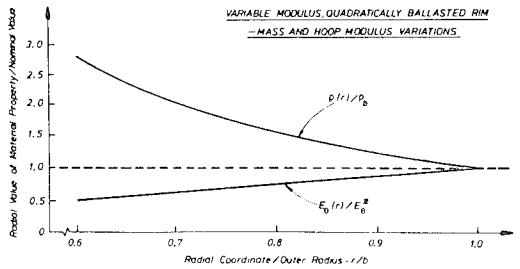

Fig. 5. Variable modulus, quadratically ballasted rim--mass and hoop modulus variations

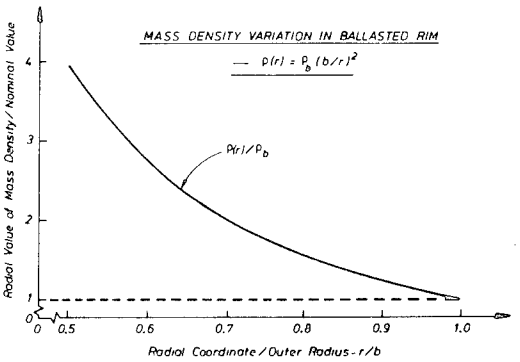

Fig. 6. Mass density variation in ballasted rim

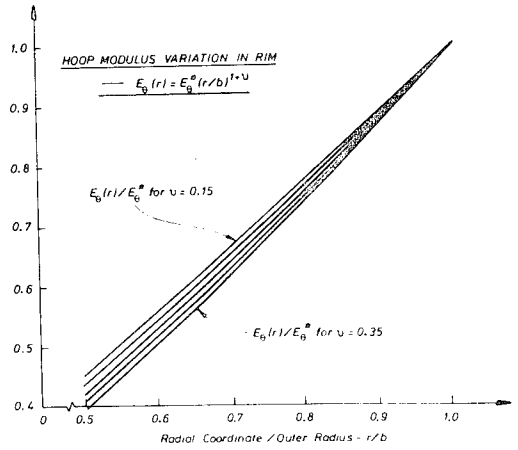

Fig. 7. Hoop modulus variation in rim

Whereas the kinetic energy storage of a thick rim composite flywheel, without ballasting or modulus variations, is limited by a high hoop and radial stress components, the thick rim composite flywheel, with the aforementioned ballasting and modulus variations, has the following approximate stress and deformation components:

$$\sigma_r \simeq 0$$

$$\sigma_\theta \simeq \rho_b \omega^2 b^2 \qquad (11)$$

$$u \simeq \rho_b \omega^2 b^3 (r/b)^{-\nu} \theta r / E_\theta^*$$

Thus, in general, the radial stress in zero whereas the hoop stress is constant and equal to the product of the mass density and the peripheral speed squared. It should be noted that the expressions in Eq. (11) were determined by numerically integrating the governing differential equation for the radial displacement given in Eq. (3) subject to the material property variations given in Eq. (10). The stresses were determined by the appropriate manipulation of Eq. (1).

Inasmuch as this constant stress thick rim is predicated on a mixture of glass fiber, epoxy, and ballast, it is of interest to denote the variation of these constituents with radius. As an example, Fig. 8 denotes the variation, by weight, of E-glass, epoxy, and powdered lead. Figure 9 depicts the variation of these constituents by volume.

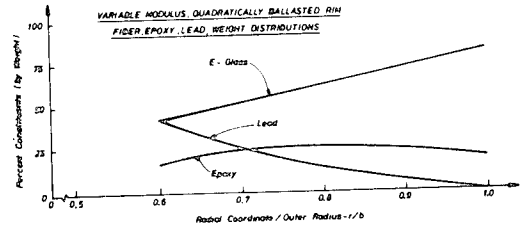

Fig. 8. Variable modulus, quadratically ballasted rim fiber, epoxy, lead, weight distributions

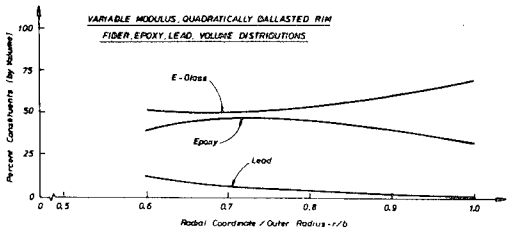

Fig. 9. Variable modulus, quadratically ballasted rim fiber, epoxy, lead, volume distributions

It should be emphasized that these figures represent the ideal theoretical distribution. In practice, however, one would make engineering approximations to both the mass and hoop modulus distributions by using "average" values rather than attempting to match the theoretical curves identically. Figures 10 and 11 reflect, for instance, the theoretical hoop and radial stress distributions in a thick rim which is wound with 16 constant, but distinct, variations of fiber, epoxy, and lead. Within each of the 16

sections, the mass density and hoop modulus are assumed to have constant values--the constant values of the mass density and elastic modulus within each section being dictated by the appropriate average ordinate value from Fig. 5 for a given radial location.

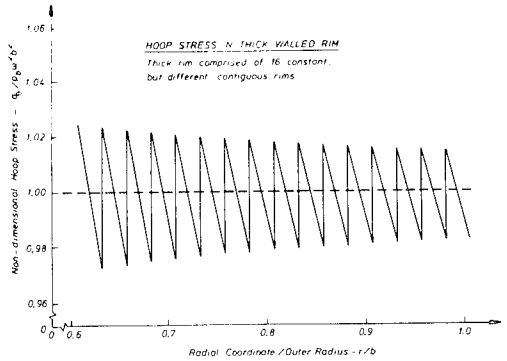

Fig. 10 Hoop stress in thick walled rim

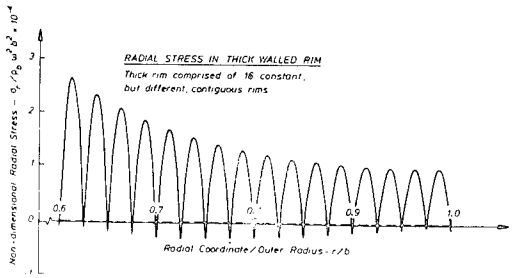

Fig. 11 Radial stress in thick walled rim

THICK RIM WITH A QUADRATIC VARIATION OF MASS DENSITY, AN EXPONENTIAL VARIATION OF STIFFNESS AND A PRESCRIBED VARIATION OF AXIAL THICKNESS (RIM HEIGHT)

One further point to consider is the influence of axial thickness on the stress and deformation quantities of a rotating rim. To this end, consider a rim with the following characteristics:

a) quadratic variation of mass density, $\rho(r) = \rho_b(r/b)^{-2}$

b) exponential variation of hoop modulus, $E_\theta = E_\theta{}^*(r/b)^{1+\nu_{\theta r}}$

c) constant value of radial modulus E_r

d) tapered rim height, $h(r) = h^*e^{-r/r^*}$

The equilibrium equation for a variable height rim can be expressed as

$$\frac{d}{dr}\{h(r)\, r\, \sigma_r\} - h(r)\sigma_\theta + h(r)\rho(r)\omega^2 r^2 = 0 \qquad (12)$$

The stress components σ_r and σ_θ can be eliminated from the above equation by manipulating the strain-displacement relations of Eq. (1) and replaced by a second order differential equation for the radial displacement u.

$$u'' + u'\{1 + \nu_{\theta r} - \nu_{\theta r}(r/b)^{1+\nu_{\theta r}-r/r^*}\}/r - u\{k^2(r/b)^{1+\nu_{\theta r}} + \nu_{\theta r}r/r^*\}/r^2 + \rho_b(r/b)^{-2}\omega^2 r(1-\nu_{\theta r}\nu_{r\theta})/E_r = 0 \qquad (13)$$

Inasmuch as Eq. (13) defies a closed form solution, a numerical integration procedure was implemented to solve for the radial displacement u. Four cases of different rim height variation were investigated for a relatively thick rim (a/b = .6); the inner radius height was chosen to be 2, 1.5, 1.25, and 1.0 times the outer radius height. Figure 12 depicts the variation of rim height for each of the 4 cases.

The result of numerically integrating Eq. (13) is that the predicted radial displacement, radial stress, and hoop stress do not differ significantly from those of a uniform height rim given in Eq. (11). The most significant aspect of these results is that as a practical matter the variable modulus, variable mass density concept rim may be easier to implement for a variable height rim than that of a constant height rim. For instance if one accepts the rule of mixtures as the basis for calculating the composite's elastic modulus then the modulus variation of Fig. 7 suggests that the fiber fraction

should increase with increasing radius. This modulus increase could be achieved in two ways: (1) increasing the number of fibers with increasing radius for a constant height rim, or (2) maintaining a constant number of fibers per radial location but decreasing the height (and hence unit volume) with increasing radius. The latter concept may be more practical in a winding process. Another advantage of the variable height concept is that the increased volume over that of the constant height rim may allow the quadratic variation of density to be more easily achieved.

ECONOMIC FEATURES OF A THICK RIM

Because the constant stress composite thick rim exhibits the stress characteristics of the thin rim concept, then a few remarks related to economics are in order. These remarks are intended to stimulate discussion on the merits of a thick rim using low cost materials such as properly ballasted E-glass rather than a multi-material thick rim using an expensive "outer jacket" of Kevlar. For small scale, low production items the economic advantages are negligible, however for large scale (200-300 TON), high production use as envisioned for off-peak electric power storage, the economic advantages are significant.

Consider, for example, the cost of glass fiber. It is a well known fact in the glass fiber industry that the SiO_2 (silica) content of glass filament has a direct relationship to the tensile strength of a filament. For instance, E-Glass filament is normally 55% SiO_2 and its ultimate single filament tensile strength is reported by Owens Corning at 500,000 PSI. Similarly, S-Glass which contains 65% SiO_2 is reported at 700,000 PSI by Owens Corning. Those familiar with the state-of-the-art, predict that fiber approaching 100% silica will have an approximate tensile strength of 1,000,000 PSI. The market price varies from 60¢ per pound for E-Glass up to $60.00 per pound for silica and quartz filament. The latter cost is a reflection of the higher production cost of one filament at one time rather than the 2,000 filaments that are produced at one time for commercial grade fibers. Thus for large scale, high production rims the economic advantages of relatively low cost E-Glass is difficult to neglect.

Consider also the cost of ballasting materials. It should be noted that the constant stress thick rim can require a substantial quantity of ballast (as much as approximately 1/4th of the total weight of the rim). With the powdered lead at roughly one dollar per pound, powdered iron at 25¢ per pound both of which have significant processing energy already invested in these products, one would appreciate the significance of eliminating this energy investment in these ballot materials if reasonable substitutes could be found. Non-magnetic red hematite-ore, which can contain 70% Fe or more before investing energy to make pig-iron, can be obtained for less than $100 per ton or 5 cents per pound. The addition of this material could, when added to other low cost materials in the composite, produce substantial overall economic results. To be specific, calculations show that if one uses powdered red hematite as ballast instead of powdered lead that a 30%-50% reduction of the total material cost can result.

CONCLUSION

The theoretical implications of varying the mass, and stiffness properties in order to achieve desirable stress states in thick rim flywheels was investigated. The theoretical investigations included:

a) Thick rim with a quadratic variation of mass density.

b) Thick rim with a quadratic variation of mass density and an exponential variation of stiffness.

In some cases, the variation of mass and stiffness properties in order to achieve desirable stress enables one to consider thick rims with an inner radius to outer radius ratio of 0.6 or lower. For instance the constant stress composite thick rim concept of variable mass density and stiffness exhibits the stress characteristics of the thin rim concept, namely, the radial stress is close to zero throughout whereas the hoop stress is constant and equal to the product of a mass density term times the peripheral speed squared.

The impact of these theoretical investigations is that thick rim flywheels may be economically attractive for large scale off-peak electric power use and, as such, these concepts should not be overlooked.

NOTATION

a	=	inner radius of rim
b	=	outer radius of rim
c	=	a/b
E_r	=	radial elastic modulus
E_θ	=	hoop elastic modulus
E^*_θ	=	nominal value of hoop elastic modulus
h_o	=	rim height at outer radius
h^*	=	reference rim height
k	=	$(E_\theta/E_r)^{1/2}$
r	=	radial coordinate
r^*	=	reference radius
u	=	radial displacement
ε_r	=	radial strain
ε_θ	=	hoop strain
ω	=	angular velocity (radians)
$\nu_{\theta r}, \nu_{r\theta}$	=	Poisson ratios
σ_r	=	radial stress
σ_θ	=	hoop stress
$\rho_{(r)}$	=	mass density as a function of radius r
ρ_b	=	mass density at outer radius of rim

REFERENCES

1. Lekhnitskii, S. G., "Anistropic Plates," Gordon and Breach, New York 1968.

2. Timoshenko, S. P., Goodier, J. N., "Theory of Elasticity," 3rd Edition, McGraw-Hill, New York, 1970.

3. Danfelt, E. L., Hewes, S. A. Chou, T-W., "Optimization of Composite Flywheel Design," Intl. Journal Mech. Sce., Vol. 19, pp. 69-78, 1977.

4. Brunelle, E. J., "The Super Flywheel: A Second Look," Journal of Engineering Materials and Technology, ASME, Jan. 1973, pp. 63-65.

5. Rabenhorst, D. W., "Primary Energy Storage and the Super Flywheel," Johns Hopkins Applied Physics Laboratory, TG 108a, Sept. 1969.

6. Morganthaler, G. F., Bonk, S. P., Composite Flywheel Stress Analysis and Materials Study," Soc. of Aerospace Material and Process Engineers.

7. William M. Brobeck and Associates, "Investigation of Multi-Ring Fiber-Composite Flywheels for Energy Storage," EPRI EM-227, Sept. 1976.

8. U.S. Flywheels, Inc., "Potentials of High Energy Density, Multi-Ring Flywheels for Application to Electric Utility Peak Power Generation," Sept. 1974.

9. "Kevlar" 49 Data Manual, E. F. DuPont du Nemours and Co., Wilmington, Del.

10. "Comparative Data-E, S, S-2 Glass," Owens-Corning Fiberglass Corp., Industrial Materials Division, Toledo, Ohio.

11. Poubeau, Pierre, Aerospatiale, Paris, France, private communication.

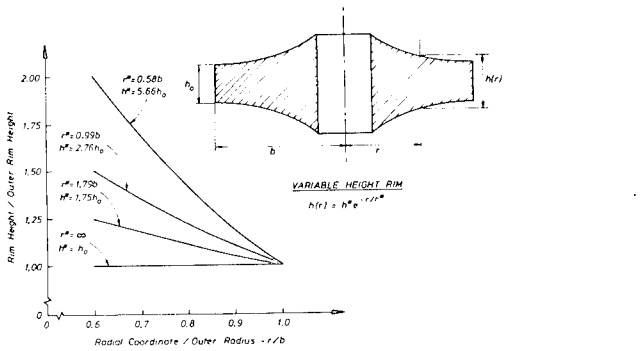

Fig. 12 Variable Height Rim Profiles

$$u = \frac{\rho_b \omega^2 b^3 (k^2 - \nu_{\theta r}^2)}{E_\theta (k^2-1)} \left\{ (r/b) + \frac{(c-c^k)(1+\nu_{\theta r})}{(c^{-k}-c^k)(k-\nu_{\theta r})} (r/b)^{-k} \right.$$

$$\left. - \frac{(c^{-k}-c)(1+\nu_{\theta r})}{(c^{-k}-c^k)(k+\nu_{\theta r})} (r/b)^k \right\} \tag{7}$$

$$\theta_r = \frac{\rho_b \omega^2 b^2 (1+\nu_{\theta r})}{(k^2-1)} \left\{ 1 - \frac{(c-c^k)}{(c^{-k}-c^k)} (r/b)^{-k-1} - \frac{c^{-k}-c)}{(c^{-k}-c^k)} (r/b)^{k-1} \right\} \tag{8}$$

$$\theta_\theta = \frac{\rho_b \omega^2 b^2 k}{(k^2-k)} \left\{ \frac{k^2+\nu_\theta}{k} + \frac{(c-c^k)(1+\nu_{\theta r})}{(c^{-k}-c^k)} (r/b)^{-k-1} \right.$$

$$\left. - \frac{(c^{-k}-c)(1+\nu_{\theta r}}{(c^{-k}-c^k)} (r/b)^{k-1} \right. \tag{9}$$

DESIGN AND FABRICATION OF A FLYWHEEL ROTOR FOR AUTOMOTIVE USE

Stephen F. Post
Francis C. Younger
William M. Brobeck & Associates
1235 Tenth Street
Berkeley, California 94710

ABSTRACT

A program for the design and fabrication of a fiber-composite flywheel is described. The objective of the program is usable energy storage in the range of 1 to 5 kWh with a total energy density in excess of 80 Wh/kg at the maximum operating speed. The design output power is 37 kW and the maximum dimensions are 35 cm diameter and 13 cm axial height. The design uses a biannulate rim of S2 fiberglass/epoxy overwrapped with Kevlar 49/epoxy. This rim is supported from an aluminum hub by polar catenary spokes filament wound with Kevlar 29/epoxy. The Kevlar 29/epoxy spokes have a lower tensile modulus than the rim materials so compatible strain levels can be achieved without excessive stress in the spokes. The stress analysis for the biannulate rim shows nearly optimum tangential stress levels in each of the two materials and a very reasonable distribution of radial stresses. Compressive radial stress occurs at the interface between the S2 fiberglass/epoxy and the Kevlar 49/epoxy. The spoke design concept permits a careful balance of spoke flexibility to assure that the spoke stiffness is adequate to maintain concentricity of the rim and hub to satisfy dynamic stability requirements while at the same time being flexible enough to allow dilation of the rim due to centrifugal loading without imposing excessive radial loads at the rim-to-spoke attachment points. Two flywheels were fabricated and delivered. A usable energy of .97 kWh is expected. A total energy density of 87 Wh/kg is expected at the maximum operating speed of 56,000 rpm.

INTRODUCTION

This paper summarizes the design and fabrication of a flywheel rotor for automotive use.* Two complete fiber-composite flywheel rotors were fabricated. These flywheels are scaled-down versions of two 5 kWh automotive flywheels built for Sandia Laboratories.

The flywheels store a maximum of 0.97 kWh of kinetic energy. Energy density is 87 Wh/kg at the maximum operating speed of 56,000 rpm. The nominal flywheel dimensions are 35 cm diameter by 13 cm axial height. The weight of the flywheel rotor assembly is 11.16 kg.

CONCEPT

The flywheel rotor design uses a biannulate rim of S2 fiberglass/epoxy overwrapped with Kevlar 49/epoxy. This combination of materials assures that the Kevlar outer portion will act as a reinforcing band about the S2-glass to maintain compressive radial stresses. This arrangement permits the combined rim to have the large radial thickness required to achieve a good space utilization.

Rim support is provided by polar catenary spokes. These spokes are tension balanced to reduce undesirable radial loading on the rim. The spoke material, Kevlar 29/epoxy, was selected to give acceptable stress levels and to produce a rigid support to maintain alignment of the rim and hub.

The hub provides support to the spokes. The hub material is aluminum with a Kevlar 49/epoxy overwrap. An interference fit puts the aluminum hub into compression when the hub is not rotating. This pre-stressing limits the tangential tensile stress in the aluminum to an acceptable value at the maximum rotation speed.

*Work performed under Lawrence Livermore Laboratory Contract #7171509.

DESCRIPTION OF FLYWHEEL

Since the maximum energy density achievable in a flywheel is proportional to the strength-to-weight ratio of the material of the flywheel, high specific strength fiber-composite materials are prime candidates for use in vehicular flywheels. The total energy stored in a fiber-composite flywheel is nearly equal to the integration of the centrifugally induced stresses in all of the fibers. Thus, to achieve the objective of over 80 Wh/kg, the use of high specific strength fibers such as Kevlar®, graphite or S2-glass is required and the geometric configuration must be such that much of the fiber is stressed centrifugally to a very high level.

The flywheel designed and fabricated as the major part of this effort utilizes several different fibers with different specific strength and elastic moduli. These fibers are arranged within the flywheel so that each fiber is stressed to approximately the same percent of its ultimate strength. Figure 1 shows the flywheel layout with the location of the various types of fiber-composite materials.

FLYWHEEL RIM

A large fraction of the flywheel mass is contained in a thick rim which is centrifugally loaded to produce very high circumferential stresses in the fibers at high rotational speeds. This rim is supported by fiber-composite spokes which are also highly stressed and add to the energy capacity. The thick rim is called a bi-annulate rim because it is built up in two distinct annular regions, each with different types of fibers. Kevlar 49® fiber is used in the outer portion where the tangential velocity is highest and heavier S2-glass fiber is used in the inner portion.

The differences in density, velocity and elastic modulus for these two annular regions is such that their dilation due to centrifugal force would be nearly but not quite equal if each region was free to expand independently. The slight difference in each of the unrestrained dilations is such that the inner portion would dilate more than the outer portion. Thus, with the two portions in physical contact the outer portion acts to constrain the inner portion and to force a

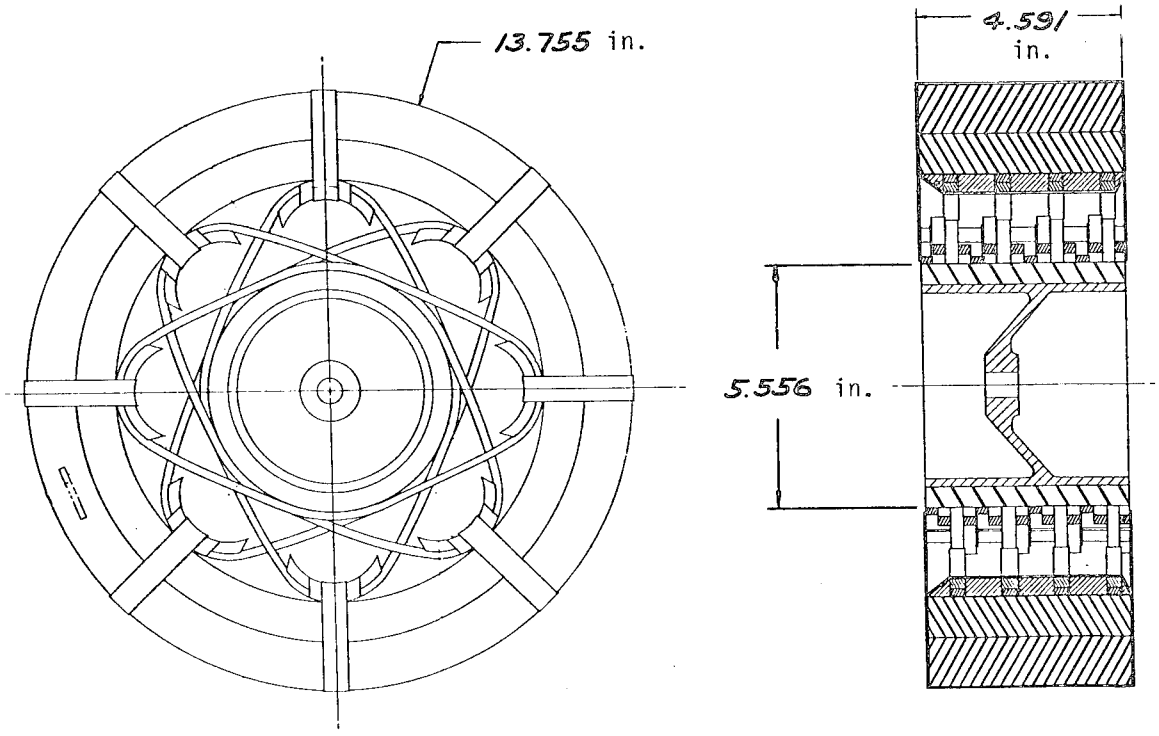

Fig. 1. Flywheel Assembly

radial compression stress at the interface between the two regions.

FLYWHEEL HUB

The hub consists of an aluminum (7075-T651) turning with a conical web joining the central attachment boss to the hub rim. This conical shape was designed to provide radial flexibility to accommodate the dilation of the aluminum hub rim without imposing excessive radial stress in the web. The aluminum hub rim is reinforced with a Kevlar 49/epoxy composite overwrap which is assembled with an interference fit. This sets up an initial radial compressive stress between the aluminum and the composite. As the flywheel speed increases, the aluminum tends to dilate more than the Kevlar 49/epoxy because the aluminum has a lower specific modulus than the Kevlar 49/epoxy composite. Thus, the compressive stress at the alumninum/composite interface increases as the flywheel speed increases and the Kevlar acts to prevent excessive circumferential stress in the aluminum.

SPOKES

A system of tension-balanced, polar-catenary spokes are used for attaching the main rim to the hub rim. This system of spokes, as shown in Fig. 2, incorporates sixteen spoke loops. The contour of the unsupported section of each spoke loop is a polar catenary, the natural shape of a flexible cord in a centrifugal force field. They are formed on a special mandrel to obtain this desired shape. This contour theoretically eliminates all bending moments in the spokes. Thus, the stresses in the spokes are pure tensile stresses.

The stress level in the spokes is maintained at a value proportional to the stress in the rim by a series of loading weights. As the speed of the flywheel increases, the centrifugal force of the loading weights increases to stretch the spokes and radially expand the spoke system to match the radial expansion of the rim caused by its centrifugal loading. The value of stress needed to stretch the spokes by the required amount is dependent upon the elastic modulus of the spokes and the dilation of the main rim. A low modulus of elasticity of the spokes and a low density is desirable. Kevlar 29/epoxy is used because it has lower density and modulus than S2-glass. The modulus is low enough to assure that the tensile stress in the spokes remains less than that in the rim. A material with much lower modulus could have been used to insure an even lower stress; however, if the modulus of elasticity is too low the spoke system will not provide adequate stiffness to maintain the concentricity of rim with respect to the hub. A critical value of stiffness has been calculated for the masses of the hub and rim using as a design point a critical speed value greatly in excess of the maximum operating speed. The cross section of the spoke was adjusted to give the required stiffness.

FLYWHEEL CHARACTERISTICS

Flywheel characteristics are summarized in Tables 1 to 4. Table 1 compares the design target with values calculated from physical measurements of flywheels #1 and #2. Table 2 shows the overall characteristic of the two flywheels. Weight and moments of inertia were measured directly. The difference in fiber fractions can be traced back to a difference in epoxy and mandrel temperature during the winding process. Tables 3 and 4 list the characteristics of the flywheel elements. Figures 3 and 4 show the computed tangential and radial stress distributions for the two flywheel rims.

Table 1. Flywheel Characteristics

	Flywheel #1	Flywheel #2	Design Target
Stored energy,kWh	0.975	0.968	0.99
Weight, lbs	24.67	24.52	24.6
Speed, rpm	55959	55959	56000
Diameter, in.	13.76	13.76	13.75
Height, in.	4.95	4.95	4.95
Energy density, Wh/kg	87.13	87.03	88.7
Polar moment, lb-in-sec^2	1.81	1.80	1.84
Kevlar 49 ring			
O.D., in.	13.76	13.76	13.75
I.D., in.	11.5	11.5	11.52
Max. tension,psi	200030	199066	210000
S-2 glass ring			
O.D., in.	11.5	11.5	11.52
I.D., in.	9.65	9.65	9.65
Max. tension,psi	175458	174116	175000
Kevlar 20 spokes(16)			
Weight, lbs	1.13	1.13	0.98
Max. tension,psi	163000	163000	163000
Loading weights			
Weight, lbs	0.687	0.687	0.69
Diametral moment, lb-in-sec^2	1.00	.99	1.02

Table 2. Overall Flywheel Characteristics

	Flywheel #1	Flywheel #2
Weight (lb)	24.67	24.52
Moment of inertia (lb-in-sec^2)	1.81	1.80
Rotational speed (rpm)	55959	55959
Stored Energy (kWh)	0.975	0.968
Energy Density (Wh/kg)	87.13	87.03
Max. outer ring stress (Kevlar 49)(psi)		
Bare fiber hoop stress (psi)	315600	329310
Comp. hoop stress(psi)	175458	174116
Radial compression (psi)	2896	1959
Radial tension(psi)	865	1175
Max. tension in spokes	127440	127440
Critical speed for radial stability (rpm)	180000	180000
Balance: C.G. of geometric center (in)	.0018	.0006

Table 3. Flywheel Hub & Spoke Characteristics

	Hub	Overwrap
Composite Hub		
Material	Alum. 7075	Kevlar 49/ Epoxy
Height (in)	4.59	4.59
Outside Dia. (in)	4.62	5.55
Inside Dia. (in)	4.24	4.62
Density (lb/m^3)	0.098	0.0463
Weight (lb)	2.66	1.59
Fiber Fraction (%)	--	65.9
Elastic Modulus (psi)	10 x 10^6	13.02 x 10^6
Spokes	**Spoke**	**Spoke Wt.**
Material	Kevlar 29/ epoxy	Alum. 7075
Width (in)	0.286	--
Thickness (in)	0.225	--
Fiber fraction (%)	75.3	--
Density (lb/in^3)	0.0476	0.098
Weight (lb)	1.139	0.687
Elastic Modulus (psi)	6.96 x 10^6	10 x 10^6

Table 4. Flywheel Characteristics

	Flywheel #1	Flywheel #2
Rings		
Outer ring		
Material	Kevlar 49/ epoxy	Kevlar 49/ epoxy
Outside Dia. (in)	13.76	13.76
Inside Dia. (in)	11.56	11.54
Height (in)	4.95	4.95
Fiber fraction (%)	63.38	60.45
Elastic Modulus (psi)	12.53 x 10^6	11.95 x 10^6
Poisson ratio	0.31	0.31
Weight (lb)	8.95	9.07
Moment of inertia (lb-in-sec^2)	372.52	374.4
Density (lb/in^3)	0.0458	0.0471
Inner ring		
Material	S-2 glass/ epoxy	S-2 glass/ epoxy
Outside dia. (in)	11.56	11.54
Inside dia. (in)	9.65	9.65
Height (in)	4.95	4.95
Fiber fraction (%)	63.5	60.9
Elastic modulus (psi)	8.62 x 10^6	8.27 x 10^6
Poisson ratio	0.282	0.282
Weight (lb)	9.98	9.19
Moment of inertia (lb-in-sec^2)	285.87	280.25
Density (lb/in^3)	0.0701	0.0671

FLYWHEEL CONSTRUCTION

The fiber composite components are fabricated by filament winding with epoxy wetted fibers using special mandrels to control the critical dimensions. Separate mandrels are required for the main rim, the hub-reinforcement rim and for the spokes. The metal parts are machined using conventional metal working equipments. The components are assembled using a fixture to assure their concentricity and alignment.

RIM FABRICATION

The biannulate rim is fabricated by a filament winding process. This process uses fibers continuously wetted with epoxy by drawing the fiber through an impregnation bath and then winding it onto a mandrel. Tight tolerances on the diameter of the mandrel and on the parallelism of the end plates control the critical dimensions.

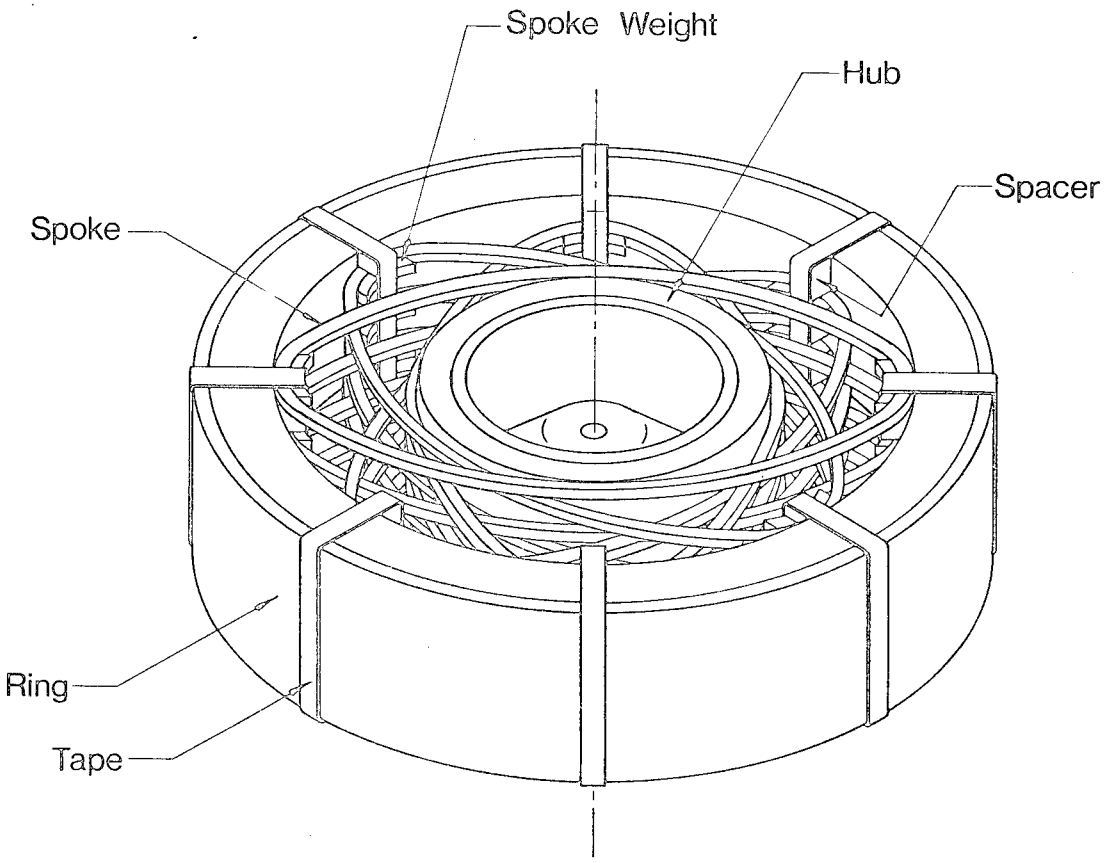

Fig. 2. Biannulate Rim Flywheel

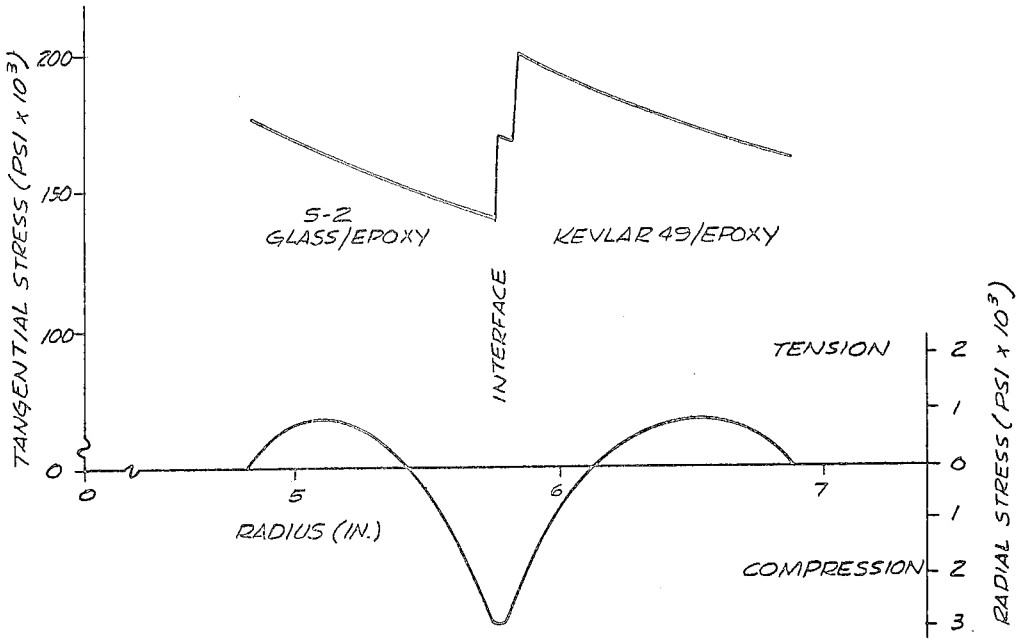

Fig. 3. Stress vs. Radius - Flywheel #1

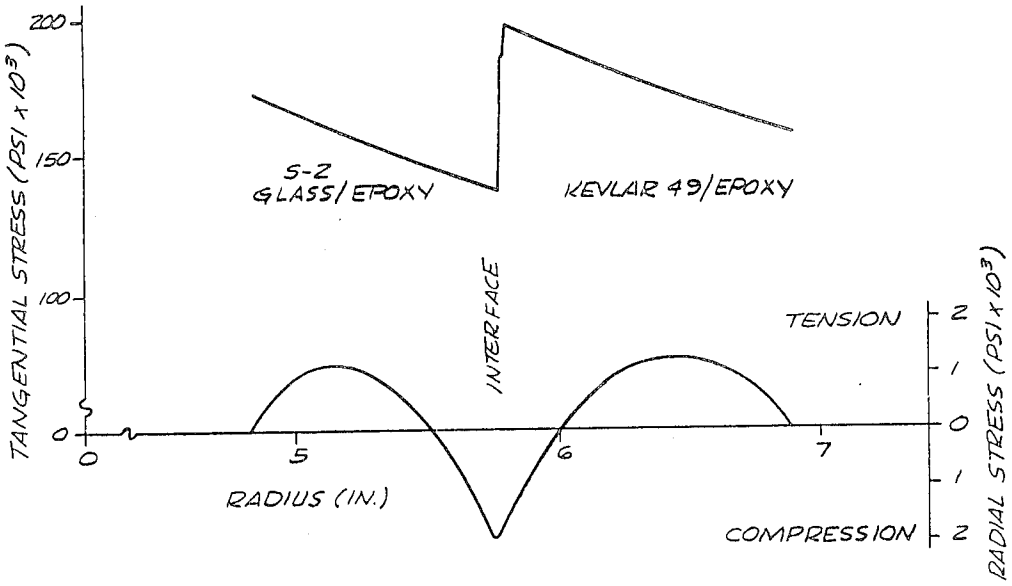

Fig. 4. Stress vs. Radius - Flywheel #2

The inner portion of the rim is wound with S2-fiberglass and the outer portion with Kevlar 49. The diameter of the interface between the S2-fiberglass and the Kevlar 49 is controlled by carefully measuring the diameter as the fiber is wound onto the mandrel and changing from S2-fiberglass to Kevlar at the appropriate place.

During the winding process fibers are taken from two spools. Initially two spools of S2-fiberglass are used to supply the fiber and later two spools of Kevlar 49 are used. At transition the fibers are intermingled by using one spool of S2-fiberglass and one of Kevlar 49.

HUB OVERWRAP

The hub overwrap rim is wet wound on a mandrel. This rim is wound with Kevlar 49 wetted with epoxy. A room temperature cure is used. This rim is assembled onto the aluminum hub with which it has a .010 inch diametral interference fit. The aluminum is shrunk by cooling it to -78°C in dry ice. The difference in the thermal expansion coefficients of aluminum and Kevlar/epoxy is such that the two parts fit together easily at this low temperature.

HUB

The hub is machined from 7075.T-651 aluminum. The final outside dimension is adjusted to give the specific interference fit with the Kevlar fiber composite hub reinforcement rim. The final machining is done after temperature cycling the hub to relieve residual stresses to assure dimensional stability of the aluminum.

The spokes are filament wound with epoxy wetted Kevlar 29 on a specially shaped mandrel to give the desired shape. The mandrel will accommodate eight spoke loops which may be wound and cured as a group. Each loop is assured the same amount of fiber by counting the number of turns during the winding process.

LOADING WEIGHTS

The loading weights are machined from aluminum. The shape of and weight of these parts are predetermined to provide the correct tension in the spokes and to uniformly distribute the compressive load over the full area where the weight bears against the spoke. Care is taken to insure that all weights are equal.

SPOKE SPACERS

The spacers fit between the loading weights and act to provide axial spacing during assembly and to provide radial support for the Kevlar 29/epoxy overwrap. These spacers are fabricated from balsa wood oriented so that the grain of the wood is essentially radial as this is the direction of greatest strength and greatest loading. The total weight of the spacers used at each azimuthal location are equal within 0.05 gram.

ASSEMBLY

The flywheel components are assembled on a fixture to insure accurate concentricity and alignment of the principal axes of the various components. The spokes are bonded to the hub reinforcement rim and to the inner surface of the main rim with epoxy. The loading weight and spoke spacers are also held in place with epoxy and with an overwrap of Kevlar 29/epoxy. The epoxy and overwrap acts to hold the static flywheel together during shipping and handling but is not required to resist operating load at high speed as the centrifugal forces due to the loading weights act to hold the spokes to the rim and hub with sufficient force to provide adequate friction to resist dynamic and torsional loads.

CONCLUSION

The two flywheels described have been built and delivered. They are scheduled to be tested in the Oak Ridge Y-12 spin test facility.

COMPOSITE MATERIAL FLYWHEEL FOR UMTA FLYWHEEL TROLLEY COACH

Theodore W. Place
AiResearch Manufacturing Company of California
2525 West 190th Street
Torrance, California 90509

ABSTRACT

A 15 kw-hr composite energy storage flywheel has been selected for the Flywheel Trolley Coach Propulsion System being developed for the Urban Mass Transportation Administration (UMTA) of the U.S. Department of Transportation. This paper describes the features of the flywheel energy storage unit and discusses similar composite flywheels from which the selected design was derived.

The design of the flywheel rotor is based on the 4-spoked hub composite rim flywheel developed by AiResearch. The flywheel is 1.067 meters in diameter, and 0.59 meters in length. The composite rim is made of separate, concentric rings of S-2 glass/epoxy and Kevlar/epoxy. The general design approach is to use a proven design and scale the size to fit the performance requirements.

Verification tests of the composite rim materials were completed prior to fabrication of the module test rotor. A tensile fatigue test on a single ring was performed for 1 million cycles at maximum design stress. Also, the composite material was tested for compatibility with the lubrication fluid being used in the Energy Storage Unit.

The flywheel rotor module is geometrically scaled from prior flywheel rotors built and tested at AiResearch. In the UMTA Flywheel Trolley Coach rotor, individual modules will be placed side-by-side to obtain the required energy storage capacity.

The five prior programs added to the confidence of designing a coach flywheel. The containment of the flywheel rotor within its housing has been demonstrated several times and the ease of containment has been impressive as compared to isotropic materials. Cyclic life of the flywheel rotor module will be demonstrated as part of the UMTA Flywheel Trolley Coach program.

INTRODUCTION

AiResearch has been involved in the study, design, and development of vehicular energy storage systems for over 11 years. Initially, steel flywheel rotor designs based on existing technology were used for rail mass transportation and for the University of Wisconsin automotive flywheel installed in a Ford Pinto.

More recently, AiResearch has built and tested several composite material flywheels. The initial studies and testing were accomplished in a company-funded research program on a multi-ring E-glass rotor. The next significant program was the U.S. Army Mobility Equipment Research and Development Command (MERADCOM) composite rotor, which utilized a multi-ring Kevlar (DuPont Trademark) and S-glass rim. The size of this flywheel rotor approximates one of the six segments that are secured together to fabricate the flywheel rotor on the UMTA Flywheel Trolley Coach. The most recent program to influence the coach rotor design was the U.S. Department of Energy Near-Term Electric Vehicle (NTEV) flywheel.

COMPOSITE MATERIAL FLYWHEEL BACKGROUND

U.S.A. MERADCOM FLYWHEEL

The MERADCOM flywheel submodule, shown in Figure 1, has the approximate diameter of the bus flywheel rotor. The knowledge gained from the MERADCOM program includes design techniques that were substantiated by the test program.

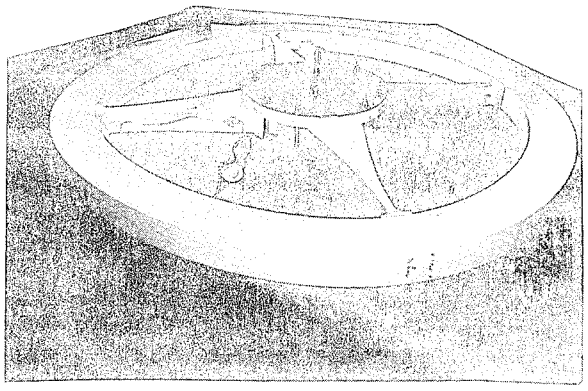

Fig. 1. U.S.A. MERADCOM Flywheel Test Rotor

Design and fabrication techniques were verified by several tests. Material tests such as a short-beam shear test and a microsection analysis demonstrated that the material properties were consistent. The hub design and spoke radial force that holds the rim on the spokes were verified by monitoring spoke strain (equal to radial force) while operating the flywheel through the speed range. A test ring cycling technique was developed to establish stress rupture data below the 100,000-cycle range. These data were used to determine the fatigue life of the flywheel. Testing was conducted that demonstrated dynamic balance of the composite material rim. The rotor was successfully operated to a maximum peripheral speed of 856 M/S.

U.S. DEPARTMENT OF ENERGY NTEV FLYWHEEL

The Near-Term Electric Vehicle (NTEV) program presented the first opportunity to adapt a composite material flywheel to a vehicle environment. Figure 2 shows the major characteristics of this flywheel system. Again, an S-glass and Kevlar multi-ring rim was used. The flywheel was subjected to 1000 cycles between 13,000 rpm and the full-speed operational condition of 25,000 rpm. This test was performed with vehicular bearings and seals. The NTEV flywheel then was run to 26,250 rpm in an NTEV flywheel housing and air was introduced into the flywheel chamber until rim failure occured by aerodynamic heating. The resulting rim disintegration was totally contained in the light-weight steel housing. The rate of momentum transfer and resulting torque to the supporting structure also were acceptable for an automotive installation.

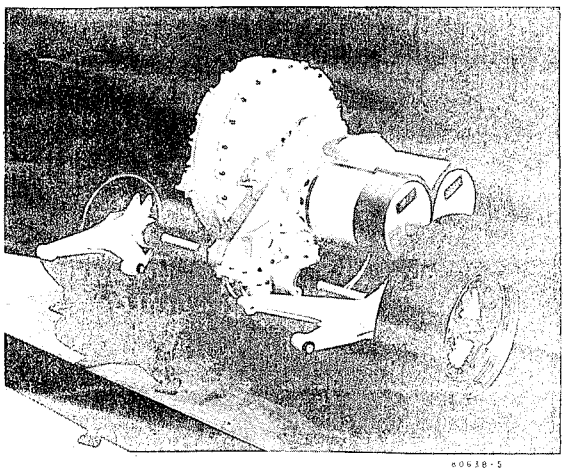

Fig. 2. Near-Term Electric Vehicle Energy Storage System

The 1000 cycle test was completed on a single flywheel. At the end of the test, the flywheel was removed and examined. A separation or gap appeared between the S-glass ring and the Kevlar rings. Several 100-hr tests were completed in test ring samples to evaluate this condition. Although a creep phenomenon occured in the initial hours, the rings stabilized during the remaining hours and the cycle tests were successfully concluded.

The flywheel has been installed in a vehicle and tested on a dynamometer, primarily to verify proper operation of the controls and vehicle functioning. A typical 6-month test period for the electric vehicle during the vehicle test phase documented 92 start cycles, with 174 hr of test time on the flywheel. Typically, the flywheel operated from 13,000 to 25,000 rpm.

FLYWHEEL SAFETY

The flywheel safety was considered from three standpoints: (1) containment of all fragments generated by a failure,

(2) prevention of the momentum transfer of the flywheel into the housing, and (3) prevention of fires.

Containment of the flywheel was demonstrated on three occasions during the DOE NTEV program. The failures were moderate, with no deformation or yield of the metal components. This moderate failure mode is attributable to the concentric ring design, in which the rings failed sequentially and acted as brakes to stop the unit.

The momentum transfer occured over a 2-sec period, reducing torques to a very low value for the containment test.

The danger of air entering the flywheel cavity, causing a fire and burst of the flywheel, also was tested. No fire was observed, and the housing temperature increase was gradual to a maximum of 175°C.

PREDESIGN FLYWHEEL ROTOR TESTS

To supplement data gathered on the MERADCOM and NTEV programs, several tests have been scheduled to demonstrate the integrity of the composite flywheel when operated in the UMTA Trolley Coach environment. These tests will provide material data and design information that reduce the risks inherent in building a full-scale flywheel.

In the first series of tests that have been completed, the effects of wetting of the composite material by vacuum oil from the flywheel bearings were evaluated. Test samples were soaked in the selected vacuum oil and these samples, along with a like number of control samples, were tested for composite interlaminar shear strength. The oil did not affect the material property of the composite.

Next, a million-cycle tension fatigue test was accomplished on three test rings at a stress level corresponding to the maximum tensile strength of the flywheel rotor. After these samples successfully passed the cycle test, a burst test demonstrated that the material still had a significant residual strength.

In addition, the fabrication technique of the composite was evaluated by a microsection analysis. Several samples were sectioned and microsections were examined for voids to establish the quality of manufacture.

The last test, yet to be completed, is a module spin test on one of the six flywheel rotor elements. This test is a proof-of-design test because it subjects a full-scale rotor segment to all stresses of actual operation. Here, 1000 cycles from zero rpm to 106 percent of maximum speed will be performed to achieve the equivalent of 10^6 operating cycles. At the successful conclusion of this test, the total flywheel rotor design will be released for fabrication.

FLYWHEEL ROTOR DESIGN

A conservative flywheel rotor design is used to reduce risk of failure and ensure a high proportion of first-time successes. The method used is to reduce the operating stress levels of the flywheel from previous experience, thereby increasing both life and reliability. Flywheels peripheral speeds and energy densities are listed in Table 1 for comparison.

Table 1. Flywheel Performance

FLYWHEEL PROGRAM	PERIPHERAL SPEED, M/S	ENERGY DENSITY, W-HR/KG
USA MERADCOM	856	53
DOE NTEV	774	44
UMTA TROLLEY COACH	700	37

As shown in Figure 3, the flywheel rotor comprises six segments that are tie-bolted together to form one rotating flywheel. The concentricity of each element is maintained by a registering diameter on the hub and the mating pilot ring on the shaft hubs.

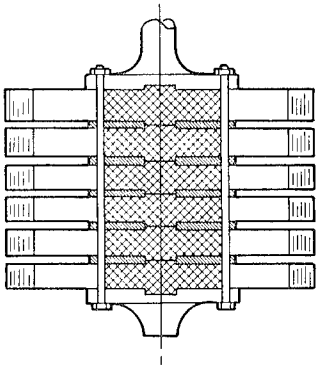

Fig. 3. UMTA Flywheel Trolley Coach Rotor

The features of the flywheel are:

- Stored energy 15 kwhr
- Outside diameter 1.067 M
- Maximum speed 12,500 rpm
- Rotor weight 557 Kg
- Rotor length 0.59 M

Each of the six flywheel rotor elements has a rim width of 96 mm. The aluminum hub is a four-spoke design with the composite rim assembled on the four spokes so that the rim attains a sub-circular shape at zero rpm. During flywheel operation, the rim grows circumferentially and approaches a true circle at maximum speed, as shown in Figure 4.

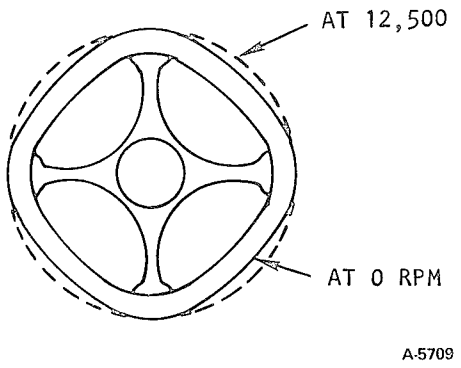

Fig. 4. Flywheel Rotor Segment

Design Analysis

A design analysis was made using published material properties, prior design experience, and trolley coach operational requirements.

The flywheel design requirements are as follows:

- ENERGY STORAGE ---------- 15 KWH
- MAXIMUM PHERIPHERAL VELOCITY ------ 700 M/SEC
- START STOP CYCLES ---------- 8,700
- CHARGE CYCLES ---------- 300,000
- BUS STOP CYCLES ---------- 7,000,000
- AMBIENT TEMPERATURE ------ 40°C TO -14°C

The UMTA Trolley Coach design requirements are as follows:

- LIFE ---------- 23 YEARS
- MAXIMUM ROLL RATE ---------- 0.5 RADIANS/SEC
- VERTICAL ACCELERATION ------ 10G

The flywheel rotor is constructed by distorting the flywheel composite rim to insert the rim over the 4-spoked hub. When the rim is released, the assembly is secured by a normal radial force.

The normal (radial) force varies throughout the cycle and is a function of the hub modulus of elasticity, the rim modulus of elasticity, and the flywheel rotor speed. The graphical presentation of normalized radial force versus speed is shown in Figure 5.

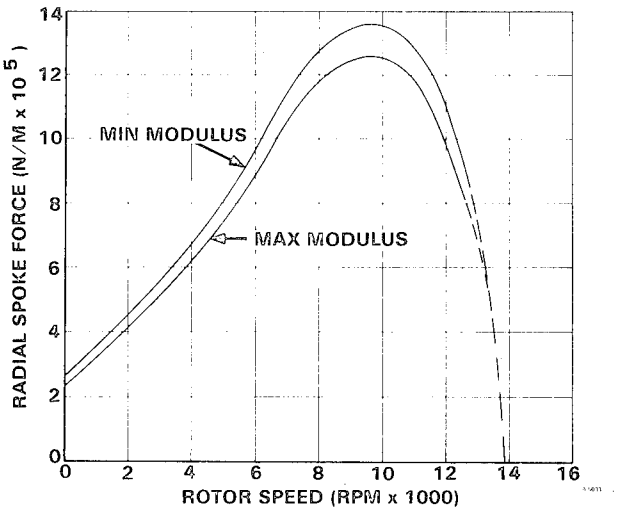

Fig. 5. Spoke Tip Radial Force

The maximum radial force was used to calculate the radial stress and the results compared to the allowable stress. Table 2 shows a margin of safety of 0.45. The effects of gyro-moment induced by the vehicle going off a 20 centimeter curb, a vertical acceleration of 10 g, or the maximum torque expected in a short circuit condition has been evaluated. The force induced has been compared to the frictional resistance of the rim-spoke interface, and the results are listed in Table 2.

Table 2. Flywheel Rim Loads

LOAD CONDITION	SPOKE TIP LOAD N	ALLOWABLE LOAD FRICTION ONLY N	STRESS (Mpa)	ALLOWABLE STRESS (Mpa)	MARGIN OF SAFETY
MAX SPOKE RADIAL FORCE (9500 RPM)	129000	---	19.0	27.6	0.45
GYRO-MOMENT (0.50 RAD/SEC)	7180	25600	1.03	20.7	19.
VERTICAL ACCELERATION (10 G)	932	25600	.138	20.7	100.
TORQUE 14.4 Nm	79.8	25600	.012	20.7	1000.

The flywheel hub duty cycle analysis is summarized in Table 3. This table shows less than 11% of the hub life will be expended during the 23 year operating period.

Table 3. Flywheel Hub Duty Cycle Life Summary

FLYWHEEL SPEED RANGE, PERCENT	CYCLE DESCRIPTION	STRESS(VON MISES) (Mpa)		CYCLES REQUIRED CR	CYCLES TO FAILURE CF	LIFE EXPENDED CR/CF
		MEAN	ALTERNATING			
0 - 100	START-STOP	117	117	8,700	2.1×10^5	.041
60 - 100	CHARGE	152	10.7	292,000	10^8	.003
80 +1	BUS STOP	138	4.38	6,974,000	$>10^8$	.070
--	TOTAL CYCLES	---	----	--	--	.114

Flywheel Environmental Considerations

Operation of the composite flywheel rotor requires a vacuum to prevent overheating and to minimize spinning losses. The required pressure of the flywheel cavity is less than 10 microns at the maximum operating speed.

Vacuum Design

The flywheel cavity was isolated by two cylindrical molecular pumps, placed at opposite ends as shown in Figure 6.

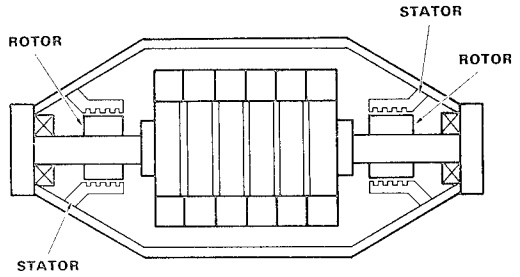

Fig. 6. Flywheel Assembly

The basic vacuum pump model was derived from analytical studies. The resulting pump size has a rotor diameter of 25 cm and a rotor length of 8 cm.

The driving cycle for the vehicle causes the flywheel speed to change from 12,500 rpm to 6,250 rpm in 12 minutes, and the flywheel speed is increased during charge in 1.5 minutes. The calculated pump pressure ratio performance will be 20 times higher at the higher speed.

Thermal Analysis

A thermal model was constructed and the stabilized temperature calculated for the flywheel rim. The rim temperature stabilized at 59°C, with an ambient temperature of 40°C.

The heat transfer mechanism is radiation of the heat from the flywheel rim to the flywheel housing, and then convection to cool the flywheel housing.

FUTURE WORK

The flywheel rotor design has been established. A single rotor module will be cycle tested to 1000 cycles. At the conclusion of the cycle test, the energy storage unit will be laboratory tested in the propulsion system and then tested in a trolley coach vehicle.

ELASTOMERIC REGENERATIVE BRAKING SYSTEMS

L. O. Hoppie
Eaton Corporation
Engineering & Research Center
P. O. Box 766
26201 Northwestern Highway
Southfield, MI 48037

ABSTRACT

Initial tests have been completed on full-scale elastomeric energy storage units intended for a regenerative braking system application on automobiles. The round-trip energy transfer efficiency of the storage units approached ninety percent, but showed a fatigue life of only a few thousand cycles. These values are in good agreement with corresponding values obtained during the testing of small-scale samples. Small scale samples of a different stressing scheme show efficiencies in excess of ninety percent, and fatigue lives in excess of 10^5 cycles. A tentative design based on this stressing scheme is described.

INTRODUCTION

Energy storage devices have been recognized as having the potential to decrease the energy consumption in a host of mobile and stationary applications. In the land transportation sector, for example, energy storage devices can be used as part of a regenerative braking system in order to capture and subsequently re-use vehicular kinetic energy which would otherwise be dissipated as heat in the friction brakes each time a vehicle decelerates. Furthermore, an energy storage device could be designed so as to provide the power not only for accelerating, but for passing and hill climbing as well. With such a device, the prime mover itself could be downsized, leading to even further reductions in fuel consumption.

In a previous paper[1], the potential advantages of an energy storage system based on storing energy in the form of strain energy in an elastomer were enumerated. It was pointed out that the volume of elastomer required is not prohibitively large, and that torque control was, at least in concept, necessarily simpler than for all other systems currently being investigated. More recently, full-size elastomeric units were tested in an attempt to:

1) Demonstrate that large amounts of energy can be efficiently transferred to and from an elastomer at high power levels;

2) Verify that empirical predictions based on small-scale test results can be applied to full-size elastomers.

Results of these tests on full-size elastomeric units are presented in this paper. Also included are recent theoretical and experimental results pertaining to an advanced scheme of elastomer stressing, and the latest iteration on the evolution of an energy transfer (torque control) device.

PRELIMINARY EVALUATION OF FULL-SIZE ELASTOMERS

Figure 1 shows a photograph of an elastomeric unit mounted on a test fixture. In this case, a 2.87" diameter rubber extrusion was wrapped around and secured to pins having a 40" centerline spacing, in order to produce four rods which are nominally adjacent to each other. The unit is sized to store 10^5J, which is the kinetic energy of a 2,500 lb vehicle traveling at approximately 30 mph. The particular arrangement and type of elastomer shown in Figure 1 were used during the preliminary full-scale tests in order to verify, at relatively low cost, the scaling laws of torque versus rotation, energy density, energy transfer efficiency, and fatigue life which were previously deduced from small-scale test results.

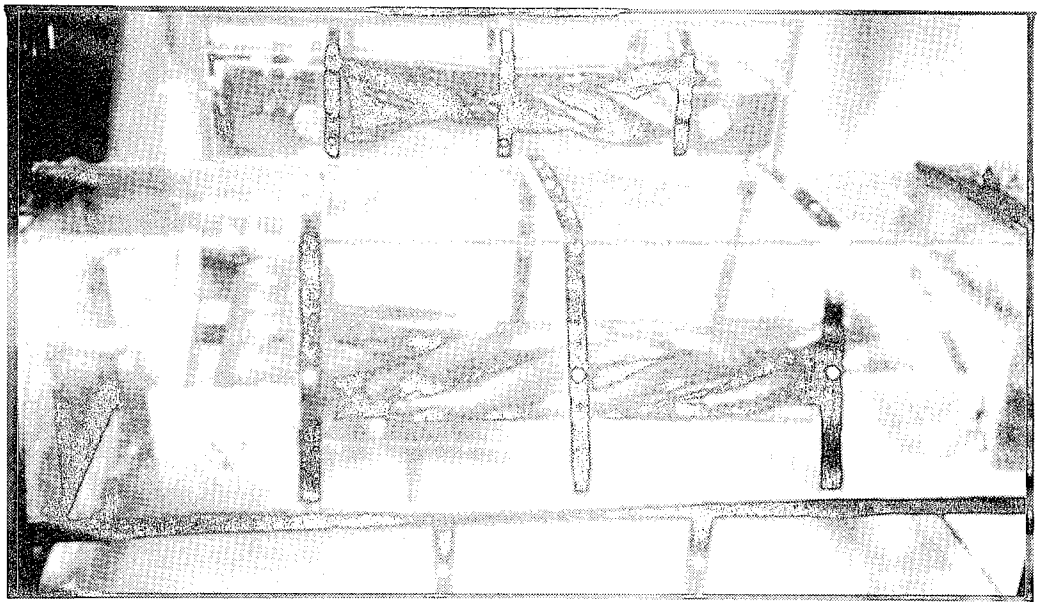

Figure 1

Full-Size Energy Storage Unit Under Test

Torque and axial load were measured by means of load cells attached to the stationary end (left-end in Figure 1) of the test fixture, while rotational position is measured at the rotating end (right-end of Figure 1). Rotation was achieved by means of a hydraulic motor which in turn was controlled by rotational position feedback.

Figure 2 shows torque and axial force versus rotation data obtained during a test in which the unit was wound until failure. The following data correspond to values pertinent to this test.

Revolutions at failure: 39 revolutions
Torque at failure: 1,020 ft-lb
Axial load at failure: 1,670 lb
Maximum axial load: 2,000 lb
Energy stored at failure: 1.35×10^5 ft-lb = 1.83×10^5 J
Volumetric energy density at failure: 177J/in^3 = 0.049W-hr/in^3
Gravimetric energy density at failure: 11.6J/g = 3,894 ft-lb/lb

Also shown in Figure 2 is the torque curve as predicted by the empirical equations deduced during the testing of small-scale samples.

The same test fixture and elastomer arrangement were used to investigate the round-trip energy transfer efficiency and fatigue life. During such tests, the elastomer was cycled between a lower limit of approximately three revolutions (the point beyond which the elastomer is in a buckling mode*) to various upper limits on the order of twenty revolutions. Typically, nearly ninety percent of the energy delivered to the elastomer was subsequently re-delivered by the elastomer, i.e., the total combined hysteresis and friction losses were only slightly in excess of ten percent of the energy delivered to the elastomer. With this elastomer arrangement, however, adjacent members abrade one another. The abrasion does not manifest itself as an excessive frictional loss, but does cause tears to develop, severely affecting fatigue life.

For example, for the tests which were performed on the full-scale unit shown in Figure 1, the fatigue life was on the order of one thousand cycles, in agreement with values previously obtained from small-scale test results.

*Sufficient twisting of an elastomer will cause knots to occur due to a buckling phenomena. Operation in the region where knots are observed is referred to as the buckling mode.

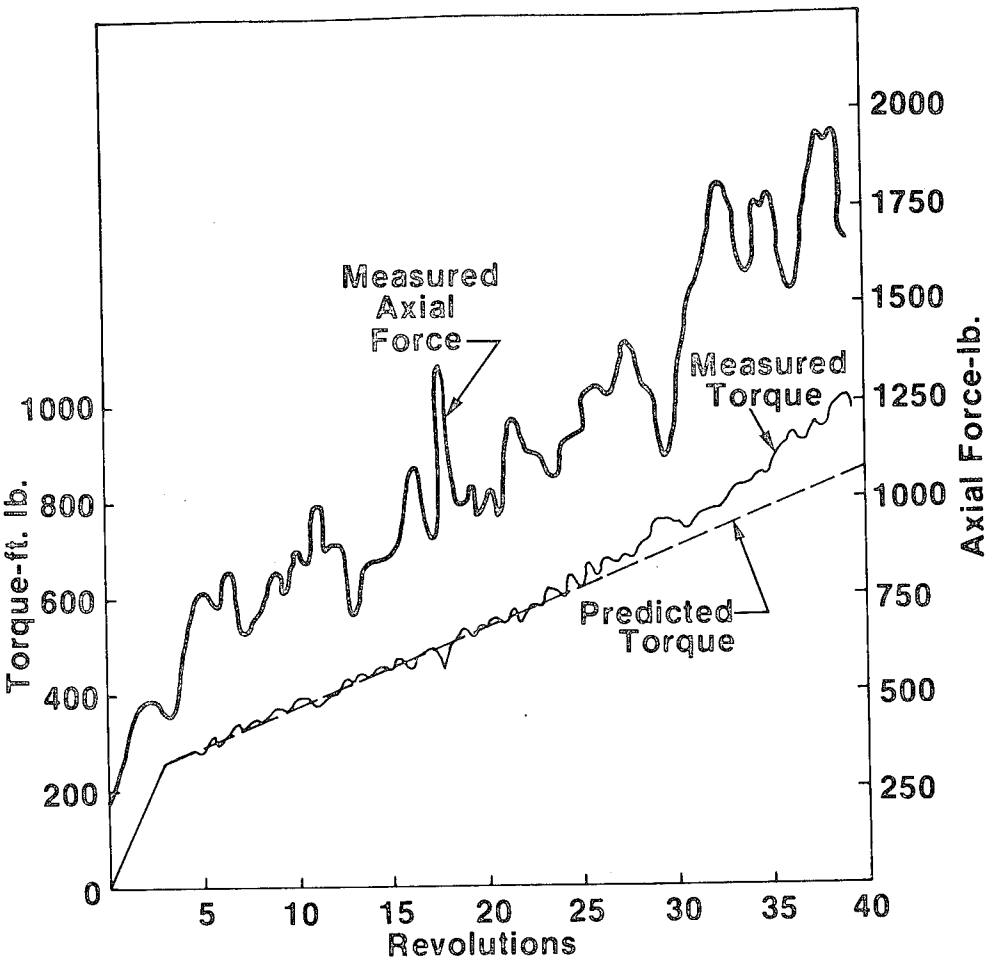

Figure 2

Torque and Axial Force Versus Revolutions on a Full-Size Elastomeric Energy Storage Unit

4 Rods Each 2.87 in. Dia. by 40 in. Length

THE PREFERRED STRESSING SCHEME

The test results described above demonstrated that large amounts of energy can be efficiently transferred to and from an elastomer at high power levels. Furthermore, the results showed that engineering information such as torque-rotation characteristics, hysteresis loss, etc., can be adequately scaled from small-scale test results. Consequently, small-scale tests were performed on stressing schemes different from the one described above in an attempt to find a stressing scheme with not only acceptable energy density and efficiency, but also with acceptable fatigue life and system adaptability.

The results of this effort led to isolated elastomeric rods initially stretched and then restrained from motion in the axial direction: energy is then delivered to or from the elastomer by rotating one end relative to the other. Figure 3 shows typical test results of a small-scale elastomeric unit stressed in this manner. Here, the effect of the final to initial length ratio, i.e., the elongation,

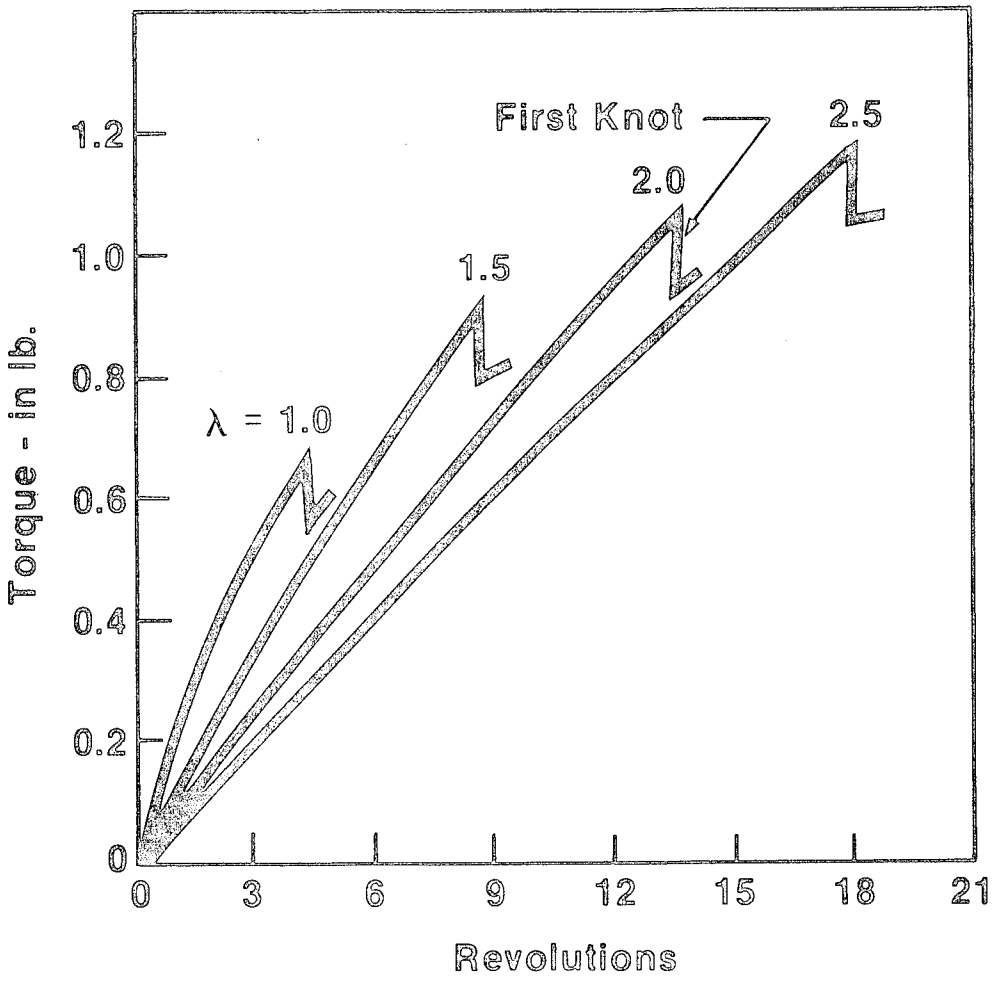

Figure 3

Effect of Initial Axial Elongation, λ, on the Torque-Rotation Characteristic of an Elastomeric Rod.

Initial Diameter: 0.375 in.
Initial Length: 3.740 in.

$$\lambda \equiv \frac{l_f}{l_i} \qquad (1)$$

on the torque rotation characteristics of the elastomer is shown. Notice first the very distinct dip in each of the curves; this is the point at which the elastomer buckles and forms the first "knot." Also notice the important result that the energy stored prior to the first knot, i.e., the integral of the torque-rotation curve from zero revolutions to the value at which the first knot appears, increases significantly with λ. In particular, these and other small-scale test results show that the energy density under these conditions varies parabolically with λ.

Rivlin[2] has considered the case of large deflections in elastomers and his theory can be applied prior to the non-linear regime, i.e., prior to the occurrence of the first knot. His theory predicts that the torque and maximum axial load are given by

$$T = \pi r_i^4 M \phi/(\lambda l_i) \qquad (2)$$

$$F_z = 2\pi r_i^2 M (\lambda - 1/\lambda^2) \qquad (3)$$

where r_i and l_i are the initial radius and length of the rod, ϕ is the rotational angle in radians, and M is a material property having units of a modulus (force per unit area).

Curve fitting to small-scale test results such as those shown in Figure 3 have shown the result

$$\phi_{Max} = \frac{\pi}{2} \left(\frac{l_i}{r_i} \right)^{3/2} \lambda \qquad (4)$$

as the rotational angle at which the first knot occurs. The maximum rotational energy which can be stored prior to the occurrence of the first knot is thus given by

$$E_{Max} = \int_0^{\phi_{Max}} T(\phi)\, d\phi \qquad (5)$$

which leads to

$$\frac{E_{Max}}{V_{Elas}} = \frac{M}{2} \left(\frac{\pi}{2} \right)^2 \lambda^2 \qquad (6)$$

as the energy density of a non-buckling rod. For soft natural rubber, M has an approximate value of 25 psi.

Fatigue tests of this stressing scheme on small-scale samples have been carried out with $\lambda = 4.0$, and at this value, the fatigue life is in excess of 10^5 cycles. Assuming an average of two stops per mile for a typical automotive application, 10^5 cycles corresponds to a life expectancy of 50,000 miles. Eliminating the effect of abrasion by not permitting knots to occur thus increases the fatigue life from an unacceptably low value to a very attractive value.

Equation 6 can be used to obtain an estimate of the amount of elastomer required for a given application. For example, if 10^5 J are required, and if it is assumed that the values $\lambda = 4.0$ and M = 25 psi are to be chosen, then approximately 1 ft^3 of elastomer would be required to capture the kinetic energy of a 2,500 lb vehicle initially traveling at approximately 30 mph. In an actual design, multiple independent rods could be employed, and the designer would be at liberty to select any desired length to diameter ratio provided that the total volume of active elastomer (excluding attachments) is approximately 1 ft^3.

TORQUE CONTROL

It has been pointed out[1] that the most important aspect of an elastomeric energy storage system is its inherent simplicity. This is because the elastomer can be thought of as a spring, and consequently forms a naturally oscillating spring-mass combination when used in conjunction with, for example, an automobile. The implication is that, at least in principle, no transmission or power conversion equipment is required; one need only connect the elastomer to the driveline of a vehicle by a simple clutch in order to convert vehicular kinetic energy into stored strain energy (potential energy) and vice versa. With a simple clutch, however, only one predesigned acceleration and deceleration profile could be executed at high efficiency.

This is not acceptable in many automotive applications, however, because of non-uniformities in acceleration and deceleration profiles imposed by various driving conditions. Consequently, some torque control is required to keep the system efficiency high during various acceleration and deceleration profiles.

Several torque control approaches have been considered for a system based on elastomeric energy storage, an example being shown schematically in Figure 4. Here, two elastomeric rods are shown coupled by a chain at one end, and by a variable sheave drive at the other end. Notice that the two sheaves are in turn connected by way of clutches to an input/output coupling consisting of three gears and a main disconnect clutch. The variable sheave drive could be any device having a continuously adjustable ratio over a narrow speed range.

Operation of the system can be understood by considering a deceleration and assuming some initial value of torque, T, in the elastomer. During deceleration, the upper clutch is disconnected, and both the lower clutch and the main disconnect clutch are engaged. Energy flows from the vehicle into the lower elastomer while a certain

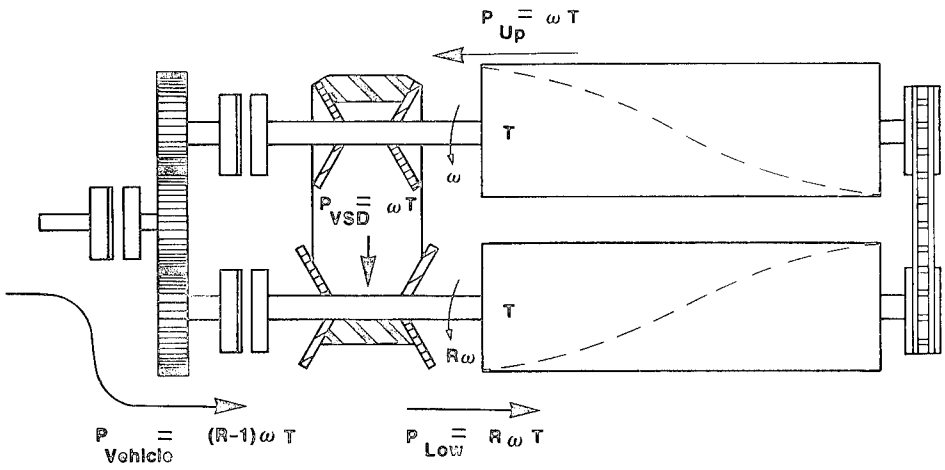

Figure 4

Torque Control Device for an Elastomeric Energy Storage System

amount of energy circulates from the upper to the lower elastomer by way of the variable sheave drive. In particular, in the absence of losses and with the upper and lower shafts rotating at speeds of ω and R ω, respectively, the amounts of power flowing at the lower and upper shafts are

$$P_{Low} = R_{\omega} T \quad (7)$$

$$P_{Up} = \omega T \quad (8)$$

while the power flowing through the variable sheave drive and the power flowing from the vehicle are:

$$P_{VSD} = \omega T \quad (9)$$

$$P_{Vehicle} = (R-1)\ \omega T \quad (10)$$

Hence, the torque applied to the vehicle during deceleration can, in principle, be smoothly and continuously adjusted from zero (R = 1) to the maximum design value ($R = R_{max}$) with nothing more complicated than a variable sheave drive. During acceleration, the upper clutch is engaged and the lower clutch disengaged. Smooth and continuous acceleration torque control is obtained by now adjusting the upper sheave to rotate faster than the lower one.

Of particular importance is the fact that the variable ratio device need be sized to carry but a fraction of the power being delivered to or from the vehicle. In particular, Equations 9 and 10 show that during deceleration, the maximum power delivered from the vehicle occurs when $R = R_{max}$, and at this value,

$$\frac{P_{VSD}}{P_{Vehicle}} = \frac{1}{R_{Max} - 1} \quad (11)$$

Since the power carried by the torque control device is relatively small, it is anticipated that a detailed design study will show that a compact variable ratio device will suffice, and that the system efficiency will still be attractive.

SUMMARY

Theoretical and experimental results have shown that large quantities of energy can be efficiently transferred to and from elastomers at high power levels. These and other aspects of the elastomeric energy storage concept make it attractive as the energy storage unit of a regenerative braking system for automotive applications. Work is underway to address the time dependent properties of elastomers, to solve engineering problems associated with the use of existing elastomeric materials, and to measure the fatigue life and efficiency of a complete full-scale system. This information will subsequently be used to ascertain the economic feasibility of such a system.

REFERENCES

(1) Hoppie, L. O., "Regenerative Braking Through Elastomeric Energy Storage," DOE, Division of Energy Storage, Conf. - 790854, pp 457 - 464

(2) Rivlin, R. S., "Large Elastic Deformations of Isotropic Materials, Part Six," Phil. Trans. A, 242, 1949.

THE FUEL ECONOMY POTENTIAL OF HEAT ENGINE/FLYWHEEL HYBRID AUTOMOBILES

Steve M. Rohde
Neil A. Schilke
Mechanical Research Department
General Motors Research Laboratories
Warren, Michigan 48090

ABSTRACT

Starting with the tractive energy requirements of automobiles over the EPA driving schedules, bounds for the fuel economy potential of idealized heat engine/flywheel hybrid vehicles were established as functions of vehicle mass and driveline efficiency. These bounds were compared with current production vehicle fuel economies and substantial fuel economy potential was noted. When the vehicle is penalized for the initial flywheel charge energy, the potential economy gains are reduced. The initial charging energy should be accounted for when comparing hybrids to conventional powerplants.

CONTROL CONSIDERATIONS FOR A FLYWHEEL HYBRID AUTOMOBILE WITH A MECHANICAL CONTINUOUSLY-VARIABLE TRANSMISSION

Norman H. Beachley and Andrew A. Frank
College of Engineering, University of Wisconsin-Madison
1513 University Avenue, Madison, WI 53706

ABSTRACT

The flywheel-transmission-internal combustion engine hybrid vehicle concept presents a number of unique control requirements. For consumer acceptance, all control functions must be accomplished automatically so that the car can be driven in the same manner as a conventional automatic transmission vehicle. In contrast to a conventional vehicle, the speed of a flywheel car is controlled by controlling the continuously-variable transmission (CVT). A torque control system is found to be the best approach. The alternative, ratio control, requires a more sophisticated system and presents a strong possibility for instability in the flywheel-drive train-vehicle system. Thus the transmission becomes a torque matching device rather than a speed matching device. With torque control, the CVT ratio itself becomes a resultant variable rather than a controlled variable, and need only be considered for secondary functions such as gear shifting. Methods of implementing torque control are described for CVT designs based on the rolling contact traction drive, the variable V-belt, hydrostatic, and slipping clutch principles. For best fuel economy it is useful to vary both the minimum and maximum allowable flywheel speeds as functions of vehicle speed, operating mode, and system parameters. It is also advantageous under certain conditions to declutch the flywheel and drive directly from the engine. These control aspects and others are treated in the paper.

INTRODUCTION

The use of a hybrid powerplant that incorporates an energy-storage flywheel has been demonstrated to offer a potential for significantly improved fuel economy and performance under urban driving conditions. Past work[1,2] has demonstrated the practicality of building and controlling such a vehicle. A great deal of effort is currently being expended on the concept to improve the system efficiency and the control algorithms to develop a viable contender for the "car of the future." The purpose of this paper is to outline the unique control requirements of a flywheel hybrid car, and to discuss control techniques that may be applicable.

Figure 1 is a schematic diagram of the basic propulsion system under consideration. Although some of the power will pass directly from the engine to the drive wheels when the engine is running, the best way to explain the concept is to consider that the car is normally driven by the flywheel, with the engine coming on to recharge it only when its speed drops below some predetermined value. Otherwise the engine is off. Regenerative braking is readily accomplished by putting energy back into the flywheel; i.e., speeding it up to absorb the kinetic energy of the vehicle itself. In addition to this basic flywheel mode, however, there is available a direct drive mode with the flywheel declutched that is advantageous for certain conditions.

One very important aspect of this concept is the requirement for a continuously-variable transmission (CVT). Since the flywheel speed cannot be changed at will and since the driver must be given free rein over the vehicle speed and acceleration, a CVT is necessary to match the speed of the flywheel and that of the car under all conditions and to provide the power transfer required to drive the car.

An experimental flywheel automobile based on Fig. 1, but without the flywheel clutch, has been designed, constructed and tested at the University of Wisconsin.[1-3] It has demonstrated the practicality and

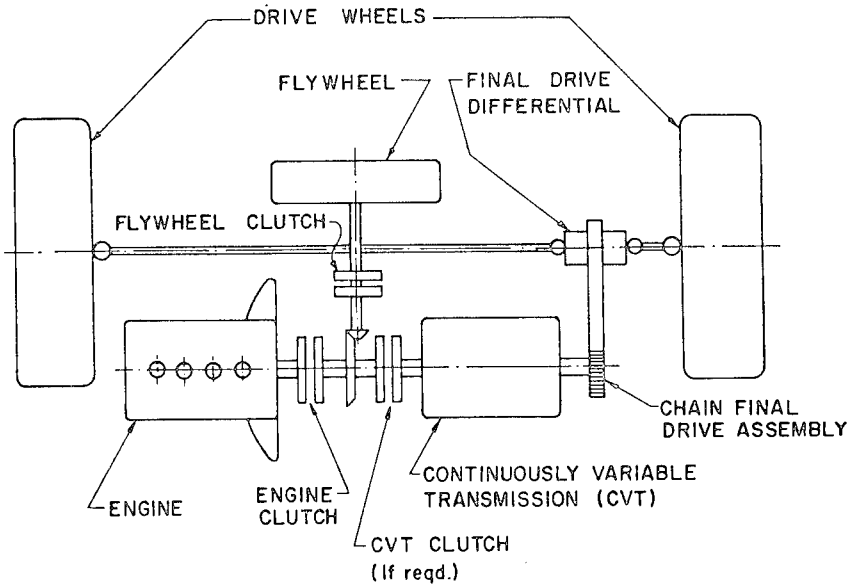

Fig. 1. Schematic diagram of a Flywheel Energy Management Powerplant (FEMP) system for a front-wheel drive vehicle.

fuel saving potential of the concept, and aided in the development and testing of certain control principles. Several other flywheel vehicle systems have been built or are currently under construction.[4-7] Data from these are also adding to our understanding of the problems involved.

A second generation vehicle is currently in the design stages at the University of Wisconsin (with the Lawrence Livermore Laboratory as the Program Manager). Whereas many of the control functions of the first experimental vehicle were handled manually, the new model will employ more sophisticated automatic controls which will not only make the car easier to drive but also make it possible to maximize system efficiency (and therefore fuel economy) under all types of driving conditions.

Since the flywheel car must be driven by controlling the CVT (rather than by controlling the engine or flywheel) it is the most important system component in terms of control. There are four basic types of CVT under consideration by us:

1) The hydrostatic power-split CVT (Fig. 2). This system utilizes a hydrostatic pump and motor, one or both of which will have variable displacement. Part of the power passes through the hydrostatic unit, and part through a straight mechanical path, the two components then being added at the output by a gear differential. (This concept was used in the University of Wisconsin experimental flywheel car and the MAN Diesel Bus.[1,4])

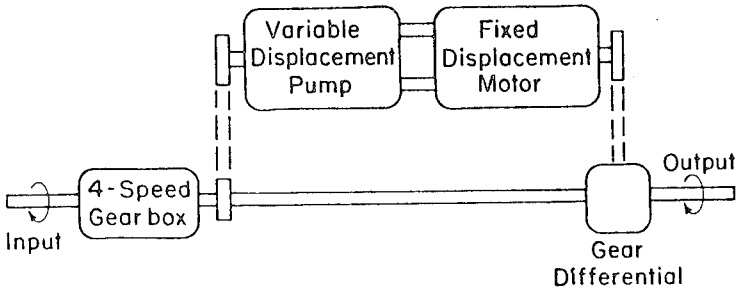

Fig. 2. Schematic diagram of a power-split hydrostatic transmission.

2) A variable V-belt CVT (Fig. 3). By varying the diameter of the sheaves, a V-belt drive can be made continuously variable. Under study are not only rubber V-belt systems, but also ones incorporating a new steel-block V-belt developed by van Doorne Transmissie of the Netherlands and others.

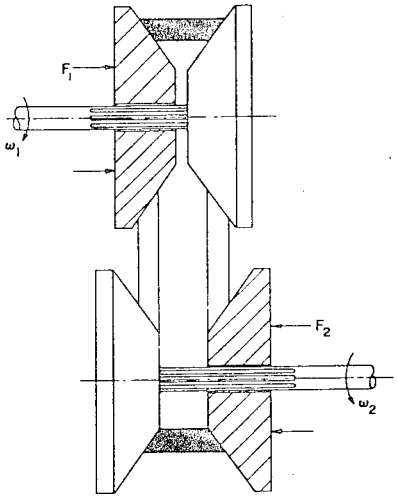

Fig. 3. A variable V-belt continuously-variable transmission (CVT).

3) Rolling contact traction drive CVT's. There are a number of versions of this general principle that might be used, with the design of Fig. 4 being one currently under development. In this design, commonly called the "toroidal drive," tilting the roller axes as indicated will change the radii of their contact with the two halves of the toroid, allowing the speed ratio of the drive to be varied in a continuous manner.

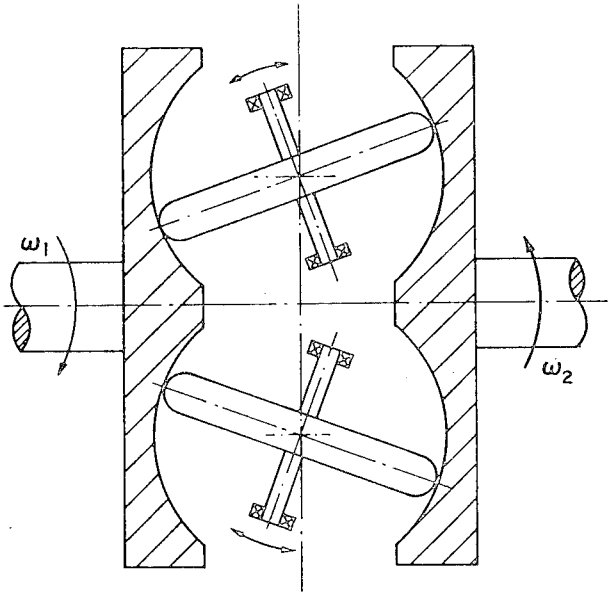

Fig. 4. The "toroidal drive," a rolling contact traction drive CVT.

4) Multi-speed gearbox with slipping clutch CVT's. An efficient CVT is obtained by using a gearbox with a large number of speed ratios (e.g., twelve or more) in series with a clutch designed for continuous slip to provide the speed ratios in between the discrete gearbox values. The attractiveness of this concept lies in the fact that except for the clutch slippage losses (relatively small with a large number of gear ratios), the system is based on components with high efficiency and low spin losses. Thus overall system efficiency can be high. To be more specific, a 12-speed slipping clutch system has been designed (Fig. 5)

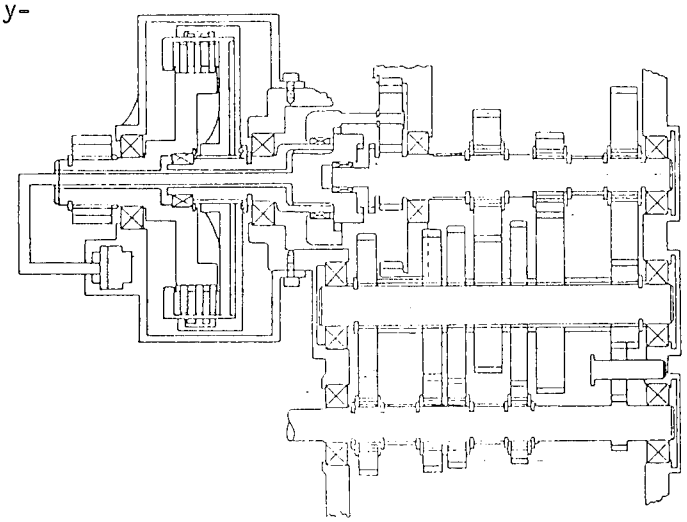

Fig. 5. A 12-speed gearbox with slipping clutch CVT (design by Michael Nohr[8]).

with 17% spacing between discrete ratios.[8] With a maximum clutch slip of 17%, average slip will be 8-1/2%, corresponding to an average efficiency of 91-1/2% for the slipping clutch element. Other system losses will of course reduce this value, but they should be small. The important fact, however, is that this efficiency can be maintained at 1-2% of the maximum load, a feature very difficult to obtain by other means.

REQUIREMENTS FOR THE FLYWHEEL PROPULSION SYSTEM

The general specifications for a satisfactory passenger car based on the

flywheel energy storage powerplant should be

1) The car must be controlled and driven in a manner similar to a present-day automatic transmission vehicle. (This is in terms of what the driver must do.)

2) There must be no instability in the driving system. This refers to potential problems such as surging, the inability to maintain a smooth constant speed, jerkiness during shifts, etc.

3) The drive train losses must be minimized. (This, of course, maximizes the fuel mileage.)

4) The engine must be operated only at conditions of maximum or near maximum efficiency; otherwise, it must be shut off.

5) Simplicity and reliability must be achieved.

In order to achieve the above goals, system controls must provide the following functions:

1) The flywheel speed (i.e., the permissible maximum and minimum values) must be controlled as a function of vehicle speed and perhaps other variables. The flywheel must be declutchable under certain conditions so that the system will provide greater fuel economy or to meet the required performance specified by the driver.

2) Gearbox shifting (required of most of the CVT candidates) must be automatically controlled, with regard to both the mechanical actuation itself and also the criteria for when a new gear ratio is required and/or desirable.

3) The actuation of clutches, some requiring fine control of the torque generated by slippage, is necessary in many of the CVT concepts.

4) The torque applied to the driving wheels (both positive and negative) must be able to be controlled at all times by the driver by means of only the accelerator and brake pedals.

The above control functions will now be considered in more detail.

CONTROL OF FLYWHEEL SPEED LIMITS (ENGINE ON-OFF STRATEGY) AND FLYWHEEL DECLUTCHING

The mechanical aspects of turning the engine "on" and "off" are quite simple. A mechanical clutch is engaged and disengaged, with the rate of engagement not being especially critical. The ignition system can be left on continuously. The fuel needs to be turned off abruptly when the engine clutch is disengaged, and then turned on when it is re-engaged. This is necessary for emissions and other considerations. An electronic fuel injection system is ideal for this function, but other systems such as a carburetor with a solenoid valve for fuel shut-off may also be satisfactory.

The choice of rpm limits (high and low) must satisfy a number of criteria. It must allow the engine to stay within its efficient range of operation. The speed range should be broad enough, based on any given flywheel inertia, so that the engine does not have to cycle too frequently (as there are losses associated with each engine start-stop cycle), but on the other hand, a narrower range allows the use of a CVT with a lower ratio range, which in most cases allows it to be designed with higher efficiency. When driving under slow urban conditions the upper flywheel speed limit should be reduced, to reduce spin losses in the flywheel, CVT, and other drive train elements, the resultant lower value of flywheel energy storage being still adequate for these conditions. When traveling at higher speeds, the lower speed limit should be raised. At higher speed, more energy and power are required for passing, grade climbing, etc., and a low engine speed dictated by a low flywheel speed (with the direct engine clutch connection as illustrated in Fig. 1) would limit the engine to low power. If the desired power beyond that available from the engine were taken out of the flywheel under such low speed (and therefore low energy) conditions, the engine-flywheel would quickly decelerate to an unusable condition. These control policies are contrary to what is proposed by many researchers, who feel the flywheel speed should be low with high vehicle speed and vice versa, to give a "constant kinetic energy" system. Experience shows the algorithm proposed here to be much more practical with a limited range CVT. Other possibilities can exist only if the CVT

overall range is much larger, which would in general result in poorer overall efficiency.

The control of the flywheel speed limits to satisfy the above requirements is best handled in a preprogrammed manner, with the limits continually changing with vehicle speed. In addition, since an automatic control system cannot anticipate what the driver is likely to do, it may also be advisable to have two alternative modes that can be selected by the driver, "performance" and "efficiency," which would have somewhat different limits and perhaps different algorithms for the same vehicle speed.

The above policy for controlling minimum and maximum flywheel speeds would allow (with a flywheel of adequate inertia) satisfactory performance without ever declutching the flywheel from the drive line. The addition of a flywheel clutch opens up new control possibilities, however, which include the prospect of reduced flywheel size.

If the engine is "full size" (a desirable feature for a general-purpose vehicle which can climb long grades at full cruising speed), then any hard acceleration can be handled by the engine itself with the flywheel disconnected. Moreover, it can do so at wide-open throttle--maximum engine efficiency conditions because of the availability of the CVT for this mode. Since the flywheel would not need to have the energy required to handle such acceleration, its proper inertia could be determined as that value required to allow it to recover most of the potential regenerative braking energy typically available and/or that value required to keep the engine on-off losses at a reasonable value. The decrease in weight and spin losses of a smaller flywheel must be balanced against the above factors in determining an optimal flywheel size for a specific vehicle operating under assumed typical conditions.

With the flywheel declutch mode, there are two control philosophies that may be used:

1) The flywheel could be left in the system except for cases in which the desired vehicle performance cannot be satisfied. This would be considered to occur whenever the flywheel speed would drop more than a certain amount (say 10%) below its preprogrammed minimum speed for the given conditions. (The engine would of course be "on" when this occurred.)

2) The flywheel could be declutched whenever it is determined (by an onboard logic system) that system economy could be improved by declutching the flywheel and using the vehicle in the CVT mode.

Combinations and variations of the above are of course possible. In any case, the engine would operate between two speed limits at wide open throttle. Figure 6 shows the engine operating characteristics under this mode of operation. Notice that the engine will operate at almost best efficiency. Also, it is possible to produce maximum engine power indefinitely. Incidentally, maximum engine power may be less than that available under flywheel drive depending on the selection of components, etc.

GEARBOX SHIFTING

All CVT designs currently being considered by us incorporate a discrete gearbox or something comparable to extend the ratio range and still maintain a high system efficiency. It is important that the system be in the proper gear at all times, to provide best efficiency and also to ensure that desired acceleration (or deceleration) will not be stopped by having the CVT reach one end of its ratio limits.

The shifting control can be handled satisfactorily in an open-loop manner. The discrete gear the vehicle should be in at any instant of time would be determined from (1) vehicle speed, (2) flywheel speed, (3) an algorithm based on efficiency data and CVT ratio limits, and, in the case of a slipping clutch system, whether the command is acceleration or deceleration.

CLUTCH ACTUATION

For the basic configuration of Fig. 1, a minimum of two clutches are required, the engine clutch and the flywheel clutch. To decrease operational complexity a third gearbox clutch could be added. The gearbox clutch is disengaged when shifting gears. Its rate of engagement afterwards must be such as to allow the CVT time to "find" the proper speed ratio; otherwise a high torque transient might occur which

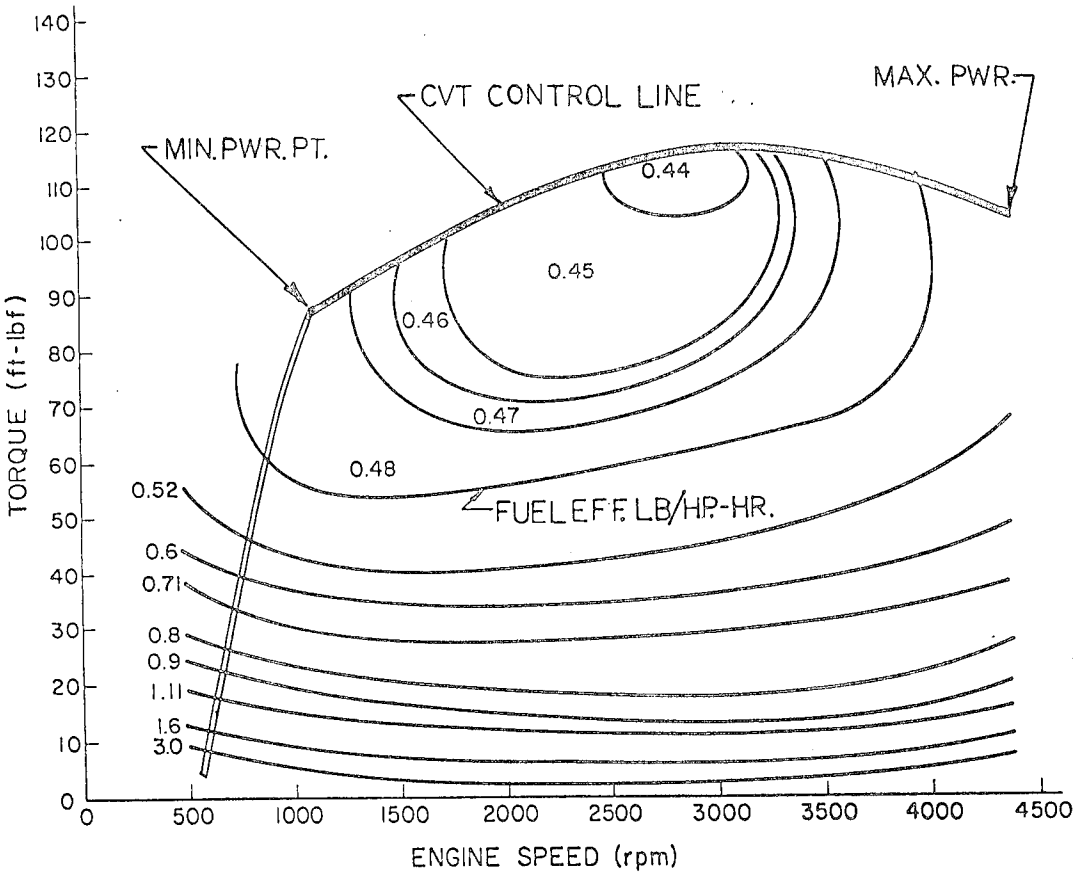

Fig. 6. Engine operation to produce maximum fuel economy with the flywheel vehicle.

could cause tire slip. It would be possible with sophisticated controls to have the CVT ratio set at the proper value so that the clutch could be engaged abruptly, but the above simpler approach would probably be adequate with a torque control system as described below. The clutch is also used in most designs as a slipping element to provide vehicle control at speeds between zero and the lowest provided by the basic CVT ratios. In this case torque is proportional to the clutch loading pressure. In a conventional car, the torque converter and engine are used for this purpose. We do not have that possibility, since torque cannot be independently controlled except at the transmission. It may be possible to design a torque-controllable torque converter for this purpose, instead of a slipping clutch. Such a system should be considered.

OUTPUT TORQUE CONTROL OF CVT'S

There is only a single CVT ratio that can exist for any particular combination of flywheel and vehicle speeds (unless there is slip between the drive wheels and the pavement). The acceleration and deceleration of the vehicle, however, is determined by the rate-of-change of the CVT ratio. Let us now consider the best way to control the CVT ratio and its rate of change.

One approach, which can be termed "ratio control," is to monitor the CVT ratio itself, determining on a continuing basis what it (and its rate of change) should be to produce what the driver has commanded and to control the CVT (with a feedback control system) in a manner that will continuously provide the proper ratio and ratio rate. This approach is theoretically feasible, but an analysis of such a system will reveal some potential problems. One complication is that the rate of change of CVT ratio depends not only upon vehicle acceleration, but also the road load and the flywheel speed. Stability is a potential problem with the required feedback control system. The

reason for instability can be explained by considering the vehicle system as two inertias (the flywheel inertia and the vehicle mass) connected by a compliant member (the drive line with all of its compliant joints, gear interfaces, etc.) with little damping. Low frequency oscillations ("surging") are found to be a likely problem for an inadequate or slightly out-of-adjustment control system. Surge frequencies fall into the 0.25 to 1 Hertz region. Unfortunately this is also the band-pass required for good vehicle response.

Although a ratio control system could be made to work, there is a much simpler and better approach: output torque control. If the torque at the output of the CVT can be controlled, then nothing else needs to even be considered. The torque sets the acceleration of the car, and that is all the driver is concerned with. Drive stability is automatically achieved; i.e., if torque at the drive wheels is kept at the value commanded by the driver, there can be no oscillations, as these can occur only with oscillating values of torque. With this approach, the CVT ratio and its rate of change are resultant variables rather than primary variables of control, and do not need to be known or even considered except to determine when a gear shift is required. Torque control is therefore the ideal approach provided that the CVT output torque can in fact be readily controlled in a reasonable manner.

We will now consider torque control techniques for various CVT designs. It should be noted at this point that perfect torque control is not essential, i.e., a given accelerator pedal position does not need to produce a specific torque within a few percent. The important consideration is that an increase in pedal displacement will produce an increase in torque in a smooth and continuous manner. The driver will provide the feedback to set the exact torque desired. (Note that in present-day cars the torque provided by a given accelerator [throttle] position is quite variable, depending upon what gear the car is in, as well as the engine speed. The driver always knows, however, that if he pushes the pedal down further the torque will increase, and vice versa.)

TORQUE CONTROL FOR MULTI-SPEED GEARBOX, SLIPPING CLUTCH CVT

With this system, torque control is extremely simple. The torque of a slipping clutch is proportional to the normal force on the friction surface. This force can be readily controlled by an accelerator pedal linked to a pressure control valve feeding a clutch loading hydraulic piston. This has to be coordinated with gear selection to produce the proper sign of the torque, since a slipping clutch provides torque only in the direction of slip.

TORQUE CONTROL OF HYDROSTATIC CVT'S

Any CVT based on hydrostatics (including the power-split versions) can have torque control implemented by means of a pressure control valve, since torque of a hydrostatic motor is directly proportional to pressure. This is the design that was used on the University of Wisconsin's experimental flywheel Pinto . A pressure-control valve manufactured by Sundstrand using feedback from the hydrostatic pressure itself was used. The system pressure is directly proportional to the angular position of the valve's input shaft (controlled by the accelerator and brake pedals through a direct mechanical linkage). Control of the vehicle torque with this design has proven to be completely satisfactory, both for forward drive and regenerative braking.

TORQUE CONTROL OF ROLLING CONTACT TRACTION DRIVES

For rolling contact traction drives, torque control is not quite as simple as for the first two types of CVT considered above. It appears, however, that torque control is probably feasible for all variations of the basic rolling contact CVT principle. To be more specific, it appears that for all such designs there is a torque or force required to hold the elements in a kinematic relationship that will give a proportional output torque. The underlying principle can be illustrated by considering the rudimentary traction drive of Fig. 7 (which, incidentally, was used in several passenger car models built around 1910). In early vehicle versions of this CVT, leather-rimmed output wheels were used, and the speed ratio was changed by merely pushing the wheel toward or away from the centerline of the input disk, the compliance of the leather making this practical. With a more modern steel-on-steel drive, however, another method is preferred, as any significant slip at the interface would

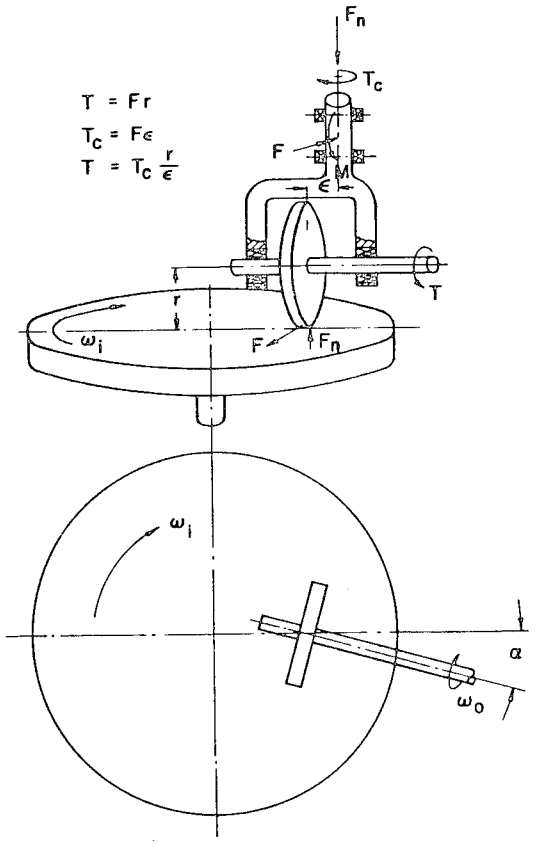

Fig. 7. A rudimentary rolling contact traction drive to illustrate torque control principles.

damage the CVT.* In this case the output wheel is "steered" toward or away from the input disk centerline by introducing a small angle α (Fig. 7) between its shaft and a radial line on the input disk. Figure 7 shows that this can be accomplished by applying a torque T_c to a trunnion shaft offset by a distance ϵ from the plane of the wheel. The control torque (T_c) is directly proportional to the CVT output torque (T) as given by the equation $T_c = \frac{T\epsilon}{r}$. When the control torque is removed, the wheel reverts to the orientation (normally where $\alpha \approx 0$) that produces no CVT output torque. Note that if the offset ϵ were to the left rather than the right the system would be unstable. As shown, the system will work satisfactorily for both forward drive and regenerative braking.

*Since the two traction surfaces are separated by a thin film of oil which allows low levels of creep, it is possible to change the CVT ratio slowly by merely pushing the output wheel to a different radius, as long as the force is not great enough to produce gross slip. The method described in the text is superior for most designs, however.

Another aspect to be considered is the normal loading between the wheel and disk. The force here should at all times be as low as possible (to reduce friction losses and increase the CVT life) but high enough to prevent slip. Loading proportional to torque is therefore desired. By using hydraulic pressure for control, it is a relatively straightforward design problem to use the same control pressure to provide both torque to the trunnion shaft and the proper normal load, even though there is a slight complication with regenerative braking where a negative CVT torque still requires positive normal loading.

Although the CVT of Fig. 7 is apparently not under serious consideration for flywheel automobiles, similar concepts based on the same general ideas are under development, and the torque control principles as described can be readily adapted to them. In fact, the principles can probably be extended to provide a practical method of torque control for any type of rolling contact traction drive.

TORQUE CONTROL OF VARIABLE V-BELT SYSTEMS

For V-belt drives (Fig. 3), both rubber and the new steel-block belt design developed by van Doorne and others, acceleration is proportional to the rate of change of speed ratio, which in this case is proportional to the rate of change of sheave diameters, with one increasing while the other decreases. This is accomplished, producing torque for acceleration, by increasing the force holding together the two halves of one variable sheave, while holding the force on the other one.

Torque, however, is required not only for acceleration, but also for steady driving to overcome the road load, gradient load, etc. Superimposed, therefore, on the above control requirement is the additional requirement that the loading force on each variable sheave must always be maintained at a level which will prevent slip, as determined from the coefficient of friction that applies to the belt-sheave interface. Moreover, it is

not satisfactory to be overly conservative (i.e., to always keep it far above the value that would allow slip) because this would cause unnecessarily high friction losses at low power levels.

The control problem, therefore, consists of keeping the two loading forces correct at all times, both on an absolute basis and also with respect to one another. We are currently studying the problem, but more data are needed before we will be able to develop a final design.

SUMMARY AND CONCLUSIONS

We have explored and discussed some control philosophies for flywheel energy storage automobiles. The objectives of all of these schemes are system simplicity, efficiency, and controllability.

The concept of flywheel speed management was discussed and concluded with the idea that flywheel speed range should be a function of the type of driving anticipated to minimize system losses.

The concept of dropping out the flywheel when no longer beneficial was also introduced. Thus the control system would automatically decouple the flywheel when it becomes a burden and recouple it when necessary to provide proper engine load. This can be done simply by sensing engine and vehicle speed if the proper transmission torque control is applied. Incidentally, the torque control scheme for flywheel drive may not be the same as for engine-CVT drive. While output torque is still the controlling factor, the direction of ratio change is reversed, i.e., more power from a flywheel drive means the flywheel must slow down whereas more power from an engine means the engine must speed up, since the engine is at wide-open throttle. The consequences of this CVT-only mode are that

1) The flywheel size may be reduced to something slightly larger than a conventional engine flywheel.

2) The vehicle system can be designed to provide a highway cruise mode without the flywheel and CVT, and the CVT can be used for high-power applications without the flywheel.

3) It is possible to utilize the advantage of a CVT vehicle while also including the load-leveling capability of the flywheel with the ability to add a highway cruise gear bypassing the CVT and flywheel.

Output torque control was discussed and found to be the desired mode of control. Other forms of torque control are possible and may have some advantage. For example, it may be desirable to control a combination of transmission input and ouput torque rather than output torque alone.[9] These control policies may provide vehicle characteristics which are desirable for certain applications and may somewhat simplify some of the problems of flywheel speed management. Output torque control has the advantage of simplicity in concept and a separation of functions.

Finally, a discussion of techniques for implementation of torque control for a variety of continuously variable transmissions was made. It should be clear that torque control can be implemented with any CVT concept, since it is basic to most systems. There are some CVT systems which may have inherent torque and ratio independence. These systems will have to be controlled by direct torque sensing at the output. Output torque sensing may be desirable for other reasons within the CVT itself. For example, the traction elements may be loaded proportional to the output torque. System response is important in many cases, since output torque can change very quickly when a vehicle runs over a bump or a hole. These kinds of problems must be addressed before a final system is selected.

ACKNOWLEDGMENTS

This research has been made possible by a contract with the Lawrence Livermore Laboratory, Mechanical Energy Storage Project. The opinions expressed represent solely those of the authors and not necessarily of the Lawrence Livermore Laboratory.

REFERENCES

1. Beachley, N. H., and Frank, A. A., "Final Report--Flywheel Energy Management Systems for Improving the Fuel Economy of Motor Vehicles," Report DOT/RSPA/DPB-50/79/1, prepared for U. S. Dept. of Transportation, Aug. 1979.

2. Frank, A. A., and Beachley, N. H., "Evaluation of the Flywheel Drive Concept for Passenger Vehicles," SAE Paper 790049, 1979.

3. Beachley, N. H., et al., "Experimental Evaluation of Flywheel Energy Management Automobile," Proc., 4th International Symposium on Automotive Propulsion Systems, April 1977.

4. Scott, D., "Regenerative Braking Cuts Bus Fuel Needs," Automotive Engineering, Vol. 87, No. 10, Oct. 1979, pp. 102-107.

5. Raynard, A. E., "Electric/Flywheel Powered Postal Vehicle Development," Proc., 1979 Mechanical and Magnetic Energy Storage Contractors' Review Meeting, Dec. 1979, pp. 465-477.

6. Anonymous, "Unique City Bus Introduced by Volvo--Stores Energy," Press Information from Volvo Bus Corporation, S-405 08, Goteborg, Sweden, June 1980.

7. Anonymous, "The Electric/Flywheel Prototype," brochure from Kinergy Research & Development, P. O. Box 1128, Wake Forest, N. C., 1978.

8. Nohr, M., "Slipping Clutch Continuously Variable Transmission Design Study," M. S. Thesis, University of Wisconsin, Madison, Wis., 1980.

9. Burrows, C. R., "An Assessment of Flywheel Energy Storage in Electric Vehicles," SAE Paper 800885, 1980.

EVALUATION OF A HYBRID FLYWHEEL/BATTERY PROPULSION SYSTEM FOR ELECTRIC VEHICLES

E.P. Cornell, F.G. Turnbull
Corporate Research and Development
General Electric Company
Schenectady, NY

T.M. Barlow
Lawrence Livermore National Laboratory
University of California
Livermore, CA

ABSTRACT

The development, fabrication, and test of a regenerative flywheel energy storage system for a battery/flywheel electric vehicle for commuter application is reviewed. The system consists of a steel flywheel coupled to a high-speed inductor motor/alternator fed by a load-commutated inverter/rectifier which does not utilize a shaft position sensor for inverter control. Computer control is used to provide component as well as overall system control and data acquisition. This flywheel energy storage system was laboratory tested over the SAE J227a Schedules D, C, and B driving cycles, using a laboratory simulation of an electric vehicle drive. Results show that maximum benefit occurs on the Schedule D cycle for which the overall system was optimized. From these tests, recommendations for additional improvements to this propulsion system are made.

INTRODUCTION

A flywheel energy storage sytem was initially conceived in 1975 by the General Electric Company and proposed for demonstration to the U.S. Department of Energy, Division of Energy Storage Systems. The overall objective of the program was to demonstrate new technology associated with a flywheel energy storage system comprised of a flywheel coupled directly to an ac synchronous motor/alternator. The motor/alternator/flywheel unit would be hemetically sealed with the rotating assembly operating in a low-pressure helium atmosphere. The motor/alternator would receive power from a solid-state inverter/rectifier unit designed to provide the necessary frequency control from a constant dc voltage power supply. The results of this program are described in References 1, 2, 3, and 4.

A follow-on effort, which is the subject of Reference 5 and this paper, was initiated with the specific objective of laboratory testing an improved flywheel energy recovery system sized for a battery/flywheel electric vehicle weighing about 3500 pounds. Computer runs have been made to simulate an electric vehicle operating under the SAE J227a Schedule D driving cycle. The goal was to determine the performance improvement that can be attributed to the use of a small flywheel in combination with the battery bank. Analysis has indicated that the flywheel can isolate the battery from a portion of the acceleration power demands of the vehicle and can also recover a substantial portion of the braking energy.

OVERALL VEHICLE SYSTEM STUDIES

In analyzing the performance of a flywheel battery-powered vehicle operating on a duty cycle such as the SAE J227a Schedule D, many operating strategies were evaluated. This involved use of the flywheel energy and the battery energy, or both, to provide propulsion energy and to accept regenerative energy during various segments of the selected driving cycle. The selected cycle and the active subsystems are shown in Fig. 1.

The five segments of the SAE driving cylce are indicated at the top of Fig. 1. The accelerate portion is divided into two modes. In the first mode, from zero vehicle speed to the "motor cornering point," indicated by the circle, all of the power is supplied from the flywheel subsystem. At the "motor cornering point," the motor back EMF equals the battery voltage and the second mode commences. During Mode 2, both the battery and the

flywheel subsystem share in supplying the accelerating power. Mode 3 begins when the vehicle has reached the desired steady speed. During this mode, all of the power is supplied from the battery. During Mode 4 (Coast) and Mode 5 (Brake), all of the recovered power is supplied to the flywheel subsystem. During Mode 6 (Idle) the flywheel subsystem is brought back to its initial speed with power from the battery. The shaded area in Fig. 1 is power supplied out of and into the flywheel subsystem to and from the propulsion motor. The cross-hatched area is the power supplied from the battery direct to the flywheel subsystem. The unshaded area represents the battery power supplied direct to the propulsion motor.

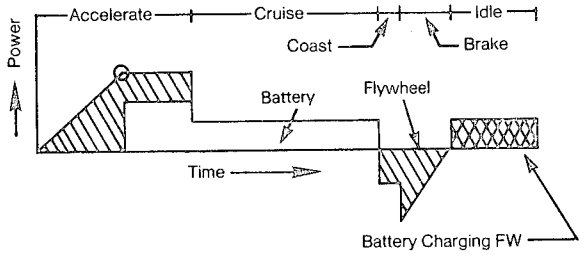

Fig. 1 Selected System Operating Strategy

Figure 2 shows schematically the overall system modeled for computer evaluation. The energy storage package was considered as a single subsystem, containing the motor/alternator/flywheel and the power conditioning equipment. As such, only one parameter, the combined in/out energy efficiency, was required to define this subsystem. This value became an input to the computer program. It was assumed that the size and the speed range of the flywheel would be designed to be sufficient to store the braking energy and to provide the needed acceleration.

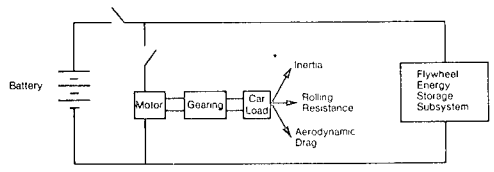

Fig. 2 Overall System Model

The battery/flywheel vehicle assumed for these simulation runs was taken as a modification of the all-battery electric vehicle that the General Electric Company has developed under separate DOE/JPL contract. The computer's performance predictions and the actual measured performance of the all-electric vehicle are presented in Reference 6. The vehicle has an empty weight of 2,000 pounds, a battery weight of 1,100 pounds, and a passenger load of 600 pounds for a gross total weight of 3,700 pounds. The computer program used the following constants: drag coefficient times frontal area ($C_D A_F$) = 5.7 sq. ft. and rolling resistance = 0.009 lb./lb. The efficiency of the drive train (motor and gears) was based on a breakdown of the losses as a function of dc armature current, dc field current, motor speed and output torque.

In assessing the results of the vehicle simulation runs, two criteria were used: first, the actual range for a repetitive J227a Schedule D cycle; and second, a comparison of this range with that computed for the pure battery electric vehicle. In the latter case, no regeneration into the battery was assumed for the reference vehicle since the amount of regeneration possible was not precisely known at that time.

Figure 3 shows the computer's predicted range of a non-regenerative all-electric vehicle and the predicted range of the battery/flywheel system operating in the modes shown on Fig. 1 as a function of flywheel in/out efficiency. The actual measured values of flywheel in/out efficiency (presented in Fig. 12) were less than the minimum value of 60% given on the curve. Extrapolation of the linear curve of range vs. in/out efficiency to a value of 50% gives the predicted increase in Schedule D driving cycle range using the flywheel package.

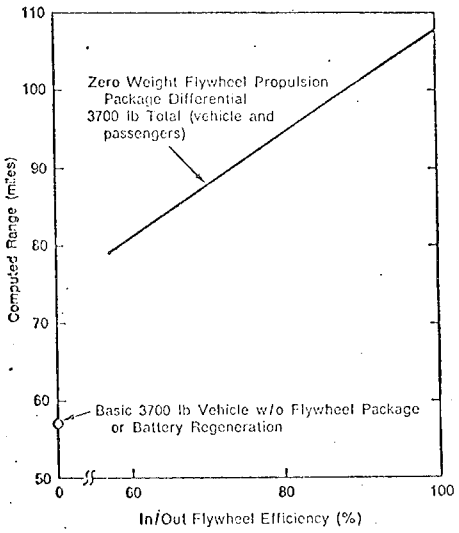

Fig. 3 Computed Range vs In/Out Efficiency on Schedule D Driving Cycle

FLYWHEEL ENERGY STORAGE PACKAGE

Inductor Motor. With respect to the flywheel drive machine the most difficult operating point of the J227a driving cycle occurs during vehicle braking and flywheel motoring. From an electrical point of view, the most severe machine load occurs at 145% of the base (or minimum operating) speed, where the commutation requirements are 230 amperes at 108 volts in the dc link. The electrical machine finally chosen from the trade-off study was a six-pole machine operating with a maximum speed of 20,000 r/min, with a rotor radius of 3.6 inches and a rotor length of 3.44 inches (active stator core length). A cross section of the machine is shown in Fig. 4.

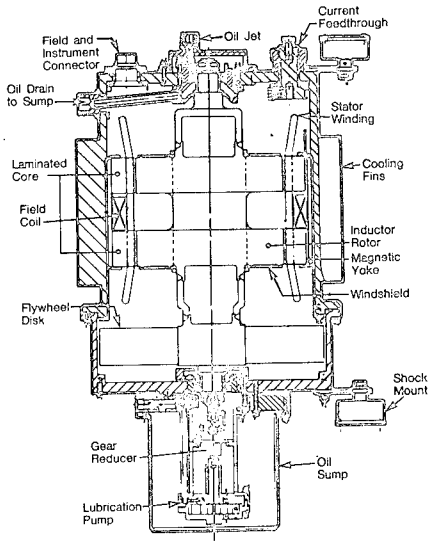

Fig. 4 Detailed Layout of Flywheel Energy Recovery Unit

Flywheel. The energy stored in the inductor motor rotor is approximately 15 watthours over the speed range of 10,000 r/min to 20,000 r/min. An additional 90 watt-hours are stored in the steel flywheel. The flywheel operates at a moderate stress level in order to produce a factor of safety of 2.0 relative to the 10^7 cycle curve for alternating stress. Although a higher stress design is possible, it was not considered advantageous in this case; doubling the design stress would only remove aproximately 10% of the total package weight from the flywheel. The flywheel weight reduction may be counterbalanced by the need for a heavier containment ring. The higher stressed wheel would also be larger in diameter and occupy more vehicle space. Additional details and photographs of the motor and flywheel assembly are contained in Reference 5.

Power Conditioner. The power conditioner is a load-commutated inverter similar to the system provided by the General Electric Company under the previous DOE Contract (No. EY-76-C-02-4010) and described in References 2 and 4. However, the new unit is lighter and smaller than the original load-commutated inverter (LCI), since it requires only six power thyristors instead of twelve. Reversal of the power flow is provided by a hybrid reverser (two diodes and two contactors) rather than a second set of six thyristors. The power circuit and the hybrid reverser are shown in Fig. 5. Additional details and photographs of the load-commutated inverter/rectifier; its control system, its forced commutation circuit for initial starting of the flywheel system, and its performance and waveforms are contained in References 7, 8, 9, and 10.

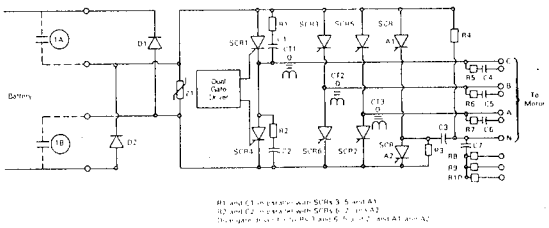

Fig. 5 Load-commutated Inverter/Rectifier Power and Commutating Circuit

Figure 6 shows the laboratory set-up with the inductor motor/flywheel package in the lower left of the photograph, the inverter/rectifier and its control located on the top of the right laboratory bench. The propulsion motor and road loss generator are located behind the bench. A photograph of that system is contained in Reference 5.

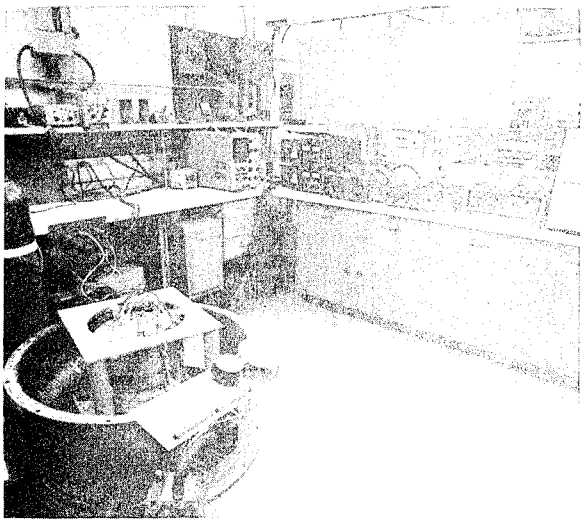

Fig. 6 Laboratory Set-up of Inductor Motor/ Flywheel Package and Power Conditioner

SYSTEM TEST CONFIGURATION

A block diagram of the entire laboratory system is shown in Fig. 7. The major components (the battery, the dc propulsion motor, the hybrid reverser, the load-commutated inverter/rectifier, the inductor machine, and the energy storage flywheel together with the electromagnetic contactors) are shown. The elements of the inverter/rectifier and the system control are indicated. The simulated vehicle is comprised of a flywheel to simulate the vehicle inertia and a dc generator and a load resistor to simulate the road load (rolling and aerodynamic) losses.

A computer-based data acquisition system measured the various electrical and mechanical parameters and provided real time and summary performance data.

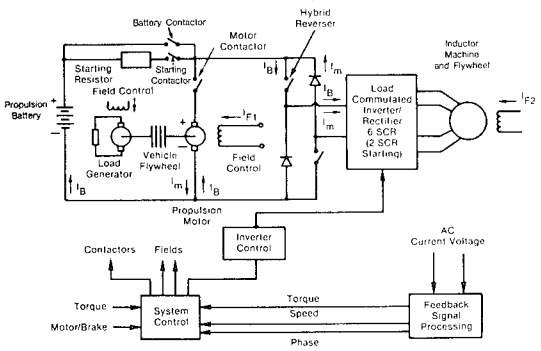

Fig. 7 Schematic Diagram of Simulated Propulsion System

SYSTEM TEST RESULTS SUMMARY

The system tests were conducted using SAE J227a driving schedules. Table 1 indicates the elapsed time in each mode together with the maximum vehicle speed in the cruise mode for the four schedules. Figure 8 presents a profile of vehicle velocity vs. time for each schedule. It is important to note that the vehicle velocity at the end of the coast interval is not specified. The flywheel/battery hybrid system divides the acceleration mode into two parts: the first using only the flywheel, and the second using both the battery and the flywheel to accelerate the vehicle.

Table 1

NOMINAL PARAMETERS OF SAE J227a ELECTRIC VEHICLE TEST PROCEDURE DRIVING SCHEDULES

Parameter	SAE J227a Schedule			
	A	B	C	D
Maximum speed, mph	10 ± 1	20 ± 1	30 ± 1	45 ± 1
Acceleration time	4 ± 1	19 ± 1	18 ± 2	28 ± 2
Cruise time	0	19 ± 1	20 ± 1	50 ± 2
Coast time	2 ± 1	4 ± 1	8 ± 1	10 ± 1
Brake time	3 ± 1	5 ± 1	9 ± 1	9 ± 1
Idle time	30 ± 2	25 ± 2	25 ± 2	25 ± 2
Total time, s	39 ± 2	72 ± 2	80 ± 2	122 ± 2

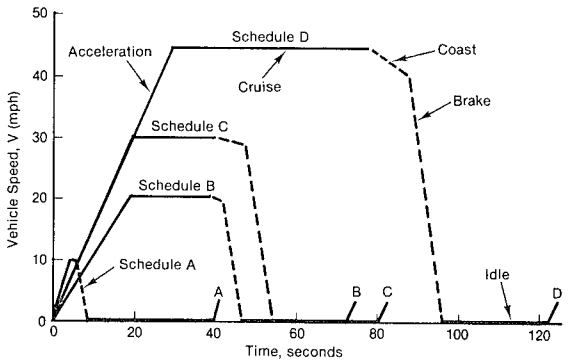

Fig. 8 Vehicle Speed vs. Time for SAE J227a Electric Vehicle Test Procedure Driving Schedules.

Schedule D Driving Cycle. The Schedule D driving cycle tests were composed of two major parts: 1) with the cruise time set at 50 seconds and starting with a fully chaged battery, the system was continuously cycled until the battery was completely discharged in order to determine the range of the vehicle; and 2) the system was operated over a small number of repetitive cycles at 108 volts with the cruise time set at values both longer and shorter than the specified value of 50 seconds in order to show the effects of varying the stops per mile.

Three complete battery discharge tests were completed using the Schedule D parameters. The test was started with a fully charged battery and continued until either the battery or the flywheel were unable to meet the vehicle speed-time profile given in the Schedule D driving cycle. A summary of the range and battery data obtained during these three runs is given in Table 2. Data were taken from three runs in order to average out any variables associated with the battery charge at the beginning of the run.

Table 2

SUMMARY DATA FROM OPERATION ON SCHEDULE D DRIVING CYCLE DURING A BATTERY DISCHARGE

Run	Total Number of Driving Cycles	Total Distance (miles)	Total Battery Energy (kWh)	Total Battery (Ah)	kWh/Mile	kWh/Cycle	Ah/Mile	Ah/Cycle	Stops/Mile
1	73	76.17	14.1	144	0.185	0.193	1.891	1.973	0.958
2	76	79.49	14.7	147	0.185	0.193	1.849	1.934	0.956
5	79	83.71	15.2	152	0.182	0.192	1.816	1.924	0.944

In an effort to show some of the system differences between a battery/flywheel hybrid vehicle and a conventional battery vehicle, the battery current vs. elapsed time for one driving cycle is shown in Fig. 9.

The measured battery current shown in Fig. 9 indicates a significant reduction in peak battery current for an equivalent all-electric battery vehicle. This reduction in peak battery current, in turn, is postulated to provide an increased battery energy capability.

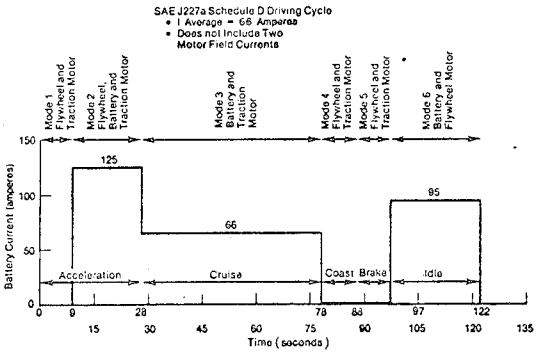

Fig. 9 Battery Current vs. Elapsed Time for SAE J227a Schedule D Driving Cycle: I Average = 66 Amperes and Does Not Include Two Motor Field Currents

The second series of tests, based on the Schedule D driving cycle, operated over a limited number of repetitive cycles, from a fixed value of d-c voltage, at an adjustable value of cruise time (both less than and greater than the 50-second cruise time specified in the Schedule D driving cycle). The system summary data were recorded; a representative sampling of the data is presented in Table 3.

Table 3

SUMMARY DATA FROM SCHEDULE D DRIVING CYCLE WITH VARYING CRUISE TIMES

Run	Energy Efficiency FM	Energy Efficiency TM	Energy Efficiency PCU	In/Out Efficiency FW	Effectiveness Factor FW	Battery kWh	Total Distance (miles)	kWh/Mile	Range Improvement Factor	Stops/Mile	Cruise Time (s)
14	0.738	0.877	0.956	0.509	1.09	0.9	4.02	0.224	1.19	1.49	20
15	0.743	0.869	0.956	0.512	1.10	0.8	3.30	0.242	1.22	1.82	10
16	0.745	0.897	0.956	0.516	1.15	0.7	2.72	0.257	1.26	2.21	2
17	0.732	0.837	0.961	0.501	1.06	1.3	6.24	0.208	1.13	0.962	50
18	0.713	0.823	0.957	0.468	1.02	1.8	10.01	0.180	1.08	0.599	100

Note: FW = flywheel
FM = flywheel motor
TM = traction motor
PCU = power conditioning unit

The battery kWh/mile vs. stops/mile is plotted in Fig. 10. The curve is a straight line with a positive slope indicating that not all of the available kinetic energy is recovered and made available for acceleration. A 100% efficient energy recovery system would have a

constant value of kWh/mile as a function of stops/mile. The zero stops/mile intercept is calculated based on the energy used during the cruise segment of the driving cycle. This would be the value of the battery energy for no stops per mile operation. The battery energy plotted in Fig. 10 does not include the field energy for the two electrical machines. It is estimated that the field requirements add approximately 3% to 4% to the average battery current.

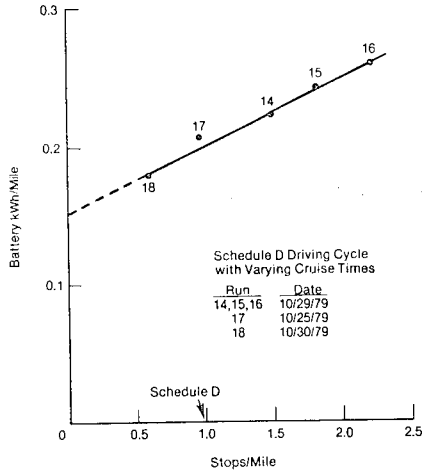

Fig. 10 Battery kWh/mi vs. Stops/Mile for Schedule D Driving Cycle with Varying Cruise Times.

In addition to the battery kWh/mile, three dimensionless ratios were calculated for each operation on the specified driving cycle. They are:

1. A Flywheel Effectiveness Factor. This is the ratio of traction motor energy in motoring to battery energy over one cycle. In an all-electric vehicle without regeneration, this ratio would be unity. Ratios greater than unity indicate that the flywheel energy storage package is supplying some net energy to the traction motor.

2. Range Improvement Factor. This is a calculated ratio based on the computer model of the lead-acid battery. The series resistor in the battery model is nonlinear and is a function of the peak battery current. In this system, the peak battery current is reduced from that in an all-electric vehicle; this should result in a greater energy storage capability of the battery, which could be indicated by a range improvement factor greater than unity.

3. Flywheel In/Out Efficiency. This ratio is a measure of the electrical energy into the flywheel energy storage package (power conditioner, inductor motor, and flywheel) divided by the output power from the same equipment operating with reverse power flow. The ratio includes the field energy losses of the inductor motor. The flywheel effectiveness and range improvement factors as a function of stops/mile on the Schedule D cycle are shown in Fig. 11.

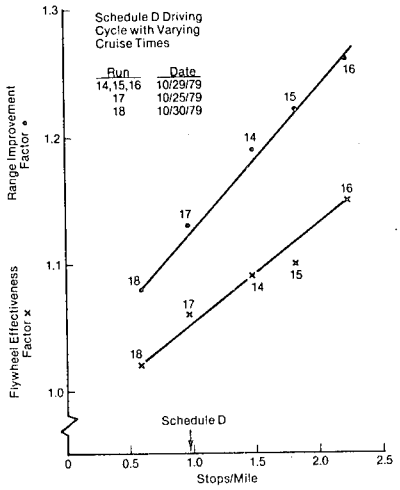

Fig. 11 Flywheel Effectiveness Factor and Range Improvement Factor vs. Stops/Mile.

These two curves are linear and show an increasing value for additional stops/mile where the flywheel energy storage system is used more frequently. These results provide quantitative data as to the greater advantage of the flywheel energy storage systems for multi-short-stop mission profiles.

The flywheel in/out efficiency is plotted vs. stops/mile in Fig. 12. For repetitive stops/mile greater than the value for Schedule D (approximately 1 stop/mile), the flywheel energy storage package maintains its energy efficiency at approximately 50% to 52%. At fewer stops/mile, the flywheel losses, and the fact that it is seldom used, result in a reduced in/out efficiency value.

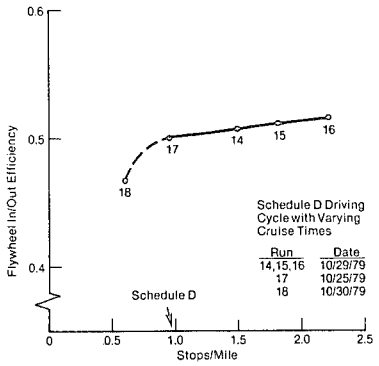

Fig. 12 Flywheel In/Out Efficiency vs. Stops/Mile.

SCHEDULE C AND SCHEDULE B DRIVING CYCLES

The test data obtained during operation of the sytem on the Schedule C and Schedule B driving cycles were similar to those described in the previous section. The tests were: 1) complete discharge of a fully charged battery to determine the total range and the total battery energy, and 2) operation over a limited number of cycles with both longer and shorter curise times in order to determine the effects of the number of stops/mile.

The summary data for the Schedule C and Schedule B battery discharge runs are given in Table 4. The battery was discharged only once on each of the driving cycles. As before, the important parameters are the number of times the driving cycle was repeated, the range attained, and the battery energy used. Here again, the data were taken until the battery or the flywheel could not meet the vehicle speed vs. time profile of the driving cycle.

Table 4

SUMMARY DATA FROM OPERATION ON SCHEDULES C AND B DRIVING CYCLES DURING A BATTERY DISCHARGE

Run	Driving Cycle Schedule	Total Number of Driving Cycles	Total Distance (miles)	Total Battery Energy (kWh)	Total Battery (Ah)	kWh/Mile	kWh/Cycle	Ah/Mile	Ah/Cycle	Stops/Mile
3	C	189	70.05	15.7	157	0.224	0.083	2.241	0.831	2.698
4	B	288	70.90	17.1	172	0.241	0.059	2.426	0.597	4.062

In a similar manner as the Schedule D driving cycle tests, the system was operated for a number of driving cycles (approximately six) to achieve steady-state operation at a fixed value of supply voltage (108), with both longer and shorter cruise times than specified by the duty cycle. Table 5 summarizes the data obtained on the Schedule C driving cycle with cruise times of 2, 5, 10, 20 (Schedule C), and 40 seconds.

Table 5

SUMMARY DATA FROM SCHEDULE C DRIVING CYCLE WITH VARYING CRUISE TIMES

Run	Energy Effictency FM	Energy Effeciency TM	Energy Efficiency PCU	In/Out Effeciency FW	Effectiveness Factor FW	Battery kWh	Total Distance (miles)	kWh/Mile	Range Improvement Factor	Stops/Mile	Cruise Time (s)
19	0.739	0.841	0.959	0.506	0.81	0.5	1.73	0.289	0.86	3.468	10
21	0.723	0.873	0.954	0.482	0.88	0.4	1.35	0.296	0.87	4.444	2
22	0.706	0.860	0.955	0.459	0.86	0.5	2.71	0.185	0.84	2.214	40
23	0.720	0.876	0.954	0.482	0.90	0.4	1.51	0.265	0.88	3.974	5
24	0.751	0.805	0.965	0.524	0.81	0.5	2.28	0.219	0.85	2.632	20

Note: FW = flywheel
FM = flywheel motor
TM = traction motor
PCU = power conditioning unit

The battery kWh/mile is plotted against stops/mile in Fig. 13. The curve has a constant positive slope, indicating that a fixed percentage of the vehicle kinetic energy is being returned to the flywheel for use during acceleration of the vehicle. Since the maximum speed of the vehicle is 30 mph in Schedule C, only approximately 44% of the Schedule D kinetic energy was available. The

flywheel effectiveness and range improvement factors are plotted vs. stops/mile in Fig. 14. The flywheel in/out efficiency is plotted in Fig. 15. Because of the smaller amount of available kinetic energy in the vehicle and the system parasitic losses, the flywheel subsystem does not provide the equivalent performance as it did on the Schedule D driving cycle. The summary data for operation on the Schedule B driving cycle with both longer and shorter cruise times are given in Table 6. The data from run 29 corresponds to the cruise time specified for the Schedule B driving cycle.

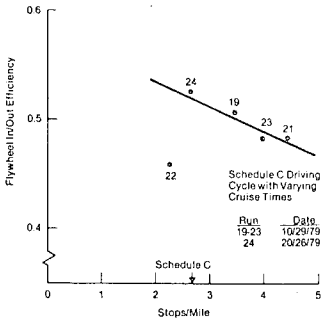

Fig. 15 Flywheel In/Out Efficiency vs. Stops/Mile

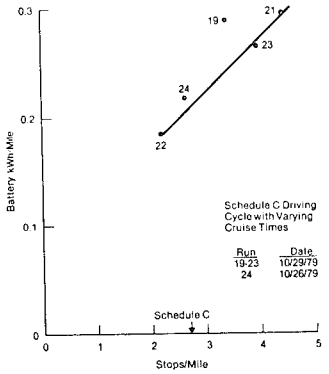

Fig. 13 Battery kWh/mi vs. Stops/Mile

Table 6

SUMMARY DATA FROM SCHEDULE B DRIVING CYCLE WITH VARYING CRUISE TIMES

Run	Energy Efficiency FM	Energy Efficiency TM	Energy Efficiency PCU	In/Out Efficiency FW	Effectiveness Factor FW	Battery kWh	Total Distance (miles)	kWh/Mile	Range Improvement Factor	Stops/Mile	Cruise Time (s)
26	0.672	0.779	0.951	0.409	0.61	0.3	1.14	0.263	0.53	5.263	10
27	0.677	0.809	0.951	0.420	0.63	0.3	1.01	0.297	0.54	5.941	2
28	0.657	0.700	0.952	0.385	0.71	0.4	2.06	0.194	0.57	2.913	38
29	0.702	0.720	0.960	0.449	0.72	0.3	1.48	0.203	0.60	4.054	19

Note: FW = flywheel
FM = flywheel motor
TM = traction motor
PCU = power conditioning unit

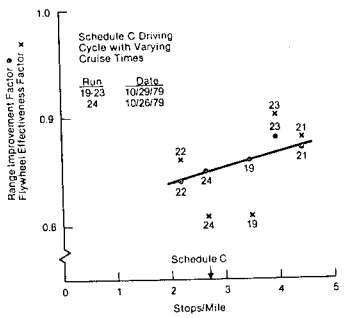

Fig. 14 Flywheel Effectiveness and Range Improvement Factors vs. Stops/Mile.

The battery kWh/mile vs. stops/mile are plotted in Fig. 16. As previously discussed, the straight line positive slope relationship indicates that a fixed percentage of the braking energy is being made available for acceleration. The range improvement and flywheel effectiveness factors are plotted in Fig. 17. The cruise speed during the Schedule B cycle is 20 mph; this results in an 80% reduction in the vehicle kinetic energy over the Schedule D cruise speed. Since there is such a small amount of energy available and the parasitic losses are fixed, the range improvement and flywheel effectiveness factors decrease as the stops/mile increase. The flywheel in/out efficiency, shown in Fig. 18, maintains a relatively fixed value of in/out efficiency.

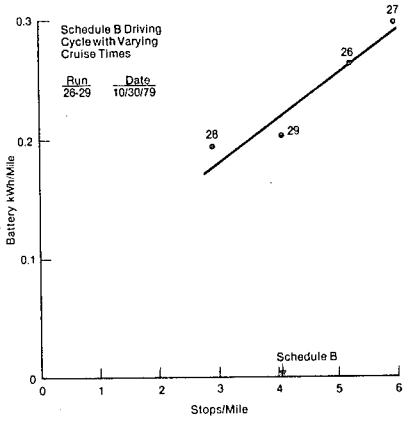

Fig. 16 Battery kWh/mi vs. Stops/Mile (Schedule B).

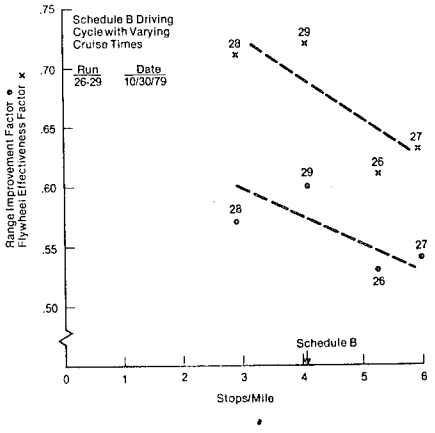

Fig. 17 Range Improvement and Flywheel Effectiveness Factors vs. Stops/Mile.

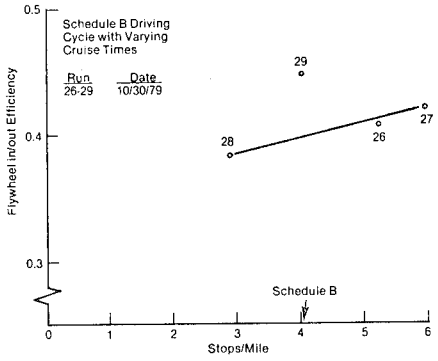

Fig. 18 Flywheel In/Out Efficiency vs. Stops/Mile.

During the Schedules B and C driving cycles, the vehicle cruise speed results in a greatly reduced amount of energy available for conversion from the vehicle inertia to the flywheel energy storage package for subsequent reuse during the next vehicle acceleration. This reduced amount of available energy reduces the in/out efficiency and the flywheel effectiveness and range improvement factors.

SUMMARY, CONCLUSIONS AND RECOMMENDATIONS

The flywheel system configuration was selected on the following bases to demonstrate flywheel energy storage system benefits in the laboratory:

1. Flywheel system benefits were maximized for the SAE J227a Schedule D driving cycle.
2. Component size was minimized.
3. High probability existed for component/system success.
4. New candidate components (continuously variable transmission, ac drives, permanent magnet disc machine) were not demonstrated.

The major conclusions resulting from the laboratory test of an improved flywheel energy recovery system sized for a battery/flywheel hybrid electric vehicle in the 3,500 pound class are:

1. The flywheel energy storage system performed as predicted in the mission for which it was designed and optimized.
2. The range of a 3,500 pound class electric vehicle with a flywheel energy storage package, operating on the SAE J227a Schedule D driving cycle, will be approximately 80 miles with presently available standard lead-acid electric vehicle batteries.
3. Performance of this flywheel energy storage system is highly dependent on the mission assigned to the electric vehicle.

4. The best performance was obtained for the SAE J227a Schedule D driving cycle (suburban cycle). The system as designed provides reduced improvement when operated on low maximum speed and low stops/mile missions.

5. Results indicate that continued effort on regenerative flywheel energy storage components and subsystems is warranted.

6. This system, implemented for laboratory evaluation of an electric vehicle flywheel energy storage system, does not represent a practical subsystem for vehicle implementation due to the following limitations:

   a. The vehicle cannot run indefinitely at constant speed below the cornering point speed.

   b. For low-speed operation, most, or all, of the vehicle acceleration energy must be supplied by the flywheel; whereas, during these conditions, extracting energy directly from the battery is desirable for efficiency reasons.

   c. During cruise conditions, flywheel energy cannot be used to supplement battery energy for passing or hill climbing.

   d. Regenerative energy cannot be converted to battery energy during prolonged negative grade operation.

   e. System components were not sized to provide performance of presently available electric vehicles; i.e., 0 mph to 30 mph in 9 seconds, 60 mph top speed, etc.

   Therefore, the system should be reconfigured with additional components to ensure that a vehicle implementation will result in highly competitive vehicular performance from operational, human factor, and safety viewpoints.

Based on the results of this laboratory test program, the following recommendations leading to improved performance are provided.

1. Extend the computer model of the flywheel energy storage package to include a more detailed calculation of the various subsystem energy losses (and therefore efficiency) as a function of operating conditions during the driving cycle rather than as a single, overall ("black box") efficiency value. This will aid in determining which subsystem is most appropriate for a particular vehicle mission. Various flywheel drive configurations should be included.

2. Evaluate advanced design synchronous motors with permanent magnet excitation in order to improve the system in/out efficiency.

3. Evaluate alternating current propulsion systems (induction motors and power conditioners) in order to improve the overall vehicle efficiency.

4. Evaluate continuously the variable transmission flywheel/propulsion systems in order to improve the overall vehicle efficiency.

ACKNOWLEDGEMENT

This work was sponsored by the U.S. Department of Energy under subcontract No. 8990503 from the Lawrence Livermore Laboratory of the University of California. Mr. Thomas Barlow of the Lawrence Livermore Laboratory was the Technical Monitor for the program.

REFERENCES

1. Guess, R.H. and Lustendader, E.L., Development of a High-Performance and Lightweight Hybrid Flywheel/Battery Powered Electric Vehicle Drive, paper presented at 4th International Electric Vehicle Symposium, Dusseldorf, Germany, August 1976.

2. Lustenader, E.L., Chang, G., Richter, E., Turnbull, F.G., and Hickey, J.S., Flywheel Module for Electric Vehicle Regenerative Braking, paper presented at 12th Intersociety Energy Conversion Engineering Conference, Washington, D.C., August 1977.

3. Lustenader, E.L., Flywheel Energy Storage System Development, paper presented at Flywheel Technology Symposium, San Francisco, CA, October 1977.

4. Lustenader, E.L., Hickey, J.S., Nial, W.R., Richter, R., Turnbull, F.G., and Chang, G., Laboratory Evaluation of a Composite Flywheel Energy Storage System, paper presented at 13th Intersociety Energy Conversion Engineering Conference, San Diego, CA, August 1978.

5. Lustenader, E.L., Edelfelt, I.H., Jones, D.W., Plunkett, A.B., Richter, E., and Turnbull, F.G., Regenerative Flywheel Energy Storage System, paper presented at 14th Intersociety Energy Conversion Engineering Conference, Boston, Massachusetts, August 1979.

6. Near-Term Electric Vehicle, Phase II, Final Report, Contract DE-AC03-76CS51294, submitted by General Electric Company, Schenectady, New York, to Department of Energy, Oakland, California, March 28, 1980, Report No. SRD-79-076.

7. Plunkett, A.B., and Turnbull, F.G., "Load-Commutated Inverter/Synchronous Motor Drive Without a Shaft Position Sensor," 1977 IEEE/IAS Annual Meeting Conference Record, Los Angeles, California, October 1977. IEEE Publication No. 77 CH1246-8-IA, pp. 748-757.

8. Plunkett, A.B., and Turnbull, F.G., "System Design Method of a Load-Commutated Inverter-Synchronous Motor Drive," 1978 IEEE/IAS Annual Meeting Conference Record, Toronto, Canada, October 1978, IEEE Publication No. 78 CH1346-6-IA, pp. 812-819.

9. Steigerwald, R.L., and Lipo, T.A., "Analysis of a Novel Forced Commutation Starting Scheme for a Load-Commutated Synchronous Motor Drive," 1977 IEEE/IAS Annual Meeting Conference Record, Los Angeles, California, October 1977, IEEE Publication No. 77 CH1246-8-IA, pp. 739-747.

10. Steigerwald, R.L., "Characteristics of a Current Fed Inverter with Commutation Applied Through Load Neutral Point," 1978 IEEE/IAS Annual Meeting Conference Record, Toronto, Canada, October 1978, IEEE Publication No. 78 CH1346-6-IA, pp. 502-516.

FEEDBACK CONTROL SYSTEMS FOR FLYWHEEL RADIAL INSTABILITIES

Mont Hubbard and Paul McDonald
Department of Mechanical Engineering
University of California
Davis, California 95616

ABSTRACT

Active control of flywheel radial instabilities is considered as an alternative to passive damping. Equations of an idealized pendulously supported flywheel are presented and cast into state variable form. Linear state feedback control laws are calculated which relate the required electromechanical control forces and torques at the support bearing to the instantaneous values of the states and which provide active damping for the undamped whirl modes. Linear-Quadratic synthesis and a pole placement method are compared. A numerical example is presented of an actively controlled ten-ton flywheel with a magnetic bearing.

INTRODUCTION

Flywheels have received increasing attention as energy storage devices in solar and wind power systems as well as in load leveling by electric utilities. In order to be economically feasible for these applications, however, higher energy densities (> 20 W-h/lb) and consequently higher shaft angular velocities will be required.

As flywheel speeds increase, so do the dynamics and vibration problems associated with their use. Many authors have investigated the stability of rotor-bearing systems, providing explanations of the destabilizing effects of various system parameters including fluid films in journal bearings[1], shaft hysteresis[2], and others. Den Hartog[3] described the mechanism by which hysteresis in the supporting shaft can excite whirl of the gyroscopic system.

In the anticipated use of flywheels in the utility load leveling application, the fundamental frequency of cycling will be one cycle/day. Thus, the system must be designed to spin up and down, passing through critical speeds each time, of the order of 10^4 cycles in a typical 30 year lifetime. Much attention must be paid, therefore, to the stability of the system at these critical speeds.

One such approach is to require a high degree of damping in the support bearing, either translational damping of radial motion of the shaft in the bearing or damping of rotation of the shaft at the bearing about the two radial axes.[4] Thomson et al.[4] derived the steady-state spin-whirl relationships and estimated the destabilizing work done by shaft hysteresis, but no specific bearing type is assumed. Also calculated are the damping constants necessary to stabilize the inherently unstable system.

Probably the most important specification in an energy storage flywheel is a low axial bearing loss and consequently long rundown times. For this reason, magnetic bearings are being considered for flywheel use.[5,6,7] Because there is no physical contact in such a bearing, losses are due to induced eddy currents and lifetimes are not limited by loading or shaft speed.[5] As has been known for more than a century,[8] however, any object suspended magnetically is unstable in one direction, thus immediately requiring active control along at least one axis to provide stability. In addition, these bearings have very low radial damping coefficients. It has not been shown that magnetic bearings can provide whirl stability in the sense of reference.[4] For these two reasons, an alternative to passive damping for guaranteeing whirl stability of the flywheel system is active control.

Two previous implementations of active suspensions in laboratory sized flywheel models[7,9] used classical compensation techniques for the control system design. In this paper, however, a state

variable approach will be taken, motivated by several recent papers[10,11,12] by Meirovitch on the state variable description of the dynamics and control of linear gyroscopic systems.

FLYWHEEL DYNAMICS AND CONTROL EQUATIONS

A schematic diagram of the general motion of the assumed flywheel-shaft system is shown in Fig. 1[13] and is similar to that treated by Thomson et al.[4] The flywheel is mounted on a nominally vertical shaft. Although future flywheels may contain more than one disk, only one disk is assumed here. The disk is axially symmetric and has polar and diametral mass moments of inertia which are related by $J_p/J_d = a$. The shaft is assumed to be supported by a single magnetic bearing which in general can have both rotational and translational compliances. Although these may be zero or negative (unstable) in the case of a magnetic bearing, both are here assumed to be zero. The (electromechanically induced) control forces and moments are assumed to act near the bearing. The shaft is assumed massless and in static equilibrium, thus serving to transmit the bearing and control moments and forces to the flywheel, which rotates at a constant angular velocity Ω about the shaft. The compliance relations for the shaft and bearing are derived in the Appendix. The equations of motion are written in a possibly non-inertial xyz reference frame which rotates about the undisturbed shaft centerline at a different constant angular velocity, ω, but whose origin has no acceleration. This general angular velocity ω allows the control system to be mechanized in a rotating coordinate system if desired. Unless otherwise specified, ω will be taken to be zero in what follows. The shaft center of mass is assumed to move in a plane perpendicular to the undeflected shaft centerline and to have a variable inertial angular velocity only in this plane. Thus, the flywheel has two translational (x,y) and two rotational (θ_x,θ_y) degrees of freedom. Although the dynamics of the actuator might become important in some systems, in this preliminary treatment actuator dynamics are neglected in order to focus on the structure of the controller.

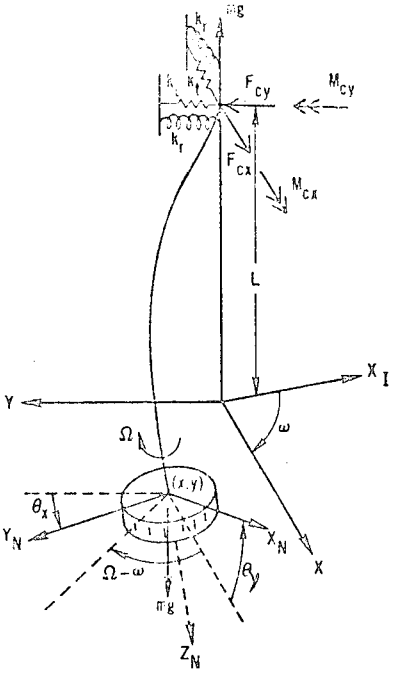

Fig. 1 Schematic diagram of flywheel and shaft with control forces and moments.

In reference[13] the equations of the flywheel system shown in Fig. 1 are derived using bond graph methods.[14] One advantage of such a method, although not immediately useful here since actuator dynamics are neglected, is that the changes in the state equations caused by the inclusion of actuator dynamics are easily derived. The shaft is shown to be an eight-port C-field which reduces to two four-ports due to symmetry (see Figure 2).

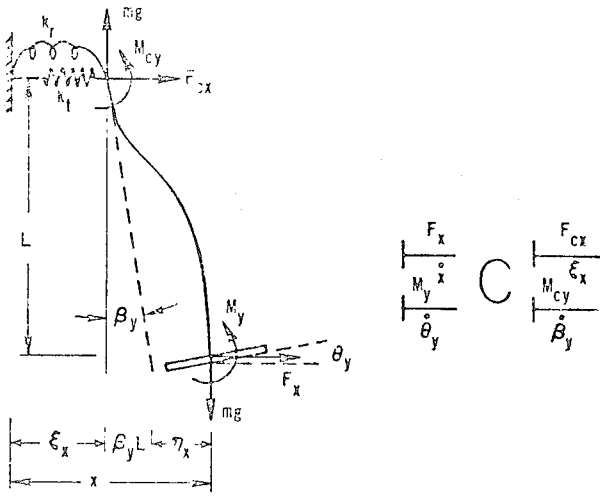

Fig. 2 Shaft schematic diagram and associated four-port compliance.

Using procedures discussed in[14] the eight equations of state can be derived directly from the total system bond graph, omitted here for brevity. These equations are of the form

$$\frac{dx}{dt} = Ax + Bu \ , \qquad (1)$$

where the state vector

$$x = (x, y, \theta_x, \theta_y, m\dot{x}, m\dot{y}, J_d\dot{\theta}_x, J_d\dot{\theta}_y)^T \ , \qquad (2)$$

the control vector

$$u = \left[F_{cx}, F_{cy}, M_{cx}, M_{cy}\right]^T \ , \qquad (3)$$

the system dynamics matrix

$$A = \left[\begin{array}{cccccccc}
0 & 0 & 0 & 0 & 1/m & 0 & 0 & 0 \\
0 & 0 & 0 & 0 & 0 & 1/m & 0 & 0 \\
0 & 0 & 0 & 0 & 0 & 0 & 1/J_d & 0 \\
0 & 0 & 0 & 0 & 0 & 0 & 0 & 1/J_d \\
\hline
m\omega^2 - k_{11} & 0 & 0 & -k_{12} & 0 & 2\omega & 0 & 0 \\
0 & m\omega^2 - k_{11} & k_{12} & 0 & -2\omega & 0 & 0 & 0 \\
0 & k_{12} & -(k_{22} + J_d\omega(a\Omega - \omega)) & 0 & 0 & 0 & 0 & 2\omega - a\Omega \\
-k_{12} & 0 & 0 & -(k_{22} + J_d\omega(a\Omega - \omega)) & 0 & 0 & -(2\omega - a\Omega) & 0
\end{array}\right] \qquad (4)$$

and the control distribution matrix

$$B = \left[\begin{array}{cccc}
0 & 0 & 0 & 0 \\
0 & 0 & 0 & 0 \\
0 & 0 & 0 & 0 \\
0 & 0 & 0 & 0 \\
-\delta_{11} & 0 & 0 & -\delta_{12} \\
0 & -\delta_{11} & \delta_{12} & 0 \\
0 & \delta_{21} & -\delta_{22} & 0 \\
-\delta_{21} & 0 & 0 & -\delta_{22}
\end{array}\right] = \left[B_1 \vdots B_2\right] \qquad (5)$$

where the constants δ_{ij}, k_{ij} are as defined in the Appendix and B_1 and B_2 are 8 x 2 matrices associated with the force and moment inputs which will be used below.

The natural modes of the uncontrolled system are purely oscillatory when the bearing stiffnesses are positive and occur at the four whirl frequencies, two direct and two retrograde.[3] Thus, one objective of active control must be to provide damping to these modes so that oscillations induced by disturbances to the system decay to zero asymptotically. This damping can require considerable power and large actuators, especially for large flywheels. Hence, another design requirement is that the power and actuator size be minimized for a given amount of active damping.

TWO CONTROLLER DESIGN METHODS

A control system design procedure which formally and explicitly addresses the trade-off discussed above is Linear-Quadratic (LQ) regulator theory.[15] In this approach it is assumed that the performance of the system is adequately described by a single scalar function, the performance index, generally taken to be an integral of quadratic forms in the state and control vectors

$$P = \lim_{t_f \to \infty} \int_0^{t_f} (x^T Q x + u^T R u)\, dt \qquad (6)$$

where Q and R are 8 x 8 positive semi-definite and 4 x 4 positive definite matrices, respectively. When Q and R are diagonal this criterion penalizes a weighted sum of the mean squares of the elements of the state and control vectors.

It is well known[15] that the optimal control u_* which yields a minimum value of the performance index (6) is given by a linear transformation of the state vector by a constant feedback gain matrix

$$u_* = -K x \qquad (7)$$

where the feedback gains are calculated from

$$K = R^{-1} B^T S \qquad (8)$$

and where the (8 x 8) matrix S is the only positive definite solution to the algebraic matrix Riccati equation

$$SA + A^TS + Q - SBR^{-1}B^TS = 0 . \quad (9)$$

The use of the LQ procedure for the design of the controller has several advantages. The structure of the compensator is known in advance and closed loop system stability is guaranteed, since the closed loop system poles are the left hand plane poles of the resulting Euler-Lagrange equations. Thus, the emphasis can be shifted toward the understanding of the physical aspects of the problem.[15] Another of the advantages is that random disturbances are easily incorporated into the system model, as will be shown below.

Finally, in multi-input multi-output systems, the feedback gains are not uniquely determined from the equations which result from pole placement methods. Thus, in general, there will be a set G of infinitely many control laws K which result in the same closed loop eigenvalues. In LQ design the remaining freedom in the choice of gains is taken to minimize P. Thus, the control variables are optimally coordinated and the gain matrix K which results from quadratic synthesis is the single choice from G, which results in minimum P. Of course, this K is also the global minimum, that is the K from all possible control laws which minimizes P.

Many computational techniques are available for the solution of the algebraic Riccati equation (9). One of the most successful is the eigenvector decomposition method proposed by MacFarlane[16] and Potter.[17] A computer program, OPTSYS,[18] which implements this method was used in the calculations below.

One of the objectives of the present study was to determine whether a suitable controller was possible using only a subset of the four originally hypothesized control variables $u = [F_{cx}, F_{cy}, M_{cx}, M_{cy}]$. In order that the Linear-Quadratic design posed above have a solution, it is required that the system be completely controllable using the control variables available. This controllability condition can be shown to be equivalent[19] to requiring that the controllability matrix be defined as

$$\mathcal{C} = [B : AB : \cdots : A^7B] \quad (10)$$

be of full rank.

Controllability calculations were made for the two cases when only forces and only moments, respectively, were included in the control set (i.e. $B = B_1$ and $B = B_2$). This study was made by using a similarity transformation to coordinatize the system and investigate controllability in "modal coordinates".[10] Mathematically speaking, any nonzero determinant of an nxn submatrix of (10) implies that there exists a control law $u = -Kx$ such that the characteristic polynomial of A-BK is arbitrary. In actual practice, however, when there is a wide range of variation of the coefficients of the control distribution matrix B expressed in modal coordinates, several orders of magnitude more control effort may be required to damp some modes than others. In this case the plant is said to be "relatively" uncontrollable. When there are also uncertainties in plant parameters (and hence uncertainties in the natural modes as well) an extremely sensitive control system design results. The controllability calculations confirmed that the system is not controllable using only forces (B_1) and also not controllable using only moments (B_2), whenever the bearing stiffnesses are zero. Hence, it was decided to proceed with the design using moments and forces.

Another method for the calculation of the feedback gain matrix K is pole placement using state feedback.[20] Here, the designer arbitrarily specifies the set of desired closed-loop eigenvalues $\Sigma = \{s_1, s_2, \ldots s_8\}$ subject only to the restrictions that if complex s_i occur, they do so in complex conjugate pairs, and that the s_i are distinct. Then assuming the system is controllable (see discussion above) the feedback gains K may be found which allow the closed loop characteristic equation

$$\Delta_{cl}(s) = \det(sI_n - A + BK) = 0 \quad (11)$$

to be satisfied for all $s = s_i \in \Sigma$, where det means "the determinant of." First equation (11) is rewritten in terms of the open loop characteristic polynomial by factoring and the use of determinant identities[20]

$$\Delta_{cl}(s) = \det[(sI_n - A)(I_n + (sI_n - A)^{-1}BK)] \quad (12a)$$

$$= \det(sI_n - A) \det(I_n + (sI_n - A)^{-1}BK) \quad (12b)$$

$$= \Delta_{ol}(s) \det(I_r + K(sI_n - A)^{-1}B) \quad (12c)$$

where r is the number of control variables (r=4 in general but r=2 if only moments or forces are used). Now K must be chosen so that the second determinant in (12c) vanishes for every s_i, i = 1, ..., 8, which will be true if some column (say the j_ith) of the matrix $I_r + K(s_i I_n - A)^{-1} B$ is zero for every i. Let the j_ith column of I_r be denoted as e_{ji} and the j_ith column of $(s_i I_n - A)^{-1} B$ be denoted as ψ_{ji}. Then we have

$$K\psi_{ji} = -e_{ji} \qquad i = 1, \ldots, 8 \qquad (13)$$

and if the j_i are chosen so that all j_i are linearly independent (this is always possible if the closed loop eigenvalues are distinct) then

$$K = -[e_{j1} \cdots e_{j8}] [\psi_{j1} \cdots \psi_{j8}]^{-1} \qquad (14)$$

In practice it is found that $j_i = j_k$ is required whenever s_i and s_k are complex conjugates so that the gain matrix K from (14) is real and the control law can be mechanized.

Any of several schemes may be used to evaluate the resolvent matrix $(s_i I - A)^{-1}$ as a function of the ith desired eigenvalue s_i. In the interactive computer program written to implement equations (13) and (14) an iterative method known as Leverrier's algorithm was utilized.[21]

NUMERICAL RESULTS

As a numerical example a specific flywheel configuration was chosen. Table I contains the parameters of a large flywheel typical of those presently being considered for the utility load leveling application. All parameters except the magnetic bearing stiffnesses k_r and k_t were taken from reference.[22] This flywheel has a tapered composite rotor with energy density of 23 Wh/lb and was mounted on a 15 cm diameter steel shaft. These parameters result in a fixed bearing translational natural frequency of 34.5 hz (217 rad/s) and the four natural open loop frequencies ω_i = 0, 0, 714.3, 0.00763 rad/s.

The state equations can be modified to include the effect of external disturbances. For example, forces and torques on the flywheel at its center of mass can be modeled by adding a term to equation (1)

$$\frac{dx}{dt} = Ax + Bu + \Gamma w \qquad (15)$$

where $\Gamma = [0 \vdots I_4]^T$.

Table I. Example flywheel parameters

Flywheel mass	m	9068 kg
Polar mass moment of inertia	J_p	2.355×10^4 kg m^2
Diametral mass moment of inertia	J_d	1.243×10^4 kg m^2
Rotational speed	Ω	377 rad/s
Shaft length	L	0.762 m
Elastic modulus (steel)	E	2.095×10^{11} N/m^2
Shaft polar area moment	I	4.237×10^{-4} m^4
Bearing translation stiffness	k_t	0 N/m
Bearing rotation stiffness	k_r	0 N-m/rad

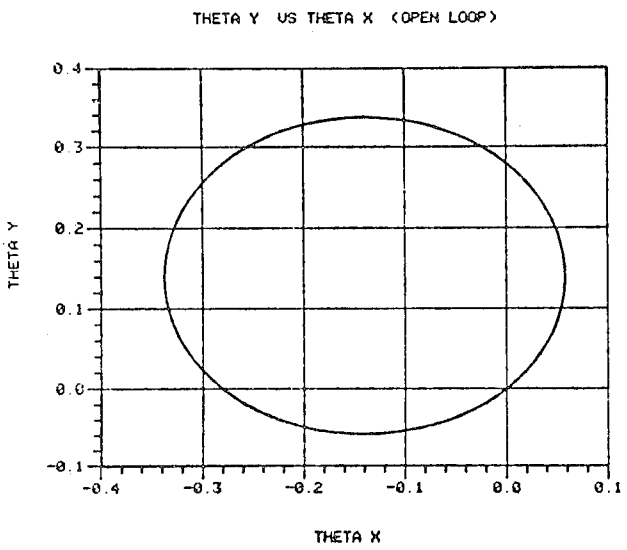

Fig. 3 Uncontrolled system response to impulsive moment at t = 0.

Figure 3 shows the results of a simulation of the uncontrolled flywheel when subjected to an impulsive disturbance force or moment at time t = 0. Here the

disturbance vector $w(t) = [0\ 0\ 1\ 1]^T\ \delta(t)$, where $\delta(t)$ is the Dirac delta function. This disturbance is equivalent to an initial condition $x(0) = (1/m)[0\ 0\ 0\ 0\ 0\ 0\ 1\ 1]^T$. In Fig. 3 the third and fourth components of the state vector are crossplotted with time implicit. As can be seen from the figure, the system is undamped with only the high frequency (714.3 rad/s) apparent.

Feedback gains were calculated using the Linear-Quadratic design method discussed above. The same state weighting matrix $Q = \text{diag}\{10^{-4} I_4 : I_4\}$ was used over a wide range of controller weighting matrices $R = \alpha I_4$, for $10^{-6} < \alpha < 10^{-12}$. Shown in Fig. 4 are the magnitudes of the real parts of the optimal closed loop system eigenvalues versus the allowable control, $u_{all} = 1/\alpha^2$. The two repeated complex pairs of roots, which migrate toward ∞ at a constant damping ratio, $\zeta = .707$, always have the largest real parts and hence are the fastest to decay to zero. The high frequency root is the next fastest damped while the extremely low frequency root is the dominant root at all values of the allowable control.

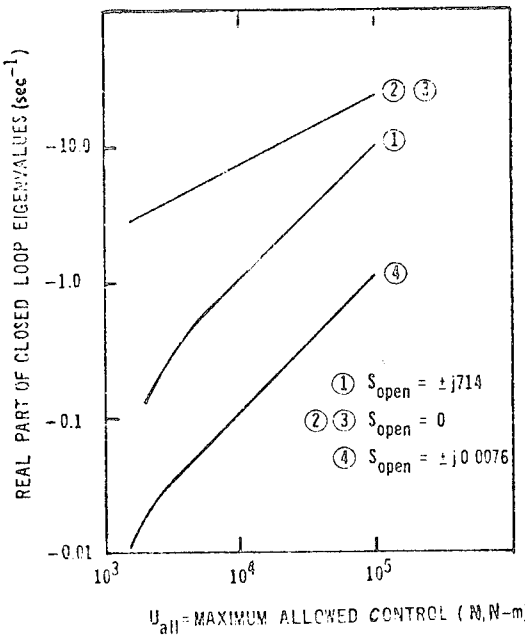

Fig. 4 Real parts of closed loop eigenvalues vs. allowable control.

Shown in Fig. 5 is a time simulation of the closed loop system with feedback gains calculated from the LQ method when u_{all} = 70,000 N, Nm. The resulting closed loop eigenvalues were -7.15±j714, -20.0±j19.3 (repeated), and -0.79±j0.0068 rad/s. The simulation is for a period of

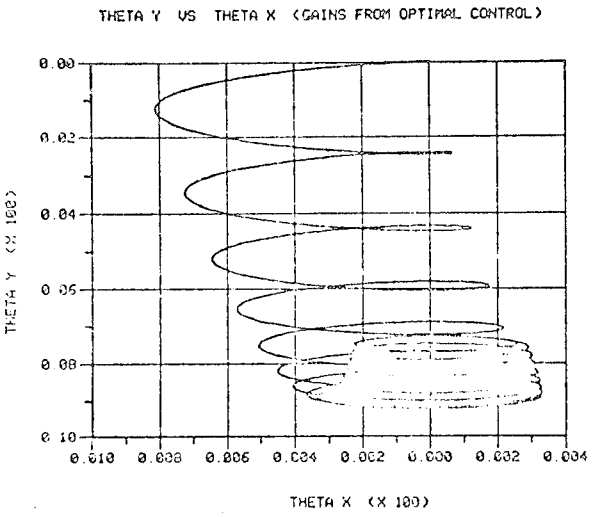

Fig. 5 Closed loop time response with Linear-Quadratic feedback gains.

0.15 seconds and shows the response to initial impulsive forces which resulted in $\dot{x}_0 = \dot{y}_0 = 1.0$ m/sec. As can be seen from the figure, both the high and intermediate frequencies are present in the results, but the small simulation time prohibits the identification of the lowest frequency which appears to be absent. Although the plotting routine used did not allow a longer time interval to be plotted, it is obvious that the system is well damped and that the oscillations are decaying exponentially to the origin.

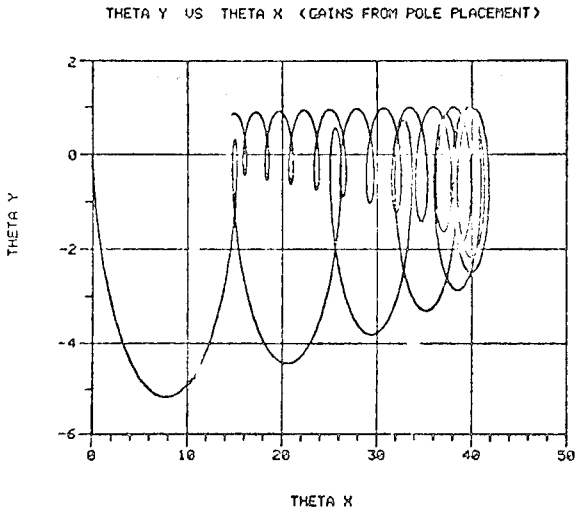

Fig. 6 Closed loop time response with pole placement feedback gains.

Since damping envelopes of the form $te^{-\sigma t}$ (rather than purely $e^{-\sigma t}$) result from repeated eigenvalues, a pole placement design was done which resulted in closed loop eigenvalues near those from the LQ design above, with the repeated roots split apart somewhat. These roots were $-10 \pm j7.14$, $-10 \pm j17.3$, $-17.3 \pm j10$, $-0.1 \pm j0.0076$, rad/s. Fig. 6 shows the results of a time simulation for these feedback gains and for the same time interval and initial conditions as in Fig. 5. Qualitatively the results are quite similar. Even though the intermediate pole placement roots are somewhat slower than the corresponding roots from the LQ design, note that these frequencies are approaching the origin faster than the LQ system did. We also note that, even with very similar closed loop poles, the eigenvectors corresponding to these poles can be quite different than the eigenvectors for the corresponding LQ poles and the pole-placement gains are generally higher. Thus, both the magnitude of the system response and the required control magnitudes can be markedly different in the two designs. The LQ design was felt to be superior for this reason.

CONCLUSIONS

The equations of motion of a pendulous flywheel were derived and written in state space form. The state variable approach allows the determination of system controllability using forces and or moments. In addition, state variable feedback controllers can be calculated as an alternative to more classical compensation techniques.

Two synthesis procedures for active control of pendulous flywheels were discussed and compared. Linear-quadratic control design was found to be superior to pole placement, because, for nearly similar closed loop eigenvalues, the control magnitudes required and the resulting transient state excursions were considerably smaller. One disadvantage of Linear-Quadratic methods, however, is that a desired set of closed loop eigenvalues can be attained only by iteration. Present investigations involve a design procedure which incorporates facets of both Linear-Quadratic and pole placement.[23] Using this technique it is possible to calculate the weighting matrices required to shift optimal closed loop eigenvalues to more desirable positions.

REFERENCES

1. B. L. Newkirk, "Varieties of shaft disturbances due to fluid films in journal bearings", Trans. ASME, Vol. 78, pp. 985-988, 1956.
2. A. T. Kimball, "Internal friction theory of shaft whirling", Gen. Elect. Rev., Vol. 27, p. 169, 1924.
3. J. P. Den Hartog, "Mechanical Vibrations", 4th Ed., pp. 261-264, McGraw-Hill, New York, 1956.
4. W. T. Thomson, F. C. Younger, and H. S. Gordon, "Whirl stability of the pendulously supported flywheel system", J. appl. Mech., Vol. 44, pp. 322-328, June 1977.
5. A. R. Millner, "Flywheels for energy storage", Technology Review, Nov. 1979, pp. 32-40.
6. A. R. Millner, "A flywheel energy storage and conversion system for solar photovoltaic applications", ASME paper 79-SOL-1, March 1979.
7. D. Eisenhaure, G. Oberbeck, and J. Downer, "Development of a low loss flywheel magnetic bearing", Proc. 14th Intersociety Energy Conversion Engineering Conference, Boston, Mass., August 1979.
8. S. Earnshaw, "On the nature of the molecular forces which regulate the constitution of the lumniferous ether", Trans. Cambridge Phil. Soc., 7, pp. 97-112, 1842 (cited in 7).
9. S. B. Hamilton, "Development of magnetically suspended momentum wheel", NASA-CR-144693, NTIS, Springfield, VA., 1973.
10. L. Meirovitch, "A new method of solution of the eigenvalue problem for gyroscopic systems", AIAA J., 12, pp. 1337-1342, 1974.
11. L. Meirovitch, "A modal analysis for the response of linear gyroscopic systems", J. appl. Mech., 42, pp. 446-450, 1975.
12. L. Meirovitch and H. Öz, "Observer modal control of dual-spin flexible spacecraft", J. Guidance and Control, 2, pp. 101-110, 1979.
13. M. Hubbard, "Whirl dynamics of pendulous flywheels using bond graphs", J. Franklin Inst., Vol. 308, pp. 405-421, 1979.
14. D. C. Karnopp and R. C. Rosenberg, "System Dynamics: A Unified Approach", John Wiley, New York, 1975.
15. M. Athans, "The role and use of the stochastic Linear-Quadratic-Gaussian problem in control systems design", IEEE Trans. Aut. Cont., AC-16, pp. 529-552, 1971.

16. A. G. J. MacFarlane, "An eigenvector solution to the optimal regulator problem", J. Elec. and Cont., 14, pp. 643-654, 1963.
17. J. E. Potter, "Matrix quadratic solutions", SIAM J. Appl. Math, 14, pp. 496-501, 1966.
18. A. E. Bryson and W. E. Hall, "Optimal control and filter synthesis by eigenvector decomposition", SUDAAR 436, Stanford University, 1971.
19. G. F. Franklin and J. D. Powell, "Digital control of dynamic systems", Addison-Wesley, Menlo Park, California, 1980.
20. W. L. Brogan, "Modern Control Theory", Quantum Publishers, New York, 1974.
21. T. Kailath, "Linear Systems", Prentice Hall, Englewood Cliffs, N.J., 1980.
22. "Economic and technical feasibility study for energy storage flywheels", ERDA Report 76-65, Rockwell International Space Division, Dec. 1975.
23. O. A. Solheim, "Design of optimal control systems with prescribed eigenvalues", Int. J. Control, 15, pp. 143-160, 1972.

NOMENCLATURE

A	system dynamics matrix
a	J_p/J_d
B	control distribution matrix
E	modulus of elasticity
e	unit vector, a column of I
F	force on shaft
G	set of admissible feedback matrices
I	area moment of inertia, identity matrix
J	mass moment of inertia
K	feedback gain matrix
k	bearing stiffness
k_{ij}	elements of stiffness matrix
L	shaft length
M	moment on shaft
m	flywheel mass
P	performance index
Q	state weighting matrix
R	control weighting matrix
S	Riccati matrix
s	Laplace variable
t	time
u	control vector
w	disturbance vector
x,y	position coordinates
x	state vector
Γ	disturbance distribution matrix
Δ	characteristic polynomial
δ	Dirac delta function
δ_{ij}	elements of B
θ_x,θ_y	flywheel orientation coordinates
Σ	set of desired closed loop eigenvalues
ψ	$(sI-A)^{-1}B$
Ω	constant flywheel spin rate
ω	angular velocity

Subscripts

b	bending
c	control
cl	closed loop
d	diametral
f	final
o	initial condition
ol	open loop
p	polar
r	rotational
t	translational
*	optimum

Superscripts

T	matrix transpose
-1	matrix inverse

APPENDIX

Derivation of Four-Port Compliance Relations for the Shaft and Bearing

Begin by decomposing the deflections of the shaft into three parts (see Fig. 2)

$$\begin{bmatrix} x \\ \theta_y \end{bmatrix} = \begin{bmatrix} \eta_x \\ \theta_y-\beta_y \end{bmatrix} + \begin{bmatrix} \xi_x \\ \beta_y \end{bmatrix} + \begin{bmatrix} \beta_y L \\ 0 \end{bmatrix} . \quad (A1)$$

The first term, merely the deflection of a built in cantilever beam with an axial stiffening force mg, can be shown (after solving the shaft differential equation) to be written as

$$\begin{bmatrix} \eta_x \\ \theta_y-\beta_y \end{bmatrix} = \begin{bmatrix} \frac{KL\cosh KL-\sinh KL}{mg\cosh KL} & \frac{\cosh KL-1}{mg\cosh KL} \\ \frac{\cosh KL-1}{mg\cosh KL} & \frac{K\sinh KL}{mg\cosh KL} \end{bmatrix} \begin{bmatrix} F_b \\ M_y \end{bmatrix} \quad (A2)$$

$$= \begin{bmatrix} \alpha_{11} & \alpha_{12} \\ \alpha_{12} & \alpha_{22} \end{bmatrix} \begin{bmatrix} F_b \\ M_y \end{bmatrix}$$

where $K = \sqrt{\frac{mg}{EI}}$ and $F_b = F_x - mg\,\beta_y$. (A3)

Note that equation (A3) includes the effect that the vertical gravity force has on the bending of the beam.

In the limit when $mg \to 0$ equation (A2) reduces to the well known constitutive relations[13] for the simple cantilever

$$\begin{bmatrix} \eta_x \\ \theta_y - \beta_y \end{bmatrix} = \begin{bmatrix} \frac{L^3}{3EI} & \frac{L^2}{2EI} \\ \frac{L^2}{2EI} & \frac{L}{EI} \end{bmatrix} \begin{bmatrix} F_x \\ M_y \end{bmatrix} . \quad (A4)$$

Now moment and force balances on the shaft give

$$M_{cy} = -M_y - F_x L + mg\,(\beta_y L + \eta_x) \quad (A5)$$

and

$$F_{cx} = -F_x . \quad (A6)$$

Substituting for η_x from (A2) and for F_b from (A3) into (A5) gives

$$\begin{bmatrix} F_{cx} \\ M_{cy} \end{bmatrix} = \begin{bmatrix} -1 & 0 & 0 & 0 \\ \alpha_{11}mg - L & \alpha_{12}mg - 1 & 0 & mg(L - \alpha_{11}mg) \end{bmatrix} \begin{bmatrix} F_x \\ M_y \\ \xi_x \\ \beta_y \end{bmatrix} . \quad (A7)$$

Similar substitution of (A3) and (A2) into (A1) yields

$$\begin{bmatrix} x \\ \theta_y \end{bmatrix} = \begin{bmatrix} \alpha_{11} & \alpha_{12} & 1 & L - \alpha_{11}mg \\ \alpha_{12} & \alpha_{22} & 0 & 1 - \alpha_{12}mg \end{bmatrix} \begin{bmatrix} F_x \\ M_y \\ \xi_x \\ \beta_y \end{bmatrix} . \quad (A8)$$

Combining (A7) and (A8) and recognizing that the force and moment on the flywheel disk are actually $-F_x$ and $-M_y$ we have

$$\begin{bmatrix} x \\ \theta_y \\ F_{cx} \\ M_{cy} \end{bmatrix} = \begin{bmatrix} -\alpha_{11} & -\alpha_{12} & 1 & L - \alpha_{11}mg \\ -\alpha_{12} & -\alpha_{22} & 0 & 1 - \alpha_{12}mg \\ +1 & 0 & 0 & 0 \\ L - \alpha_{11}mg & 1 - \alpha_{12}mg & 0 & mg(L - \alpha_{11}mg) \end{bmatrix} \begin{bmatrix} F_x \\ M_y \\ \xi_x \\ \beta_y \end{bmatrix} \quad (A9)$$

$$= C^{-1} \begin{bmatrix} F_x & M_y & \xi_x & \beta_y \end{bmatrix}^T \quad (A10)$$

where C is a symmetric stiffness matrix, and hence is energy conserving and obeys Maxwell's reciprocity relations.[14]

Inverting (A10) gives the desired compliance relation

$$\begin{bmatrix} F_x, M_y, \xi_x, \beta_y \end{bmatrix}^T = C \begin{bmatrix} x, \theta_y, F_{cx}, M_{cy} \end{bmatrix}^T . \quad (A11)$$

Because the shaft is symmetric, the same compliance relations are true in the orthogonal directions, namely

$$\begin{bmatrix} F_y, -M_x, \xi_y, -\beta_x \end{bmatrix}^T = C \begin{bmatrix} y, -\theta_x, F_{cy}, -M_{cx} \end{bmatrix}^T . \quad (A12)$$

For simplicity, the first two rows of C are denoted

$$\begin{bmatrix} C_1 \\ C_2 \end{bmatrix} = \begin{bmatrix} k_{11} & k_{12} & \delta_{11} & \delta_{12} \\ k_{12} & k_{22} & \delta_{21} & \delta_{22} \end{bmatrix}$$

since these coefficients appear in the system dynamics and control distribution matrices (4) and (5).

DYNAMIC ANALYSIS OF A MAGNETICALLY SUSPENDED ENERGY STORAGE WHEEL* ** +

DOE/ET/20279-102

Prof. L.L. Bucciarelli
School of Engineering, MIT
Dr. A. Rangarajan
M.I.T. Lincoln Laboratory
P. O. Box 73
Lexington, Massachusetts 02173

ABSTRACT

The results of an analysis conducted in support of the design of a 1-kwh flywheel fabricated and tested recently at the MIT Lincoln Laboratory are presented. The flywheel is a prototype of a 40-kwh residential unit that will be used to store energy obtained from photovoltaic arrays.

The 1-kwh system is designed to operate between 7500 and 15,000 rpm. The flywheel, made of seven 15-inch-diameter steel disks, weighs about 400 pounds, and is suspended vertically by a flexible quill shaft from a set of six magnetic bearings. The magnetic bearings minimize frictional losses and should require little maintainance over the design life of the system. The quill shaft, which permits self-alignment of the wheel's principal axis with the spin axis, was sized so that there are no critical frequencies in the operating range. An integral motor/generator unit is used to spin the wheel up when power is available and to generate power when required.

The analysis describes the methods used to obtain:

1. Whirl modes and frequencies as a function of spin-rate using the normalized eigenvectors of the system at rest (spin-rate = 0.0).

2. Dynamic response for given damping and flywheel imbalances.

3. Estimates of the amount of internal (hysteretic) damping that can cause self-excited instabilities.

Results of the analysis compare well with preliminary test results.

INTRODUCTION

MIT Lincoln Laboratory is in the process of developing a magnetically levitated flywheel for energy storage and power conditioning in residential applications. A 1-kwh capacity prototype (Fig. 1) with a 400-pound flywheel and operating between 7500-15,000 rpm has been designed and is currently being tested. The flywheel, made of steel disks, is supported by a set of six magnetic bearings via a flexible shaft (quill). (In the full-scale unit, the flywheel will be made of composite materials resulting in more efficient energy storage and less severe containment problems in the event of

*This work was sponsored by the U.S. Department of Energy.

**The U.S. Government assumes no responsibility for the information presented.

+Presented at the Flywheel Technology Symposium, Scottsdale, Arizona, 26-30 October 1980.

wheel failure.) A motor/generator unit is used to motor the wheel when power is available and as a generator when electricity is required. The vertical position of the flywheel is maintained by actively controlling the strength of the magnetic field responsible for providing lift. The lateral position of the shaft, on the other hand, is passively maintained; if off-axis displacement occurs, a restoring force is generated due to the presence of the magnetic field.

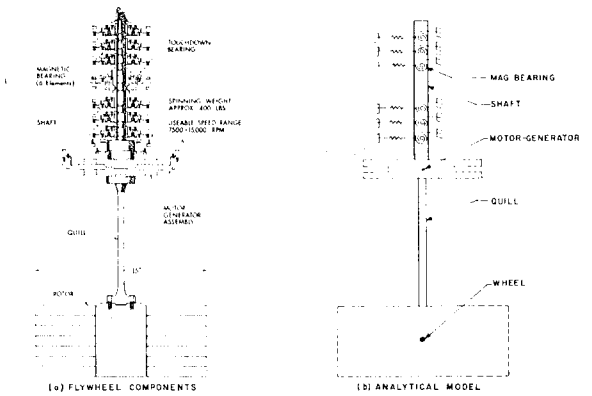

1 Kwh EXPERIMENTAL FLYWHEEL

Fig. 1

The flexible quill accommodates any imbalance or misalignment that may exist initially in the wheel or that might develop during the course of its life. In the operating speed range, the flywheel seeks to position its c.g. on the axis of rotation. If the flywheel were attached directly to the shaft supporting the bearings, without an intervening quill, this self-centering action could lead to excessive excursion of the shaft relative to the bearing stators.

The purpose of this analysis was to provide a rationale for sizing structural elements. This required consideration of a variety of problems: determination of natural frequencies of the system, including gyroscopic effects, to ensure that there are no critical frequencies in the operating range; determination of the response of the system to imbalances and misalignments of the wheel to ensure that the dynamic deformations at the magnetic bearings stay within bounds; determination of the amount of internal (or hysteretic) damping relative to the amount of external damping at the bearings, such that self-excited oscillations do not occur.

To carry through this analysis, a system of linear differential equations, which includes the gyroscopic effect of the wheel is presented. Using the first five modes of the non-spinning shaft as generalized coordinates, the whirl modes over the spin-speed range from 0 to 1000 Hz are determined. The local stability of these whirl states is then explored and, an estimate derived of hysteretic damping required to induce unbounded growth of a whirl mode with time. Finally, the forced response problem, where the forcing function is generated due to wheel eccentricities is considered.

EQUATIONS OF MOTION

The equations of motion of the rotating shaft with respect to a rectangular Cartesian coordinate frame fixed in space are:

$$\begin{bmatrix} M & 0 \\ 0 & M \end{bmatrix}\begin{Bmatrix} \ddot{q}_y \\ \ddot{q}_z \end{Bmatrix} + \Omega\begin{bmatrix} 0 & G \\ -G & 0 \end{bmatrix}\begin{Bmatrix} \dot{q}_y \\ \dot{q}_z \end{Bmatrix} + \begin{bmatrix} C & 0 \\ 0 & C \end{bmatrix}\begin{Bmatrix} \dot{q}_y \\ \dot{q}_z \end{Bmatrix} + \begin{bmatrix} K & 0 \\ 0 & K \end{bmatrix}\begin{Bmatrix} q_y \\ q_z \end{Bmatrix} + \mu\begin{bmatrix} 0 & K_H \\ -K_H & 0 \end{bmatrix}\begin{Bmatrix} q_y \\ q_z \end{Bmatrix} = \begin{Bmatrix} Q_y \\ Q_z \end{Bmatrix} \quad (1)$$

The shaft is assumed to be rotationally symmetric and inertias are lumped at the nodes. Elements of the skew symmetric gyroscopic matrix containing [G] are the rotary inertias of the disks taken about the spin axis of the shaft. In this analysis of the MIT Lincoln Laboratory flywheel, only the gyroscopic effects of the flywheel and of the motor/generator were considered significant. We include the effects of structural damping through the term $\mu\ [K_H]$ where $[K_H]$ is the stiffness matrix of those elements which introduce hysteretic damping. The matrix, [C], is the viscous damping matrix. Damping was assumed to be present only at the magnetic bearings. The nodal displacements (Fig. 2) are given by:

$$[q_y] = [v_1 \psi_{z_1}\ v_2 \psi_{z_2} \cdots v_n \psi_{z_n}]$$
$$[q_z] = [w_1 \psi_{y_1}\ w_2 \psi_{y_2} \cdots w_n \psi_{y_n}] \quad (2)$$

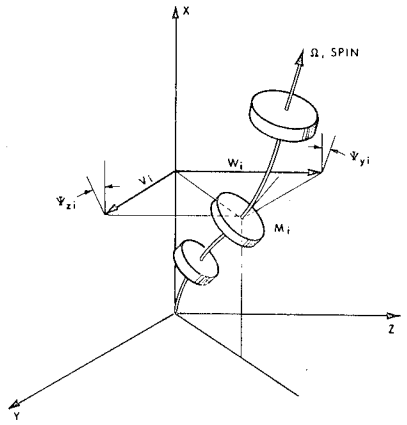

THE COORDINATE SYSTEM

Fig. 2

The applied forces at the first node arising out of any imbalance in the flywheel are given by:

$$Q_{y_1} = m\Omega^2 e \cos\Omega t$$
$$Q_{z_1} = m\Omega^2 e \sin\Omega t \qquad (3)$$

where m is the mass of the wheel and e is the static imbalance (c.g. offset with respect to the spin axis). Any dynamic imbalance (inclination of the principal axis with respect to the spin axis) can be taken into account in a similar manner.

NATURAL FREQUENCIES AND MODE SHAPES - NON-SPINNING SHAFT

In the analysis of possible whirl states and investigation of the stability of these states, we will use the mode shapes of the non-rotating shaft as generalized coordinates. These are solutions to the eigenvalue problem obtained from the equations of free vibration.

$$\begin{bmatrix} M & 0 \\ 0 & M \end{bmatrix} \begin{Bmatrix} \ddot{q}_y \\ \ddot{q}_z \end{Bmatrix} + \begin{bmatrix} K & 0 \\ 0 & K \end{bmatrix} \begin{Bmatrix} q_y \\ q_z \end{Bmatrix} = 0 \qquad (4)$$

Because we have assumed a rotationally symmetric shaft, the eigenvalue problem in 2n degrees of freedom reduces to one in n degrees of freedom. In modal form, Equation (4) becomes:

$$[K]\{\psi\} - \omega_c^2 [M]\{\psi\} = 0 \qquad (5)$$

The system can now be modeled as a planar structure as shown schematically in Fig. (1b). The magnetic bearings were modeled as linear elastic springs; the axial deformations were assumed to be decoupled from lateral deformations. These two assumptions are consistent with a linear analysis based on small deformation theory. It is of interest to note that the magnetic bearings possess negative stiffness in rotation and, accordingly, were modeled as such. The bearings, each having a positive stiffness in translation, were positioned along the shaft to ensure that the overall rigid body rotational stiffness was positive. The flywheel was modeled as a point mass with associated inertias.

We let ω_{c_j} be the j^{th} natural frequency $[\psi_j]^{c_j}$ the corresponding mode shape, and choose to normalize the latter with respect to the mass matrix:

$$[\psi_i][M]\{\psi_j\} = \begin{cases} 0 & i \neq j \\ 1.0 & i = j \end{cases} \qquad (6a)$$

hence

$$[\psi_i][K]\{\psi_j\} = \begin{cases} 0 & i \neq j \\ \omega_{c_i}^2 & i = j \end{cases} \qquad (6b)$$

The eigenvalues and the normalized eigenvectors were obtained using STRUDL[1], a structural design language, available in a time-sharing mode at MIT Lincoln Laboratory. The model had eleven nodes and twenty-two degrees of freedom. The lowest five eigenvalues and normalized eigenvectors obtained from this analysis were then read directly by another computer program that was developed to perform the dynamic analysis of the spinning system. The mode shapes obtained from the STRUDL analysis are shown in Fig. (3)

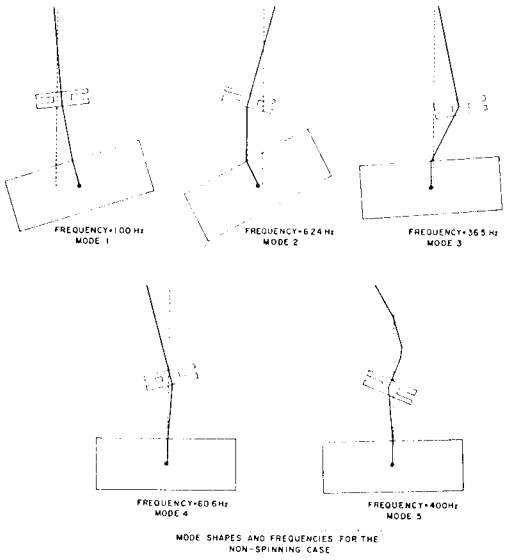

Fig. 3

It is now possible to rewrite the equation of motion in terms of the modal coordinates, if we set:

$$\{q_y\} = [\psi][\omega_c^{-1}]\{\eta\} \tag{7a}$$

$$\{q_z\} = [\psi][\omega_c^{-1}]\{\zeta\} \tag{7b}$$

Eq. (1) may be written as:

$$\begin{bmatrix}\omega_c^{-2} & 0\\ 0 & \omega_c^{-2}\end{bmatrix}\begin{Bmatrix}\ddot{\eta}\\ \ddot{\zeta}\end{Bmatrix} + \Omega\begin{bmatrix}0 & A\\ -A & 0\end{bmatrix}\begin{Bmatrix}\dot{\eta}\\ \dot{\zeta}\end{Bmatrix} + \begin{bmatrix}D & 0\\ 0 & D\end{bmatrix}\begin{Bmatrix}\dot{\eta}\\ \dot{\zeta}\end{Bmatrix} + \begin{bmatrix}\mathbb{1} & 0\\ 0 & \mathbb{1}\end{bmatrix}\begin{Bmatrix}\eta\\ \zeta\end{Bmatrix} + \mu\begin{bmatrix}0 & B\\ -B & 0\end{bmatrix}\begin{Bmatrix}\eta\\ \zeta\end{Bmatrix} = \begin{Bmatrix}F_\eta\\ F_\zeta\end{Bmatrix} \tag{8}$$

where

$$[A] = [\omega_c^{-1}][\psi]^T[G][\psi][\omega_c^{-1}] \tag{9a}$$

$$[D] = [\omega_c^{-1}][\psi]^T[\mathbb{C}][\psi][\omega_c^{-1}] \tag{9b}$$

$$[B] = [\omega_c^{-1}][\psi]^T[K_H][\psi][\omega_c^{-1}] \tag{9c}$$

are all real, symmetric, and positive semi-definite.

WHIRL-MODE STATES

It is well known that the gyroscopic motion of the spinning disks will alter the system's natural frequencies and mode shapes[2,3]. In the following analysis, we determine how these vary with spin speed, Ω. The eigenvalue problem for the whirl-mode shapes and frequencies is obtained from:

$$\begin{bmatrix}\omega_c^{-2} & 0\\ 0 & \omega_c^{-2}\end{bmatrix}\begin{Bmatrix}\ddot{\eta}\\ \ddot{\zeta}\end{Bmatrix} + \Omega\begin{bmatrix}0 & A\\ -A & 0\end{bmatrix}\begin{Bmatrix}\dot{\eta}\\ \dot{\zeta}\end{Bmatrix} + \begin{bmatrix}\mathbb{1} & 0\\ 0 & \mathbb{1}\end{bmatrix}\begin{Bmatrix}\eta\\ \zeta\end{Bmatrix} = 0 \tag{10}$$

by seeking solutions of the form:

$$\{\eta\} = \{r\}\cos\omega t \tag{11a}$$

$$\{\zeta\} = \{r\}\sin\omega t \tag{11b}$$

This implies that the shaft undergoes planar bending, the plane of bending itself whirling around at frequency ω. If ω is positive, we have forward whirl, if negative, retrograde whirl.

Again, the problem reduces to one in five degrees of freedom,

$$-\omega^2[\omega_c^{-2}]\{r\} + \omega\Omega[A]\{r\} + [\mathbb{1}]\{r\} = 0 \tag{12}$$

Introducing an auxiliary vector,

$$\{q\} = \omega[\omega_c^{-1}]\{\eta\} \tag{13}$$

enables us to write the eigenvalue problem in the standard form

$$\begin{bmatrix}-\Omega[A] & \omega_c^{-1}\\ \omega_c^{-1} & 0\end{bmatrix}\begin{Bmatrix}\eta\\ q\end{Bmatrix} - \lambda\begin{bmatrix}\mathbb{1} & 0\\ 0 & \mathbb{1}\end{bmatrix}\begin{Bmatrix}\eta\\ q\end{Bmatrix} = 0 \tag{14}$$

where $\lambda = 1/\omega$.

Since the matrix on the left is real and symmetric, we are assured that all eigenvalues, ω_j, will be real.

Fig. (4) shows the loci of the eigenvalues (the whirl frequencies, ω_j) as a function of spin rate, Ω. The solid curves are forward whirl states, the dotted retrograde (ω should be read as $-\omega$ when viewing the latter). The gyroscopic effect is most pronounced on the second mode. In this case, the

forward-whirl frequency always remains greater than the spin speed of rotation - because the ratio of the moment of inertia about the spin axis to that about a transverse axis passing through the c.g. of the flywheel is greater than 1.0. The points on these curves, where the spin speed Ω equals the whirl frequency ω, are designated "critical frequencies".

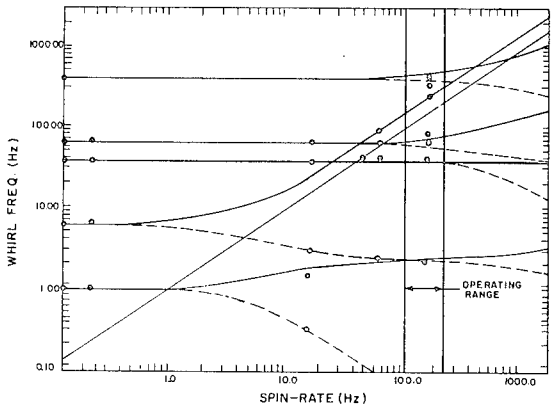

Fig. 4

After conducting a parametric study, it was found that a quill 8 inches long and 7/16 inch in diameter yielded critical frequencies lying outside the operating range and yet ensured that lateral displacement of the shaft in that same range would not be excessive. Preliminary experimental results, shown as dots in Fig. (4), indicate that the prediction of the whirl states and critical frequencies is reasonably good.

STABILITY OF WHIRL STATES

Structural damping, represented by the term in Eq. (1) containing the factor μ, can lead to self-excited oscillations, i.e., to instability. Internal damping provides a mechanism for transferring energy of spin about the shaft axis to kinetic and strain energy of whirling. In what follows, the possibility of instability in the vicinity of the whirl states at any given spin rate is investigated.

Premultiplying by Eq. (8) by $[\dot{\eta}\ \dot{\zeta}]$, integrating by parts, and noting that

$$[\dot{\eta}\ \dot{\zeta}]\begin{bmatrix} 0 & A \\ -A & 0 \end{bmatrix}\begin{Bmatrix} \dot{\eta} \\ \dot{\zeta} \end{Bmatrix} = 0 \qquad (15)$$

due to the symmetry of [A], we obtain:

$$\frac{d}{dt}\left\{\frac{1}{2}[\dot{\eta}\ \dot{\zeta}]\begin{bmatrix} \omega_\zeta^{-2} & 0 \\ 0 & \omega_\zeta^{-2} \end{bmatrix}\begin{Bmatrix} \dot{\eta} \\ \dot{\zeta} \end{Bmatrix} + \frac{1}{2}[\eta\ \zeta]\begin{bmatrix} k & 0 \\ 0 & k \end{bmatrix}\begin{Bmatrix} \eta \\ \zeta \end{Bmatrix}\right\}$$
$$= -[\dot{\eta}\ \dot{\zeta}]\begin{bmatrix} D & 0 \\ 0 & D \end{bmatrix}\begin{Bmatrix} \dot{\eta} \\ \dot{\zeta} \end{Bmatrix} + \mu\left[[\dot{\zeta}][B]\{\eta\} - [\dot{\eta}][B]\{\zeta\}\right] \qquad (16)$$

In the vicinity of the j^{th} whirl mode, $[\phi_j]$ at whirl frequency ω_j, we have

$$\{\eta\} = \{\phi_j\}\cos\omega_j t$$
$$\{\zeta\} = \{\phi_j\}\sin\omega_j t \qquad (17)$$

The above equation then reduces to

$$\frac{d}{dt}\{E_j\} = -\omega_j^2[\phi_j][D]\{\phi_j\} + \mu\omega_j[\phi_j][B]\{\phi_j\} \qquad (18)$$

where E_j is the total energy of the j^{th} whirl mode; kinetic plus strain energy. It is seen that the total energy will increase without limit if the external damping, [D], is not sufficiently large relative to the hysteretic damping, μ [B]. That is, for stability, the latter must be confined as follows:

$$\mu < \frac{\omega_j[\phi_j][D]\{\phi_j\}}{[\phi_j][B]\{\phi_j\}} \qquad (19)$$

Now the sign of the hysteresis factor μ is fixed by

$$\mu = \frac{(\Omega-\omega)}{|\Omega-\omega|} \qquad (20)$$

Assuming, without loss of generality, that Ω is positive and, for the moment, condidering forward-whirl-mode behavior, $\omega > 0$ Eq. (18) shows that for instability we must have $\mu > 0$

and hence

$$\Omega > \omega \qquad (21)$$

Thus we note that hysteresis induced self-excited oscillations are always at a frequency lower than the spin speed. A similar observation was made by Bolotin[4].

This analysis also leads to the conclusion that for this particular damping mechanism, retrograde whirl modes can never be unstable, for if ω_j is negative, then the right-hand side of Eq. (18) is always negative. Hence, in this case, $\frac{dE_j}{dt}$ is always less than zero.

Figure (5) shows the value of μ required for instability of the forward whirl modes as a function of spin rate Ω. In evaluating Eq. (19), the matrix $[K_h]$ was taken as the stiffness matrix of the whole structure, [K]. This implies that all structural elements contribute equally to structural damping. Viscous damping was assumed to be derived solely from the copper in the magnetic bearings incorporated for that very reason. The damping associated with each of the six bearings was taken as 4.34 in-lb-sec in rotation and zero in translation.

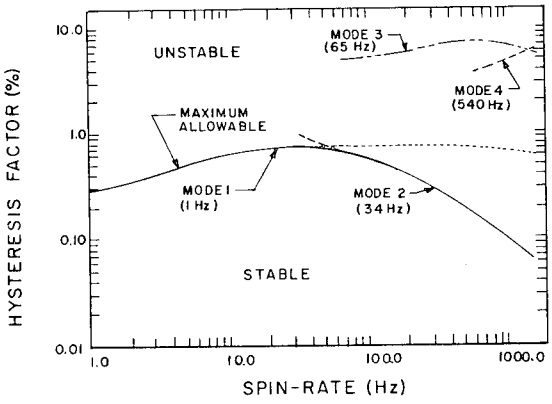

MAXIMUM ALLOWABLE HYSTERESIS
Fig. 5

FORCED RESPONSE

Any eccentricity in the location of the flywheel center of mass relative to the spin axis (or any inclination of the principal axis) will generate a forcing function with a frequency equal to the spin rate and an amplitude proportional to the square of the spin rate. To obtain estimates of the excursion of the shaft as the flywheel is brought up to speed, Eq. (1) was solved with a forcing function.

$$Q_{y_1} = me\Omega^2 \cos\omega t \qquad Q_{\psi_{z_1}} = (I_d - I_p)\epsilon_\theta \cos\omega t \tag{22a}$$

$$Q_{z_1} = me\Omega^2 \sin\omega t \qquad Q_{\psi_{y_1}} = (I_d - I_p)\epsilon_\theta \sin\omega t \tag{22b}$$

and damping matrix based, as before, on our best estimates of the damping characteristic of the magnetic bearings. The effect of hysteretic damping was neglected in this part of the analysis.

For this particular forcing function, the maximum response occurs in forward whirl at frequencies equal to the spin rate, Ω (at the intersection of the $\Omega = \omega$ line on Fig. (3) with the forward-whirl-mode contours). Figure (6) shows the response predicted for the displacement of a point just above the motor/generator as a function of Ω. The eccentricity was taken as 10^{-4} inches of c.g. off-set and 0.01^o inclination of the principal axis with the spin axis. Of particular concern was the resonance around 40 Hz. Consideration was given to adding more external damping but this option was not pursued. In the actual spin-up of the wheel, large displacements at 40 Hz were seen, but sufficient torque was available to drive through this critical frequency, safely avoiding excessive dynamic excursions.

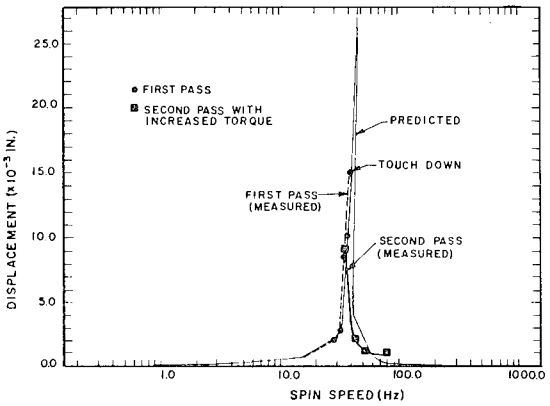

FORCE – RESPONSE

Fig. 6

SUMMARY AND CONCLUSIONS

This multi-faceted analysis provided a framework for design of the MIT Lincoln Laboratory flywheel. One major concern was to ensure that no critical frequencies were found in the operating range (125-250 Hz). This constraint was met by use of a

quill, 8 inches long and 7/16 inches in diameter. The forced response analysis showed also that the quill would permit self-centering of the flywheel and yet not lead to excessive displacement of the magnetic bearings.

Stability analysis of the whirl states suggested that hysteretic damping on the order of 0.1-1 percent might lead to unbounded growth of the lower whirl modes. Indeed, at a spin rate of Ω = 180 Hz a growth of the 2-Hz whirl mode, which is due to internal damping is seen. Increasing the amount of external damping is one way to eliminate this mode of instability and is a remedy being pursued.

REFERENCES

1. ICES STRUDL-II, The Structural Design Language, Engineering User's Manual, M.I.T., Cambridge, MA, 1968.

2. W.T. Thompson, F.C. Younger and H.S. Gordon, "Whirl Stability of Pendulously Supported Flywheel System," Transactions of ASME, June 1977.

3. T.L.C. Chen and C.W. Bert, "Whirling Response and Stability of Flexibly Mounted, Ring-Type Flywheel Systems," prepared for Sandia Labs under contract number 07-7843, SAND 78-7073, February 1979.

4. Bolotin, Non-Conservative Problems in the Theory of Elastic Stability, McMillan Company, N.Y., 1963, p. 139-198.

FORCED WHIRLING RESPONSE OF A PENDULOUSLY SUPPORTED FLYWHEEL WITH NONLINEAR OIL-TYPE DAMPING†

C.A. Kocay
Graduate Student

and

C.W. Bert
Perkinson Professor of Engineering
Mem. ASME

School of Aerospace, Mechanical and Nuclear Engineering
The University of Oklahoma
Norman, Oklahoma

ABSTRACT

In this investigation, the steady-state synchronous motion of a flywheel system excited by various combinations of rim unbalance and initial tilt is analyzed. The system consists of a rim-type, composite-material flywheel attached to its hub by relatively flexible composite-material bands, and driven by an air turbine through a vertical, slender quill shaft. External damping is provided by an oil-type bearing on the quill shaft. Attention is directed to a nonlinear representation of the damper modeled as a short bearing with a full film of oil. Gyroscopic effects are also included in the system model, which has eight degrees of freedom with respect to complex generalized displacements. Solution is obtained by means of a specially developed iterative algorithm, and response curves are presented and interpreted.

INTRODUCTION

Current flywheel research and development efforts are aimed at the creation of a relatively lightweight flywheel capable of high-density storage of mechanical energy. To meet these requirements, the flywheel must be able to operate at high rotational speeds and withstand the high stresses accompanying these speeds. For these reasons researchers are incorporating composite materials in their designs, since composites have both excellent tensile strength characteristics and high strength-to-density ratios. One such composite-material flywheel, designed and experimentally tested by Sandia Laboratories[1-2], is the motivation for this investigation.

This paper presents the results of an analytical investigation of the forced whirling behavior of a rim-type, composite-material flywheel where the attachment of the rim to its hub is by means of relatively flexible composite-material bands (Fig. 1). The flywheel system considered here models a typical pendulous testing configuration in which an air turbine drives a slender, flexible quill shaft on which the flywheel hub is mounted (Fig. 2). An oil bearing, located between the air turbine and the flywheel hub, acts as a damper by restricting the lateral motion of the flywheel shaft. The system model consists of four discrete rotor masses corresponding

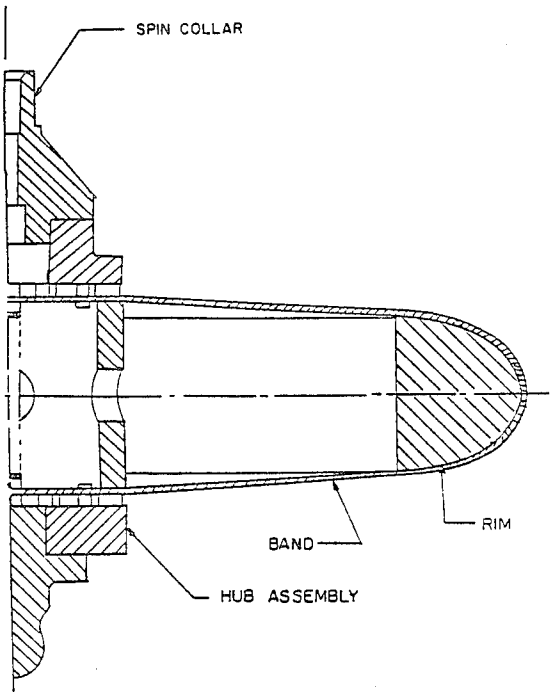

Fig. 1. Cross-sectional view of one-half of the Sandia "wagonwheel" flywheel with a 25.4 cm (10.0 in.) outside radius.

†The research reported here was supported by the Department of Energy through a contract from Sandia Laboratories, Albuquerque, New Mexico.

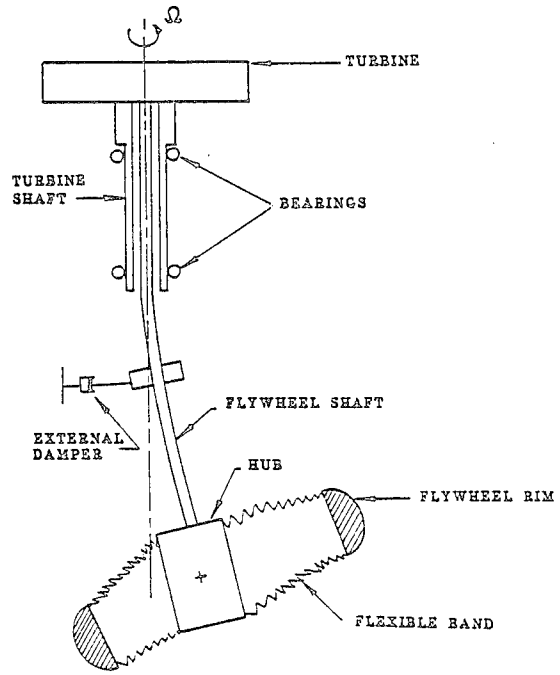

Fig. 2. Schematic diagram of the Sandia flywheel system as installed in the Sandia-Livermore spin-test facility.

to the rim, hub, oil-type-bearing damper, and air turbine. Each mass element is allowed two degrees of freedom (in-plane displacement and out-of-plane tilting) which results in an eight-degree-of-freedom dynamic system of equations in terms of complex generalized displacements. Gyroscopic action of the discrete mass elements is taken into account in the formulation of the equations of motion.

This work is an extension of the forced whirling analysis by Chen and Bert[3] of this same flywheel system. Here, greater complexity is introduced into the governing differential equations by the more realistic modeling of the oil-type damper as a nonlinear-behaving squeeze-film bearing. Other differences with respect to Ref. 3 are a revised stiffness matrix[††] and the consideration of various forcing combinations caused by rim in-plane eccentricity and out-of-plane initial tilt rather than considering these two types of unbalance only separately.

In a recent paper Salamone and Gunter[4] discussed the synchronous forced response of an overhung rotor with a rigid disk. In this work, combinations of both in-plane unbalance and disk skew (initial tilt) of the disk were also considered. However, their rotor system was much simpler. In the analysis presented here, the rotor system considered has multiple forward critical speeds, two of which are within the speed range of interest and a third one just beyond.

PRACTICAL APPLICATION

Since the flywheel system studied here is typical of present testing configurations, the results of this study have significant practical implications. It is shown that the motion of the flywheel hub is predicted to exceed allowable limits when rotating at the high end of the speed range of interest. These excessive displacements are obtained when a typical measured value of the initial tilt (as opposed to mass eccentricity) is included in the system equation. Since a certain amount of initial tilt will always be present no matter how precisely a flywheel is balanced, it is concluded that the present testing arrangement should be modified for high-speed flywheels. The authors suggest that the pendulous configuration (with its many advantages) be retained but that a stiffer flywheel shaft be used.

DAMPER CONSIDERATIONS

A cross section of the Barbour Stockwell damper installed as part of the Sandia-Livermore spin-test system is shown in Fig. 3. The damper consists essentially of two halves, each having a radius R = 3.8 cm

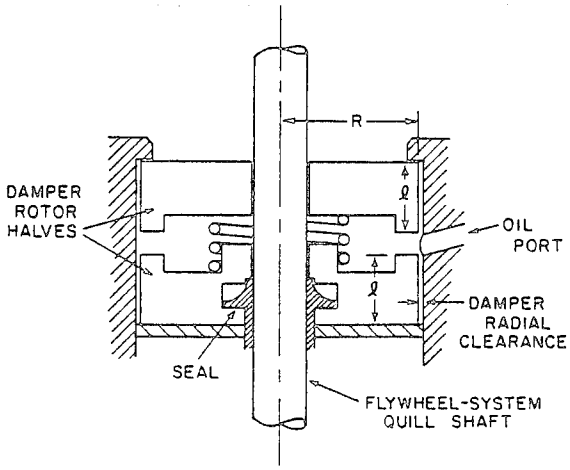

Fig. 3. Schematic diagram of the Barbour Stockwell damper installed as part of the flywheel spin-test system.

[††]The revision of the stiffness matrix is the reason that the critical speeds reported here are higher than those of Ref. 3.

(1.5 in.) and axial length ℓ = 1.9 cm (0.75 in.), separated by an axial distance of 0.64 cm (0.25 in.). The radial clearance between the flywheel shaft and the damper-rotor halves is 0.05 mm (0.002 in.), while the radial clearance between the rotor and the housing is c = 0.10 cm (0.04 in.)(greatly exaggerated in Fig. 3). The central-cavity portion of the damper contains a relatively stiff spring which tends to keep the two halves spread apart. An external oil port leads directly to the central cavity making this volume a small oil reservoir.

If one assumes negligible pressure losses at the top and bottom seals of the damper, the hydrodynamic pressure created by damper whirling will be relieved only near the central cavity. A symmetric axial pressure distribution will be achieved if the inlet pressure at the oil port is great enough to cause all of the damper's circumferential surface to have a film of oil, i.e., there is no cavitation. For this Barbour Stockwell damper, 280 KPa (40 psig) is the typical inlet gage pressure and should be more than sufficient. Thus, a "short-bearing" approximation, using a damper axial length L = 2ℓ = 3.8 cm (1.5 in.), appears to be most appropriate to compute the hydrodynamic forces.

Since the radial clearance between the flywheel shaft and the damper rotor is 0.05 mm (0.002 in.), the damper rotor of Fig. 3 can be considered as a journal bearing with respect to the flywheel shaft. In a squeeze-film damper, radial and orbital motion of the bearing element is permitted, but rotation is prevented by some type of mechanical constraint. However, no such constraint is apparent in the Barbour Stockwell damper. Nevertheless, assuming that the damper is at all times full of oil, the rotational velocity of the damper rotor should be considerably less than that of the flywheel shaft. Thus, the flywheel system damper of Fig. 3 is taken to act as a squeeze-film damper. The damping forces resulting from this approximation are expected to be reasonably accurate.

Recent literature on squeeze-film dampers has been extensive; see for example Refs. 5-9. For a "short-bearing" squeeze-film damper with a full film of oil, i.e., no cavitation, around the circumference of the damper, Gunter, et al.[5] obtained the following expression for an equivalent damping coefficient

$$C_d = \frac{\pi \mu R (L/c)^3}{(1-\varepsilon^2)^{3/2}} \qquad (1)$$

where μ = oil viscosity, R = damper rotor radius, L = damper axial length, c = damper radial clearance, and ε = dimensionless eccentricity ratio (i.e., the ratio of damper radial displacement to damper radial clearance).

ASSUMPTIONS

In the present analysis, the following engineering assumptions are made:

1. The turbine bearings (ball bearings) are considered to be isotropic and act as simple supports without damping.
2. All rotating components are axisymmetric.
3. Air-friction losses are neglected, since the flywheel system, as tested, is enclosed in a protective housing having internal air pressure at 8.7 Pa (8.6×10^{-3} atm.)[2].
4. All temperature effects are neglected.
5. Although the flywheel shaft is vertical, the pendulum effect, which is small, is neglected.
6. The shafts and flywheel bands are modeled as discrete, massless flexible elements.
7. The flywheel rim, hub, damper rotor, and air turbine are considered as discrete rigid masses.†††
8. The damper is modeled as a short-bearing, squeeze-film damper with no cavitation of the oil film. Damping forces are assumed to be produced only in response to in-plane, i.e., lateral, velocities of the damper rotor.
9. Other than damping, all nonlinear effects are neglected (potential sources of nonlinearity include large deflections, bearing-stiffness nonlinearities, bearing clearances, and material nonlinearities).
10. Since solutions for synchronous motion only are sought here, internal damping due to material hysteresis and internal friction can be ignored (see Ref. 11, p. 72).
11. The system rotates at a constant angular velocity, i.e., torsional vibration and coupling between torsional and lateral vibrations are neglected.
12. Axial vibration, associated with vertical motion of the air turbine on its air-flotation bearing, is neglected.

†††The rim has relatively high natural frequencies[10], all of which are well above the operating speeds considered.

GOVERNING EQUATIONS

The governing differential equations used in this analysis were essentially presented in Ref. 3 and generalize the derivation of Dimentberg[11], ch. 4, to a multi-degree-of-freedom system. In matrix form these equations can be written as

$$[M]\{\ddot{q}\} - i[G]\{\dot{q}\} + [C]\{\dot{q}\} + [K]\{q\} = \{F\}e^{i\Omega t} \quad (2)$$

where $i \equiv \sqrt{-1}$, $\{q\} \equiv$ generalized displacement vector, $[M] \equiv$ generalized inertia matrix, $[G] \equiv$ gyroscopic effect matrix, $[C] \equiv$ external damping matrix, $[K] \equiv$ stiffness matrix, $\{F\} \equiv$ generalized force vector, $\Omega \equiv$ running speed, $t \equiv$ time, and a dot denotes a derivative with respect to time. Now

$$\{q\} = \{r_r, \phi_r, r_h, \phi_h, r_d, \phi_d, r_t, \phi_t\}^T \quad (3)$$

where r is the complex in-plane translation and ϕ is the complex out-of-plane tilting of a mass element, and the subscripts r, h, d, and t, here and hereafter, refer to the rim, hub, damper, and air-turbine, respectively. The sign convention for r and ϕ is shown in Fig. 4.

$$[M] = \begin{bmatrix} m_r & & & & & & & \\ & I_{mr} & & & & & & \\ & & m_h & & & 0 & & \\ & & & I_{mh} & & & & \\ & & & & m_d & & & \\ & & & & & I_{md} & & \\ & & 0 & & & & m_t & \\ & & & & & & & I_{mt} \end{bmatrix} \quad (4)$$

where m_r is the mass of the rim, I_{mr} is the mass moment of inertia of the rim about a diametral axis, etc.

$$[G] = \begin{bmatrix} 0 & & & & & & & \\ & J_{mr}\Omega & & & & 0 & & \\ & & 0 & & & & & \\ & & & J_{mh}\Omega & & & & \\ & & & & 0 & & & \\ & & & & & J_{md}\Omega & & \\ & & 0 & & & & 0 & \\ & & & & & & & J_{mt}\Omega \end{bmatrix} \quad (5)$$

where J_{mr} is the polar mass moment of inertia of the rim, etc. See Table 1 for the values of the mass and inertia parameters appearing in [M] and [G] corresponding to the Sandia flywheel system studied here.

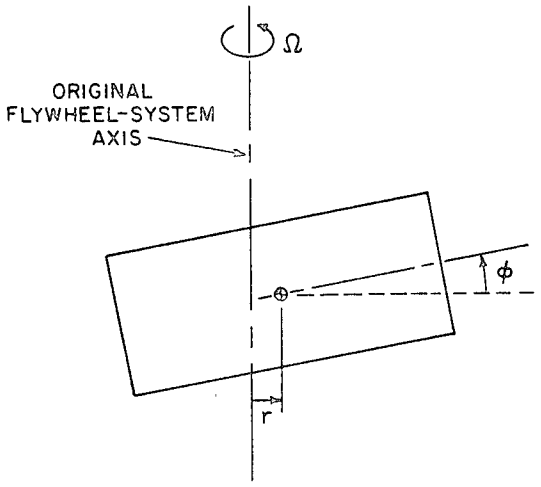

Fig. 4. Sign convention used: a typical rotating mass element having positive values of r and ϕ at an instant when both generalized displacements are in phase.

$$[K] = \begin{bmatrix} K_{11} & 0 & K_{13} & 0 & 0 & 0 & 0 & 0 \\ 0 & K_{22}(\Omega) & 0 & K_{24}(\Omega) & 0 & 0 & 0 & 0 \\ K_{13} & 0 & K_{33} & K_{34} & K_{35} & K_{36} & 0 & 0 \\ 0 & K_{24}(\Omega) & K_{34} & K_{44}(\Omega) & K_{45} & K_{46} & 0 & 0 \\ 0 & 0 & K_{35} & K_{45} & K_{55} & K_{56} & K_{57} & K_{58} \\ 0 & 0 & K_{36} & K_{46} & K_{56} & K_{66} & K_{67} & K_{68} \\ 0 & 0 & 0 & 0 & K_{57} & K_{67} & K_{77} & K_{78} \\ 0 & 0 & 0 & 0 & K_{58} & K_{68} & K_{78} & K_{88} \end{bmatrix} \quad (6)$$

where the values of the stiffness elements K_{pq}, some of which are functions of running speed due to centrifugal stiffening of the flywheel band action, were derived in Ref. 12, Appendices A and C. These stiffness values differ slightly from those used in Ref. 3 and are listed in Table 2.

$$\{F\} = \{m_r r_\varepsilon \Omega^2, (I_{mr} - J_{mr})\phi_\varepsilon \Omega^2 e^{-i\beta}, 0, 0, 0, 0, 0, 0\}^T \quad (7)$$

where r_ε is the in-plane eccentricity and ϕ_ε is the out-of-plane initial tilt of the flywheel rim, and β is the relative phase lag between these two excitation sources.

The only term of Eq. (2) yet to be defined is the external damping matrix [C]. As already discussed in the Assumptions, the only appreciable external damping is that due to in-plane motion of the system

Table 1. Mass and inertia parameters for Sandia "wagonwheel" flywheel.

Quantity	Symbol	Value
Rim mass	m_r	7.53 N-sec^2/m (0.043 lb-sec^2/in.)
Hub mass	m_h	4.11 N-sec^2/m (0.0235 lb-sec^2/in.)
Damper mass	m_d	1.47 N-sec^2/m (0.0084 lb-sec^2/in.)
Turbine mass	m_t	3.50 N-sec^2/m (0.020 lb-sec^2/in.)
Rim mass moment of inertia about its axis	J_{mr}	0.363 N-m-sec^2 (3.215 lb-in-sec^2)
Hub mass moment of inertia about its axis	J_{mh}	0.0061 N-m-sec^2 (0.054 lb-in-sec^2)
Damper mass moment of inertia about its axis	J_{md}	0.00107 N-m-sec^2 (0.0095 lb-in-sec^2)
Turbine mass moment of inertia about its axis	J_{mt}	0.0076 N-m-sec^2 (0.067 lb-in-sec^2)
Rim mass moment of inertia about a centroidal diameter	I_{mr}	0.185 N-m-sec^2 (1.636 lb-in-sec^2)
Hub mass moment of inertia about a centroidal diameter	I_{mh}	0.0279 N-m-sec^2 (0.247 lb-in-sec^2)
Damper mass moment of inertia about a centroidal diameter	I_{md}	0.00067 N-m-sec^2 (0.0059 lb-in-sec^2)
Turbine mass moment of inertia about a centroidal diameter	I_{mt}	0.0045 N-m-sec^2 (0.040 lb-in-sec^2)

Table 2. Non-zero elements of the stiffness matrix [K].

Stiffness elements which vary with rotational speed (Ω in rad/sec)

$K_{22}(\Omega) = 4.772 \times 10^5 + 1.010 \times 10^{-3}\Omega^2$ N-m/rad
$(4.223 \times 10^6 + 8.936 \times 10^{-3}\Omega^2$ lb-in/rad)

$K_{24}(\Omega) = -4.772 \times 10^5 - 1.010 \times 10^{-3}\Omega^2$ N-m/rad
$(-4.223 \times 10^6 - 8.936 \times 10^{-3}\Omega^2$ lb-in/rad)

$K_{44}(\Omega) = 4.868 \times 10^5 + 1.010 \times 10^{-3}\Omega^2$ N-m/rad
$(4.308 \times 10^6 + 8.936 \times 10^{-3}\Omega^2$ lb-in/rad)

Constant-value stiffness elements

$K_{11} = 2.144 \times 10^8$ N/m (1.224×10^6 lb/in)	$K_{56} = 1.176 \times 10^5$ N/rad (2.644×10^4 lb/rad)
$K_{13} = -2.144 \times 10^8$ N/m (-1.224×10^6 lb/in)	$K_{57} = -8.995 \times 10^5$ N/m (-5.136×10^3 lb/in)
$K_{33} = 2.177 \times 10^8$ N/m (1.243×10^6 lb/in)	$K_{58} = -7.927 \times 10^4$ N/rad (-1.782×10^4 lb/rad)
$K_{34} = -1.459 \times 10^5$ N/rad (-3.279×10^4 lb/rad)	$K_{66} = 2.418 \times 10^4$ N-m/rad (2.140×10^5 lb-in/rad)
$K_{35} = -3.324 \times 10^6$ N/m (-1.898×10^4 lb/in)	$K_{67} = 7.927 \times 10^4$ N-m/m (1.782×10^4 lb-in/in)
$K_{36} = -1.969 \times 10^5$ N/rad (-4.427×10^4 lb/rad)	$K_{68} = 4.669 \times 10^3$ N-m/rad (4.132×10^4 lb-in/rad)
$K_{45} = 1.459 \times 10^5$ N-m/m (3.279×10^4 lb-in/in)	$K_{77} = 9.913 \times 10^8$ N/m (5.660×10^6 lb/in)
$K_{46} = 5.446 \times 10^3$ N-m/rad (4.820×10^4 lb-in/rad)	$K_{78} = 3.797 \times 10^7$ N/rad (8.536×10^6 lb/rad)
$K_{55} = 4.224 \times 10^6$ N/m (2.412×10^4 lb/in)	$K_{88} = 1.617 \times 10^6$ N-m/rad (1.431×10^7 lb-in/rad)

damper. Thus, making use of Eq. (1), we have

$$C_{55} = C_d = \frac{\pi\mu R(L/c)^3}{[1 - (|r_d|/c)^2]^{3/2}} \tag{8}$$

and all other elements of [C] are taken to be equal to zero.

METHOD OF SOLUTION

Due to the nonlinearity in the damping coefficient C_{55}, the otherwise linear differential equations governing the forced motion of the flywheel system (2) become a set of nonlinear differential equations. However, since only one term in these equations is nonlinear, the attack taken here is to treat that single external-damping term C_{55} as a constant, solving the resulting linear system equations, and iterating with respect to the value assumed for C_{55}.

Assuming a synchronous solution of the form

$$\{q\} = \{\bar{q}\}e^{i\Omega t} \tag{9}$$

and substituting into Eq. (2), one obtains the following matrix equation

$$\{-[M]\Omega^2 + [G]\Omega + i[C]\Omega + [K]\}\{\bar{q}\} = \{F\} \tag{10}$$

At each rotational speed Ω, an initial value C_{d_o} is assumed for C_{55} (all other elements of the external damping matrix [C] are zero) and Eq. (10) is solved by standard numerical routines to yield a complex solution vector $\{\bar{q}\}$. The fifth element of this vector, the complex in-plane damper displacement r_d, is substituted into Eq. (8) to obtain the solution-demanded damping coefficient $C_{d_1}^*$. If C_{d_1} does not match the assumed value C_{d_o} to within the desired convergence requirement, a Gauss-Seidel iteration scheme with point relaxation (see for example, Ref. 13) is invoked which then determines the next assumed value C_{d_1}. This process is continued until convergence of the damping coefficient is attained, whereupon the last computed solution vector $\{\bar{q}\}$ is also accepted.

As might be expected the generalized displacements forming the solution vector have sharply changing amplitudes when the rotational speed is in the proximity of a natural frequency of the system. These

resonant amplitudes are very sensitive to the amount of damping. Conversely the damping coefficient of Eq. (8) varies sharply with damper in-plane displacement, especially as the magnitude of r_d approaches the value of the damper radial clearance c.

Such sharp variances can cause significant difficulties for an iteration scheme and, in fact, necessitated several modifications in the scheme used here. These modifications consisted in (a) the setting of fairly narrow, but adjustable, bounds on the values of $C_{d_i}^*$, (b) shrinking the relaxation factor after a number of non-convergent iterations, and (c) taking the average of previous non-convergent values as the new assumed value C_{d_i} if the number of iterations exceeds a certain number. These modifications, and how they are incorporated, are shown in the flow chart of Fig. 5.

After obtaining the generalized synchronous solution $\{\bar{q}\}$ of the system, one further calculation is required. The lateral motion of this flywheel system, as installed in the Sandia spin-test facility, is limited by a phenolic collar attached to a stationary steel ring[2]. This phenolic buffer collar limits the lateral motion at the base of the spin collar (see Fig. 1) to a maximum of 0.7 mm (0.028 in.).

The distance along the flywheel system axis from the center of the hub to the height of the spin collar at which this buffer collar acts is 10.3 cm (4.07 in.) as measured on a drawing of the Sandia spin-test setup. One can obtain the magni-

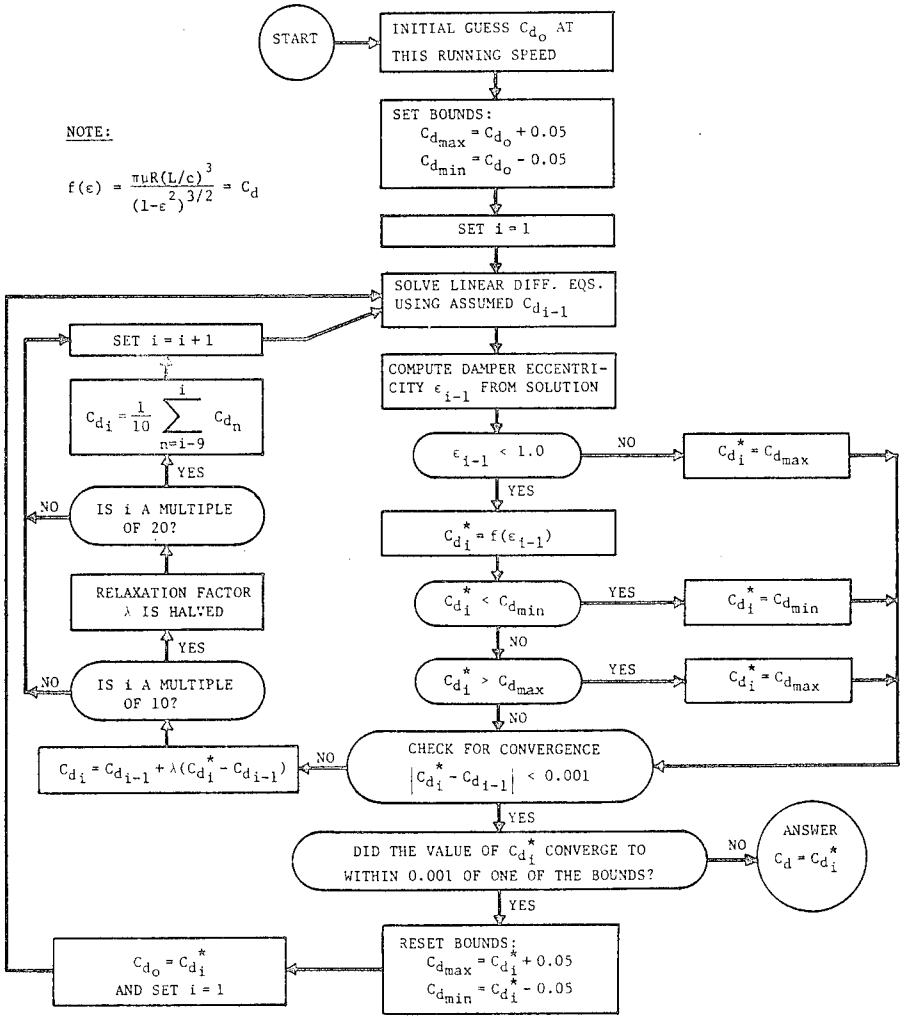

Fig. 5. Flow chart of iterative algorithm used in the solution of the system equations.

tude of the in-plane motion at this point, at the base of the spin collar, in terms of the synchronous generalized displacements of the hub by the expression

$$\rho_h = |r_h - 10.3\ \phi_h| \qquad (11)$$

Here r_h and ϕ_h are the complex synchronous solutions for in-plane displacement and out-of-plane tilting of the hub, and ρ_h is the magnitude of the in-plane displacement at the motion-limited point. The minus sign in Eq. (11) is necessary due to the sign convention used for in-plane displacements and out-of-plane tilt angles, as shown in Fig. 4.

NUMERICAL RESULTS

The value of the oil viscosity μ in the damper was taken to be 3.2×10^{-2} N-sec/m^2 (4.6×10^{-6} lb-sec/in.^{2}) which corresponds to SAE 10 oil at 39°C (103°F). This value of viscosity should be less than for the oil used and should therefore yield conservative (i.e., higher) generalized displacement results in terms of response magnitudes.

The results for four different unbalance conditions of the rim are presented:

a) in-plane displacement eccentricity r_ε only
b) out-of-plane initial tilt ϕ_ε only
c) combined r_ε and ϕ_ε with zero phase angle between the resulting excitations; that is, $\beta=0$ in the forcing term, Eq. (7)
d) combined r_ε and ϕ_ε with a phase angle of π radians between the resulting excitations; that is, $\beta=\pi$

For all of the above, the values for r_ε and ϕ_ε were taken to be 0.025 cm (0.010 in.) and 0.13 degrees, respectively. These values were provided by Sandia Laboratories as typical of the flywheels tested. The numerical results for the generalized synchronous displacements of the rim, hub, damper, and air turbine are presented in Figs. 6-13 for system rotational speeds of 0 to 42,000 rpm. The variation of the external damping coefficient C_d with rotational speed is shown in Fig. 14 for each of the unbalance conditions.

From the solution of the homogeneous system equations corresponding to Eq. (2) and with no external damping ([C]=[0]), the first-order critical speeds in or near the speed range of interest were found to be at 800 rpm, 15,500 rpm, and 43,700 rpm. All of the amplitude peaks shown in Figs. 6-13 are seen to occur near these first two critical speeds. The last critical speed is just outside the speed range of the figures, but can nevertheless be related to amplitude increases occurring near 42,000 rpm.

Since the air-turbine amplitudes for both in-plane displacement and out-of-plane tilting are negligibly small on the scale chosen for these figures, the amplitudes and phase angles of r_t and ϕ_t will not be discussed further. It should also be noted that r_d, the damper in-plane displacement, is always less than 1 mm (0.04 in.), the radial clearance of the damper.

For rim-unbalance conditions (a), see Figs. 6 and 7. Amplitude peaks occur at approximately 800 rpm for the rim, hub, and damper for both lateral displacement and tilting. However, only r_d and ϕ_d show significant peaks at approximately 15,000 rpm. The phase-lag behavior of the in-plane displacements differs considerably from that corresponding to out-of-plane tilting. At the 800-rpm peaks, the in-plane displacement responses transition from a 0-degree to a 180-degree phase lag. This phase lag increases to 360 degrees for r_d at 15,000 rpm but barely ripples and remains at 180 degrees for r_r and r_h. For the out-of-plane tilting responses, the phase lag also increases from 0 to 180 degrees at 800 rpm. However, then the phase lags appear to "anticipate" the second critical speed, returning back to near 0 well before 15,000 rpm and then shifting back to 180 degrees at approximately 15,000 rpm. For the remainder of the speed range, amplitudes and phases remain constant except for a slight increase in $|\phi_h|$ at 42,000 rpm.

For rim-unbalance condition (b), see Figs. 8 and 9. Amplitude peaks again occur at approximately 800 rpm for the rim, hub, and damper for both lateral displacement and tilting. Again, as in condition (a), only r_d and ϕ_d show significant peaks at the second critical speed. Contrary to condition (a), tilting amplitudes show increases at the high end of the speed range with ϕ_h going off scale at 37,000 rpm, well in advance of the third critical at 43,700 rpm. Here, the damper in-plane amplitude r_d is also increasing at 40,000 rpm. Phase-lag behavior again differs for the in-plane and out-of-plane responses. The phase lags corresponding to

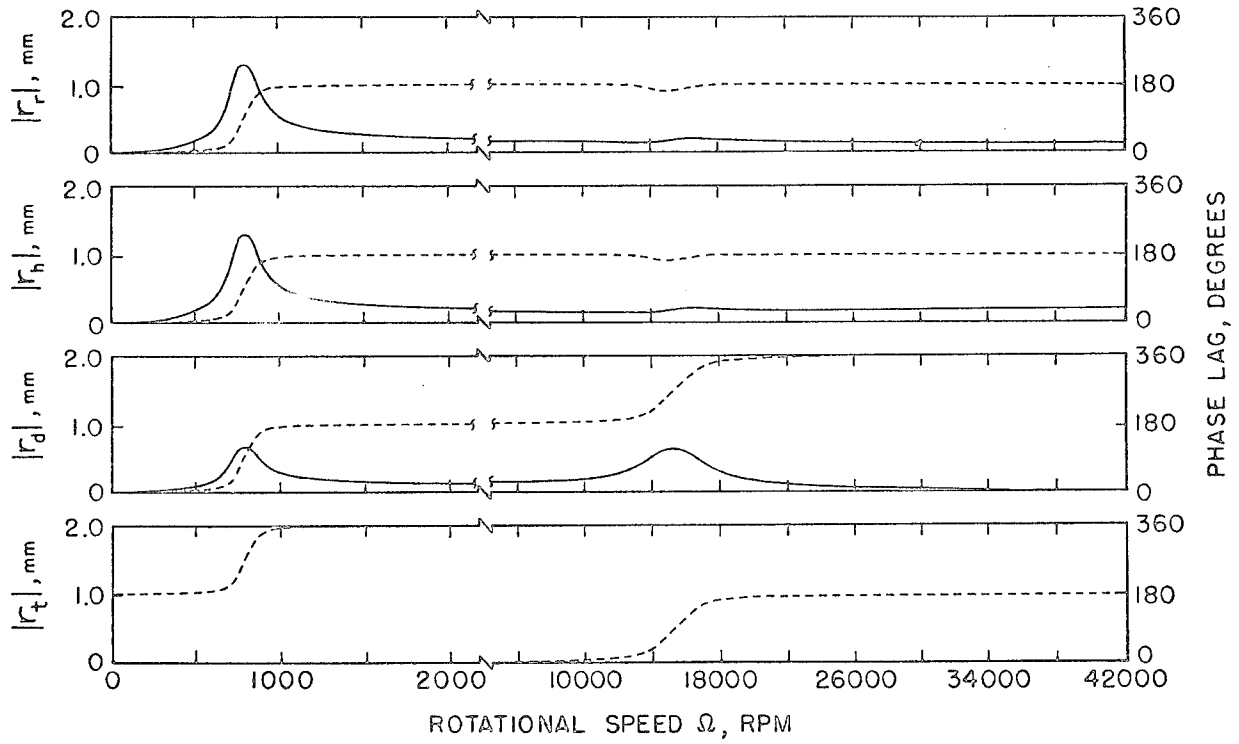

Fig. 6. In-plane displacement amplitudes (solid lines) and phase angles (dashed lines) versus rotational speed for condition (a), r_ε = 0.025 cm (0.010 in.).

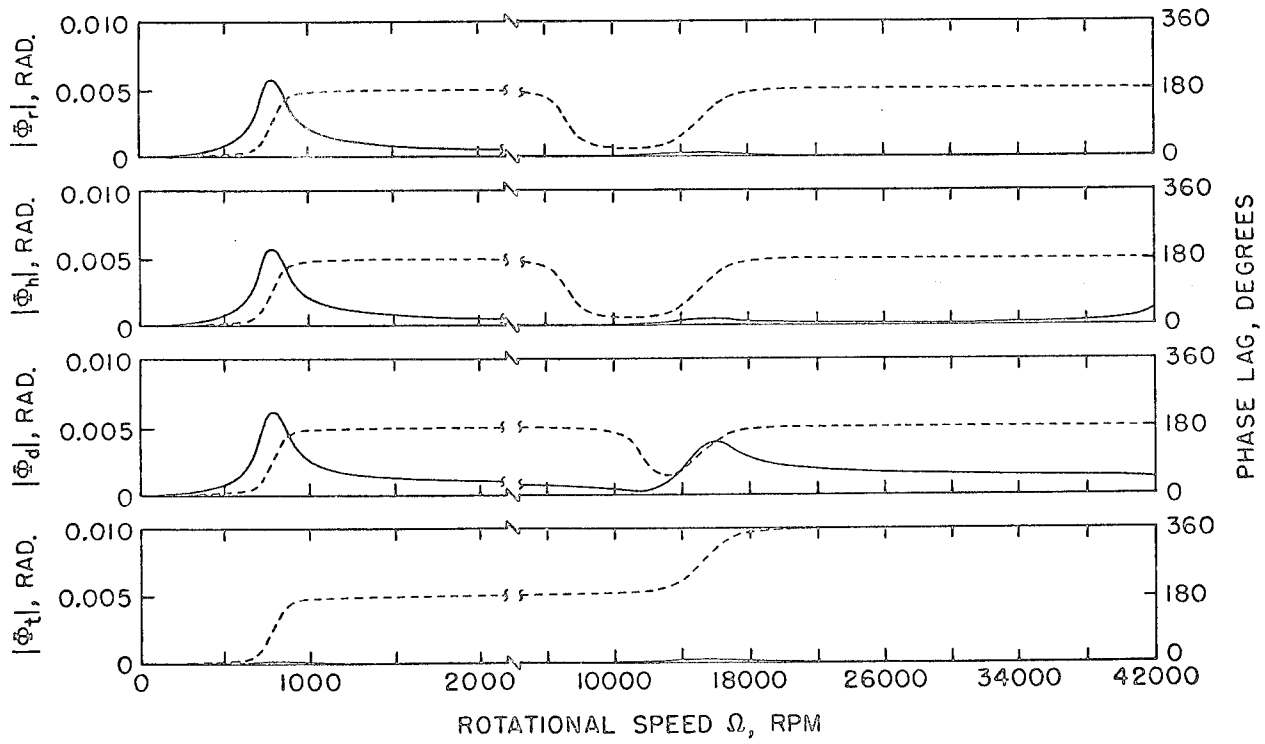

Fig. 7. Out-of-plane tilting amplitudes (solid lines) and phase angles (dashed lines) versus rotational speed for condition (a), r_ε = 0.025 cm (0.010 in.).

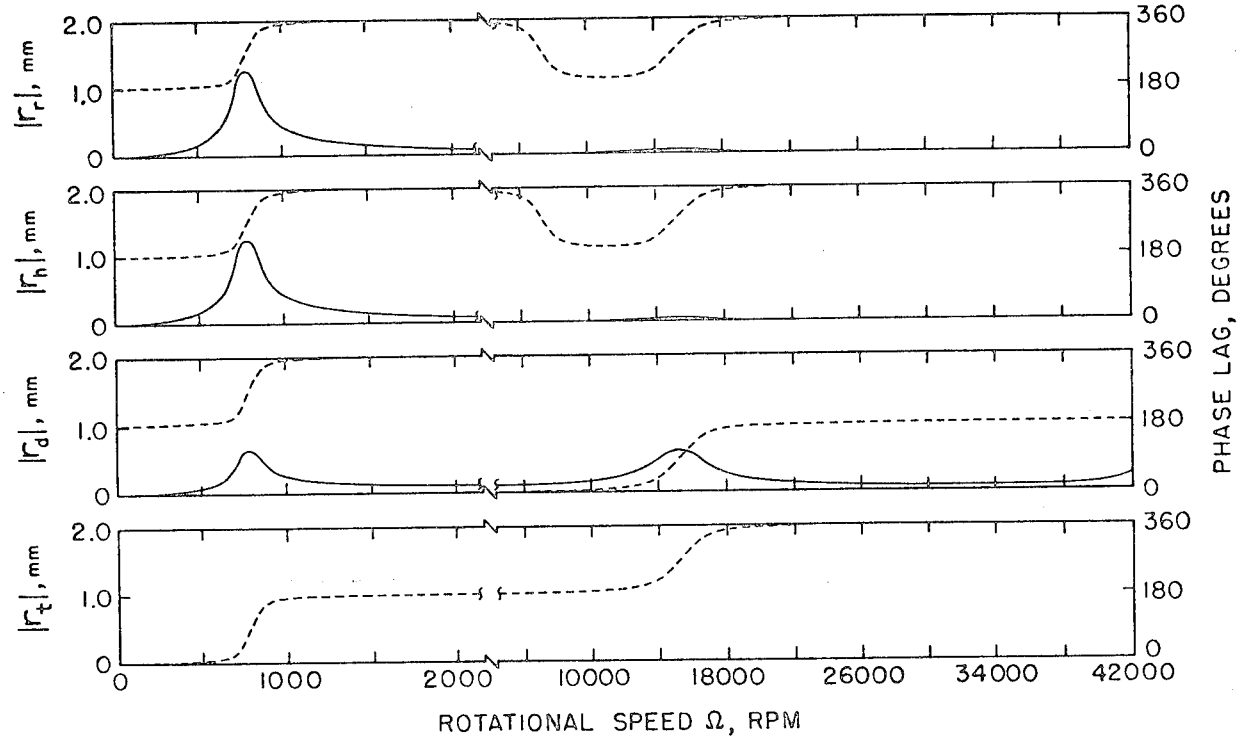

Fig. 8. In-plane displacement amplitudes (solid lines) and phase angles (dashed lines) versus rotational speed for condition (b), ϕ_ε = 0.13 degrees.

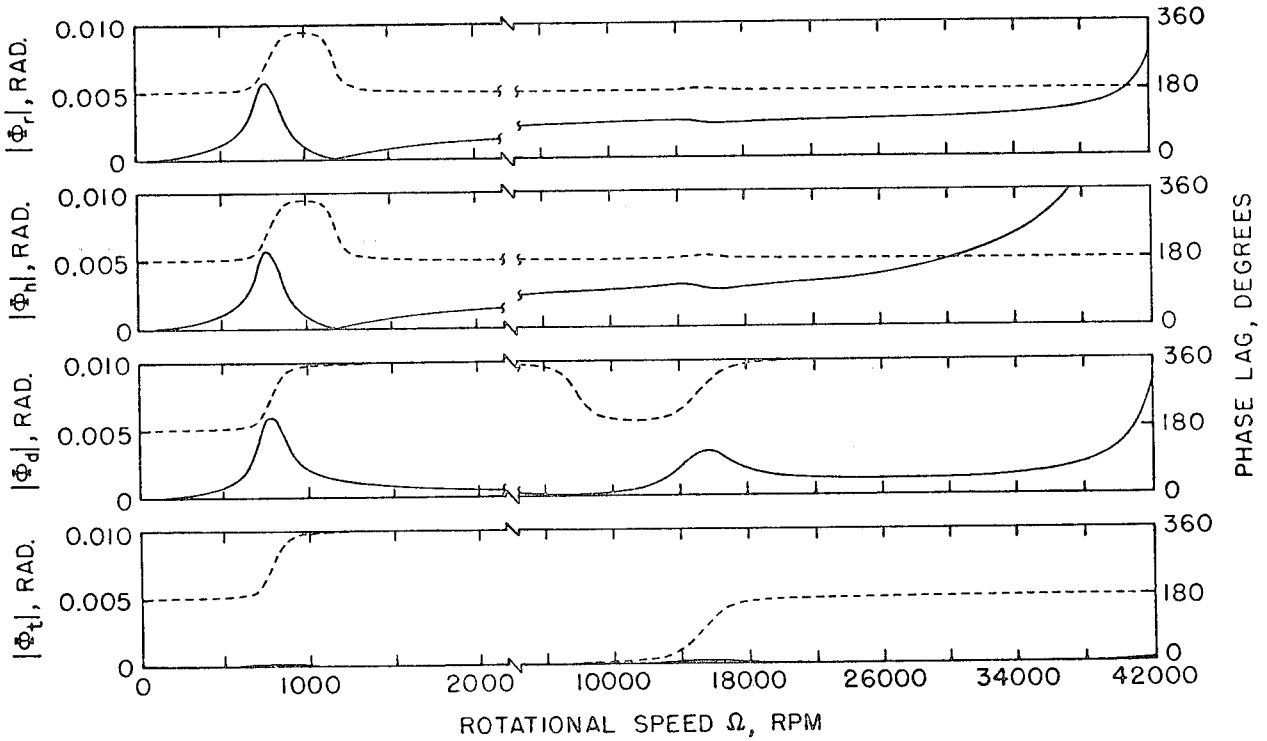

Fig. 9. Out-of-plane tilting amplitudes (solid lines) and phase angles (dashed lines) versus rotational speed for condition (b), ϕ_ε = 0.13 degrees.

in-plane displacements increase from 180 to 360 degrees at the first critical speed. Then the phase lags for r_r and r_h "anticipate" the second critical, dropping back to 180 degrees at about 8,000 rpm and shifting again to 360 degrees at approximately 15,000 rpm. At 15,000 rpm the phase lag for r_d simply increases from its post-first-critical value of 360 degrees (equivalent to 0) to 180 degrees. For the tilting responses, all phase lags increase from 180 to 360 degrees at the first critical speed, but then the phase lags corresponding to ϕ_r and ϕ_h quickly drop back to 180 degrees and remain there through the second critical speed. The phase lag of ϕ_d "anticipates" the second critical speed and drops from 360 to 180 degrees at approximately 8,000 rpm and then climbs back to 360 degrees at about 15,000 rpm. All phase lags remain constant after the second critical speed through 42,000 rpm.

For rim-unbalance condition (c), see Figs. 10 and 11. The amplitude peaks at the first and second critical speeds are nearly eliminated. The best indications that a critical speed has been passed are the phase lags of the responses. In the cases of r_r, r_h, ϕ_r, and ϕ_h, the phase lags start at 180 degrees, dip sharply toward zero just prior to the first critical, and go back to 180 degrees for the remainder of the speed range. The phase lag for ϕ_d begins similarly at 180 degrees with a large dip just before 800 rpm and returning to 180 degrees. Then a similar but smaller dip is encountered just before the second critical. However, at approximately 33,000 rpm, the phase lag of ϕ_d makes a rapid, not quite straight vertical, jump from 180 to 360 degrees where it remains through 42,000 rpm. This rapid phase shift corresponds to the speed at which the amplitude of ϕ_d hits zero, so it is no cause for alarm. For r_d the phase lag starts at 0, increases to 180 degrees at 800 rpm, increases to 360 degrees at the second critical speed, but drops back suddenly to 180 degrees near 22,000 rpm, where it remains through 42,000 rpm. That this drop is so abrupt is again not a cause for alarm since the amplitude of r_d is essentially zero from approximately 20,000 to 23,000 rpm. Although the amplitudes of the responses do not especially "peak" at the critical speeds, the amplitudes corresponding to ϕ_r and ϕ_h do grow steadily as rotational speed increases. Also, the three tilting amplitudes corresponding to ϕ_r, ϕ_h, and ϕ_d appear very similar, at the higher end of the speed range, to those obtained in condition (b). Here also the amplitude of ϕ_h goes off scale at approximately 37,000 rpm.

For rim-unbalance condition (d), see Figs. 12 and 13. Qualitatively over the entire speed range shown, the in-plane amplitudes and phase lags here behave just like those for condition (a), in-plane eccentricity r_ε only. Compare Fig. 6 with Fig. 12. The out-of-plane tilting amplitudes and phase angles for condition (d) behave just like those for condition (b), initial tilt ϕ_ε only, except that the phase lags here are shifted by -180 degrees with respect to the values obtained for (b). Compare Fig. 9 with Fig. 13.

It should be noted that even though the results for condition (d) are easily related qualitatively to conditions (a) and (b), this is an exception rather than the general rule for combination unbalance conditions not reported above.

It should also be noted that the system-response solutions as presented in Figs. 6-13 are, in general, smooth curves. Especially at resonant speeds where amplitudes increase sharply, no "chopping" of the response curves is seen to occur. The variation of the external damping coefficient C_d, as calculated by the authors' iteration scheme, is shown in Fig. 14 and it similarly exhibits smooth behavior. This response smoothness increases confidence that the results are computationally correct and that the described iteration scheme can successfully cope with sensitive nonlinear terms.

The final numerical results presented involve the magnitude of the in-plane displacement at the base of the spin collar on top of the hub. This quantity, calculated according to Eq. (11), is shown in Fig. 15 as a function of the rotational speed. The four rim-unbalance combinations are presented together for easier comparison. Also shown is the 0.7-mm limit at which the spin collar would hit the phenolic buffer employed in the Sandia-Livermore spin-test setup.

Only in the case of unbalance condition (c), r_ε and ϕ_ε with β=0, would the spin collar not encounter the displacement limit at the first critical speed. However, given a flywheel with one of the other unbalance conditions, it would most

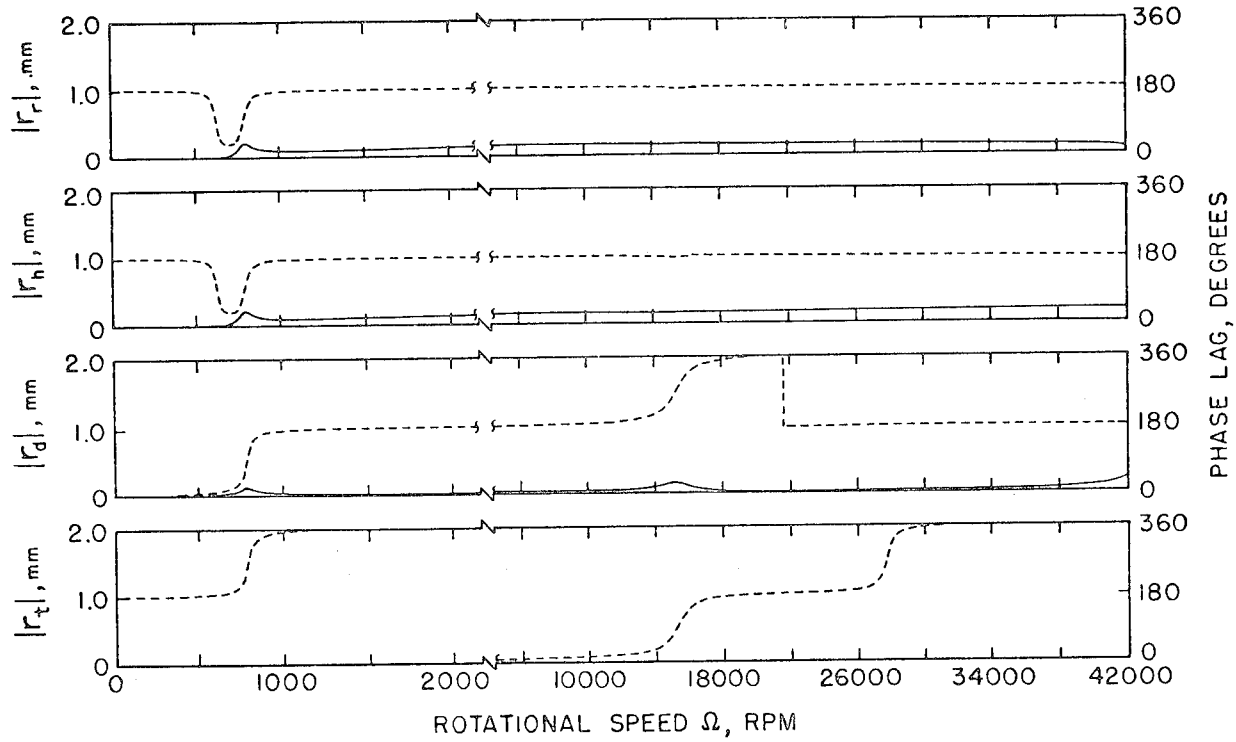

Fig. 10. In-plane displacement amplitudes (solid lines) and phase angles (dashed lines) versus rotational speed for condition (c), r_ε = 0.025 cm (0.010 in.) and ϕ_ε = 0.13 degrees with β=0.

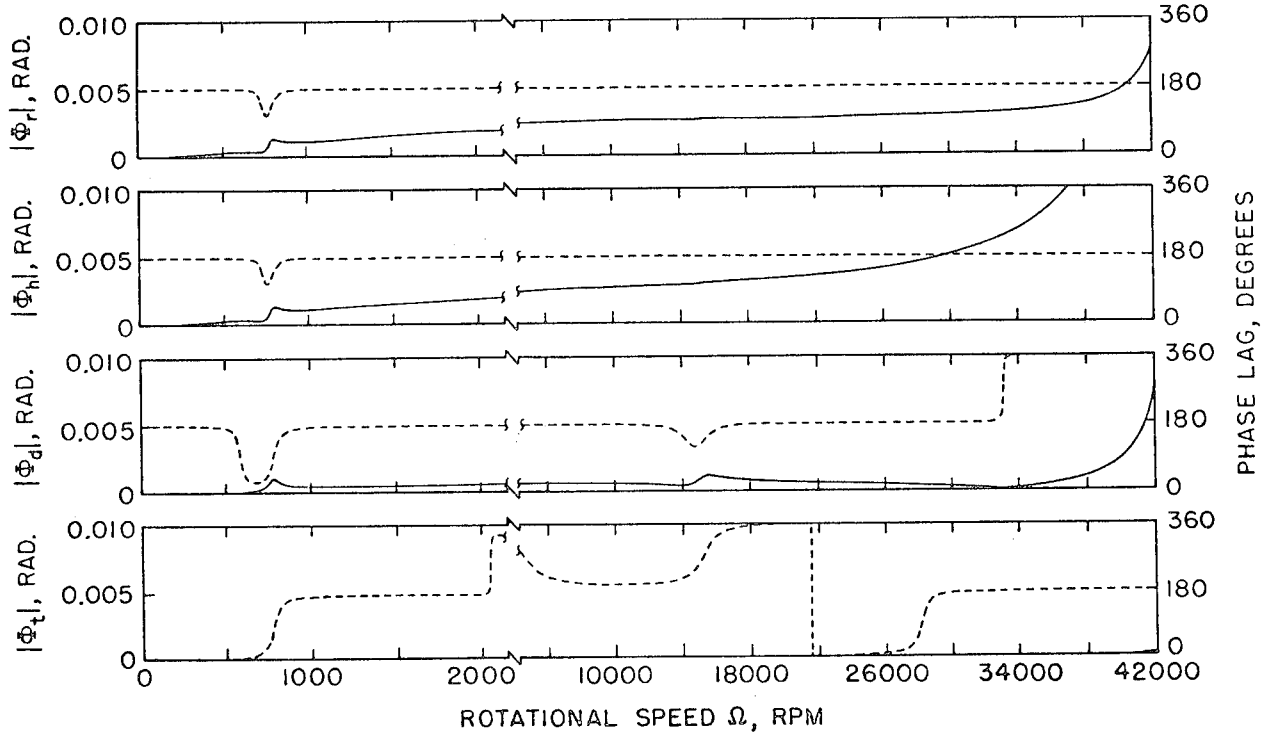

Fig. 11. Out-of-plane tilting amplitudes (solid lines) and phase angles (dashed lines) versus rotational speed for condition (c), r_ε = 0.025 cm (0.010 in.) and ϕ_ε = 0.13 degrees with β=0.

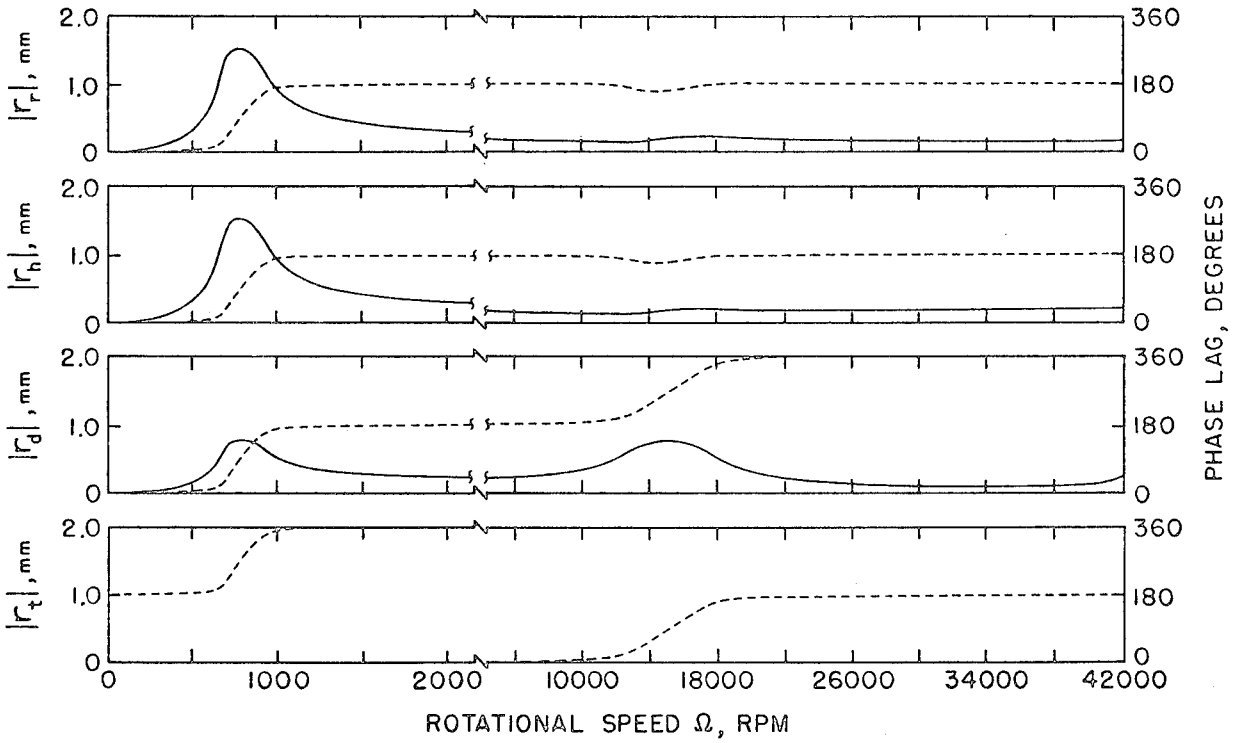

Fig. 12. In-plane displacement amplitudes (solid lines) and phase angles (dashed lines) versus rotational speed for condition (d), r_ε = 0.025 cm (0.10 in.) and ϕ_ε = 0.13 degrees with $\beta=\pi$ radians.

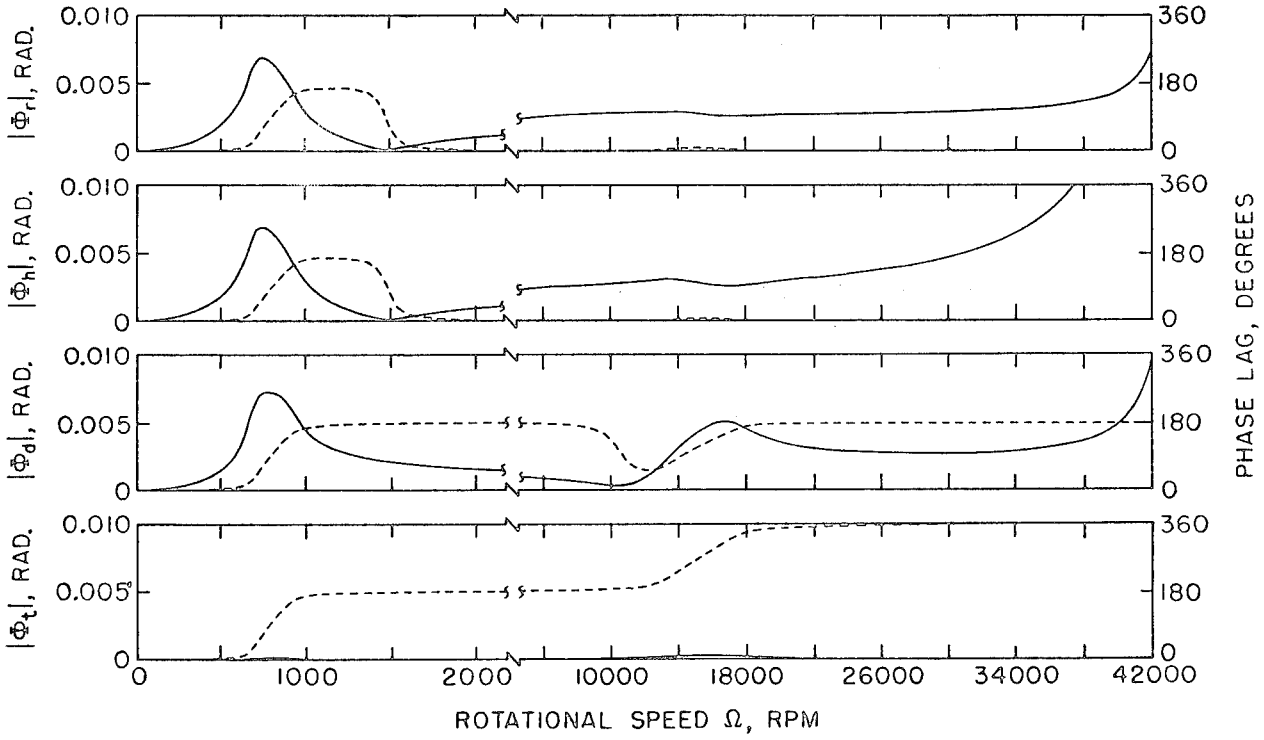

Fig. 13. Out-of-plane tilting amplitudes (solid lines) and phase angles (dashed lines) versus rotational speed for condition (d), r_ε = 0.025 cm (0.010 in.) and ϕ_ε = 0.13 degrees with $\beta=\pi$ radians.

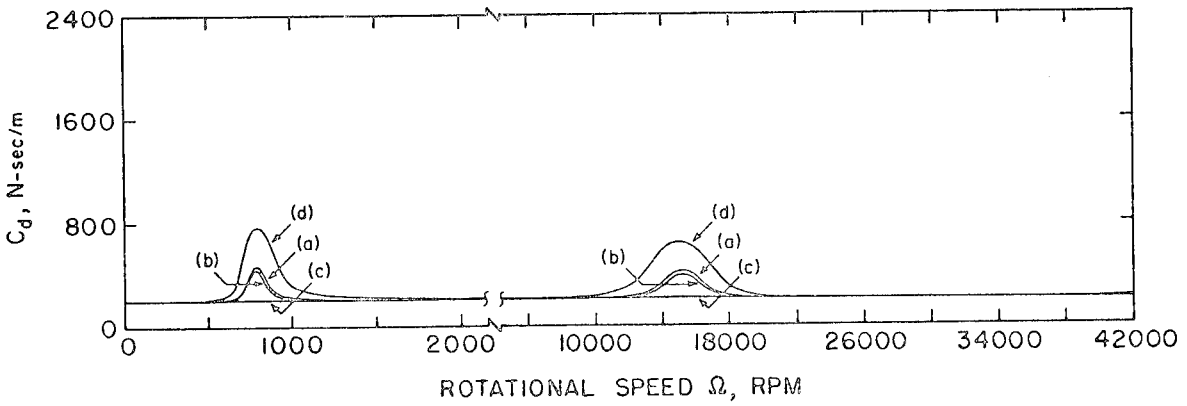

Fig. 14. Damping coefficient C_d as a function of rotational speed for different rim-unbalance conditions: (a) r_ε only, (b) ϕ_ε only, (c) r_ε and ϕ_ε with $\beta=0$, and (d) r_ε and ϕ_ε with $\beta=\pi$ radians.

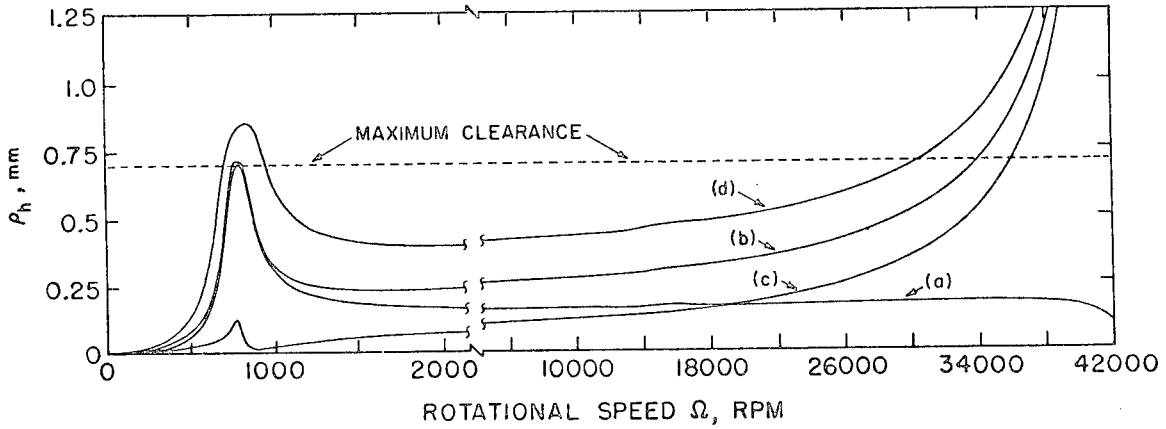

Fig. 15. Magnitude of in-plane displacement at base of spin collar ρ_h versus rotational speed for different rim-unbalance conditions: (a) r_ε only, (b) ϕ_ε only, (c) r_ε and ϕ_ε with $\beta=0$, and (d) r_ε and ϕ_ε with $\beta=\pi$ radians.

likely be easy to accelerate through this critical speed and avoid hitting the stop.

As might be predicted from the hub generalized displacements of Figs. 6-13, no significant increase in spin collar in-plane displacement is exhibited upon passing the second critical speed of 15,500 rpm. In fact, the curve corresponding to unbalance condition (a), r_ε only, exhibits a low, constant amplitude up until the end of the speed range at 42,000 rpm where the amplitude decreases. This behavior does not resemble at all the curves for the other unbalance conditions which each contain ϕ_ε, an initial tilt of the rim. For these other cases, the amplitude gradually and continually rises from a point just after the first critical speed until it exceeds the displacement limit well short of the 43,700 rpm third forward critical speed.

The spin-collar displacement corresponding to unbalance condition (d), r_ε and ϕ_ε with $\beta=\pi$, exceeds the displacement limit at slightly over 30,000 rpm. In contrast, for condition (c), r_ε and ϕ_ε with $\beta=0$, the displacement limit is exceeded at approximately 36,000 rpm. For unbalance condition (b), ϕ_ε only, the displacement limit is exceeded at the intermediate value of approximately 34,000 rpm.

ADDITIONAL COMMENTS AND SOME PRACTICAL SUGGESTIONS

The calculation of critical speeds is insufficient in assessing possible dynamic problem areas. For example, the second critical of the present rotor system excites a mode characterized by maximum motion at the damper while rim and hub generalized displacements are almost unaffected. The system's damper easily limits this motion and this critical speed is seen to be not "critical" at all.

The system response at the first critical speed lies in a fairly narrow speed range. It is the authors' belief that this speed also should be judged not "critical" on the basis that acceleration of the flywheel system could easily permit crossing this narrow range. However, the motion of the system associated with the third critical speed does limit the permissible speed range.

Motion near the third forward critical speed is characterized by rim and hub tilting which is 180 degrees out of phase with damper tilting. Since it is assumed that damper tilting (as opposed to damper translation) does not generate any damping moments, the tilting amplitudes of the rim and hub (when emphasized by rim initial tilt) begin to increase without bound as the third critical speed is approached. Rim and hub tilting amplitudes begin to rise well before the tilting of the damper. Thus, it is very unlikely that damper improvements could decrease these large tilting angles. The best means of extending the safe speed range appears to be reduction of the couple unbalance (initial tilt) existing in the rim.

The primary significance of this analysis with regards to composite-material flywheel testing has been the demonstration of couple unbalance as an inhibitor to the attainment of higher rotational speeds. All reasonable means should be employed to ensure that couple unbalance of a flywheel is minimized. Furthermore, in light of the second conclusion stated below, a test engineer could monitor rim and hub tilting amplitudes during spin tests, diagnose couple-unbalance behavior, and still have time to halt the test prior to a costly flywheel failure.

CONCLUSIONS

From the analytical results presented here, the following conclusions can be made with regard to the flywheel system model examined in this paper.

1) Both in-plane and out-of-plane resonance-type responses of the rim and hub are excited at the system's first critical speed but not the second.
2) The best indications of residual couple unbalance in the rim (as would be caused by initial tilt) are the out-of-plane tilting responses of the rim and hub. These amplitudes, under steady-state conditions, exhibit a relative minimum at speeds slightly higher than the first critical and then begin to rise gradually but steadily as the rotational speed continues to increase.
3) The presence of couple unbalance in the rim can cause the spin collar to hit its displacement limit at a rotational speed much lower than the third forward critical speed. For the typical values of in-plane eccentricity and out-of-plane tilting assumed in this paper, the worst combination caused the displacement limit to be exceeded at slightly over 30,000 rpm which is only 70% of the third forward critical speed.

REFERENCES

1 Reedy, E.D., "A Composite-Rim Flywheel Design," SAMPE Quarterly, Vol. 9, No. 3, Apr. 1978, pp. 1-6.

2 Reedy, E.D., Jr. and Street, H.K., "Composite-Rim Flywheels: Spin Tests," SAMPE Quarterly, Vol. 10, No. 3, Apr. 1979, pp. 36-41.

3 Chen, T.L.C. and Bert, C.W., "Whirling Response and Stability of Flexibly Mounted, Ring-Type Flywheel Systems," Journal of Mechanical Design, Trans. ASME, Vol. 102, No. 2, Apr. 1980, pp. 369-377.

4 Salamone, D.J. and Gunter, E.J., "Synchronous Unbalance Response of an Overhung Rotor with Disk Skew," ASME Paper 79-GT-135, Mar. 12-15, 1979.

5 Gunter, E.J., Barrett, L.E., and Allaire, P.E., "Design of Nonlinear Squeeze-Film Dampers for Aircraft Engines," Journal of Lubrication Technology, Trans. ASME, Vol. 99, No. 1, Jan. 1977, pp. 57-64.

6 Vance, J.M. and Kirton, A.J., "Experimental Measurement of the Dynamic Force Response of a Squeeze-Film Bearing Damper," Journal of Engineering for Industry, Trans. ASME, Vol. 97, No. 4, Nov. 1975, pp. 1282-1290.

7 Pan, C.H.T., "An Improved Short Bearing Analysis for the Submerged Operation of Plain Journal Bearings and Squeeze-Film Dampers," ASME Paper 79-Lub-33, Journal of Lubrication Technology, Trans. ASME, to appear.

8 Cunningham, R.E., "Steady-State Unbalance Response of a Three-Disk Flexible Rotor on Flexible, Damped Supports," Journal of Mechanical Design, Trans. ASME, Vol. 100, No. 3, July 1978, pp. 563-573.

9 Bansal, P.N. and Hibner, D.H., "Experimental and Analytical Investigation of Squeeze Film Bearing Damper Forces Induced by Offset Circular Whirl Orbits," Journal of Mechanical Design, Trans. ASME, Vol. 100, No. 3, July 1978, pp. 549-557.

10 Bert, C.W. and Chen, T.L.C., "On Vibration of a Thick Flexible Ring Rotating at High Speed," Journal of Sound and Vibration, Vol. 61, No. 4, Dec. 22, 1978, pp. 517-530.

11 Dimentberg, F.M., Flexural Vibrations of Rotating Shafts, Butterworths, London, 1961.

12 Kocay, C.A. and Bert, C.W., manuscript in preparation.

13 Hornbeck, R.W., Numerical Methods, Quantum Publishers, New York, 1975, pp. 101-106.

SIMPLIFIED GYRODYNAMICS OF ROAD VEHICLES WITH HIGH-ENERGY FLYWHEELS

Professor Alan T. McDonald
School of Mechanical Engineering
Purdue University
West Lafayette, Indiana 47907

ABSTRACT

Concern has been expressed about the safety of using high-energy flywheels in vehicles that operate in mixed traffic on public highways. Concern focuses on the need to contain the kinetic energy and angular momentum of the energy storage element. Usually the potential is cited for large gyrodynamic moments during normal maneuvers, collision-avoidance, or in post-collision situations.

Gyrodynamic properties of kinetic energy wheels are analyzed in this paper. Basic equations are reduced to parametric forms and used to construct a nomograph. The parameters considered are kinetic energy, angular momentum, precession rate, and reaction torque. The nomograph may be used to find the reaction torque applied to a vehicle during arbitrary maneuvers; its application is illustrated by two detailed examples. The examples show the decisions required of the analyst, and guide the choice of appropriate parameter values.

The nomograph permits quick calculation of gyrodynamic reactions for alternative components and maneuvers. It should be useful to those involved in parametric studies of highway vehicles with high-energy flywheels. The nomograph and the examples presented show that gyrodynamic reactions are small for reasonable designs.

INTRODUCTION

Any rotating mass exhibits gyrodynamic behavior by resisting changes in orientation of its spin axis. Flywheels used for energy storage in automotive applications are subjected to the maneuvers of the vehicle. The resulting gyrodynamic reactions may be large. Questions frequently are raised about the design and safety aspects of these energy storage systems.

Grodynamic theory is poorly understood by nonspecialists. However, calculation of the magnitude and directions of torque reactions in flywheel systems subjected to maneuvers is straight-forward. Because questions continue to be raised it is useful to present a simplified analysis of flywheel system gyrodynamics that is accessible to the nonspecialist.

The purposes of this paper are to:

(1) provide a primer on gyrodynamics with emphasis on physical results
(2) identify and quantify vehicle maneuvers typical of normal operation and accident situations
(3) simplify calculation of gyrodynamic reactions to a graphical procedure using a nomograph
(4) illustrate use of the nomograph with example calculations

The paper is organized into sections dealing with each of these topics, followed by a concluding discussion. Details of the mathematical developments are in the Appendix.

FUNDAMENTALS OF GYRODYNAMICS

A spinning flywheel rotor is shown schematically in Fig. 1. The rotor revolves at angular speed, ω, about the spin axis shown in the figure. The corresponding angular velocity, $\vec{\omega}$, is the vector that describes the flywheel motion. It has magnitude ω and sense (direction) given by the "right-hand" rule* as shown in the figure.

The mass moment of inertia, or simply moment of inertia of the rotor is given by

$$I = \int_{M(\text{rotor})} r^2 dm \qquad (1)$$

where dm is the mass of a differential element located at radius, r, from the spin axis. The rotor energy content, angular momentum, and gyrodynamic reactions depend on the moment of inertia and angular speed of the rotor.

Basic Equations

The basic equations describing the energy content, angular momemtum, and gyrodynamics of a flywheel are summarized in this section. (Complete details are given in the Appendix.)

The physical size of a flywheel package is usually specified in terms of its energy storage capacity. Knowledge of the amount of stored energy and the corresponding angular speed permits calculation of the moment of inertia of the rotor. The energy stored by a flywheel of any configuration may be expressed as

$$E = \frac{1}{2} I\omega^2 \qquad (2)$$

where E is the stored energy.

Equation 2 gives the fundamental relationship among the rotor moment of inertia, rotor angular speed, and energy storage capacity of the flywheel package. Although the relationship is simple, its application is slightly more complicated because flywheel energy storage capacity can be specified in several ways. These include measures of either the total or useful energy storage capacities, as discussed in the Appendix. The form of Eq. 2 is the same in each case; only the constant of proportionality changes. The moment of inertia may be calculated from known values for E and ω as

$$I = \alpha \frac{2E}{\omega^2} \qquad (3)$$

where α is a constant of proportionality that ranges from 1.1 to 1.3. (Evaluation of the constant of proportionality is illustrated in the Appendix.)

Once the rotor moment of inertia is calculated from Eq. 3, the angular momentum may be evaluated as

$$\vec{H} = \vec{I}\vec{\omega} \qquad (4)$$

Angular momentum is also a vector quantity that possesses both magnitude and sense. Its magnitude is a measure of the resistance of the spinning rotor to changes in orientation of its spin axis. The direction of $\vec{H}$ is also given by the right-hand rule and is identical to that of $\vec{\omega}$. The sense of $\vec{H}$ is important in determining the sense of a reaction torque.

For a given flywheel geometry, the magnitude or $\vec{H}$ depends uniquely on the energy content and operating speed of the flywheel. The magnitude of $\vec{H}$ is given by

$$H = I\omega \qquad (5)$$

Substituting for I from Eq. 3 gives

$$H = \alpha \frac{2E}{\omega} \qquad (6)$$

* Visualize wrapping the fingers of the right hand about the spin axis in the direction corresponding to ω. The thumb would then indicate the direction of $\vec{\omega}$.

These equations illustrate two important general results that must be considered when selecting a flywheel design and its operating parameters. Equation 5 shows that for a given flywheel (I specified) the maximum angular momentum value occurs at maximum operating speed. This means that the largest torque reactions will occur when the flywheel is operating at maximum speed. No lower speed need be considered in the gyrodynamic analysis.

Equation 6 expresses the same information in a different way. It shows that for a flywheel of constant stored energy (αE fixed) the maximum angular momentum is reduced when the maximum rotor speed is increased. This suggests that the maximum operating speed should be chosen as large as possible. Referring again to Eq. 3, we see that for fixed energy high angular speed, ω, gives small moment of inertia, I. Because I is proportional to $1/\omega^2$, the final relationship becomes that shown in Eq. 6.

The final basic equation needed is the relation between changes in orientation of the flywheel axis and reaction torque. If torque, $\vec{T}_a$, is applied to a spinning flywheel package, its angular momentum will change according to [1]:

$$\vec{T}_a = \frac{d\vec{H}}{dt} \tag{7}$$

Equation 7 states that the rate of change of angular momentum is equal to the torque applied to the flywheel package. However, Eq. 7 is not in the most convenient form for our purpose. A better form would be in terms of the equal and opposite reaction torque

$$\vec{T} = -\frac{d\vec{H}}{dt} \tag{8}$$

Here $\vec{T}$ is the torque exerted by the flywheel package in response to the $d\vec{H}/dt$ imposed on it by vehicle motion.

When a vehicle containing a flywheel maneuvers, some or all of its rotation is imposed on the flywheel package.* The rate of rotation imposed is called precession and may be related to the motion of the vehicle as discussed in the following paragraphs.

The concept of precession is illustrated graphically in Fig. 2. To understand the diagram, assume that the flywheel and its containment are attached to a vehicle. When the vehicle maneuvers, some of its rotation is forced upon the flywheel package. As shown in [1], precession rate is equal to the rate of rotation of the flywheel package, which is shown in the figure as $\vec{\Omega}$. Both the magnitude and orientation of $\vec{\Omega}$ depend upon the vehicle maneuver. They are completely unrelated to $\vec{H}$ or to $\vec{\omega}$ which are design and operating characteristics of the flywheel rotor.

Figure 2(a) illustrates schematically the definitions of the three vector quantities, $\vec{\omega}$, $\vec{H}$, and $\vec{\Omega}$, and illustrates again the right-hand rule convention used to define them. Part (b) of the figure illustrates the effect of the precession rate, $\vec{\Omega}$, imposed on the flywheel package. The angular momentum vector at an initial instant is shown by solid lines. At a slightly later instant, its orientation becomes that shown by dashed lines. The difference between the two orientations, when divided by the small time interval, becomes the rate of change of angular momentum. The vector relationship among the quantities is

$$\frac{d\vec{H}}{dt} = \vec{\Omega} \times \vec{H}$$

or

$$\frac{d\vec{H}}{dt} = \vec{H} \times \vec{\Omega} \tag{9}$$

where x represents the cross product between two vectors.

Combining Eqs. 8 and 9 gives the desired relationship among precession rate, angular momentum, and reaction torque exerted by the flywheel package

$$T = \vec{H} \times \vec{\Omega} \tag{10}$$

* The amount of rotation imposed on the package may be reduced by mounting it in gimbals, as with a ship's compass.

The interpretation and physical significance of this result are discussed in detail in the following section, and illustrated in the EXAMPLE CALCULATIONS section later in the paper.

Physical Description of Reaction Torques

Reaction torques arise when the flywheel package resists changes in the orientation of its spin axis caused by vehicle motion. Both the magnitude and sense of the reaction torque must be determined to specify it completely.

The magnitude of the reacton torque is given by

$$T = H\Omega \sin\Theta_{H\Omega} \qquad (11)$$

where $\Theta_{H\Omega}$ is the smallest angle measured from $\vec{H}$ toward $\vec{\Omega}$, as shown in Fig. 3. The maximum reaction torque occurs when $\vec{H}$ and $\vec{\Omega}$ are perpendicular, for them $\Theta_{H\Omega}$ equals 90 degrees and its sine is unity.

The sense of the reaction torque is found by applying the right-hand rule again, as illustrated in Fig. 3. The reaction torque, $\vec{T}$, must be perpendicular to both $\vec{H}$ and $\vec{\Omega}$. It must be normal to the plane that contains $\vec{H}$ and $\vec{\Omega}$ as shown in Fig. 3(b). The sense of $\vec{T}$ is determined by imagining that $\vec{H}$ rotates into $\vec{\Omega}$ through angle $\Theta_{H\Omega}$. When the fingers of the right hand indicate such a rotation, the right thumb points in the direction of the reaction torque, $\vec{T}$. (There is no reaction torque when $\Theta_{H\Omega}$ is zero because then the imposed motion is aligned with the flywheel spin axis.)

Vehicle maneuvers can result in motions about three coordinate axes. The various possibiliites may be described using the coordinate system defined in Fig. 4 to identify vehicle motions.

The longitudinal coordinate axis points in the direction of vehicle motion. Roll involves rotation of the vehicle about the longitudinal axis. Using the right-hand convention, positive roll is defined as clockwise when facing in the direction of vehicle travel. Lateral and vertical coordinate axes are also shown in Fig. 4. Pitch is rotation about the lateral axis. In positive pitch, the front of the vehicle rises relative to the rear. Yaw is rotation about the vertical axis. In positive yaw, the vehicle nose moves left relative to the tail as seen by an observer facing forward.

Each vehicle rotation component that causes precession can produce reaction torque components. The results depend on the orientation of the flywheel spin axis. Three spin axis orientations are possible, one in each corrdinate direction. The reaction torque components that correspond to each vehicle rotation are summarized in Table 1. In the table, the

Table 1. Reaction Torque Components Produced by Vehicle Rotations

Orientation of Flywheel Spin Axis	Imposed Vehicle Rotation (positive direction assumed)		
	Roll	Pitch	Yaw
Lateral	+Yaw	0	-Roll
Vertical	-Pitch	+Roll	0
Longitudinal	0	-Yaw	+Pitch

first column contains the three possible orientations of the flywheel spin axis (the angular veolocity is assumed positive for each orientation). The remaining columns contain the signs of the reaction torque components produced by the positive vehicle rotations shown in the colunm headings.

Consider a flywheel placed with its axis longitudinal in the vehicle. The angular momentum vector, $\vec{H}$, will then point toward the front, since positive flywheel rotation is assumed. Roll causes no reaction torque, because roll produces no change in the flywheel spin axis. Pitch tends to rotate the vehicle about the lateral axis in the direction shown in Fig. 4. Thus $\vec{\Omega}$ for this motion is aligned with the lateral axis. Rotation of the $\vec{H}$ vector into the $\vec{\Omega}$ vector using the right-hand rule results in a reaction torque vector pointed down along the yaw axis. It is thus a torque component that tends to

produce a negative yaw, and is so labeled in the table. Finally, yaw will produce the $\vec{\Omega}$ vector aligned with the yaw axis. Rotation of the $\vec{H}$ vector into the $\vec{\Omega}$ vector using the right-hand rule results in a reaction torque vector pointed along the lateral axis, a positive pitch reaction.

Each of the other table entries can be worked out in similar fashion. The effect of a sign change in either the flywheel angular velocity or in the imposed rotation is to change the sign of the resulting reaction torque component.

The wheelbase, L, is significantly longer than the track dimension, t, of most vehicles. Therefore, torque reactions that tend to pitch or yaw the vehicle are relatively unimportant compared to roll reactions. Roll reactions can be produced by only two combinations of flywheel placement and vehicle motion. One is a lateral flywheel axis placement combined with yawing motions. The other is with a vertical flywheel axis orientation combined with pitching motions. These combinations are discussed in more detail in the next section.

VEHICLE MANEUVERS

The remaining task is to relate the overall vehicle motion to the precession rate, $\vec{\Omega}$. In actual vehicle operation, precession can occur about three axes, when the vehicle:

(1) yaws rounding corners
(2) pitches from a horizontal path, or
(3) rolls about its longitudinal axis

Normal maneuvers would include only the first two cases; an emergency conceivably could introduce any or all of the three cases.

Normal Operation

Consider first motion around corners. Cornering results in yaw, as discussed in the previous section. Assume motion at steady speed, V, along a path of constant radius, R, as shown in Fig. 5. From the geometry of the figure,

$$s = R\Theta$$

and

$$V = \frac{ds}{dt} = R\,\frac{d\Theta}{dt} = R\Omega$$

Thus the precession rate magnitude is

$$\Omega = \frac{V}{R} \qquad (12)$$

The lateral acceleration experienced by the vehicle will be given by

$$a_r = \frac{V^2}{R} \qquad (13)$$

Observations [2] suggest that under normal conditions, drivers operate vehicles such that $a_r < 0.3$ g, where g is the acceleration of gravity. Tire adhesion limits the maximum value of a_r, even under emergency conditions, to values below about 0.6 g. Combining Eqs. 12 and 13 gives either

$$\Omega = \sqrt{\frac{a_r}{R}} \qquad (14a)$$

or

$$\Omega = \frac{a_r}{V} \qquad (14b)$$

Thus the precession rate, Ω, increases with lateral acceleration. At any fixed value of lateral acceleration, it increases as maneuver radius is reduced, i.e. as a turn becomes "sharper". Physically this latter conclusion results from the vehicle turning through a larger yaw angle during any time interval.

The relationships expressed by Eqs. 12, 13, and 14 may be displayed graphically as shown in Fig. 5. The chart may be used to evaluate vehicle precession rate in yaw using as inputs either vehicle speed and turn radius or lateral acceleration and turn radius. Use of the charts is illustrated in the EXAMPLE CALCULATIONS section.

Pitch motions in normal operation could be caused by changes in road surface slope. Such departures from a horizontal path could occur in several ways, two are shown in Fig. 6*. Both can be analyzed using the methods developed in the Appendix. The results suggest that curbs are much more significant than ramps, and that a small vehicle is more affected because of its shorter wheelbase dimension. Figure 6 contains a summary of the comparisons. It shows pitch precession rate, Ω, to be a function of the parameter V/L, the vehicle speed divided by wheelbase length.

Significant roll motions are unlikely during normal vehicle operation.

Emergencies and Accidents

Emergency situations could result from system failures such as loss of vacuum in the flywheel housing or bearing failure. Although torque reactions would be produced by such failures, they would not involve gyrodynamics. Thus they could be analyzed by conventional methods.

Accident situations require consideration of all the gyrodynamic possibilities. Motion about any vehicle axis could be exaggerated as the result of collisions with fixed objects or impacts from other vehicles.

Yawing motions have been discussed previously with the results presented in Fig. 6. When no collision occurs, tire adhesion limits the yaw rate to values below about 0.5 rad/sec. Collisions could introduce somewhat higher yaw rates. The worst situation might be a collision between one end of the vehicle and a stationary object, converting all of the vehicle kinetic energy to spin about the vertical axis. The maximum spin rate would probably be less than the ratio of forward speed to wheelbase length, V/L, as shown in the Appendix. However, for a small car at legal speed limit this might imply a yaw rate as great as 10 rad/sec.

* The curb-climbing maneuver was suggested by an analysis presented in Ref. 3.

A similar conversion of kinetic energy to angular motion about the roll axis could also produce large angular speeds. Using the ratio V/t could produce a roll rate as high as 30 rad/sec after a vehicle strikes a curb. Such a precession would, according to Table 1, be reacted into yawing or pitching tendencies. Of course, the maximum vehicle moment of inertia is about these axes.

Dimensional reasoning suggests that the vehicle moment of inertia for yaw and pitch will be greater than for roll by at least the ratio $(L/t)^2$. As suggested in the previous two paragraphs, the corresponding reaction torques about these two axes would be approximately in the ratio t/L. Since $L/t > 1$, this confirms that responses to torques in yaw and pitch will be much less than the response to roll torques. In combination with Table 1, this analysis shows that vertical is the most favorable orientation for the flywheel spin axis.

DEVELOPMENT OF NOMOGRAPH

All of the basic equations described earlier may be displayed in simple graphs. Together with a graph of the results derived for precession rate in the last section, they may be combined into a nomograph which can be used to estimate reaction torques quickly and easily.

The first basic equation was for the usable kinetic energy of a flywheel. The usable kinetic energy is related to the vehicle mass and operating speed for a hybrid vehicle as shown in Fig. 7. The figure is constructed by plotting total vehicle weight versus usuable flywheel kinetic energy (assuming that the sum of vehicle kinetic and flywheel usable energies is constant, and that the operating speed range of the flywheel is 2). The maximum design operating speed of the vehicle is the constant parameter along the sloping lines in the log-log plot.

To enter the nomograph, the appropriate value of usable flywheel kinetic energy may be determined approximately from Fig. 7. One enters on the ordinate at the appropriate vehicle weight, reads across to the intersection with maximum design operating speed, then reads down to the abscissa to determine the energy requirement. (Direct entry on the abscissa with the value of flywheel usable stored energy is also possible.)

The second basic equation needed is the relation between flywheel kinetic energy and angular momentum. This relationship was expressed by Eq. 3 and is displayed in Fig. 8. In the figure angular momentum is plotted versus flywheel usable stored energy. The diagonal lines represent constant angular speeds. The graph is entered along the abscissa with the predetermined value of the flywheel usable stored energy. This value is projected up to the intersection with a maximum flywheel operating speed line. The intersection is then projected horizontally to the ordinate to determine the corresponding value of flywheel angular momentum.

Evaluation of the vehicle precession rate in yaw was discussed previously in connection with Fig. 5. It is assumed here that the vehicle precession rate has been thus determined.* If more than one component of precession is present, the following discussion applies to each component.

Equation 11 provides the necessary relation among angular momentum, precession rate, and reaction torque. Figure 9 was developed from Eq. 11 and is used as follows. Enter Fig. 9 at the ordinate with the angular momentum value determined previously. Project horizontally to the right. Also enter the figure with the precession rate component determined previously from Fig. 5. Project vertically upward. The intersection of these two projections corresponds to the reaction torque component produced by the angular momentum and precession rate conditions imposed. The magnitude of the resulting reaction torque is found by interpolating among the slanted lines. Its axis direction and sense may be determined from Table 1.

This completes development of the elements needed to assemble a nomograph for the approximate evaluation of gyrodynamic reaction torques caused by known motion inputs to the flywheel package. The completed nomograph is assembled in Fig. 10; its use is illustrated in the next section by detailed solution of two example situations.

Complaint suspension sytems for flywheel packages need more detailed analysis. Compliance allows the position of the flywheel spin axis to rotate relative to the vehicle. Even if the rotor were originally aligned with one vehicle axis, more than one reaction torque component would be introduced with the passage of time. Such effects are described briefly in the Appendix. A more comprehensive treatment may be found in [4].

EXAMPLE CALCULATIONS

The two cases that have been chosen to illustrate use of the nomograph are:

(1) flywheel-propelled bus
(2) flywheel-augmented automobile

Each of these cases is solved in detail below for the limit maneuver of 0.6 g lateral acceleration at a vehicle speed of 20 mph.

Flywheel-Propelled Bus

Specifications:

W = 30,000 pound weight
E = 12 kW-hr usable flywheel energy
ω = 12,000 rpm maximum operating speed
L = 25 ft wheelbase
t = 6 ft track dimension

Maneuver:

a_y = 0.6 g lateral acceleration
V = 20 mph

* It is also assumed that the flywheel package suspension is stiff, so that the package precesses with the vehicle. This point is discussed in more detail in the Appendix.

Analysis: Flywheel usable stored energy is known. Enter nomograph or Fig. 8 at E = 12 kW-hr and project upward to intersection with slanting line representing ω = 12,000 rpm. At this intersection project horizontally to find $\vec{H}$ = 40,000 ft-lbf-sec. Project this value horizontally or enter Fig. 9.

The vehicle precession rate is determined from Fig. 5 for the specified maneuver. Enter Fig. 5 with vehicle speed, V = 20 mph, and project horizontally to the right. At the intersection with a_r = 0.6 g, project downward to find Ω = 0.7 rad/sec. Project this value downward (or enter Fig. 9).

At the intersection of H = 40,000 ft-lbf-sec and Ω = 0.7 rad/sec, read the reaction torque value, T = 30,000 ft-lbf. Then determine its sense from Table 1. With the spin axis horizontal and positive precession in yaw, the reaction torque will tend to produce positive pitch on the vehicle. Thus it will tend to lift the front of the vehicle.

The vehicle wheelbase is L = 25 ft. The reaction torque of 30,000 ft-lbf would unload the front axle by approximately 1200 pounds. The load on the rear would increase by the same amount. Compared to the static front and rear axle loads of about 10,000 and 20,000 pounds, respectively, these changes are of little significance.

With the spin axis placed laterally, a roll reaction would be produced for this maneuver. However, there would be no danger of overturning the vehicle. The maximum possible change in load distribution would be +/-2,500 pounds per side. This would be insignificant compared to the static distribution of 15,000 pounds per side.

For this case an accident that converted vehicle kinetic energy into angular motion could produce a precession rate in yaw only slightly in excess of 1.2 rad/sec. The corresponding value in roll could approach 5 rad/sec. However, either motion component would still produce small wheel reactions compared to the static loads.

Flywheel-Augmented Automobile

Specifications:

W = 3,600 pounds
Hybrid system, Vmax = 60 mph
ω = 25,000 rpm
L = 8 ft
t = 5 ft

Maneuver:

a_r = 0.6 g lateral acceleration
V = 20 mph

Analysis: With a hybrid system, it is assumed that the flywheel usable energy storage required to absorb the vehicle kinetic energy upon regenerative braking is to be determined. It is found from Fig. 7 or the nomograph by projecting vehicle weight horizontally from the ordinate. At the intersection with the sloping line that represents Vmax = 60 mph, the required usable stored energy is seen to be E = 0.2 kW-hr. Project this value upward (or enter Fig. 8 at the abscissa).

The flywheel angular momentum is determined at the intersection of the energy projection and the line representing ω = 25,000 rpm. The corresponding value is approximately H = 600 ft-lbf-sec. Project this value horizontally to the right (or enter Fig. 9 on the ordinate).

The precession rate for this maneuver has been determined to be Ω = 0.7 rad/sec. Project this value upward from the abscissa (Fig. 9). The intersection with the angular momentum projection is at a reaction torque value of approximately T = 300 ft-lbf. This value would correspond to wheel reactions in the order of 40 to 60 lbf peraxle. Such small reactions would be entirely negligible for a vehicle of this weight. Other possible reaction components may be evaluated using the methods presented in the previous example.

CONCLUSIONS

A simplified analysis of the gyrodynamics of kinetic energy wheels has been presented in this paper. The basic parameters of kinetic energy, angular momentum, precession rate, and reaction torque were combined into a nomograph. The nomograph permits rapid estimation of the reaction torques caused by vehicle maneuvers, and will be useful for preliminary design analysis.

Use of the nomograph was illustrated by two examples worked out in detail. The examples demonstrated the use of the simplified techniques presented. The results also led to conclusions that gyrodynamic reaction torques may be insignificant for typical design situations.

REFERENCES

[1] Fox, R. W. and McDonald, A. T., Introduction to Fluid Mechanics, 2nd ed. New York: Wiley, 1978.

[2] Rice, R. S. and Dell Amico, F., "An Experimental Study of Automobile Driver Characteristics and Capabilities," Calspan Report No. ZX-5208-K-1, Prepared for General Motors Corporation under Contract No. CC-222, March 1974.

[3] "Analysis of Gyrodynamic Sensitivity of Flywheel-Propelled Street Vehicles," AiResearch Manufacturing Company of California, Report No. 75-11647, June 23, 1975.

[4] Otaki, H., "Some Analysis of Gyroidal Effect and the Development of a Flywheel Powered Vehicle," Society of Automotive Engineers, Paper No. 800835, 1980.

APPENDIX

The moment of inertia of a flywheel rotor is given by

$$I = \int m(\text{rotor}) r^2 dm \qquad (A.1)$$

In Eq. A.1, dm is the mass of a differential element located at radius, r, from the spin axis. dm may be expressed as

$$dm = \rho d\forall = \rho 2\pi r\, t(r) dr \qquad (A.2)$$

so that for uniform rotor density the moment of inertia is a function of rotor shape that may be expressed as

$$I = 2\pi\rho \int_0^R r^3 t(r) dr$$

For a disc of uniform thickness, t,

$$I(\text{disc}) = 2\pi\rho t \int_0^R r^3 dr =$$

$$\rho\pi R^2 t \frac{R^2}{2} = M \frac{R^2}{2} \qquad (A.3)$$

where M is the rotor mass.

Some flywheel design concepts use materials of varying density. To analyze those cases, density must also be expressed as a function of radius; it must be left under the integral sign when Eq. A.2 is evaluated.

The moment of inertia of a rotor can also be measured experimentally. The usual procedure is to mount the flywheel rotor as a stiff torsional pendulum. The moment of inertia can be calculated from the measured period or frequency of oscillations.

The total energy stored by a flywheel rotor of any configuration may be expressed in terms of its moment of inertia and angular speed as

$$E_t = \frac{1}{2} I \omega^2 \qquad (A.4)$$

It is not practical to extract so much energy that the flywheel stops rotating. Operation is usually between a maximum speed determined by stress and life considerations, and a minimum speed chosen as a compromise between

energy storage and output speed range. The usable stored energy is an important measure of flywheel energy storage capacity. The usable stored energy may be expressed in terms of the operating speeds as

$$E_u = \frac{1}{2} I (\omega_{max}^2 - \omega_{min}^2) \qquad (A.5)$$

In terms of the maximum operating speed,

$$E_u = \frac{1}{2} I \left[\omega_{max}^2 \left[1 - \left(\frac{\omega_{min}}{\omega_{max}}\right)^2\right]\right.$$

or

$$E_u = \frac{1}{2} I \omega_{max}^2 (1 - \beta^2) \qquad (A.6)$$

where the operating speed ratio is defined as $\beta = \omega_{min}/\omega_{max}$. A typical value is $\beta = 0.5$. At any intermediate operating speed, $\omega_{min} \leq \omega \leq \omega_{max}$, the usable energy content is

$$E_u = \frac{1}{2} I \omega_{max}^2 \left[\left(\frac{\omega}{\omega_{max}}\right)^2 - \beta^2\right] \qquad (A.7)$$

The physical size on an energy storage wheel is commonly specified in terms of its maximum usable energy storage capacity.

Equation A.6 may be written in the form of Eq. 1 in the body of the paper. Then the moment of inertia may be expressed as

$$I = \frac{1}{1 - \beta^2} \frac{2E_u}{\omega_{max}} \qquad (A.8)$$

Comparison with Eq. 1 shows the constant of proportionality to be

$$\alpha = \frac{1}{1-\beta^2} \qquad (A.9)$$

For $\beta = 0.50$, $\alpha = 1.33$, and for $\beta = 0.33$, $\alpha = 1.12$, which are representative of values typically used in practice.

Yawing motions that result from normal cornering were analyzed in the body of the paper. Pitching motions were mentioned but not analyzed in the paper. Two cases were identified: ramps and curbs; more detailed analyses follow.

The geometry of Fig. 6 suggests that ramp climbing may be analyzed in terms of ramp angle, θ, vehicle speed, V, and wheelbase length, L. The maximum pitch precession rate occurs momentarily after the front wheels contact the ramp. At that instant, the velocity component of the front, perpendicular to the line joining wheel centers, is approximately

$$V_f = V \tan\theta$$

The corresponding precession rate is

$$\Omega_{pitch} = \frac{V_f}{L} = \frac{V \tan\theta}{L} \qquad (A.10)$$

For a 10-degree ramp negotiated at V = 55 mph by a vehicle with wheelbase L = 8 ft, V/L = 6.88 mph/ft, and

$$\Omega \; 55 \frac{mi}{hr} \times \tan 10^0 \times \frac{1}{8 \; ft} \times 5280 \frac{ft}{mi} \times \frac{hr}{3600 \; sec} = 1.78 \; rad/sec$$

as shown in Fig. 6. Precession rates are smaller for larger vehicles as the figure shows.

The curb-climbing maneuver can also be analyzed approximately using the geometry of Fig. 6. Basically the approximation is that the front of the car climbs the curb of height, h, during the time it takes the vehicle to travel from the point where the tire first contacts the curb until the centerline of the wheel is directly above the curb. Using angle, γ, defined as in Fig. 6, the geometry gives

$$r(1 - \cos\gamma) = h$$

or

$$\cos\gamma = 1 - \frac{h}{r}$$

where r is the wheel radius. Once γ is known, the distance travelled is approximated by $r\sin\gamma$, so that the travel time is

$$\Delta t \cong \frac{r\sin\gamma}{V}$$

The increment of precession angle during Δt is

$$\Delta\theta \cong \frac{h}{L}$$

so that

$$\Omega \cong \frac{\Delta\theta}{\Delta t} = \frac{hV}{Lr\sin\gamma}$$

Finally, the substitution may be made that

$$\sin\gamma = (1-\cos^2\gamma)^{1/2} =$$

$$[1 - (1 - \frac{h}{r})^2]^{1/2}$$

to obtain the precession rate as

$$\Omega \cong \frac{hV}{Lr[1-(1-h/r)^2]^{1/2}} \qquad (A.11)$$

For a passenger car with L = 8 ft and r = 12 in. mounting a 4-in curb at V = 55 mph (80.7 ft/sec)

$$\Omega \left(\frac{4 \text{ in.}}{12 \text{ in.}}\right) \quad 80.7 \frac{\text{ft}}{\text{sec}} \quad \text{x}$$

$$\frac{1.}{8 \text{ ft}} \quad \frac{1}{[1-(\frac{4}{12})^2]^{1/2}} = 3.57 \text{ sec}^{-1}$$

or 3.57 rad/sec. The variation with V/L is linear, as shown in Fig. 6. For a bus, Ω = 1 rad/sec, even for a 6-in. curb, because of its larger tires and longer wheelbase.

In an accident situation, it is likely that a moving vehicle will collide with a massive stationary object. The worst case of such a collision would be the situation where one end of the vehicle struck the object as the vehicle was moving sideways with its initial speed. In the resulting collision, the end of the vehicle would remain stationary and the center of mass would continue to travel, imposing a large precession rate on the vehicle. The spin rate could be estimated in this worst case by assuming momentum is conserved during the collision. This would surely overestimate the actual spin rate for any realistic situation.

If momentum is conserved, the impulse that acts against the vehicle during the collision would reduce its linear momentum, and at the same time increase its angular momentum. The momentum balance equations for the initial and final situations would read

Initial momentum: mV_o

Final momentum: $mV_f + \frac{I\omega}{L/2}$

For a rod of uniform density, $I = mL^2/12$. Also, from the mechanics of the collision, $\omega = V/L/2 = 2V/L$, where L is the wheelbase length. Substituting and combining the two momentum equations gives

$$V_f = \frac{3V_o}{4}$$

and

$$\omega = \frac{2V_f}{L} = \frac{3V_o}{2L} \qquad (A.12)$$

Evaluating Eq. A.12 for a passenger car gives

$$\omega = \frac{3}{2} \text{ x } 80.7 \quad \frac{\text{ft}}{\text{sec}} \text{ x } \frac{1}{8 \text{ ft}} = 15.1 \text{ rad/sec}$$

Although this is a large value, it is unlikely that it would ever be achieved for at least three reasons:

(1) the collision with a fixed object is unlikely to conserve momentum
(2) the moment of inertia of an actual vehicle is much larger than that of a rod of uniform density
(3) the probability of a collision directly at the end of the vehicle is quite low

The corresponding precession value for the bus case is about 3 times smaller due to the longer wheelbase of the bus.

The other post-accident possibility is the rollover. The reasons just quoted cannot quite so readily be applied to the rollover. A rollover accident might be characterized like the collision just described. However, the relevant length is the height between the vehicle center of mass and the road surface. This height is approximately half the track dimension of the vehicle. This length is 3 to 5 times smaller than half the wheelbase. Therefore, precession rates in the roll

direction might be 3 to 5 times larger than those calculated in yaw.

Precession about the roll axis gives rise to reaction torques about either yaw or pitch axes according to Table 1. The moment of inertia of the vehicle that resists these reactions is the greatest about these axes. Without considering a specific vehicle it is impossible to draw further general conclusions.

Some designers have advocated mounting a flywheel energy storage package in a compliant suspension so it can rotate more or less freely with respect to the vehicle during maneuvers. If the motion is truly free, like the gimbals of a ship's compass, there will be no reaction torques when the vehicle maneuvers. Instead the flywheel package will maintain the original orientation of its axis throughout the vehicle motion. If the flywheel spin axis is vertical, then one would expect the flywheel package to "seek" that direction at all times. If the vehicle went up hill and down, it would eventually return to a level attitude, at which time the flywheel would be in its original position.

Use of a compliant suspension with considerable stiffness would limit the motion of the flywheel package relative to the vehicle. This might be an advantage if electrical cables were used to transmit energy. However, the suspension stiffness would introduce a new dynamic problem: the coupling between the vehicle and the flywheel package. This problem is addressed in a limited way in Ref. 4; its discussion is beyond the scope of this paper.

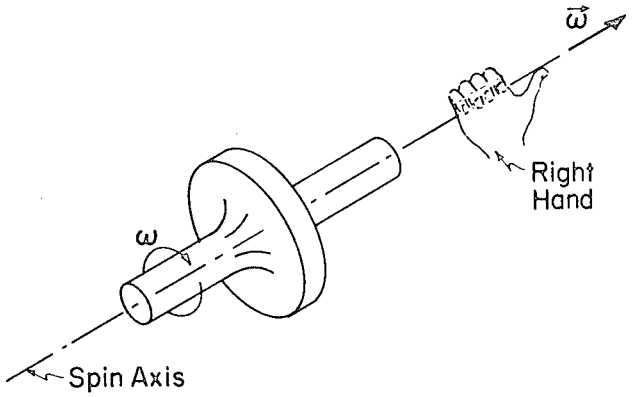

Fig. 1 Geometry of Flywheel Rotor and Notation for Description of Angular Velocity

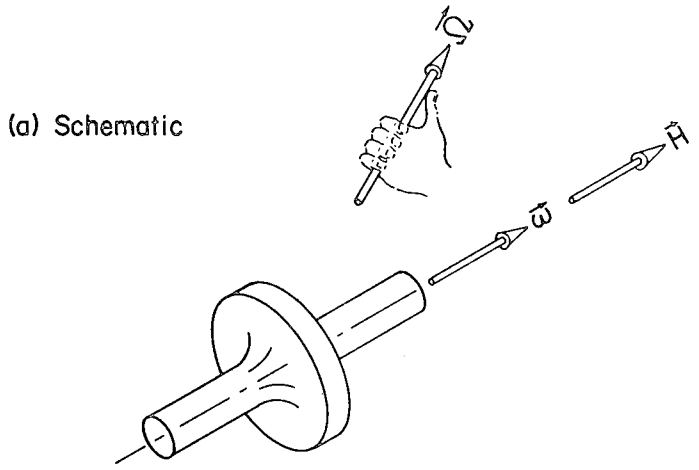

(b) Effect of precession rate on angular momentum

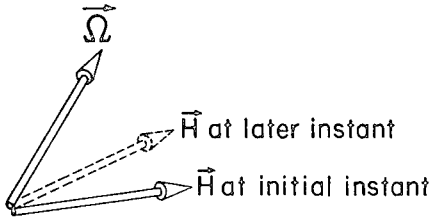

Fig. 2 Schematic Showing Angular Velocity, Angular Momentum, and Precession Rate Vectors, and Rate of Change of Angular Momentum

(a) Definition of $\theta_{H\Omega}$

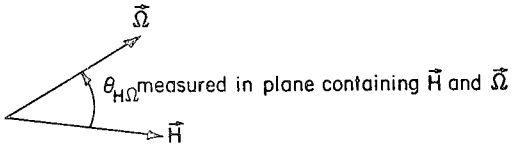

(b) Sense of reaction torque, $\vec{T}$

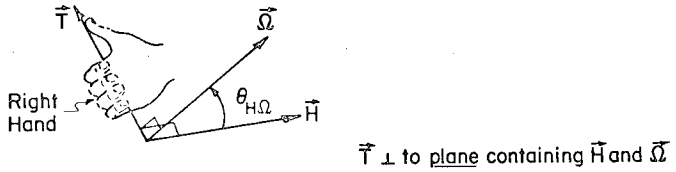

Fig. 3 Schematic Showing Angle between Angular Momentum and Precession Rate Vectors, and Defining Sense of Reaction Torque

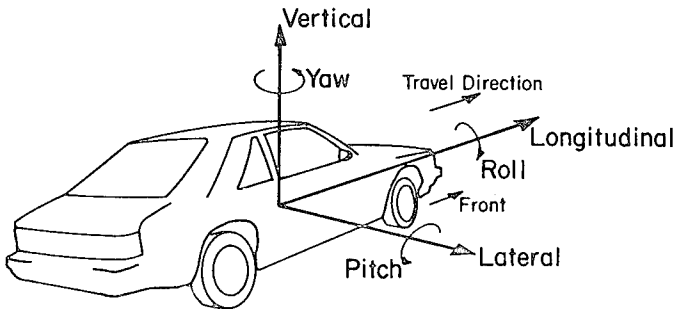

Fig. 4 Coordinate System Used to Describe Vehicle Motions

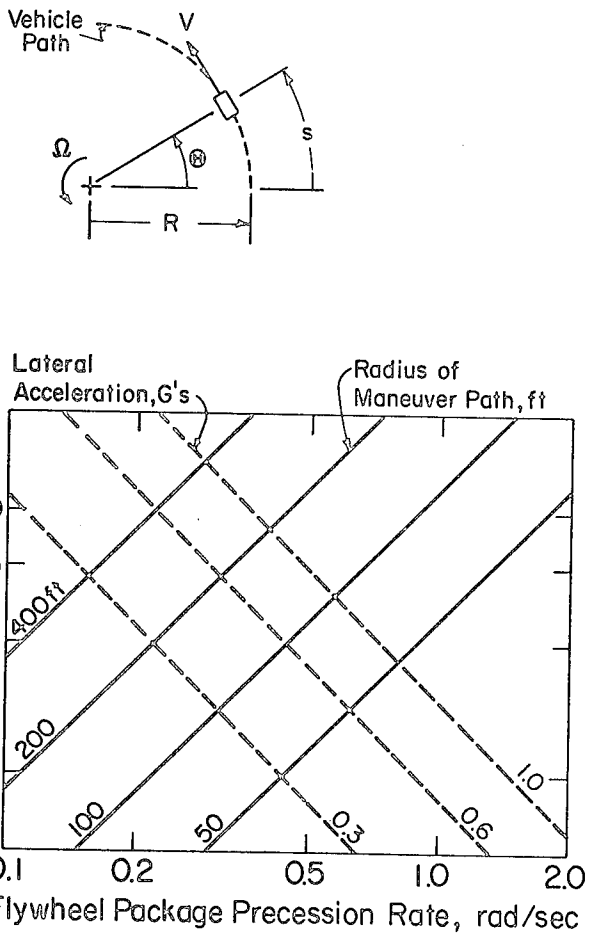

Fig. 5 Vehicle Cornering Maneuver Speed vs. Precession Rate, Showing Lines of Constant Radius and Constant Lateral Acceleration

(a) Changes in surface contour

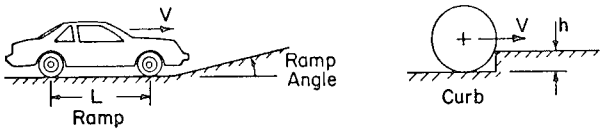

(b) Summary of pitch precession rate results

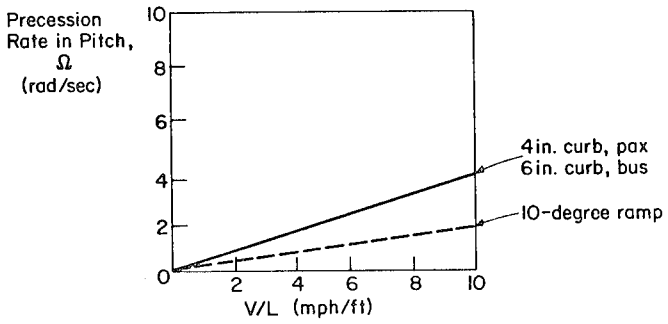

Fig. 6 Precession Rate in Pitch on Ramp or Curb vs. Vehicle Speed and Geometry Parameter

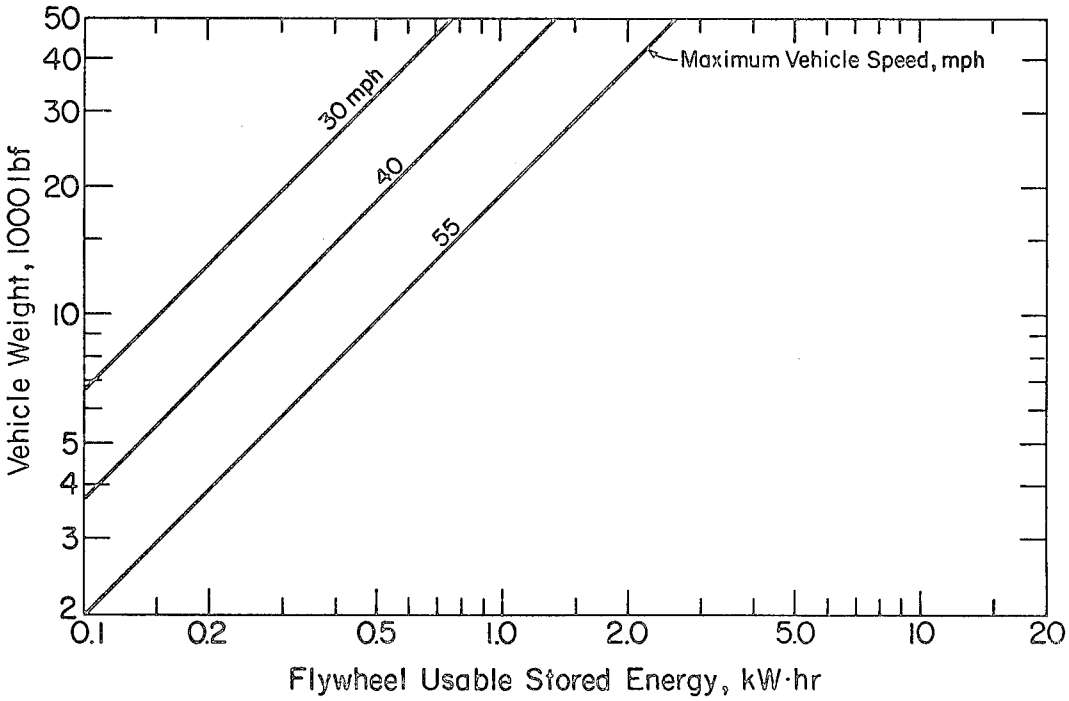

Fig. 7 Vehicle Weight vs. Flywheel Usable Stored Energy with Vehicle Speed as a Parameter

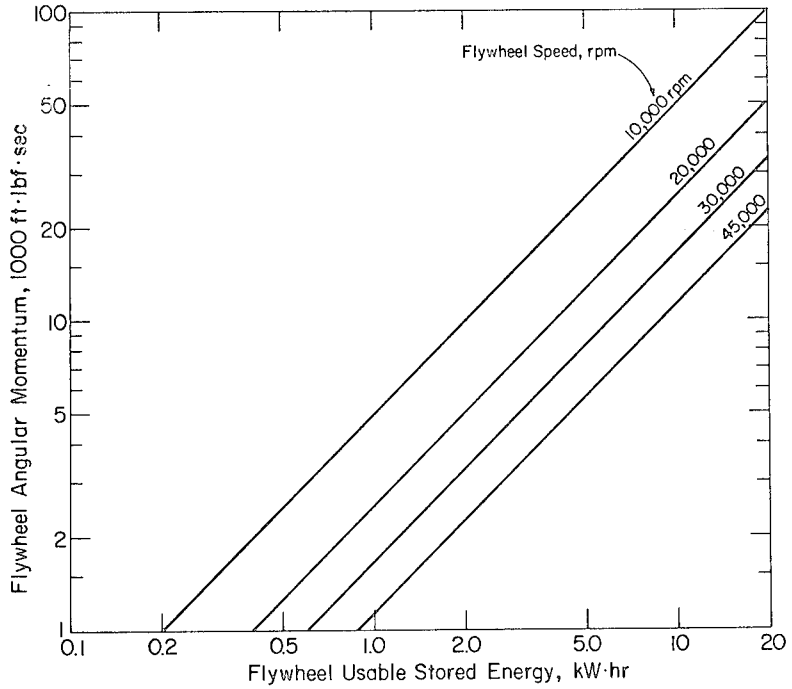

Fig. 8 Flywheel Angular Momentum vs. Flywheel Usable Stored Energy with Maximum Operating Speed as a Parameter

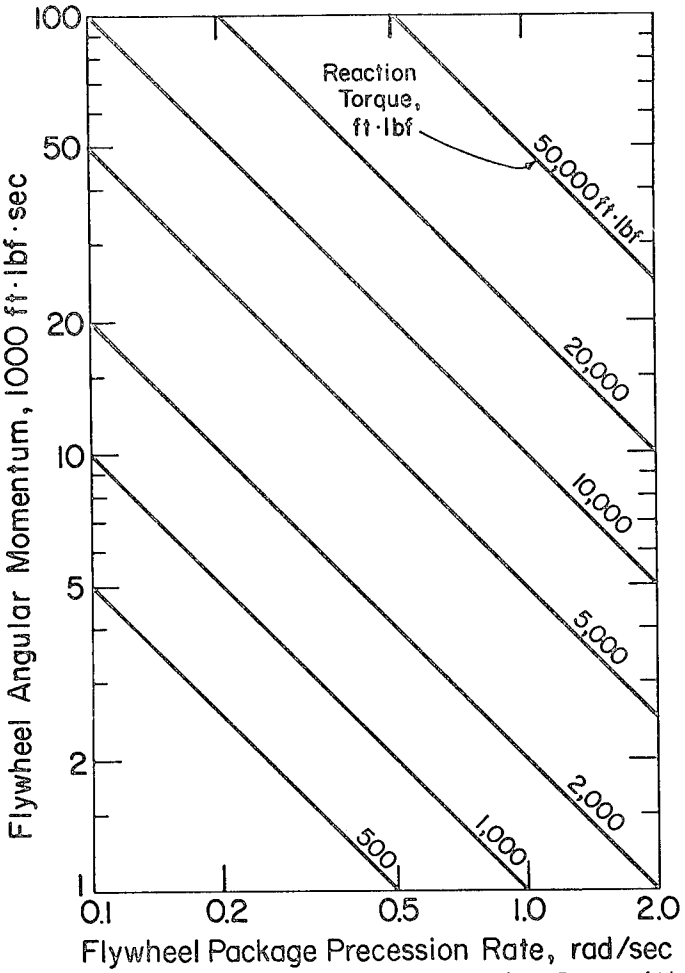

Fig. 9 Flywheel Angular Momentum vs. Precession Rate with Flywheel Reaction Torque as a Parameter

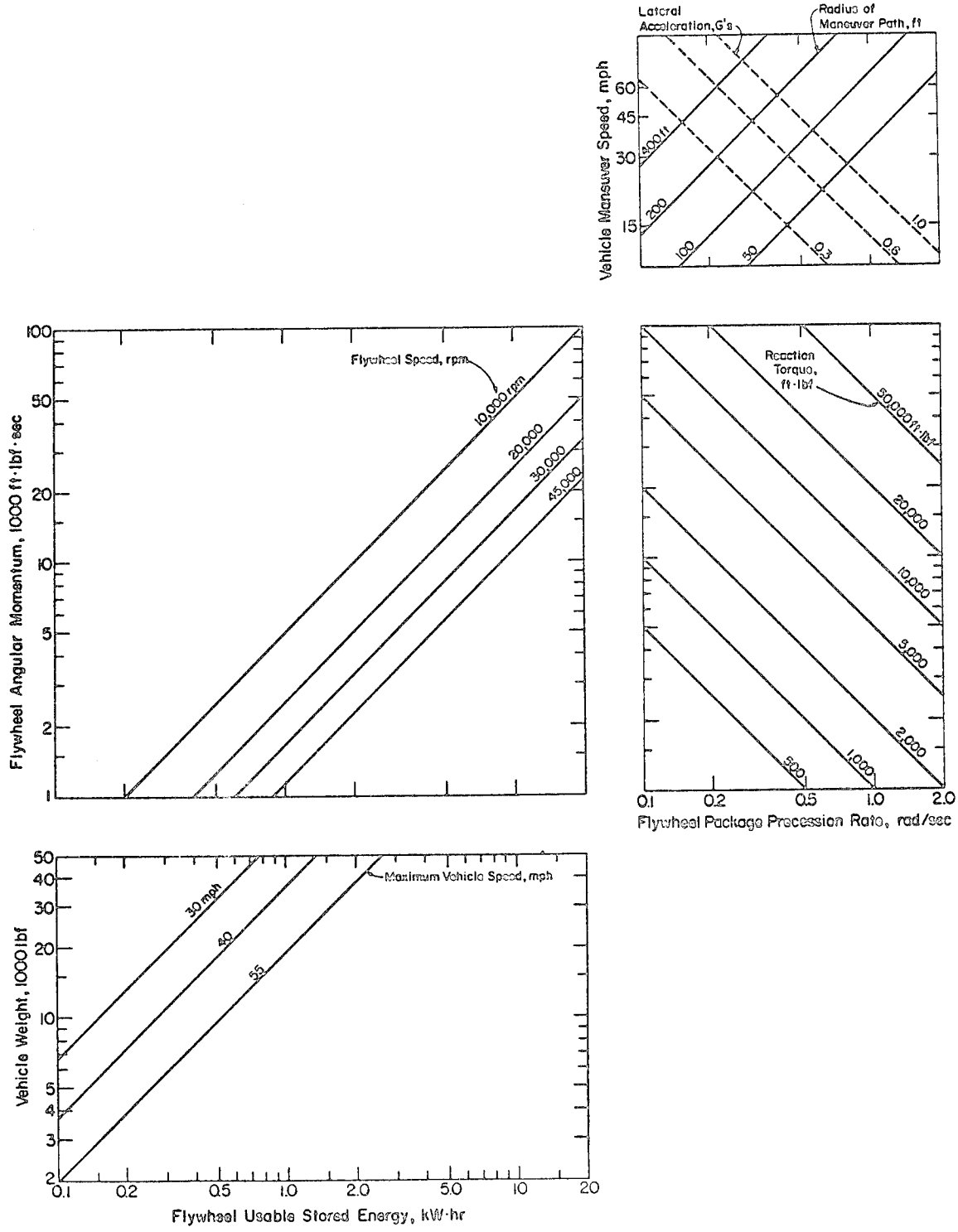

Fig. 10 Nomograph for Estimating Reaction Torque During Maneuvers of Flywheel Package

DOE/ET/20279-100

PERFORMANCE TESTING AND ECONOMIC ANALYSIS OF A PHOTOVOLTAIC FLYWHEEL ENERGY STORAGE AND CONVERSION SYSTEM* ** +

R. D. Hay, A. R. Millner++ and P. O. Jarvinen
Massachusetts Institute of Technology
Lincoln Laboratory
P. O. Box 73
Lexington, Massachusetts 02173

ABSTRACT

A subscale prototype of a flywheel energy storage and conversion system for use with photovoltaic power systems of residential and intermediate load-center size has been designed, built and tested by MIT Lincoln Laboratory. System design, including details of such key components as magnetic bearings, motor generator, and power conditioning electronics, is described. Performance results of prototype testing are given and indicate that this system is the equal of or superior to battery-inverter systems for the same application. Results of cost and user-worth analysis show that residential systems are economically feasible in stand-alone and in some utility-interactive applications.

INTRODUCTION

This report describes the MIT Lincoln Laboratory development program for inertial energy storage systems to be used with residential photovoltaic installations. Inertial energy storage will compete with batteries which are now the only practical electrical energy storage component available. Desirable characteristics of any energy storage system are: low standby losses, high operating efficiency, and high energy density. In contrast to storage batteries, inertial energy storage systems have the capacity for short duration high discharge rates without degradation. This characteristic can be used to advantage in a residence where a high peak to average load exists. In industry, high demand charges can be reduced by using inertial energy storage to supply peak power needs. The development of magnetic bearings and high-performance flywheel rotors makes possible economically attractive energy storage systems which can meet these requirements. The input and output electronics are integrated with the motor/generator for maximum performance and reliability at minimum cost.

The design and testing of a laboratory 1/10 scale 1-4 kWh flywheel system is described, as are the preliminary design of a residential 40-kWh peak energy storage system and the results of industrial cost studies of the residential unit. A larger 500-kWh-peak energy storage load center has been costed using scaling laws and input data derived from the small units. A summary of user-worth studies is presented which relates the amount of energy stored to the area of PV collector in terms of a net cost benefit to the potential buyer. The specifications for the three inertial energy storage systems are shown in Table I.

DESCRIPTION OF 1/10 SCALE LABORATORY SYSTEM

The features and characteristics of this system have been previously described [1, 2] but a brief review is given for clarity. Figure 1 is a section through the magnetic bearing and shaft assembly without the external supports. The principle components are:

- Flywheel rotor
- Motor/generator
- Six magnetic bearings
- Shaft
- Quill
- Touchdown bearings

*This work was sponsored by the U. S. Department of Energy.
**The U. S. Government assumes no responsibility for the work presented.
+Presented at the 1980 Flywheel Technology Conference, 26-30 October 1980, Scottsdale, Arizona.
++Dr. Millner's present address is: Tri-Solar Corporation, 6 Alfred Circle, Bedford, Massachusetts 01730.

10139-11

TABLE I
FLYWHEEL SYSTEM PARAMETERS

PARAMETERS	UNIT	SUBSCALE	40 kWh RESIDENCE	500-kWh LOAD CENTER
ENERGY STORED	kWh	1 TO 4	40	500
ROTOR WEIGHT	lbs	350	2,700	33,000
ENERGY AVAILABLE	kWh	0.6 TO 2.5	25	325
MAXIMUM SPEED	krpm	15	12	6.5
POWER INPUT	kW	0.50	8	100
POWER OUTPUT				
STEADY STATE	kW	0.50	8	100
PEAK	kW	0.625	10	100
INPUT O.C. VOLTAGE MAXIMUM	VOLTS DC	400	400	800
INPUT S.C. CURRENT MAXIMUM	AMPS DC	2.5	40	260
INPUT VOLTAGE RANGE	VOLTS DC	220-330	220-330	440-660
INPUT CURRENT MAXIMUM	AMPS DC	2.3	35	230
OUTPUT VOLTAGE	RMS VOLTS DC	110	220 C.T.	440
MAXIMUM OUTPUT CURRENT	RMS AMPS PER PHASE	5.6	45	130
PHASES	NO.	1	1	3

C71-1020

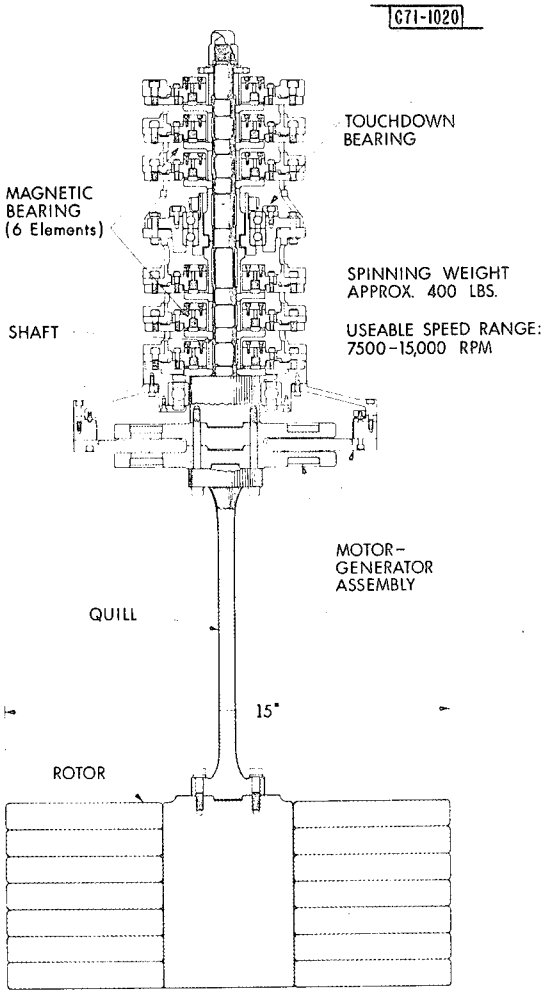

Figure 1
1/10-scale experimental flywheel.

The touchdown bearings are used to support the shaft only if the magnetic levitation is removed, otherwise there is no contact. The quill allows the flywheel to be self-aligning if the rotor is not perfectly balanced. The present flywheel, which has a specific energy of 10 Wh/kg, is made from steel discs pressed onto a hub. One or more advanced design ($\sim$40 Wh/kg) flywheel rotors of potentially low fabrication cost will be procured and will be substituted for the steel rotor to test a configuration typical of a residential energy storage system. The steel rotor is balanced within 1.3×10^{-6} kgm, however the quill mounting is designed to operate with an imbalance up to 4.3×10^{-4} kgm.

Figure 2 shows the complete assembly ready to be placed in the vacuum tank. A thick enclosure surrounds the steel flywheel as a safety shield for containment in the unlikely event of a quill or flywheel failure. This heavy shield would be completely unnecessary for a filamentary composite rotor which has a characteristically benign failure mode should a failure take place. All large components were spin tested to 10% over the 15,000-rpm maximum operating speed.

Figure 3 is a block diagram of the electronic systems. DC from the array is switched by the SCR motor drive into the motor/generator armature windings. Hall generators provide motor phase signals for unidirectional rotation at starting. The ouput cycloconverter is powered from the motor-generator armature terminals. Power can flow directly from the motor bridge to the cycloconverter or be put into or withdrawn from the flywheel through the armature coils. The cycloconverter transforms the variable voltage and frequency three-phase motor AC to single-phase 60 Hz, 117 V. Power flow is governed by the relative voltages of the motor drive, the back EMF of the armature and the cycloconverter. For storing energy the motor drive voltage is always constrained to be equal to or greater than the back EMF which is proportional to shaft speed. The cycloconverter input voltage is always equal to or less than the back EMF. The cycloconverter type of frequency changer was selected for the 1/10-scale Laboratory system because of its potential for stand-alone frequency stability and adaptability in using less expensive SCR semiconductors.

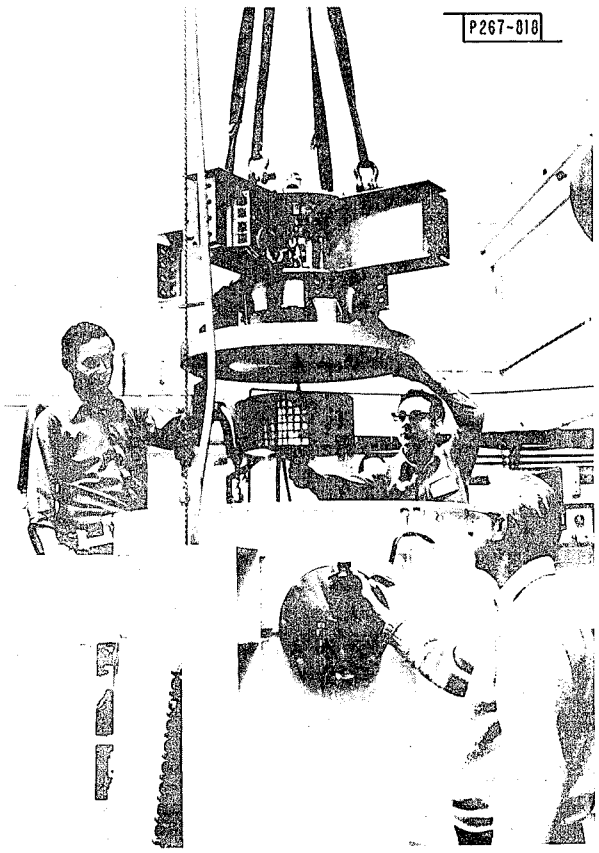

Figure 2
Flywheel assembly and vacuum tank.

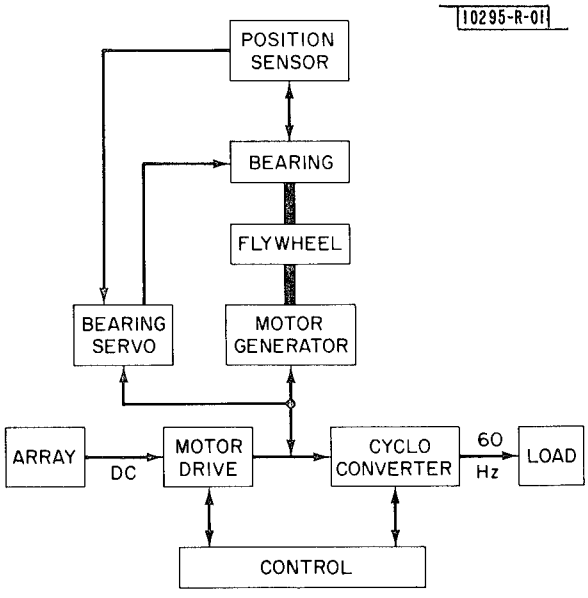

Figure 3
Flywheel system schematic.

The bearing servo functions to control the axial position and thus maintains constant magnetic flux (and lift force) in the air gap. An error signal from the axial position probe modulates the current in the bearing flux control coil to maintain equilibrium. Long-term position stability has been found to be excellent. Peak current for lift-off is supplied by a storage battery.

It is important to note that this is an experimental/developmental energy storage system. The experience gained in building and operating the system will be used in the design of prototype residential units.

EXPERIMENTAL MEASUREMENTS

Diagnostic instrumentation consists of transverse shaft position probes located in the upper and lower magnetic bearing sections. In addition, temperature thermistors are imbedded in the armature stator and attached to the mounting structure. Other measurements of power, voltage, wave shape, etc., were taken with standard laboratory instruments. After completing the flywheel assembly, initial lift-off of the magnetic bearings was achieved without difficulty. Zero-speed-vibration characterization measurements were taken of the suspended shaft and flywheel. These tests confirmed the resonant modes which were calculated with a computer model of the system [3].

Power loss and efficiency were calculated from measured current and voltage in or out of the component being tested. In the case of AC power, the output power factor, which has been measured to be greater than 0.95, is assumed to be unity. The measurement precision is approximately $\pm$ 3 W or 3% of the measured power, whichever is greater.

Results of initial measurements indicate that there is a fixed loss, exclusive of magnetic bearing power, of 4 W at 7500 rpm, which increases to 6 W at 10,000 rpm. This is a greater loss than anticipated and is at least partially due to circulating armature currents in the parallel halves of each phase. This loss averages 1.5% of the stored energy per hour for the steel flywheel. With the expected elimination of circulating armature currents and the installation of a 4-kWh high-performance rotor, this component of the tare loss would decrease to 0.4% of stored energy per hour.

RESULTS FROM INITIAL TESTS

Using the motor drive, the flywheel was spun up in the vacuum tank to the minimum operating speed of 7500 rpm after passing through the whirl resonances at 40 and 70 rps. The motor drive has performed excellently up to 550-W input and the motor-commutation circuit transfer from forced to self-triggering works smoothly. The total input power efficiency, shown in Figure 4, was found to be a constant 92% with no significant variation with power level or shaft speed. The total output power efficiency (output power divided by flywheel energy rate change, Figure 4) was found to be approximately constant at 80%, with a slight falling off at low power. This lower efficiency is due primarily to the poor wave form and power factor on the input side of the cycloconverter at the generator frequency, resulting in increased reactive power transfer between the cycloconverter and generator. The indicated throughput power efficiency is about 75% for outputs of over 200 W but falls to ~60% at low power. This efficiency was measured with the maximum energy transferred to or from the rotor limited to 50% of either the input or output power. Any energy transferred was credited to input or output according to sign.

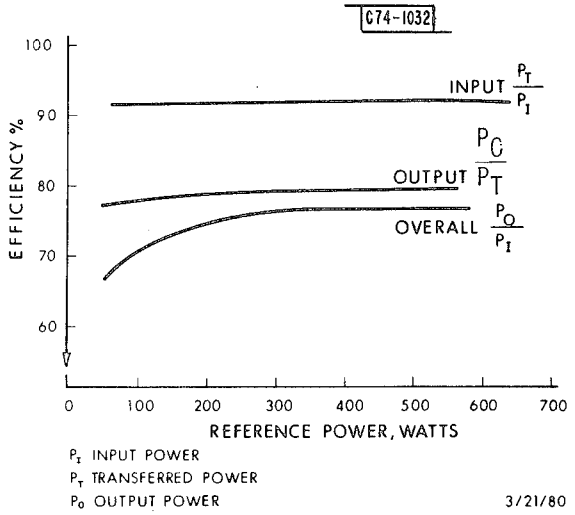

Figure 4
Measured flywheel efficiency.

There is a measureable enhancement in throughput efficiency with simultaneous operation of input and output electronics compared to multiplying separate input and output measurements. Methods to improve the low power efficiency are being investigated. The cycloconverter has been tested to 700-W output and has powered a variety of small AC appliances. The output waveform is excellent with current harmonic distortion of 0.5%.

Table II lists the measured component and system total efficiency. For comparison, the expected efficiencies for a deep discharge storage battery system are shown to be similar.

10097-R-01

TABLE II

MEASURED EFFICIENCY FLYWHEEL ENERGY STORAGE AND CONVERSION SYSTEM
vs
BATTERY INVERTER AND MAXIMUM POWER TRACKER SYSTEM

FLYWHEEL BASED SYSTEM		
DC MOTOR ELECTRONICS	94 PERCENT	
DC MOTOR	96	
AC GENERATOR	90	
BEARINGS AND TARE	95	(1-1/2% Stored Energy Per Hour)
GENERATOR ELECTRONICS	88	
TOTAL	68 PERCENT	

BATTERY BASED SYSTEM	
MAXIMUM POWER TRACKER	96 PERCENT
BATTERY	80
INVERTER	85
TOTAL	65 PERCENT

4/28/80

As an alternative to the cycloconverter, a system consisting of a rectifier, a DC-DC down converter, and either a 60-Hz utility-interactive or a stand-alone inverter, is being completed and will be tested. Results will be reported at a later time. Previous experience with inverters has shown that conversion efficiencies of 80 to 90% can be achieved.

During the course of the testing, an unexpected excitation of the 2-Hz whirl resonance was encountered within the operating range at about 170 rps (10,000 rpm). With sustained operation at this speed, the amplitude of the 2-Hz resonance increased slowly until bearing touchdown was encountered. An experimental investigation of the rotating system resonance spectrum is being conducted to find the cause of the observed whirl instability. The damping value built into the present

magnetic bearings is very small at 2 Hz and is apparently insufficient to suppress this frequency. Additional damping is being added to the system to correct this condition. Under experimental conditions, the bearing system has remained stable against external vibrations (<100 Hz) with peak amplitudes of 0.0002 m of 0.001 rad ($\sim$0.03 arc minute). These values are larger than amplitudes of commonly found earth vibrations. Since there are no spin resonances in the operating speed range, exciting a resonance from external vibrations is not expected to occur.

SCALING PERFORMANCE TO 40-kWh-PEAK STORAGE

It is expected that the operating efficiencies for the 40-kWh system components will be equal to or higher than those of the reported 1/10-scale system. Efficiencies should improve with increasing size, especially the tare loss which would drop to 0.3% per hour energy loss. Table III lists the expected fixed losses and the operating efficiency for the residential-size system. The results of the 1/10-scale flywheel-system tests, when scaled to the 40 kWh-size, indicate that the performance goals are achievable.

101040-H

TABLE III
RESIDENTIAL UNIT ESTIMATED LOSSES
40 kWh, 8 kW DC, 10 kW AC

FIXED LOSS	200 WATTS (2% of Full Load)
STORAGE LOSS	0.3% PER HOUR
INPUT ELECTRONICS:	
FULL LOAD	8%
HALF LOAD	7%
OUTPUT ELECTRONICS	
FULL LOAD	8%
HALF LOAD	7%
M/G LOSS (Input-Output)	
FULL LOAD	4%
HALF LOAD	2%

RESULTS OF 40-kWh SYSTEM COST STUDIES

Estimating the cost of manufacturing and selling inertial energy storage systems is perhaps more important than achieving technical performance goals. Figure 5 is a design layout of a residential-size system. Based on this layout, cost studies have been done by three industrial contractors using the 1/10-scale flywheel details scaled up to the required size for manufacturing cost estimates. Table IV presents the preliminary results of this work for the major components in quantities of 10,000 units per year. An estimate previously made by Lincoln Laboratory is shown for comparison although no figures for system checkout or markup are included. These costs, based on the present design with current (1980) technology, should be considered as upper limits. Large cost differences between the different estimates for specific components are evident. Investigation into the basis for estimating a given component shows a variety of approaches but the final cost totals are fairly close so the variations in component costs tend to average out. Analysis of the cost studies is in progress to resolve the reasons for differences and to present a comprehensive summary of the studies. Redesign to reduce the number of parts, thus simplifying fabrication and assembly, has been suggested as a means to decrease costs. Material substitution is another cost-cutting technique which is particularly applicable to the high-cost samarium-cobalt permanent magnets. It is estimated that these improvements could reduce costs by 30% or more, so that second-generation system costs are expected to be less than those shown in Table IV. These options are being investigated.

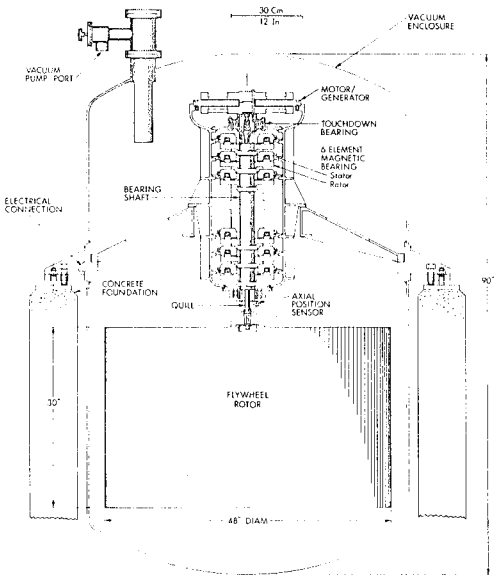

Figure 5
Residential flywheel energy storage unit.

P0275-H-01

TABLE IV

MANUFACTURING COST ESTIMATES[1]
40 kWh, 8 kW
FLYWHEEL ENERGY STORAGE UNIT
• 10,000 UNITS PER YEAR 1980 TECHNOLOGY AND DOLLAR COSTS

ORGANIZATION	THEODORE BARRY	GARRETT AIRESEARCH	KELSEY-HAYES RESEARCH	MIT LINCOLN LABORATORY[3]
FLYWHEEL ROTOR	4,000[2]	4,000[2]	4,000[2]	5,000
MOTOR-GENERATOR	2,200	2,100	2,300	1,200
MAGNETIC BEARING ASSEMBLY	2,600	4,100	5,100	2,500
VACUUM SYSTEM AND ENCLOSURE	2,400	1,100	1,500	1,200
ELECTRONICS	1,200	3,500	2,600	1,800
SYSTEM CHECKOUT	200	500	1,200	–
INSTALLATION	1,000	1,500	900	800
SUB TOTAL	13,600	16,800	17,600	12,500
MANUFACTURING MARKUP AND DISTRIBUTION	3,400	5,000	2,700	–
TOTAL	17,000	21,800	20,300	–

(1) PRELIMINARY
(2) FLYWHEEL COST SPECIFIED BY MIT LINCOLN LABORATORY
(3) A.R. MILLNER, A FLYWHEEL ENERGY STORAGE AND CONVERSION SYSTEM MIT LL REPORT COO-4094-48

In considering areas of cost reduction, the rotor stands out as the most expensive single part. High-energy density rotors are required to make inertial energy storage cost competetive with other storage systems. One possibility is epoxy-impregnated filamentary rotors, which have undergone considerable development and have an estimated quantity production cost of $140 per kWh stored. Alternative rotor designs made with unbonded filaments (Kevlar, glass or steel) or amorphous metal ribbon (METGLAS*) are also under development [4] and present the possibility of attaining $50 per kWh in production. This latter figure would result in a halving of the rotor cost shown in Table V.

The power necessary to maintain the vacuum surrounding the rotor is a requirement which directly affects system efficiency. Surface outgassing will be great enough to require pumping so as not to exceed an absolute pressure of $\sim 10^{-3}$ torr, where air drag is unimportant. This can be done either periodically or continuously, or alternatively, the vacuum enclosure can be sealed off and a getter or adsorption pump used with initial roughing accomplished with a temporary pumping system. The volume of gas to be pumped is small (≤ 10 l/s) and the choice of a pumping method will depend on the cost and reliability of the pumping system, including the average power required to operate it.

* ® Allied Chemical Corporation

The 40-kWh design is being upgraded to incorporate suggestions and recommendations from the industrial cost studies. Attention is being directed to reducing the cost of components, besides the rotor: the magnetic bearing assembly, the motor generator, and the electronics package.

FLYWHEEL ENERGY STORAGE ECONOMICS

To be economically attractive for photovoltaic PV systems, flywheel energy storage must be appropriately sized to the array power and be available at a price that a buyer is willing to pay. A range of cost estimates for a flywheel system is shown in Table V. The "high" 1980 estimate is based on the cost studies summarized in Table IV, including an allowance for cost-reducing manufacturing improvements expected in the second-generation residential flywheel systems.

P01114-H

TABLE V

RESIDENTIAL FLYWHEEL SYSTEM COST ESTIMATES
1980 DOLLARS

	"HIGH" 1980 TECHNOLOGY ($)	"MEDIUM" 1985 HIGH ESTIMATE ($)	"LOW" 1985 LOW ESTIMATE ($)
STORAGE CAPACITY $/kWh	375	200	120
INPUT $/kWDC	130	90	40
OUTPUT $/kWAC	220	185	60
20 kWh TOTAL AT 8 kW	10,300	6,200	3,200
40 kWh TOTAL AT 8 kW	17,800	10,200	5,600

The "medium" and "low" 1985 technology costs represent probable and optimistic cost estimates based on improved component design with continuing system development for a flywheel system with 1985 technology. These subsystem and total costs are used in the economic analysis which follows.

A system-worth analysis conducted by MIT Energy Laboratory [5] considered the economic feasibility of energy storage with photovoltaic input in both utility-interactive and stand-alone installations. The objectives of the report were to determine optimal flywheel sizing for a single-family residence with an 8-kW-peak PV array in various operating modes and to make a determination of the sensitive financial parameters which would affect market penetration.

The results of this analysis are presented as a value which is the difference between the benefits and the cost to the homeowner of a PV installation. This Break-Even Capital Cost (BECC) is defined as:

$$\text{BECC} = \sum_{i=1}^{\text{life}} \frac{\text{BENEFITS-COSTS}}{(1+r)^i}$$

where

BENEFITS = Total dollar equivalent of utility electricity displaced by the PV flywheel system, plus, for stand-alone applications, distribution-line costs otherwise incurred.

COSTS = All costs of the system not to be included in the BECC figure (see below).

LIFE, i = Assumed lifetime of the system: 20 years.

r = Discount rate. (The true cost of borrowing money.)

The System BECC must account for all costs associated with (1) the flywheel storage unit, (2) the PV modules, and (3) all balance-of-system (BOS) costs, including mounting, electrical wiring of the PV modules, and all maintenance over the life of the system.

The Flywheel BECC includes the costs associated with power conditioning and is the system BECC less the cost of non-flywheel components such as PV modules.

The MIT Energy Laboratory report showed that for a utility-interactive residence in Phoenix with a flat-rate price structure and 0% buy-back from the utility, system BECC is \$5,000 with an 80-m^2 array and no flywheel (Figure 6a). This figure increases to \$11,500 and \$13,000 for a system with flywheels of 20-and 40-kWh usable capacity, respectively. Flywheel BECC under the same conditions is a function of assumed balance-of-system costs

C74-1030

UTILITY INTERFACE PV FLYWHEEL

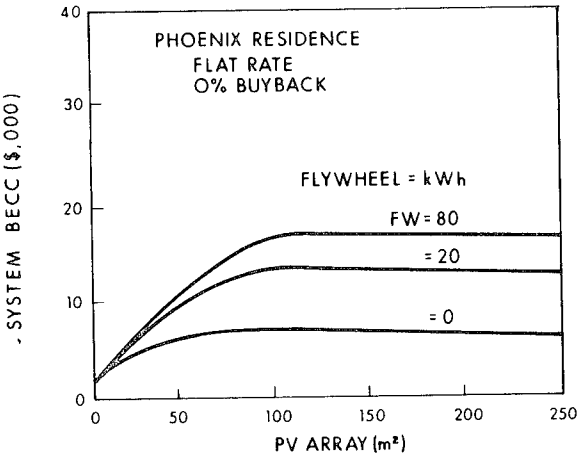

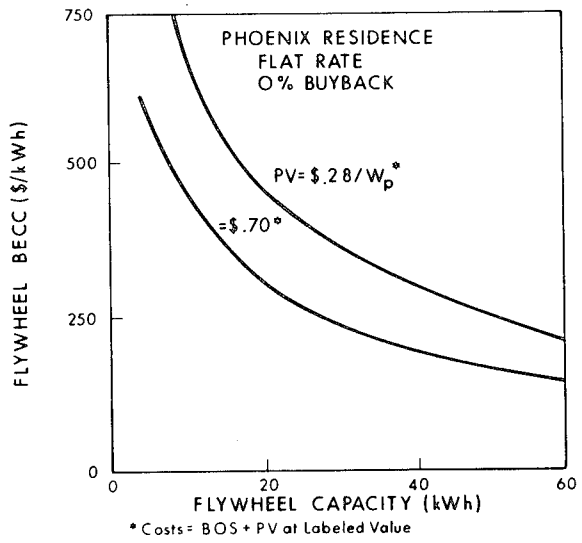

Figure 6a. System BECC vs. PV array.
Figure 6b. Flywheel BECC vs. capacity.

and PV module costs. For a 20-kWh-capacity flywheel and PV modules at the 1985 cost goal of $0.70 Wp (1980$) including BOS costs, the flywheel BECC is $300/kWh (Figure 6b). Note that this worth value is above the preliminary medium cost estimate of Table V showing that flywheels are an economical addition to a PV system when utility buyback rates are low.

In general, the addition of storage serves to increase the optimum capacity of installed PV when hardware costs are assumed low enough to yield a positive return on investment. When storage is dedicated to the PV array alone, it is shown to have the greatest value when buyback rates by the utility for excess PV-generated electricity are low. This is true since marginal benefits to a fixed-storage capacity decline as buyback rates are increased. Depending on flywheel and other BOS cost assumptions, at some utility buyback rate below 50%, the addition of storage capacity effects an increase in investment net benefits.

Using the most reasonable set of cost and financing projections for 1985, a PV-flywheel system will begin to look economically attractive when the cost of electricity, in 1980 dollars, exceeds 0.09/kWh (starting cost, assuming 3%/year real escalation thereafter, Figure 7). Variations in time-of-day rate setting by the utilities are only significant in affecting storage economics if electricity is bought and sold directly from the storage device, thus acting in a dispersed-system storage mode. It was also found that the discount rate, r, is an important parameter in influencing system worth.

For stand-alone (non-grid-connected) applications, the optimum configuration and sizing for the PV and flywheel (Figure 8) was found to be quite insensitive to relative component costs. Flywheel capacity rated in peak-kWh-storage figures is optimum at roughly 2.5-4.0 times the array size rated in kWp. In addition, the optimum size of a flywheel and PV system is highly sensitive to the desired service reliability. For stand-alone applications, an auxiliary generator is assumed to supply the power differential between that available from the PV system and storage and the requirements of the load.

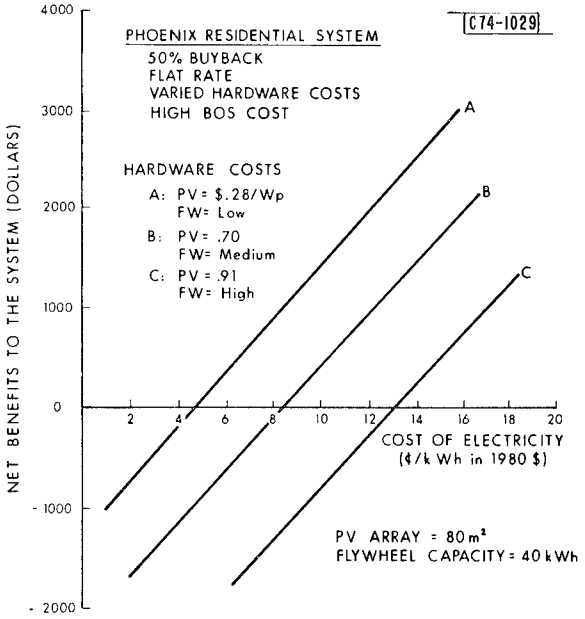

Figure 7
Utility interface PV and flywheel system new benefits vs. cost of electricity.

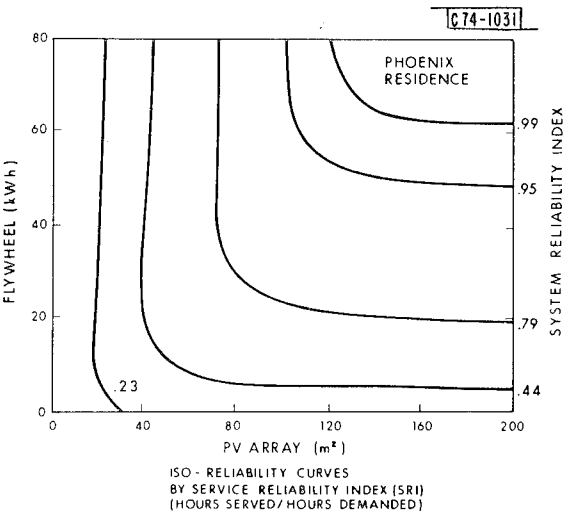

Figure 8
Remote stand-alone residential system: PV and flywheel only.

500-kWh, 100-kW LOAD CENTER

The characteristics and the fabrication costs of a large 500-kWh inertial-energy storage system for a load center are based on geometric and energy scaling relationships derived from the 40-kWh residential system design [6]. Obviously, a simple scaling in size is not a substitute for an engineered design, but it can form a basis for rudimentary fabrication

cost estimates and suggest important features to be included in a 500-kWh energy storage system design.

The industrial cost studies included scoping estimates of the 500-kWh load center which are summarized in Table VI. The MIT Energy Laboratory user-worth study described above also analyzed a load center typified by a PV-powered apartment complex with energy storage.

101041-H

TABLE VI
100-kW LOAD CENTER
1980 TECHNOLOGY
COST ESTIMATE

STORAGE CAPACITY $/kWh		340
ELECTRONICS $/kW		250
500 kWh / 100 kW	TOTAL	$195,000
UNIT COST TOTAL $/kWh		390

The preliminary results of the user-worth study reflect the same conclusions found for residential energy storage, i.e.: that there are diminishing returns for increased storage capacity and that the inclusion of storage has the effect of increasing optimum PV array size. The results also predict lower breakeven capital costs for the load center. This indicated difference in costs requires further investigation because of the rudimentary character of the design upon which estimates were based. A detailed design for a 500-kWh energy storage system is needed to obtain accurate cost estimates and the basis of the economic model must be reviewed for appropriateness for this application.

CONCLUSION

Results obtained to date indicate that flywheel energy storage and conversion systems can be built with high throughput efficiency and low fixed losses. The 1985 flywheel costs goals will be met by further refinement of the residential flywheel design presented here. When 1985 cost estimates are met, the worth of the system is greater than the cost for residential stand-alone applications and for utility-interactive applications with low buyback rates.

ACKNOWLEDGMENTS

Designing, overseeing construction, and checkout of the electronics was excellently done by Neil Rasmussen. This project was supported by the Photovoltaic and Energy Storage branches of the Department of Energy.

REFERENCES

1. A. R. Millner, "A Flywheel Energy Storage and Conversion System for Photovoltaic Applications," International Assembly on Energy Storage, Dubrovnik, 28 May - 1 June 1979.

2. R. D. Hay, A. R. Millner, "Flywheel Energy Storage Interface Unit for Photovoltaic Applications," 14th Intersociety Energy Conversion Engineering Conference, Boston, MA 5-10 August 1979.

3. L. L. Bucciarell, A. D. Rangarajan, "Dynamic Analysis of a Magnetically Suspended Flywheel," 1980 Flywheel Technology Symposium.

4. D. W. Rabenhorst, "Demonstration of a Low-Cost Flywheel in an Energy Storage System," Proceedings of 1979 Mechanical and Magnetic Energy Storage Meeting, Washington, DC, 1979.

5. T. L. Dinwoodie, "Flywheel Energy Storage for Photovoltaics: An Economic Evaluation of Two Applications," MIT-EL-80-002 (February 1980).

6. A. R. Millner, "Scaling Laws for Flywheel System Comparison," MIT Lincoln Laboratory, COO-4094-63, November, 1979.

THE ACCELERATING FLYWHEEL

Dr. David G. Ullman
Department of Mechanical Engineering
Union College
Schenectady, New York 12308
Member ASME

John Corey
Mechanical Technology Incorporated (MTI)
Latham, New York
(Formerly with Union College)
Member ASME

ABSTRACT

A flywheel energy storage unit which can accelerate inertial loads from rest without an external transmission has been designed, built and tested. The preliminary development of this flywheel, a configuration of Band Type Variable Inertia Flywheel (BVIF), is presented. This includes a development of the equations of motion which governs the BVIF mechanism, the properties of a BVIF powering an inertial load, and the design and testing of a prototype model. It will be shown that the BVIF is an energy storage system capable of smoothly accelerating inertial loads to an even terminal speed.

VARIABLE LIST

b band width
E energy
h band thickness
I polar moment of inertia
L single band length
m mass
n number of bands
P power
r_1 hub radius
r_2 outer radius of material wrapped around the hub
r_3 inner radius of material in outer casing
r_4 inner radius of out casing
r_5 outer radius of casing
T torque
Θ angular position
ρ mass density
ω angular speed

Subscripts

B band
eff effective
fixed nonvariable
i inner hub shaft
I moment of inertia
o outer casing shaft
ω angular rate
L load

INTRODUCTION

Many of the end uses of energy depend on its availability in mechanical form, usually as rotating shaft power. Consequently, great advantage would be had in terms of simplicity and overall system efficiencies if energy for such uses could be stored in a rotating mass. Such a device is by definition a flywheel, one of the oldest and most commonly used energy storage mechanisms.

Nonetheless, the uses of flywheels to date have been largely limited to reducing variations in the speeds of shafts driven by pulsed or irregular inputs or supplying peak forces in machine tools such as punch presses. The reason for this underutilization is an inherent difficulty in the power delivery capabilities of conventional flywheels. Specifically, the energy content, E, of a flywheel is a function of the polar moment of inertia, I, and the angular velocity, ω, ($E = \frac{1}{2}I\omega^2$), where the moment of inertia is a function of the mass and the effective radius of that mass from the axis of rotation ($I = \int_m r^2 dm$). For a fixed-inertia system such as the common rotating disk flywheel, then, the energy equation

prescribes reduction in angular velocity as the only means of extracting energy. Most shaft loads, however, require a constant or increasing speed for their operation, so the only means of connecting a fixed-inertia flywheel to such loads is through some type of continuously variable transmission (CVT) or its electrical analog, a motor-generator system. The addition of such a unit to the system usually produces reduction in efficiency and increases in system complexity, weight, and cost. The design and development of effective flywheel energy transmission systems must precede any significant usage of flywheels as energy storage systems.

The flywheel described in this report releases energy in a manner intended to eliminate the need for a CVT or motor-generator by uncoupling the flywheel's energy content from its angular velocity. It is a variable-inertia flywheel (VIF), in which the moment of inertia term I, of the energy equation becomes a variable, allowing net energy release even if the speed term, ω, is constant or accelerating. For the flywheel under consideration here, the mechanism is a coiled thin band wound between an inner hub rotating with angular velocity ω_i and a concentric cylindrical outer casing rotating with angular velocity ω_o. Thus the BVIF is a two-degree-of-freedom device. The layout is much like the installation of a clockwork's mainspring except that no springiness is intended or assumed. As shown in Fig. 1 there are two inter-wound bands for balance but there could be more if desired. Variation in the moment of inertia is accomplished by relative rotation of hub and casing which winds the band material in onto the hub or out against the casing. This device is referred to as the Band-Type Variable Inertia Flywheel (BVIF). Figure 1 also defines the conventions used in all the ensuring discussion. The positive directions for all angular rates and torques are taken to be positive in the counter-clockwise direction shown. The subscripts used for these quantities are: "i" when referring to the inner hub, the inner rotating element, "o" when referring to the casing, the outer rotating element. The torques on hub and casing are due to the band segment between the tightly wound material about the inner hub and that pressed by centrifugal forces in the outer casing. This segment of the band is in tension. The bands exert a positive torque on the hub and a negative torque on the casing when wrapped in the direction shown. The band-wrap direction is defined to be positive when $\omega_o > \omega_i$ causes the bands to accumulate on the hub; negative if $\omega_o > \omega_i$ causes the bands to move out to the casing.

The development history of the BVIF leading to the research reported here is presented in References 1-4. Reference 1 presents an introduction to the variable inertia concept, discusses many potential configurations and studies one configured like a flyball governor. Reference 2 is a digested version of Reference 1. In Reference 3 the Band Type Variable Inertia Flywheel is initially studied. Its equations of motion are derived and three potential ways of connecting it to external systems are developed. These three are as shown in Fig. 2 as Type I, the inner hub connected to the load and the outer casing free; Type II, the inner and outer elements geared together reducing the BVIF to a one-degree-of-freedom system; and Type III, the inner hub, outer casing and load are connected to the three elements of a planetary gear set. In Reference 3 the Type II system was studied and found to be able to power a friction load at near constant speed but not have good inertia load powering capabilities.

This paper is a synopsis of research reported on in Reference 4 where the Type III BVIF, the one with the planetary gear set, has been more deeply studied. The operation of this system is explained by derivation of the equations of motion and their application to the Type III system. A comparison of computer simulation results to experimental data is offered as verification of the equations.

THE BVIF EQUATIONS OF MOTION

The equations of motion of the BVIF (regardless of which Type system) have been derived using Lagragian techniques in References 3 and 4. In Reference 4 the approach is made both through kinetic energy and separately through potenital energy formulations. This dual approach is intended to gain insight into the complex variations of angular rate, band torque and moments of inertia which characterize the operation of a BVIF. Also in Reference 4, for completeness,

the equations of motion have been derived using the standard Newtonian approach. This latter development is presented here assuming a perfect, no-loss system. This assumption is relaxed in later sections of the paper.

According to Newton's 2nd Law, the sum of the torques on a body must equal the time-rate of change of angular momentum or,

$$\Sigma T = \frac{d}{dt}(I\omega).$$

Visualizing the BVIF as a two degree-of-freedom system, drawing free-body diagrams on inner and outer inertias (see Fig. 3), and summing forces on each provides:

$$T_i + T_B = \frac{d}{dt}(I_i\omega_i), \qquad (1)$$

and

$$T_o - T_B = \frac{d}{dt}(I_o\omega_o). \qquad (2)$$

T_B is the only unevaluated term here. To develop an equation for this band torque in terms of the variables defined in Fig. 1, consider a small mass, dm, in the band and moving from radius r_2 to r_3. A rotation of the inner hub, $d\theta_i$, causes a length of band, $dL = d\theta_i r_2$ to unwind. Since band accumulation between windings is not allowed, a casing rotation equal to $d\theta_i \frac{r_2}{r_3}$ is required to absorb dL from the hub. If θ is defined by

$$\theta = \theta_i - \theta_o,$$

then

$$d\theta = d\theta_i - d\theta_o = d\theta_i - d\theta_i \frac{r_2}{r_3}$$

and

$$\frac{dL}{d\theta} = \frac{d\theta_i r_2}{d\theta_i - d\theta_i \frac{r_2}{r_3}} = \frac{r_2 r_3}{r_3 - r_2}.$$

Now, $dm = nhb\rho dL$, so by substitution and rearrangement,

$$d\theta = \frac{dm}{nbh\rho}\left(\frac{r_3 - r_2}{r_3 r_2}\right).$$

As the torque, T_B, does work (causes an energy change) in the band as it moves through the relative angle θ then

$$E = T_B\theta$$

or

$$dE = T_B d\theta.$$

For the bit of band mass, dm, moving from r_2 to r_3, the change in energy is:

$$dE = \tfrac{1}{2}dm r_3^2\omega_o^2 - \tfrac{1}{2}dm r_2^2\omega_1^2.$$

Combining and rearranging the expressions for dE and $d\theta$ gives

$$T_B = \tfrac{1}{2}nhb\rho\left(\frac{r_2 r_3}{r_3 - r_2}\right)(r_3^2\omega_o^2 - r_2^2\omega_i^2), \qquad (3)$$

this characterizes the band torque in terms of the basic system. From the Reference 3 derivation, the expressions for the other variables used are:

$$I_i = \frac{\pi\rho b}{2}(r_2^4 - r_1^4) + I_{i_{fixed}} \qquad (4a)$$

and

$$I_o = \frac{\pi\rho b}{2}(r_4^4 - r_3^4) + I_{o_{fixed}}, \qquad (4b)$$

so

$$\dot{I}_i = 2\pi\rho b r_2^3 \dot{r}_2 \qquad (4c)$$

and

$$\dot{I}_o = -2\pi\rho b r_3^3 \dot{r}_3, \qquad (4d)$$

where

$$\dot{r}_2 = \frac{nh}{2\pi}\frac{r_3}{r_3 - r_2}(\omega_o - \omega_i) \qquad (4e)$$

and

$$\dot{r}_3 = \frac{r_2}{r_3}\dot{r}_2. \qquad (4f)$$

The variables r_2, r_3 can be used as macroscopic, observable coordinates for the system motion. They depend on the intrinsic coordinates, θ_i and θ_o according to equations 5,

$$r_2 = \frac{(r_{3_o}^2 - r_{2_o}^2) - [(r_{3_o} - r_{2_o}) + K_s(\theta_i - \theta_o)]^2}{2[(r_{3_o} - r_{2_o}) + K_s(\theta_i - \theta_o)]} \qquad (5a)$$

and

$$r_3 = \frac{(r_{3_o}^2 - r_{2_o}^2) + [(r_{3_o} - r_{2_o}) + K_s(\theta_i - \theta_o)]^2}{2[(r_{3_o} - r_{2_o}) + K_s(\theta_i - \theta_o)]} \qquad (5b)$$

where $K_s = \frac{nh}{2\pi}$ and r_{2_o}, r_{3_o} are the values of r_2 and r_3 at time equal to zero.

The above equations constitute a complete modeling of the basic BVIF as a free-standing system with the assumption of perfect, no-loss operation. These factors will be added in the subsequent sections of this paper. Also, from equations 1-5 it is evident that the BVIF is a two degree of freedom system with the angular velocities or positions of the hub and casing as independent coordinates. It is obvious that these equations are highly nonlinear and that the seven independent equations 1, 2, 3, 4a, 4b, 4e and 4f contain 9 unknowns (T_i, T_o, T_B, ω_i, ω_o, I_i, I_o, r_2, r_3). To complete the set of equations the connection of the BVIF to the outside system must be defined.

TYPE III BVIF SYSTEM SIMULATION

The Type III BVIF is by far the most complex dynamically of the BVIF configurations studied to date due to the inclusion of a planetary gear set. However, the complexity offers the most promise for versatility in operation. In this configuration (see Fig. 2), the two shafts of the BVIF (hub and casing) are connected to a load shaft via a planetary (epicyclic gear train) so that at any given time all three shafts can be rotating at different angular rates. The load shaft is notated with the subscript L. The equations of motion do not reduce but rather expand into a set of 11 simultaneous nonlinear equations which can be solved for the torques and accelerations of hub, casing and load shafts. In addition to the seven equations derived earlier there are also additional equations for the load and the planetary gear set. The load torque and angular rate (2 more unknowns) are related by

$$T_L = I_L\dot{\omega}_L + T_F + T_{AERO}\omega_L^2; \qquad (6)$$

where the load is assumed to consist of an inertia I_L, Coulomb friction, T_F, and aerodynamic loss, T_{AERO}. Plus from Reference 5, the torque and rotational relationships for planetary gear sets:

$$T_i = -T_L/(1-gr) \qquad (7a)$$

and

$$T_o = gr \cdot T_L/(1-gr) \qquad (7b)$$

and

$$\dot{\omega}_L = \dot{\omega}_i/(1-gr) - gr\cdot\dot{\omega}_o/(1-gr). \qquad (7c)$$

The gear ratio, gr, is defined as the ratio of θ_i to θ_o when $\theta_L = 0$. Note that the rotation equation (7c) holds for angular position, θ, and angular acceleration, $\dot{\omega}$, as well and that the representation of the gear set in Fig. 2 is purely arbitrary. Any of the elements of the epicyclic train may be attached to the three shafts of the Type III without altering the equations so long as gr is defined as above. Also with the addition of variables T_L and ω_L and equations 6 and 7, there are eleven nonlinear equations and unknowns.

With the planetary gear set in the Type III BVIF it is quite possible to accelerate the load while both hub and casing are slowing down. The acceleration of the load depends on the rate of change in the difference between inner and outer velocities, rather than their absolute values. In fact, for appropriate choices of gr, the load can be made to accelerate positively no matter what the magnitudes or even directions of the two flywheel velocities. In principle a great energy yield may be possible if the flywheel speeds can be brought low while the load shaft speeds up.

TYPE III BVIF - TYPICAL OUTPUT CHARACTERISTICS AND SENSITIVITY TO PARAMETER VARIATION

To demonstrate the output characteristics of a Type III BVIF accelerating inertial load and show the effects of parameter variation a specific example will be used. The dimensions for this example are from the prototype BVIF described in the next section of this paper. The major dimensions for this model are:

r_1 = 0.5 in
r_4 = 5.0 in
n_{band} = 2
h_{band} = .002 in
b_{band} = 1.0 in
L_{band} = 9700 in

$\rho_{steel} = .00073\ lb\cdot s^2/in^4$

$I_{i_{fixed}} = .05\ lb\cdot s^2\cdot in$

$I_{o_{fixed}} = .74\ lb\cdot s^2\cdot in$

$I_{max} = 1.32\ lb\cdot s^2\cdot in\ @\ r_2=.5\ in$

$I_{min} = 0.98\ lb\cdot s^3\cdot in\ @\ r_2=3.5\ in$

The planetary gear set used has a ratio of .75. This value was not selected based on any benefits of this value but because of availability of hardware. In these simulations the entire mechanism is assumed frictionless. Friction effects will be discussed.

In this section the operation of the above dimensioned Type III BVIF will be described in great detail. This will be followed by a discussion of the effect of variation of some of the major dimensions and initial conditions.

For example the baseline initial conditions used are $\omega_i = \omega_o = 500$ rad/sec (4775 rpm) and $r_{2_o} = 3.0$ in. The load is purely inertial and $I_L = .20\ lb\cdot s^2\cdot in$. Initially the inertial load is at rest. The simulation of this example is made in three steps. At time zero the entire BVIF is rotating at 500 rad/sec and a clutch between the load and BVIF is disengaged. At time zero-plus the BVIF is allowed to go free so the various shafts can rotate at different speeds which will happen due to centrifugal forces on the bands. At one second the load clutch is engaged taking one second for the BVIF load shaft and the load to reach a nonslip common speed. From two seconds on the BVIF is directly powering the load with no clutch slip or gear change. The results of this simulation are shown in Fig. 4a-f and 5.

The angular rate time history of the BVIF is shown in Fig. 4 along with the band position r_2. For the first second of the run the BVIF is free so centrifugal force is driving the band material outward ($\dot{r}_2<0$). This causes the inner hub to accelerate due to loss of mass and the casing to decelerate as it gains mass. The load shaft having low inertia speeds up in response to the torques on it through the planetary. Between one and two seconds the clutch is engaged slowing the load shaft. The 190 rad/sec shown for ω_L at two seconds is the speed of the load shaft and the load itself at that time. Prior to one second the load was at rest and with the torque supplied through the slipping clutch accelerated from 0 to 190 rad/sec in the one second interval. From the two second point on the load is accelerated with no clutch slip. To do this $\omega_i<\omega_o$ so the band winds in, $\dot{r}_2>0$. At 8 seconds $\omega_L = \omega_i = \omega_o$ and $\dot{r}_2 = 0$. From this time onward $\omega_o > \omega_i$ and the band winds out into the casing, $\dot{r}_2<0$. This continues until the band is fully out wound. At this time $\omega_L = 800$ rad/sec and the inertial load has been smoothly accelerated from rest with only an initial clutching.

In Fig. 4b the moments of inertia of the system are plotted. Here the moment of inertia of the material rotating at speed ω_i, I_i, is seen to increase initially as the band winds in. Then, as the band winds out I_i falls to $I_{i_{fixed}}$. Similarly the moment of inertia of the material rotating at ω_o, I_o, drops initially then increases steadily. The moment of inertia of the BVIF as seen by the load itself is called the effective moment of inertia, I_{eff}. This ficticious inertia represents the entire BVIF as if all the elements were rotating with angular velocity ω_L. The effective moment of inertia can be derived either by considering the equations of motion which is quite lengthy or by treating the BVIF as a black box so that

$$T_L = \frac{d}{dt}(I_{eff}\omega_L)$$

and solving for I_{eff}. This latter treatment has been used in the computer simulations. As seen in Fig. 4b, I_{eff} drops steeply during the high acceleration portion of the run then levels off as the terminal velocity is reached. Essentially the entire system of BVIF plus load must conserve angular momentum so

$$\frac{d}{dt}[(I_{eff} + I_L)\omega_L] = 0$$

or

$$\dot{I}_{eff}\omega_L = -(I_{eff} + I_L)\dot{\omega}_L .$$

Thus $\dot{I}_{eff}$ must be negatively large to give high acceleration to the load in the early portion of the run as can be seen. Figure 4c is the torque-time history of each element of the system. Also included is the history of r_2, or band position. Note that T_B, the band torque is the overwhelming protion of T_i, justifying the usage of the potential energy/band

tension mode of energy removal rather than relying on the inertial change effects to produce usable torque. Note also that all the torques can be approximated as being proportional to r_2. This supports the decision to use in-wound band as the initial condition, in order that the torque curves would have the early peak and trailing long-term response.

Figures 4d, e and f along with Fig. 5 show the power flow within the system. In Fig. 4d the power flow through the planetary is shown. Power P_L is the power given up to the load. P_o is the power transferred to the outer casing through torque T_o. P_i is the power input to the planetary from the hub through torque T_i. As can be seen the sum of these powers equals zero at all times. Power P_i, for example, is derived from the band torque T_B and the rate of change of the energy stored in the mass rotating at speed ω_i. This can be shown as

$$P_i = \frac{d}{dt}E_i + P_B$$

$$= \frac{d}{dt}[\tfrac{1}{2}I_i\omega_i^2] + P_B$$

$$= I_i\omega_i\dot{\omega}_i + \tfrac{1}{2}\omega_i^2\dot{I}_i + P_B \quad .$$

$$= P_{I_\omega} + P_{I_I} + P_B \quad .$$

The first term is due to change in speed and the second due to change in inertia. These two terms and their sum is plotted in Fig. 4e for the inner hub and similarly in 4f for the outer casing. Before discussing the information on these plots Fig. 5 is introduced.

In this figure the various powers from Figs. 4d, e and f are shown in a power flow diagram at selected times. Initially, at time zero, all elements of the BVIF are at the same speed and there is no load thus there is no power flow anywhere within the mechanism. At one second, just prior to clutch engagement, the band is unwinding due to centrifugal force. Thus the inner moment of inertia is dropping, releasing energy but, by conservation of angular momentum the inner hub is accelerating which takes energy. The net effect is that the inner hub is absorbing energy. The opposite is occurring in the outer casing and power is flowing through the band, because of the band torque, from the outer casing to the inner hub. At two seconds the clutch is fully engaged and now there is also power flow through the planetary to the load. The band is winding in (see Fig. 4a) thus $\dot{I}_i$ is increasing, absorbing energy, and both ω_i and ω_o are increasing absorbing energy. However, $\dot{I}_o$ is decreasing at such a high rate as to supply power to the above plus the load (note $P_{I_\omega} + P_{I_I} + P_{o_\omega} + P_{o_I} = -P_L$). As ω_i accelerates ω_o starts to decrease, $\dot{\omega}_o < 0$ as seen at 4 seconds. Now both parameters associated with the outer casing are giving up energy. The same is true at six seconds. Near eight seconds the angular rates become equal and change from $\omega_o > \omega_i$ to $\omega_i > \omega_o$. At this junction the band starts winding out rather than in. Also, at the same time, $\dot{\omega}_i$ is very small. Thus the power terms associated with $\dot{I}_i$, $\dot{I}_o$ and $\dot{\omega}_i$ are all small. From 8 seconds on the band is winding out, thus $\dot{I}_i$ is decreasing and giving up power. However, $\dot{I}_o$ is absorbing power at a faster rate, so the net effect of moment of inertia change is to absorb power. But, the angular speeds are both decreasing at a rate fast enough to overwhelm the inertia effects. In fact, net power is being given up by both segments of the BVIF during the remainder of the run.

In considering at the power flow diagrams one point is noteworthy. Before eight seconds, when the moments of inertia appear to be decreasing, the power flow recirculating through planetary gears and BVIF is on the order of three times what is given up to the load. However, after eight seconds when the apparent moment of inertia is increasing (the effective moment of inertia is still dropping however) the recirculating power is the same order of magnitude as the power to the load. This implies the BVIF is more efficient in its power flow when outwinding.

Based on the simulation presented above and numerous others the effect of changing various parameters on the output will be discussed. There are two sets of parameters, physical measures and initial conditions. The effects of the band thickness, h, and length, L, and number of bands, n are to affect the total amount of band material in the BVIF. In Reference 3 it was shown that the greatest change in moment of inertia was when

$$nLh = \frac{\pi}{2}(r_4^2 - r_1^2) \ .$$

Thus any deviation from this will reduce the available moment of inertia variation potential. The height of the bands, b, and the outer radius of the band casing, r_4, alter the total energy storage capability of the BVIF, the height in direct proportion and the radius as squared. Obviously if r_4 is altered then the band length, thickness or number of bands will need to be altered as discussed above. The hub radius, r_1, has only a weak effect on the design and generally should be kept as small as possible. The band density, ρ, has proportional effect on total energy storage. The band material should be as dense as possible. The fixed inertias, $I_{i_{fixed}}$ and $I_{o_{fixed}}$, reduce the effectiveness of the BVIF. Thus they should be as small as possible.

The effect of the initial speed of the BVIF is to increase the energy stored. The shape of the curves in Fig. 4 do not change other than in time scaling in an inverse proportion. In this example $\omega_{i_o} = \omega_{o_o} = 500$ rad/sec and the run lasted 30 seconds. If another run was to be made with another initial speed, ω, then the time for the run, t_f, would be

$$t_f = \frac{500 \cdot 30}{\omega} \ .$$

So if $\omega = 1000$ rad/sec then $t_f = 15$ sec.

The effect of load moment of inertia and of the initial band position as measured by r_{2_o} can best be discussed in terms of Fig. 6. This figure is the result of many simulated runs where the initial band position as measured by r_{2_o} and the inertial load were varied. The approach to the figure can best be seen by example. Say that $r_{2_o} = 3.0$, most of the material is inwound and $I_L = .20$ lb$\cdot$s$^2\cdot$in, point A in the Figure. When the load is engaged the BVIF will initially wind in the bands until $r_2 = 3.5$ which is $r_{2_{max}}$. Then the bands will totally unwind into the outer casing. In accomplishing the wind and unwind the BVIF will release 56% of its initial stored energy. This is the same run as presented in Figs. 4 and 5. If $I_L = .05$ for example the band would not inwind at all, $r_2 = r_{2_{max}} = 3.0$ and just outwind until all the band material was in the outer casing. The BVIF would have released only 28% of its stored energy in performing this task.

It is interesting to note that the final speed of a load accelerated from rest is a function of initial speed only. (An exception to this statement is at very low load inertias, .05 lb$\cdot$s$^2\cdot$in or less). In general the ratio of final load speed to initial BVIF speed is 1.60 ± 10%. Thus for this case the initial BVIF speed was 500 rad/sec and the final was 795 rad/sec near the 800 rad/sec calculated by the general ratio.

From the above it can be concluded that the Type III BVIF can accelerate a frictionless inertial load irrespective of initial band position, angular rate, or, within bounds, moment of inertia of the load. In actuality the moment of inertia of the load as seen by the BVIF can be modified by fixed ratio gearing as, of course, can the speed of the load. Gearing such as described can only be designed with a specific load in mind. Thus the next step in BVIF development will be the application of the Type III BVIF to a specific load such as a vehicle.

No mention has yet been made about some practical aspects of BVIF design such as dynamic balance and energy density. Balance considerations will be mentioned in the next section. In discussing energy density for the BVIF care must be taken as the BVIF is both the energy storage unit and a major part of the transmission system. However, analysis in Reference 4 has shown that, assuming the outer ring carries the entire centrifugal load of the bands (the band carry none of their own load) and the bands are steel and the outer ring is Kevlar (working stress 130,000 ksi) the energy density is 5.9 watt hr/lb. Left out of this value are the load carrying capacities of the end plates which support the outer ring, the load carrying capacity of the bands themselves and the weight of the end plates, gears, bearings and containment. But, even if 3 watt hr/lb is realizable it still may be acceptable in an era of 40 watt hr/lb fixed inertia flywheels because the BVIF is not only a flywheel but a transmission system as well.

BVIF PROTOTYPE TESTING

In order to verify the dynamic simulation results and gain knowledge of the BVIF's true potential, a prototype model was designed, constructed and tested. The design of the prototype model is based on the proof-of-concept model described in Reference 3. Like the previous version, this prototype is 10½" in diameter and 1 3/8" thick at the rim. The band material occupies a cavity 10" in diameter and 1.05" high. The maximum design rotational rate is 5000 rpm. The stresses resulting from this speed are quite conservative in keeping with the primary design objective of verifying the equations of motion not in producing a high energy density system.

The resulting prototype configuration and its test stand are presented in photographic Figs. 7 and 8. The prototype as seen in Fig. 7 only shows the outside of the casing. Internally, as shown in Fig. 8, the center hub is really a spool to help reduce internal friction. Essentially, the physical properties of this prototype are as used for the simulations in the previous section.

To support the analysis the prototype model was used to accelerated an inertial load. The simulation was modified by the addition of bearing, gear, and windage friction (no vacuum was used). The gear and bearing friction values were measured (Reference 4) and the windage values were empherical (Reference 3). A typical comparison of results is shown in Fig. 9. Here the two measured values, the loadshaft rpm and the inner hub shaft rpm are plotted with simulated values. As can be seen the simulation is always within 10% of the measured values. The effects of the friction can be seen by comparing Figs. 4a and 9. The major features are that the ratio of maximum load speed to initial BVIF speed is lower and the rpm tapers off with time. There was no effort beyond using a good grade of bearings to reduce friction in the prototype testing.

In operating the prototype speeds of up to 3500 rpm were run. At thes speeds there was no apparent problem with balancing. With the use of two bands and the high inertial loads, mass was always symetric about the axis. Potential problems which might be encountered in a moving base application are unknown, but the amount of material mass between the tight wound outer and inner sections of band are very small and, thus, little problem is foreseen.

CONCLUSIONS AND RECOMMENDATIONS

1. The Band-Type Variable Inertia Flywheel (BVIF) is a system capable of storing and delivering energy in usable form. This is a single mechanism, which, unlike conventional flywheels does not require any intermediate transmission equipment. A BVIF has been built and operated which is capable of smoothly accelerating a directly-connected inertial load from rest to a final speed without clutch-slipping losses or any additional transmission devices.

2. There are essentially three ways to attach loads to a BVIF. The first is an open-loop system with two degrees of freedom, referred to as the Type I. The Second (Type II) is a single-degree-of-freedom unit with a fixed ratio between hub speed and casing speed. Third (Type III) has two degrees of freedom like Type I but includes power recirculation through a gear train like Type II. Of these, the Type III has been identified as the most promising configuration.

3. The Type III BVIF is capable of accelerating inertial loads smoothly and with stability to a terminal speed. That final speed can be greater than the initial flywheel speed, and both inner and outer elements of the BVIF slow down. The Type III BVIF is ideally capable of yielding more than half of its stored energy to the load during such an operation.

4. Prototype testing in the Type III mode has produced real-world evidence of Type III BVIF capacity. Further work remains to be done to fully characterize the nature of such systems.

5. Throughout this study the BVIF was treated only in the mode of giving up stored energy. A study is needed on the effects of BVIF design parameters and load conditions on the energy absorption or storage mode.

6. The next step in BVIF development is to integrate it into a system with a prime mover. The BVIF with its accelerating capability seems a good choice for hybridizing with a prime mover to add additional power during

acceleration and absorbing power during braking.

REFERENCES

1. Ullman, D.G., "A Variable-Inertia Flywheel As an Energy Storage System", Ph.D. Disseration, Ohio State University, March 1978.

2. Ullman, D.G. and Velkoff, H., "An Introduction to the Variable-Inertia Flywheel (VIF)", Journal of Applied Mechanics, Vol. 46, No.1 March 1979.

3. Ullman, D.G., "Preliminary Development of the Band-Type Variable-Inertia Flywheel (BVIF)", Sandia Laboratories, Albequerque, N.M., (SAND 79-7089), November 1979.

4. Ullman, D.G., and Corey, J., "Second-Stage Development of the Band-Type Variable-Inertia Flywheel", to be published by L.L.L., 1980.

5. Merritt, H.E., "Gear Trains," Pitman and Sons, Ltd., London, England, 1947.

6. Beachley, N.H., and Frank, A.A., "Increased Fuel Economy in Transportation Systems by Use of Energy Management-Second Series Program," D.O.T., December 1975.

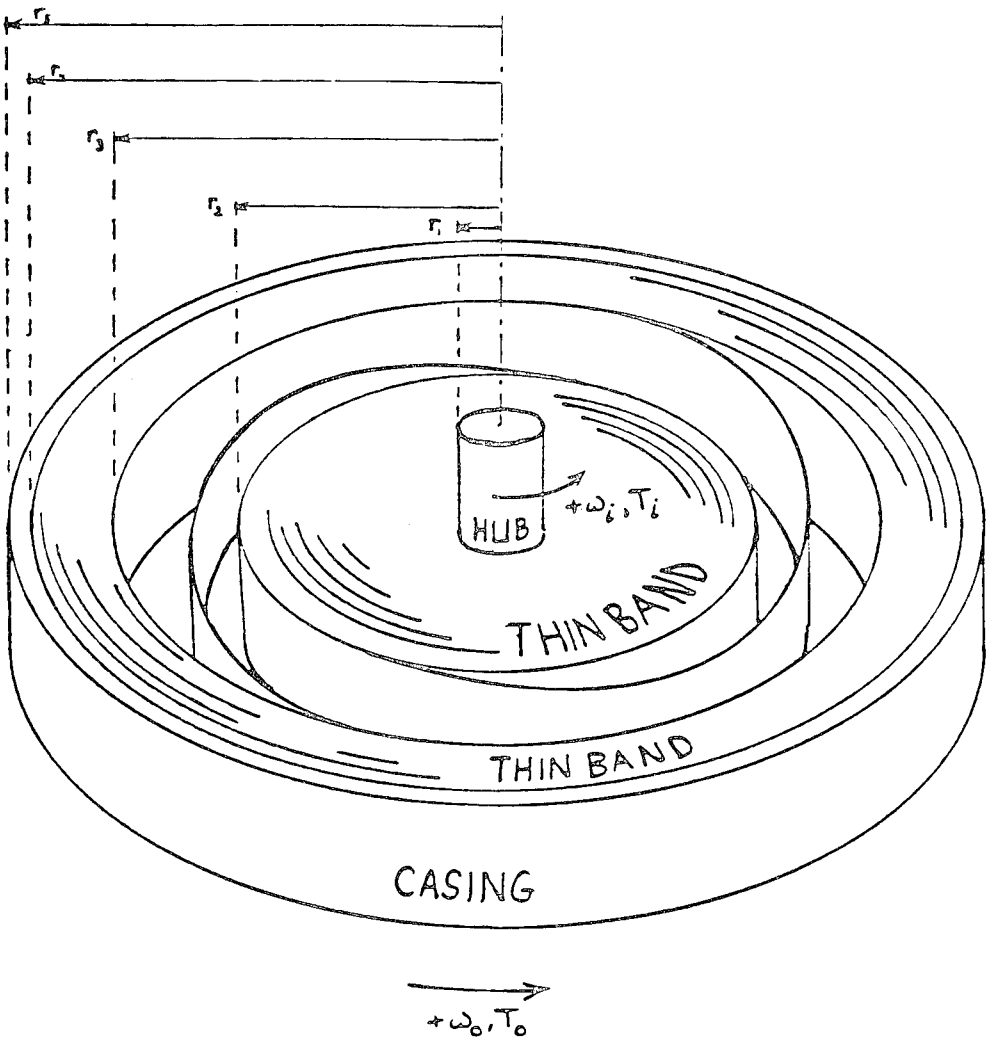

FIGURE 1

BVIF GEOMETRY WITH SIGN CONVENTIONS

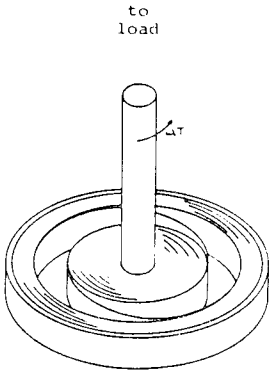

TYPE I

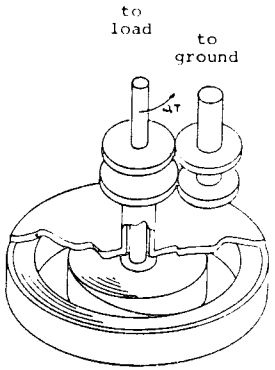

TYPE II

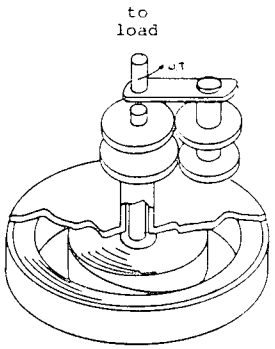

TYPE III

FIGURE 2

BVIF CONFIGURATIONS

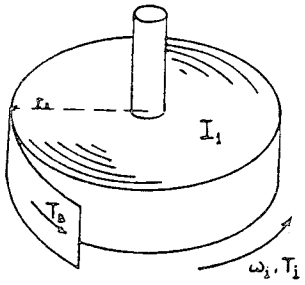

INNER INERTIA FREE-BODY DIAGRAM

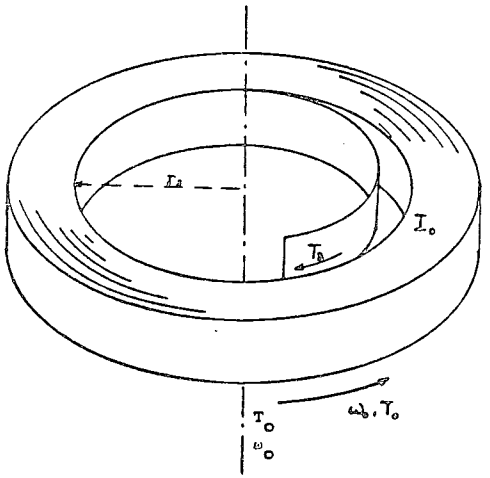

OUTER INERTIA FREE-BODY DIAGRAM

FIGURE 3

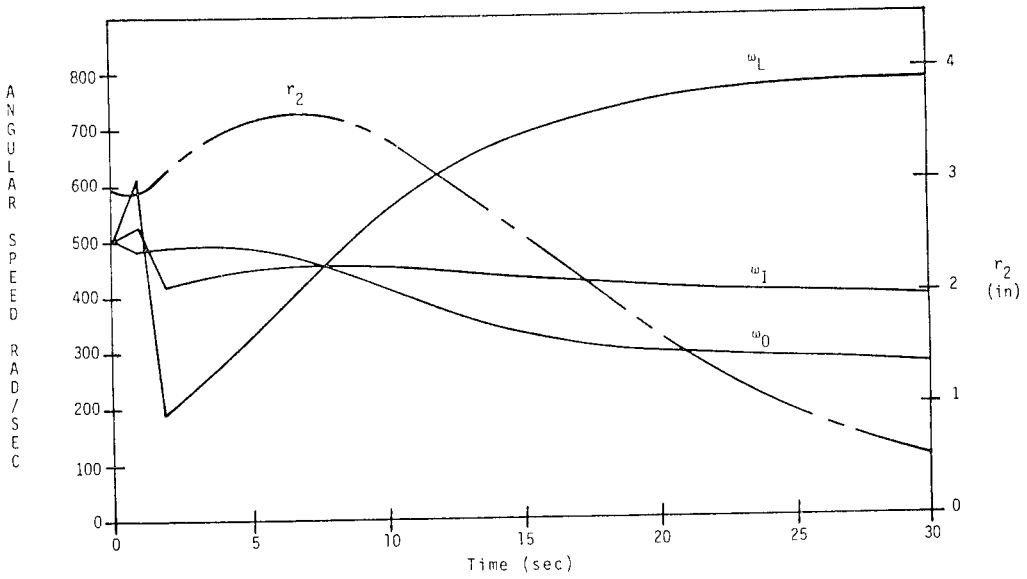

Figure 4a. Type III BVIF Simulation: Angular Rates and Band Position. Time History.

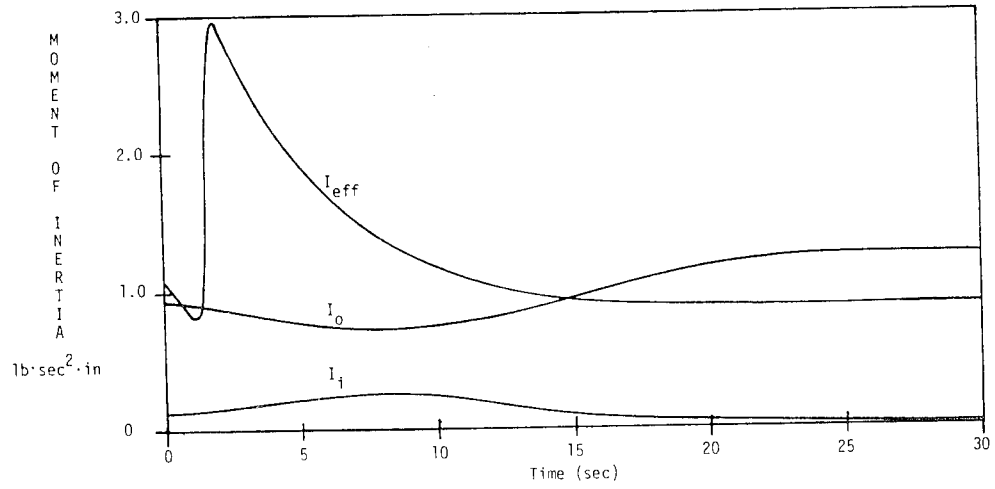

Figure 4b. Type III BVIF Simulation: Moments of Inertia. Time History.

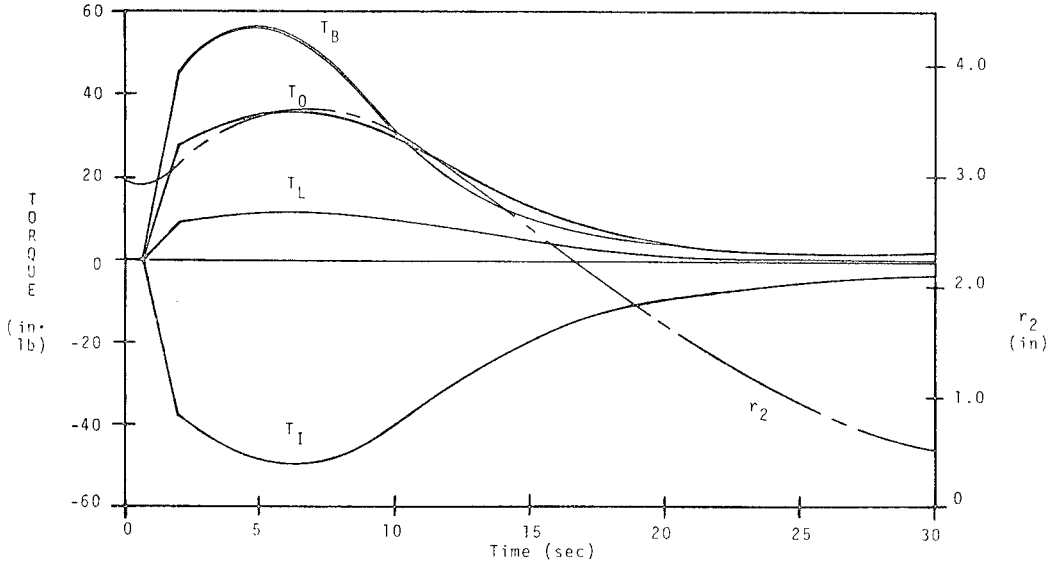

Figure 4c. Type III BVIF Simulation: Torque. Time History.

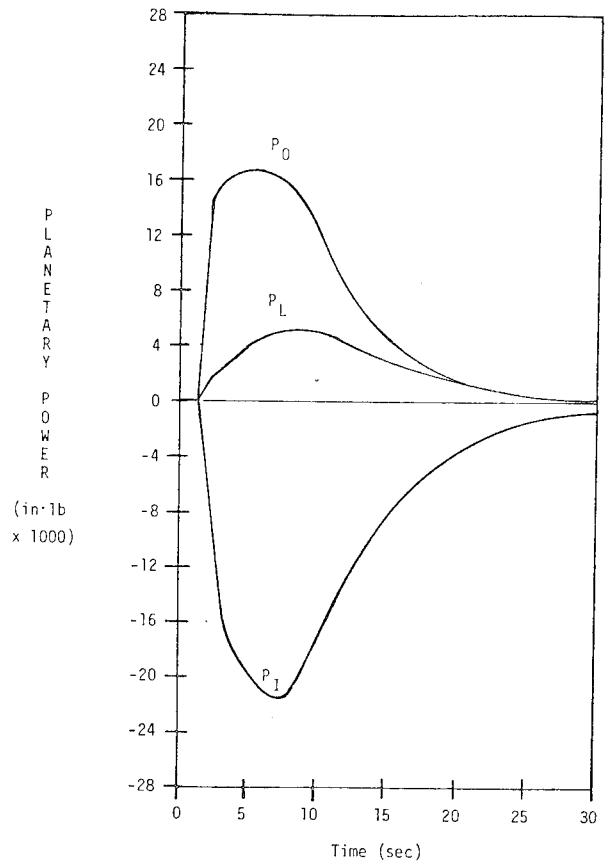

Figure 4d. Type III BVIF Simulation: Planetary Power.

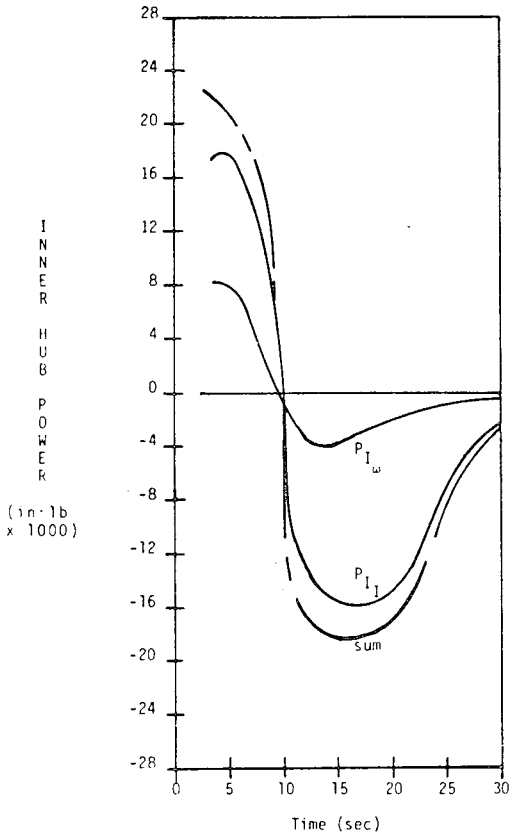

Figure 4e. Type III BVIF: Inner Hub Power. Time History; Plotted After Completed Clutch Engagement for Clarity.

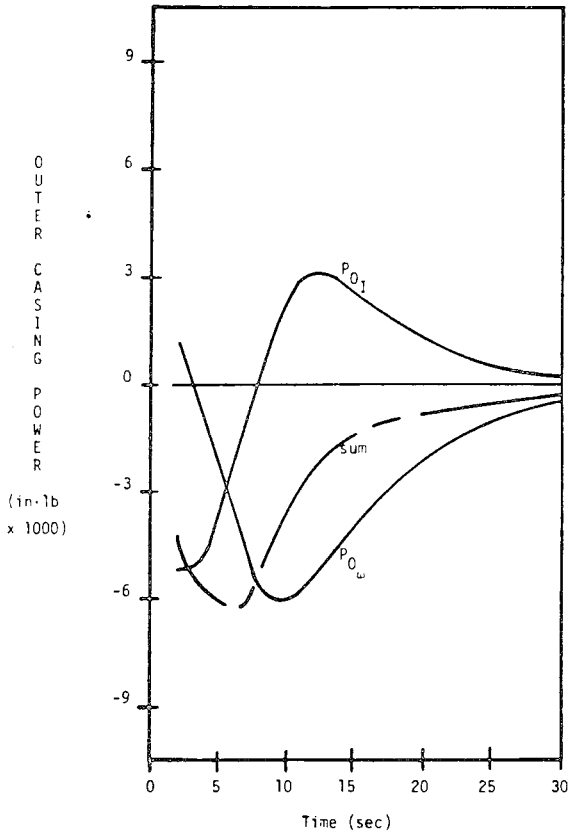

Figure 4f. Type III BVIF Simulation: Outer Casing Power. Time History; Plotted After Completed Clutch Engagement for Clarity.

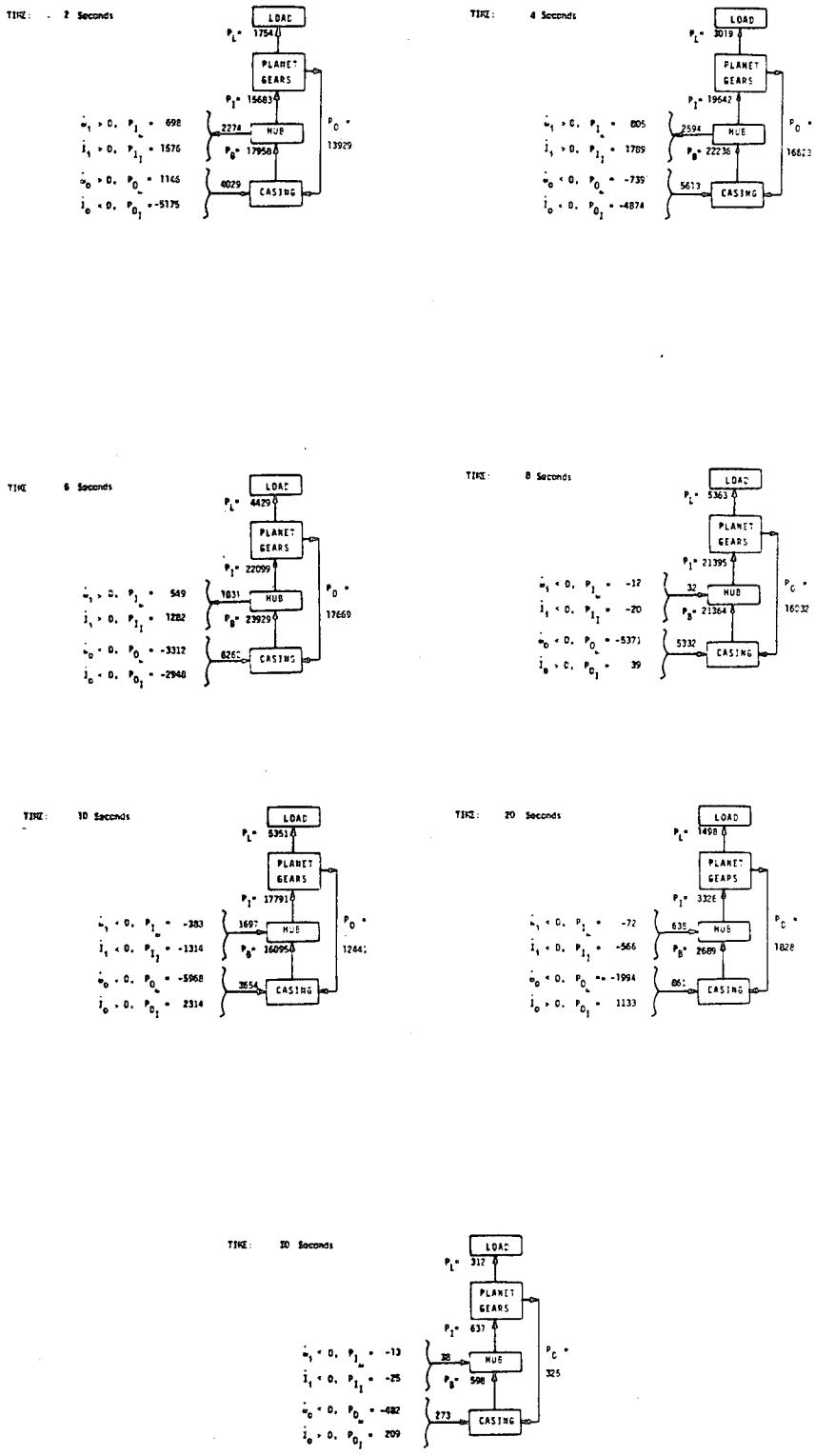

FIGURE 5

POWER FLOW IN BVIF EXAMPLE

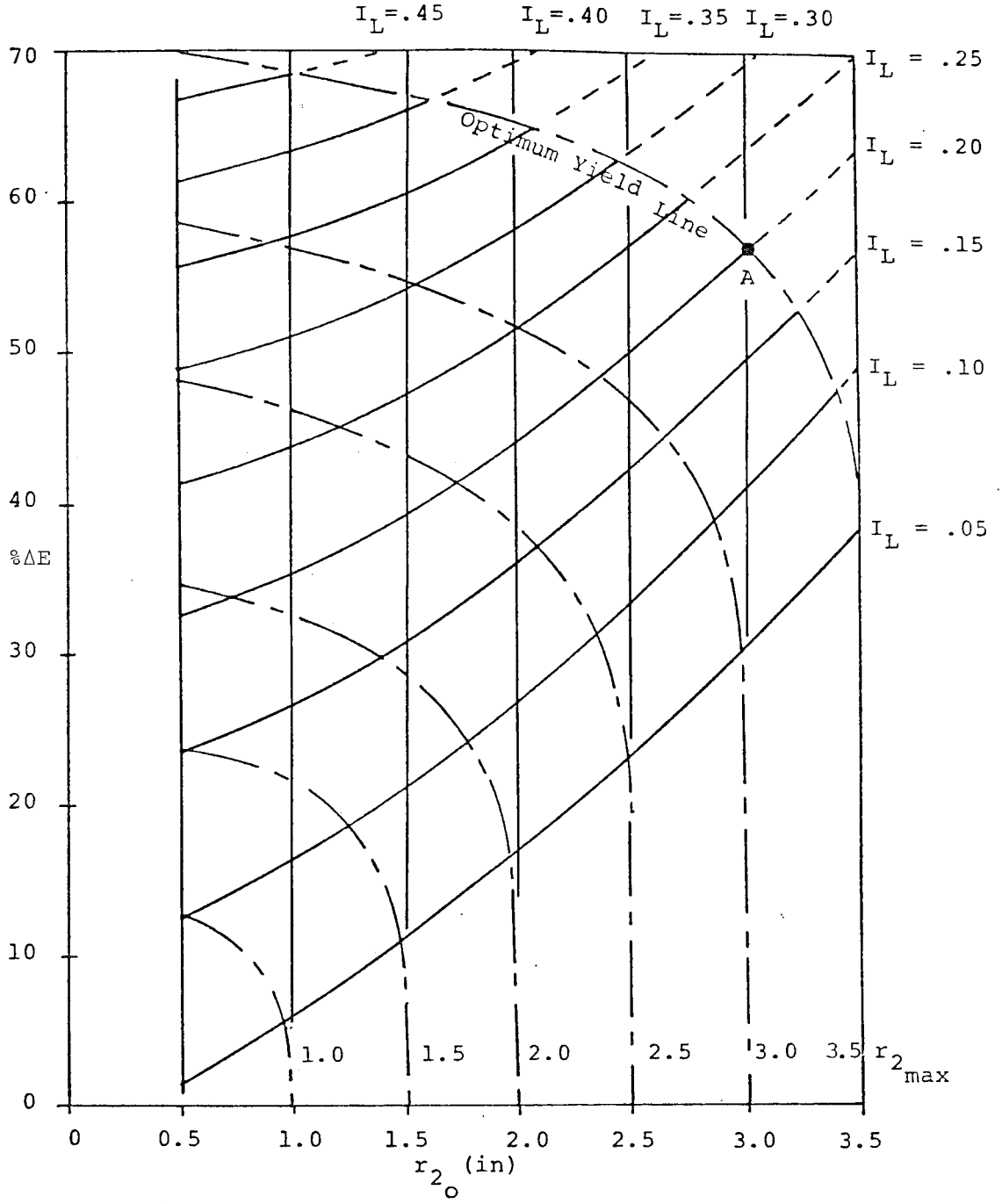

FIGURE 6

FRACTIONAL ENERGY YIELD VS r_{2_o} : Type III BVIF FOR 8 VALUES OF LOAD INERTIA, I_L WITH LINES OF MAXIMUM BAND WIND.

I_L INCLUDES FIXED LOAD SHAFT INERTIA = .05

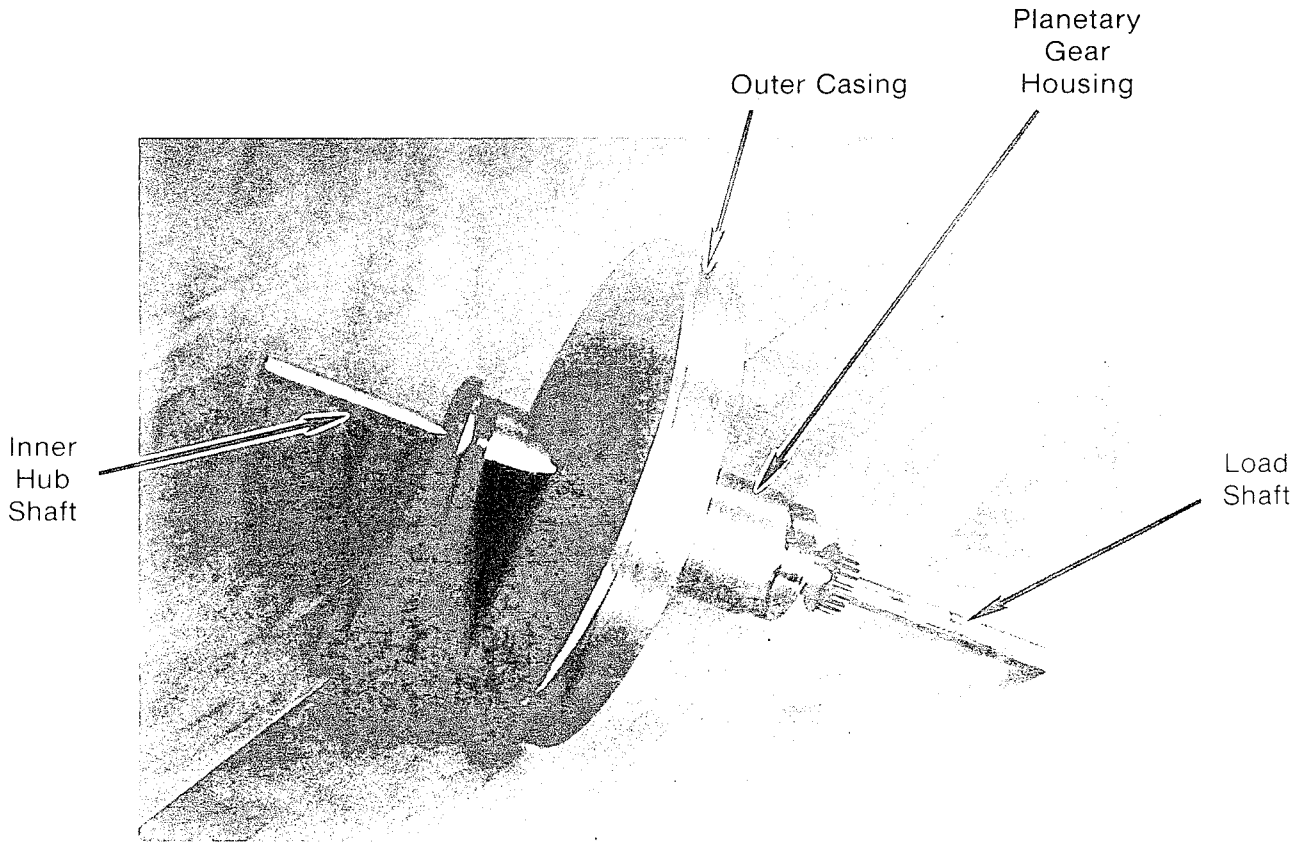

FIGURE 7

PROTOTYPE BVIF

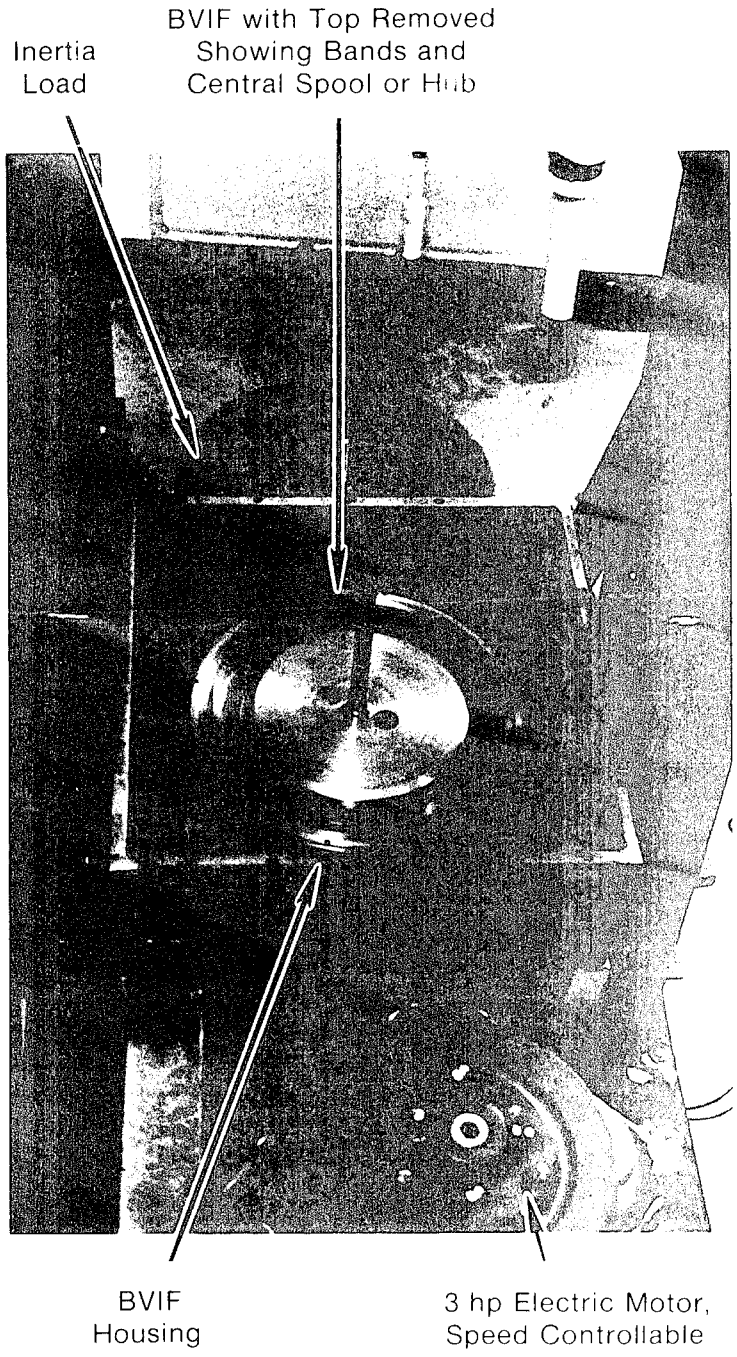

FIGURE 8
BVIF TEST STAND

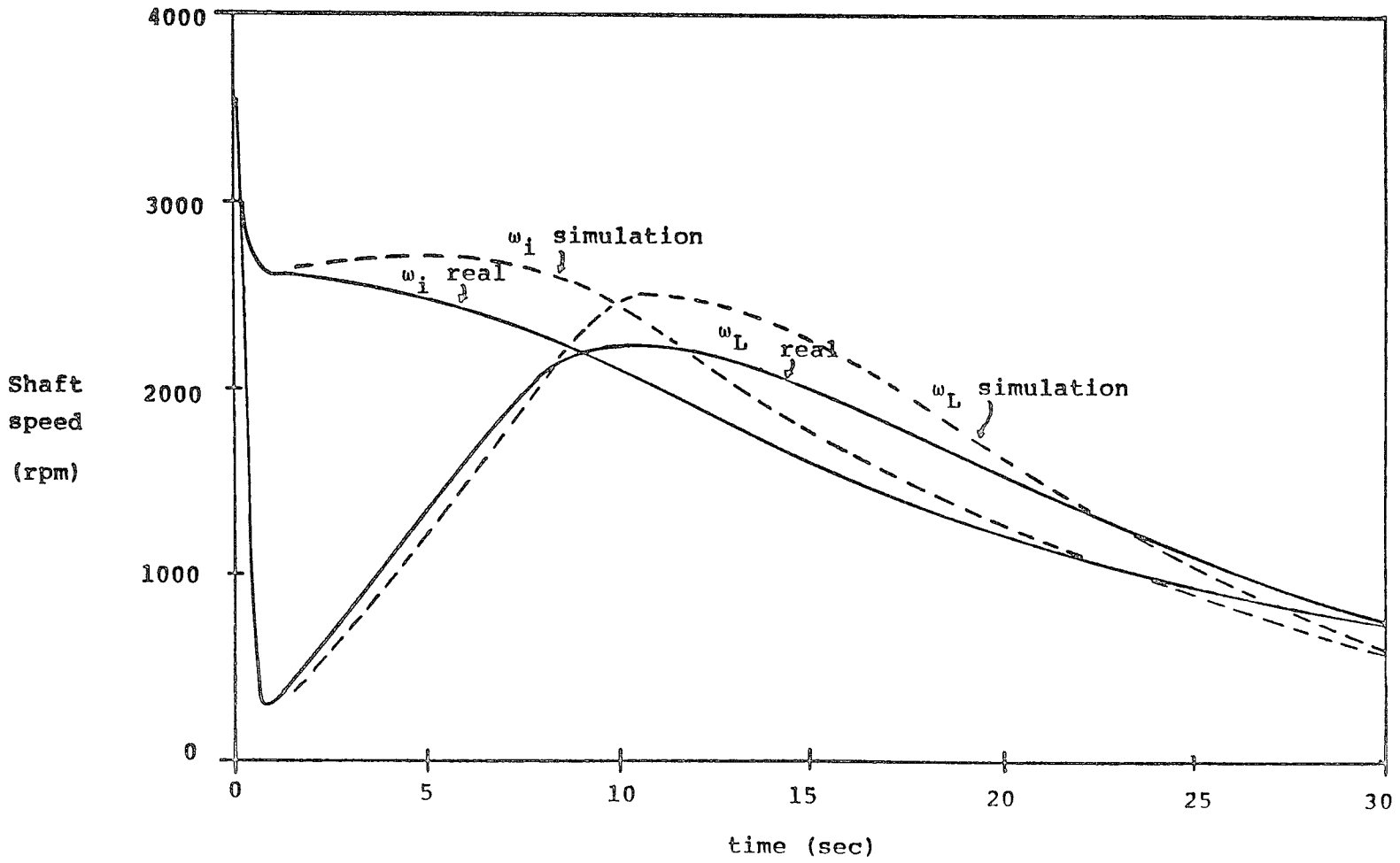

FIGURE 9

COMPARISON OF TYPE III MODEL WITH LOSSES TO ACTUAL PROTOTYPE RUN HISTORY

CONCEPTUAL DESIGN OF A FLYWHEEL ENERGY STORAGE SYSTEM

William H. Bauer
Francis C. Younger
William M. Brobeck & Associates
1235 Tenth Street
Berkeley, California 94710

ABSTRACT

A conceptual design of a flywheel energy storage system suitable for on-site interfacing with residential photovoltaic (PV) energy sources has been developed. The basic design objective was to provide a generous margin of safety and above average reliability and efficiency at the lowest practical cost. The basic concept utilizes a constant voltage motor/generator directly coupled to a flywheel rotor. The motor voltage level is maintained at the optimum operating voltage of the PV array. Power is drawn from the flywheel-driven motor/generator (operating as a generator) when the voltage output of the array drops below its optimum value. Power is delivered to the flywheel via the motor/generator (operating as a motor) when the voltage rises above the optimum value. A fiber-composite rotor driving a separately-excited motor satisfies the basic requirements. The flywheel operates in a vacuum and has a combination of magnetic thrust support and ball bearings to achieve acceptable efficiency and low run-down losses. The use of a hermetically-sealed magnetic power coupling eliminates the need for a rotary vacuum seal. Cost of the system has been determined for production models to be produced in annual quantities up to one-hundred thousand.

CONCEPT

The Flywheel Energy Storage System (FESS) concept integrated with a residential photovoltaic (PV) supply is shown in Fig. 1. The FESS acts as an energy buffer between the direct current PV supply and the alternating current utility power source to permit an optimum utilization of the available solar energy. The PV supply represents a variable voltage dc source with its voltage dependent upon its temperature and current and upon the solar insolation. With increasing insolation, the available PV energy will rise and may exceed the load demand of the home; excess power is then diverted for storage in the flywheel shown in the pit below the garage floor. This stored energy is subsequently recovered to supply electrical energy to the home when the available solar energy is inadequate to satisfy the demand.

Fig. 2 shows the general flow of power and main system elements. The generator coupled to the flywheel provides the electrical to mechanical energy conversion using adjustable field current to provide control of the power flow. The generator converts mechanical energy into electrical energy to discharge the flywheel when there is a demand for its energy or it acts as a motor to reverse the energy flow when there is a surplus of solar energy.

The link shown between the solar unit, the generator, and the power conditioner is a dc link set at the voltage which optimizes the power output of the PV cells. This optimum value of voltage depends upon the temperature of the PV cells and the solar insolation. The voltage is controlled by the field excitation of the generator and the flywheel speed. As the flywheel speed increases, the field current is reduced to maintain the desired voltage. The power conditioner provides the required conversion from 250 volts dc to 60 Hz/220 volt single phase ac.

The flywheel/generator system is shown in Fig. 3. The main elements are the flywheel, motor/generator, vacuum vessel and the flywheel suspension system.

The FESS design concept was developed specifically for a 10-kWh storage capacity system with a 5-kW maximum power output.

However, special emphasis was placed on assuring that the concept was adaptable for upward scaling to 50-kWh storage capacity and 10-kW maximum power output. Table 1 provides a comparative listing of the design features that primarily serve to distinguish the 10-kWh and 50-kWh storage capacity configuration.

The design has a generous factor of safety and high reliability. It is designed for a life expectancy of at least twenty years during which 10,000 charge/discharge cycles may be encountered.

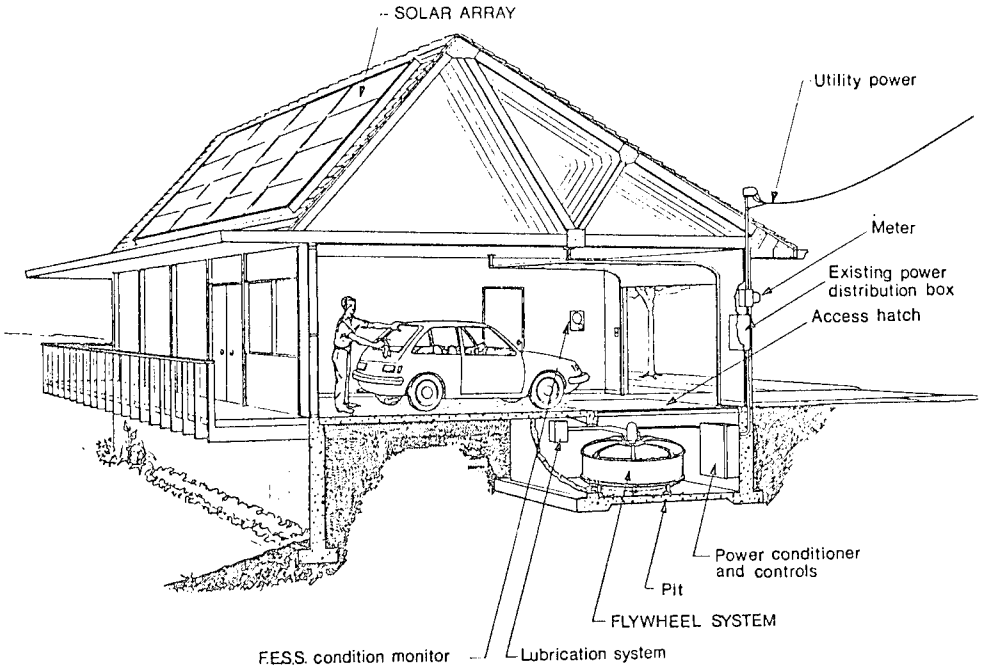

Fig. 1. Residential Flywheel Energy Storage System

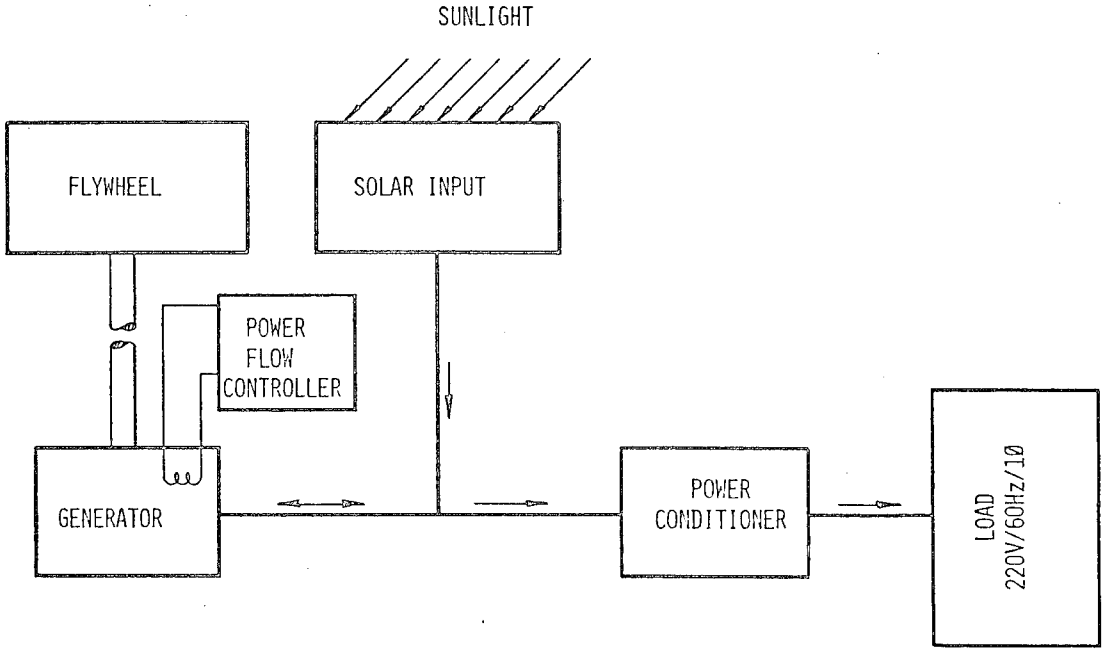

Fig. 2. Power Flow Schematic for FESS

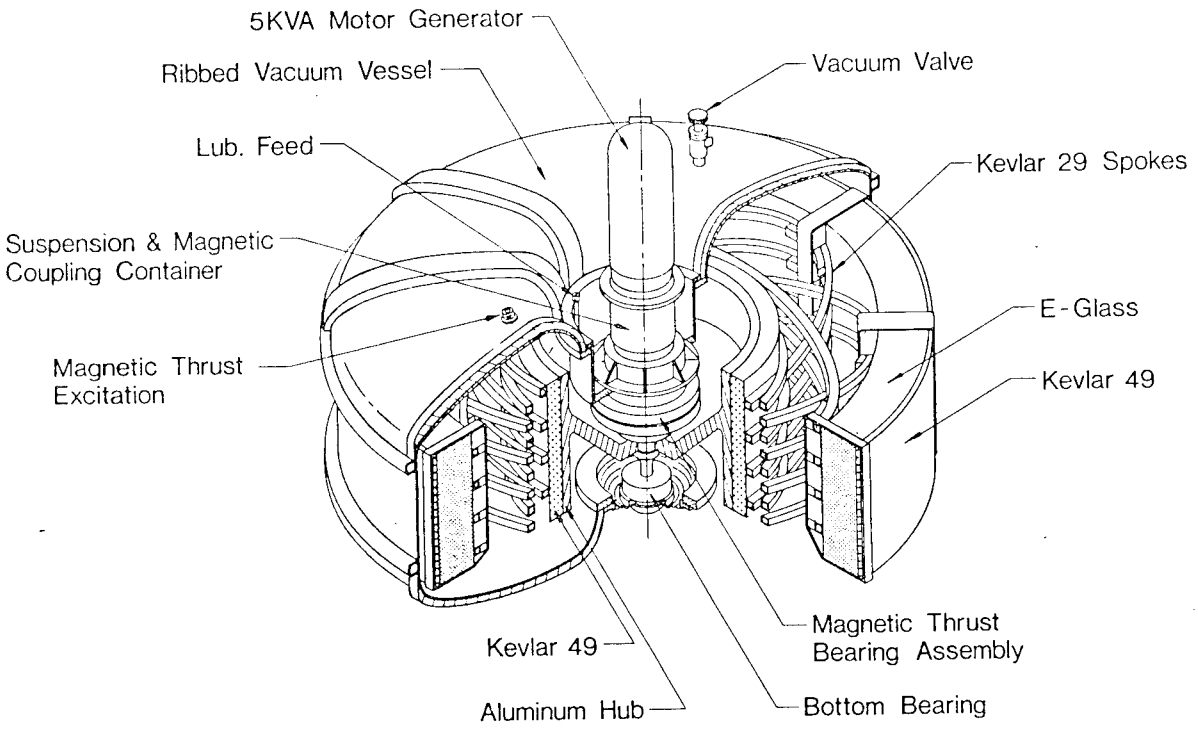

Fig. 3. Ten-kWh FESS Cut-Away View

Table 1. FESS Design Features.

Design Energy Storage	10 kWH	50 kWh
Working speed, rpm		
Maximum	9,800	5,730
Minimum	4,900	2,860
Rotor characteristics		
Outside diameter, in.	49.88	85.29
Inside diameter, in.	40.88	69.90
Height, in.	13.12	22.43
Weight, lb	906	4,530
Maximum stored energy,kWh	13.5	67.5
Maximum energy density, Wh/lb	14.9	14.9

DESCRIPTION OF COMPONENTS

TEN-kWh ROTOR

The rotor as shown in Fig. 4 is a biannulate rim supported by tension-balanced polar-catenary spokes which connect the central hub to the rim. The biannulate rim consists of a thick portion filament wound with E-glass/epoxy and a thin circumferential overwrap of Kevlar 49/epoxy. The outside diameter is 1.267 m (49.88 in.) and the inside diameter is 1.038 m (40.88 in.). The glass/Kevlar interface diameter is 1.249 m (49.16 in.). The rim axial length is 333 mm (13.12 in.). The relatively large amount of the inexpensive E-glass keeps the cost down and the high modulus Kevlar 49 overwrap suppresses the radial tension stresses which otherwise would occur in a thick rim. This design permits a high volumetric energy density as a large percent of the swept volume of the flywheel is occupied by highly stressed fiber-composite material. The rim weight is 278 kg (613 lbs) and the total weight is 411 kg (906 lbs). For 10-kWh of available energy, the peak stored energy is 13.5 kWh at 9,800 rpm, and the energy density is 32.8 Wh/kg (14.9 Wh/lb).

A 584-mm (23-in.) diameter hub reduces the radial space between the hub and rim to allow the Kevlar 29 spokes to be short enough to provide adequate rigidity to maintain hub/rim concentricity.

The rotor assembly incorporates sixteen spoke loops, with each loop providing four spokes for a total of 64 spokes. Each spoke is .89 inch thick by .82 inch wide. The contour of the spokes is a polar catenary, the natural shape of a flexible cord in a centrifugal force field. This contour theoretically eliminates all bending

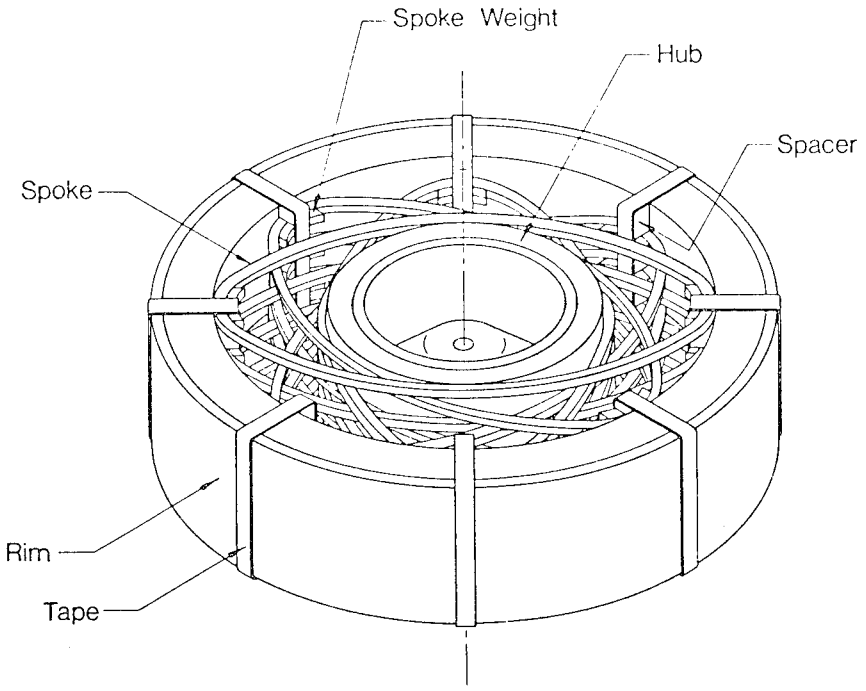

Fig. 4. Biannulate Rim Flywheel

moments in the spokes, and helps to reduce the maximum stress to a moderate level.[1] The spokes have adequate rigidity to assure that the rotor behaves as a rigid body, i.e., all of its significant vibrational modes are at sufficiently high frequencies to prevent self excitation. Centrifugal loading of the spokes and rim help to insure this rigidity.

The spokes contain steel loading weights at the junction with the rim. The centrifugal force on these weights causes the spokes to expand radially. The weights are sized to produce an expansion to match that of the rim thereby virtually eliminating radial loading on the rim. The low modulus of elasticity of the Kevlar 29 allows the loading weights to be small enough to minimize spoke tension stresses. There are a total of 32 weights (i.e. two per spoke loop) and each weighs 1.7 pounds.

The hub is made from aluminum alloy and is strengthened by a pre-stressed Kevlar 49 overwrap which partially resists the centrifugal loading on the aluminum portion. A section view of the hub was shown in Fig. 3. The radial stresses in the hub are minimized by the conical shape. The overwrap fits onto the aluminum with a diametral interference of .013 inches to produce a compressive preload which acts to reduce the maximum tensile stress in the aluminum caused by centrifugal loading.

SUSPENSION SYSTEM

The suspension system shown in Fig. 5 consists of a combination of precision ball bearings and a magnetic thrust bearing. The magnetic thrust bearing supports 90 percent of the rotor weight. The upper part is electrically energized to attract the lower part. Both parts are silicon iron with an outside diameter of 273 mm (10.75 in.). The gap between the two parts remains constant even if the rotor is experiencing a small precession with nutation.

The precision ball bearings maintain the required radial alignment of the rotor relative to the drive motor and support ten percent of the rotor weight. The housing for the main suspension bearings is attached to the vacuum vessel through an annular rubber pad. The resiliency of this pad permits a limited amount of radial motion of the rotor to accommodate a small amount of rotor unbalance without imposing excessive radial loads on the bearings. A small amount of precessional motion is also permitted. The lower bearing support is also mounted in rubber to permit a limited amount of motion. The rubber mounting pads provide damping to prevent dynamic instability. The system operates above the

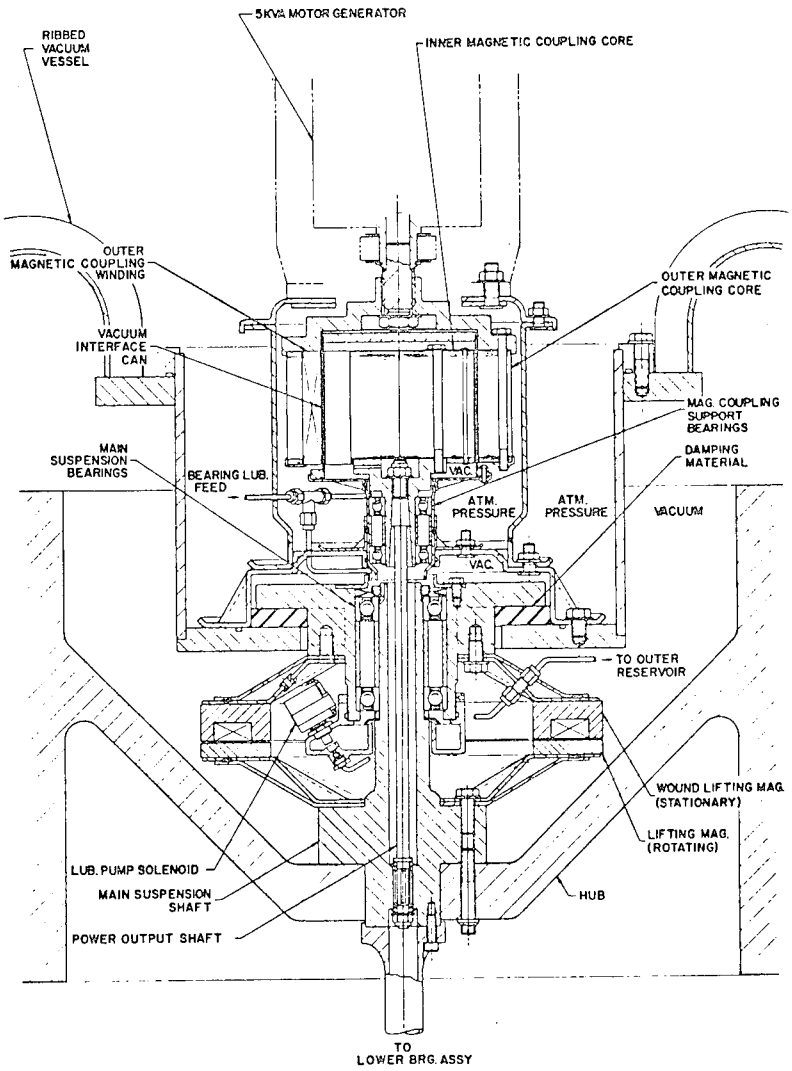

Fig. 5. Ten-kWh FESS Suspension and Magnetic Coupling

critical speed where asynchronous whirl modes can be excited unless adequate damping is provided.[2]

The upper bearings are lubricated by an oil drop system. Oil is injected into the top of the housing one drop at a time. The drop turns into mist as it hits the high speed rotating parts. Surplus oil is collected in a reservoir below the housing. A small solenoid-powered plunger intermittently pumps this oil to an evacuated exterior reservoir, from which it again flows to the top of the housing to repeat the cycle. Because of their light loading, the lower bearings can be lubricated with grease.

MAGNETIC COUPLING

The purpose of the magnetic coupling is to transfer torque through the vacuum vessel without the use of a dynamic seal. Both the inner and outer cores are constructed from laminated transformer silicon steel. The outer portion of the coupling is driven by the motor and holds the magnet coil windings. The inner portion which is coupled to the flywheel via a 12.7-mm (.5-in.) diameter quill shaft is driven synchronously as a salient-pole machine running on reluctance torque. The gap between the inner and outer portion is occupied by a vacuum barrier shown as a "vacuum interface can." The cylindrical wall of the can is made from G-10, an epoxy composite, 4.12-inch diameter by .03-inch thick in the 10-kWh system. In order to reduce run-down losses, the coupling is electrically activated only during charging or discharging.

MOTOR/GENERATOR

The motor/generator unit is an air-cooled, separately-excited, three-phase alternator.

VACUUM VESSEL

The vacuum vessel shown in Fig. 3 is made from twelve gage (.105 inch) steel stampings. Ribs are used to provide the required rigidity against the vacuum load and to provide adequate bearing support.

An O-ring seal is used to keep vacuum integrity. A valve provides a connection for a vacuum pump for periodic pump down. When the FESS is first assembled and pumped down, an initial outgassing period will be encountered. Baking out the system will speed up this outgassing process.[3] Once properly outgassed, the closed system is expected to remain at a sufficiently low pressure for many months, as the epoxy resin has a negligible vapor pressure.[4]

CONTROL SYSTEM CONCEPT

The FESS control system shown in Fig. 6 maintains the optimum flow of power from the PV supply by diverting excess power from the PV supply to the flywheel when the available solar power exceeds the demand of the home and by taking power from the flywheel when the demand is greater than that available from the PV supply. For a given insolation and temperature of the PV cells, there is an optimum dc voltage where the maximum power is drawn from the PV supply. If the load demand increases above this maximum power output, it would cause the voltage output of the PV supply to drop excessively. This voltage drop will be opposed by power diverted from the flywheel if the output voltage of the generator is set at the optimum value. Similarly, if the load demand decreases, the voltage of the PV supply tends to rise as the current falls. This rise in voltage and loss of current will also be prevented by having the output voltage set at the optimum value because as the PV output voltage rises, the generator becomes a motor and diverts power to the flywheel.

The FESS control system continuously monitors the dc bus voltage and sets it to a value which maximizes the power output of the PV supply. The set point voltage is produced through an integrated circuit pulse width modulator that regulates the field current of the generator.

Electronic commutation of the three-phase motor is provided by a three-phase waveform generator that develops the control signals for the power transistors which drive the motor. The developed signal is a periodic three-phase square wave. The frequency of operation is a direct function of the rotor speed as the clock signal is generated from the rotor position sensor. The rotor position sensor is comprised of a number of optical sensors, a slotted position wheel, and some logic. As the slots pass through the sensors digital pulses are generated. The pulses are then combined to form the clock for the waveform generator. One of the sensor outputs also serves as the input to the synchro-switch as an aid in controlling the magnetic coupling synchronization.

A unique feature is that the line voltage is monitored to prevent common devices from turning on simultaneously. This allows the conduction angle of the waveform to approach a maximum of 120^{o}.

High and low level detectors are used as alarm signals that indicate abnormal velocities of the flywheel. Other than its normal operating range, the flywheel can be in one of two conditions. It can be discharged to the point at which little useful energy remains or it may be charged to the point at which no more energy can safely be added to the flywheel. The high or low level detector will indicate either of these states.

RELIABILITY AND SAFETY

The overall design life of the system is 20 years. Certain parts such as the rolling bearings and the slip ring brushes were designed for periodic replacement. Stresses in rotating parts were kept as low as possible to ensure reliable operation. As the mechanical system is hermetically sealed, it is anticipated that reliability similar to that of hermetically sealed refrigeration units can be achieved. High-reliability industrial-grade electronic components were called out to ensure a 20-year lifetime with minimum service requirements.

The safety hazard in the event of total failure of the wheel and vacuum vessel is eliminated by installation of the unit

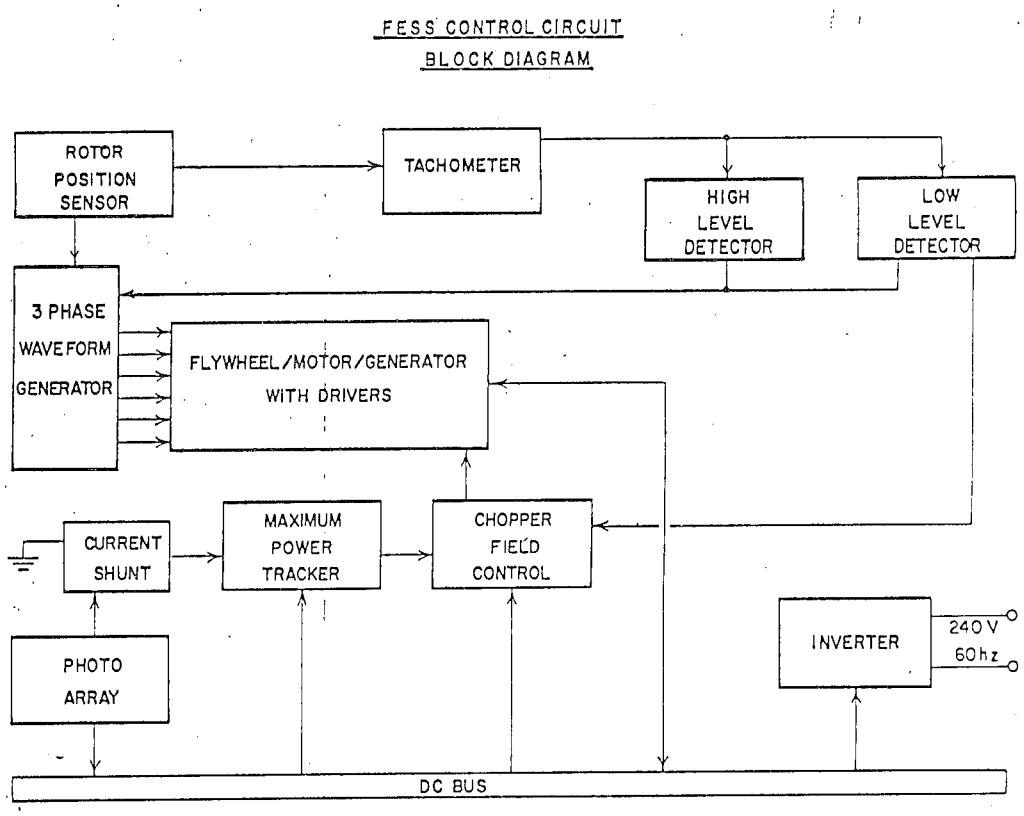

Fig. 6. Block Diagram of Control System

in a pit. The pit which provides environmental isolation and noise isolation also provides for rotor failure. Electrical wiring placed in conduit in accordance with local building codes is not expected to provide any safety hazards as the voltages and currents involved are similar to those found in present house wiring systems. Special effort should be taken, however, to ensure that insulation on wiring on the dc bus from the solar panels remains intact. The 250 volt dc bus is considerably more dangerous than the ac voltages found in present house wiring.

EFFICIENCY

Run-down losses for the 10 kWh design at 10,000 rpm are shown in Fig. 7. Total losses are 150 watts which correspond to 1.5 percent per hour.

Run-down losses vary with speed. A graph of losses vs. speed is shown in Fig. 8.

Power conversion losses are illustrated in a pie graph in Fig. 9. The losses total 465 W.

Power conversion efficiency is a function of power level and speed. A graph of the round-trip (charge and discharge) efficiency as a function of speed at two power levels is shown in Fig. 10. At the maximum power level of 5 kW, the average round-trip efficiency over the operating range is 71 percent. This value drops with lower power level until it reaches zero at zero power.

PRODUCTION COST

Productions costs[5] are summarized in Table 2. For a production quantity of 100,000 the cost for the system is $5,057 including the controller and inverter.

Table 2. Cost estimate for 10-kWh FESS.

Qty	Mechanical Parts	Controller Peak Power Tracker	Inverter	Total
10^2	7085	536	795	8416
10^3	5845	478	276[a]	6599
10^4	4955	441	235	5631
10^5	4445	412	200	5057

[a]Represents the change from a commercially purchased unit to an in-house design.

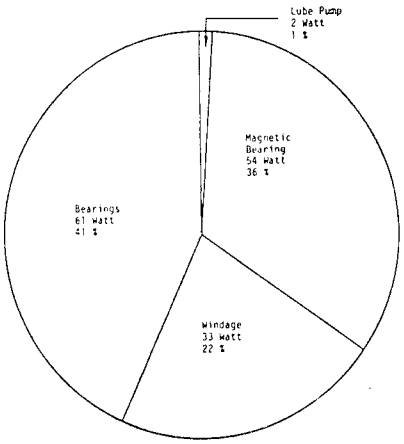

Fig. 7. Run-Down Loss Chart

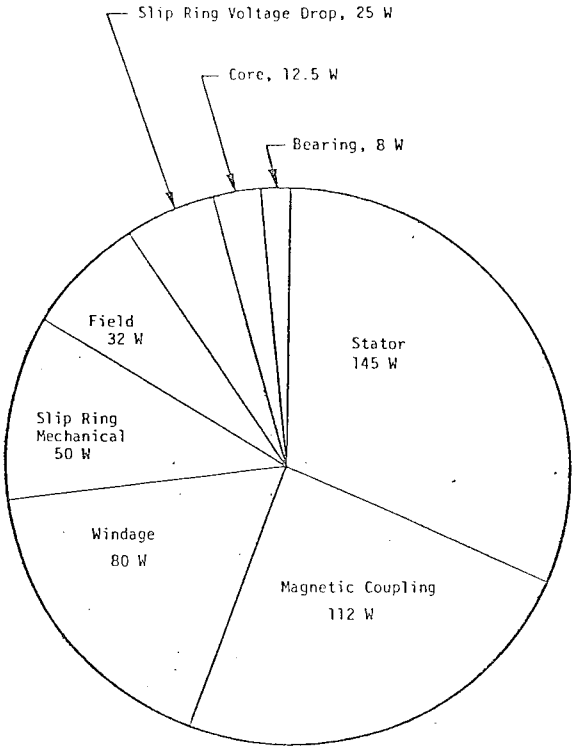

Fig. 9. Power Conversion Losses

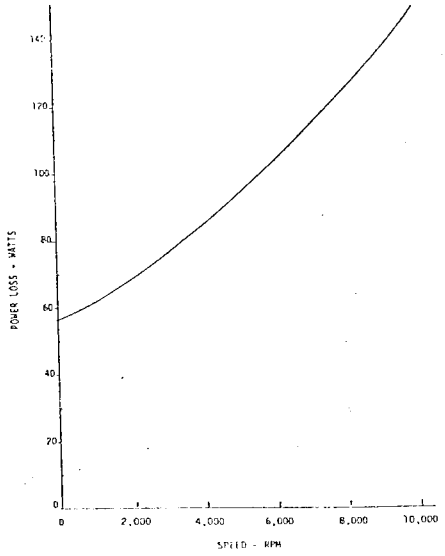

Fig. 8. Run-Down Loss vs. Speed

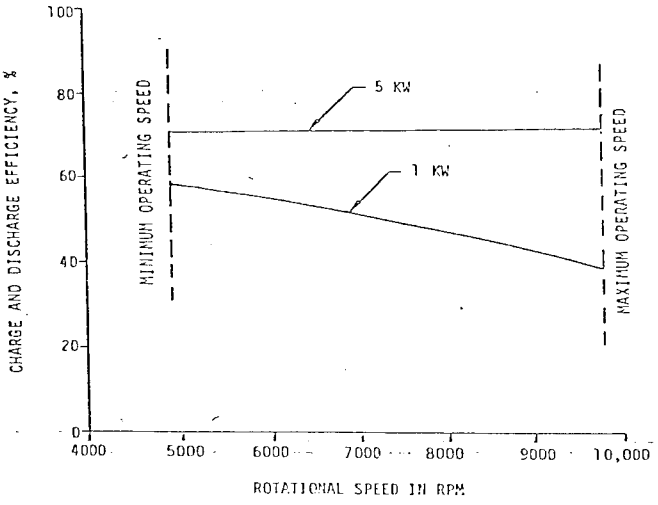

Fig. 10. Charge/Discharge Efficiency

REFERENCES

1. Younger, F. C., "Tension-Balanced Spokes for Fiber-Composite Flywheel Rims," 1977 Flywheel Technology Symposium, CONF-771053, March 1978.

2. Thomson, W. E., Younger, F. C., and Gordon, H. S., "Whirl Stability of the Pendulously Supported Flywheel System," Journal of Applied Mechanics, Vol. 44, Transactions of the ASME, Vol. 99E, June 1977, pp. 322-328.

3. Poehlmann, H. C., "Outgassing Tests of Fiber/Epoxy Composite Materials," Sandia Laboratories, Report No. SAND78-7075, February 1979.

4. Markley, F., Roman, Jr., and Vosecek, R., "Outgassing Data for Several Epoxy Resins and Rubbers for the Zero Gradient Synchrotron," 1961 Transactions of the Eighth Vacuum Symposium and Second International Congress, Pergamon Press, 3rd Ed., 1962.

5. Sandia Report No. 79-7088, Conceptual Design of a Flywheel Energy Storage System - Final Report," Sandia Laboratories, Report No. SAND79-7088, December 1979.

COMPOSITE FAILURE ANALYSIS FOR FLYWHEEL DESIGN APPLICATIONS*

P.V.McLaughlin, Jr., A.Dasgupta, and Y.W.Chun†
Department of Mechanical Engineering
Villanova University, Villanova, PA 19085

ABSTRACT

Laminate analysis is used to develop design information concerning the failure characteristics of quasi-isotropic laminated composite plates containing 2n-ply symmetric layups at equal angles of π/n. These laminates are elastically isotropic and have strength behavior which approaches isotropic if n is sufficiently large. This study determines the causes of a so called "biaxial strengthening effect" where laminate strength in equal biaxial tension may be 1.5 times the uniaxial tensile strength. It also determines the strength anisotropy of elastically isotropic composite laminates, and develops design curves for several laminate configurations using candidate material systems - a graphite/epoxy, an S2-glass/epoxy cured by vacuum bag/autoclave (VB/AC) process (about 50% fiber volume fraction), and S2-glass/epoxy cured by a matched metal die compression molding (MMDCM) process (about 60% fiber volume fraction). Results of the laminate analysis predictions are compared with test data, and conclusions are drawn concerning applicability of laminate analysis techniques and several different failure criteria as design tools for flywheel structures.

INTRODUCTION

Because of their high strength-to-weight ratios, "benign" failure characteristics and tailorability of mechanical properties, fiber composite materials have emerged as prime candidates for high speed flywheel rotor applications. Unlike steels and other isotropic materials, composites exhibit generally anisotropic failure characteristics, even when laminated in a configuration which produces isotropic stress-strain behavior.[1] Also, composite materials can have a significant biaxial strengthening effect, depending on the material system and layup configuration.[2] Lastly, because composites are heterogeneous materials, their failure behavior is further complicated by interlaminar stresses[3] and complex internal cracking.[4] All of these aspects of composite failure make the design of composite flywheels a difficult task.

Since fiber composite materials lend themselves to strength and elastic property tailorability, it is common to "design" the material system (layup, fiber material, and matrix) for specific design situations by use of constant strain laminate analysis,[5] which allows determination of laminate average elastic properties as functions of unidirectional ply properties and orientations and predicts stresses in individual layers for any given applied laminate average stress. It has been the practice for designers and analysts to use laminate analysis in conjunction with a layer failure theory and layer failure data to predict laminate failure by assuming that the laminate fails at load levels which cause the first ply to reach its failure stress. Although extremely good predictions of laminate elastic constants and layer stresses are obtained with laminate analysis, less success has been obtained with failure predictions. Two types of in-plane failure can occur: one is primarily due to matrix or fiber-matrix interface failure under transverse normal and/or axial shear stresses, and the other is primarily due to fiber failure (or buckling, in the case of compression) under axial normal stress. In fiber-dominated laminates (those with n=3 or more ply orientations), laminate failure usually

*The support of the Lawrence Livermore Laboratory for this research is gratefully acknowledged. The authors wish to thank Dr. S.V. Kulkarni, LLL Project Engineer, for his help and constructive criticism throughout this effort.

†Associate Professor, Graduate Student, and Assistant Professor, respectively.

occurs at stress levels well above, and never below, predicted layer matrix failures. For this reason, laminate stresses which cause first ply matrix failures can be considered a lower bound to laminate strength. A more realistic estimate of laminate failure for $n \geq 3$ can be considered to be predicted first layer fiber failure, which has been shown inductively[1] to give an upper bound to laminate failure under all but the most extreme cases of non-proportional loading.

In the present investigation, laminate analysis has been used to investigate, for design purposes, the failure characteristics of quasi-isotropic laminated composite plates, where 2n-ply symmetric layups at equal angles of π/n are elastically isotropic and have strength behavior which approaches isotropic if n is sufficiently large.[1] This study determines the causes of a so called "biaxial strengthening effect" where laminate strength in equal biaxial tension may be 1.5 times the uniaxial tensile strength. It also determines the strength anisotropy of elastically isotropic composite laminates, and develops design curves for several laminate configurations using candidate material systems - a graphite/epoxy, an S2-glass/epoxy cured by vacuum bag/autoclave (VB/AC) process (about 50% fiber volume fraction), and S2-glass/epoxy cured by a matched metal die compression molding (MMDCM) process (about 60% fiber volume fraction). Laminate failure analysis predictions are presented for several failure criteria - maximum strain, quadratic interaction, maximum stress, and "netting analysis". Results are compared with test data, and conclusions are drawn concerning applicability of laminate analysis techniques and failure criteria as design tools for flywheel structures.

LAMINATE FAILURE ANALYSIS

GENERAL

Linear elastic constant strain laminate failure analysis was performed on quasi-isotropic [0/±60], [0/±45/90], [0/±30/±60/90], and [0/±20/±40/±60/±80] (α-9, see ref. 6) laminates made from graphite/epoxy (Celion 6000/Narmco 5213) and S2-glass/epoxy (3M SP-250-S2) fiber composite materials. Two types of glass/epoxy materials were analyzed - one cured by the vacuum bag/autoclave process (VB/AC) resulting in about 50% by volume of fibers, and the other cured by a matched metal die compression molding process (MMDCM) which has about 60% by volume of fibers. Unidirectional composite properties were used as inputs to a laminate analysis computer program, and elastic properties and failure stresses were generated for four layer failure criteria (maximum strain, maximum stress, quadratic interaction, and netting, all discussed below).

Most laminate analysis codes, including the code used in this study, treat composite material behavior as linear elastic to failure. While axial tensile stress-strain behavior is linear to failure, axial shear and transverse compression are highly nonlinear[7,8] (Figure 1). Transverse tensile behavior of a layer can be nonlinear, especially if the layer is constrained between other non-parallel layers. Axial compressive stress-strain behavior may be highly nonlinear, depending upon shear stress-strain and failure properties of the matrix[9]. When performing a linear elastic laminate analysis, it is necessary to choose a single linear approximation to the nonlinear behavior. If stresses are low, an initial tangent modulus (Figure 1) approximation will produce accurate results for layer stresses and strains. If stresses are close to failure levels, a secant-to-failure modulus will give good results. Unfortunately, at incipient laminate failure, some layers are highly stressed and some are not, making choice between tangent and secant-to-failure approximate stress-strain curves difficult.

SELECTION OF STRESS-STRAIN PROPERTIES

In the present study, it was assumed that axial tensile, compressive, and transverse tensile behavior were all linear, leaving only transverse compressive and axial shear behavior to be approximated by tangent or secant-to-failure lines. Since it is possible for axial shear stresses to be high when transverse compressive stresses are low and vice-versa, it was necessary to construct several sets of properties for each material - all tangent moduli, all tangent moduli except axial shear, and both transverse normal and axial shear secant-to-failure moduli. In addition, macroscopic failure behavior in axial shear is known to be highly ductile in a [±45] configuration where cross plies prevent total separation after cracking,[7,8,10] but quasi-brittle when a layer is unconstrained by cross plies such as in a short-

beam shear test of unidirectional material.[11] These considerations gave a total of six possible linear idealizations of stress-strain behavior to failure of a unidirectional fiber composite layer, as shown in Table 1. It is noted that this ignores any effects of adjacent constraint layers upon transverse tensile "ductility" and failure, and any nonlinearity in axial compression.

Complete data on unidirectional properties were not available, and estimates had to be made from data for similar materials. A summary of the six sets of approximate properties for each of the one graphite/epoxy and two S2-glass/epoxy materials is presented in Tables 2a,b, and c. Failure analysis was performed for all six sets of properties for each material, and final results selected according to the ranges of validity shown in Table 1. Failure criteria used in the analysis are described in the following section.

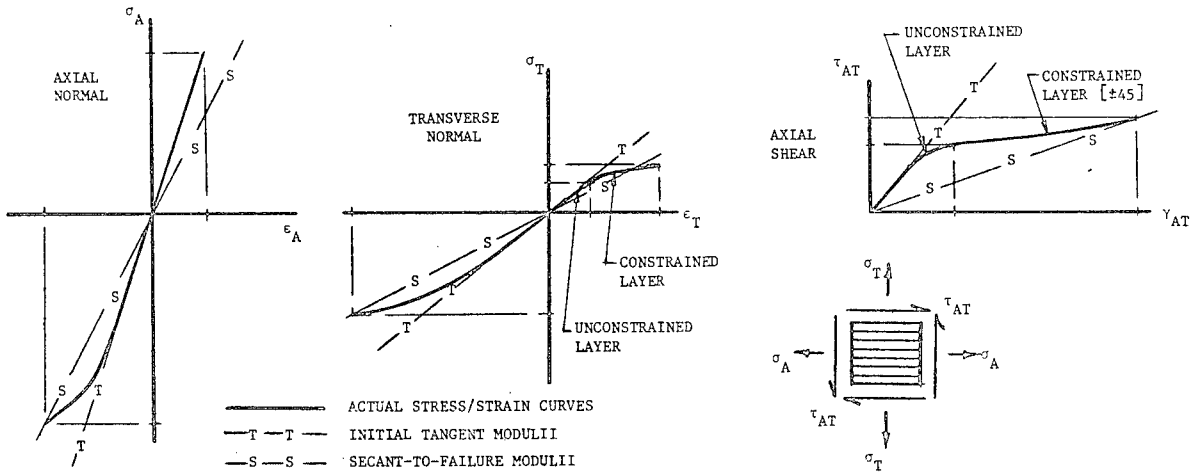

Figure 1. Typical stress-strain curves for [0] fiber composites[7,8,20] showing tangent and secant modulus linear approximations.

Table 1. Linear approximations of unidirectional fiber composite material stress-strain behavior used in present study.

Approximation Type	Axial		Transverse		Axial Shear		Range of Validity
	Tens	Compr	Tens	Compr	Constrained [±45]	Unconstrained (Short Beam Shear)	
Tan Mod Shear Cons	T	T	T	T	T	--	All values of ax tens, ax compr, trans tens; low values of trans compr, ax shear.
Tan Mod Shear Uncon	T	T	T	T	--	T	
Sec Shear Shear Cons	T	T	T	T	S	--	All values of ax tens, ax compr, trans tens; low values of trans compr; high values of ax shear.
Sec Shear Shear Uncon	T	T	T	T	--	S	
Sec Shear/ Trans Comp Shear Cons	T	T	S	S	S	--	All values of ax tens, ax compr; low values of trans tens; high values of trans comp, ax shear.
Sec Shear Trans Comp Shear Uncon	T	T	S	S	--	S	

T = Initial Tangent Modulus (See Fig. 1)
S = Secant-To-Failure Modulus
Comp = Compression
Tens = Tension
Cons = Constrained Layer
Uncons = Unconstrained Layer
Ax = Axial
Trans = Transverse

Table 2. Tangent and secant modulus property approximations.

a. Celion 6000/NARMCO 5213 Graphite/Epoxy

Approximation Type	Moduli, 10^6 psi			ν_A	Failure Stresses, 10^3 psi				τ_{AT}	A_{AT} 10^{-10} psi^{-2}	Failure Strains, 10^{-3}				γ_{AT}
					σ_A		σ_T				ϵ_A		ϵ_T		
	E_A	E_T	G_{AT}		Ten	Com	Ten	Com			Ten	Com	Ten	Com	
Tan Mod Shear Cons	21.0	1.4	0.7	0.3	259.0	177.0	7.0	20.0	10.4	-2.82	12	11	5.2	30	110
Tan Mod Shear Uncon	21.0	1.4	0.7	0.3	259.0	177.0	7.0	20.0	9.35	-2.82	12	11	5.2	30	67
Sec Shear Shear Cons	21.0	1.35	0.095	0.3	259.0	177.0	7.0	20.0	10.4	-2.82	12	11	5.2	30	110
Sec Shear Shear Uncon	21.0	1.35	0.14	0.3	259.0	177.0	7.0	20.0	9.35	-2.82	12	11	5.2	30	67
Sec Shear/ Trans Comp Shear Cons	21.0	0.7	0.095	0.3	259.0	177.0	7.0	20.0	10.4	-2.82	12	11	5.2	30	110
Sec Shear/ Trans Comp Shear Uncon	21.0	0.7	0.14	0.3	259.0	177.0	7.0	20.0	9.35	-2.82	12	11	5.2	30	67

b. 3M SP-250-S2 (VB/AC) S2-Glass/Epoxy

Approximation Type	Moduli, 10^6 psi			ν_A	Failure Stresses, 10^3 psi				τ_{AT}	A_{AT} 10^{-10} psi^{-2}	Failure Strains, 10^{-3}				γ_{AT}
					σ_A		σ_T				ϵ_A		ϵ_T		
	E_A	E_T	G_{AT}		Ten	Com	Ten	Com			Ten	Com	Ten	Com	
Tan Mod Shear Cons	6.2	1.65	0.78	0.3	230.0	134.0	7.9	28.0	12.3	-2.665	37	22	5	70	130
Tan Mod Shear Uncon	6.2	1.65	0.78	0.3	230.0	134.0	7.9	28.0	11.7	-2.665	37	22	5	70	76
Sec Shear Shear Cons	6.2	1.65	0.095	0.3	230.0	134.0	7.9	28.0	12.3	-2.665	37	22	5	70	130
Sec Shear Shear Uncon	6.2	1.65	0.154	0.3	230.0	134.0	7.9	28.0	11.7	-2.665	37	22	5	70	76
Sec Shear/ Trans Comp Shear Cons	6.2	0.4	0.095	0.3	230.0	134.0	7.9	28.0	12.3	-2.665	37	22	5	70	130
Sec Shear/ Trans Comp Shear Uncon	6.2	0.4	0.154	0.3	230.0	134.0	7.9	28.0	11.7	-2.665	37	22	5	70	76

c. S2-Glass/Epoxy (MMDCM)

Approximation Type	Moduli, 10^6 psi			ν_A	Failure Stresses, 10^3 psi				τ_{AT}	A_{AT} 10^{-10} psi^{-2}	Failure Strains, 10^{-3}				γ_{AT}
					σ_A		σ_T				ϵ_A		ϵ_T		
	E_A	E_T	G_{AT}		Ten	Com	Ten	Com			Ten	Com	Ten	Com	
Tan Mod Shear Cons	7.27	2.0	0.89	0.3	270.0	150.0	8.83	23.2	14.9	-2.874	37	21	4.5	67	115
Tan Mod Shear Uncon	7.27	2.0	0.89	0.3	270.0	150.0	8.83	23.2	12.0	-2.874	37	21	4.5	67	67
Sec Shear Shear Cons	7.27	2.0	0.13	0.3	270.0	150.0	8.83	23.2	14.9	-2.874	37	21	4.5	67	115
Sec Shear Shear Uncon	7.27	2.0	0.172	0.3	270.0	150.0	8.83	23.2	12.0	-2.874	37	21	4.5	67	67
Sec Shear/ Trans Comp Shear Cons	7.27	0.35	0.13	0.3	270.0	150.0	8.83	23.2	14.9	-2.874	37	21	4.5	67	115
Sec Shear/ Trans Comp Shear Uncon	7.27	0.35	0.172	0.3	270.0	150.0	8.83	23.2	12.0	-2.874	37	21	4.5	67	67

E_A=Axial Young's Modulus
E_T=Transverse Young's Modulus
G_{AT}=Axial Shear Modulus
ν_A=Axial Poisson's Ratio
σ_A=Axial Normal Failure Stress
σ_T=Transverse Normal Failure Stress
τ_{AT}=Axial Shear Failure Stress
A_{AT}=Quadratic Interaction Coefficient
ϵ_A=Axial Normal Failure Strain
ϵ_T=Transverse Normal Failure Strain
γ_{AT}=Axial Shear Failure Strain

Graphite/Epoxy properties deduced from references 8, 19, 20, 22.

Glass/Epoxy properties deduced from references 7, 8, 21, 23.

FAILURE CRITERIA

Current practice in predicting laminate failure by laminate analysis techniques utilizes one or more of the following failure criteria:

Maximum Strain. Failure is assumed to occur when axial normal, transverse normal, or axial shear strains reach critical values in tension or compression, resulting in the following equations:

$$\varepsilon_A^t, \text{ or } -\varepsilon_A^c = \frac{\sigma_A}{E_A} - \frac{\nu_T}{E_T}\sigma_T$$

$$\varepsilon_T^t, \text{ or } -\varepsilon_T^c = \frac{\sigma_T}{E_T} - \frac{\nu_A}{E_A}\sigma_A \qquad (1\ a,b,c)$$

$$\gamma_{AT}^o = \tau_{AT}/G_{AT}$$

where σ is normal stress, τ is shear stress, ε is normal strain, γ is shear strain, E is Young's modulus, ν is Poisson's ratio, G is shearing modulus, A is axial (fiber) direction, T is transverse to fiber direction, superscripts t and c indicate failure in tension and compression, respectively, and superscript o indicates failure in shear. The maximum strain failure criterion is shown in Fig. 2a for $\tau_{AT} = 0$.

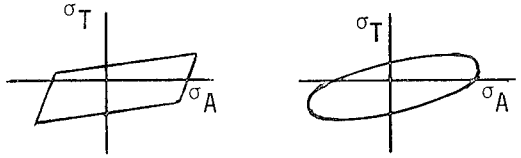

(a) MAXIMUM STRAIN

(b) QUADRATIC INTERACTION

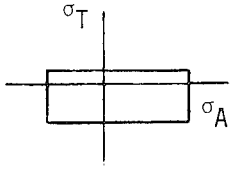

(c) MAXIMUM STRESS

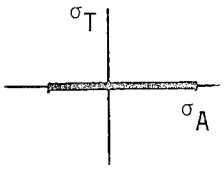

(d) NETTING

Fig. 2. Layer failure criteria

Quadratic Interaction. Several researchers[12-15] have proposed stress polynomial failure criteria which account for unequal properties in tension and compression as well as complicated interaction effects. The simplest of these is a quadratic interaction equation, which, when satisfied, predicts failure:

$$A_{AA}\sigma_A^2 + A_{TT}\sigma_T^2 + A_{AT}\sigma_A\sigma_T + A_S\tau_{AT}^2 + A_A\sigma_A + A_T\sigma_T = 1 \qquad (2)$$

The A's are constants which depend upon failure stresses in uniaxial and combined stress states. Of the six constants, only A_{AT} (called the quadratic interaction coefficient) requires a layer failure test under combined σ_A and σ_T stress. The rest can be determined from uniaxial data. In the present study, since combined stress data were unavailable, the quadratic interaction coefficient was assumed to be:

$$A_{AT} = -\frac{1}{\sigma_A^c \sigma_T^c} \qquad (2a)$$

where σ^c are failure stresses in compression. This assumption agrees reasonably well with experimentally determined interaction coefficients reported in reference 14. A typical quadratic failure criterion is shown for $\tau_{AT} = 0$ in Fig. 2b.

Maximum Stress. Failure is assumed to occur when axial normal, transverse normal, or axial shear stresses reach critical values in tension or compression:

$$\sigma_A = \sigma_A^t, -\sigma_A^c$$

$$\sigma_T = \sigma_T^t, -\sigma_T^c \qquad (3\ a,b,c)$$

$$\tau_{AT} = \pm\tau_{AT}^o$$

where τ_{AT}^o is the failure stress in axial shear, and σ^t and σ^c are failure stresses in tension and compression, respectively. The maximum stress failure criterion is shown in Fig. 2c for $\tau_{AT} = 0$.

Netting Analysis. Although somewhat of a misnomer, netting analysis of composites refers to performing a laminate analysis with $E_T = G_{AT} = \nu_{AT} = \nu_{TA} = 0$ (i.e., only elastic properties in the fiber or axial direction are assumed non zero) which approximates a laminate having each layer heavily cracked parallel to the fibers so that the layer carries load in axial tension and compression only. Stress concentrations in adjacent layers due to the cracks are ignored. The resulting layer failure criterion used in netting analysis is shown in Fig. 2d.

Designers and analysts of composite

structures generally use either the maximum strain or quadratic interaction failure criteria, since they have been shown to give good results in actual practice. The one drawback of the quadratic interaction criterion is a difficulty determining the mode of failure (i.e., fiber-dominated or matrix-dominated), which is not a problem for the maximum strain criterion. In the present study, computations were made for all four failure criteria for comparison purposes.

In a constant speed rotating disc, there will be normal radial and circumferential stresses, σ_r and σ_t, respectively. Shear stresses τ_{rt} will occur upon disc acceleration and deceleration, but are considered of secondary importance in high speed, low acceleration applications. Interlaminar shear and normal stresses will also exist at disc edges and throughout a tapered laminated disc. A typical plane stress distribution in a rotating flat disc is shown in Fig. 3. Both σ_r and σ_t are equal at the center. Radial stress decreases to zero at the outside radius; circumferential stress decreases, but not to zero. Circumferential stress is always greater than or equal to radial stress. Therefore, laminate failure results are presented in the form of failure interaction curves (loci of failure points in stress space) for flywheel circumferential and radial stresses, and as design curves for circumferential failure stress versus ratio of radial to circumferential stress, σ_r/σ_t. Results are discussed in the following sections.

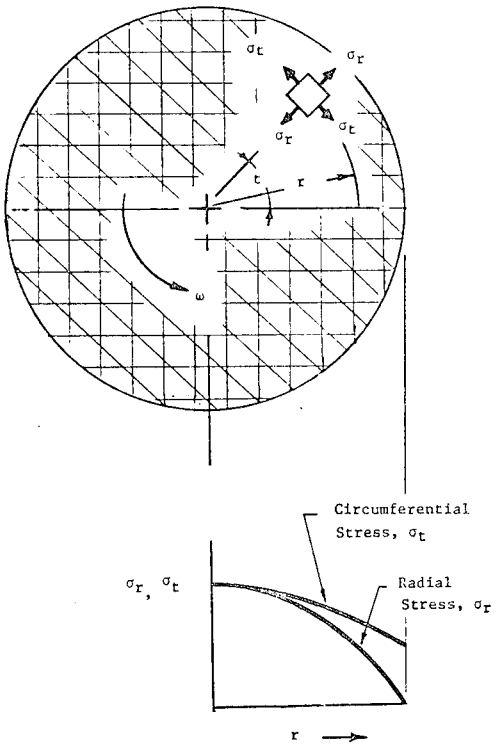

Fig. 3. Typical planar stress distribution in rotating isotropic laminated disc with no central hole

FAILURE INTERACTION CURVES

Laminate failure predictions were obtained under circumferential (σ_t) and radial (σ_r) stress for the four quasi-isotropic laminate configurations [0/±60], [0/±45/90], [0/±30/±60/90], and [0/±20/±40/±60/±80] made from graphite/epoxy and glass/epoxy. All six property variations of each material were analyzed, and failure interaction curves representing first layer matrix failure (lower bound on laminate strength) and first fiber failure (upper bound on laminate strength) were plotted.

It was found that layer shear failure was not a failure mode in any of the laminates for any of the material properties used. Since graphite/epoxy is extremely stiff in the axial direction (E_A/E_T = 15, E_A/G_{AT} = 30), and all laminates were fiber-dominated laminates, there was very little difference between laminate moduli calculated from tangent and secant elastic properties. Further, all laminate failures under σ_r, σ_t were found to be due to layer failures in either axial tension, axial compression, or transverse tension. Therefore, secant modulus versus tangent modulus results gave nearly identical failure interaction curves for graphite/epoxy.

For S2-glass/epoxy, transverse stiffness is the same order of magnitude as axial stiffness (E_A/E_T = 3.6, E_A/G_{AT} = 8). As a result, tangent modulus and secant modulus results were significantly different, even though shear failure or transverse compression failure did not occur.

Representative failure interaction curves are presented for [0/±60] and [0/±45/90] graphite/epoxy using the maximum strain failure criterion in Figs. 4

through 6, and similar quadratic interaction results for [0/±60] graphite/epoxy in Figs. 7 and 8. Since results for both glass/epoxies are qualitatively similar to graphite/ epoxy results, only summary failure interaction curves are presented in Figs. 9 and 10. A complete set of both graphite/epoxy and S2-glass/epoxy results can be found in ref. 16. The following points are noteworthy upon comparing results for the different laminates and materials:

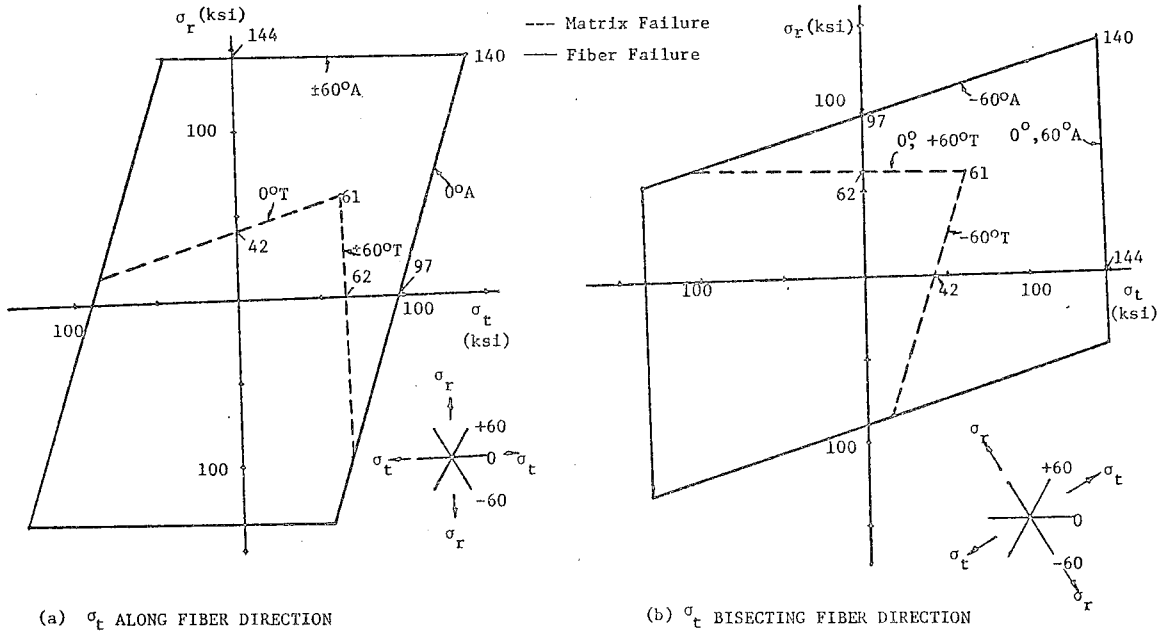

(a) σ_t ALONG FIBER DIRECTION

(b) σ_t BISECTING FIBER DIRECTION

Figure 4. Failure interaction curve for Celion 6000/Narmco 5213, $[0/\pm60]_S$ graphite/epoxy laminate, max. strain criterion.

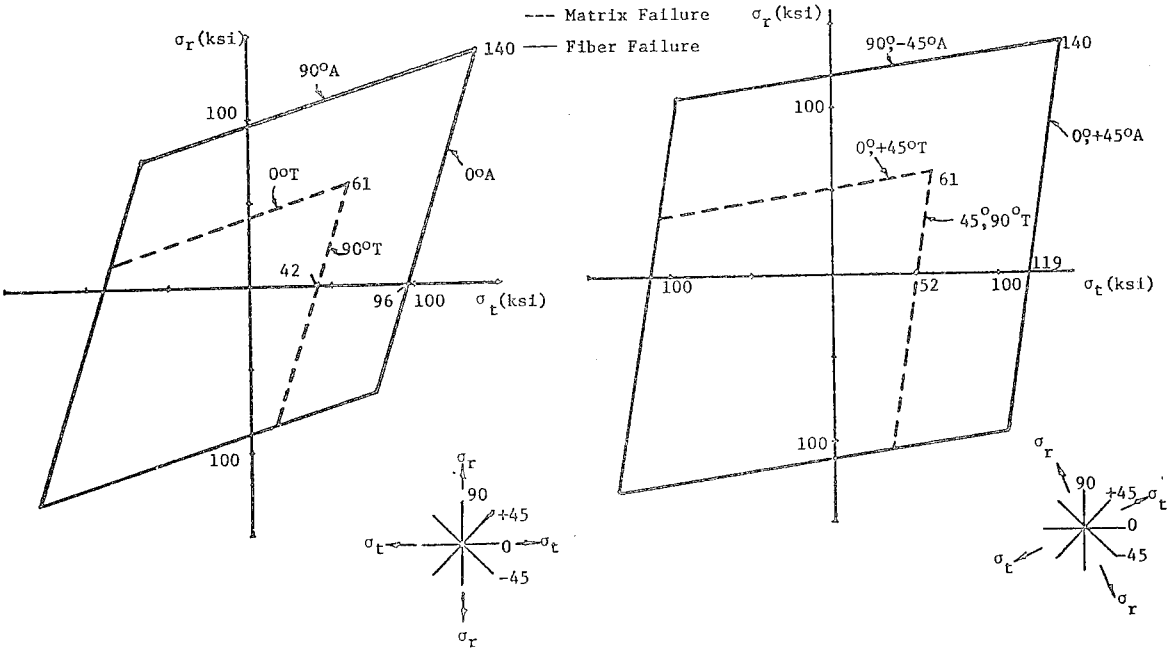

(a) σ_t ALONG FIBER DIRECTION

(b) σ_t BISECTING FIBER DIRECTION

Figure 5. Failure interaction curve for Celion 6000/Narmco 5213, graphite/epoxy $[0/\pm45/90]_S$ laminate, maximum strain criterion.

ANISOTROPY

Figure 4a shows the failure interaction curves for graphite/epoxy, maximum strain failure, of a [0/±60] laminate with σ_r the 0° direction, and σ_t splitting the 60° fibers in the 90° direction. Solid lines represent fiber failure (axial tension or compression), dotted lines represent first matrix failure (transverse tension). If σ_t were along the fibers and σ_r in the 90° direction, the resulting

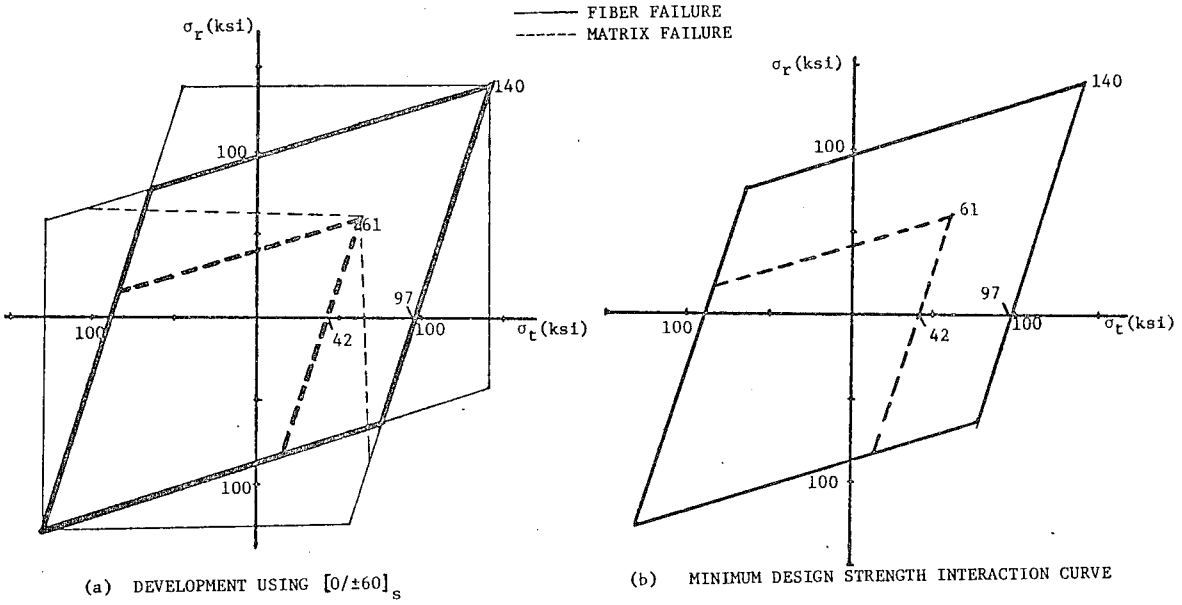

(a) DEVELOPMENT USING $[0/\pm60]_s$

(b) MINIMUM DESIGN STRENGTH INTERACTION CURVE

Figure 6. Minimum design strength interaction curve for all Celion 6000/Narmco 5213 graphite/epoxy laminates, maximum strain criterion.

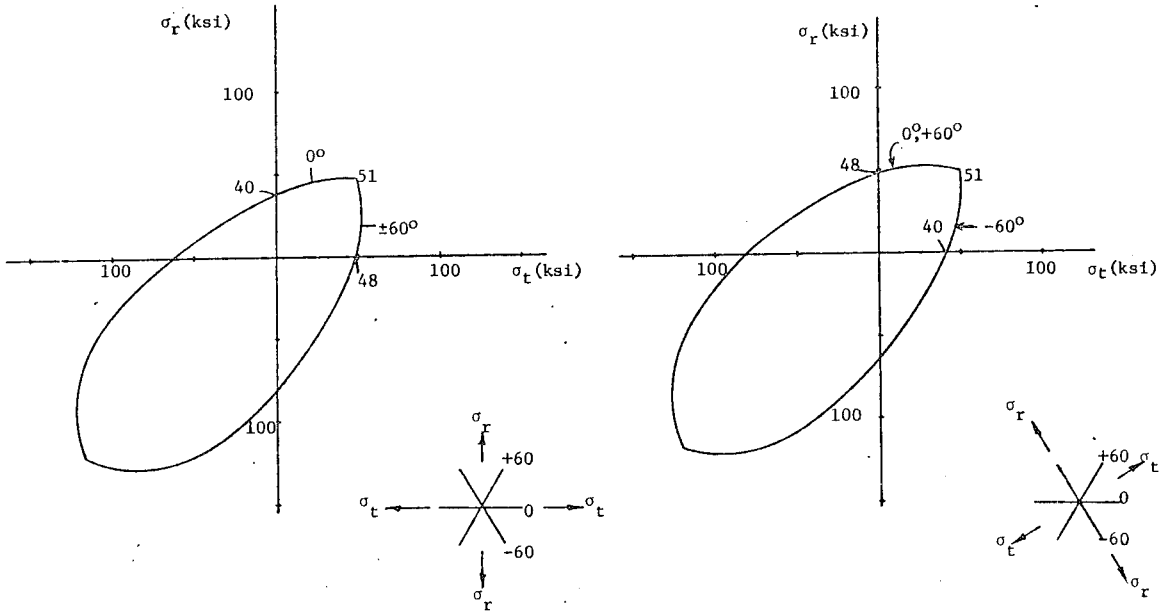

(a) σ_t ALONG FIBER DIRECTION

(b) σ_t BISECTING FIBER DIRECTION

Figure 7. Failure interaction curve for Celion 6000/Narmco 5213, graphite/epoxy $[0/\pm60]_S$ laminate, quadratic interaction criterion.

interaction curve is as shown in Fig. 4b. The tensile strength in the fiber direction is nearly 1.5 times that in the 90° direction if matrix failure precipitates laminate failure, and 1/1.5 if fiber failure is the dominant factor in laminate failure. It is seen that, irrespective of failure mode, the [0/±60] laminate exhibits a high degree of strength anisotropy even though it is elastically isotropic. Failure surfaces are shown in Figs. 5a and 5b for a [0/±45/90] graphite/

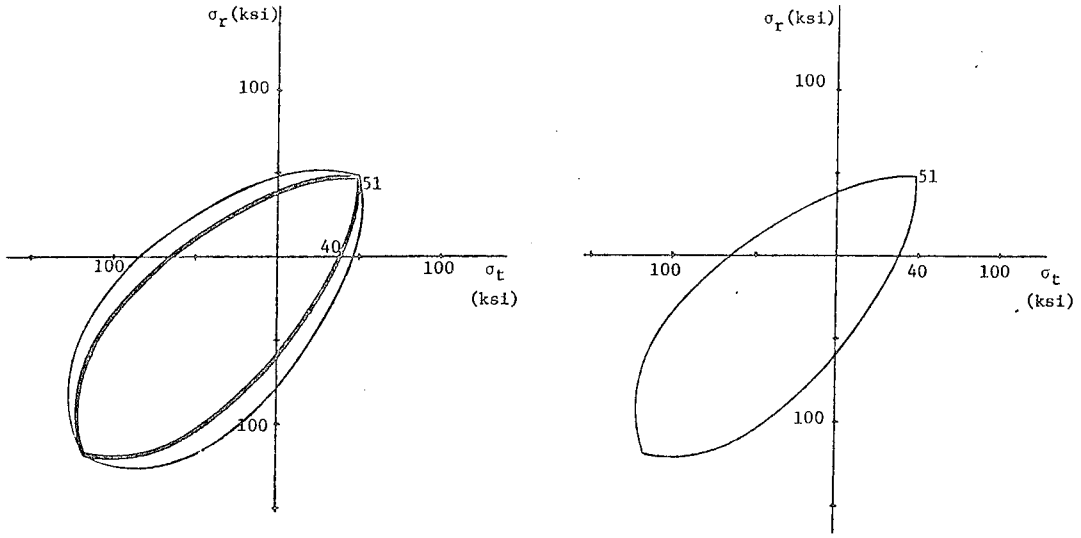

(a) DEVELOPMENT USING $[0/\pm60]_s$

(b) MINIMUM DESIGN STRENGTH INTERACTION CURVE

Figure 8. Minimum design strength interaction curve for all Celion 6000/Narmco 5213 graphite/epoxy laminates, quadratic interaction criterion.

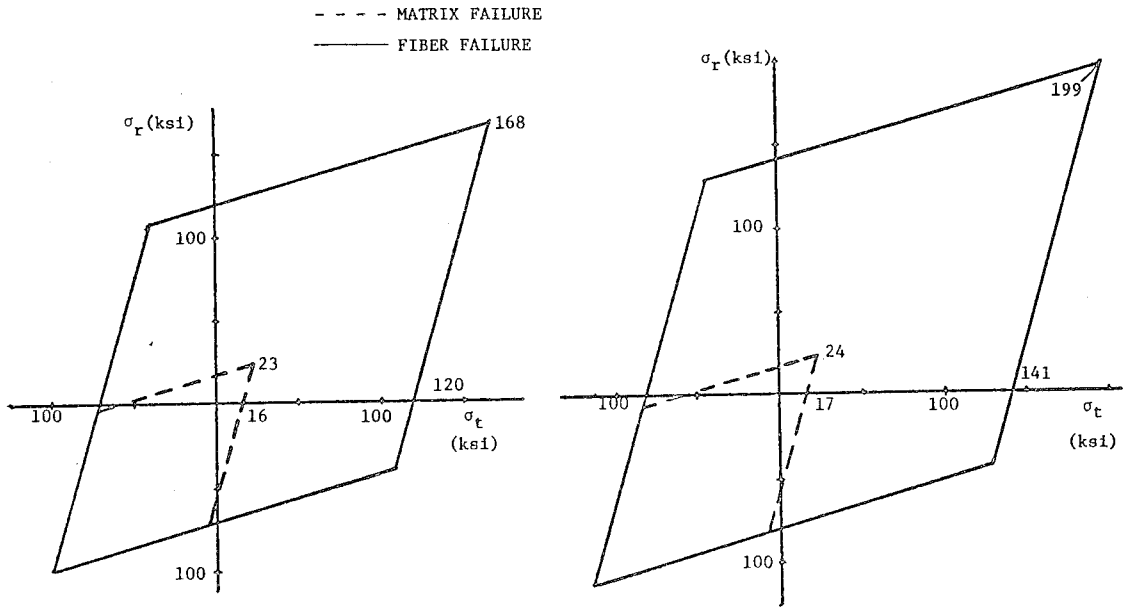

(a) VACUUM BAG/AUTOCLAVE CURED

(b) MATCHED METAL DIE COMPRESSION MOLDED

Figure 9. Minimum design strength for all quasi-isotropic laminates of 3M SP-250-S2 S2-glass/epoxy, maximum strain failure criterion.

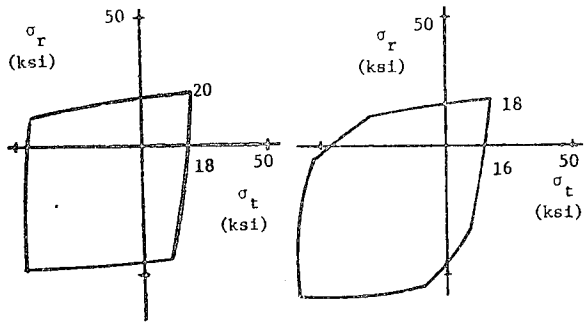

(a) VACUUM BAG/AUTOCLAVE CURED (b) MATCHED METAL DIE COMPRESSION MOLDED

Fig. 10. Minimum design strengths for all quasi-isotropic laminates of 3M SP-250-S2 S2-glass/epoxy quadratic interaction layer failure criterion.

epoxy laminate. Anisotropy results for all laminates are presented in Table 3. It is noted that as the number of layer orientations increases from three for the [0/±60] to nine for the α-9 laminate, the strength anisotropy decreases considerably. The maximum strain off-axis-to-axial strength ratio decreases from 1.5 for n=3 to less than 1.04 for n=9. Failure surfaces for the [0/±60] laminate by the quadratic interaction criterion are shown in Figs. 7a and 7b. Anisotropy results for quadratic interaction, maximum stress, and netting analysis failure criteria are qualitatively the same as maximum strain, as shown in Table 3. Anisotropy of S2-glass/epoxy laminates is also shown in Table 3, and is similar to the graphite/epoxy.

MINIMUM DESIGN STRENGTH INTERACTION CURVES

When any quasi-isotropic laminate is used in a flywheel, it is obvious that the radially symmetric nature of σ_r and σ_t will cause axes of radial and circumferential stresses to act at all angles to the fiber direction. A designer is therefore not interested in maximum strengths for a given laminate, but minimum strengths for failure resistance. Since σ_r and σ_t axes parallel to and

Table 3. Laminate anisotropy comparisons, ratios of off-axis strength to axial strength.

Failure Criterion	[0/±60]	[0/±45/90]	[0/±30/±60/90]	[0/±20/.....] α-9
a. GRAPHITE/EPOXY				
Max Strain M[a]	-1.5[b]	1.25	1.1	-1.05
F	+1.5	1.25	1.1	+1.04
Quadratic	-1.2	1.15	1.05	-1.02
Max Stress M	-1.35	1.2	1.05	-1.03
F	+1.5	1.25	1.1	1.04
Netting Analysis	1.5	1.25	1.1	1.04
b. S2-GLASS/EPOXY (VB/AC)				
Max Strain M	-1.47	1.23	1.09	-1.04
F	1.47	1.23	1.09	1.04
Quadratic	-1.19	1.10	1.04	-1.02
Max Stress M	-1.33	1.17	1.07	-1.03
F	1.43	1.21	1.09	1.04
Netting Analysis	1.5	1.24	1.1	1.04
c. S2-GLASS/EPOXY (MMDCM)				
Max Strain M	-1.47	1.23	1.09	-1.04
F	1.47	1.23	1.09	1.04
Quadratic	-1.24	1.13	1.05	-1.02
Max Stress M	-1.32	1.17	1.06	-1.03
F	1.43	1.22	1.09	1.04
Netting Analysis	1.5	1.24	1.09	1.04

[a] M = Matrix failure (transverse tension)

F = Fiber failure (axial tension)

[b] Negative sign indicates off axis weaker than axial.

splitting fiber directions represent the full range of strength anisotropy variations, the lowest failure predictions from the two failure surfaces will provide minimum design strengths for the composite flywheel designer. The method of developing minimum design strength failure interaction curves for a given laminate is shown in Fig. 6a for [0/±60] maximum strain failure predictions. The failure interaction curves for σ_t along a fiber direction (Fig. 4a) and σ_t bisecting fiber directions (Fig. 4b) are superimposed. The lowest failure stresses of the curves become the desired minimum design strength interaction curves (see also Fig. 6b). The procedure and results are shown in Figs. 8a through 8b for the quadratic interaction failure criteria and [0/±60] graphite/epoxy laminate.

When results of the remaining laminates, [0/±45/90], [0/±30/±60/90], and the α-9, were obtained, it was found that the minimum design strengths were identical to the [0/±60] results. This leads to the important result that the minimum design strength failure interaction curve based on analytical predictions of first layer failure is a material system property for all quasi-isotropic laminates. It is noted that this result has been verified for in-plane loads only, and may not be true if out-of-plane effects such as interlaminar stresses and stress concentrations due to adjacent cracked layers are present.

The minimum design strength failure interaction curves for graphite/epoxy (maximum strain and quadratic interaction failure) are shown in Figs. 6b and 8b. Results for S2-glass/epoxy, VB/AC and MMDCM processes, are shown in Figs. 9 and 10.

BIAXIAL STRENGTHENING EFFECT

A study of minimum design strength failure interaction curves for all materials analyzed shows that failure stresses under biaxial stress states are significantly higher than uniaxial failure stresses. At first, this biaxial strengthening effect was thought to exist only for the maximum strain theory of failure. However, laminate strength is higher under equal biaxial stresses for quadratic interaction, maximum stress, and netting analysis failure criteria as well. Table 4 shows ratios of biaxial strength to uniaxial strength for all materials considered, broken down by failure criterion and matrix- or fiber-dominated failure mode. In all cases except matrix failure by maximum stress, biaxial strengths are between 1.3 and 1.5 times higher than uniaxial strengths.

The mechanism of this strengthening under biaxial stresses has been studied. The effect is due to the highly anisotropic elastic behavior of unidirectional composite layers, coupled with the laminated plate nature of composite laminates. Even though a laminate is elastically isotropic, stresses in individual layers are considerably different from average laminate stresses due to layer anisotropy. In a laminate under uniaxial tension in, say, the X-direction, some layers oriented close to the Y (90° to X) direction will contain compressive axial stresses due to the negative transverse straining from Poisson's effect. These layers will have negative stress components in the X-direction. Even though there will be a high stress in the layer which precipitates laminate failure, X-direction components of non-failing compressive layer stresses will subtract from laminate average stress in the X-direction, lowering the average

Table 4. Ratios of minimum biaxial tensile strength to minimum uniaxial tensile strength for graphite/epoxy and S2-glass/epoxy.

Failure Criteria	Material Type		
	CELION 6000 Gr/EP	3M SP-250-S2	
		VB/AC	MMDCM
Max M[a]	1.45	1.39	1.41
Strain F	1.45	1.39	1.41
Quadratic	1.32	1.10	1.12
Max M	1.05	0.98	0.99
Stress F	1.41	1.26	1.27
Netting	1.48	1.50	1.50

[a]M = Matrix failure (transverse tension)

F = Fiber failure (axial tension)

stress at laminate failure. In equal biaxial tension, all layers have tensile stresses in all directions, and hence the laminate average stress at failure will be higher.

The importance of this biaxial strengthening effect to the design of laminated flywheels is clear. Not only are stress levels important to failure, so is the type of stress state. For example, if no biaxial strengthening effect existed, failure of an isotropic, flat, solid disc would initiate at the center of the disc where stresses are highest. However, even though stresses are smaller at the outer radius, only uniaxial circumferential stress σ_t exists. Therefore, failure may initiate at the outer radius of the flywheel. There is flywheel failure evidence to support this conclusion.[6]

TANGENT VERSUS SECANT MODULUS RESULTS

For graphite/epoxy, tangent modulus properties give nearly the same results as secant properties for the maximum strain failure theory. Quadratic interaction results, however, show differences in failure prediction for tangent and secant properties. For glass/epoxy, tangent modulus results are different from secant modulus results regardless of failure criterion used.

This can be explained by noting that in composites with extremely stiff fibers (graphite/epoxy), laminate elastic constants are not affected by changes in transverse normal or axial shear properties. Strains in layers, therefore, are nearly the same for tangent and secant modulus materials. Maximum strain failure results will be similar for the two materials. Stresses in layers, however, will depend upon layer moduli, and be different for tangent and secant properties. Stress-limited failure criteria will therefore produce different failure predictions for tangent and secant properties.

In composites where fiber direction stiffness is not large, changes in transverse normal and axial shear moduli will have a significant effect on laminate stiffnesses. Maximum strain laminate failure results will therefore be different for tangent and secant moduli. Stress-limited failure criteria such as quadratic interaction will be expected to give even greater differences.

FIBER FAILURE (UPPER BOUND) VERSUS MATRIX FAILURE (LOWER BOUND)

First fiber and first matrix layer failures as upper and lower bounds to laminate failure have already been discussed. For the maximum strain failure criterion and graphite/epoxy material, the matrix and fiber failure predictions are somewhat far apart, but are considerably closer together than for glass/epoxy. Matrix failures for glass/epoxy are predicted at about one-tenth the fiber failure stress. Since matrix failures seldom are direct causes of laminate failure, these results are not cause for concern. However, as discussed shortly, the fiber-dominated laminate failure predictions give some results which are contrary to experimental data.

COMPARISON WITH EXPERIMENTAL RESULTS

Since all material property information was not available and several elastic and failure properties had to be estimated, it was expected that direct comparisons of analytical results and experimental data would not be close. Trends in predictions and qualitative comparisons, however, should be able to be made.

Table 5a shows a comparison of laminate failure predictions by quadratic interaction, maximum strain (matrix and fiber), and netting analysis failure criteria, and test results for several graphite/epoxy and glass/epoxy laminates stressed along a fiber direction. Quadratic interaction and maximum strain matrix failures are well below test results, and maximum strain fiber failure predictions are higher than test results, but considerably closer than matrix failure predictions. Graphite/epoxy predictions are much closer to test results than are S2-glass/epoxy predictions. Netting analysis predictions, which assume matrix cracks parallel to fibers, give results which are very close to test data. This is not surprising since laminate analysis predicts that matrix cracks have formed due to transverse tensile stresses well before fiber failure stresses are reached, and indicates the desirability of analytically modeling matrix cracking and layer nonlinear behavior.

Table 5. Comparison of laminate strengths from "first failure" analytical predictions with test results.

a. TENSILE LOAD PARALLEL TO FIBER DIRECTION

Material	Laminate	Failure Stress, ksi				
		Quadr. Inter.	Maximum Strain		Netting	Test[a]
			Matrix	Fiber		
Gr/Ep	$[0/\pm45/90]_s$	40	42	96	84	70-79[8,18]
Celion 6000/5213	$[0/\pm30/\pm60/90]_s$	40	42	96	84	74[8]
S2-Gl/Ep	$[0/\pm45/90]_s$	16	16	120	77	84[8]
3M SP250-S2	$[0/\pm30/\pm60/90]_s$	16	16	120	76	71[8]
VB/AC	$[\alpha-9]$	16	17	120	77	80[8]

b. TENSILE LOAD BISECTING FIBER DIRECTIONS

Material	Laminate	Failure Stress, ksi				
		Quad. Inter.	Maximum Strain		Netting	Test[a]
			Matrix	Fiber		
Gr/Ep	$[0/\pm45/90]_s$	45	52	119	104	47-50[8,18]
Celion 6000/5213	$[0/\pm30/\pm60/90]_s$	42	46	106	92	50[8]
S2-Gl/Ep	$[0/\pm45/90]_s$	18	20	148	95	44[8]
3M SP250-S2	$[0/\pm30/\pm60/90]_s$	17	18	131	84	49[8]
VB/AC	$[\alpha-9]$	16	16	125	77	41[8]

[a]Superscripted numbers give sources of test data (see references)

Even though the along-axis analytical predictions show reasonable agreement with experiment, it has been found that results of uniaxial tensile tests with load direction bisecting fiber directions (off-axis tests) do not agree well with analysis. Table 5b presents comparisons between off-axis laminate strength by analysis and test[8]. Tests show that higher strengths occur when loading along fibers; analysis predicts the reverse for all theories but maximum strain first matrix failure of the [α-9] laminate. It is extremely likely that matrix cracking and/or specimen edge delaminations may have an effect upon fiber failure which is not recognized in the laminate analysis, or that matrix cracking in many layers is followed by large scale delamination and ultimate laminate failure prior to fiber failure. These conclusions are supported by observations during tests[8].

The laminate analysis predictions generated for this study have been examined to see if some combination of multiple layer failures might consistently give reasonable agreement with failure test results and show off-axis strengths weaker than along-fiber strengths. Vicario and Toland[24] discuss a laminate failure prediction which assumes that laminate failure does not occur until each and every layer has failed. This prediction methodology can be used with any layer failure criterion, and for convenience will be called an "all layers" failure methodology to distinguish from first layer failure already discussed. In order for the "all layers" method to produce realistic results, it is necessary to reduce elastic properties of layers that fail in either matrix or fiber failure modes. This is especially important for layer failure by fiber breakage, as the laminate stiffness is significantly altered. Matrix failures will also cause some laminate stiffness changes, especially for low modulus fiber composites such as S2 glass, but stiffness reduction is considerably less than when fibers fail.

Since in the present analysis elastic property modifications were not made when individual layer stresses reached failure levels, the "all layers" failure methodology was modified to predict failure when either all layers fail by axial shear or transverse tension, or any layer fails by fiber failure. The former criterion of all matrix failures might simulate the phenomenon of large scale delamination initiated by extensive matrix cracks in all layers, and the latter first fiber criterion would preclude the possibility of multiple fiber failures being required prior to laminate failure. The only laminate stiffness changes ignored by this methodology would be those due to matrix cracking. Even though these can be quantitatively significant for glass/epoxy materials, results obtained should show qualitative trends in laminate failure behavior. For convenience, this modified "all layers" failure methodology will be called "all matrix/first fiber."

Laminate analysis failure predictions were generated by the "all layers/first fiber" methodology for maximum stress and maximum strain layer failure criteria. Since fiber and matrix failures are indistinguishable for the quadratic interaction layer failure criterion, the unmodified "all layers" failure methodology was used for it. Results of "all layers/first fiber" with maximum strain failure and "all layers" with quadratic interaction failure are compared with test data in Table 6. The following points are noted:

- Netting analysis (Table 5) still gives better quantitative failure predictions for tensile loading along fiber directions, regardless of material or laminate type.
- When load direction bisects fiber directions (off-axis loading), analytical "all layers" failure predictions are twice as high for graphite/epoxy and [α-9] glass/epoxy laminates, but agree reasonably well with test results for S2-glass/epoxy [0/$\pm$45/90] and [0/$\pm$30/$\pm$60/90] laminates.
- Quadratic interaction "all layers" failure consistently predicts off-axis weakening, but has the worst quantitative predictions.
- Maximum strain "all matrix/first fiber" failure predicts off-axis weakening and agrees quantitatively with the S2-glass/epoxy off-axis test results.
- None of the predictive methodologies studied here provide consistent qualitative and quantitative agreement between laminate failure predictions and test results.

Table 6. Comparison of laminate strengths from "all layers failed" analytical predictions and test results.

a. TENSILE LOAD PARALLEL TO FIBER DIRECTION

Material	Laminate	Failure Stress, ksi		
		Quadratic Interact. "All Layers"	Maximum Strain "All Matrix/1st Fiber"	Test
Gr/Ep Celion 6000/5213	$[0/\pm45/90]_s$	99	96	70-79
	$[0/\pm30/\pm60/90]_s$	99	96	74
S2-Gl/Ep 3M SP250-S2	$[0/\pm45/90]_s$	119	120	84
	$[0/\pm30/\pm60/90]_s$	119	120	71
VB/AC	$[\alpha-9]$	119	120	80

b. TENSILE LOAD BISECTING FIBER DIRECTIONS

Material	Laminate	Failure Stress, ksi		
		Quadratic Interact. "All Layers"	Maximum Strain "All Matrix/1st Fiber"	Test
Gr/Ep Celion 6000/5213	$[0/\pm45/90]_s$	84	100	47-50
	$[0/\pm30/\pm60/90]_s$	92	106	50
S2-Gl/Ep 3M SP250-S2	$[0/\pm45/90]_s$	46	38	44
	$[0/\pm30/\pm60/90]_s$	65	53	49
VB/AC	$[\alpha-9]$	85	78	41

DESIGN CURVES FOR CIRCUMFERENTIAL STRESS AT FAILURE

In most flywheel rotors, the circumferential or hoop stress σ_t is larger than the radial stress σr. Most stress analyses of rotating discs provide both σ_t and σr for design or failure analysis purposes. With this information, a designer can calculate the ratio of $\sigma r/\sigma t$, go directly to the proper laminate minimum design strength failure interaction curve, and plot a line with slope equal to $\sigma r/\sigma t$ and the point $(\sigma r, \sigma t)$ as shown in Fig. 11. The design's factor of safety will then be the ratio of the length of the line from the origin to the line's intersection curve (F in Fig. 11) to the length of the line from the origin to the point $(\sigma r, \sigma t)$, A in Fig. 11.

Since σ_t is greater than σr, a more

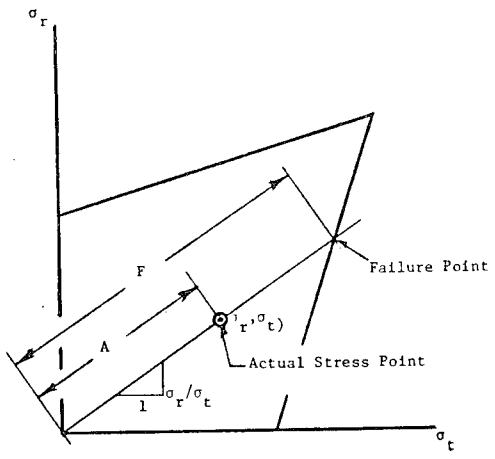

Fig. 11. Use of minimum design strength failure interaction curves to determine factor of safety.

convenient way of presenting the design information has been developed. Data from minimum design strength failure interaction curves has been replotted as tangential failure stress σ_t versus ratio of σ_r/σ_t (Figs. 12a-c). The designer obtains σ_r and σ_t from a stress analysis of the flywheel. He then calculates σ_r/σ_t and enters the appropriate failure stress design curve to obtain σ_t at failure. The factor of safety is then equal to σ_t at failure divided by σ_t from the stress analysis (see Fig. 12 for an example). This procedure is clearly simpler than using failure interaction curves.

COMPARISON OF FAILURE ANALYSIS METHODS

Results obtained from the laminate analysis calculations and comparisons with experimental results have given some clear indications as to the directions to be followed for further design/analysis procedures. They fall into two main categories: type of layer failure criterion which gives most realistic results, and type of laminate analysis method which best predicts stress-strain and failure information for design use.

FAILURE CRITERION COMPARISONS

Analytical and experimental results show clearly that those failure criteria which predict laminate failure by first ply matrix failure yield strengths considerably below a laminate's actual potential. Since the quadratic interaction failure criterion does not distinguish between fiber and matrix failure of a layer, it is impossible to tell which mode of failure is being predicted. A comparison of laminate strength predicted from first ply matrix failure (maximum strain and maximum stress criteria) to first layer failure using layer quadratic interaction criterion is given for graphite/epoxy in Fig. 13a. Clearly, the quadratic interaction criterion is predicting failure at matrix cracking levels. The quadratic results are compared in Fig. 13b to fiber-dominated failure modes for maximum stress, maximum strain, and netting criteria. Also shown is experimental tensile strength. It is obvious that quadratic interaction predictions on a first layer failure basis are not representing ultimate laminate

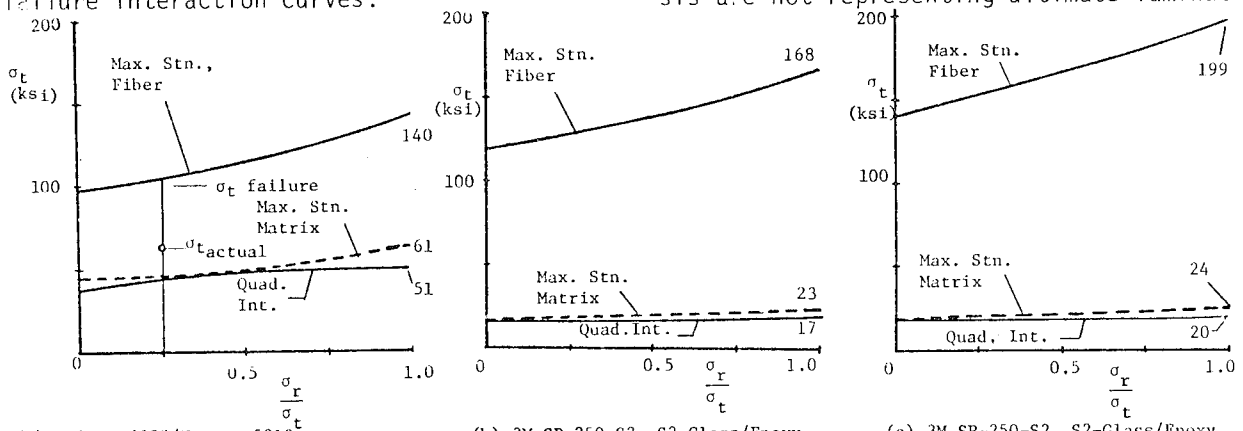

(a) Celion 6000/Narmco 5213 Graphite/Epoxy

(b) 3M SP-250-S2, S2-Glass/Epoxy (Vacuum Bag/Autoclave Cured).

(c) 3M SP-250-S2, S2-Glass/Epoxy (Match Metal die Compression Molded)

Figure 12. Circumferential failure stress, σ_t, vs. ratio of radial to circumferential stress, σ_r/σ_t. Minimum strength maximum strain (max.stn.) and quadratic interaction (quad.int.) failure criteria, quasi-isotropic laminates.

failure, although it may well be predicting matrix cracking. Similar results for glass/epoxy (VB/AC) are shown in Figs. 14a and 14b. Conclusions are that quadratic interaction should not be used on a first layer failure basis in laminate strength predictions using classical laminate analysis. It is noted that excellent results

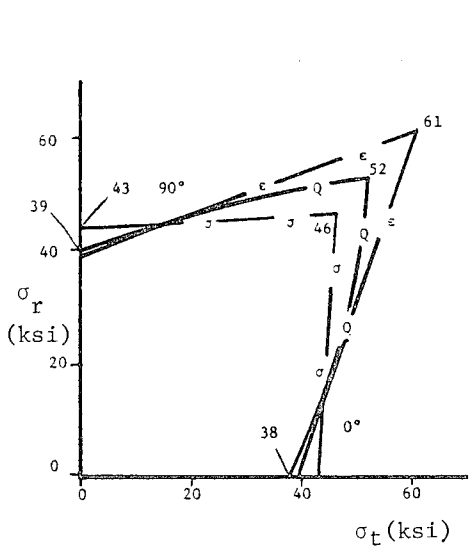

(a) MATRIX DOMINATED FAILURE

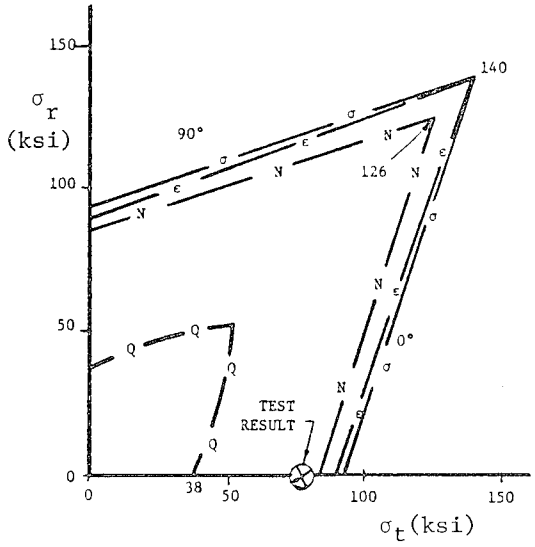

(b) FIBER DOMINATED FAILURE

Fig. 13. Comparison of failure predictions by maximum strain (ε), maximum stress (σ), netting analysis (N) with quadratic interaction (Q) and test results. Celion 6000/Narmco 5213 graphite/epoxy, [0/±45/90] laminate, σ_t along fiber direction.

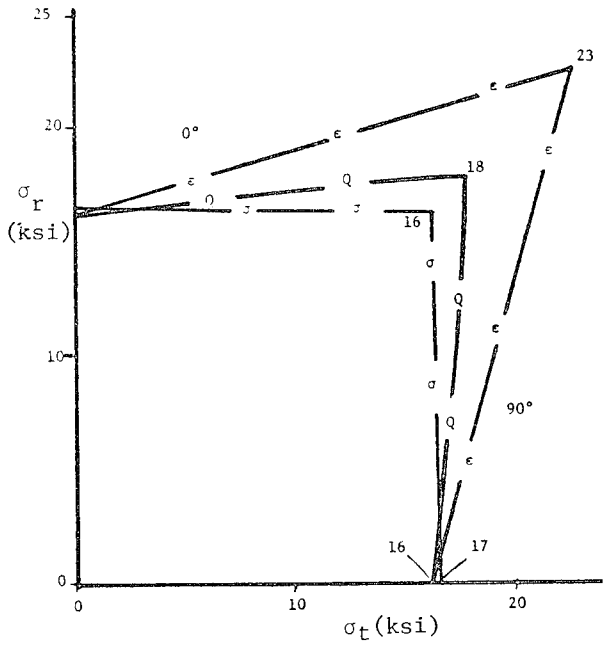

(a) MATRIX DOMINATED FAILURE

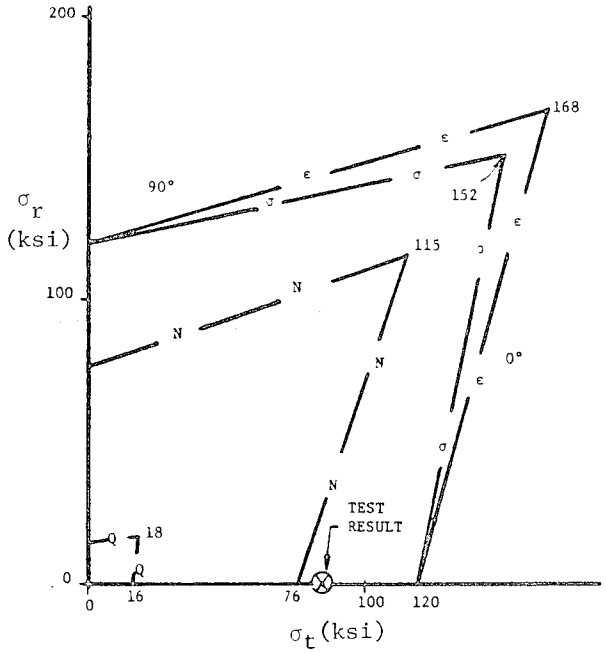

(b) FIBER DOMINATED FAILURE

Fig. 14. Comparison of failure predictions by maximum strain (ε), maximum stress (σ), with quadratic interaction (Q). 3M SP-250-S2 S2-glass/epoxy (vacuum bag/autoclave cured), $[0/\pm45/90]_s$ laminate, σ_t along fiber direction.

have been obtained when fitting laminate failure data to a quadratic failure criterion. This procedure can work well provided that proper failure data are available for all layups under consideration for a particular design.

Attempts to take matrix cracking and widespread delamination into account using "all layers" or "all matrix/first fiber" failure methodologies has only been partially sucessful, with no one methodology consistently giving good qualitative and quantitative predictions. It is possible that one of these approaches or a modification thereof, when used with a laminate analysis methodology which correctly models post-cracking stress-strain behavior, will produce more accurate analytical predictions. There is evidence that the inclusion of out-of-plane effects such as interlaminar stresses and reduction of fiber-direction failure strengths due to stress concentrations from cracked adjacent layers will be necessary.

LAMINATE ANALYSIS METHODOLOGY

It is apparent that laminate analysis gives better predictions of failure stresses when layer stiffness reduction due to matrix cracking is taken into account. Netting analysis, while being a step in the right direction, perhaps goes too far in that all layers are considered extensively cracked with no transverse restraint. The actual physical phenomenon of matrix cracking is statistical, with cracks occurring in weakest locations first. Layer stiffness is reduced only in the immediate vicinity of the crack, and only in the overstressed layers. The uncracked portion of cracked layers, and the layers which have not yet cracked due to matrix failure, still contribute significantly to laminate stiffness. The true layer behavior in transverse tension or shear is therefore closer to that exhibited by a [±45] laminate[8,10], which has characteristics of a ductile metal. Linear elastic laminate analysis will not suffice.

One approach to the problem would be to use a nonlinear laminate analysis technique such as decribed in reference 17. In this program, the stress-strain behavior in axial shear and transverse compression is described by a modifed exponential second stress deviator invariant equation, allowing experimental stress-strain curves to be closely approximated in transverse normal stress and in-plane shear. The program applies stresses in small increments, and iterates until stresses and strains fit both equilibrium and stress-strain equations. This type of computer program, while producing desired results, is relatively expensive to run compared to linear elastic laminate analysis programs, primarily due to the small stress increment size and the iterative nature of the solution method.

Clearly, a method which retains the speed of linear elastic analysis, but which has considerably better accuracy, is desirable for repetitive design analysis calculations. A fairly simple method of obtaining greater accuracy in laminate analysis is to approximate each of the nonlinear stress-strain curves by two straight lines. Such an approximation fits the actual nonlinear curves very closely[16]. The obvious advantage of bilinear approximations is that while stepwise elastic behavior occurs, there are no iterations necessary as in the case of a nonlinear program.

CONCLUSIONS

Laminate failure analysis of graphite/epoxy and glass/epoxy quasi-isotropic laminates under in-plane stresses and comparison with experimental data have shown the following:

Fiber composite laminates exhibit considerable strength anisotropy, with [0/±60] layups being most anisotropic and having ratios of axial strength (along fibers) to off-axis strength (bisecting fibers) as high as 1.5.

Failure stresses for fiber composite laminates are considerably greater in equal biaxial tension than in uniaxial tension, when first matrix or first fiber failures control laminate failure. This biaxial strengthening effect is layer anisotropy-dependent, but independent of layer failure criterion. Flywheel failures may, as a result, initiate at the outer edge, rather than the center where stresses are higher.

Laminate failure predictions based upon first fiber-dominated layer failure correlate well with experimental results for tests parallel to a fiber direction, but do not predict experimental strengths in the off-axis direction. First matrix-dominated layer failures do not correlate

well with laminate ultimate failure data. The use of multiple failed layers as an approximation to the effects of extensive matrix cracking and delamination has been only partially successful in providing better correlation with off-axis test results. A failure prediction methodology which accurately represents the effects of matrix cracking and/or delamination on laminate failure is clearly needed. Quadratic interaction first layer failure criterion produces essentially the same results as maximum strain or maximum stress matrix failures. It is therefore not recommended that quadratic interaction be used on a first layer failure basis in conjunction with classical laminate analysis to predict ultimate failures for laminated flywheel rotors.

Analytically developed minimum design strength first failure interaction curves for quasi-isotropic laminates are identical for a given material system, independent of laminate stacking sequence.

Linear elastic laminate analysis does not realistically represent actual stress-strain behavior due to layer nonlinear behavior. Development of a laminate analysis using bilinear approximation to nonlinear layer stress-strain equations is recommended. In this context, the failure strain of a [0/90] laminate could be used as layer axial failure strain instead of unidirectional results. This will automatically incorporate constraint and stress concentration effects of adjacent cracked layers. Also, transverse stress-strain curves "backed out" of [0/90] tensile test results should be used to reflect the gradual modulus change of a transverse layer due to increasing frequency of cracks.

Nonlinear effects will probably be more important for materials such as glass/epoxy where unidirectional axial and transverse stiffnesses are closer in magnitude, than for materials such as graphite/epoxy where ratio of axial to transverse stiffness is very high.

Minimum design strengths presented in the form of circumferential failure stress σt, plotted against ratio to radial to circumferential stress, $\sigma r/\sigma t$, are more convenient for design purposes than minimum design strength interaction curves.

REFERENCES

1. McLaughlin, P.V., Jr., Majumdar, S., and Phillips, J.W., "Elastic Behavior, Brittle Failure and Plastic Flow of Filamentary Materials", International Journal of Solids and Structures, Vol. 9, 1973, pp. 951-965.

2. McLaughlin, P.V., Jr., and Rosen, B. W., "Combined Stress Effects Upon Failure of Fiber Composites", Final Report, Contract No. N62269-73-C-0800, Materials Science Corp., Report No. TFR/7404, April 1974.

3. Pipes, R.B., "Interlaminar Stresses in Composite Laminates", AFML-TR-72-18, May, 1972.
   See Also:
   McLaughlin, P.V., Huang, S.N., and Rosen, B.W., "Investigations of Failure Mechanisms in Fiber Composite Laminates", Final Report, Contract No. N62269-74-C 0662, Materials Science Corp., Report No. TFR/7508, June, 1975.

4. Reifsnider, K.L., and Talug, A., "Characteristic Damage States in Composite Laminates", Research Workshop in Mechanics of Composite Materials, Duke University, October, 1978.
   See Also:
   Henneke, E.G., II, and Reifsnider, K.L., "Observation of Fatigue Damage in Graphite Epoxy Composite Laminates", Proceedings, 15th Annual Meeting Society of Engineering Science, 1978, pp. 303-308.

5. Ashton, J.E., Halpin, J.C., and Petit, P.H., Primer on Composite Materials: Analysis, Technomic Publishing Co., Stanford, Conn., 1969.
   See Also:
   Muha, T.J., "Users Manual for the Laminate Point Stress Analysis Computer Program, SQ5 as Revised by AFFDL/FBC", Report No. AFFDL-TM-74-107-FBC, July, 1974.

6. Kulkarni, S.V., "Composite Laminate Flywheel Rotor Development Program", Proceedings of the 1979 Mechanical and Magnetic Energy Storage Contractors' Review Meeting, December, 1979, p. 387.

See Also:
Nimmer, R.P., "Laminated Flywheel Disc With Filament Wound Outer Ring", same Proceeding, p. 407.

7. Clements, L.L., and Moore, R.L., "Composite Properties for S2-Glass in a Room-Temperature-Curable Epoxy Matrix", Lawrence Livermore Laboratories, University of California, Report No. UCRL-81517, Rev. 1, November, 1978.

8. Duke, J.C., Jr., "A Comparison of Quasi-Isotropic Fiber Reinforced Composite Laminates", Report No. UCRL-15225, Lawrence Livermore Laboratory, November, 1979.

9. Chatterjee, S.N., and McLaughlin, P.V., Jr., "Inelastic Shear Instability in Composite Materials Under Compression", Proceedings, Third EMD Specialty Conference, ASCE, September, 1979, pp. 649-652.

10. Rotem, A., and Hashin, Z., "Failure Modes of Angle Ply Laminates", Journal of Composite Materials, Vol. 9, 1975, pp. 191-206.

11. Advanced Composites Design Guide, Third Edition, Air Force Materials Laboratory, Wright-Patterson Air Force Base, Ohio, 1973.

12. Goldenblat, I.I., and Kopnov, V.A., "Strength Criteria for Anisotropic Materials", Izvestia Akademii Nauk SSR, Mekhanika, No. 6, 1965, pp. 77-83.

13. Malmeister, A., "Geometry of Theories of Strength", Mekhanika Polimerov, Vol. 2, No. 4, 1966, pp. 519-534.

14. Tennyson, R.C., MacDonald, D., and Nanyaro, A.P., "Evaluation of the Tensor Polynomial Failure Criterion for Composite Materials", Journal of Composite Materials, Vol. 12,

15. Tsai, S.W., and Wu, E.M., "A General Theory of Strength for Anisotropic Materials", Journal of Composite Materials, Vol. 5, 1971, pp. 58-80.

16. McLaughlin, P.V., Jr., Dasgupta, A., and Chun, Y.W., "Composite Failure Analysis for Flywheel Design Applications", Final Report to Lawrence Livermore Laboratory, Subcontract No. 6448409, Villanova University, March, 1980.

17. Hashin, Z., Bagchi, D., and Rosen, B.W., "Nonlinear Behavior of Fiber Composite Laminates", NASA CR-2313, April, 1974.

18. Kulkarni, S.V., Stone, R.G., and Toland, R.H., "Prototype Development of an Optimized, Tapered-Thickness, Graphite/Epoxy Composite Flywheel", Lawrence Livermore Laboratory, University of California, Report No. UCRL-52623, November, 1978.

19. Celion Carbon Fibers - Materials Properties of Composites, Celanese Corporation, Technical Brochure, 1979.

20. Advanced Composites Design Guide, Third Edition, Air Force Materials Laboratory, Wright-Patterson Air Force Base, Ohio, 1973.

21. "Scotchply" Brand Reinforced Plastics Product Information Brochure SP-RTD-19(127.3)11, 3M Company.

22. Kliger, Howard, Celanese Corporation, Personal Communication.

23. Davis, J.W., 3M Company, Personal Communication.

24. Vacario, A.A., Jr., and Toland, R.H., "Failure Criteria and Failure Analysis of Composite Structural Components", Chapter 2 in Structural Design and Analysis, Part I, C.C. Chamis, ed., Composite Materials, Vol. 7, Academic Press, 1974, pp. 51-97.

MATERIAL DESIGN PROPERTIES OF CELLULOSIC FLYWHEEL ROTOR CORES

David L. Hagen, Scott A. Gaff, Arthur G. Erdman
Mechanical Engineering Department
University of Minnesota, Minneapolis, MN 55455

ABSTRACT

Preliminary studies of cellulosic rotors indicate that plywood cores in compound rotors and rotors wound with high performance paper appear promising. This paper discusses material properties that are critical to designing a plywood rotor core. The results of tensile test data are given showing the distribution of strengths measured for vacuum dried hexagonal birch plywood. These are compared with similar tests at ambient conditions to show the approximately 10% decrease in performance upon drying, and the implications discussed. The use of high resolution tensile stress-strain test data coupled with precise digitally integrated acoustic emission measurements is proposed to estimate long term strength. Preliminary data for such measurements on plywood is presented. Measurements of the tensile fatigue of plywood samples are discussed. The hygroscopic nature of cellulose requires that careful consideration be given to drying of the material, and to the moisture release and outgassing rates in a vacuum. Data is presented for comparative drying rates of plywood disks and cylinders in a vacuum. Similar phenomena are expected for other rotor materials.

INTRODUCTION

Flywheel systems have the potential for stationary energy storage applications if they can be made cost effective. Since the rotor represents a major portion of the overall cost, efforts have been directed towards finding materials with high performance per unit cost and with low assembly costs. Cellulosic materials were suggested by D. W. Rabenhorst at the Applied Physics Lab, as potential candidates for low cost flywheel rotors (1). Later reviews by the present authors showed that these cellulosic materials still looked promising (2). Preliminary research into the various aspects involved in designing and manufacturing cellulosic rotors is reported in (3). Spin tests of plywood disks by Rabenhorst demonstrated preliminary technical feasibility (4). Tapered birch plywood disks were used as convenient cores around which higher performance materials such as Kevlar, fiberglass and steel hose wire were wound.

Further work was done at the University of Minnesota on developing plywood rotors and in conducting preliminary studies of the material properties of plywood for such rotors (5). Associated studies were made of the rotor supports, system dynamics and controls. A model demonstration system was built using a plywood rotor. A detailed economic study of the costs of cellulosic materials and of assembling cellulosic rotors was then made for the Applied Physics Laboratory (6). This indicated that plywood rotors were marginally competitive with E-glass or steel hose wire rotors, primarily due to comparatively higher container costs. Wound rotors of so called "Superpaper" made of highly oriented fibers however appear to provide potentially the lowest energy storage costs in a rotor of all the materials examined. Further studies of the sensitivity of flywheel system economics show a strong dependence on the rotor volume and container costs for cellulosic materials as compared with conventional high performance rotors (7,8). Plywood or similar pseudoisotropic materials definitely appear to be useful materials to make cores around which to wrap E-glass or steel hose wire while contributing to the energy storage potential of the rotor. Low container costs should make wound "Superpaper" rotors competitive with steel hose wire rotors.

Given the potential economic competitiveness of cellulosic rotors, their technical feasibility must be demonstrated in detail before they can be commercialized. Reliable methods of designing, assembling and balancing plywood and paper

rotors are therefore needed. The design of high performance applications requires detailed information on the strength and fatigue distribution of these cellulosic materials under vacuum conditions. These material properties control the energy storage capabilities of the rotors and the resulting storage economics. Further work was therefore conducted to address these issues (7,9). Several new methods of attaching hubs durably to cellulosic rotors were developed. Methods of balancing pseudoisotropic or wound rotors were created using semi-automatic alignment methods which eliminate removing or adding material. Further design parameter were developed for use in preliminary design of the stiffness of rotor supports to accomodate material properties, dynamics and transmission limitions.

The following discussion will concentrate on the detailed results to date of the tensile testing program and how these pertain to the rotor design. Preliminary results will be given on the analyses of load deformation curves accompanied by acoustic emission measurements. These may be potentially useful for evaluating the damage rate and the long term strength. Preliminary results will also be presented on the drying rates and diffusion coefficients of plywood rotors, as these will affect the economics and feasibility of using cellulosic rotors in a vacuum.

TENSILE TESTS

The testing program was designed to evaluate the three major technical factors of intrinsic energy (tensile strength/density); distribution, moisture effects, and veneer orientation. To evaluate the intrinsic energy distribution accurately it was decided to test at least 100 samples in each series for their tensile strength and density. The different orientations would be tested with material that was vacuum dried and also with material conditioned to 50% relative humidity (RH) to evaluate the effects of moisture loss. Finally tests would be run on plywood parallel to the grain and at the angle bisecting the grain angle in adjacent plies. Commercially available Finnish birch plywood was obtained and 450 tensile samples were cut for these series of tests.

Calculations and burst tests indicate that pseudoisotropic material made up with a 0°, 60°, -60° hexagonal configuration is considerably stronger than if made in the conventional 0°, 90° crossply configuration (9). Preliminary tests and discussions with the plywood distributors indicated that there might also be further effects of quality control and hot press versus cold adhesives in reducing the strength of commercially available birch plywood. An order for 75 sheets of hexagonal birch plywood 460 mm (18") square made with a 0°, 60°, -60° veneer orientation was therefore placed with Lenderink Inc. of Belmont, Michigan (10). As a control, 25 similar sheets were ordered with a conventional 0°, 90° crossply orientation.

Some of the sheets are being used for fatigue tests. Six sheets of the 0°, 60°, -60° plywood were sent to the Applied Physics Laboratory for future burst testing to compare actual spin tests with this series of tensile and fatigue tests.

RESULTS

The results of the tensile tests of the Finnish Baltic birch are given in previous reports (7,9). The means and standard deviations for both the vacuum dried samples and those equilibrated to 50% RH are summarized in Table 1. The results indicate that this commercially available material has a very broad distribution of strengths with standard deviations ranging from 12 to 22%. As initially anticipated, there was a significant drop in the tensile strength after vacuum drying the plywood, ranging from 5 to 20%. This drop ranges from 25 to 102% of the standard deviation of the strengths respectively. The few samples with very low tensile strengths could probably be readily detected through nondestructive testing methods or eliminated through proof testing.

Calculations of the strengths of hexagonal plywood show that the strength along the directions 90°, 30°, -30° are 25.6% of that along one of the veneer directions. This is a 54% improvement over the similar 45° orientation with 0°, 90° crossply plywood. Tests of the custom made birch plywood of this configuration are shown in Fig.s 1 and 2. The results are summarized in Table 2. Note that the mean strength and intrinsic specific energy values of hexagonal plywood perpendicular to the face grain (90°) are 57.0% and 54.8%, respectively, of their

corresponding values parallel to the face grain (8). These percentage relationships represent an approximate 92% improvement in performance going from the cross ply configuration to the hexagonal configuration for the weakest direction in the plywood. The properties in this weakest direction are expected to correlate best with actual spin burst tests of disks of such pseudoisotropic material. Some spin tests of E-glass pseudoisotropic disks run at the Applied Physics Laboratory resulted in pseudoisotropic strengths 34.6% and 45.6% of the uniaxial strengths, respectively, for cross ply and hexagonal ply construction (11). This change in orientation resulted in a 32% improvement.

The initial tests of the hexagonal plywood show a drop in strength when the material is vacuum dried similar to the conventional cross ply plywood. (See Fig. 1,2.) Part of this may be due to prestressing the material due to differential shrinkage. This effect is shown in the samples of the hexagonal plywood bending and warping when they are vacuum dried. The bending would be caused by unequal material properties or uneven moisture distribution during manufacture. The warping occurs because the hexagonal plywood has a helical geometry as compared to the cross ply material which is symmetrically constructed and does not exhibit such warping. The magnitude of this twisting effect is expected to be proportional to the change in moisture content from when it was manufactured to after it is dried. The plywood should therefore be manufactured with as low a moisture content as is practical.

The standard deviations of the strengths of the custom made hexagonal birch plywood are considerably smaller than that of the commercially availables conventional birch plywood (See Tables 1 and 2.) Furthermore, the samples cut from the same board have strengths that are grouped much closer together. This could indicate that there are significant differences in the material used in the construction or changes in the bonding procedures as to quantity of adhesive or its curing. The very low strength measurements came from boards which could probably be detected by use of non-destructive means such as flexural modulus measurements. This would leave the remainder of the boards with a standard deviation of less than 5%. These effects can be examined further in testing the remaining boards.

The data in Tables 1 and 2 has provided some of the fundamental information on the distribution of strengths of plywood that is necessary to be able to use plywood in such an engineering application with a given confidence level. The broad distribution seen in conventional commercially available plywood was substantially reduced in custom-made clear hexagonal plywood. The strength of this hexagonal yellow birch plywood in the weakest region bisecting adjacent plies was also double that of the conventional crossply imported birch. Vacuum drying the plywood reduced the strengths on the order of 10% as was anticipated from trends observed in related literature.

The general trend has been established, with sufficient data for statistically accurate measures of the performance and changes. This is particularly important at the low strength end of the distribution where the design parameter must be set.

HIGH RESOLUTION TENSILE AND ACOUSTIC EMISSION TESTS

Conventional ramp or fatigue tensile tests typically produce data only on the stress at fracture or the duration of a stress cycle before fracture. Typically numerous lengthy tests must be performed over some time. This is particularly true if sufficiently accurate data is to be obtained to extrapolate results to the ultimate duration of load over the projected operating stress conditions. It would be useful if information of the rate of fracture as a function of stress could be obtained during short term tests. The ultimate strength and duration of load could presumably be inferred from such data.

There is some evidence in the literature which indicates that the rate of permanent deformation or damage increases rapidly when stressed above a given value which is approximately 50% of the short term strength (10). This is also the approximate constant stress level that is projected to be sustainable over 30 years or longer. If this level could be reliably measured in a short term test and be correlated with the long term strength, it would greatly simplify the efforts of measuring the useable strength for new species or moisture conditions.

The concept of a proportional limit as the beginning of major plastic deformation and material damage is widely used in metal testing. Such conventional analysis of load deformation curves is difficult to apply to wood since it exhibits considerable viscoelasticity. Any estimate of a proportional limit based on a given offset or visual estimation is dependent on the rate at which the test was conducted and is not an inherent absolute material property. Some examples of stress strain curves of tensile specimens conducted at several constant strain rates are given in Fig. 5. Transitions in the curvature are not strikingly obvious, and may be hidden in the experimental error. Imaginative and painstaking tests have therefore been required to separate the effects of recoverable viscoelastic response in the wood from irrecoverable viscous permanent deformation or creep. Some tests involve a cycle of loading and unloading the material to determine the residual deformation. This is plotted as a function of stress to observe any rapid increase in the parameter. Ivanov, for instance, used a constant rate of loading and unloading to constantly increasing levels (13). The residual deformation at the bottom of each cycle was plotted against stress. Sugyama monitored the creep rate as a function of time for different stress levels (14). The creep rate after a given time was plotted versus stress and showed a break in the curve.

Acoustic emissions occuring in samples during tensile tests have been monitored, though very few such experiments have been made on wood (15). The rates of acoustic emissions show a rapid increase after the stress reaches a certain level (16). If the acoustic emissions are caused by failure of individual tracheids, this presumably indicates damage to the material. Consequently the sample would become more flexible as well as weaker. The viscoelasticity would be expected to provide a certain curvature to the graph which would be dependent on the stress. Apart from the viscoelastic deformation, the load deformation graph might presumably curve at higher stresses as the modulus of the material was reduced. The viscoelastic deformation may also increase more rapidly as a result. Accurate analysis of the slope of the load deformation curve may therefore reveal a pronounced change in the rate of curvature above a certain stress region. This change in the rate of curvature should correlate with the acoustic emissions. An exploratory study of the load deformation graph coupled with monitoring the acoustic emissions was therefore proposed. These tests would be compared with the strength and the long term durability to see if some correlation could be made.

Examining the system using a first order analysis, the stiffness of the sample can be modeled as made up of a series of groups of fibers in parallel. The change of the overall spring constant is thus related to the fracture of the component fibers. The acoustic energy released when those fibers are broken is proportional to the stiffness of the fibers times the square of the strain at failure. If the fibers are hypothesized to fail at equal strains, then the acoustic energy released should be proportional to the square of the signal. Ignoring side effects, nonlinearities, damping, resonances, etc., we hypothesized that the integration of the square of the acoustic emission signal will be proportional to the change in stiffness or modulus of the tensile sample during the test. (See Fig. 8.) Both are expected to increase more rapidly with stress above a given stress region which could correlate with the long term strength. High resolution measurements of the load deformation curve coupled with the acoustic emissions were therefore proposed. The equipment to perform these tests was specified or designed and procured or built as follows (See Fig. 21).

EQUIPMENT

The combined requirements of high resolution, accuracy and speed in sampling data during tensile testing indicated that a micro-computer based data acquisition system was necessary to monitor and record the data, and to provide the preliminary data manipulation and reduction. The curvature seen in tensile tests is on the order of 10%, part of which is due to the recording equipment. In order to resolve the nonlinear effects to the 1% level, an equipment precision and accuracy of 0.01% was chosen. This is considerably more stringent than most equipment available for stress and strain measurements. The stress and strain data are alternately taken and then averaged over sixteen or more points. This helps reduce noise and

improve the resolution to give full 16 bit (parts/ 65536) significance to the data. Using this approach, 200 pairs of averaged points can be recorded on floppy disk each second. During a one minute run, this results in over 10,000 pairs of points. To accurately measure the slope a least squares fit could then be made every hundred points.

To monitor the acoustic energy released, it was decided to periodically digitize, square, and sum an amplified and filtered signal. Existing literature suggest that there is probably useful information in the unexplored low ultrasonic range as well as in the audio range (11,15). The 1 kHz to 100 kHz range was therefore chosen for examination. A 30 kHz resonant sensor with 65 dB preamplification is being used with the mechanical noise below 1 kHz filtered out. A high speed digitizing squaring and summing circuit with 12 bit resolution and 400 kHz throughput was designed and assembled. A TRW # TDC 1010J chip capable of multiplying and accumulating two 16 bit numbers in an eighth of a microsecond is used. Higher throughput rates and resolution can therefore be designed using faster digitizing chips for analysis of stiffer materials with higher emissions frequencies. This suggests a 65 dB signal-to-noise ratio indicating that the limiting factor will be noise from the test equipment.

Resolution and sensitivity in much acoustic emission research has been limited by noise transmitted from the machine through the grips or directly through the air. Noise from the test equipment has been effectively eliminated by introducing an acoustic isolator consisting of multiple layers of metal and polymer in between the machine and the grips (17). Wedge grips incorporating this principle were therefore designed. Seperate isolators and anechoic foam around the sample were also used.

Some preliminary results suggesting these trends were obtained from data obtained with conventional tests. Some typical stress strain graphs obtained during the tensile testing program are traced in Fig. 5 for 3 different strain rates. The curvature of one such curve taken from the regular test series was estimated by sighting a straight edge to the curve at different points. The changes from the curvature at 10% of the breaking strain (after the initial preload and starting perturbations) is shown in Fig. 6. (Further discussion in Appendix.)

TENSILE FATIGUE TESTS OF PLYWOOD

A typical stationary flywheel energy storage system may be designed for a life of 30 years of diurnal cycling or 10,000 cycles. This cyclic fatigue affects the durability of the rotor. The actual nature of the effects, however, is not clear from data existing in the literature, particularly for vacuum dried plywood.

Conventional fatigue tests of wood on a rapid cyclic fatigue machine have been performed and show that wood is quite durable (18,19). The damping or internal friction results in considerable heating in the sample. This is significant since wood as a viscoelastic material exhibits a creep rate that is exponentially proportional to the absolute temperature (19). The creep under constant stress also degrades the material. Constant stress has been shown to be more detremental than daily applying and removing the stress up to several hundred cycles (14). This indicates that the duration under stress may be more significant.

This concept has been developed recently in the form of several damage theories (30,31). These theories use a relation between the stress and the damage rate and integrate it over the expected stress history. To obtain data as to the effects of fatigue and stress on vacuum dried plywood, it was proposed to study such fatigue on an available cyclic fatigue machine. Comparable tests would be run at ambient conditions to compare the results with other studies. Four or five decades of time could resonably be tested on such a machine if stresses were chosen to give mean times to failure of 0.1 hrs (6 min), 1 hr, 10 hrs, and 100 hrs (4 days). These could be compared with the ramp tests on the Instron which could be performed in 0.01 hrs (0.5 min). A flywheel with a range of transmission ratios of 1:3 will result in a minimum to maximum load ratio of 1:9. The fluctuating and mean loads were chosen to simulate this in a sinusoidal cycle.

A pseudoisotropic cellulosic rotor will probably use a hexagonal assembly where the veneer directions are 0°, 60°, and -60°. The weakest region of the plywood is probably the region bisecting

the grain direction in adjacent plies, i.e., perpendicular to the face grain where the angle to the veneers is 90°, 30°, and -30°, respectively. Due to the length of the tests, it was decided to concentrate initially on this direction using the vacuum dried custom made hexagonal birch plywood. The samples to be tested in tensile fatigue are identical to those used in the ramp tensile tests. The testing must be done in a controlled atmosphere of dry nitrogen or 50% RH.

EQUIPMENT

The cyclic fatigue test machine available to the project was developed by B. J. Lazan at Syracuse University and is one of a number fabricated and used by the Aeronautical Engineering Department at the University of Minnesota (22). The machine uses an adjustable eccentric mass driven by a synchronous electric motor at 3600 rpm (60 Hz) to produce a fluctuating load. A pair of springs is used to maintain a tensile preload on the sample.

The machine automatically maintains the preset preload-spring extension by lowering the bottom spring support in the advent of extension of the sample due to elasticity or creep. Failure of the sample causes the eccentric cage to contract a micro switch which shuts off the power and applies a brake.

The fatigue test machine was designed for relatively stiff materials such as steel or aluminum which have a Young's modulus E in the range of 71-210 GPa (10-30 Mpsi). Birch plywood by comparison has a modulus on the order of 3.5 GPa (0.5 Mpsi), which complicates the dynamic equations and stress applied. The flexibility of the wood requires two corrections:

1) The fluctuating load causes a significant displacement of the eccentric cage. At the bottom and top of the cycle these displacements are in series with the preload spring, changing the load they apply. The mechanism which maintains the constant spring extension will cause the maximum load to remain at $F_x = F_c + F_a$, but the average and minimum loads F_a and F_n will have different values.

2) The flexibility of the wood drastically lowers the spring constant of the system and therefore lowers the natural resonance frequency of the spring mass system. Initial calculations have shown a natural resonance frequency of the spring mass system of approximately 80 Hz compared to a driving frequency of 60 Hz, resulting in a transmissibility significantly greater than unity (9). The actual transmissibility depends on the spring constant and damping coefficient of the particular sample being tested.

The equations describing the dynamics of the fatigue test machine have been formulated (7). The difficulties of absolute calibration lead to adapting the equipment to accomodate a load cell for initial calibration. Subsequent tests can make use of the rate of preload to establish the initial elasticity, and the dynamic motion of the cage can be used to follow subsequent changes. Thus a number of samples can be tested under known conditions.

ROTOR DRYING RATES AND METHODS

The hygroscopic nature of cellulose and the accompaning shrinkage or swelling with changes in moisture content are fundamental properties that must be taken into consideration when designing and assembling such rotors. If cellulose is equilibrated at ambient conditions of 50% relative humidity, it will contain around 8% to 10% moisture. If the cellulosic material is then measured at 10 microns Hg pressure, the eventual equilibrium moisture content would be about 0.00028%. This water which represents 8-10% of a rotor's moist weight would have to be removed or prevented from desorbing for a cellulosic rotor to be operated in a vacuum. The time and effort required to dry the rotor and maintain vacuum are critical factors in overall economics of using cellulosic materials in flywheel rotors.

If cellulosic disks are bonded into a rotor and then placed in a vacuum, the outer surfaces will dry rapidly and shrink. It will take quite some time for the moisture in the center of the rotor to diffuse out. This results in the other surface material shrinking much faster than the center causing the plies to separate around the edges (7).

To solve this dual problem of splitting due to unequal shrinkage, and of the long time required to dry a large rotor, it is necessary to dry the disks before they are assembled into a rotor. Similarly the veneers must be dried as much as practical and adhesive chosen for

minimum moisture content when the disks are assembled. The corolary of this splitting problem, is that if a dried rotor is placed in a humid environment, it will rapidly absorb moisture on the outside which will swell, causing the interior plies to separate. Assembled rotors must therefore be kept in a carefully controlled environment and be allowed to change moisture very slowly.

One possible solution to this problem is to coat the rotor with a hermetic epoxy coat such as has been developed by boat builders (23). Such a coat would probably be useful in minimizing the rate of removal of moisture or volatile chemicals from a vacuum dried rotor while in a vacuum. This could minimize the pumping requirements and possibly permit periodic pumpdowns if an hermetic rotor pressure/burst container is used. The cyclic stresses experienced by the rotor during operation would probably destroy the integrity of a completely hermetic coat and preclude the corresponding use of a moist rotor.

The rate at which moisture can be removed from a rotor or disk affects the pumping requirements and the drying costs. Moisture loss has been assumed Fickian or gradient dependent by most reports in the literature (24). There is some controversy as to whether the diffusion is dependent on the moisture content or vapor pressure gradients and if this is valid for bound water (25). Some preliminary experimental data showing the rate of moisture loss while vacuum drying plywood cylinders is shown in Fig. 10.

To evaluate the drying times and desorption rates of cellulosic rotors, the effective diffusion coefficients must be measured. Vacuum drying of timber has been experimented with since the early part of this century, and large commercial equipment is presently available for this purpose (26). Little data however is available on the relevant drying coefficients for plywood or paper.

The interaction of water with cellulose has been the subject of considerable examination, and has been extensively reviewed (27-31). There is substantial evidence that water in cellulosic materials is in two major categories of strongly or weakly bound or adsorbed water up to the fiber saturation point. (Beyond saturation there are considerable quantities of free or bulk water present. The transition between the two categories is not sharp, and there is evidence for further differentiation as to the availability of the water, and the degree of bonding. In the present case, we are primarily concerned with conditions dryer than ambient on down to a moderate vacuum. In this region, there is typically a monolayer or less of water present, and the simple adsorption theories such as the BET equation are probably adequate in a first analysis. The BET equation describes the average moisture content in terms of the relative humidity as:

$$M(h) = \frac{h\ M_o\ C}{(1-h)(1+(B-1)h)}$$

where Mo is the monomolecular coverage and

$B = A \exp(-\Delta U/RT)$. where T is the absolute temperature, ΔU= adsorption energy, and the preexponential factor A is approximately unity (24).

For very low humidities, such as under moderate vacuum conditions, the average moisture content relative to that at 50% relative humidity reduces to:

$$M(h) = h(1+0.5(C-1))M(0.5)$$

At 294 K (70 F) and 10 milliTorr for instance, M=0.00028%. Thus at pressures substantially less than atmospheric, the moisture content at equilibrium varies fairly linearly with pressure.

The strong bonding coupled with low permiability and relatively large volumes would make attaining this equilibrium state very slow. The movement of moisture through dry wood is usually considered controlled by viscous and Knudsen or slip flow diffusion of water vapor. At low pressures, the mean free path becomes comparable to the dimensions of the cellulosic pores so that the Knudsen flow will dominate the permiability.

The diffusion of the moisture can be modeled using Fick's second law which in one dimension is:

$$\frac{\partial M}{\partial t} = D \frac{\partial^2 M}{\partial x^2}$$

where t= time, x= Distance in the flow direction, and D= diffusion coefficient. (There has been some controversy over the

use of Fick's law in terms of concentrations. There is also some question as to the applicability of the formulations for the movement of bound water where the energy barrier to lateral movement is less than that for evaporation (25). This equation is similar to the calculations of heat conduction except that the diffusion coefficient is generally not constant, but varies with temperature and pressure and thus with position and time. This complicates the solution and would require intricate numerical calculations to solve.

As a first approximation, we can assume that the diffusion coefficient D is approximately constant with time and thus pressure. To model drying a cylindrical plywood rotor or plywood disks, a cylindrical configuration is assumed to have radius r and length l. Separate average diffusion coefficients Dr and Dl are assumed for the radial and axial directions respectively. The fractional change in the average moisture content or in the average of the pressure squared throughout the body at time t is defined as

$$E(t)= \frac{M(t) - M(0)}{M(\infty) - M(0)} = \frac{P(t)^2 - P(0)^2}{P(\infty)^2 - P(0)^2}$$

A dimensionless time parameter τ is defined proportional to time as:

$\tau_\lambda = 4tD/L$ for flow through a parallel sided body of thickness L and $\tau_\rho = tD/r$ for flow through a cylinder of radius r.

The average moisture content in a cylinder is then given by

$$\bar{E}_\rho(\tau) = 1.0-0.693 \exp(5.78\ \tau),\ \tau \geq 0.1$$

and the average moisture content in a parallel sided body is given by

$$\bar{E}_\lambda(\tau) = 1.0 - 0.811 \exp(-2.47\ \tau)\ \tau \geq 0.2$$

The average fractional content remaining in a cylinder of finite length can be found by multiplying the separate radial and axial components:

$$(1-\bar{E}(t)) = (1-\bar{E}_\rho(t))(1-\bar{E}_\lambda(t))$$

$$= 0.562 \exp(-2.47\tau_\lambda - 5.78\tau_\rho),\ \tau \geq 0.2$$

To obtain equations relating to measureable quantities we differentiate this equation with respect to time to obtain the rate of change of moisture content as:

$dM/dt=0.562\ b \exp(-bt)$ where b is

$b=9.88D_\lambda/L^2 + 5.78D_\rho/R^2$

Taking the natural logrithm of the absolute value of this and multiplying by RL we have

$$-RL \ln(\mathrm{abs}(dM(t)/dt)) = -RL \ln(0.562\ b) + (\alpha 5.78\ D_\rho + 9.88\ D_\lambda/\alpha)\ t$$

where the aspect ratio of the cylinder is $\alpha = L/R$. The diffusion coefficients may be closely correlated with each other, so if we take the ratio of radial to axial diffusion coefficients as

$$Q=D_\rho/D_\lambda$$

we have

$$R\ L \ln(\mathrm{abs}(dM(t)/dt)) = -RL \ln(0.562\ b) + (\alpha Q\ 5.78 + 9.88/\alpha)\ D_\lambda\ t$$

Thus we have an equation of an easily measureable quantity that is linearly proportional to time. By measuring the mass loss rates of cylinders of various aspect ratios during vacuum drying we can solve for the diffusion coefficients and their ratio. The variation of these coefficients can then be monitored with time or moisture content or average pressure squared.

Plots of such measurements for various aspects ratios is shown in Fig. 11. From such data, the diffusion coefficients were calculated. The variation in D_λ and the ratio D_ρ/D_λ with time could be calculated with better data.

CONCLUSIONS

The tensile strength and intrinsic energy distribution data obtained should enable serious evaluation of the technical and economic merits of plywood rotors. The shape of the strength distribution curve is significantly affected by material strengths and assembly methods which could be monitored through nondestructive methods and through careful quality control methods. The intrinsic energy distribution curve is not as variable as the strength. This should allow evaluation of the lower 10% of the distribution through proof testing fairly reasonably.

The high resolution testing procedures coupled with monitoring the acoustic emissions appear to provide a new and useful approach to evaluating the performance of materials and monitoring the phenomena during testing. Further analysis of this method coupled with fatigue tests would appear promising.

Table 1. Tensile strength of 9 ply 1/2" finnish birch plywood.

Face Veneer Orientation	RH%[a]	Number Of Samples	Mean Strength X MPa	Psi	Standard Deviations Psi	%	Drying Drop Δ%	Δ/S %
Parallel = 0°	50	45	71.8	10,409	2,313	22.2		
	0	31	57.6	8,352	1,380	16.5	-19.8	-1.02
Normal = 90°	50	51	69.4	10,066	2,142	21.3		
	0	33	65.9	9,560	1,868	19.5	- 8.0	-0.6
Mid Ply = 45°	50	60	20.4	2,965	367	12.4		
	0	40	18.8	2,729	378	13.9	- 5.0	-0.25

[a]Samples equilibrated at 73°F and 50% relative humidity or vacuum dried to less than 20 millitorr pressure and tested in dry nitrogen atmosphere.

Table 2. Tensile strength of 16 ply 1/2" hexagonal yellow birch plywood and its intrinsic specific energy.

Face Veneer Orientation	RH%	Number of Samples	Mean Strength MPa	Psi	Standard Deviations Psi	%	Drying Drop Δ%	Δ/S %
Parallel = 0°	50	100	72.7	10,549	1,090			
	0	1	58.5		-	-	-22.0	-
Mid Ply = 90°	50	99	41.5	6,014	973	16.2		
	0	97	34.2	4,965	873	17.6	- 8.8	-0.76

Face Veneer Orientation	RH%	Number of Samples	Intrinsic Specific Energy KJ/KG	σ/ρ WH/LB	Standard Deviation KJ/KG	%
Parallel = 0°	50	43	96.1	12.1	7.56	7.9
Perpendicular = 90°	50	56	53.5	6.75	9.1	17.0

APPENDIX

Note: Comprehensive coverage of the questions of the strength and fracture of wood is found in the proceedings of the First International Conference on Wood Fracture held August 14-16, 1978, Banff, Alberta Canada, and sponsored by the Forintek, Canada Corp. Western Forest Products Laboratory, Vancouver British Columbia V6T 1X2 published July 1979. A similar comprehensive coverage of the field of acoustic emission technology is found in the publication Acoustic Emission: A Bibliography with Abstracts by Thomas P. Drouillard published by Plenum, New York, 1979.

Acoustic Emissions & Tensile Tests Contd. Note the significant change in slope that occurs around the 50% strain region. The RMS value of the acoustic emissions occuring during this time are shown in Fig. 7 Summing the square of the peak voltage to estimate the acoustic energy released gives the graph in Fig. 8. Note how the curves in both Fig. 7 and Fig. 8 increase rapidly after the 50% strain region. Plotting the acoustic energy released versus the change in the modulus of elasticity shows a remarkably linear correlation considering the manual data estimation methods. The intercepts of the curves in Fig. 6,8 and 9 can be used to evaluate a stress level which could probably be used as the long term value of sustainable stress. The phenomena shown in these preliminary results will be analyzed in detail with the high resolution data qathering equipment described. This approach appears useful to distinguish between viscoelasticity and fracture or plastic deformation.

The moisture loss tests suggest that the material must be dried as thoroughly in as thin sections as possible before assembly. Epoxy coatings show some promise for maintaining the moisture status in a rotor and in minimizing vacuum pumping requirements. Epoxy coated rotors assembled and equilibrated under ambient conditions also appear to be suitable for low cost lower performance applications where evacuation and optimum performance are not required.

Further consideration of plywood for rotor cores around which to wrap higher performance materials would appear warranted. Similarly high performance "Superpaper" rotors should also be considered in the depth that plywood has to evaluate its promise as a rotor material.

ACKNOWLEDGEMENTS

The authors would like to acknowledge the contributions made to this study by the numerous individuals and institutions who have worked with or discussed the project with us. Support for the work mentioned has been provided by the Minnesota Energy Agency, and the Department of Energy through the Sandia and Lawrence Livermore Laboratories. The Forestry Department of the University of Minnesota kindly provided the tensile testing facilities and loan of the humidity equipment. Special thanks are due to Jon Blomgarden, Terry Brier, Greg Stenberg, Stuart Levy and Cathy Hagen for their invaluable assistance and enthusiasm.

REFERENCES

1 David W. Rabenhorst, "Applicability of Wood Technology to Kinetic Energy Storage." Johns Hopkins University, Applied Physics Laboratory APL/JHU Digest, Vol. 11, No. 5, May/June 1972, pp2-12.

2 David L. Hagen and Arthur G. Erdman, "Flywheels for Energy Storage: A Review with Bibliography." Design Engineering Tech. Conf., ASME Paper No. 76-DET-96, Montreal September 26-29, 1976.

3 A. G. Erdman, D. A. Frohrib, T. P. Carlson, D. L. Hagen, W. L. Garrard, "The Design of a Wind Energy Storage System with a Cellulosic Flywheel." Proc. 1977 Flywheel Technology Symposium, pp. 201-212, October 5-7, 1977, San Francisco, CA, CONF-771053.

4 D. W. Rabenhorst, "Composite Flywheel Development Program- Final Report." Johns Hopkins University, Applied Physics Laboratory: APL/JHU SDO-4616A NSF Grant No. AER 75-20607, May 1978.

5 A. G. Erdman, D. A. Frohrib, W. L. Garrard, D. L. Hagen, T. P. Carlson, "The Development of a Cellulose Flywheel System for Rural Wind Energy Storage: Final Report." University of Minnesota for the Minnesota Energy Agency, July 1978.

6 D. L. Hagen, A. G. Erdman, D. A. Frohrib, "Design of Flywheel Rotors Utilizing Cellulosic Materials." Paper No. 799080, 14th Intersociety Energy Coversion Engineering Conference, Boston MA August 6, 1979.

7 D. L. Hagen, A. G. Erdman, "Economics of Cellulosic Rotors." University of Minnesota, Final Report to the Applied Physics Laboratory, May 1979.

8 A. G. Erdman, D. A. Frohrib, W. L. Garrard, D. L. Hagen, T. P. Carlson, "The Development of a Cellulose Flywheel System for Rural Wind Energy Storage: Phase II. Final Report." University of Minnesota for the Minnesota Energy Agency, December, 1979.

9 Tom Lenderink, Lenderink Inc., Belmont MI 49306

10 D. P. McGuire and D. W. Rabenhorst, "Composite Flywheel Rotor/Hub Attachment through Elastomeric Interlayers." Proc. 1977 Flywheel Technology Symposium, USDOE 1978.

11 D. L. Hagen, "The Properties of Natural Cellulosic Materials Pertaining to Flywheel Kinetic Energy Storage Applications." Proc. 1977 Flywheel Technology Symposium, October 5-7, 1977, San Francisco, pp409-428.

12 Iu. M. Ivanov, "The Limit of Plastic Flow of Wood," U.S.D.A. Forest Prod. Lab. Translation No. 111 by H. P. Kipp (August 1955)

13 Hideo Sugiyama, "On the Effect of the Loading Time on the Strength Properties of Wood: A Review of Japanese Research," Wood Science and Tech. 1.289-303 (1967)

14 G. R. DeBaise, A. W. Porter, R. E.

Pentoney, "Morphology and Mechanics of Wood Fracture," Materials Research and Standards, 6(10), 493-499 (October 1966)

15 W. E. Wood, and D. Dilipkumar, "Acoustic Emission Analysis of Finger Joints: A Feasibility Study", Oregon Graduate Center, Beaverton, OR, September 27, 1977.

16 W. E. Wood and D. Dilipkumar, "A Composite Grip Design for Elimination of Extraneous Noise During Acoustic Emission Testing", J. Test. Eval., Vol. 6, No. 6, 1978, pp. 369-370.

17 Wayne C. Lewis, "Fatigue of Wood and Glued Joints Used in Laminated Construction," Forest Prod. Res. Soc.,5.221-229 (1951) Laminated Construction," Forest Prod. Res. Soc.,5.221-229 (1951)

18 K. Egner and A. Rothnund, "Zusammenfassender Bericht uber Dauerzugversuche mit Holzern," Materialprufungsanstalt Tech.

19 J. D. Barrett R. O. Foschi, "Duration of Load and Probability of Failure in Wood. Part I. Modelling Creep Rupture. Part II. Constant Ramp and Cyclic Loadings." Canadian J. Civil Eng. Vol. 5, No. 4, 1978, pp505-532.

20 C. C. Gerhards, "Time Related Effects of Loading on Wood Strength: A Linear Cumulative Damage Theory." Wood Science Vol. 11, No. 3 January 1979, pp139-144.

21 B. J. Lazan, "Dynamic Creep and Rupture Properties of Temperature Resistant Materials under Tensile Fatigue Stress." Am. Soc. Test. Materials, Vol. 49, 1949 pp 757-787.

22 Gougeon Brothers, Inc., Bay City, Michigan, "Wooden Blade Feasibility Feasibility Study, Final Report." November 1978 to NASA-Lewis Research Center, Cleveland Ohio.

23 J. F. Siau, Flow in Wood, Syracuse Wood Science Series, 1, Syracuse University Press, 1971.

24 Perifra, (company manufacturing Sirocco Vacuum drying equipment) 49, Rue d"Hautevine, Paris X.

25 A. Venkateswaren, "Sorption of Aqueous and Nonaqueous Media by Wood and Cellulose." Chemical Reviews Vol. 70 No. 6, December 1970.

26 Christen Skaar, Water in Wood, Syracuse University Press 1972.

27 William T. Simpson, "Predicting Equilibrium Moisture Content of Wood by Mathematical Models." Wood and Fiber, Vo. 5, No. 1, Spring 1973.

28 Stanley P. Rowland, "Cellulose: Pores, Internal Surfaces, and the Water Interface." Textile and Paper Chemistry Technology, American Chemistry Society Symposium 1976.

29 William Simpson, "Sorption Theories for Wood." Symposium on Wood Moisture Content-Temperature and Humidity Relationships, at Virginia Polytechnic Institute, Blacksburg, Oct. 29, 1979, USDA Forest Service.

30 George Bramhall, "The Validity of Darcy's Law in the Axial Penetration of Wood." Wood Science and Technology, Vol. 5(1971,p121-134.

31 Eugene M. Wengert, "Predicting Average Moisture Content of Wood in a Changing Environment." Wood and Fiber, Vol. 7 No. 4 Winter 1976 p264-273.

32 Howard N. Rosen, "Distribution of Water in Hardwoods: a Mathematical Model." Wood Science and Technology, Vol. 8 (1974), p283-299.

33 John F. Siau, "A Model for Unsteady -State Gas Flow in the Longitudinal Direction of Wood." Wood Science and TEchnology Vol. 10 (1976) p149-153.

34 J. D. Babbitt, G. Bramhall, (Letters to Editor.) Wood Science, Vol9 No.4 (April 1977), pp151-153.

35 J. W. S. Hearle, "Thermodynamic Relations Among Stresses, Deformations, and Moisture Adsorption." Textile Research Journal, Dec. 1957, pp940-945.

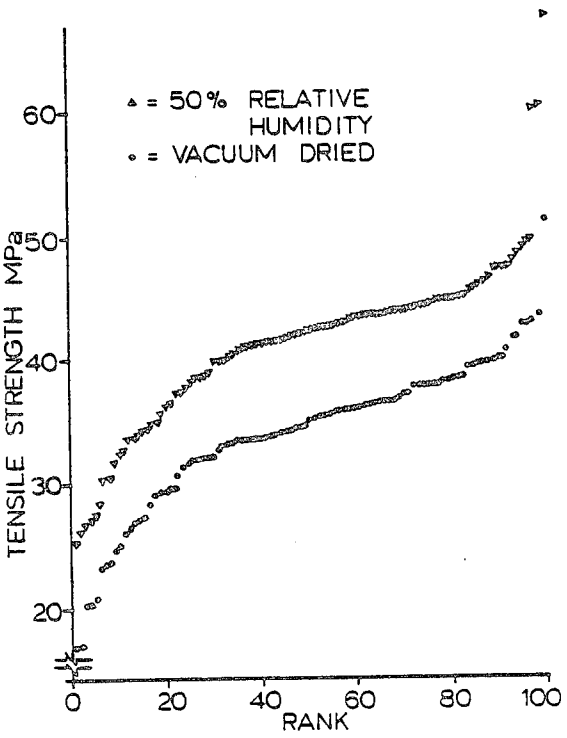

Fig. 1 Tensile Strength of Hexagonal 16 ply Yellow Birch Plywood Perpendicular to the Face Veneer Grain.

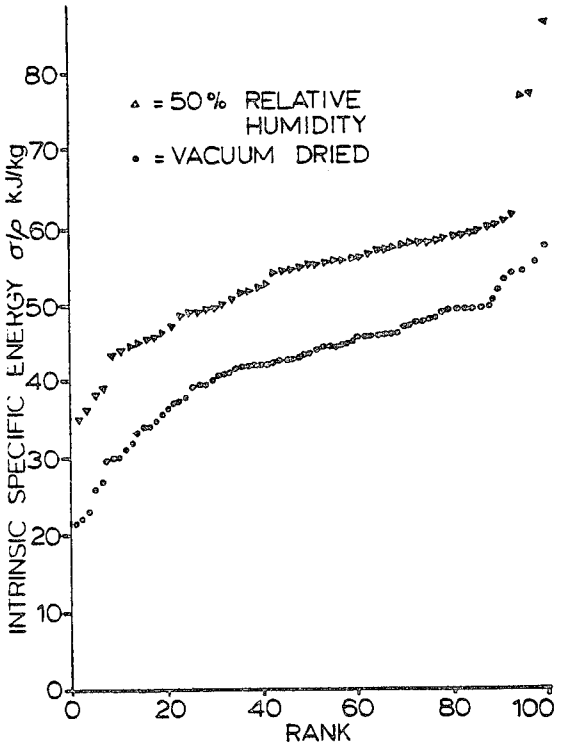

Fig. 2 Intrinsic Specific Energy Distribution of Hexagonal Yellow Birch Plywood Perpendicular to the Face Veneer.

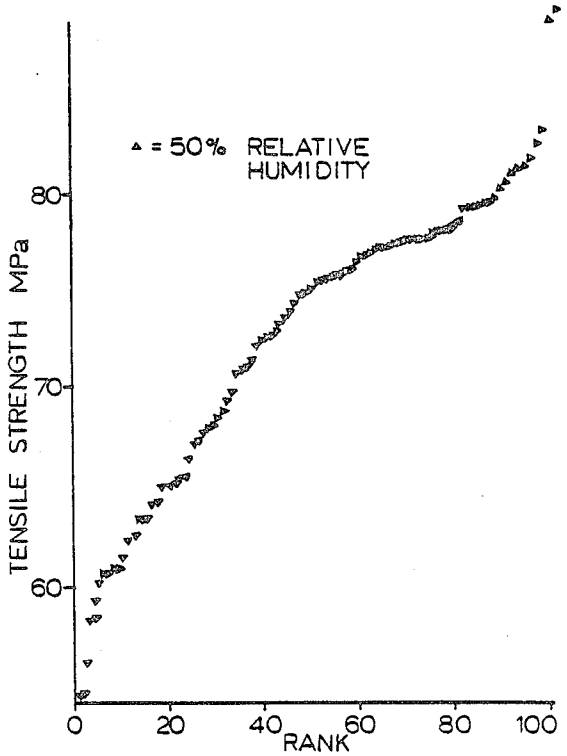

Fig. 3 Tensile Strength of Hexagonal Yellow Birch Plywood Parallel to the Face Veneer Grain.

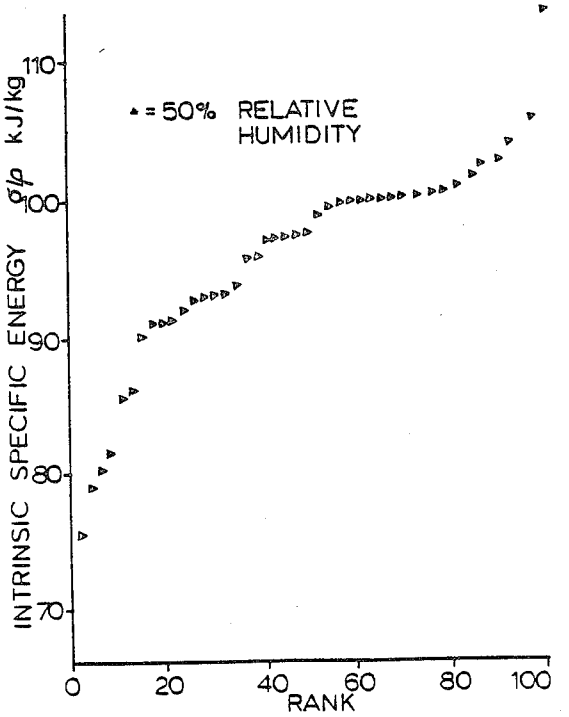

Fig.4 Intrinsic Specific Energy Distribution of Hexagonal Yellow Birch Plywood Parallel to the Face Veneer Grain.

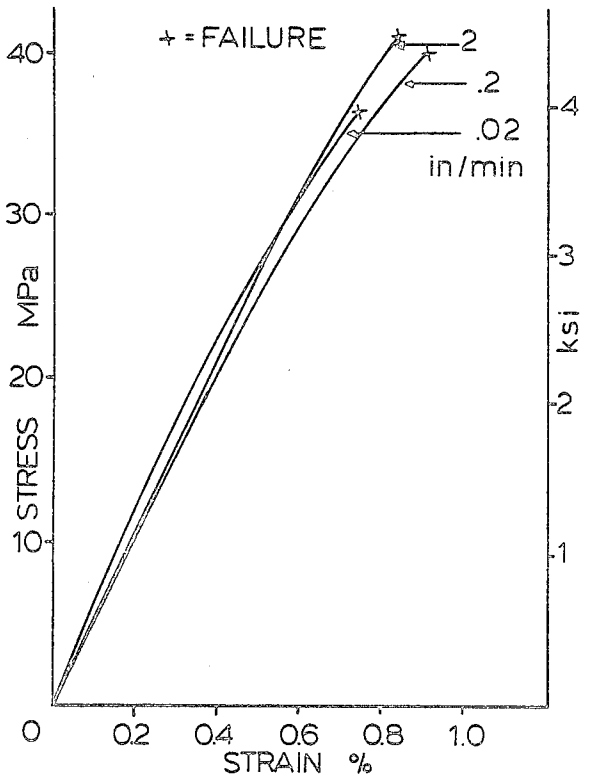

Fig. 5 Tensile Test of Yellow Birch Hexagonal Plywood Perpendicular to the Face Veneer Grain @ Constant Strain Rate.

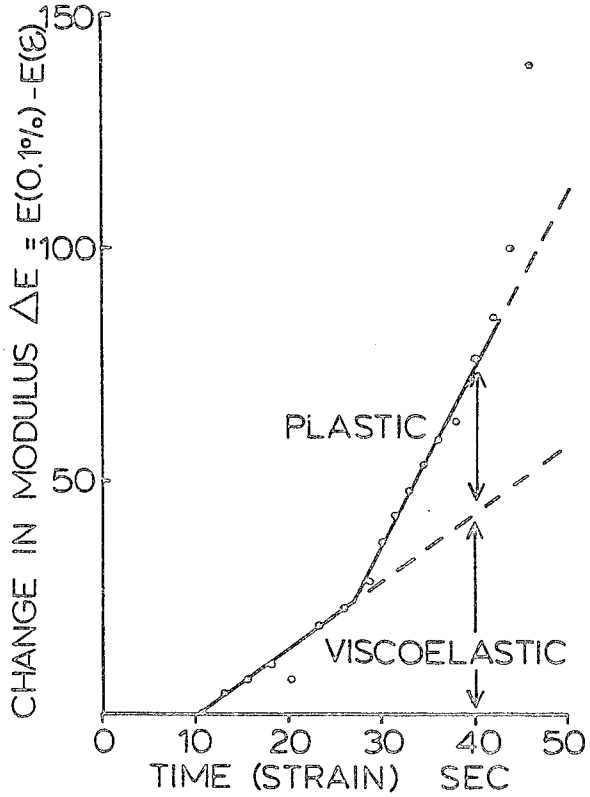

Fig. 6 Change in Modulus of Elasticity with Strain in Tensile Test of Yellow Birch Plywood @ Constant Strain Rate.

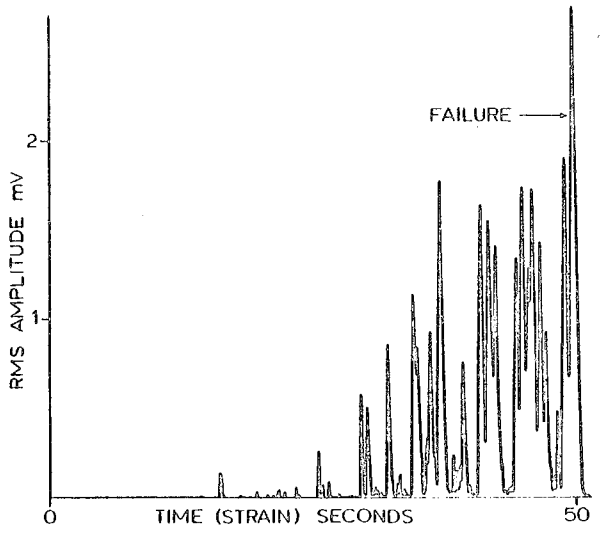

Fig. 7 True RMS of Acoustic Emissions During Tensile Test of Birch Plywood (Vacuum Dried)at Constant Strain Rate.

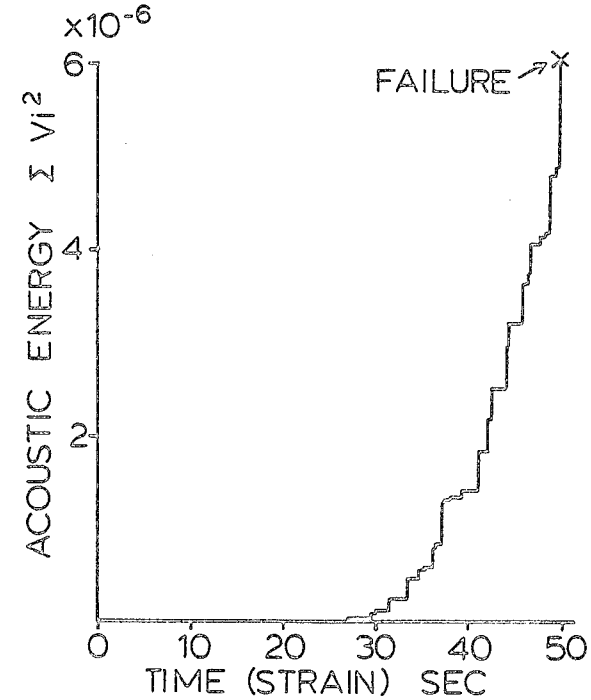

Fig. 8 Acoustic Energy Released During Tensile Test of Birch Plywood at Constant Strain Rate.

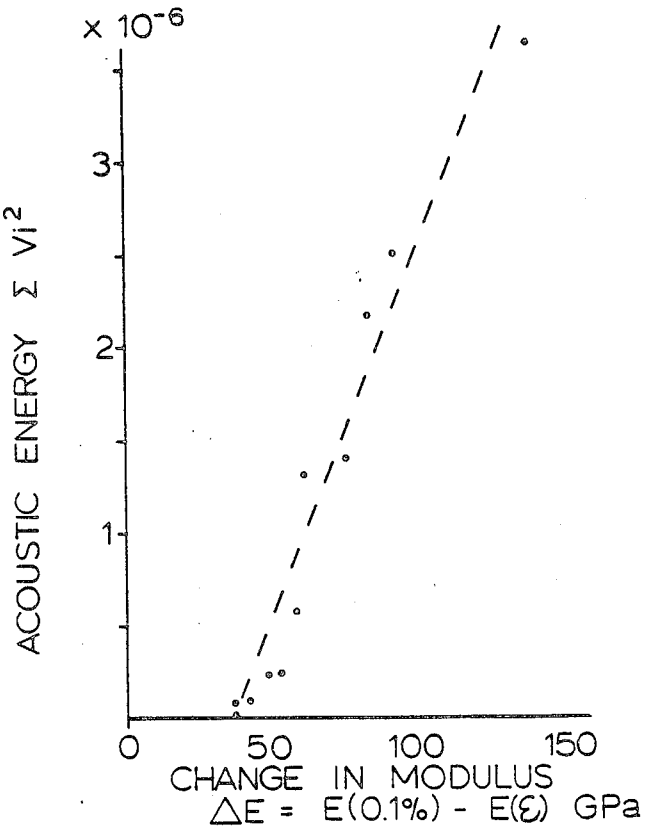

Fig. 9 Correlation of Acoustic Energy Released in Fiber Fracture with Change in Modulus of Elasticity.

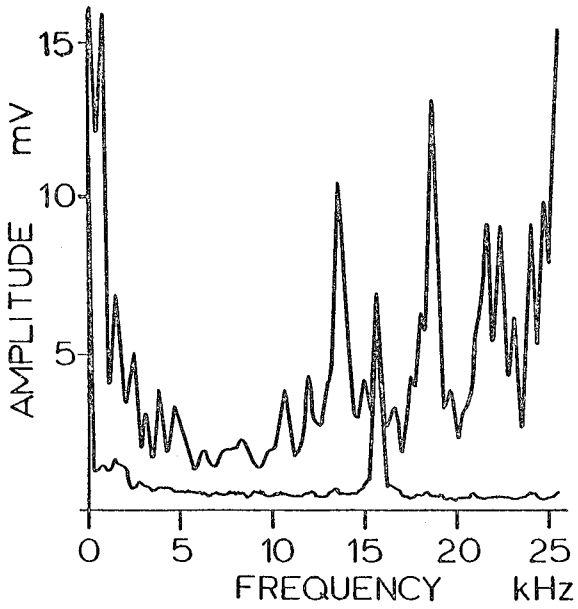

Fig. 10 Frequency Analysis of Acoustic Emissions with 30 kHz Sensor for the two halves of a constant strain rate tensile test.

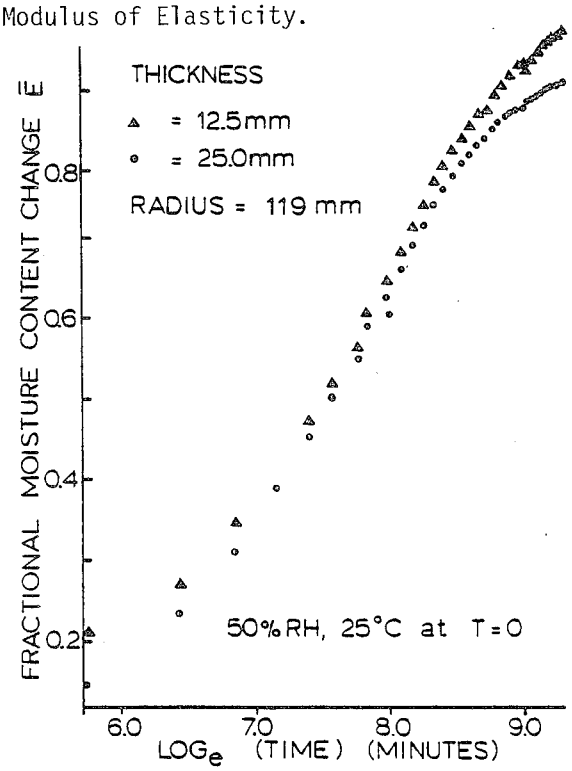

Fig. 11 Fractional Moisture Loss Tests of Birch Plywood Disks during Vacuum Drying.

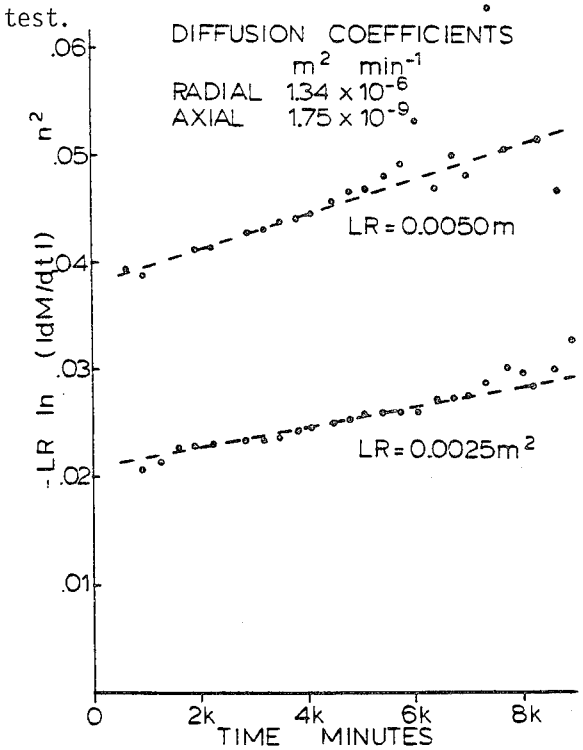

Fig. 12 Variation in Reduced Moisture Loss Rates with Time for Birch Plywood Disks during Vacuum Drying.

REMARKS ON THE STRESS STATE IN ROTATING ORTHOTROPIC DISKS

G. GENTA, M.M. GOLA, A.GUGLIOTTA
Politecnico di Torino - Istituto della Motorizzazione
10100 - TORINO Italy

ABSTRACT

It is well known that the stress distribution in orthotropic rotating disks of constant thickness without a central hole is axisymmetrical. In a previous paper the present authors have shown that the same happens also in the case of pierced disks of constant thickness provided that the elastic compliances of the material satisfy a certain relationship. In the present paper an axisymmetrical stress distribution is found for the orthotropic constant stress disk, and reasonably strong clues are given to support the assumption that the stress distribution in orthotropic disks without a central hole of any profile is axisymmetrical. The same property holds for rotating disks with a central hole, provided that the elastic compliances of the material satisfy the already mentioned equation. In all cases in which an axisymmetrical stress distribution was found, it could be calculated using a one-dimensional technique. This property can be used to optimize the shape of orthotropic disks using any simple one-dimensional method for the calculation of the stresses.

AIM OF THE WORK

Composite material flywheels can be built in several ways, namely by filament winding or by using different types of laminates. The cheapest solution is to use normal cross-ply laminates instead of the more costly quasi-isotropic ones. Cross-ply laminates, like normal plywood, which can also be regarded as a good material for low cost flywheels does not show axisimmetrical properties, and the calculation of the stress distribution must be performed using at least a two-dimensional technique, when the plane stress or plane strain assumptions are possible.

It is however well known in the literature that the stress distribution in unpierced orthotropic disks of constant thickness is axysimmetrical, i.e. function of the radius only [1] [2], even if the material density is a function of the radius[3].

The A.A. have shown in a previous work[4] that the same property applies to constant thickness disks with a central hole if the elastic compliances of the material satisfy a particular equation.

The aim of the present work is to show that there are strong clues to suggest that any orthotropic disk of arbitrary shape shows a stress distribution which is a function of the radius only and which can be calculated by a simple one-dimensional procedure, like the one used for isotropic disks if one of the following conditions applies:

- The disk has no central hole
- The elastic compliances of the material satisfy the already mentioned equation.

It will be also shown that the "constant stress profile" which holds for isotropic materials leads, in the case of orthotropic materials, to an axisymmetrical constant stress state in which the circumferential stresses are equal to the radial ones.

Of course, in such cases, the displacement and deformation fields are both functions of the angle.

Apart from the "constant-stress disk", the A.A. have not been able to prove that the stress distribution is axisymmetrical with an analytical procedure, but have in fact run numerical calculations of stress distribution in unpierced disks with a large variety of different profiles.

The procedure used is, in substance, a finite element technique, already described in previous works on similar subjects [5] [6] [7]. In all cases, the stress distribution has proved to be axisymmetrical, since small local deviations can be explained in terms of convergence problems.

The same procedure shows that, in presence of a central hole, the stress state is dependent on the angle, except if the material satisfies the special conditions mentioned above; this can be considered as a test of the reliability of the method.

DISKS WITHOUT A CENTRAL HOLE

CONSTANT STRESS DISK

The constant stress profile in the case of isotropic materials with the plane stress assumption, is:

$$h = h_o \exp [- B (r/r_e)^2] \qquad (1)$$

where:

$$B = \rho \omega^2 r_e^2/2 \sigma . \qquad (2)$$

This solution is in general true only for isotropic materials. As an example, a disk having the profile defined by eq. (1) and built with a cylindrically orthotropic material (e.g. a composite material obtained by the filament winding technique) is not a constant stress disk.

As a matter of fact, it is impossible to make a strictly-speaking constant-stress disk with such materials as the conditions $\sigma_r = \sigma_c$ = constant doesn't satisfy the strain compatibility equations[8]. In the case of an orthotropic material it is possible to prove that the relationship:

$$\begin{cases} \sigma_r = \sigma_c = \sigma = \text{constant} \\ \tau_{rc} = 0 \end{cases} \qquad (3)$$

will satisfy the strain compatibility equation.

From eq. (2) the strains in radial and circumferential direction can be calculated as:

$$\begin{cases} \varepsilon_r = (S'_{11} + S'_{12}) \sigma \\ \varepsilon_c = (S'_{22} + S'_{12}) \sigma \\ \gamma_{rc} = (S'_{16} + S'_{26}) \sigma . \end{cases} \qquad (4)$$

They are independent of the radius r and function of the angle θ through the elastic compliances S'_{ij} referred to the radial (1) and circumferential (2) directions.

With the usual relationships[9] between the compliances S_{ij} referred to the xy system (Fig. 1) and the S'_{ij}, eq. (4) become:

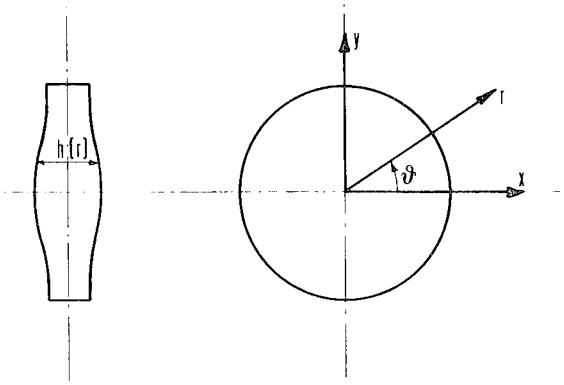

Fig. 1 - Systems of reference.

$$\begin{cases} \varepsilon_r = \sigma \left[\frac{1}{E_1} (\cos^4\theta - \sin^4\theta) + (\frac{1}{E_1} + \frac{1}{E_2}) \sin^2\theta - \frac{\nu_{12}}{E_1} \right] \\ \varepsilon_c = \sigma \left[\frac{1}{E_1} (\sin^4\theta - \cos^4\theta) + (\frac{1}{E_1} + \frac{1}{E_2}) \cos^2\theta - \frac{\nu_{12}}{E_1} \right] \\ \gamma_{rc} = 2 \sigma \sin\theta \cos\theta (\frac{1}{E_2} - \frac{1}{E_1}) . \end{cases} \qquad (5)$$

The strain compatibility equation can be written as:

$$r(\gamma_{rc})_{,r\theta} + (\gamma_{rc})_{,\theta} - r^2 (\varepsilon_c)_{,rr} - 2r (\varepsilon_c)_{,r} + r (\varepsilon_r)_{,r} - (\varepsilon_r)_{,\theta\theta} = 0 . \qquad (6)$$

Remembering that the strains are independent of r, eq. (5) and (6) yield:

$$2 \left[(\frac{1}{E_2} - \frac{1}{E_1}) \sin\theta \cos\theta \right]_{,\theta} - \left[\frac{1}{E_1} (\cos^4\theta - \sin^4\theta) + (\frac{1}{E_1} + \frac{1}{E_2}) \sin^2\theta - \frac{\nu_{12}}{E_1} \right]_{\theta\theta} = 0 . \qquad (7)$$

Performing one derivative operation, equation (7) becomes:

$$2 \left[(\frac{1}{E_1} - \frac{1}{E_1}) \sin\theta \cos\theta \right]_{,\theta} - 2 \left[(\frac{1}{E_2} - \frac{1}{E_1}) \sin\theta \cos\theta \right]_{,\theta} = 0 \qquad (8)$$

which is an identity.

As solution (3) has proved to satisfy the strain compatibility equation (6), it can be introduced into the usual equilibrium equations[10] which in the case of $\tau_{rc} = 0$ become:

$$(h\ r\ \sigma_r)_{,r} - h\ \sigma_c + h\ \rho\omega^2\ r^2 = 0. \quad (9)$$

It is therefore possible to find the disk profile h(r).

As eq. (9) does not depend on the nature of the material, the same solution (1) of the isotropic case is found.

It is to be noticed that the stress state is, in this case, equal for isotropic and orthotropic materials while the displacement field is not.

With simple calculations, the stresses in x and y directions can be found and the displacement field can easily be calculated:

$$\begin{cases} u_x = \frac{1}{E_1}(1 - \nu_{12})\ \sigma\ .\ x \\ u_y = (\frac{1}{E_2} - \frac{\nu_{12}}{E_1})\ \sigma\ .\ y\ . \end{cases} \quad (10)$$

The displacement in x direction depends only on x coordinate, the one in y direction depends only on y.

UNPIERCED DISKS OF ARBITRARY PROFILE NUMERICAL ANALYSIS

Since the present authors neither have found in the literature, nor have obtained themselves, a solution concerning the problem of the disk of any shape, a numerical analysis was attempted.

The procedure is one already used in previous works [6 7] and there described in detail.

It substantially consists in developing the radial u , and the circumferential displacement v in trigonometric series of only the even terms (the others are absent for symmetry):

$$\begin{cases} u = u_k \cos 2k\theta \\ v = v_k \sin 2k\theta\ . \end{cases} \quad (11)$$

Moreover, annular elements are defined, with inner radius r_i and outer radius r_e ; in each of these elements both the radial displacement u and the circumferential v are interpolated by a third degree polynomial in which the coefficients are the function and its derivatives to the radius at r_i and r_e.

A general formula for the family of osculating polynomials of this kind has been recently given in [11].

Therefore:

$$\begin{cases} u_k(r) = [a_{k_1}; a_{k_2}; a_{k_3}; a_{k_4}] \cdot \\ \qquad \cdot [u_i; (\frac{du}{dr})_i; u_e; (\frac{du}{dr})_e]^T \\ v_k(r) = [b_{k_1}; b_{k_2}; b_{k_3}; b_{k_4}] \cdot \\ \qquad \cdot [v_i; (\frac{dv}{dr})_i; v_e; (\frac{dv}{dr})_e]^T . \end{cases} \quad (12)$$

In order to limit the cost of the analysis the series in (11) were truncated at k = 2 included. This choice is justified also by the fact that in the case of the flat unpierced disk the trigonometric functions present in the expression of the displacement fields, obtained from[1], have only the argument 2θ and 4θ.

The analysis is performed for the plane stress case. Fig. 2 shows the results in non dimensional form concerning a conical disk, chosen as an example, having outer radius of 500 mm, thickness at the outer radius 10 mm and thickness at the revolution axis 100 mm.

The material was characterized by the following plane stress stiffness matrix , with dimensions MN/m^2:

$$[Q] = \begin{bmatrix} 40310 & 1260 & 0 \\ 1260 & 5040 & 0 \\ 0 & 0 & 1000 \end{bmatrix} . \quad (13)$$

Fig. 2a refers to the unpierced disk, and shows that both the radial stress σ_r and the circumferential stress σ_c are independent of angle, θ, i.e. the state of stress is axisymmetrical, since the curves related to θ = 0, 30°, 60°, 90° are superimposed.

Of course, this does not hold for both strain and displacement field [2 4 6 7]. The shear stress τ_{rc} are identically equal to zero.

A closer observation of fig. 2-a will show, however, that the stress distribution seems not to be exactly axisymmetrical near the outer edge of the disk; as it will become apparent later, this is entirely due to the fact that the trigonometric polynomials were truncated at k = 2, while some more terms would be needed for a better

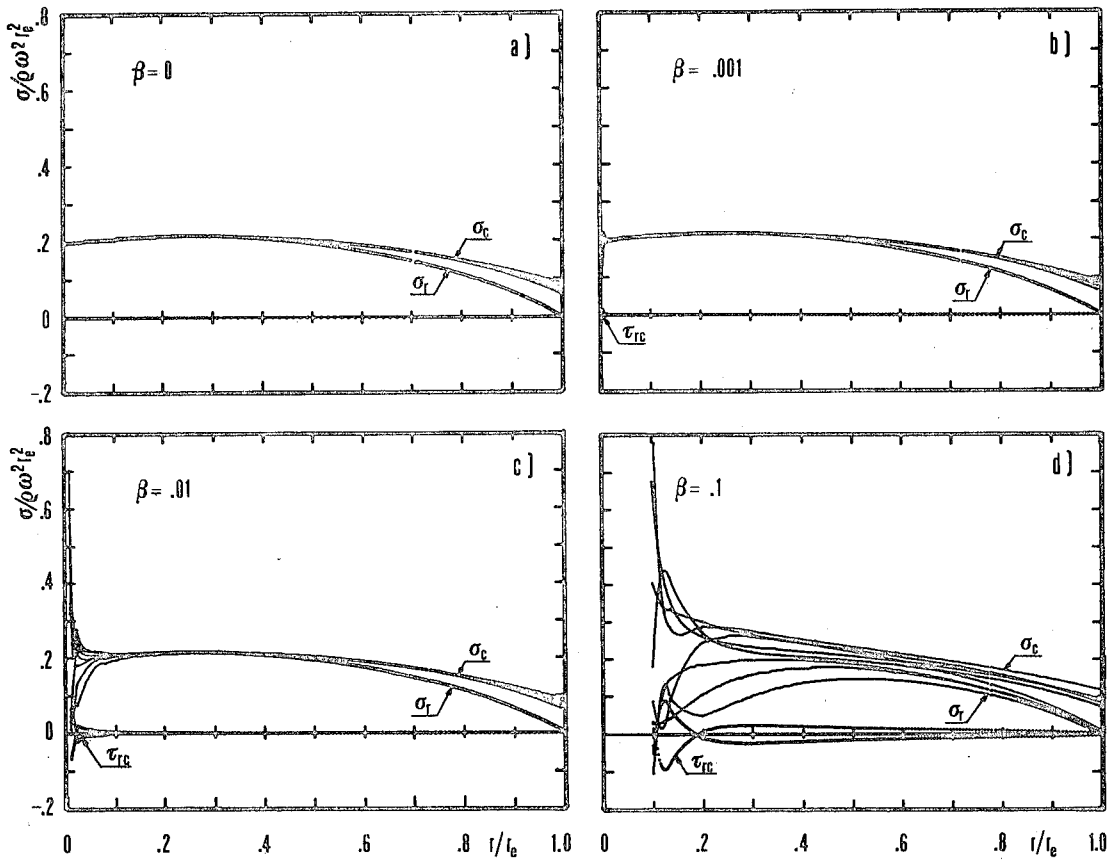

Fig. 2 - Stress distribution in conical disks with radius 500 mm, outer thickness 10 mm and thickness at rotation axis 100 mm.
a) Unpierced disk
b), c), d) Pierced disks with β = 0,001; β = 0,01; β = 0,1 respectively.
Orthotropic material.

———— σ_r and σ_c
..... τ_{rc}

approximation of the displacement field , which would result in a more closely axisymmetrical calculated stress state.

Curves of fig. 2-b are related to the same basic disk, but having very small central hole with ratio $\beta = r_i/r_e = 0{,}001$: as it can be expected, the curves are the same of fig. 2-a, except local peaks near the centre. However, the numerical estimation of these peaks cannot be thought to be correct. Fig. 2-c and 2-d refer to central holes having values of β equal to 0,01,and 0,1. It can be seen that when the hole is large enough, as in fig. 2-d, its effect is no longer local, and the state of stress no longer axisymmetrical. As in fig. 2-b, also in figs.2-c and 2-d the solution near the innner edge is not completely correct, since the interpolating functions are not able to correctly comply with the boundary conditions due to the very high local gradients.

It has been said before that the scatter of the curves in fig.2-a, particularly evident for the circumferential stress near the outer edge, is due only to the truncation of the interpolating polynomials, but that the solution is, in reality, an

axisymmetrical state of stress. A proof of this statement could be given by repeating the analysis with more terms, but this would increase costs and computing time , besides being unnecessary in the light of what follows.

A first clue is based on the fact that if the real curves are superimposed for most of their length they cannot scatter as in fig. 2-a: in fact the resultant force of σ_c calculated on any diametral section of the disk must be equal independently of the diameter chosen, what would not happen in the case of fig. 2-a. A second clue was obtained by examining an unpiered disk made of a general orthotropic material, but having equal stiffness on the two principal orthogonal directions, i.e.:

$$E_1 = E_2 = 40000 \text{ MN/m}^2; \quad \nu_{12} = 0,3 ;$$

$$G = 5000 \text{ MN/m}^2.$$

In this case the solution for the displacement field should involve less trigonometric terms, since their base period must be $\pi/2$. Therefore the limited number of terms involved in the present analysis should in general be sufficient, and in effect, as it is shown in fig. 3, the curves for $\theta = 0$, $15°$, $30°$, $45°$ do superimpose within the thickness of the pen.

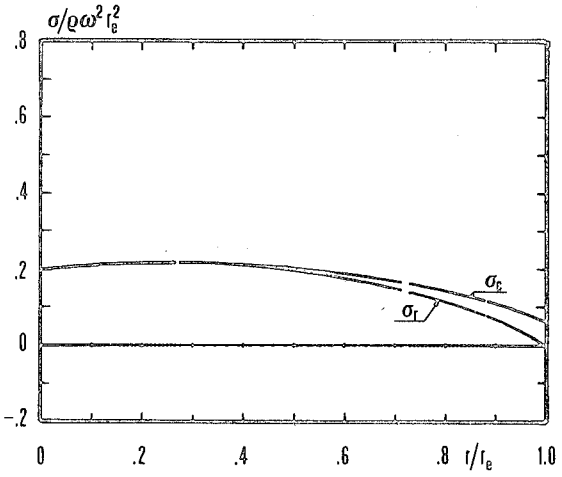

Fig. 3 - Stress distribution in the same disk of fig. 2a but with an orthotropic material having $E_1=E_2$.

This shows, togeter with the fact that in fig.2-a the scatter is very limited, that the displacement field is well defined already by the very first terms in expansion (11). Of course,no conclusion of this kind is possible when a hole is present.

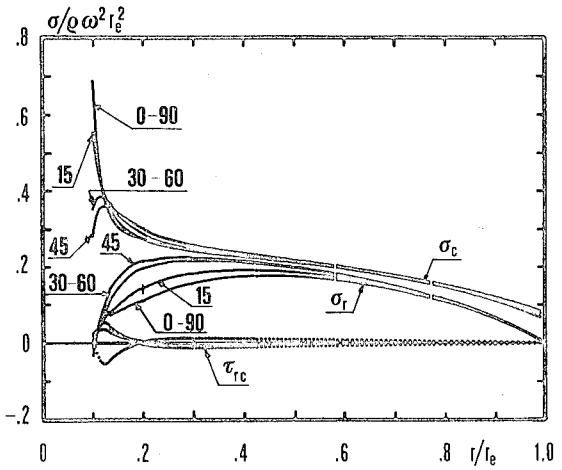

Fig. 4 - Stress distribution in the same disk of fig. 2-d, but with an orthotropic material having $E_1=E_2$

Considering infact fig. 4 related to the same material considered in fig. 3,but with the presence of a central hole, with a 100 mm diameter, it cannot be said how much of the scatter is due to the numerical approximation and how much to the real solution itself; such analysis was considered to be beyond the scope of the present work.

All these considerations suggest that:

a) the numerical procedure used and the order of truncation gave results which are sufficiently approximated for the unpiered disk.

b) The stress distribution in conical unpierced disks is indipendent of angle θ and the small deviations are very probably due to truncation.

With this experience, is was attempted the solution of an unpierced disk of a very complex shape in fact, a disk of "any" shape, since it was generated by joining seven annular conical elements, and choosing thicknesses and radial depths as Montecarlo numbers.

In fact, it is evident that such a disk is just a mathematical creature, since physically no plain stress could be really possible.

Fig. 5 shows both the disk's shape and the curve for σ_c and σ_r at angles $\theta = 0°$, $30°$, $60°$, $90°$; the material had the same characteristics of the one employed for the case of fig. 2. It can be seen that the scatter of the curves at varying angle θ is very limited, and, in the light of the examples produced before, is very probably due to truncation.

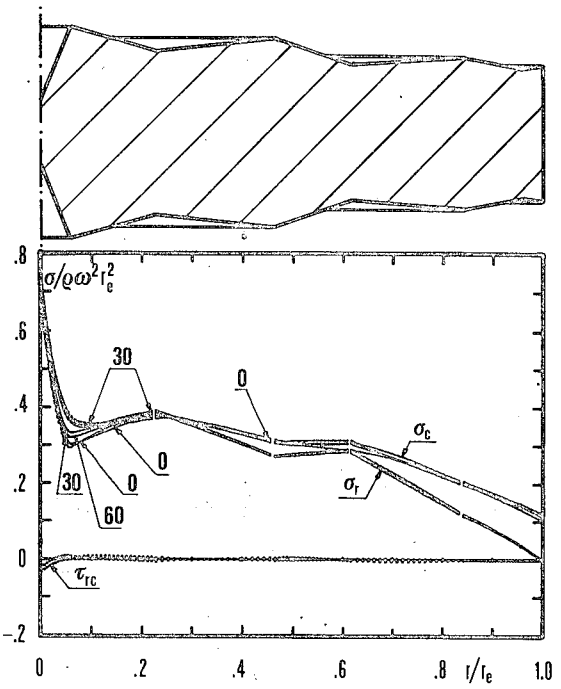

Fig. 5 - Shape and stress distribution of an unpierced disk made of seven annular conical elements. Orthotropic material.

However, when rapid variations are present with the radius, interpolation with cubic polynomials may not be sufficient and this may influence the distribution of the values among the trigonometric expansions, since the set of solution for the a_{kj} and b_{kj} of (12) is found by imposing that the value of the elastic energy be an overall minimum; this may account for the fact that the greater scatter is present at point of greater slope variation in fig.5.

As it can be found with simple calculations from [1] [2] [3], the stress distribution in an orthotropic constant thickness unpierced disk is identical to the one in an isotropic one having a Poisson's ratio given by:

$$\nu = - \frac{S_{11} + S_{22} + 6S_{12} - S_{66}}{3(S_{11}+S_{22})+2\,S_{12}+S_{66}} \quad . \qquad (14)$$

If the plane strain assumption is to be used instead of the plane stress one, the elastic compliances β_{ij} must be introduced in eq.(14) instead of S_{ij}.

The stress distributions in the disks of fig. 2a and fig. 5 were then calculated using a common one-dimensional technique, namely Manson's method[12], giving a result which is so close to the one obtained with the finite element technique that the lines on the graphs were completely superimposed. Where the finite element technique gave some scattered results, the line representing the one-dimensional solution lies between the various curves σ (r) related to the different angles

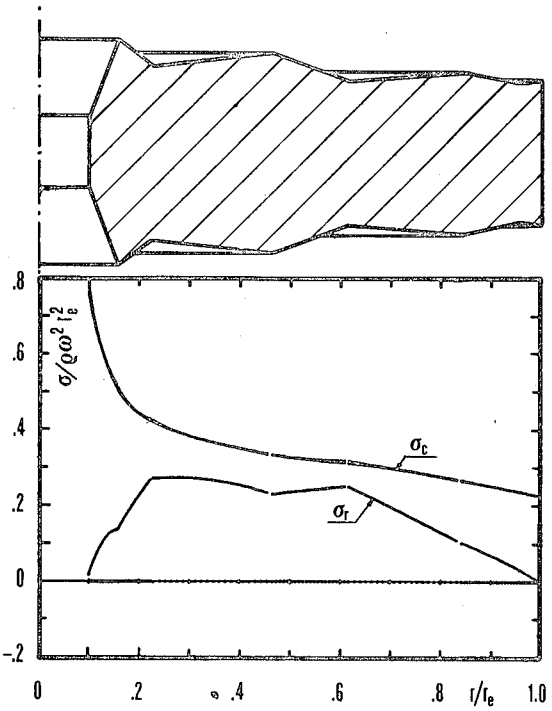

Fig. 6 - Shape and stress distribution of a disk similar to the one of fig. 5 but with a centrale hole (β=0,1) Orthotropic material satisfying condition (17).

In conclusion, it may not be an excess of confidence to state that an unpierced disk of any shape is characterized by an axisymmetrical stress distribution which can be calculated using a one-dimensional technique.

DISKS WITH A CENTRAL HOLE

CONSTANT THICKNESS DISK

Modelling the disk as a cylindrical body in which the stresses are constant in the direction of the axis, it is possible to introduce two stress functions F and ψ [4] [9] [13] such that, in xyz system (fig.1):

$$\begin{cases} \sigma_x = (F)_{,yy} + U \\ \sigma_y = (F)_{,xx} + U \\ \tau_{xy} = -(F)_{,xy} \end{cases} \qquad \begin{cases} \tau_{xz} = (\psi)_{,y} \\ \tau_{yz} = -(\psi)_{,x} \end{cases} \tag{15}$$

where U is the potential function of body forces that, in the case of a rotating disk, is

$$U = \frac{1}{2} \rho \omega^2 (x^2 + y^2) \, . \tag{16}$$

It can be demostrated[4] that with these functions, with the appropriate boundary conditions, and with the additional condition that the elastic compliances of the material satisfy the equation:

$$S_{11} + S_{22} - 2S_{12} - S_{66} = 0, \tag{17}$$

the solution is:

$$\begin{cases} \sigma_r = \rho \omega^2 r_e^2 K_1 [1 + \beta^2 - \beta^2/\chi^2 - \chi^2] \\ \sigma_c = \rho \omega^2 r_e^2 K_1 [1 + \beta^2 + \beta^2/\chi^2 - K_2 \chi^2] \\ \tau_{rc} = \tau_{yz} = \tau_{xz} = 0 \end{cases} \tag{18}$$

where change has been made to polar coordinates, r and c indicate respectively radial and circumferential, and

$$K_1 = \frac{3(S_{11}+S_{22})-2 S_{12}}{8 (S_{11} + S_{22})} \, , \qquad K_2 = \frac{S_{11} + S_{22} - 6 S_{12}}{8 (S_{11} + S_{22})} \, . \tag{19}$$

Thus, the stress distribution is clearly independent of the angle. Of course, if the material is isotropic, that is:

$$S_{11} = S_{22} = \frac{1}{E} \; ; \quad S_{12} = -\frac{\nu}{E} \tag{20}$$

eq. (19) yield:

$$K_1 = (3+\nu)/8 \quad ; K_2 = (1+3\nu)/8 \tag{21}$$

that, together with eq. (18), give the well known corresponding solution.

ARBITRARY PROFILE, MATERIAL SATISFYING CONDITION (17) - NUMERICAL ANALYSIS

The same finite element technique used for unpierced disks was then applied for the calculation of the stress distribution in several pierced disks with different profiles made of materials satisfying condition (17). In all cases an axisymmetrical stress state has been found. In fig. 6 the profile of a pierced disk obtained with random numbers is shown together with the stress state.

The plane stiffness matrix of the material is the following:

$$[Q] = \begin{bmatrix} 40310 & 1260 & 0 \\ 1260 & 5040 & 0 \\ 0 & 0 & 4210 \end{bmatrix} \; MN/m^2 \, .$$

A one-dimensional calculation was then attempted, using an isotropic material whose Poisson's ratio is given by eq. (14), which taking into account condition (17), becomes:

$$\nu = -\frac{2 S_{12}}{S_{11}+S_{22}} = \frac{2 E_2}{E_1 + E_2} \nu_{12} \, . \tag{22}$$

Again the results are completely superimposed to the ones obtained by the finite element technique.

There are therefore strong clues to believe that the stress distribution in any disk, pierced or unpierced made with an orthotropic material satisfying condition (17) is axisymmetrical and can be easily calculated using a one-dimensional technique.

CONCLUSION

It can be analytically demonstrated that unpierced rotating disks made of orthotropic materials are characterized by a state of stress which is independent of the polar angle θ, in the following cases:

a) when the disk is of constant thickness

b) when the disk has a shape of uniform stress.

In the case of constant thickness, the stress state has been analytically proved to be axisymmetrical when the material satisfies condition (17) also for the pierced disk.

No analytical solution was known to the A.A. for the case of disks of any shape; however, they were led to suspect that the axisymmetry of the stress state is a more general result, valid for unpierced disks independently of their thickness distribution along the radius.

Numerical analysis was performed, with a specially arranged finite element proce-

dure, using annular elements capable of both displacement compatibility and stress equilibrium at the boundaries. The approximation due to the truncation of the interpolating polynomials has been discussed.

These authours believe that it can be reasonably concluded that the state of stress in unpierced disks is indipendent of the angle for any shape of disk.

However, this conclusion is not really proved, but relies on very strong clues ; it is hoped that these will stimulate efforts to find their general analytical proof or disproof.

Similar conclusions can be drawn for pierced disks of any shape, provided that the material satisfies condition (17); infact analysis on a disk of very complicated shape, generated by random numbers, has given a remarkably evident axisymmetry of the stresses.

In all cases in which an axisymmetrical stress distribution was found, it could be calculated by any one-dimensional method provided that an isotropic material with Poisson's ratio given by eq. (14) or eq. (22) is used. Also this looks to be a general property.

This property allows to use very simple and fast calculation techniques to solve the stress distribution in orthotropic disks, making it possible to optimize their shape by a trial and error procedure.

SYMBOLS

h	disk thickness at radius r
r	radius
r_e, r_i	outer radius, inner radius
u	radial displacement
v	circumferential displacement
x,y	cartesian system of reference
E_i	Young modulus in i direction
Q'_{ij}	elements of the plane stiffness matrix
S_{ij}	elastic compliances refered to xy system
S'_{ij}	elastic compliances refered to rθ system
β	ratio r_i/r_e
β_{ij}	plane strain elastic compliances
γ	shear strain
ε	strain
θ	polar angle
ν	Poisson's ratio
ρ	density
σ	stress
τ	shear stress
ω	angular velocity
χ	ratio r/r_e
$(\ )_{,x}$	differentiation with respect to the variable x.

REFERENCES

1 Chang, C.I., "The Anisotropic Rotating Disk" *Int. Journal of Mechanical science*, vol. 17, 1975, pp. 397-402.

2 Chang, C.I., "A Closed Form Solution for an Orthotropic Rotating Disk", *Journal of Applied Mechanics*, decem - ber 1974, p. 1122.

3 Chang, C.I., "Stresses and Displace -. ments in Rotating Anisotropic Disks with variable Densities", *A.I.A.A. Journal* vol. 14, n. 1, Jan. 1976, pp.116-118.

4 Genta G., Gola M., "The stress state in orthotropic rotating disks", Istituto della motorizzazione, Politecnico di Torino, 1979.

5 Belingardi G., Genta G., Gola M.: "Una applicazione del principio dei lavori virtuali al calcolo di dischi rotanti in materiale anisotropo" V Congresso AIAS, Bari 1977.

6 Belingardi G., Genta G., Gola M.: "A study of the stress distribution in rotating orthotropic disks", *Composites* aprile 1979, pp.72-80.

7 Genta G., Gola M.: "Volani in legno lamellare. Caratterizzazione del materiale, calcolo delle tensioni e prove di centrifugazione" VI Congresso AIAS, Brescia, 1978.

8 Belingardi G., Genta G.: "Sull'analisi delle tensioni in dischi rotanti in materiale ortotropo sottoposti a variazioni di temperatura", III Congresso Nazionale AIMETA, Cagliari, octo - ber 1976.

9 Lekhnitskii S.G., *"Theory of elasticity of an anisotropic elastic body"*, Holden Day, New York, 1963.

10 Lakshminarayana H.V., Srinath H.: "Elastic stresses in rotating ortho - tropic discs of variable thickness" , *Journal of strain analysis*, vol. 8, n. 3, 1973, pp. 176- 181.

11 Gola M., Gugliotta A.: "A Formula for Polynomials Having Prescribed Values of a Function and its Derivatives of any Order at Both Ends of the 0-1 Interval." Istituto della Motorizzazione, Politecnico di Torino, Dec. 1979.

12 Manson S.S.: "Determination of Elastic Stresses in Gasturbine", NACA Report 871, 1947.

13 Sendeckyi G.P.: "Some Topics in Anisotropic Elasticity", *Composite Materials*, vol. 7, Academic Press, N.Y., 1975.

HYBRID ELECTRIC POWER SYSTEMS USING FLYWHEELS

Eberhart Reimers
U.S. Department of Energy,
Office of Advanced Conservation Technologies,
Division of Thermal and Mechanical Energy Storage Systems,
600 E. Street NW,
Washington, D.C. 20545

Thomas M. Barlow
Mechanical Engineering Department,
Lawrence Livermore National Laboratory,
University of California,
Livermore, CA 94550

ABSTRACT

The flywheel is used as an energy storage device in hybrid electric vehicle propulsion systems and in a utility power residential system. Current experimental equipment designs are performance-optimized by combining state-of-the-art and "space age" technologies, system configurations, and component concepts with little regard to the user's cost. The high cost, in turn, delays commercialization of new equipment concepts. One way to maximize equipment utility at lowest first cost is to limit the major development effort to the flywheel rotor and its ancillaries, while attempting to utilize commercially available components in a suitable system configuration. In most cases this can be done with little weight penalty, and within acceptable limits prescribed for the particular application. This paper analyzes two potentially low-cost system design alternatives, both of which incorporate commercial machinery and a standard flywheel module rated at 17 kW·h. The first design alternative describes a hybrid electric propulsion drive that utilizes the flywheel as a load leveler and as a source of short-term peak power. In the second design alternative the flywheel is utilized as a source of long-term power in a residential power supply externally charged by an intermittently energized solar photovoltaic-wind power supply. Most importantly, in both cases the electric machinery is utilized at highest component utility, which is one of the requirements to reduce first equipment cost.

INTRODUCTION

Existing technologies and system configurations can be utilized to expand the use of flywheels. Hybrid electric and mechanical power systems for either transportation or stationary power applications seem to be well-suited for the multiple disposition of power from a centrally located power source. The conversion of multiple forms of power into electrical power in conjunction both with a practical peak power energy storage device, namely a flywheel, and with no-break reconnectible windings in electric machinery is attainable at high component utility. Utilizing only commercially available components, such systems can be constructed at relatively low first-equipment cost.

The design of flywheels, solid-state power conditioners, and appropriate logic controls are described in the general literature. Thus, only specific problems of power transfer for the hybrid electric propulsion drive and the utility power residential system are considered in this paper, which emphasizes the control of squirrel-cage induction motors with switched windings, and the control of the continuously variable transmission (CVT) in conjunction with a constant-speed synchronous machine.

GENERAL DISCUSSION

HYBRID ELECTRIC DRIVE

The performance of large hybrid ac electric propulsion systems for off-road

vehicles or material handling equipment can be substantially improved by the use of an energy storage flywheel, whereby the flywheel supplies peak power well in excess of maximum engine power of a relatively constant-speed heat-engine power plant. Kinetic energy storage in the flywheel permits the engine to be operated over a narrow range of its torque-speed curve, and eliminates the need for rapid engine-throttling controls to provide vehicle peak power or acceleration profiles. This reduces the complexity of emission control measures for exhaust systems. The power plant is sized on the basis of continuous power for maximum cruising speed. Time-limited peak power requirements for acceleration and high-torque hill climbing at low speed will be supplied by the flywheel.

The flywheel capacity is calculated in terms of typically 200% peak power overload capability for a 5-min period. Since the flywheel supplies energy by a change in angular velocity, the required flywheel energy storage capacity is typically 35 kW°h for a 200-hp turbine drive to provide 50 kW°h over a 20% speed range at 24 000 rpm; and 17 kW°h when operated over a speed range of 12 000 to 24 000 rpm. The flywheel is either "clutched in" to bring it up to synchronous speed, as shown in Fig. 1, or connected to the planet gears of a continuously variable mechanical transmission for improved energy retrieval. The speed of the ring gear for this transmission is the controlled variable, which is controlled by a variable displacement hydrostatic motor. The alternator acts as an electromechanical power processor furnishing power to the motors during the propulsion mode, or it stores power returned from the motor as kinetic energy in the flywheel in the event this is a requirement.

UTILITY POWER RESIDENTIAL SYSTEM

On-site energy storage requirements for solar photovoltaic (PV) power systems are currently satisfied by energy storage batteries. Those requiring regulated ac-output power use solid-state inverters for power conditioning. Studies conducted to define future PV power systems generally assume continued use of such elements because of the generally held conviction that no other system can compete economically with batteries and inverters. However, studies performed at the Massachusetts Institute of Technology's Lincoln Laboratory indicate that flywheel energy storage with integrated power-conditioning electronics can be technically and economically competitive

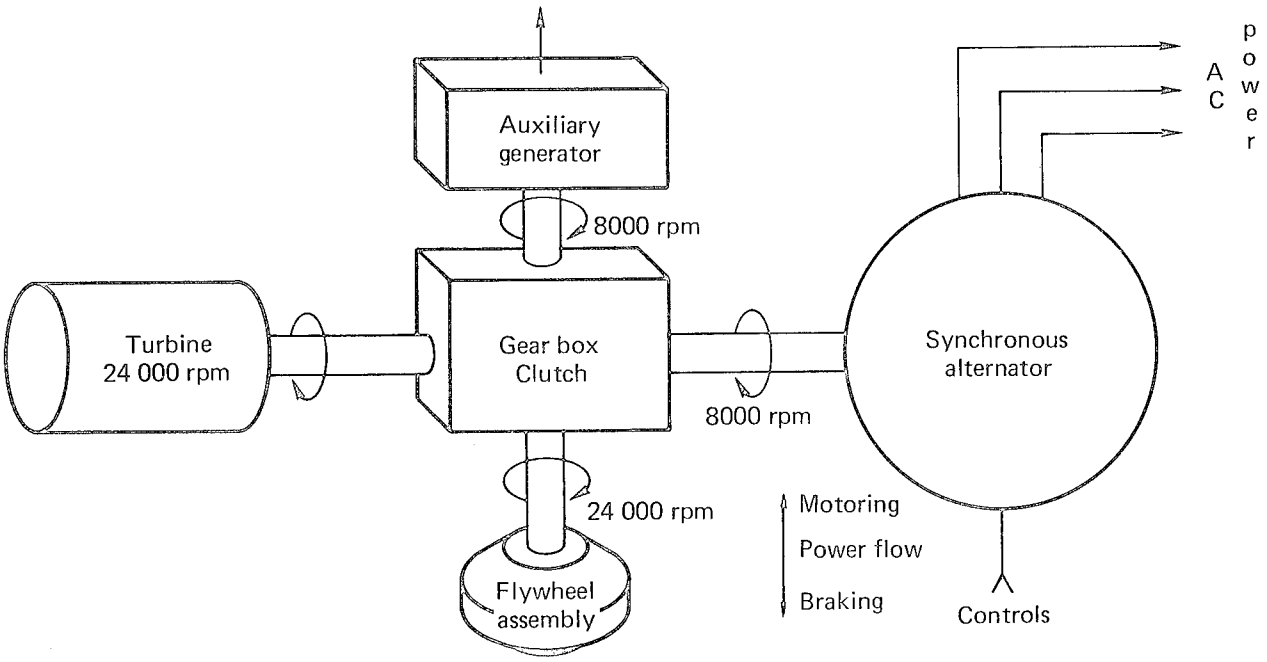

Fig. 1. Alternator power supply with high-speed energy storage flywheel.

with either present-day or advanced batteries. The design of such a system is currently in progress and is described in the literature.[1]

Prior art utilizes a solar cell array to charge the lead acid energy storage battery. Shown in Fig. 2, the solar photovoltaic cell array consists of a series string of cells (SC), whereby the string is connected through a diode (D1) across the positive and negative terminals of the battery (D). Diode (D1) assures unidirectional current flow into the battery from the photovoltaic energy source and blocks current flow in the opposite direction. Depending on the energy requirements, many series strings can be parallel-connected, whereby each string is individually isolated with its own series diode (D1).

To sustain the battery as an uninterruptible energy source under all load and environmental conditions, it is usually necessary to provide excess photovoltaic energy capacity, such as to supply adequate energy to the battery for varying levels of solar radiation and ambient temperature. Since solar conversion efficiency is a function of sunlight and ambient temperature, the battery charge to be maintained during a winter day for a constant load profile will unavoidably result in an overcharge during bright summer days and days with a light overcast. This would result (and actually is one of the serious drawbacks of present-day installations) in boil-off of the electrolyte, which requires regular attendance to refill the battery or other control measures. However, photovoltaic cells also are essentially constant-current sources that can be short-circuited without damage. Since the supply of current is limited, the energy can be supplied directly to a shunt-field-excited dc machine in conjunction with a gear-speed increaser and an automotive-type centrifugal clutch. The machine is then the electromechanical conversion device that stores energy in the flywheel or, when required, provides dc energy to a solid-state dc-to-precise-ac inverter. After start-up, solar photovoltaic energy is stored in the flywheel over its usable operating range between typically half speed and full speed. Motor speed is the controlled variable by virtue of shunt-field excitation. An overvoltage at the armature has only a minor impact on motor speed.

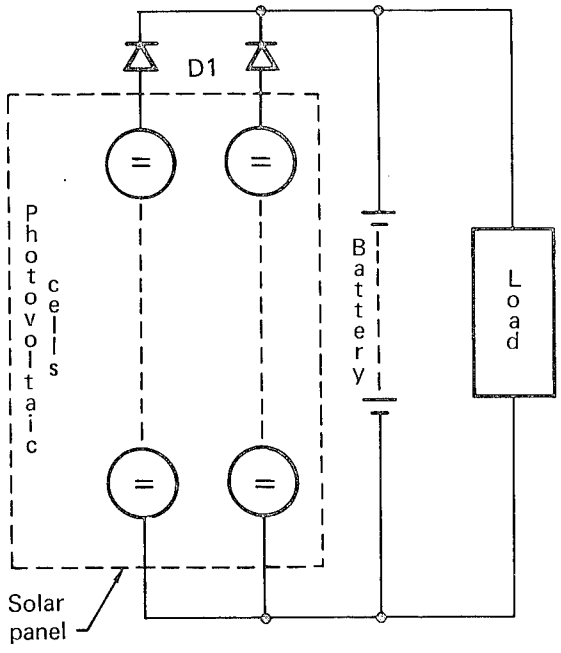

Fig. 2. The typical solar photovoltaic panel. Blocking diode D1 assures unidirectional power flow into the battery. Circuit contains no provisions against overcharge.

It suffices here to note that the solid-state dc-to-precise-ac inverter is typically of the pulse-duration-modulation variety and utilizes a Tschebyscheff filter to supply precise 60-Hz utility power as described elsewhere,[2] and as available from industry.[3]

HYBRID ELECTRICAL PROPULSION DRIVE

An expanded system concept for an ac motorized wheel drive application utilizes a stepless winding reconnection methodology to fully utilize both the alternator and ac wheel motor propulsion characteristics.

At low wheel speeds the alternator is required to provide power for a high-torque profile for the wheel motors typically at a low armature (stator) voltage and a large current amplitude. Because power is furnished through a phase-controlled rectifier bridge, this current contains a large reactive component. For the low-voltage condition, the aircraft-type alternator supplies typically two times its nominal current rating and consequently operates with a typical 75%

efficiency. This is a reduction of 19% from its 92% efficiency when operating at full voltage, nominal current, and a 0.8 lagging power factor.[4] As an alternative, the reconnection of split stator windings from series to parallel or vice versa results in an improvement of the operating efficiency but also in a temporary loss of power during reconnection. This reconnection disables the vehicular propulsion drive for brief periods, a condition that cannot be tolerated.

As a solution to the alternator reconnection problem, a stepless reconnection scheme is proposed that enables switching the alternator windings from series to parallel or vice versa in phase sequence at the instant the current crosses the zero axis. This method maintains high alternator efficiencies without a temporary loss of power to the propulsion drive. This system schematic and reconnection sequence is shown in Fig. 3.

The constant-power speed range of a conventionally wound squirrel-cage induction motor for the wheel drive, which contains one stator winding per motor phase, can be temporarily extended by increasing its flux to a point at which the effective air-gap voltage is 50% of the impressed voltage across the motor stator. The voltage, current, and slip frequency profile for this conventional operating mode is shown in Fig. 4. Thermal fatigue within the motor normally limits the duty cycle for such extended operation. Furthermore, with this motor configuration the current requirement results in poor component utilization of the upstream solid-state power conditioning equipment.

Figure 5 shows the circuit diagram and current/voltage profiles for an improved approach. The constant-power speed range of a conventional induction motor is extended by switching its four primary windings from parallel into series in three discrete steps. As a result, motor current remains constant through the entire constant-horsepower speed range, thus improving the component utilization of the upstream power conditioning equipment. However, this motor technique has the inherent disadvantage that power must be removed from the wheel when reconnecting windings. This transient removal of power cannot be tolerated when keeping the vehicle in motion on difficult terrain. External cabling

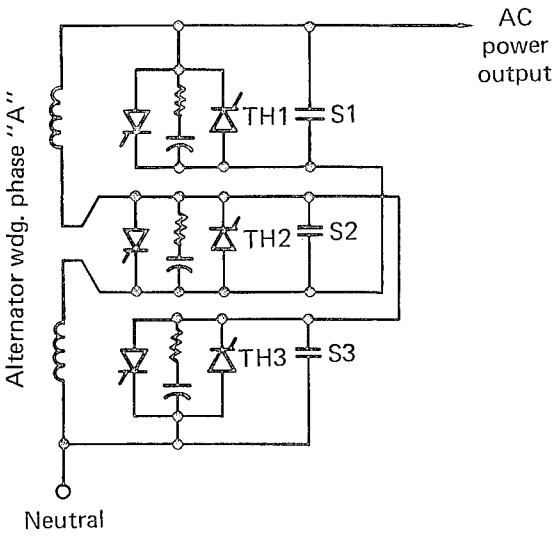

Winding configuration: from series into parallel		
Sequence	Switch No:	Operating condition
1	TH2	On
2	S2	Break
3	TH2	Off
4	TH1, TH3	On
5	S1, S3	Make
6	TH1, TH3	"On"
Winding configuration: from parallel into series		
7	TH1, TH3	On
8	S1, S3	Break
9	TH1, TH3	Off
10	TH2	On
11	S2	Make
12	TH2	"On"

Sequence 3/4 and 9/10: switch at zero voltage or current cross-over

Fig. 3. Alternator with no-break reconnectible windings from series into parallel or vice versa (only one-phase winding shown).

complexity and hardware packaging may offer formidable problems, which in turn can adversely affect the weight and bulk of such a system configuration and thereby impair its reliability and serviceability.

A previously developed technology concept makes it possible to extend the constant-horsepower speed range by integral switching of the windings of four

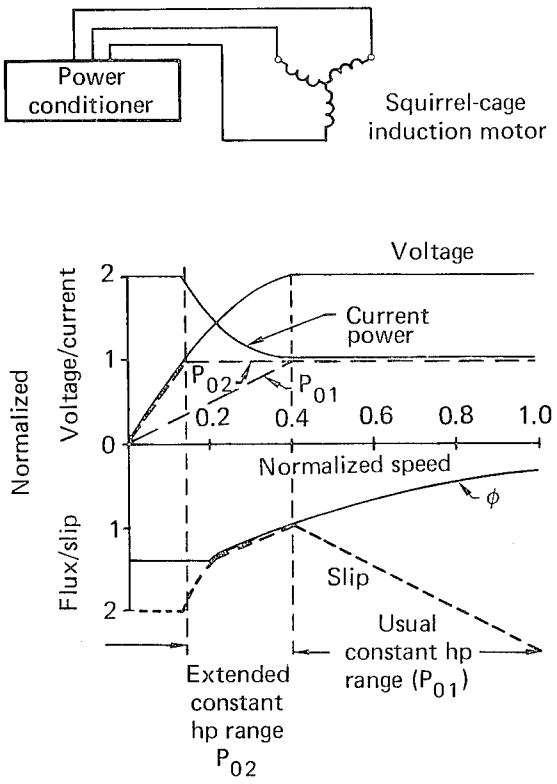

Fig. 4. Constant speed range extension with single ac motor utilizing one winding/phase.

squirrel-cage induction motors with a no-break gear shifter.[5] The rotors of the adjoining motors are mechanically locked to each other through a common gear-speed reducer. The individual motor stator windings, schematically shown in Fig. 6, are reconnected from series into parallel by a two-pole, two-position slide contactor, one segment for each motor phase, suitable for mounting inside a motorized wheel or drive-shaft assembly. Utilizing three switch decks, shown in Fig. 7, the four motors are series-connected during the low-speed operating mode. Increasing wheel speed results in a control signal that initiates reconnection of the motors into two parallel groups, each containing two series-connected motor stator windings. A further vehicle speed increase results in the parallel connection of all four motors (though it should be understood that many applications can be satisfied with the gear shifting of two motors only). This four-motor winding reconnection method has the inherent advantage that the system power flow need not be interrupted when switching the individual stator windings from series into parallel and vice versa. Furthermore, the squirrel-cage induction motor is capable of operating at constant hp over a typically 2.36:1 speed range in the case where it is assumed that the supply voltage remains constant while the slip frequency is the controlled variable. When utilizing four motors with reconnectible windings, it is possible to attain a constant-horsepower profile for an ac wheel over a speed range of 13:1 without penalizing the upstream power-conditioning equipment. Such an ac motor wheel configuration is also capable of providing a short-term 200% peak-power acceleration profile within the motor operating speed range through manipulation of the airgap flux and its slip frequency.[6]

Under the conditions that the ac wheel supply voltage is a function of the motor speed profile, the motor voltage is solely manipulated by the electric motor operating mode and/or the alternator to provide the necessary volt-second/cycle profile for a variable frequency range of 27:1. This corresponds to a vehicle

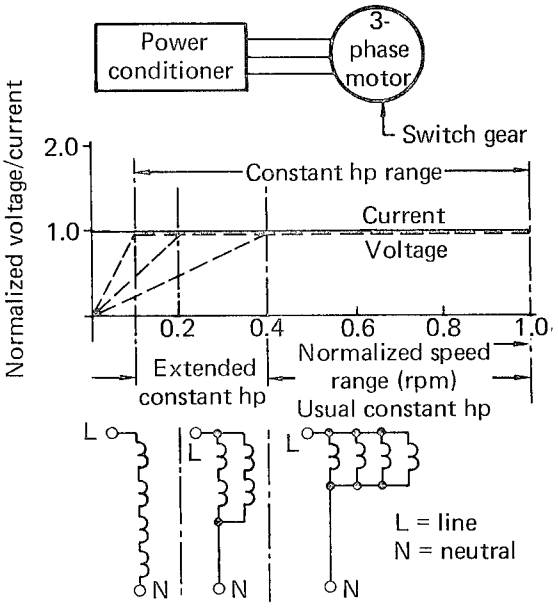

Fig. 5. Constant hp speed range extension with single ac motor utilizing four windings/phase. Each winding reconnection is accompanied with a break of power. Motor contributes to rotating mass inertia of wheel.

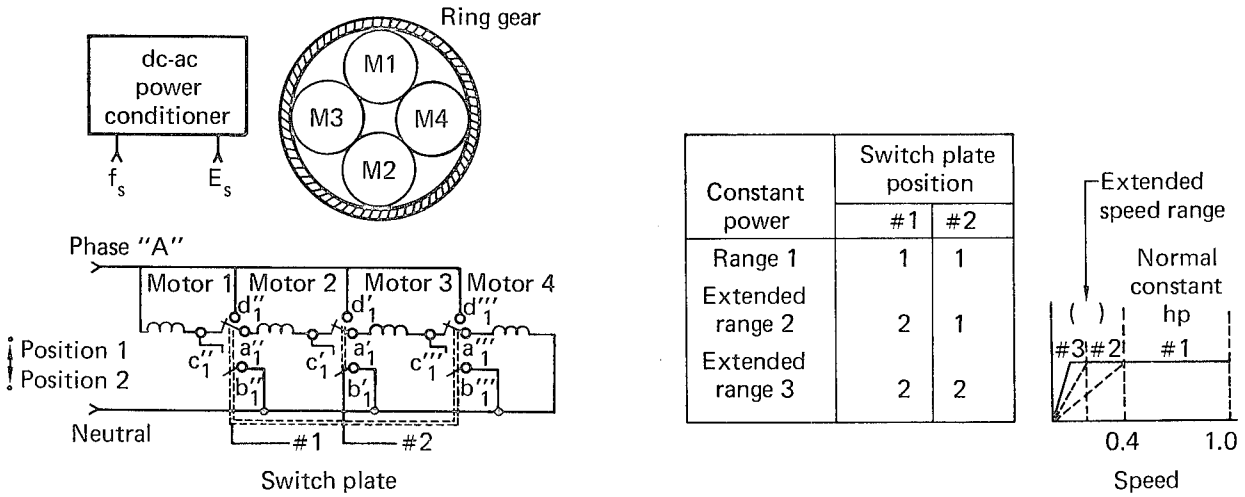

Fig. 6. Constant hp speed range extension through winding reconnection of four ac motors connected to a common ring gear speed reducer. Power flow to the wheel is maintained under all operating conditions by virtue of switching methodology.

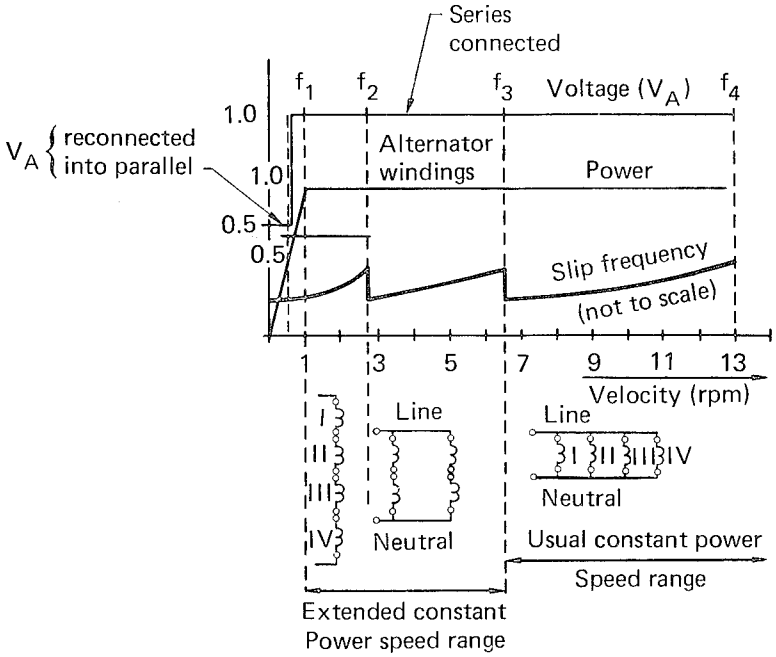

Fig. 7. Schematic presentation of wheel utilizing four ac motors (only one-phase winding shown).

operating capability between 60-mph maximum speed and standstill, if a 4% slip frequency in the wheel motors is assumed at nominally rated shaft torque. Motor operation at either a lower slip frequency or reduced power at standstill requires typically only a 4:1 voltage control, assuming the alternator operates in the low-voltage mode. Thus, the solid-state power conditioner requires only a rudimentary control methodology to process a bidirectional power flow, whereby the reactive power requirement of the motors can be satisfied by the alternator.

During the switching interval, the stator winding of the second as well as the fourth motor is temporarily short-circuited. However, a power source line-to-line short circuit is not possible because the winding of the first motor is connected in series during this transient period. This is shown in Fig. 8.

The short-circuit transient amplitude that circulates through the contactor is equal to the last known current amplitude of the stator winding with a typical discharge time constant of 50 ms for conventional machines. Hence, the contactor life expectancy is not seriously impaired. During the switching operation, the short-circuited motor has only a slight drag since virtually no power is returned from the wheel-driven rotor to the stator because of its temporary zero-slip frequency operation. Only the energy stored in the stator winding is expendable. The solid-state power conditioning equipment operates with substantially improved component utilization since the extended wheel speed range at constant horsepower is obtained under constant motor supply current conditions. The simplified performance profile for an individual machine during the winding reconnection switching interval is shown in Fig. 9.

AC WINDING RECONNECTION METHODOLOGY

The mechanical equivalent for a contactor switch plate and the winding reconnection sequence is shown in Fig. 10 for one phase supply and two motors only. The contacts are initially arranged such that wiper "c" connects with "b" before breaking contact "a" when switching the motors from series into parallel. Contact "a", and thus the motor No. 2 stator winding, is then connected to the phase supply through wiper blade "d". In other words, when switching the motors from the low-speed into the high-speed operating mode,

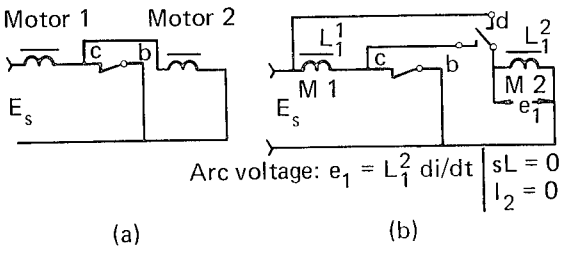

Fig. 8. Contact position during motion: (a) motor No. 2 is temporarily short-circuited, (b) motor No. 2 before reconnection across the line.

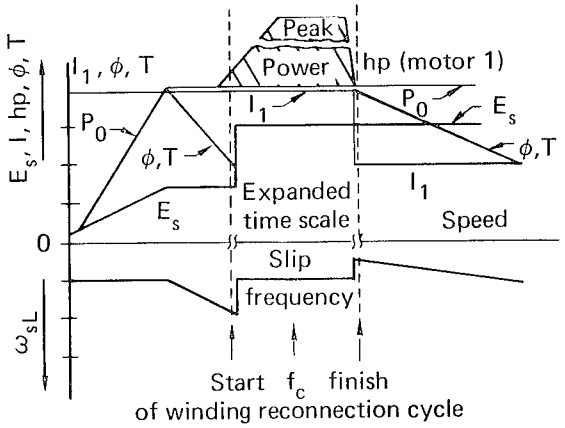

Fig. 9. Simplified winding reconnection sequence for two ac motors (only one-phase winding shown).

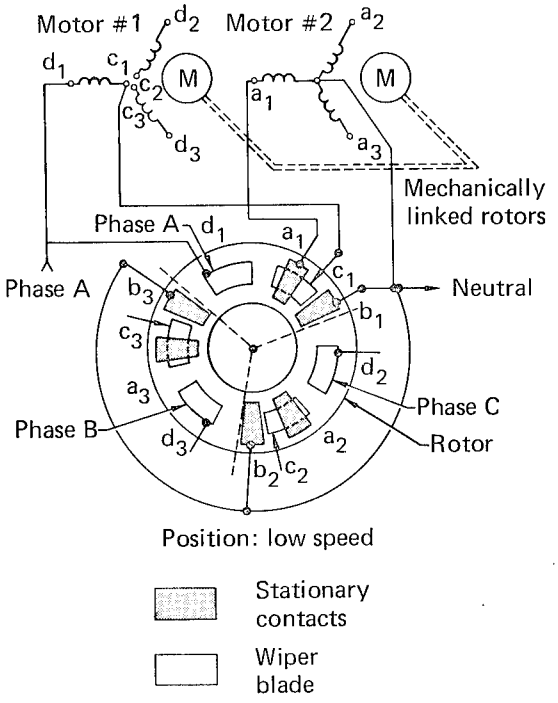

Fig. 10. Simplified motor No. 2 performance profile during the winding reconnection switching interval.

or from a series-winding to a parallel-winding connecting mode, switching action occurs in three distinct sequential steps, although the contactor switch plate is in continuous motion between its points of rest. The contactor plate is set initially into motion and contactor "b-c" closes. Motor No. 1 is now reconnected across the line to the neutral bus in its entirety, whereas motor No. 2 is short-circuited momentarily through contactor "a-c-b". Before the switching action, both motors were virtually operating at an identical flux and current level. However, the closing of contact "a-c" causes the motor to immediately operate at zero-slip frequency with its rotor freewheeling. Hence, the energy stored in the primary leakage inductance is expended through contactor "a-c", whereby the free-wheeling current is typically 180-deg phase-displaced to the current in contactor "b-c" as sustained by motor No. 1.

For a moment motor No. 1 carries the total torque profile until motor No. 2 has been reconnected. The machine does so since it is now supplied with two times volts/cycle (Es/ω_s). The total line current, however, is to remain constant since an increase of the machine's flux level will be accompanied by a momentary 50% decrease in its slip frequency $\pm(\omega_{sL})$,* as set forth by the simplified Eq. (1) for machine torque capability (T):

$$T = (E_s/\omega_s)^2 \cdot (\pm)\ (\omega_{sL}/R_2) \quad , \qquad (1)$$

where R_2 = rotor resistance.

While contactor "b-c" remains in the closed position, contactor "a" is now in the intermediate position and open toward either "c" or "d". The contactor "a" arc voltage amplitude (e_1) is approximated by Eqs. (2a) and (2b) with

$$e_L - L_1\ (di/dt) + N(d\phi/dt)V \quad , \qquad (2a)$$

$$e_L - L_1\ (di/dt) + i(dL/dt)V \quad . \qquad (2b)$$

*The sign of the slip frequency determines whether the wheel is in the motoring mode, or if power is returned to the flywheel through the alternator and appropriate solid-state control means.

The second term can be assumed negligible since the motor is operated essentially at low flux and within the linear portion of the saturation curve. However, energy stored in the primary leakage inductance must be expended somewhere, either through an arc, an arc suppressor, R-C snubber, or other free-wheeling loop.

Finally, the contactor is assumed to have reached its second stable condition, meaning contact "a-d" is closed also. All motors operate now across the line. Previously it was established that the motor rotors were mechanically linked through a common gear and that the contactor switch plate switches rapidly from stable position 1 to stable position 2. At the instant of reconnection, motor No. 2 essentially recovers its flux, with its MMF vectors slightly phase-displaced in regard to the motor No. 1 MMF vector because of the previous history of zero-slip frequency in motor No. 2. The total line current still remains constant. Each motor carries now half the load torque profile at 50% of the original current amplitude. The slip frequency is furthermore reduced and typically 25% of the slip frequency prior to the winding reconnection cycle, as shown previously in Fig. 9.

Before finalizing the physical layout for the winding reconnection mechanism, other switching methods need to be analyzed. Of particular interest would be the reconnection of the windings in phase sequence somewhere midstream from a low flux mode toward a higher flux mode or vice versa within a narrow speed range. The sequential switching of phase windings assures that two phases remain operative at all times in the controlled flux and slip mode. Thus, the danger of winding burnout is minimized. Contact arcing is expected to be virtually eliminated because switching will be initiated whenever the current vector is at zero. Furthermore, because of mutual coupling the stored energy in each winding will be transferable instantaneously to other phase windings. During this very short transient, the motors can sustain typically two-thirds of the original power profile, assuming the neutrals are returned to the power supply. Most likely the rotating mass inertia of the motors will sustain the power profile during this interval.

HYBRID ELECTRIC STATIONARY POWER SYSTEM

The advent of the continuously variable transmission (CVT) enables the design of a solar photovoltaic utility power stationary system, including a residential system, in conjunction with a synchronous machine and the previously described 17-kW°h flywheel rotor. The schematic for such a system is shown in Fig. 11. The flywheel is capable of sustaining a 2-kW°h constant-load profile for 5 h in conjunction with a CVT energy transfer efficiency of 75%. However, flywheel energy density, bearing support, and other ancillary requirements are more easily manageable in stationary flywheel applications, and therefore are potentially attainable at lower cost.[7] During start-up of the flywheel, the CVT is capable of providing a 16:1 gear ratio in conjunction with a two-speed fixed gear ratio transmission. Hence, the flywheel can be operated in the synchronous mode as low as 656 rpm, and as high as 10 500 rpm.

In the normal operating mode, flywheel speed varies between 5250 and 10 500 rpm or 12 000 and 24 000 rpm, respectively, when coupled to an additional gear. The amount of energy either stored or removed from the rotor determines flywheel speed, and as such the momentary CVT gear ratio within its limits 2.917:1 and 5.833:1.

In the motoring mode the synchronous machine transfers intermittently available solar photovoltaic power to the flywheel, as supplied by the external solar panel through the solid-state dc-to-ac power conditioner. Simultaneously, the machine supplies precise ac power to the local power grid.

It is noteworthy that the synchronous machine stores energy electromagnetically as a "rotating condensor," and is capable of filtering out disturbances and waveform distortions originating in the inverter. The machine is usually operated in the magnetically over-excited state to reflect a leading power factor

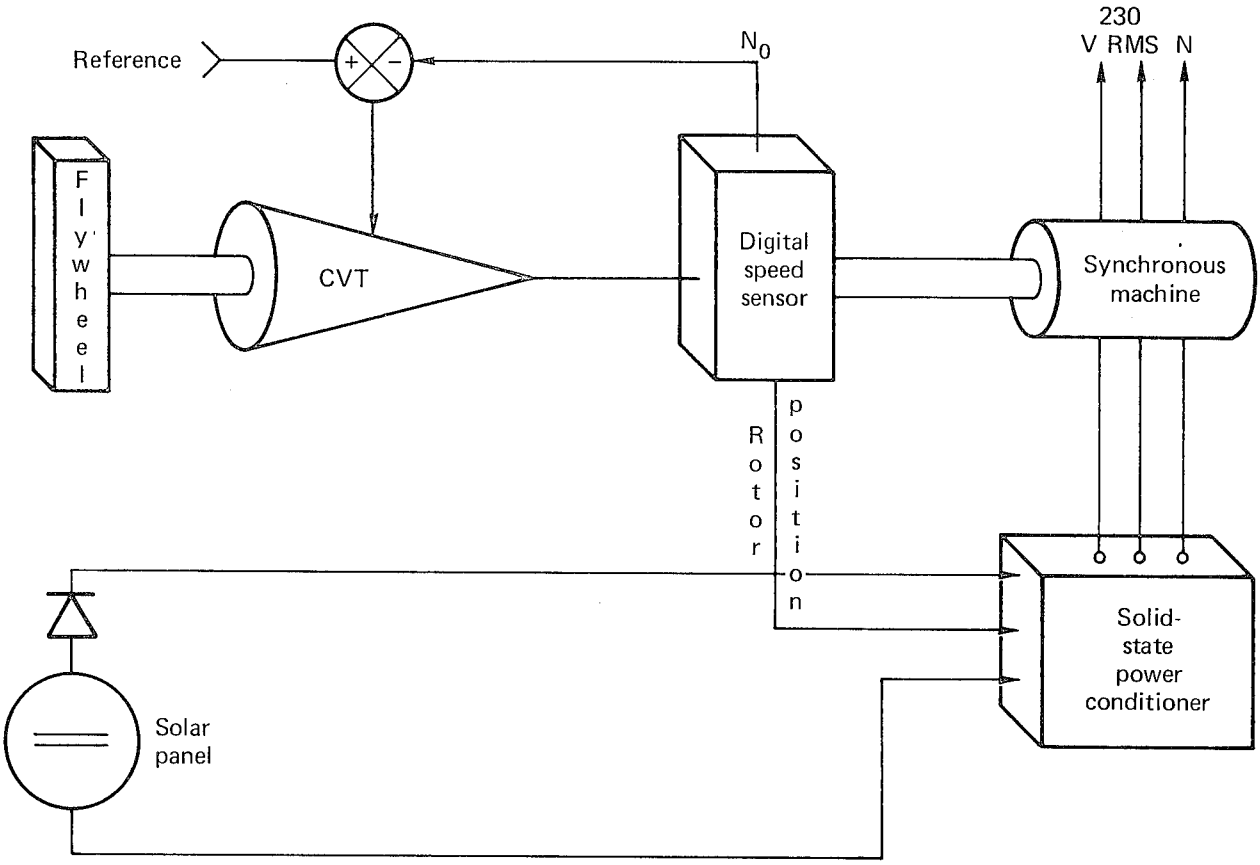

Fig. 11. Schematic for solar photovoltaic residential power system.

toward the solar photovoltaic power conditioner to aid the commutation of its solid-state power switches at appropriate phase angles. However, incorporation of a series-shunt filter resonant-type solid-state inverter, shown schematically in Fig. 12, enables the photovoltaic supply to perform as a functionally independent subsystem.

The commercial synchronous machine contains usually two coil windings per phase. The windings can be separated into two groups and reconnected similarly as shown in Fig. 13(a)-(c). The first group operates in conjunction with a solid-state dc-to-ac inverter to transfer three-phase ac power from the 150-V dc solar photovoltaic panel to the flywheel. The second group provides single-phase, three-phase ac power at 240 V rms to the local utility grid.

Typically, the available slot area for the stator windings of a commercial synchronous machine is utilized only to 35%. Hence, an additional winding can be imbedded at a slight surcharge, and reconnected to provide single, split-phase power at 240 V rms, as shown in Fig.

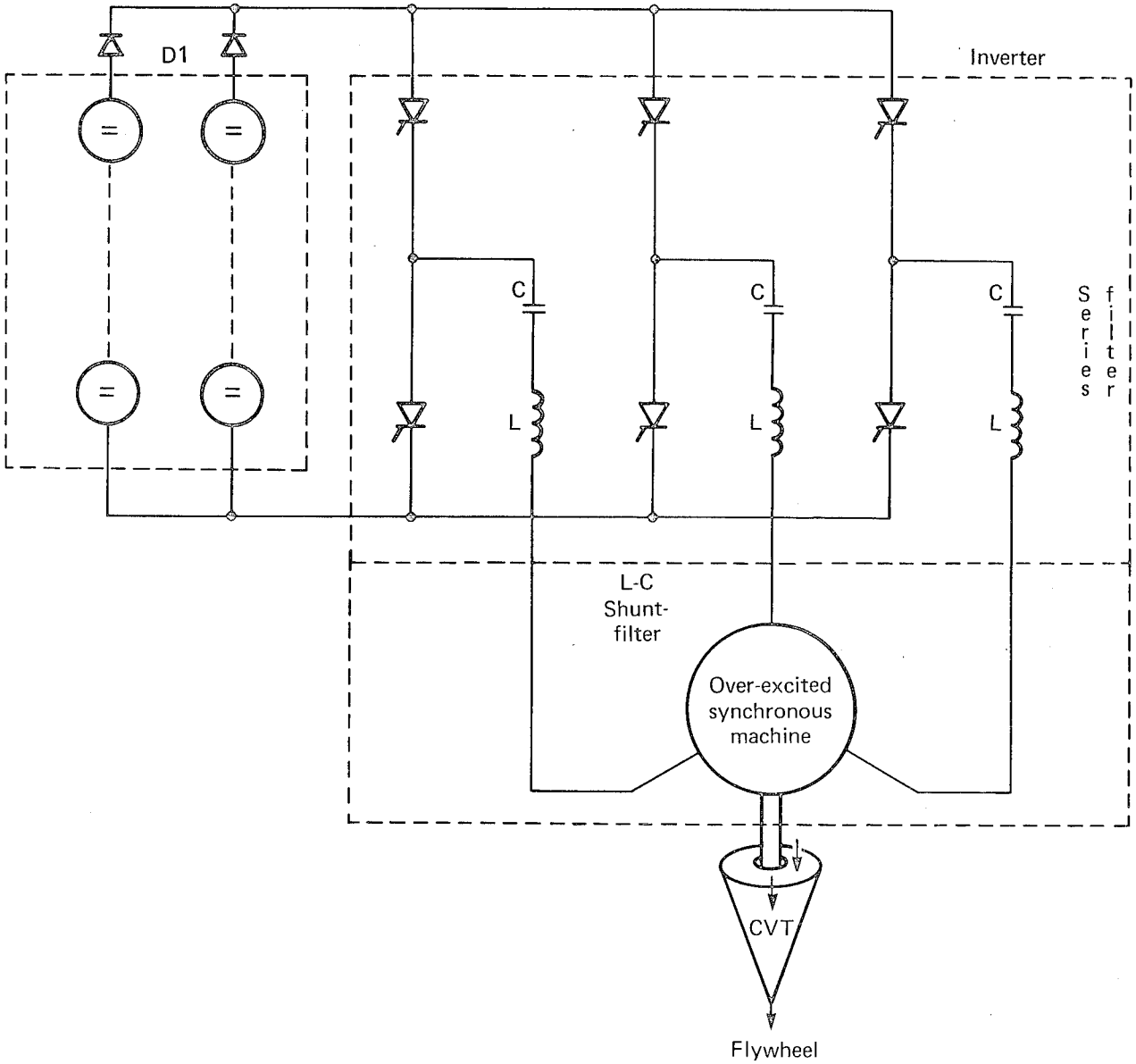

Fig. 12. The series-shunt filter type, naturally commutated inverter is well suited as a building block for a utility-grade solid-state power supply in conjunction with a synchronous machine.

13(c). When operating from a typically 300-V dc solar photovoltaic panel, the winding ratio of the secondary/primary winding is then 0.73:1. Maintenance of this winding ratio makes it possible to operate the machine in the over-excited magnetic-flux mode to support natural commutation of the power conditioner, or "rotating condenser" action.

Synchronous machine speed must be maintained at $N_0 = 1800 \pm 36$ rpm to

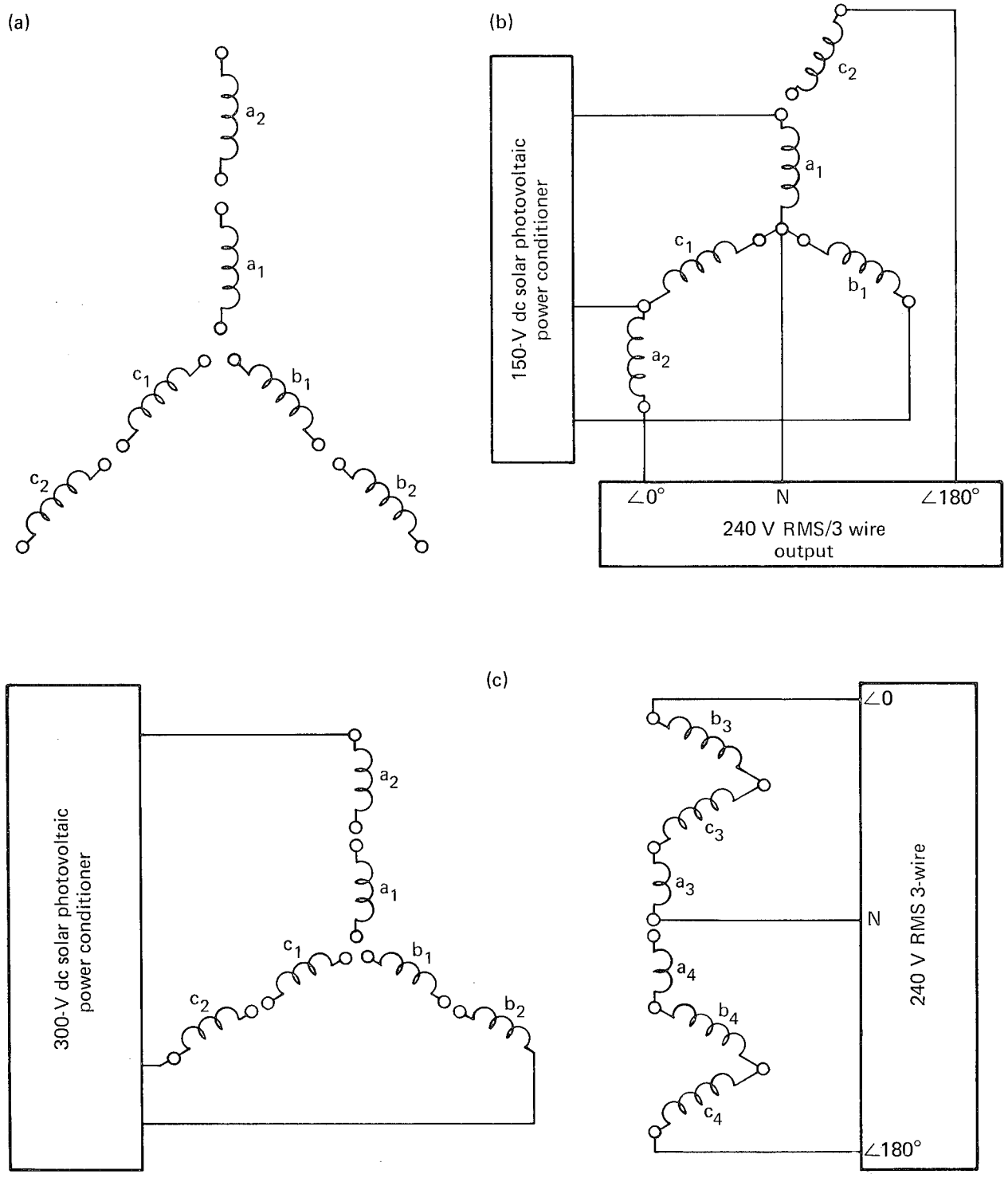

Fig. 13. Winding reconnection methodology: (a) conventional; (b) low-voltage mode using existing windings; and (c) high-voltage mode using auxiliary windings.

sustain utility-grade ac power. Because flywheel speed is a continuously but slowly changing variable, the only critical disturbance reaching the CVT occurs when the rotor position changes from a lagging to a leading torque load angle when changing from the motoring to the generator mode. Although a stiff transmission will maintain a relatively constant machine speed without perturbance during a rapid change in the load-torque profile, a soft transmission, particularly in conjunction with an automotive-type torque converter, is not capable of damping out a change of the machine's load torque angle (δ), or the angular displacement of the rotor as described in Appendix A. Such transmission requires an external power monitor to sense and inject a perturbance into the CVT to maintain constant machine speed during this interval. The control methodology for such CVT is shown in Fig. 14.

CONCLUSIONS

The flywheel represents a safe and economical method to provide short-term peak power for an earthmover or other utility vehicle requiring a large, rudimentary electrical drive system. In the case of the earthmover's probable drive cycle, the recovery and subsequent storage of braking energy does not seem to be warranted. This in turn requires the installation of only a rudimentary solid-state power conditioner to control the frequency and speed of the multimotor drive. Incorporation of a multimotor winding switching methodology appears to be cost-competitive with existing Ward-Leonard dc motor-generator drive systems. It is noteworthy that present dc

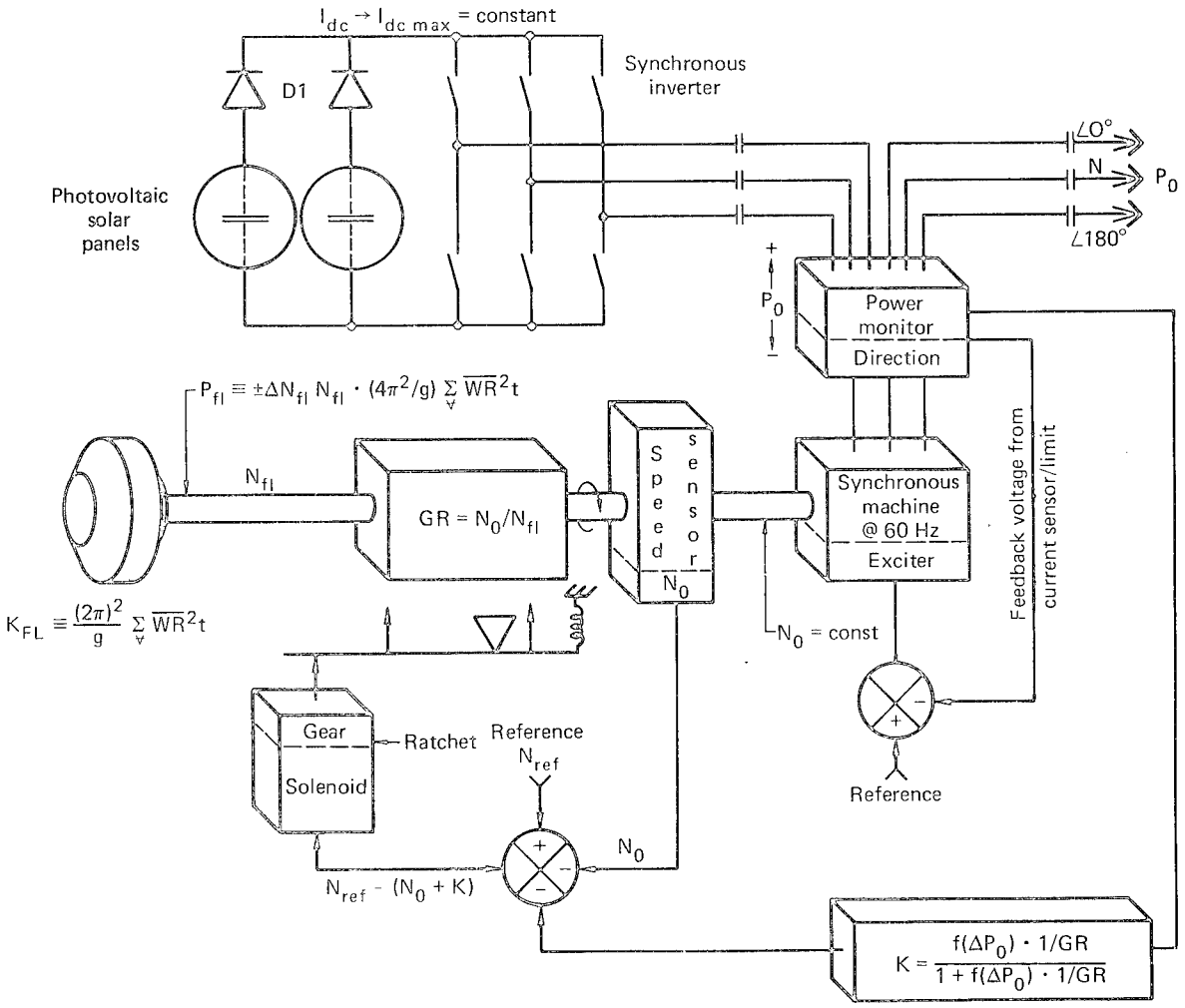

Fig. 14. Control methodology for CVT with soft power transfer characteristic.

drives neither contain an energy storage flywheel nor a recuperative brake capability.

The utility power residential system in conjunction with a constant-speed synchronous machine can use the less efficient, but low cost band-type CVT and still retain its economic viability. The weight penalty incurred in such a system is uncritical for the residential system. Because synchronous machines are widely deployed in industry, their use in conjunction with energy storage devices may find ready acceptance as load levelers and uninterruptible power supplies.

The cost-benefits of this technology must be demonstrated to potential users through practical means. User acceptance of first-generation equipment will be attainable more readily if equipment design is based on simplicity of construction, operational reliability, and maintainability, as well as availability of spare parts. For this reason, first-generation equipment needs to contain only rudimentary solid-state power processing and logic control subsystems. As the market potential for energy storage device applications develops because of further cost reductions, re-engineering of the product and subsequent design of more sophisticated equipment may then be warranted.

APPENDIX A.

NOMENCLATURE

T_D	:	damping torque
T_{SH}	:	shaft torque
T_J	:	inertia torque
T_E	:	electrical torque
W	:	rotor height
R	:	rotor radius
J	:	inertia
δ	:	torque angle
ω_n	:	undamped frequency
ω_d	:	damped angular frequency
ζ	:	damping ratio
P_{SH}	:	shaft power
P_J	:	inertia power
P_E	:	electrical power
P_D	:	damping power
P_S	:	synchronizing power
N_0	:	shaft speed
P	:	number of pole pieces

SYNCHRONOUS MACHINE CRITICAL PARAMETERS

For synchronous operation the shaft power (P_{SH}) is

$$P_{SH} = P_J + P_E$$

$$= P_J(d^2\delta/dt^2) + P_D(d(\delta/dt) + P(\delta),$$

where P_J is the inertia power/unit acceleration.

(A-1)

Assuming torque angle δ is measured in electrical radians, then P_J is

$$P_J = J(2/P)\cdot(2\pi N_0/60 \quad , \ (W)$$

where

$$J = \overline{(WR^2)}/32.7 \ . \ (ft\text{-}lb/s^2) \qquad (A\text{-}2)$$

Inertia power in the synchronous mode is considered constant since actual machine speed is assumed to be within 1% of synchronous speed at all times.

The electromagnetic power (P_E) comprises the two power components P_D and $P(\delta)$, where

P_D = damping power per unit departure from synchronous speed,

$P(\delta)$ = synchronous power corresponding to the torque angle (δ).

The damping power P_D ($d\delta/dt$) is

$$P_D(d\delta/dt) = 2\pi N_0 \cdot T_D \cdot (746/33{,}000) \times (\pi/180)\cdot(2/P) \ (W/el.deg/s) \ .$$

(A-3)

If $P(\delta)$ is the amplitude of the sinusoidal power curve, then $P(\delta) = P_M \sin\delta$, or $P(\delta) = P_S\delta$ if the torque angle is small @ $(+)\pi/6 < \delta < (-)\pi/6$, where P_S is the slope of the power angle curve at the origin.

Generally T_D, P_S $\overline{WR^2}$, p and electrical data are known machine constants.

Equation (A-1) is set to zero to calculate machine parameters, including the load torque angle (δ) Eqs. (A-4) to (A-8)

Undamped frequency:

$$\omega_n = (P\delta/P_J)^{\frac{1}{2}} \quad . \text{ (RAD/s)} \qquad \text{(A-4)}$$

Damping factor:

$$\zeta = P_D/\left[2(P_J-P_S)^{\frac{1}{2}}\right] \quad . \qquad \text{(A-5)}$$

Damped angular frequency is

$$\omega_d = \omega_n\left[1-(\zeta)^{2\ \frac{1}{2}}\right] \text{(RAD/s)}$$

$$fd = \omega_d/2\pi \quad . \quad \text{(Hz)} \qquad \text{(A-6)}$$

Load torque angle (steady state) is

$$\delta_1 = P_{SH}/P(\delta) \quad . \quad \text{(El. deg)} \qquad \text{(A-7)}$$

Maximum excursion of load torque angle for small damping, $\zeta < 1$ is

$$\delta = \delta_1\left[1-1/(1-\zeta^2)^{\frac{1}{2}}\right] \cdot \varepsilon^{-\zeta\omega_n t} \cdot \sin\left[\sqrt{1-\zeta^2})\omega_n t + \phi\right] \quad , \qquad \text{(El. deg)} \qquad \text{(A-8)}$$

where

$$\phi = \tan^{-1}(1-\zeta^2)^{\frac{1}{2}}/\zeta \quad .$$

Actual transient performance of the machine will depend on the stiffness of the continuously variable transmission. A stiff transmission will minimize the machine's load torque angle because the flywheel provides the necessary damping as a kinetic energy buffer. However, a less stiff transmission in conjunction with a hydraulic torque converter cannot dampen out the momentary machine instability and its resultant temporary change of frequency in response to a sudden change of the load torque profile.

REFERENCES

[1] A. R. Millner and T. Dinwoodie, "System Design, Test Results, and Economic Analysis of a Flywheel Energy Storage and Conversion System for Photovoltaic Applications," IEEE 1980 PVSC Conference Record No. C00-4094-70.

[2] E. Reimers, "Design Rationale for an Integrated Power Module Inverter," IEEE 1977 IAS/IPSCC Conference Record.

[3] W. Tuten, Creative Technology Inc., Scottsdale, AZ, private communication (1980).

[4] Aerospace Data 78-601, Westinghouse Electric Company, Aerospace Electric Division, Lima, OH.

[5] E. Reimers, "Hybrid Electric Propulsion Utilizing Reconnectible Motor Windings in Wheels," IEEE 1973 IAC Conference Record, pp. 913-921.

[6] A. E. Fitzgerald and C. Kingsley, Jr., Electric Machinery, 2nd ed. (McGraw-Hill, New York, 1952), pp. 267-271, 548-549.

[7] D. W. Rabenhorst et al., "Low Cost Flywheel Demonstration Program," Applied Physics Laboratory, Johns Hopkins University, Report No. DOE/EC/1-5085, April 1980.

ACKNOWLEDGEMENTS

Work performed under the auspices of the U.S. Department of Energy by the Lawrence Livermore Laboratory under Contract W-7405-Eng-48.

UTILIZATION OF FIELD-MODULATED MACHINES FOR FLYWHEEL APPLICATIONS

David Eisenhaure, William Stanton, Emery St. George, and Tim Bliamptis
The Charles Stark Draper Laboratory, Inc.
555 Technology Square
Cambridge, Massachusetts 02139

ABSTRACT

In most stationary flywheel applications, it is necessary for the flywheel system to interface with utility-supplied electrical power. The conventional approach to this problem is to generate variable frequency and transform this to 60-Hz power through the use of solid-state electronics. Historically, this approach has yielded acceptable performance, although it does not tend to be economically favorable for systems sized at the residential level. Field-modulated systems represent an alternative approach to flywheel power conversion which had been largely ignored despite significant advantages. Such a field-modulated approach requires ac excitation of machine fields rather than dc. This ac field excitation allows the output power to be converted to 60 Hz through the utilization of extremely inexpensive solid-state electronics. Common problems with field-modulated systems, which have prevented their exploitation, are output waveform distortions, high field-power requirements, and a requirement for a fixed load. The Charles Stark Draper Laboratory, Inc. (CSDL) has developed a field-modulated concept that eliminates these problem areas through the use of two separately excited fields oriented in quadrature. CSDL has constructed and laboratory tested a 1-kW heteropolar inductor motor/alternator incorporating these concepts. Test results have been in good agreement with theoretical predictions and have generally supported the feasibility of the concept.

INTRODUCTION

This paper describes the utilization of field-modulated machines for interfacing between a flywheel and a 60-Hz electrical grid. The requirements for high efficiency and low cost are conflicting, especially in light of difficult technical considerations in this application. These difficulties arise from the necessity of maintaining performance characteristics over a wide range of power and flywheel speed. In order to be best suited for flywheel application, the power converter must meet the following requirements.

(1) Provide waveforms with low harmonic content requiring minimal filtering.

(2) Provide controlled output power, voltage and frequency from a variable-speed shaft.

(3) Have a single electromechanical unit for a motor/generator.

(4) Supply power in stand-alone or line-coupled modes.

(5) Provide controlled reactive power-handling ability.

(6) Be cost and weight effective.

(7) Provide electronics compatible with bidirectional power flow.

The various classes of frequency converters capable of meeting these requirements are depicted in Fig. 1.[1] These systems are either mechanical or electromechanical; the electromechanical systems further subdivide into those employing a motor/generator to produce the 60-Hz power, and those employing semiconductors.

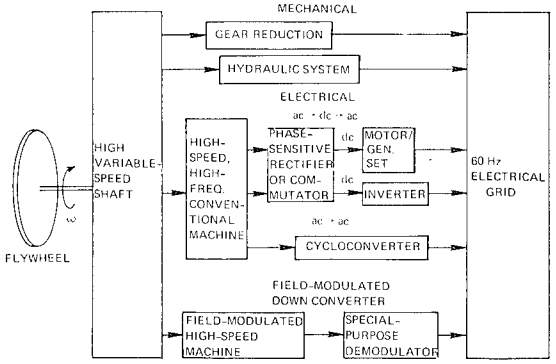

Fig. 1. Conventional energy conversion approaches.

The semiconductor systems may be classed as:

(1) Electronically modulated frequency conversion.

(2) Field-modulated frequency conversion.

The electronically modulated class of converters could have a dc link as in a rectifier and inverter, or might be ac/ac as in a cycloconverter. The field-modulated converter has a generator output that is amplitude-modulated and appropriately demodulated to provide the lower frequency output.

The characteristics of the motor/generator have a significant effect on the choice of alternatives. These characteristics will be discussed briefly before proceeding with the discussion of field-modulated conversion techniques. With the high shaft speeds required for this application, brushes are very undesirable (unreliable; high maintenance). All connections to the rotor should, therefore, be made with either rotary transformers or separate exciters. In fact, for high-speed applications, stress considerations may limit the rotor diameter to a size for which a wound rotor is impractical. Two alternatives to a wound rotor are a permanent-magnet rotor machine and a variable reluctance machine (inductor alternator).

The permanent-magnet machine has two significant problems for this application. First, since the field is constant, continuous losses are incurred in the stator iron even in the coast period. This problem can be reduced by suspending the stator coils and rotating the back iron with the rotor. Second, since the generated voltage is probably two to three times V_{line} at maximum shaft speed, a step up from V_{line} is needed for energy insertion. The permanent-magnet machine will generally have a lower armature reaction than an equivalent wound machine. Low armature reaction requires special care in the power electronics design. The permanent-magnet machine, however, remains an important candidate even with the aforementioned problems.

The variable reluctance machine (inductor alterntor) seems to be a good choice for the input/output job at this time. Since its field is on the stator, the problems of high-speed brushes and wound-rotor stress limits are avoided. Field-modulation control is possible with the inductor alternator.

The primary motivation for choosing a field-modulated converter over other alternatives is economics. A field-modulated converter may be implemented with an extremely simple power stage composed of low-cost semiconductors. The remainder of this paper describes field-modulated control, its economic advantages, and the operation of the CSDL testbed system.

ALTERNATIVES FOR FIELD-MODULATED CONVERSION SYSTEMS

All field-modulated conversion systems have two characteristics in common. First, they utilize either one- or two-phase ac rather than dc field excitation. Second, their purpose is to provide output waveforms containing very low harmonics at a fixed frequency.

The simplest proposed approach to field-modulation is to modulate the field at a frequency such that the difference frequency is the desired frequency. To implement this, the field must be rotating and must rotate such that the difference frequency is the desired output frequency. A two-phase modulation of $\phi \cos \omega_m t$ and $\phi \sin \omega_m t$ can be used to generate the required field. One phase of the output voltage for this system is given by

$$V_o = A\left(1 - \frac{\omega_m}{\omega_g}\right) \sin \left(\omega_g - \omega_m\right)t \qquad (1)$$

$$\omega_L = \omega_g - \omega_m \qquad (2)$$

where

ω_g is generated frequency.

ω_m is modulation frequency.

ω_L is the desired output frequency (line frequency).

The second term in Eq. (1) is the transformer-coupled voltage. The ratio of modulation power to output power for this system is then

$$\frac{P_{mod}}{P_{output}} = -\frac{\omega_m}{\omega_g - \omega_m} \qquad (3)$$

This technique has the advantage of requiring no power conversion electronics, but suffers from high field-power requirements, especially for high-speed flywheels where $\omega_g >> \omega_m$.

Assuming a ratio of ω_g to the desired output frequency of 10, the value for ω_m is nine tenths of ω_g. For this case, the ratio of modulation power to output power is nine. This technique is clearly unacceptable because of the size of the power in the modulating field.

The remaining field-modulated conversion systems require simple output electronics. These systems are more suitable for flywheel applications, however, and operate by generating a suppressed carrier modulation of the form

$$E_o = A \sin \omega_m t \sin \omega_g t$$

where

ω_g is the electrical equivalent of shaft speed.

The load voltage can be recovered by rectifying this waveform with both a positive and a negative rectifying group, and then demodulating at the modulation frequency to provide the load voltage. With rectifiers, the system is not usable for inductive loads unless an intermediate storage capacitor is used. Usually, loads are tuned to be slightly capacitive. Equation (4) is what the ideal output voltage would look like. The actual generated voltage using a single-phase field modulated by $\sin \omega_m t$ is of the form

$$E_o = A\left(\sin \omega_m t \sin \omega_g t + \frac{\omega_m}{\omega_g} \cos \omega_m t \cos \omega_g t\right) \quad (4)$$

The second term is the transformer-coupled voltage due to the ac field. From this, the modulation power (which is the transformer-coupled power, neglecting field and stator efficiencies) is proportional to

$$A^2 \left(\frac{\omega_m^2}{\omega_g^2}\right)$$

Since the output power due to the shaft is proportional to A^2, the ratio of modulation power to output power is given by

$$\frac{P_{mod}}{P_{output}} = \frac{A^2\left(\frac{\omega_m^2}{\omega_g^2}\right)}{A^2 + A^2\left(\frac{\omega_m}{\omega_g}\right)^2}$$

or

$$\frac{P_{mod}}{P_{output}} = \frac{\left(\frac{\omega_m}{\omega_g}\right)}{1 + \left(\frac{\omega_m}{\omega_g}\right)^2}$$

For reasonable ratios of ω_m/ω_g, (such as 0.1), the modulation power as a percentage of total output power is seen to be a very small quantity.

The second approach to suppressed-carrier field-modulation utilizes a two-phase rather than a single-phase field. This technique can eliminate both the zero-crossing distortion and harmonic effects due to finite machine impedance. This method utilizes two-phase field modulation with the amplitude of the second field set at ω_m/ω_g times the amplitude of the first. With this field, the output voltage becomes

$$E_o = A\left[1 - \left(\frac{\omega_m}{\omega_g}\right)^2\right] \sin \omega_m t \sin \omega_g t \quad (6)$$

This equation does not contain the zero-crossing distortion term that was in the single-phase field-modulation approach. The transformer-coupled power (modulation power) for this system as a ratio to output power is, for $\frac{\omega_m}{\omega_g} << 1$

$$\frac{P_{mod}}{P_{output}} = -\left(\frac{\omega_m}{\omega_g}\right)^2 \quad (7)$$

The harmonic distortion has been reduced without increasing the required modulation power. This is achieved by controlling the amplitude of the second phase of the field such that the speed voltage due to that field negates the transformer-coupled voltage due to the first field. This technique appears to have real promise, especially if coupled with a specially configured machine. The CSDL refinements of this concept are defined in the following section.

CSDL TWO-PHASE SUPPRESSED-CARRIER FIELD-MODULATION CONCEPT

The CSDL system was synthesized so as to satisfy the previously stated engineering requirements for the flywheel conversion system. In order to arrive at a system

that uses the machine and silicon controlled rectifier (SCR) switches more efficiently, the following additional requirements were imposed.

The machine should be designed so that its generated voltage will:

(1) Drive current continuously in each of its phases. } Improved efficiency

(2) Cause zero crossings of current to be coincident with SCR switchings. } Lower EMI

(3) Utilize output impedance of the machine to limit current amplitude for parallel operation. } Simplified control schemes

The CSDL design technique combines waveform requirements, switching characteristics, and machine impedance to determine the required back electromotive force (EMF) for an optimal performance defined by the requirements listed. The particular analysis that follows is for two-phase field modulation that controls the amplitude and phase of a single-phase output of lower frequency. In general, more than one phase at the generator frequency would be summed to reduce the harmonic content of the lower frequency output. The CSDL frequency-conversion concept is best summarized by Fig. 2.

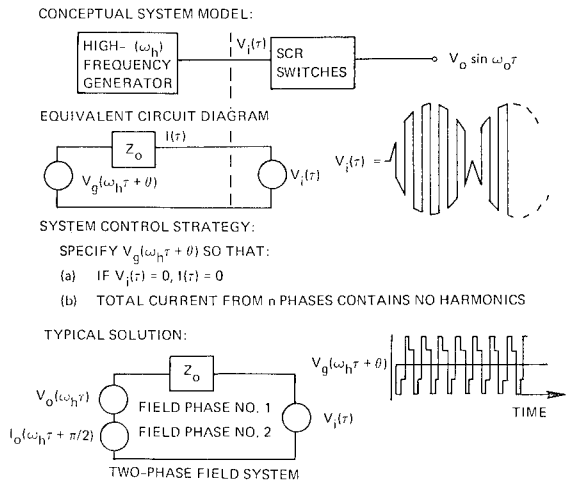

Fig. 2. Conceptual development of special-purpose flywheel conversion system.

Figure 3 shows system implementation and phase definition. For two phases of high-frequency generation converted to a single phase of lower frequency, the system would be diagrammed as in Fig. 4.

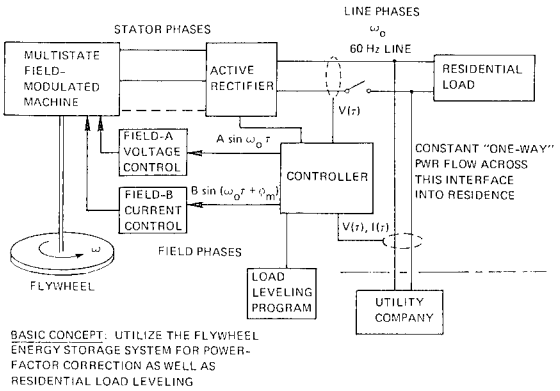

Fig. 3. CSDL frequency conversion concept.

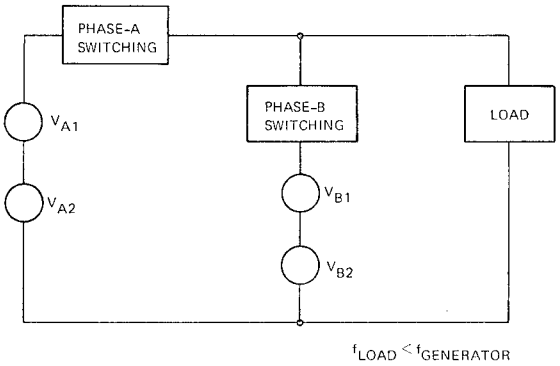

Fig. 4. System for two phases of high-frequency generation converted to a single phase of lower frequency.

With reference to Fig. 4, the 1 subscript in each case refers to the voltage due to one field phase. The two fields are in quadrature, as are the Phase A and Phase B outputs. For a resistive load, the modulation signals for the two field phases are in phase. The output waveforms for different power-factor loads are shown in Fig. 5. To more easily portray the concept, the back EMFs drawn are for the case when $(f_g/f_L = \infty$. This case exists if the output is dc (for which no modulation is required), or is approximately true when $f_g >> f_L$. The ratio of generated frequency to load frequency is 10, which was used to develop Fig. 5. This approximation is consistent with the desired system operation, since only a minor amount of harmonics is generated by the approximation.

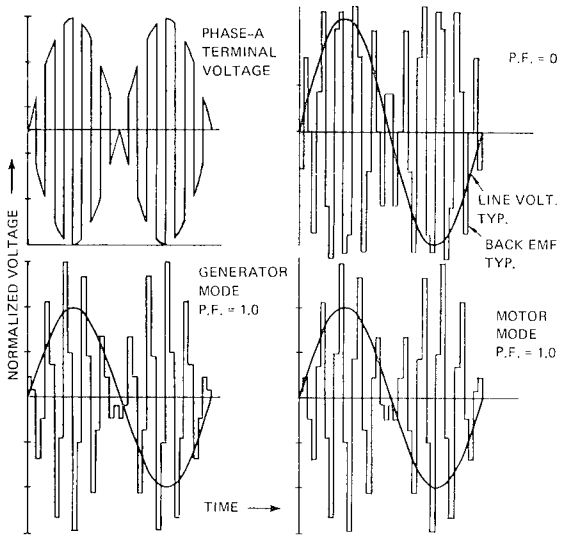

Fig. 5. Two-phase system voltages.

To further clarify the concept, assume that the generator is two-phase and is to feed a dc load through an active switching network. One phase of the generating system might look like the schematic in Fig. 6. Assume that the appropriate SCRs

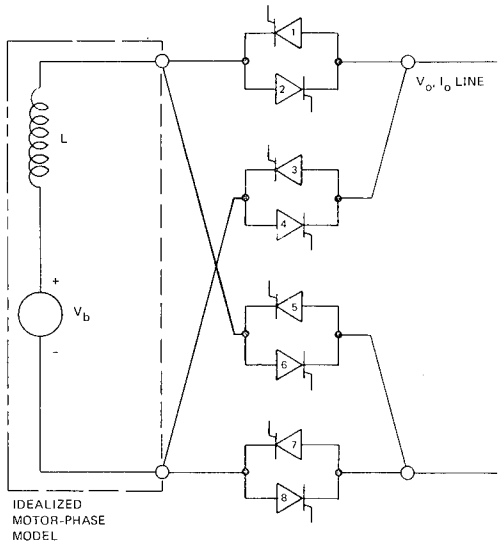

Fig. 6. Motor-phase and switching model.

for current flow are switched at the generator frequency. The voltage on the generator side of the switches will be a square wave of voltage at the generator frequency. If the generated voltage had the form shown in Fig. 7, and was in phase with the switches, the current would be driven to zero at the switching times. In Fig. 7, the voltage square wave is the top drawing. In the next lower drawing, the

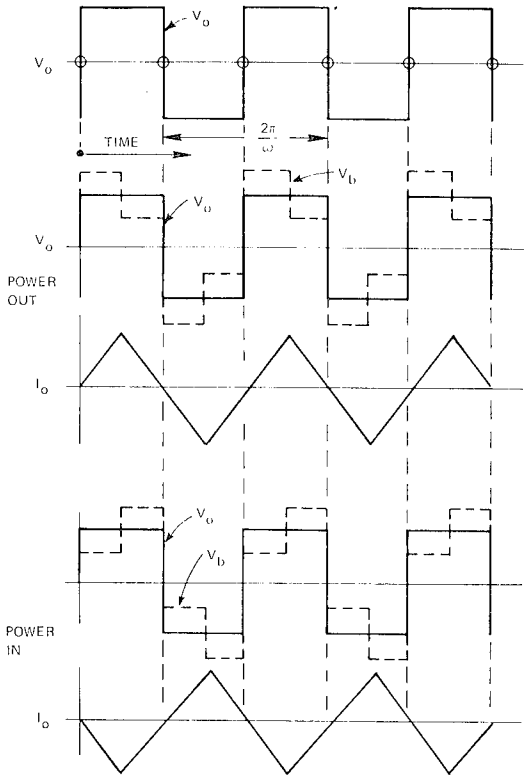

Fig. 7. Idealized voltage waveforms.

generated voltage is superimposed on the square wave with dotted lines. The difference voltage is available to drive the machine inductance, which results in the generator current shown in the third drawing. These drawings correspond to power flow from source to load. The bottom two drawings depict regeneration.

The waveforms shown in Fig. 8 represent the outputs of one phase of a dual-field, dual-phase machine.

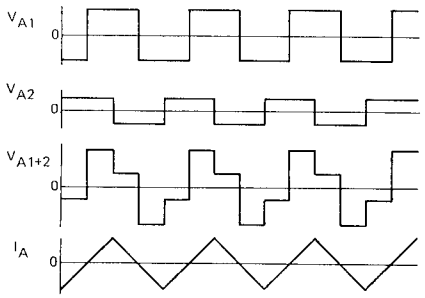

Fig. 8. Waveform-generation method.

The top waveform is generated by Field 1, and the next lower waveform is generated by Field 2. The generated voltage is the sum of these two voltages, as shown in the third drawing. Switching the SCRs appropriately performs the rectification process such that the output current has the form shown in Fig. 9. The top waveform is due to one phase of the assumed two-phase generating system. The next lower waveform is due to the second phase. The sum, then, ideally is a dc level with zero ripple.

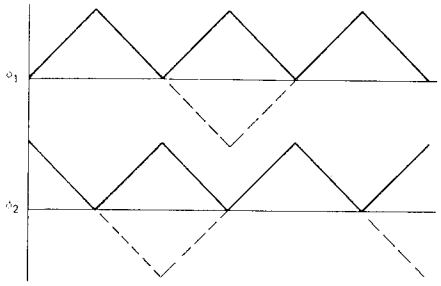

Fig. 9. Two-stator-phase current waveforms.

SYSTEM CONTROL FOR SUPPRESSED-CARRIER FIELD MODULATION

The system controls have to perform voltage regulation, and over-current and over-voltage protection in the stand-alone mode. For the line-coupled mode, it must pick up the additional duties of frequency synchronization, and amplitude and phase control of the load current. The latter two items allow the control of power-extraction level and possible power-factor correction.

This power-conversion system uses a specially designed electrical machine consisting of two independently controlled field windings. There may be two or more generator phases, as previously discussed. The system includes a switching circuit that demodulates the higher frequency signal, established in the armature winding by the machine operation, to a lower frequency line or load. The lower frequency signal may be zero frequency (dc), as well as ac.

The first field-control circuit senses the phase difference between the optimum zero crossings and the actual zero crossings of the higher frequency signal. It drives the first field winding to adjust the phase of the higher frequency signal, and minimize that phase difference. In effect, the phase difference between the output voltage and output current of the machine is being monitored in this way. The internal voltage of the machine, which determines the optimum zero crossings, may be monitored using an encoder that indicates the relative position of the rotor and stator. The actual zero crossings indicative of the output-current zero crossings may be determined by a polarity indicator on sensed current. Any phase difference between the two generates an error signal that is fed to the first field, which drives the machine to correct that error.

The second field-control circuit is used for modulating the higher frequency signal carried by the armature winding with the lower frequency signal, and for monitoring the output of the switching circuit. The control circuit senses the amplitude difference between the selected signal (voltage or current) at the lower frequency, and a reference level, and drives the second field winding to adjust that parameter towards the reference level. If the switching circuit is coupled to a line, current would normally be sensed, and the reference would be a current level. The two are combined in a comparator, and an error signal drives the second field to adjust the amplitude and phase of the output current relative to the output voltage.

For the system under discussion, bi-directional power requires the machine to be a motor-generator, but for other applications the machine might only be a motor or only a generator. When the system is operating in the stand-alone mode, that is, when it is not coupled to an external power source, the comparator in the second field-control circuit monitors the voltage on the output from the switching circuit, and the reference is a voltage level.

The switching circuit in Fig. 10 is controlled by a firing circuit which synchronously actuates the switches in a sequence dependent upon the mode of operation of the machine: motor or generator.

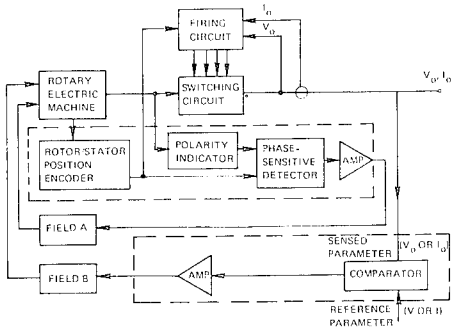

Fig. 10. Converter control system schematic.

and the optimum zero-crossover point of the voltage output from the machine.

The Field-A control circuit includes a polarity indicator which provides a signal each time the higher frequency signal crosses zero, and a rotor/stator position encoder which (by reference to the position of the rotor relative to the stator) provides a signal indicating the optimum zero-crossover time. The outputs of the polarity indicator and the encoder are submitted to a phase-sensitive detector, which provides an error to an amplifier if there is a detected phase difference. The amplifier, in response to an error signal, drives Field A to adjust the phase of the output current relative to the output voltage so that the error is eliminated.

The Field-B control circuit includes a comparator which senses either the voltage or the current on the output line and compares it with a reference to provide an error signal. That error signal is provided to an amplifier that drives Field B such that the error between amplitude and phase of the output current or voltage and the reference is minimized.

The switching circuit is fired in a pattern synchronous with the high-frequency signal from the machine by means of a firing circuit, which includes a one-of-eight decoder having eight outputs labeled 0 through 7, and having three inputs: one from an exclusive OR gate, one from a polarity sensor, and one from the rotor/stator position encoder. The inputs to the exclusive OR gate are from polarity sensors on the machine current and voltage. The firing control circuit is diagrammed in Fig. 11. When the polarities of the output voltage and current are different, the exclusive OR gate at the input to the decoder indicates operation in the motor mode; when they are the same, it indicates generator mode. The eight outputs of the decoder labeled 0-7 are fed through four OR gates, which respectively operate SCR switches 1 and 8; 4 and 5; 2 and 7; and 3 and 6 (see Fig. 6).

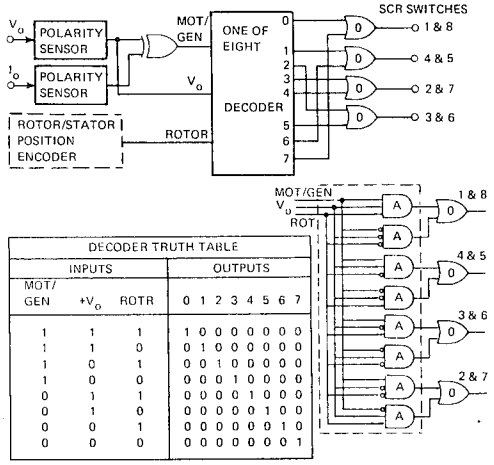

DECODER TRUTH TABLE

INPUTS			OUTPUTS							
MOT/GEN	$+V_o$	ROTR	0	1	2	3	4	5	6	7
1	1	1	1	0	0	0	0	0	0	0
1	1	0	0	1	0	0	0	0	0	0
1	0	1	0	0	1	0	0	0	0	0
1	0	0	0	0	0	1	0	0	0	0
0	1	1	0	0	0	0	1	0	0	0
0	1	0	0	0	0	0	0	1	0	0
0	0	1	0	0	0	0	0	0	1	0
0	0	0	0	0	0	0	0	0	0	1

Fig. 11. Firing control circuitry and truth table.

A truth table for the decoder is shown in the lower left of Fig. 11. A "1" indicates motor operation, and a "0" indicates generator operation in the motor-generator column. In the V_0 column, "1" indicates positive output voltage, and "0" indicates negative output voltage. In the rotor column, "1" means that the rotor position indicates positive machine voltage, and "0" means negative machine voltage. Thus, in the motor mode when V_0 is positive, first SCRs 1 and 8 will be fired when the back EMF is positive, and SCRs 3 and 6 will be fired when the back EMF is negative. In the generator modes, SCRs 2 and 7 will be fired for positive back EMF, and then SCRs 4 and 5 will be fired for negative back EMF. For negative V_0, in the generator mode, SCRs 3 and 6 are fired for positive back EMF and SCRs 1 and 8 for negative back EMF. In the motor mode for negative V_0, SCRs 4 and 5 are fired for positive back EMF, and SCRs 7 and 2 for negative back EMF. In each of the two modes, motor and generator, the sequence repeats itself. The decoder may be implemented by a group of AND gates and inverters as in the lower right part of Fig. 11.

ECONOMICS

The field-modulated approach exhibits superior economic performance due to the simplicity of its power stage, its ability to utilize low-cost semiconductors, and its intrinsically low harmonic content. These factors are summarized in Table 1. While the effects of power-stage simplification and low-cost semiconductors on the system economics are straightforward, the effects of harmonics on system economics are less obvious. Loss of system efficiency due to the harmonic content of the output waveform depends on system load characteristics. As an example, almost 100 percent of the rms harmonic content of the output waveform is wasted in induction motor drives. Harmonic currents in the motor can substantially reduce the motor efficiency from that which could be obtained with low harmonic waveforms. This decrease in efficiency can result in substantially increased costs due to energy loss.

Table 1. Summary of economic factors.

Factor	Suppressed-Carrier Field Modulation	Motor/Generator — dc Link Inverter
Required Filtering	None required — system approach results in a back EMF voltage that is optimally filtered by the natural machine inductance. Result is a low harmonic waveform	Two stages of power — level filtering required adds substantially to capital cost. Filter losses increase life-cycle cost
Required Power Switching	One stage required — approach results in efficient use of SCR capacity (cost of SCRs per kilowatt of output is low)	Two stages required — extra stage results in increased capital cost over FM system. SCR losses add to life-cycle cost
Machine Utilization	Continuous loading of all machine phases results in a minimum volume of copper required for a particular machine efficiency	Depends on the dc line → machine interface. In some configurations, it requires 2 to 3 times as much copper to obtain the same efficiency as the CSDL system
Capability to Power Factor Correct by Reactive Power Control	Yes	Yes

CSDL TEST-BED SYSTEM

As mentioned in the introduction, the electrical machine chosen for demonstration of the suppressed-carrier field-modulation concept was a heteropolar inductor alternator. Machines of this type are characterized by having both their output windings and their excitation-field windings located on the machine stator. This concept is particularly desirable for flywheels due to high rotor stresses and the potential difficulty implementing a wound field on the rotor. A two-phase field was developed for the inductor alternator, and the machine was configured to produce the waveforms depicted in the previous section.

The assembled inductor motor/alternator[3] is depicted in Fig. 12, including the drive motor and related instrumentation. The specially wound stator for this machine, together with the machine rotor, are shown in Fig. 13. It should be noted that the rotor is constructed solely of lamination stacks, and that the machine utilizes two stator elements each excited by one phase of the two-phase field.

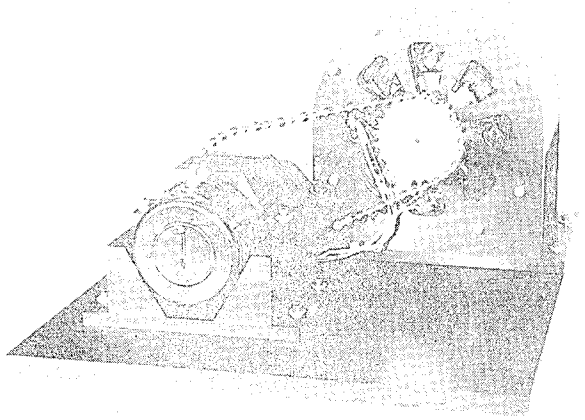

Fig. 12. Assembled inductor motor/alternator.

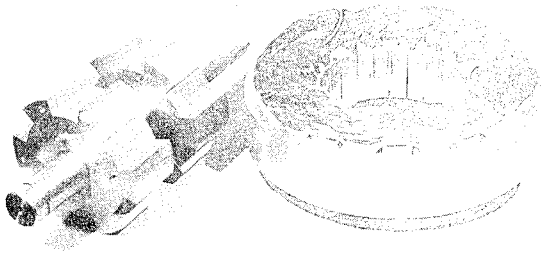

Fig. 13. Wound stator together with rotor.

The machine has been tested in both motor and generator modes and the experimental results agreed very closely with those predicted by the theory outlined in the previous section. Figures 14 and 15 represent the terminal characteristics of the machine when generating 60-Hz electrical power. Figure 14 represents the terminal voltage of one phase of the machine, while Fig. 15 represents one phase of current before rectification. Figures 16 and 17 show the performance of the machine with dc field excitation to show more precisely the relationship between output waveforms. Figure 16 shows the relationship between voltage and current of the machine, while Fig. 17 shows the open-circuit back EMF. It should be noted that the machine will produce either dc or ac power by merely changing the field excitation.

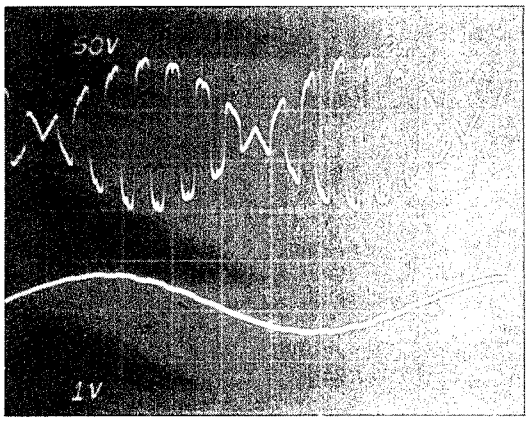

Fig. 14. Terminal voltage of one phase of the machine (above) and field excitation current (below).

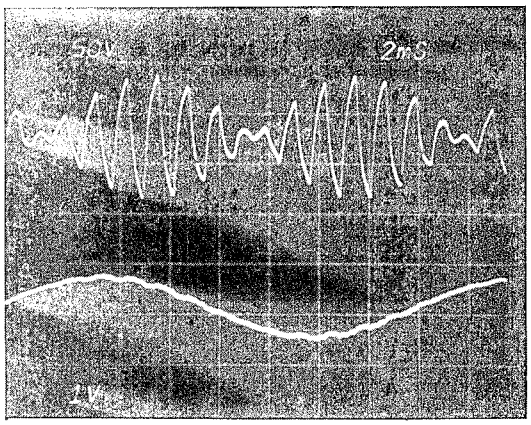

Fig. 15. One phase of current before rectification.

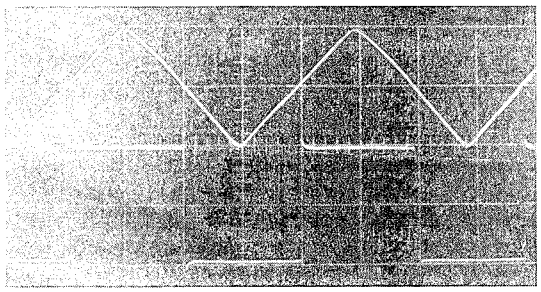

Fig. 16. Relationship between voltage (below) and current (above) in generator mode.

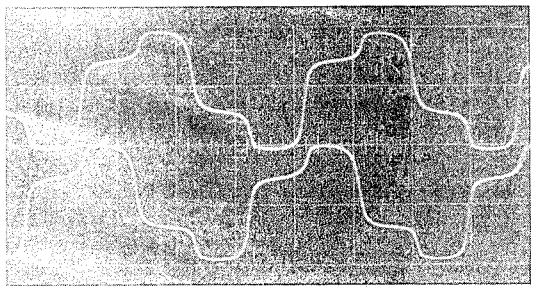

Fig. 17. Open-circuit back EMF of the machine.

CONCLUSIONS

Theoretical predictions indicate that good quality 60-Hz power can be produced from a variable-speed flywheel shaft utilizing field-modulation techniques. These techniques can result in systems that satisfy all system requirements for flywheel applications. Testing of the CSDL baseline system has shown that the actual performance agrees very closely with theoretical predictions.

Field-modulated machines were originally chosen for their potential cost reduction through reduction of system complexity and improvements in efficiency. Experience to date has verified the capability of these systems to provide savings in both these areas. In applications that require flywheels to interface with 60-Hz power, field-modulated machines should be considered a viable alternative to more conventional approaches.

REFERENCES

[1] D.B. Eisenhaure, G.A. Oberbeck, S. O'Dea, and W. Stanton, *Final Report on Research Toward Improved Flywheel Suspension And Energy Conversion Systems*, R-1108, (The Charles Stark Draper Laboratory, Inc., Cambridge, MA, Nov. 1977.)

[2] U.S. Patent 4, 179, 729, *Rotary Electric Machine and Power Conversion System Using Same*, W. Stanton, D.B. Eisenhaure, G.A. Oberbeck, and K. Fertig, April 15, 1977.

[3] D.B. Eisenhaure, E. St. George, W. Stanton, and T. Bliamptis, *Development of a Dual-Field Heteropolar Power Converter*, Report in process, (The Charles Stark Draper Laboratory, Inc., Cambridge, MA, March 31, 1980.)

MOSFET BASED POWER CONVERTERS FOR HIGH-SPEED FLYWHEELS

David Eisenhaure, William Stanton, Richard Hockney, Tim Bliamptis
The Charles Stark Draper Laboratory, Inc.
555 Technology Square
Cambridge, Massachusetts 02139

ABSTRACT

High-speed energy storage flywheels place severe requirements on the design of solid-state power converters, for a flywheel coupled power converter must combine high efficiency over a wide range of power and flywheel speed with relatively low production costs. Recent developments in high power MOSFET transistors have significantly increased the technical and economical viability of solid-state power converters for flywheel applications. This paper reviews and compares the control requirements for both induction and permanent magnet machines. The characteristics of The Charles Stark Draper Laboratory's baseline drive systems in both these areas are given. The general requirements for a Pulse Width Modulated (PWM) inverter are outlined together with the application advantages of MOSFET devices. The general efficiency characteristics of semiconductor alternatives in motor drive applications are developed in the context of improved economic performance.

INTRODUCTION

The rapid depletion of mineral resources coupled with an increasing public reluctance to accept the nuclear alternative has sparked unprecedented interest in various "soft" energy systems. The interface requirements for such systems often include some form of intermediate energy storage, which is necessary in order to decouple the energy source from the demand characteristics of the load. Flywheel energy storage is a potential solution to this need. It is characterized by high reliability, long life, and low cost, and has the potential, with proper development, of storing energy efficiently at relatively high energy densities.

Flywheels in stationary applications have special design problems associated with the electrical conversion system because of the power and energy requirements of these applications. These subsystems require state-of-the-art advancement to make flywheel energy storage cost effective. The Draper Laboratory believes that the most difficult problem associated with the use of flywheels in such applications will be the development of low-cost conversion systems at suitable power densities.

The Draper Laboratory has been developing a variety of brushless machine systems suitable for flywheel applications that appear to have the potential for both low cost and high broad-band efficiency. The rotating machines considered for these systems include wound-rotor, induction, inductor, permanent-magnet, and special purpose machines. The converters considered for use with these machines include dc link inverters, phase controlled rectifiers, cycloconverters, and special-purpose switching systems. This paper concentrates on the utilization of newly developed field-effect power transistors (MOSFET) in a PWM inverter. With proper control, this inverter can be utilized with either induction or permanent-magnet flywheel drives.

The primary advantages of MOSFET transistors in flywheel applications are their extremely short switching times and minimal drive requirements. High device speeds are particularly advantageous when permanent magnet motors are utilized, for the combination of high drive frequency requirements for flywheel applications and low characteristic inductance of permanent magnet machines lead to extremely high modulation frequency requirements. High switching speeds reduce or eliminate

filtering requirements while maintaining 60-Hz grid interface capability. The low drive requirements of these devices lead to substantial circuit simplification and contribute to high operating efficiencies. These devices have a number of additional advantages including ease of paralleling, extended Safe Operating Area (SOA), and an integral reverse rectifier.

The Draper Laboratory is involved in the development of a microprocessor-controlled 15 kW, three-phase inverter utilizing this technology. This development involves the design, construction, and test of a prototype inverter. Trade-offs between switching losses and motor losses are computed, and optimized. The completed system is designed to maintain high efficiency throughout its power and speed range. The successful application of this technology to a PWM inverter suited for flywheel drive has potential for high efficiency and performance coupled with low costs.

Thus, two major motivations for utilization of induction motor drive systems are the extreme reliability and unmatched price/performance characteristics. In addition, squirrel cage induction motors can be operated at high speeds because of their inherent ruggedness and lack of brushes. For constant horsepower, operation at higher machine speed reduces size and weight, and to a point, the cost of a machine.

An induction motor operated in a controlled slip mode (variable frequency, variable voltage) is capable of supplying very high torque at stall without having to sacrifice low slip characteristics at normal operation. Since the machine is operated at low slip over the entire speed range, a major improvement in efficiency is realized.

Power generation is also easily obtained by operating in the negative slip region. The CSDL baseline system is shown in Fig. 1. Slip control of an induction motor is achieved by measuring the shaft speed and controlling the excitation frequency so that the difference between the shaft speed and the rotating magnetic field in the armature is controlled. It is known that an induction machine controlled in this manner has improved torque and efficiency characteristics over the full speed range.

Most previous implementations use a constant slip frequency control. While this type of control strategy represents a significant improvement over "open loop" control, it does not effectively utilize the capabilities of the induction motor. CSDL has currently employed a variable slip control which maximizes efficiency for any torque-speed point within the machine capability. This approach can be implemented reliably and at low cost by utilizing modern microprocessor technology.

The CSDL optimum efficiency slip control scheme consists of a variable slip frequency controller that sets the motor excitation such that the efficiency of the system is at a maximum subject to imposed constraints. For purposes of clarity, inverter coupling effects are not considered in this portion of the analysis. The impact of non-ideal inverter characteristics will be analyzed in a subsequent section. A more complete analysis would include power stage inefficiencies. It should be noted, however, that in maximizing the motor efficiency, the current required is usually a minimum. Since the losses in the controller are approximately proportional to the current, the implication is that controller efficiency increases.

The induction motor drive is subject to three constraints: voltage, current, and flux. It should be noted that the voltage and current constraints are chosen to optimize controller design, and not necessarily because of motor design limitations. Determination of these constraints is part of the system design problem.

For any induction motor (or class of motor) a unique control law can be derived which maximizes the efficiency of that motor at any operating point (torque and speed) subject to these constraints. Fig. 2 is representative of an induction motor operated under CSDL's maximum efficiency control law. The maximum torque in the low-speed range, 0 to 0.45, is limited by available system current. In the mid-speed range, 0.45 to 0.75, maximum torque is limited by both available system current and voltage. For high-speed operation, maximum torque is limited because available voltage can provide diminishing current and torque for increasing speed. The dotted line in the mid-speed range indicates achievable torque within the system current constraint if a larger voltage capability existed.

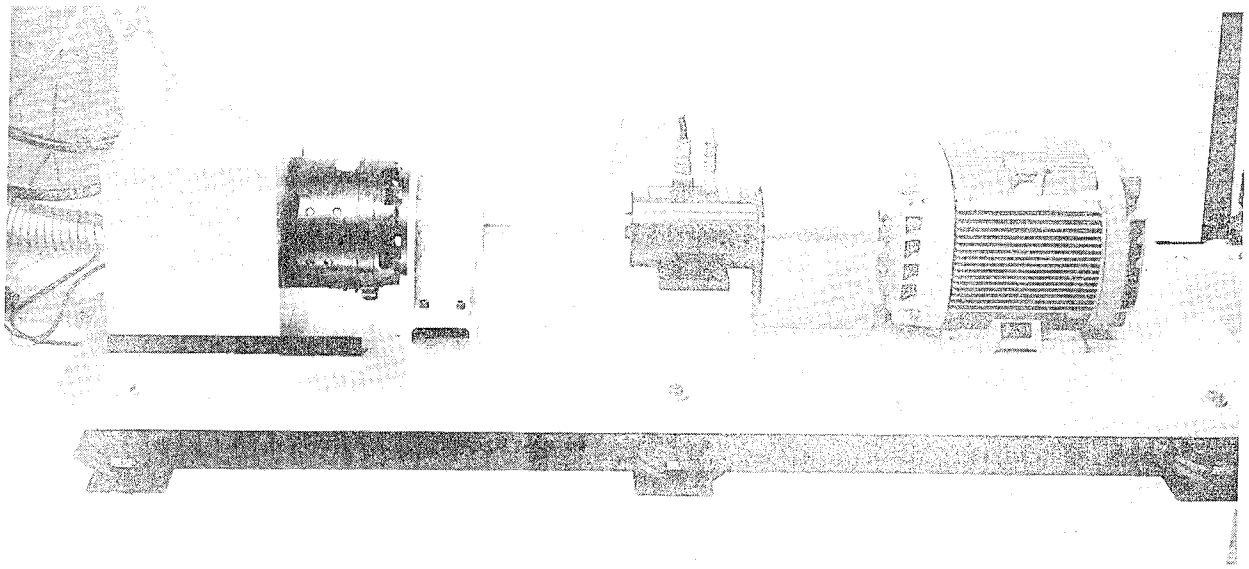

Fig. 1. CSDL baseline induction motor drive.

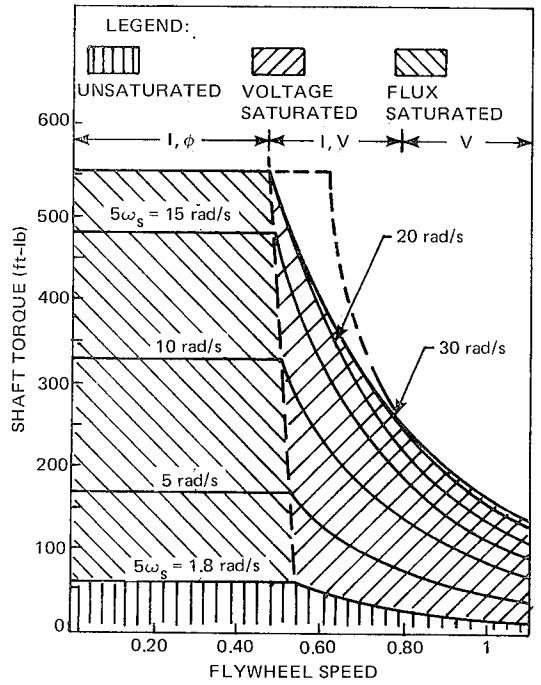

Fig. 2. Optimum slip control strategies for induction motors.

Within the locus of maximum torque capability, there are three distinct modes of operation. At low torques, indicated by vertical lines, the motor can be run at the uncontrained maximum-efficiency slip-frequency without exceeding any of the imposed constraints. At larger values of torque, maximum efficiency implies flux saturation at low speeds, indicated by lines sloping upward to the left, and voltage saturation at higher speeds, indicated by lines sloping upward to the right. A given level of torque in the flux saturated region is provided at constant values of current and slip.

Increasing torque is accomplished by increasing current and slip—slip must increase as current increases to avoid violating the flux constraint. Torque at any speed in the voltage limited region is obtained by applying the maximum available voltage at optimum slip frequencies. The solid lines in this graph indicate available torque at constant slip-frequencies which do not violate the flux constraint at low speeds or the voltage constraint at higher speeds.

OPTIMUM TORQUE ANGLE PERMANENT MAGNET FLYWHEEL DRIVE

This section provides a brief summary of brushless dc motor commutation techniques for polyphase machines. The linear first-order effects of the machine will be presented based upon the equivalent electrical circuit model.

To provide a basis for discussing brushless commutation techniques as well as the so-called optimum torque angle drive, the equivalent circuit in Fig. 3

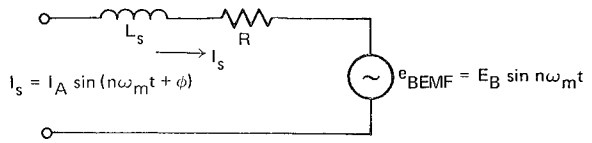

Fig. 3. Equivalent electrical schematic of one phase of a polyphase dc motor.

is used. This simplified model assumes a sinusoidally wound machine which consists of winding inductance and resistance in series with a back EMF (BEMF) which is a function of rotor position and rate. If this polyphase machine is current excited with sinusoid of frequency equal to that of BEMF and arbitrary phase, ϕ, the electrical power converted to mechanical power is

$$P_m = I_A E_B \cos \phi$$

Maximum conversion efficiency is obtained when $\phi = 0$ because motor losses ($I_A^2 R$) for a given current amplitude are independent of phase. Since stator flux is in phase with stator current, I_A, and rotor flux leads BEMF by 90°, it is then easy to deduce that $\phi = 0$ corresponds to the optimum torque angle, 90°.

A generalized block diagram of an optimum-torque-angle PM motor controller which operates on the principal of maintaining $\phi = 0$ is shown in Fig. 4. The shaft encoder provides a position signal for current control, and can be either continuous or incremental. A resolver is an example of a continuous position indicator. Fig. 5 is a diagram of a PM machine controller which could use any of several incremental position transducers.

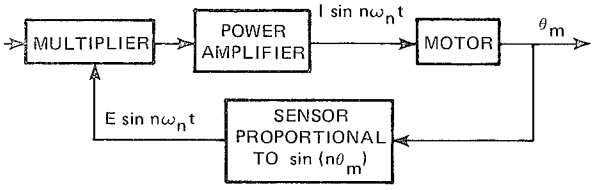

Fig. 4. Commutation with continuous angle encoding.

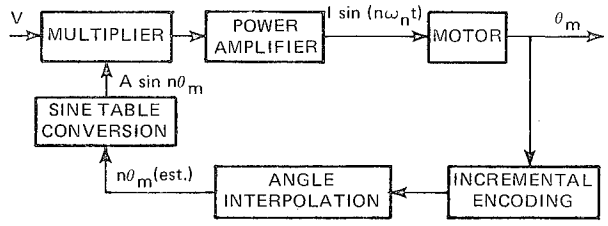

Fig. 5. Commutation with incremental encoding.

For any of the commutation methods, several electronics methods exist for signal handling, such as pulse position or amplitude multiplication instead of linear multiplication. It is not the intent of this summary, however, to provide a coverage of those techniques, but rather to provide an overview of brushless commutation techniques for dc motors. Basic angular sensing methods were discussed along with the concept of optimum torque angle drive. A final point is that, when the R/L break frequency of the motor is sufficiently above the maximum expected stator excitation frequency ($n\omega_m$), a voltage source can replace the stator current source since the stator impedance will introduce negligible phase shift between current and voltage.

CSDL has developed a 5-hp PM machine to allow laboratory test and evaluation of control concepts. This motor is shown in Fig. 6 and is being tested in conjunction with the PWM-FET inverter. For a given nominal efficiency level, PM machines exhibit higher harmonic losses than induction motors in PWM operation because of their lower stator inductance.

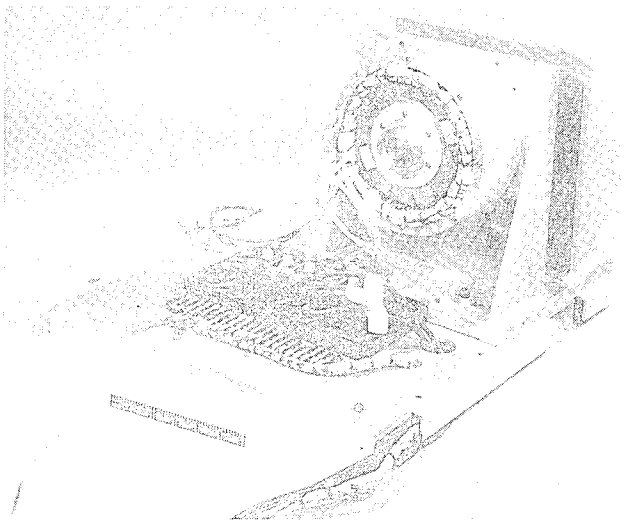

Fig. 6. 5-hp PM machine.

MOTOR CONTROLLER—INDUCTION

The induction motor controller shown in Fig. 7 could easily be reconfigured for PM operation by replacing rate control with position control. This controller consists of a power stage and a slip controller. It is essentially a variable-frequency, variable-amplitude current source. Current amplitude is

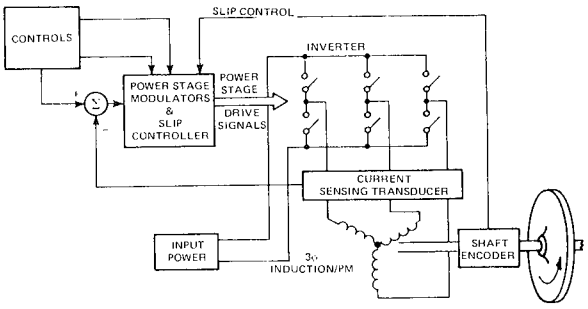

Fig. 7. Power stage and slip controller.

controlled via the driver circuitry, which includes pulse width modulators as shown in Figure 8. The filtered motor current is compared to the commanded current, and the error is forced to null in a servo loop. Since flux saturation of an induction motor is a function of stator current and slip frequency, the controller computes the actual slip frequency and determines a current limit for the current servo, thereby avoiding motor saturation. The power stage of the CSDL MOS-FET inverter is shown in Figure 9.

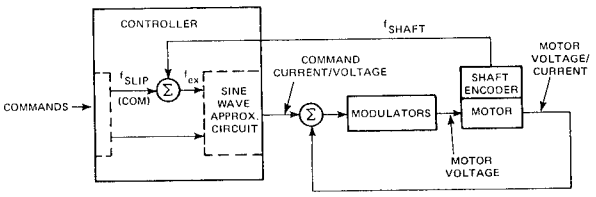

Fig. 8. Pulse width modulators.

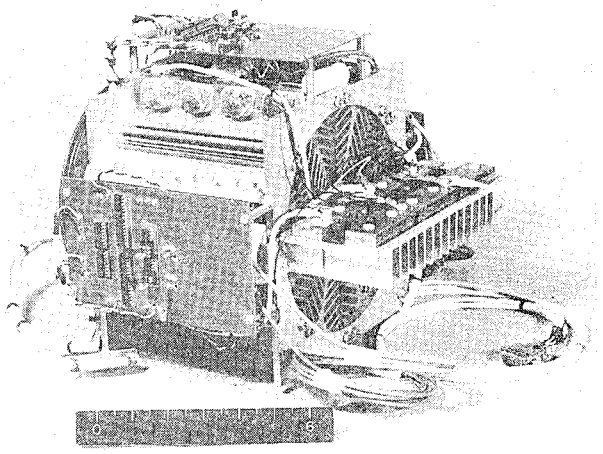

Fig. 9. Baseline HEXFET inverter under construction.

The slip control circuitry uses an incremental shaft speed sensor and commands a motor excitation frequency that is higher than the shaft speed for torque production and lower than shaft speed for regeneration. Generation is commanded by changing the sign of commanded slip. The emphasis to date has involved the determination and demonstration of a practical slip control implementation using the operating regimes described in Fig. 2.

CHARACTERISTICS OF MOS-FET DEVICES IN PWM INVERTER APPLICATIONS

Field-effect transistors have only recently become available as power devices, and are currently being produced with individual device ratings of 4.4 kW. At these power levels, FETs have become a serious competitor to bipolar transistors in medium power applications and, more specifically for flywheel applications, in pulse-width modulated inverters. These devices have a number of advantages compared to bipolar transistors, such as minimum drive requirements, low switching losses from extremely fast transition, and ease of paralleling. Their primary technical disadvantage has been a relatively high on-resistance. This has been reduced through innovative geometries in newer devices. At present, cost of equivalently rated MOSFETs exceed those of bipolar transistors by a factor of 2-10. The large price differential is understood to be a temporary effect, caused by stiff demand, short supply, and the vendor's desire to recoup R&D costs.

SWITCHING AND HARMONIC LOSS MECHANISMS IN PWM INVERTER SYSTEMS

The primary loss mechanisms that can be traded off in PWM inverter design are switching losses in the power semiconductor and motor losses due to harmonics. Since the motor harmonic current is generated as a direct result of the switching algorithm selected, these loss mechanisms are directly coupled to one another. The combination of these loss mechanisms can be minimized by selecting an optimum carrier frequency. This optimum carrier frequency is a function of both motor speed and load. In order to show how the optimization of these loss mechanisms is interdependent on both motor and semiconductor characteristics, a full load and full speed situation will be analyzed.

The relative switching efficiencies of the three most popular types of power semiconductors including FETs, bipolar junction transistors (BJT), and silicon controlled rectifiers (SCR) are indicated in Fig. 10. The FETs clearly give superior performance throughout, and will efficiently operate in regions which are not possible for SCRs and even BJTs. The value of this advantage is obviously dependent on the switching frequency. For a maximally efficient pulse-width-modulated system, the carrier frequency should be set at the point where the sum of the load losses and switching losses is at minimum. (Device losses are approximately constant with respect to frequency for a given load.)

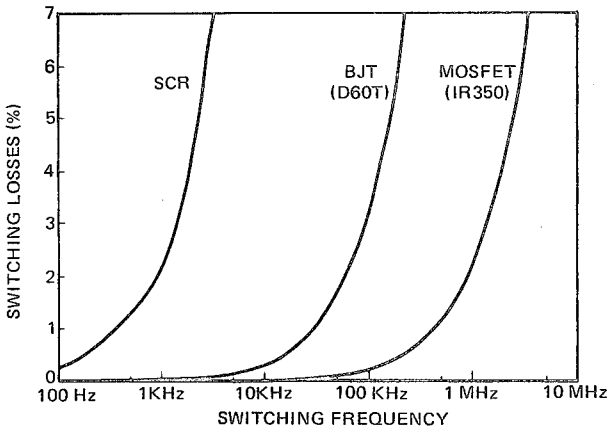

Fig. 10. Relative switching efficiencies of three areas of power semiconductors.

Fig. 11 gives normalized motor harmonic losses as a function of normalized carrier frequency for full voltage PWM operation. These losses are plotted for various values of N_m, a dimensionless grouping of motor operating parameters that determine the motor susceptability to PWM-induced harmonic losses. This parameter is a function of both machine type as well as design specifics.

Induction motors, because of relatively higher machine inductance, tend to have a lower N_m than an equivalently rated PM motor at the same excitation frequency. Similarly, an induction motor designed for higher starting torques will have a higher N_m than one designed for high efficiency. These curves span the range of practical motors for flywheel drive applications.

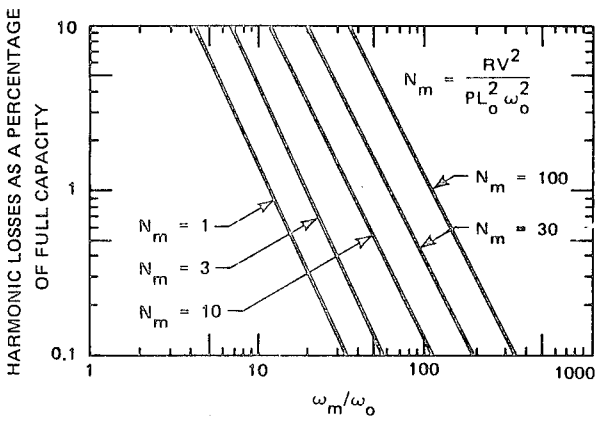

Fig. 11. Harmonic losses in machines as related to their electrical characteristics.

PWM losses are minimized by selecting a carrier frequency which is a tradeoff between the decreasing harmonic losses and increasing switching losses with increased carrier frequency. The combined effect of harmonic and switching losses is plotted in Fig. 12 for differing values of a normalization quantity, N_m. These curves demonstrate that FET devices are advantageous for all applications. They do, however, have particular advantages for N_m and, therefore, PM motors. Fig. 13 repeats Fig. 12 for SCRs and clearly demonstrates that SCRs are not competitive for the 400-Hz excitation frequency chosen.

The 15 kW HEXFET inverter is being tested as a drive for both a 2-pole, 10 hp, 60-Hz induction motor and a 12-pole, 5 hp, 500-Hz PM brushless dc motor. Each of the six switches is formed by paralleling four HEXFETS rated at 400 V, 11 A; the highest ratings presently available. Because HEXFETS have inherent current sharing properties, ballast resistors, a source of inefficiency in bipolar inverters, are unnecessary.

RELIABILITY

Transistorized inverters require fewer parts due to less extensive snubbing circuitry, the absence of inductive commutation components, and reduced sensitivity to dv/dt induced turn-on. These

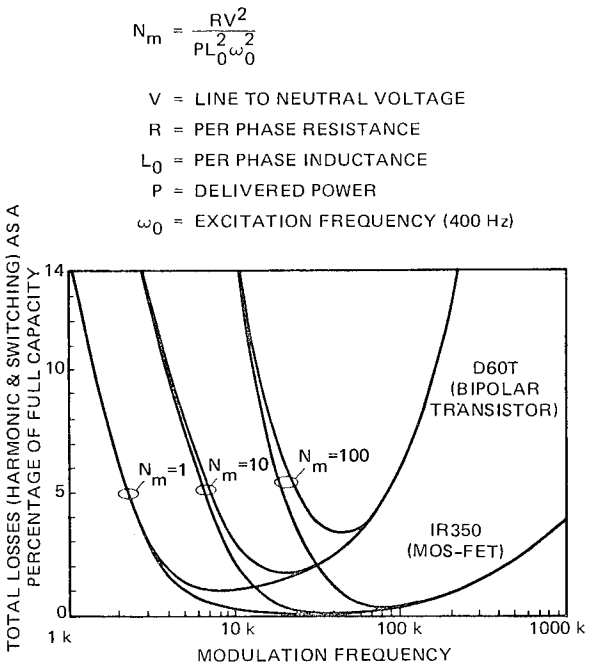

Fig. 12. Efficiency comparison for bipolar and MOSFET PWM inverters.

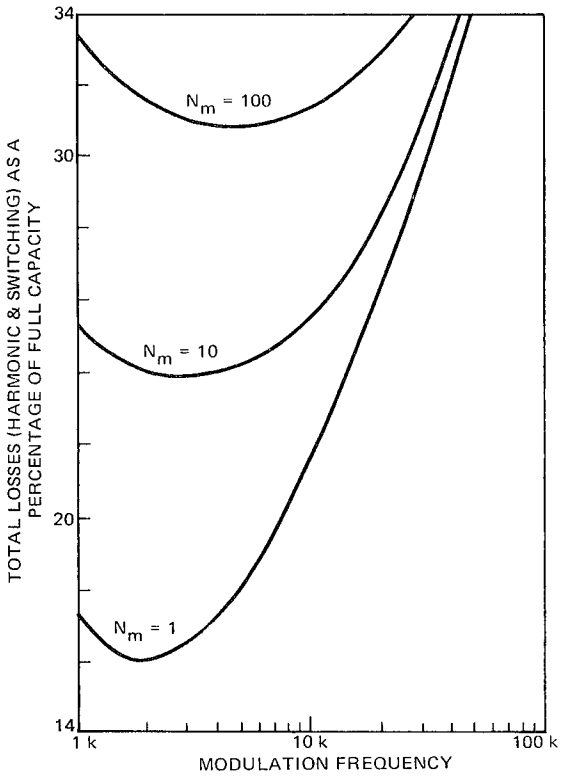

Fig. 13. Efficiency of SCR PWM inverters for various motor characteristics.

factors all contribute to higher reliability. HEXFETS share these advantages of BJTs over SCRs, but in addition have less severe second breakdown characteristics, require less complex drive circuitry, and require no current sharing resistors. It stands to reason that, if the reliability of the power MOSFET device itself proved comparable to that of competing technologies, MOSFET inverters will exhibit superior reliability performance.

ECONOMICS

Both capital expenditure and operating costs of a system are important in determining cost effectiveness. The capital costs for BJT and FET inverters are at present higher than those for SCR inverters despite the fact that semiconductor costs are only a part of the inverter cost. Reduced operating costs provided by increased efficiency can, however, justify higher capital expenditures.

The initial capital expenditure for a solid-state inverter is a function of not only semiconductor costs but also the type of controls desired, the peak and average power ratings, line voltage, and inverter architecture. The predominant cost of the inverter is still that of the semiconductors, and the cost of MOSFETS is presently significantly higher than that of either SCRs or BJTs. However, commutation costs for SCRs and drive requirements for BJTs are important secondary costs, which a MOSFET inverter does not have. Costs of BJTs and SCRs have also declined due to improvements still in progress.

These improvements are the result of production experience and lower marginal costs, which are due to distribution of fixed costs across larger market volumes. It is clear that MOSFETS should also experience significant cost reductions, and within five years could be 10 percent to 25 percent of their present cost in current dollars.

Because power MOSFET technology is in its infancy, these numbers are highly speculative, and it is therefore clearly premature to evaluate the overall economics of FET inverters. The savings from potential increases in efficiency for MOSFET inverters over SCRs and BJTs significantly improves the cost competitiveness of MOSFET inverters. Fig. 14 shows the

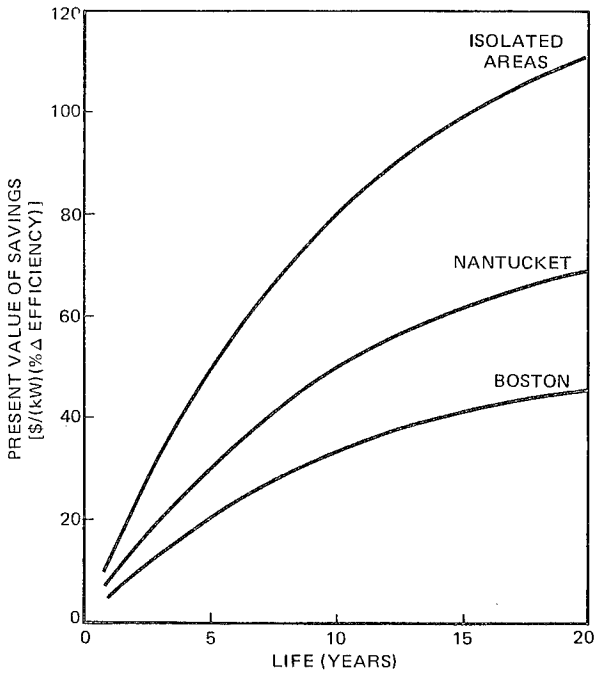

Fig. 14. Present value of energy savings obtained at various utility rates.

present value for energy savings obtained at utility rates of 6¢/kWh for Boston, 9¢/kWh for Nantucket, and 15¢/kWh for isolated areas. The curves show that a 1-percent increase in efficiency in an inverter for a Nantucket application with a 20 year life has a present value of $70/kWh; a 5-percent efficiency improvement in a 10 kW unit would yield a present value of $3,500 in savings. Assumptions used to create these curves are 100-percent utilization and a cost of money of 10 percent. While practical utilization factors will be lower, the curves clearly indicate a strong economical incentive for efficiency improvements.

CONCLUSIONS

Power MOSFET devices offer the potential of PWM flywheel drives with substantially improved efficiencies over those obtainable with other semiconductors. While these devices are currently much more expensive than other semiconductors, this cost should come down with competition. The utilization of these devices should be considered in applications where flywheel drive efficiency is critical.

FLYWHEEL BEARING DESIGN FOR AUTOMOTIVE APPLICATIONS

William H. Bauer
William M. Brobeck
William M. Brobeck & Associates
1235 Tenth Street
Berkeley, California 94710

ABSTRACT

Flywheel systems of the capacity required to replace the batteries of electric cars require bearings with very low friction losses. The requirements of these bearings are discussed and quantized for a typical case. A magnetic thrust bearing and liquid-film radial bearings are proposed to meet these requirements. Calculated dimensions, load capacities and power losses of these bearings are given for a particular flywheel system design.

INTRODUCTION

The application of flywheel energy storage to automobiles has generally been considered suitable for load leveling only. The concept of the "mechanical battery," a flywheel unit capable of storing and delivering all the energy required to propel the vehicle has not received much credence. One reason for this seems to be the opinion that the run-down loss of a flywheel system is so large that storage times would be impractically short and overall efficiency impractically low as a result of this loss.

The components of the run-down loss in a typical system are:

Windage,
Vacuum pumping power,
Generator no-load losses, and
Bearing friction.

It is not difficult to show that there is a good possibility of making the first three loss components vanishingly small. Below 10^{-5} Torr, an easily attainable pressure, windage loss is negligible.[1] With a sealed vacuum system pumped by absorption, there is no pump power. The generator losses without excitation of the magnetic field can also be made insignificant. Bearing friction remains to be evaluated. Its estimation is the subject of this paper. It will be shown that bearing friction loss while it cannot be reduced to zero can be made small enough to be no obstacle to the use of flywheel storage as the sole source of propulsion energy for an electric car.

REQUIRED RUN-DOWN RATE

The bearing system requirements can be divided into those of friction and support. Taking the friction requirements first, the quantity to be established is the allowable run-down rate. A typical passenger car, traveling 10,000 miles per year at an average of 40 miles per hour is in use 250 hours out of the 8760 hours per year. Ninety-seven percent of the time it is out of use. This large part of the time is the time that bearing friction is important. Fortunately, when the car is not in use the flywheel system is subjected to only the force of gravity. The bearing configuration can be changed from the road condition to the standby condition so as to greatly reduce the losses while the car is parked.

Situations in which the run-down rate would be most important would be extended parking where no charger was available or having to abandon the car because of an impassable road or other trouble. As a practical worst case, assume that the car is parked with the flywheel half discharged and that it will be retrived in a week. Further assume that a remaining charge of 25 percent will be enough to get the car to a charging station. To meet this requirement the flywheel can decelerate from 50 to 25 percent of full charge in seven days. If the friction force is proportional to the speed a loss rate of ten percent per day would be allowable. If the power loss is constant the allowable rate is 3.6 percent of the full charge per day. With the combination of magnetic and liquid film bearings to be

discussed the allowed loss rate would be between these values.

Another basis for setting the allowable run-down rate is the allowable standby energy loss. Assume a capacity of ten kilowatt hours of total stored energy at maximum operating speed of which 7-1/2 kWh is delivered in each discharge cycle. Assume also that the car will be driven on stored energy through 500 charge and discharge cycles per year. Further assume that the bearing losses can equal four percent of the delivered energy. This allows 150 kilowatt hours of bearing loss in 8760 hours, an average of 17 watts. The corresponding run-down rate is 5.4 percent per day. (The losses in the generator and charger will increase this to the order of 25 watts drawn from the ac line.). This loss, which is less than ten percent of the load of a typical household refrigerator, should be acceptable.

The above considerations appear to determine the allowable bearing losses. A loss rate of 12.5 watts on standby at full speed corresponding to four percent per day will be considered satisfactory.

BEARING LOADS

Bearing loads can be considered to arise from the following causes:

Rotor weight,
Linear accelerations,
Angular accelerations, and
Magnetic forces.

As an example, a flywheel rotor system, including the rotating part of the generator, weighing 700 pounds and storing ten kilowatt hours at 15,000 rpm will be assumed. 7.5 kilowatt hours will be delivered during discharge to 7,500 rpm. The general arrangement with bearings to be described later is shown in Fig. 1. As the axis is assumed to be vertical the weight of 700 pounds is the thrust bearing load during standby.

If the bearings are directly supported from the frame of the car, a rough calculation(A)* shows that angular accelerations on the road can produce radial bearing loads that would be excessive for any practical bearing. The gyroscopic effect of the flywheel will tend to hold the car level against roll or pitch. Because transmission of the gyroscopic forces through the bearings would increase the bearing loads, the flywheel unit will be assumed to be mounted in gimbals. The gimbal support will insulate the flywheel system from angular acceleration in roll and pitch. A small restoring torque will be applied to return the plane of the wheel to its normal position with respect to the car after a change in angle. Angular acceleration about the rotation axis has no effect on the bearing loads.

Linear acceleration forces will be due to the path of the car along the road and over bumps and to its acceleration and deceleration. Forces in the horizontal direction depend on the way the car is driven. A horizontal acceleration of 70 percent of gravity is used based on a coefficient of friction between the tire and the road of 0.7.[2]

Vertical road loads will be limited by the vehicle mass and suspension spring rate. The natural frequency of a typical suspension is one cycle per second.[3] Assuming a sudden step of six inches gives an acceleration of 0.6 g.(B) This will be used as the maximum vertical acceleration to be resisted.

Magnetic forces arise from the attraction between the stator and rotor of the generator. These forces average to zero when the rotor and stator are concentric. Although there may be variations during a revolution such variation is not expected to produce appreciable variation in bearing loads due to the large mass involved. However, magnetic forces place a stringent requirement on radial bearing stiffness. The decentering force rate of the generator shown in Fig. 1 has been calculated to be the order of 150,000 pounds per inch.(C) The radial bearings and their associated structure must provide a stiffness exceeding that force rate between the generator stator and rotor to prevent the rotor and stator pulling into contact with each other. This situation which exists in any generator or motor is easily handled by oil-film or rolling-element bearings. However, satisfying this requirement may be a serious problem in the design of the bearing supporting structure.

Unbalance of the rotating system also imposes requirements on the radial bearings.(D) With fiber-composite flywheel construction, an eccentricity of the center of gravity of .010 inches should be provided for.[4] Because the flywheel

*Letters in parentheses refer to Appendices

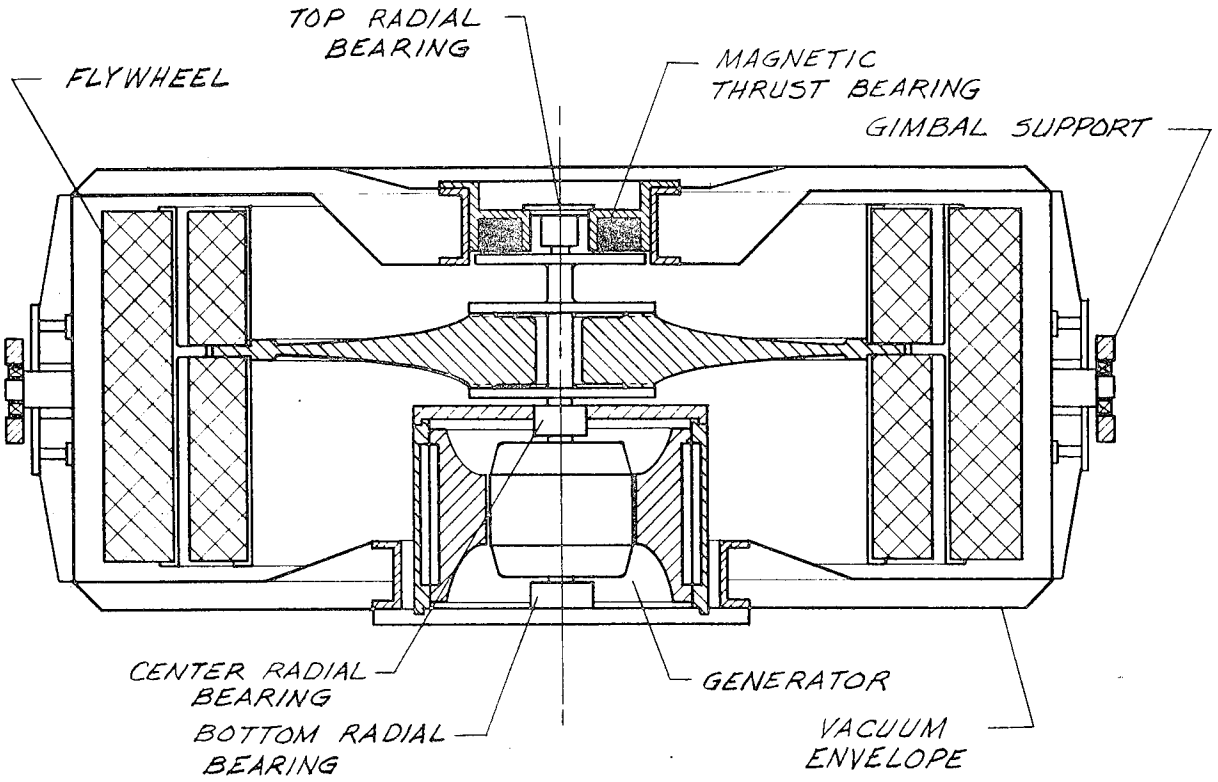

FIGURE 1 - FLYWHEEL STORAGE UNIT

will operate above its lowest critical speed, its center of mass will rotate with the assumed .010 inches radius. Furthermore, dynamic as well as static unbalance can exist. The axis of rotation may tilt with respect to the geometric axis by .010 inches in the axial length of the wheel.

To ensure stable operation of the flywheel, means must be provided to damp out whirl motion due to gyroscopic forces. This damping can be provided by mounting one of the flywheel bearings in an elastomeric cushion. Incipient whirl motion will cause deflection of the cushion and hence absorption of the whirl energy through hysteresis in the cushion material.

In addition to the above requirements, there are other requirements that must be met. The bearings should have a long, preferably infinite life because the other elements of the system, the flywheel itself and the generator, have the potential for operation without maintenance or deterioration. The bearings must operate in a high vacuum and they should be quiet.

Table 1 summarizes the bearing requirements as discussed in the foregoing.(E)

Table 1. Summary of bearing requirements.

Allowable friction loss	12.5 watts at full rpm (4% of deliverable stored energy per day at maximum speed)
Standby thrust load	700 lbs (rotor weight)
Transient thrust load	420 lbs (.6 times rotor weight)
Maximum transient load:	
Top bearing	100 lbs
Center bearing	580 lbs
Bottom bearing	125 lbs
Standby radial load	100 lbs
Radial stiffness	Greater than 150,000 lbs/in

BEARING SELECTION

Of the types of bearings that are suitable for use in a high vacuum, we can identify rolling-contact (ball or roller), magnetic and liquid-film (plain) bearings. Rolling-contact bearings do not have the unlimited life required for a maintenance-free system. (Note that 97 percent of the flywheel's time will be spent on standby and most of it at full speed.) Magnetic bearings have the possibility of adequately low losses and adequately high load capacity. However, it appears impossible to obtain sufficient radial stiffness with magnetic bearings. On the other hand, liquid-film bearings appear to meet the radial stiffness requirements and to combine high load capacity with low friction loss. The configuration which will be analyzed, therefore, consists of a magnetic thrust bearing and oil-film radial bearings for the flywheel system shown in Fig. 1.

Because of the conflicting requirements of cushion support of at least one of the flywheel bearings and the high radial stiffness required for support of the generator rotor, a system of three radial bearings is indicated. The flywheel-end bearing will be cushioned while the other two will be rigidly attached to the generator stator. The motions due to unbalance of the flywheel will be absorbed by attaching extension shafts to the flywheel hub through bonded elastomeric rings on both sides of the hub. This construction will differ in detail depending on the type of hub or spoke system used.

MAGNETIC THRUST BEARING

Fig. 2 shows the design of a lifting magnet to support the rotating system. The magnet strength is chosen to equal the rotor weight increased by a modest vertical acceleration of 20 percent of gravity. For the transient thrust load given in Table 1, the support would transfer to ball bearings. Although such bearings have a limited life under continuous operation, they should last indefinitely if required only to support momentary overloads.

The magnet gap is controlled by a servo responding to a magnetic or optical pickup. The vertical stiffness is determined by the gain of the servo loop which will be limited by the onset of instability. The transient properties of the magnet and the properties of the supporting structure will determine how small a gap will be practical to use. This calculation will not be attempted here. Instead, it will be assumed that a gap of .040 inches (1 mm) will be satisfactory during road operation and .015 inches will be satisfactory during standby.

The power losses of the magnet can be divided into coil excitation power (copper loss) and eddy current and hysteresis losses (iron loss). The coil power is decreased by increasing the size and weight of the magnet and by decreasing the gap. The coil power required by a magnet having the dimensions given, together with the other parameters of the bearing are stated in Table 2.[F] To this must be added the power loss in the servo system.

Table 2. Characteristics of magnetic thrust bearing (servo system not included).

Overall diameter	9 inches
Overall height	2-3/4 inches
Maximum flux density at pole tips	10,000 gauss
Gap during road operation	.040 inches
Gap during standby	.015 inches
Coil power in road operation	14 watts
Coil power during standby	2.5 watts
Maximum load capacity	920 lbs
Normal load	700 lbs
Iron loss due to .001 inch total indicated run out of armature disk	Less than one watt
Armature disk material	Laminated transformer iron
Weight of copper	14 lbs
Weight of iron	21 lbs
Total weight	35 lbs

Iron losses are caused by the lack of azimuthal uniformity of the magnetic field in the gap. If the iron were completely uniform and the surfaces exactly parallel and perpendicular to the rotation axis, there would be no iron losses. The losses for a given inaccuracy can be reduced by lamination of the magnet core and the rotating armature. Reasonable assumptions as to mechanical inaccuracies indicate negligible losses in laminated core and armature material.[G]

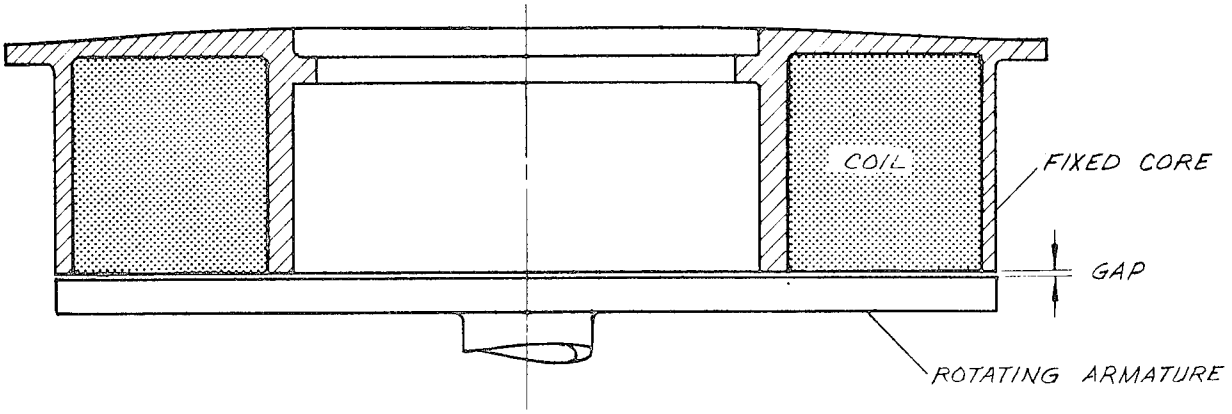

FIGURE 2- MAGNETIC THRUST BEARING

LIQUID-FILM RADIAL BEARINGS

As has been discussed, liquid-film bearings appear to be the best and possibly the only satisfactory means of radial support. The standby friction loss of these bearings under the light loads involved is due to the viscous drag of the liquid film. Under the heavier loads of road operation, the shaft moves to an eccentric position reducing the film under the load and increasing the pressure which acts to support the load. The limiting load is reached when the shaft contacts the bearing sleeve which occurs at a film thickness comparable to the roughness of the surfaces. This action of plain bearings has been studied extensively and is well understood. The film thickness as a function of load for a typical bearing is shown in Fig. 3. Of the three radial bearings assumed, the center bearing, which is near the plane of the center of gravity of the rotor, will be the most heavily loaded of the three. The top and bottom bearings have very light loads under all conditions. Table 3 gives losses under standby conditions. Losses under road conditions are essentially the same except when the overload ball bearings come into action. Even then the losses are negligible compared to the power output in road operation.

Table 3. Characteristics of liquid-film radial bearings.

	Top	Center	Bottom
Diameter - inches	.5	.6	.5
Length - inches	.5	.6	.5
Radial clearance - inches	.001	.001	.001
Liquid viscosity - centipoises	1	1	1
Maximum speed - revs/sec	250	250	250
Standby loss - watts at 250 RPS	2	4	2
Maximum load - lbs	100	580	125
Minimum film thickness - micro-inches at 125 RPS and maximum load(H)	17	6	14
Total standby power loss in liquid film bearings at 250 RPS(H)		8 watts	

The minimum film thickness of six microinches provides a large factor of safety over the commercially obtainable smoothness of the order of one microinch on parts of the size and shape required.[5] Fig. 4 shows a possible design for a liquid-film bearing provided with a radial overload ball bearing. Under overload conditions, the spring supporting the film bearing will compress causing the shaft to be restrained by the ball bearing. The ball bearing inner race normally clears the shaft and remains stationary.

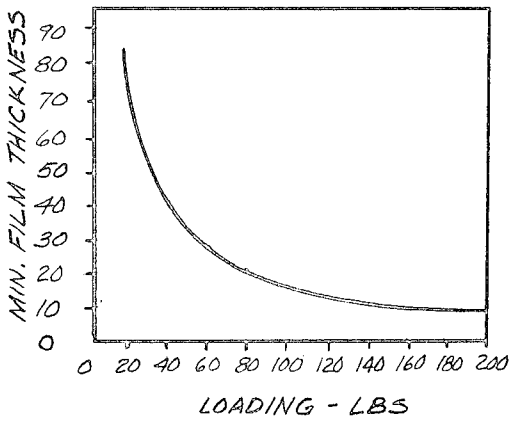

FIGURE 3

MINIMUM FILM THICKNESS VS. LOADING

½ IN. X ½ IN. JOURNAL BEARING
VISCOSITY = 1 CENTIPOISE
SPEED = 7500 RPM
.001 IN. RADIAL CLEARANCE

A circulating pump is provided to keep the bearing supplied with oil. The oil flow required, which is very small, is proposed to be produced by a plunger operated by an electro-magnet. At intervals of several seconds, the magnet is pulsed causing the plunger to pump the small quantity of liquid required to maintain the bearing in the flooded condition. A small accumulator is used to maintain constant pressure on the bearing.

With lightly-loaded radial fluid-film bearings on a vertical shaft, the phenomena of shaft whirl can be expected. Whirl is a rotation of the shaft axis with respect to the bearing axis which, if it builds up in amplitude, can destroy the bearing. Whirl may also be induced by gyroscopic effects. Whether or not destructive whirl occurs depends on the combined properties of the rotating part, the bearings and the structure supporting the bearings. Fortunately, all of these are under control of the designer. Design

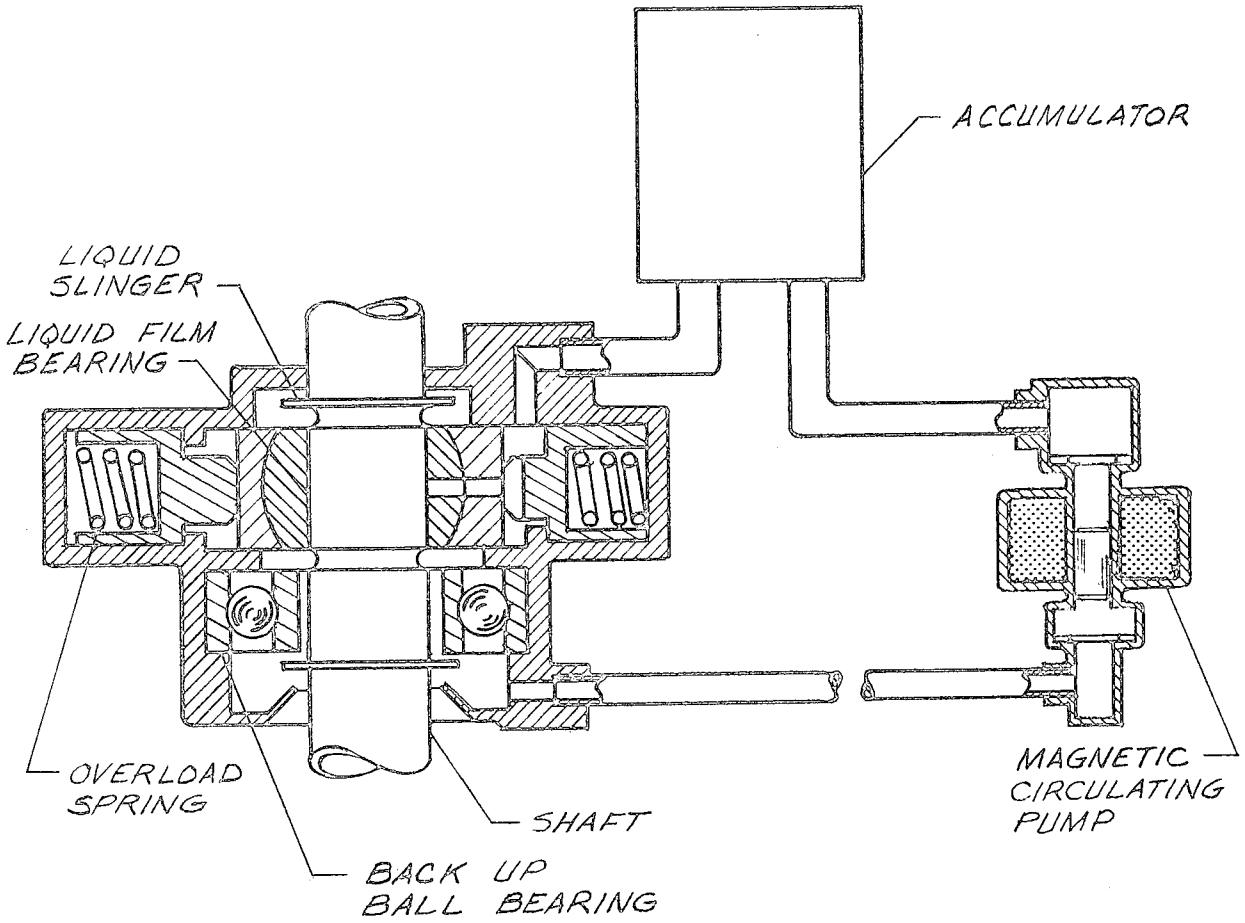

FIGURE 4 - LIQUID FILM BEARING ARRANGEMENT

features to prevent whirl do not have to be confined to one element of the system alone. Many such features have been invented to control shaft whirl under similar conditions but the proof of their success in any particular application must be demonstrated in actual operation.

The fluid film bearing torque, being viscous drag, will vary in proportion to the shaft speed. The power required by the thrust bearing magnet will be independent of speed and so the torque required to generate that power will increase as the speed falls. Neither of these effects will be significant in the usual standby operation because the flywheel will normally be fully charged less than one hour after the car is parked and will be "topped off" before its speed has dropped more than a few percent.

The liquid which provides the supporting film must have a sufficiently low vapor pressure to prevent significant windage loss and must have low viscosity to reduce the standby power loss. Organic liquids have been developed for diffusion vacuum pumps that have the necessary low vapor pressure. It is not known, however, if those compounds meet the viscosity requirements. It may be necessary to develop a new organic compound to meet the combined requirements of vapor pressure and viscosity.

In the example, the total calculated bearing standby loss is ten watts, two and a half for the magnetic bearing and eight for the fluid-film bearings. To this must be added the power required by the magnetic bearing servo for which the remaining two of the allowed twelve and one-half watts can be allocated. The fact that the servo system requires very little range of control while the flywheel is in the standby condition should make its power requirement small.

CONCLUSION

The results of design studies of magnetic and fluid-film bearings for a typical automotive flywheel-generator system have been presented. It can be concluded that bearings can be designed to resist the loads imposed in road operation and to have adequately low run-down losses provided that a fluid of suitable viscosity and vapor pressure can be obtained and that shaft whirl can be prevented. Although a considerable development effort may be required, the prospects of meeting these requirements appear to be good.

APPENDICES

(A) Gyroscopic force on bearings of rigidly mounted flywheel.

Angular velocity in roll

Assume roll natural frequency 1 Hz
Roll amplitude 6 in. in 60 in. = .1 radian
Roll velocity = .1 x 2π = .2π radians/sec = ω_R

Flywheel velocity = $\frac{15000}{60} \times 2\pi$

= 1571 radians/sec = ω_F

Flywheel energy = 10 kWh
= 10 x .746 x 33000 x 3600
= 8.86 x 10^8 ft lbs = E

Flywheel moment of inertia = $\frac{2E}{\omega_F^2}$

= $\frac{2 \times 8.86 \times 10^8}{(1571)^2} = 718 \frac{\text{ft lbs}}{\text{sec}^2}$

Flywheel torque = $I\omega_F\omega_R$
= 718 x 1571 x .2π
= 709,000 lb ft

Bearing spacing 2 ft.

Bearing load $\frac{709,000}{2}$ = 354,000 lbs

This extreme load would probably never be reached because the sprung part of the vehicle would accelerate in pitch. However, the large bearing load calculated in this way makes use of a gimbal mounting appear advisable.

(B) Vertical acceleration of one end of the vehicle .

Natural frequency = $\frac{\omega}{2\pi}$ = 1 Hz

Maximum acceleration with an amplitude of 6 inches = $6\omega^2 = 6 \times 4\pi^2 = 237 \frac{\text{inches}}{\text{sec}^2}$

$\frac{237}{12 \times 32.2}$ = .61 g

(C) Decentering magnetic force of an electrical machine Ref. 6.

$\frac{\text{Force}}{\text{Displacement}} = \frac{2\pi RL}{8\pi} \frac{B^2}{\text{Gap}} = \frac{RLB^2}{4 \times \text{Gap}} = K$

B = 10,000 gauss, gap assumed 1 mm
R = Rotor radius assumed 10 cm
L = length = 10 cm

$$K = \frac{10 \times 10 \times (10{,}000)^2}{4 \times .1} = 2.50 \times 10^{10} \frac{\text{Dynes}}{\text{cm}}$$

$$= \frac{2.50 \times 10^{10} \times 2.54}{981 \times 454} = 142{,}000 \frac{\text{lbs}}{\text{in}}$$

(D) Unbalanced Force

Weight of bearing shell and housing - assumed 1-1/2 lbs
Eccentricity of center of gravity - .010 inches
Rotating speed - 15,000 rpm

$$\text{Force} = MR\omega^2 = \frac{1.5}{32.2}\left(\frac{.010}{12}\right)\left(15000 \times \frac{2\pi}{60}\right)^2$$

$$= 96 \text{ lbs}$$

(E) Radial bearing loads.

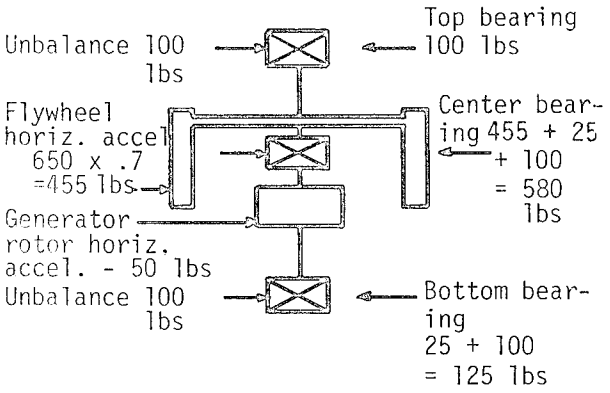

(F) Magnet power required.

Steady load	700 lbs
Maximum load	900 lbs
Operating gap	.040 in.
Standby gap	.015 in.

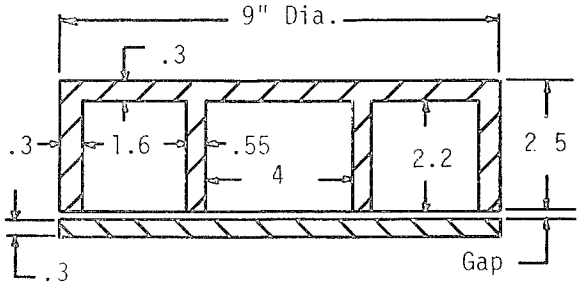

Maximum flux density 10,000 gauss
Pole area = $8.7\pi \times .3 + 4.55\pi \times .55$
$= 16.0 \text{ in}^2$

$$\text{Magnetic pressure} = \frac{B^2}{8\pi} = \frac{(10{,}000)^2}{8\pi}$$

$$= 3.98 \times 10^6 \frac{\text{Dynes}}{\text{cm}^2}$$

$$\frac{3.98 \times 10^6 \times (2.54)^2}{981 \times 454} = 57.6 \frac{\text{lbs}}{\text{in}^2}$$

Magnetic force = 16.0 x 57.6 = 922 lbs

Weight of copper $1.6 \times 2.2 \times .6 \times (2 + .55 + .8)2\pi \times .321 = 14.2$ lbs
(Space factor .6 - Density of copper .321 $\frac{\text{lbs}}{\text{in}^3}$)

Ampere turns at 700 lbs and .040 inches gap

$$NI = \frac{B\ell}{.4\pi} = \frac{(10{,}000)\left(\frac{700}{922}\right)\frac{1}{2}(.1 \text{ cm})(2)}{.4\pi}$$

$$= 1386 \text{ amp turns}$$

Resistance of one-turn coil

$$R = \frac{L\rho}{A} = \frac{2\pi(2 + .55 + .8)}{1.6 \times 1.7 \times .6} \times (.73 \times 10^{-6}$$

ohm inches at 40 c) $= 9.4 \times 10^{-6}$ ohm

$$\text{Power} = I^2R = (1386)^2 \times 9.4 \times 10^{-6}$$
$= 18$ watts

Ampere turns at 700 lbs and .015 inches gap

$$NI = 1386\left(\frac{.015}{.040}\right) = 520 \text{ amp turns}$$

$$\text{Power} = (520)^2 \times 9.4 \times 10^{-6} = 2.5 \text{ watts}$$

Magnet Weight

$$\text{Iron } \left[(9)^2 \frac{\pi}{4}(.3)(2) + (4.55\pi)(2.2)(.55) + (8.7\pi)(2.2)(.3)\right].28 = 20.6 \text{ lbs}$$

Copper 14.2 lbs
Total 20.6 + 14.2 = 34.8 lbs

(G) Losses in magnet iron.

Iron losses may be very difficult to calculate with good accuracy. However, their order of magnitude can be estimated as follows:

Assume the gap to be .015 inch and the flux density to be 10,000 gauss.

Assume the speed to be 15,000 rpm and the total indicated run out of the disk .001 inch.

Then the flux variation in the disk will be the order of $\frac{1}{15}(10{,}000)$ or ± 330 gauss.

Assume the disk material to be transformer iron which at 60 Hz and 10 kg peak has .223 watts/lb eddy current loss and .269 watts/lb hysteresis loss (USS transformer 52).

At 250 Hz (15,000 rpm) the calculated eddy current loss is

$$.223\left(\frac{250}{60}\right)^2\left(\frac{330}{10{,}000}\right)^2 = .0042 \text{ watts/lb}$$

and hysteresis loss

$$.269\left(\frac{250}{60}\right)\left(\frac{330}{10{,}000}\right)^{1.6} = .0048 \text{ watts/lb}$$

Total loss .0042 + .0048 = .009 watts/lb

If the entire core and disk were made of this material the total loss would be .009 x 20.6 lbs = .18 watts.

(H) Minimum film thickness and power loss.

Sample calculation for top bearing

h_n = minimum film thickness
R = Radius, .25 in.
C = Radial Clearance, .001 in.
μ = Viscosity, 1 centipoise or 1.45×10^{-7} reyn ($lb\text{-}sec/in^2$)
N = Speed, 7500 rpm or 125 rev/sec

P, loading per unit area:

$$P = \frac{W}{2RL} = \frac{(100)}{(2)(.25)(.5)} = 400 \text{ psi}$$

S, Sommerfield Number:

$$S = \left(\frac{R}{C}\right)^2\frac{\mu N}{P} = \left(\frac{.25}{.001}\right)^2\frac{(1.45 \times 10^{-7})(125)}{400}$$

$$= .0028$$

From Figure 49, page 5-41, Reference 7, the minimum film thickness variable H is determined to be .017.

$$h_n = HC = (.017)(.001) = 17 \times 10^{-6} \text{ in.}$$

Power Loss, Hp

From Equation 8-12, Page 218, Reference 8,

$$Hp = \frac{2\pi^3\mu N^2 D^3 L}{Cd}$$

Where Cd is the diametral clearance, equal to 2C.

Assume the maximum speed of 15,000 rpm or 250 rev/min.

$$Hp = \frac{2\pi^3(1.45 \times 10^{-7})(250)^2(.5)^3(.5)}{(2)(.001)}$$

$$= 17.6 \text{ in·lb/sec} = 1.98 \text{ watts}$$

REFERENCES

1. Baer, M.R., "Aerodynamic Heating of High Speed Flywheels in Low-Density Environments," Sandia Report SAND 78-0957, October, 1978.

2. "Passenger Car Wheels - Performance Requirements and Test Procedures," Society of Automotive Engineers, SAE J328a.

3. Observed on a typical American passenger car.

4. Experience with fabrication of composite flywheels at William M. Brobeck & Associates.

5. Baumeister & Marks, Marks Handbook for Mechanical Engineers, Seventh Ed., McGraw Hill, p. 13-107.

6. Behrend, B.A., AIEE Transactions, Vol. 17, p. 617.

7. O'Connor & Boyd, Standard Handbook of Lubrication Engineering, McGraw-Hill, 1968.

8. Wilcock & Booser, Bearing Design and Application, McGraw-Hill, 1957.

FACTORS AFFECTING THE CONTROL OF A MAGNETICALLY SUSPENDED FLYWHEEL

David Eisenhaure, James Downer, and Richard Hockney
The Charles Stark Draper Laboratory, Inc.
555 Technology Square
Cambridge, Massachusetts 02139

ABSTRACT

This paper discusses the identification and solution of several unique control problems involved in the design of the feedback compensation of a magnetic suspension for use with a stationary energy-storage flywheel. Compliance-induced housing resonance, the inherent instability of permanent-magnet suspensions, and magnetically induced dynamics are of particular concern to control engineers. Without proper control design, the existence of finite, lightly-damped housing stiffness can cause oscillations in the independently controlled axial and radial suspension systems. Two alternatives for the suppression of these oscillations are notch filters in the compensation networks and mechanical stiffening of the housing. The latter technique moves the oscillation frequency to a point far beyond the bandwidth of the system. These alternatives were implemented separately, and their results were compared. System performance was substantially improved through incorporation of either alternative. The final configuration uses a combination of these two alternatives. This configuration allows extremely high bearing stiffness to be obtained without introducing undesirable oscillations.

INTRODUCTION

This paper reviews the control of a flywheel magnetic bearing developed by The Charles Stark Draper Laboratory, Inc. (CSDL). This bearing was developed as part of an ongoing Internal Research and Development (IR&D) program designed to demonstrate the economic and engineering superiority of ultralow-loss magnetic bearings through analysis of a scale model flywheel suspension. The baseline suspension design includes a nominal 10-lb wheel capable of achieving speeds up to 25,000 r/min.

A test-bed energy-storage module was designed, fabricated, and tested at CSDL.

BACKGROUND

For any flywheel energy-storage system (FESS) to be effective, the energy dissipated by the system must be small when compared with the stored energy. Magnetic bearings suggest themselves for FESS applications because their potential for low loss is excellent. The main advantages of these bearings include long life and very low drag.

The energy consumption for gas and magnetic bearings may be calculated using formulas from the literature and CSDL sources.[1] For gas bearings

$$\text{Power} = \frac{0.8\ \mu R^4 \omega^2}{C} \qquad (1)$$

where

μ = gas viscosity

ω = speed (rad/s)

R = radius of the bearing

C = bearing clearance

For magnetic bearings

$$\text{Power} = aM\left(K_H B^n f + K_E B^2 f^2\right) + I^2 R \qquad (2)$$

where

aM = mass of the controller affected by the flux

B = strength of the control magnetic field

f = frequency

The parameters K_H, K_E, (hysteresis and eddy-current coefficients, respectively), and n are properties of the material.

Experimental determination of the energy consumption of advanced ball bearings (for FESS applications) has been performed.[2] This drag increases as the product of load and bearing bore increases. Since the bore must increase with load, the drag increases rapidly with system size at a given speed.

Figure 1 describes the energy and cost savings that can be achieved by using magnetic bearings instead of either of the two most common types of suspension (ball or gas bearings).[1,2]

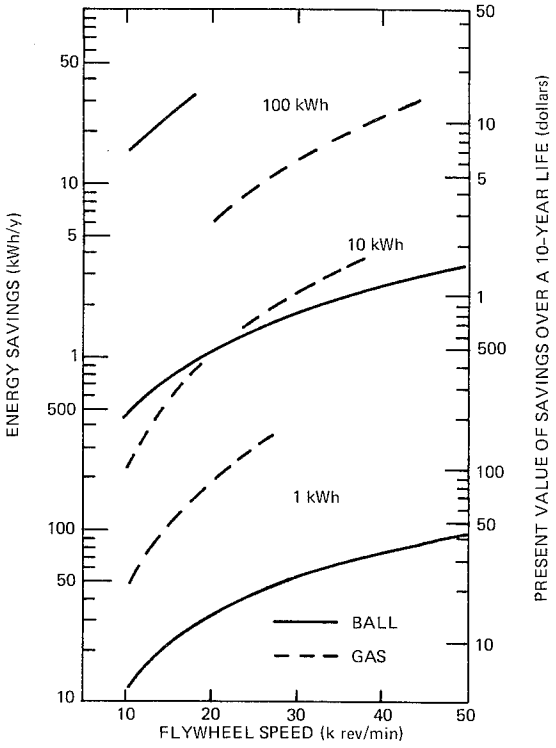

Fig. 1. Energy savings advantages of magnetic bearings over conventional suspensions.

SYSTEM DESCRIPTION[3]

Figure 2 is a photograph of the system. It is a scaled-down version of an expected load-leveling installation. Figure 3 is a layout view showing the internal components of the system. The position of the wheel is maintained by a pair of radial magnetic bearings and a single magnetic-thrust bearing. Both bearing types are permanent magnet (PM) biased electromagnets.

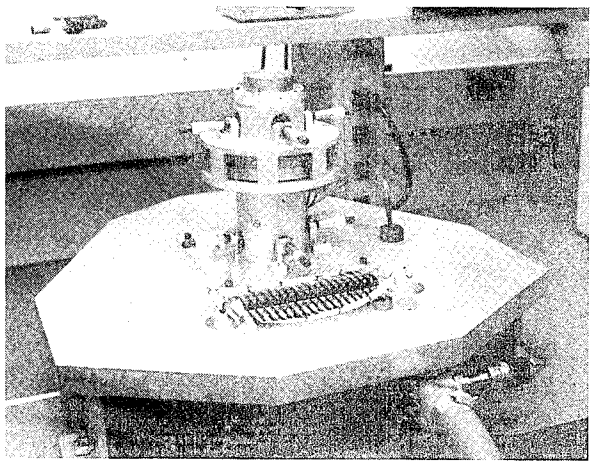

Fig. 2. Flywheel magnetic bearing test bed.

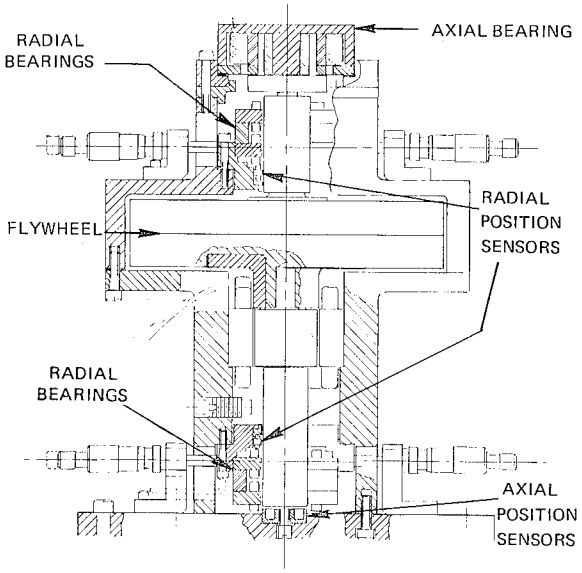

Fig. 3. Magnetic suspension flywheel assembly.

MAGNETIC SUSPENSION LOSS ANALYSIS

The most significant types of energy loss associated with magnetic-suspension systems are magnetic-core losses (Hysteresis and eddy-current),[4] copper losses, and windage drag.

The radial bearing losses are higher than the axial bearing losses because of the differential flux densities passing through the rotor laminations at each rotation. Appropriate rotor material

selection minimizes these core losses. MN60 high-permeability, low-loss ferrite was chosen because of its small hysteresis loop and high resistivity. Proper component fabrication restricts the eddy currents primarily to an area of the rotor opposite the poles of the radial suspension units. The main disadvantage with using ferrites is the difficulty in machining this highly brittle material. It has a tensile strength of approximately 2500 $lb/in.^2$ and must be ground to final dimensions by a specialized process.

The flywheel was deliberately designed to have a vertical axis of rotation. This ensures that the suspension required to support the greatest load has low losses. Had the axis of rotation been horizontal, the radial bearings would need to generate larger forces with corresponding larger core losses.

The drag on a rotating disk has been studied by numerous investigators.[6] It can be shown that an acceptable level of drag (0.1 W) will result if the wheel spins in a vacuum of less than 23 microns of mercury.

STRUCTURAL CONSIDERATIONS

The baseline flywheel system consists of a nominal 10-lb wheel spinning at 25,000 r/min. Figure 4 shows the flywheel shaft assembly.

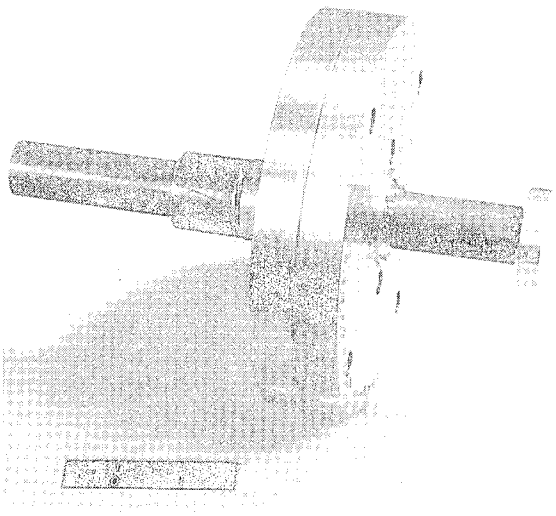

Fig. 4. Flywheel shaft assembly.

Due to its lack of structural integrity, ferrite is unsuitable for use as a shaft. It was necessary to bond ferrite sleeves to thermally compatible stainless steel shafts to reduce core losses.

Because of the need to support a large weight, the axial suspension must drive flux through a magnetic path including part of the flywheel shaft assembly. Ferrite is unsuitable for this application because of its low flux saturation limit. For this reason, an end cap of cold rolled steel was installed at the top of the flywheel shaft assembly.

In a load leveling application, an efficient, two way, electromechanical energy conversion device would be needed for the storage and retrieval of energy from the flywheel. Since only the bearings are under study herein, a spin-up motor is all that is required. A small three-phase, 400-Hz induction motor was chosen and modified. The rotor was secured, through a moderate press fit, to the flywheel shaft while the stator was mounted in the housing (Fig. 5)

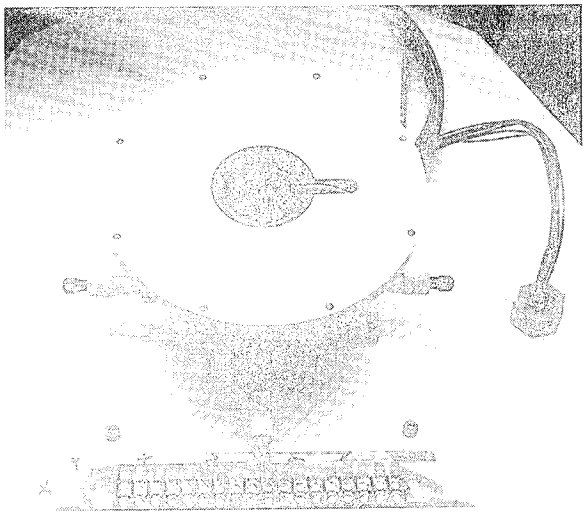

Fig. 5. Lower housing with inducation motor stator.

Due to the rotational inertia of the flywheel, a large amount of power must flow into the rotor to produce the torque required for spin-up. Some of this power is dissipated as heat in the rotor. This heat could cause problems due to the lack of convection in an evacuated chamber. Conduction heat transfer paths were supplied for both the rotor and stator.

A copper heat-transfer sleeve was installed above the rotor to transfer heat into the flywheel (Fig. 6).

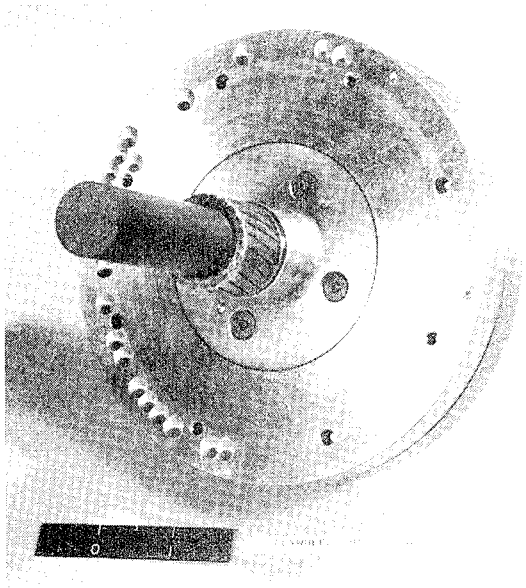

Fig. 6. Flywheel heat-transfer sleeve.

The entire housing is aluminum and will conduct heat down into a heat sink base plate (see Fig. 2).

Due to the possibility of bearing failure, backup bearings in both the radial and axial directions have been included.

MAGNETIC DESIGN

Earnshaw's theorem[6] shows that at least one axis of a passive, three-axis magnetic suspension will be unstable. The usual procedure is to actively control only one axis. Actively controlled stiffness, however, tends to be approximately 10 times as high as passive stiffness. The advantage of high stiffness is manifold. It allows for more repeatable performance with lower losses in areas of concern, and greater flexibility in the choice of spring and damper rates.

Actuators. Radial suspension is produced by a pair of permanent-magnet biased electromagnets (Fig. 7). Each bearing consists of an axially magnetized ring magnet and two stator disks. The stators each have four wound poles spaced to coincide with the two principal axes. The coil windings add to the permanent-magnet flux on one side of the rotor and oppose it on the opposite side so that a net force is produced in the desired direction.

The permanent-magnet bias produces both gain for the system and an unstable

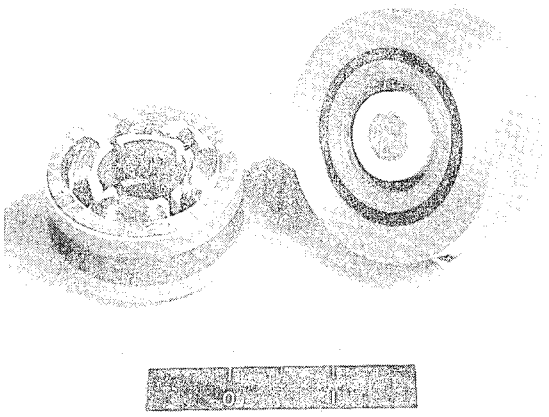

Fig. 7. Magnetic actuators.

spring effect due to its attractive nature. The magnet will tend to pull the rotor in the direction of its offset from center rather than correct for the offset. For this reason, the stable force due to the control current in the control coils must be larger than the unstable spring effect to produce a "net stable" spring constant.

Design considerations for the radial suspension deal with constraints of minimum current, flux saturation of the ferrite sleeves, and maximum force levels. The suspensions are designed so that, at the maximum rotor displacement, the maximum current allowed by the control circuit produces flux saturation in the ferrite sleeves and a 2-lb net stable force.

The axial magnetic-force generator (MFG) operates on a slightly different principle than its radial counterpart. A cutaway view of this device and the top of the flywheel shaft is shown in Fig. 8.

An axially magnetized Alnico V ring magnet acts as the major flux source. Because of the direct relationship of tractive force and flux density, a small cross-sectional area pole has been placed in the center of the magnet. This is the largest load carrying component of the MFG.

Primarily, the flux of the magnet is constrained to a path which consists of the magnet, back iron, center pole, and rotor end cap. This magnetic path is similar to that found in a permanent magnet version of the flat-faced armature type of lifting magnet commonly used in such varied applications as scrap metal moving, magnetic clutching, and magnetic braking.[7]

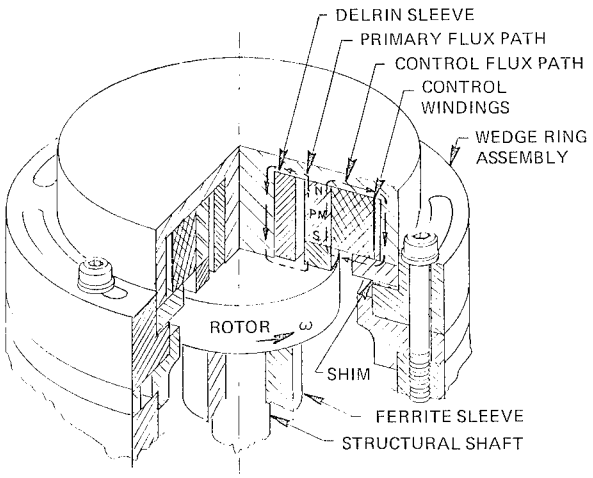

Figure 8. Axial magnetic suspension system.

An alternate path for flux is provided by the housing of the suspension as a result of its construction from the same magnetically soft material (cold rolled steel) as the primary flux path. Flux following this secondary route is generally restricted to a path consisting of the housing and ring base as well as the air gap between the ring base and the keeper ring of the magnet.

Active control of the force exerted on the rotor end cap by the MFG is obtained by shunting flux between the two paths to either reduce or enhance the air gap flux density and, therefore, the tractive force. Flux switching is accomplished through the use of the control windings placed in the annular air space between the permanent magnet and the housing.

The nominal length of the air gap between the MFG and the rotor is such that the majority of the shaft weight is supported by permanent-magnet traction alone. This minimizes the use of control current with its associated I^2R losses. An optimum air gap length is one at which the weight of the rotor equals the pull of the magnet. This length is constantly changing because of partial demagnetization of the magnet as it traverses minor hysteresis loops. Therefore, the length of the nominal air gap is not always expected to be optimal. It was anticipated however, that 90-95 percent of the energy required for suspension of the rotor would come from the permanent magnet rather than from control current.

Nonmagnetic components of the system include a wedge-ring assembly and a shim for mechanical alignment of the MFG relative to the housing as well as a sleeve surrounding the center pole. This latter device protects the tractive surfaces of the MFG from direct metal-to-metal contact with the rotor during high-amplitude transients without disturbing the flux distribution.

Sensors. The radial and axial position signals are produced by varying the impedance of electromagnetic coils (Fig. 9).

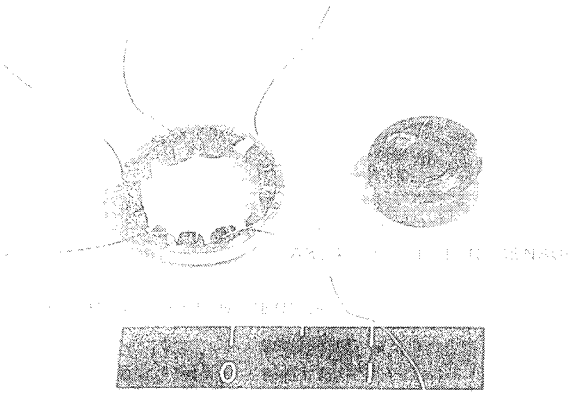

Fig. 9. Sensors.

The radial position sensors or microsyns contain radially opposed coils. As the rotor moves toward one set of coils, that set's impedance increases while that of the opposite coil decreases. The difference in voltage drops across these coils is a measure of rotor displacement.

The axial sensor operates on the same principle but contains only one coil. A permanent inductor installed within the controller is used for comparison.

SUSPENSION SYSTEM DYNAMICS

Due to the inherent instability of a permanent-magnet biased magnetic bearing, closed-loop feedback control must be applied to each of the bearings.

To design an effective compensation network for use with these bearings, a model that accurately predicts the dynamic behavior of the plant and actuators must be developed. As an initial step toward this goal, an assumption of completely decoupled radial and axial dynamics has

been made. This assumption breaks the system modeling task into two somewhat simplified subtasks.

A zero-order approximation, to a permanent-magnet biased magnetic bearing, which treats the flywheel housing as rigid mechanical ground and neglects internal suspension dynamics, is useful only for demonstrating the nature of the plant. The suspension force may be thought of as the combination of an unstable spring effect and a constant gain from current

$$F = -K_u X + K_s I_c \qquad (3)$$

where

F = suspension force

X = flywheel position

K_u, K_s = constants

I_c = control current

By applying Newton's law to the flywheel, the following transfer function emerges

$$\frac{X(S)}{I_c(S)} = \frac{K_s}{M_f S^2 - K_u} \qquad (4)$$

where

S = Laplace variable

M_f = flywheel mass

This transfer function shows an effect that is common to both the axial and radial systems, the existence of a pair of real poles equally spaced about the imaginary ($j\omega$) axis. The frequency response for this combination of minimum and nonminimum phase poles is characterized by a constant 180-degree phase shift over the entire spectrum.

AXIAL SUSPENSION MODEL[8]

The axial suspension system may be thought of as a mechanical subsystem and a magnetic subsystem joined by electromechanical coupling to derive an adequate working model.

Mechanical Subsystem. The finite stiffness of the flywheel housing causes vibration. The problem of determining the natural frequencies of this structure is difficult. By examining only the largest compliances, a lumped stiffness and mass approximation may be made.

It would appear that the most compliant part of the flywheel housing is the partially open enclosure that surrounds the wheel. Application of equations from the theory of elasticity[9] verify that the stiffness of this portion of the structure is nearly one order of magnitude lower than the next most compliant section. The second most compliant member is the back iron of the force generator that supports the heavily loaded center pole and permanent magnet.

These two stiffnesses may be combined into an equivalent housing stiffness. For modeling purposes, the lower housing will be assumed to be rigid and attached to mechanical ground. The upper housing, MFG, and other components attached to the enclosure will be treated as a rigid mass mounted on the housing spring. The flywheel and the suspension each experience magnetic tractive force in opposite directions. This is shown schematically in Fig. 10.

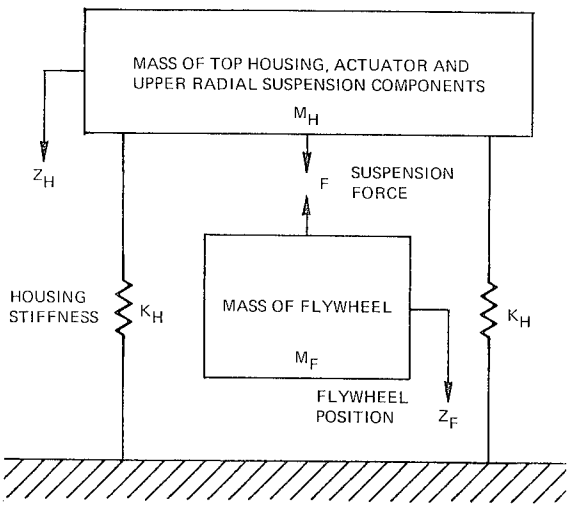

Fig. 10. Axial mechanical schematic.

Magnetic Subsystem. Both conservative and lossy effects are present in the MFG. These effects are described as follows.

In all but a few simple geometric configurations, the problem of determining the distribution of magnetic flux in free space is an easy one. By reducing the available

air space to a network of simply shaped paths, the permeance of the volume may be calculated by a semiempirical technique.[7]

A reduction of the magnetic bearing field to a network of simply shaped flux paths has been performed.

During normal operation, the permeances of the iron flux paths are large compared to those of the air paths, but they are still included in the model since flux saturation may occur at small air gaps. It is assumed that flux density is uniform over their cross-sections.

No effort (such as the use of laminated stock) has been made to reduce eddy currents in the MFG and rotor. All conducting paths in the system, when subjected to a time varying magnetic flux, are sites of eddy currents. Hysteresis loss has been ignored in this analysis.

Constitutive relationships for these two effects are

$$F = \frac{1}{P}\phi \qquad \text{(conservative)}$$

$$F = G_e \frac{d\phi}{dt} \qquad \text{(lossy)} \qquad (5)$$

where

F = magnetomotive force

P = permeance of the magnetic path

G_e = conductance of the eddy current path

ϕ = flux

The force exerted on the end cap is determined by the amount of magnetic energy made available for useful work by an infinitesimal change in the air-gap length. The energy stored and force exerted are therefore

$$W_m = \frac{\phi^2}{2P_g}$$

$$F = -\frac{\partial W_m}{\partial G} = \frac{-\phi^2}{2\mu_o A}$$

where

W_m = magnetic energy

P_g = permeance of the useful air gap ($\mu_o A/G$)

F = force

G = air-gap length

μ_o = permeability of free space

A = cross-sectional area of the air gap

The sign of the force indicates that it opposes an opening of the gap (i.e., that it is attractive).

Axial System Transfer Function. Based on Eqs. (5) and (6), as well as Fig. 10, the differential equations that govern this system may be written and reduced via block-diagram techniques and algebraic manipulation to a transfer function relating flywheel motion to control current for the frequency range of interest

$$\frac{Z_f}{I_c}(S) = \frac{5.01\left[\left(\frac{S}{\omega_3}\right)^2 + 1\right]}{\left[\left(\frac{S}{\omega_1}\right)^2 - 1\right]\left(\frac{S}{\omega_2} + 1\right)\left[\left(\frac{S}{\omega_4}\right)^2 + 1\right]} \qquad (7)$$

A qualitative explanation of each factor is possible. The minimum/nonminimum phase pole pair at ω_1 (25 Hz, 157 rad/s) illustrates the inherent instability of a permanent-magnet biased bearing. The existence of lossy and conservative magnetic effects in the MFG manifest themselves as a real pole at ω_2 (92 Hz, 578 rad/s). Mechanical resonance induced by housing compliance produces the complex zero pair at ω_3 and the complex pole pair at ω_4 (117 and 122 Hz, 735 and 767 rad/s, respectively). The frequency of the zero pair is determined by the housing mass and stiffness

$$f_3 = \frac{1}{2\pi}\sqrt{K_H/M_H} \qquad \text{(Hz)}$$

This near cancellation of a complex pole pair by a complex zero pair produces drastic changes in both the magnitude and phase angle at frequencies near ω_3 and ω_4.

This theoretical model agrees with the measured frequency response (see Fig. 11) of the system up to approximately 350 Hz to the degree that material properties (resistivity, permeability, modulus of elasticity...) are known.

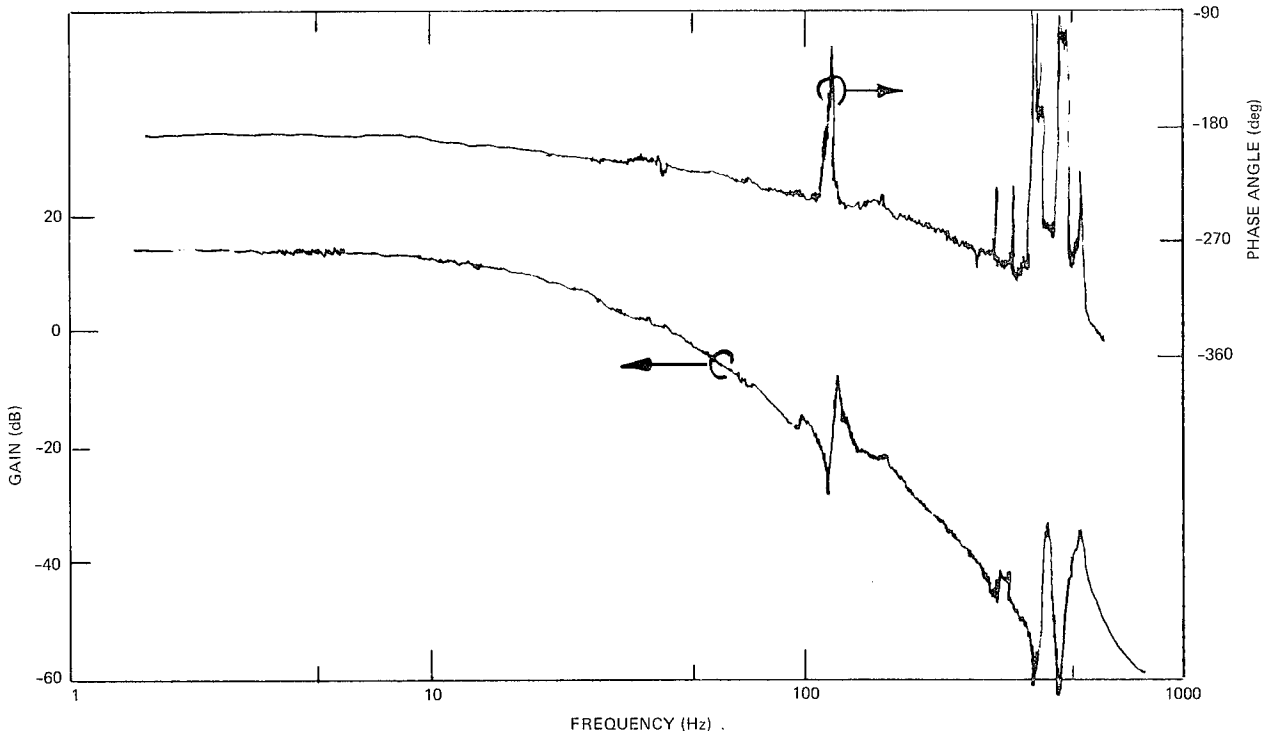

Fig. 11. Axial plant frequency response.

Higher frequency peaking in the measured frequency response are visible near 420 and 510 Hz. These are higher-order resonance phenomena which also manifest themselves as near pole-zero pair cancellations.

A pair of accelerometer spectra for the axial plane are shown in Fig. 12(a) and (b). The former shows the accelerometer mounted to the upper housing while the latter shows the output of the accelerometer when attached to the flywheel.

Comparison of the peaking phenomena in the frequency response with the spectrum of the flywheel shows agreement to the level of accuracy of the two measuring instruments.

An increase in the range of usefulness of the system transfer function, Eq. (7), from 350 to 800 Hz may be realized by introducing the results of this spectrum analysis.

If the zero and pole frequencies near 420 Hz (411 and 439 Hz, 2582 and 2758 rad/s) are denoted by ω_5 and ω_6, respectively, and those near 510 Hz by ω_7 and ω_8

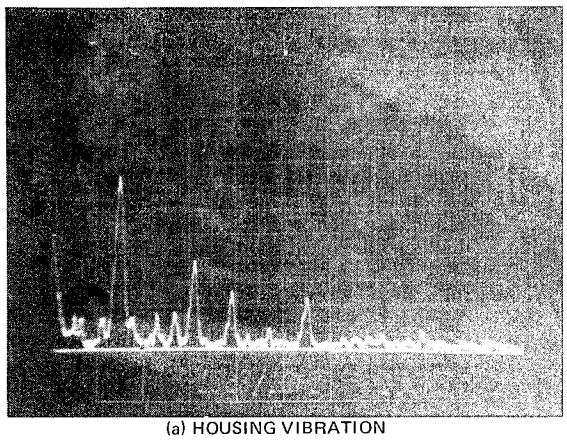

(a) HOUSING VIBRATION

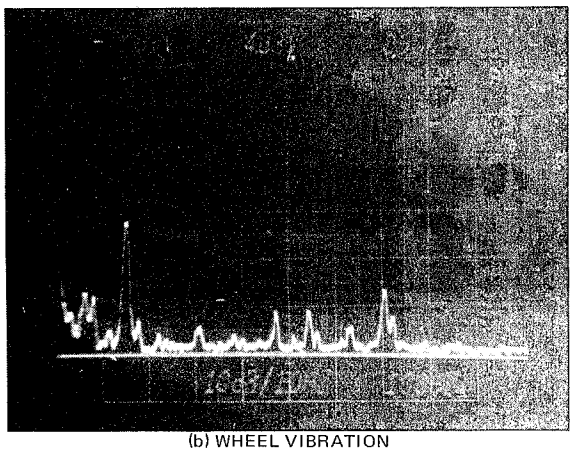

(b) WHEEL VIBRATION

Fig. 12. Vibration spectrum of the axial suspension.

(480 and 540 Hz, 3016 and 3393 rad/s), a transfer function that is adequate for controller design may be written as follows

$$\frac{Z_f}{I_c}(S) = \frac{5.01}{\left[\left(\frac{S}{\omega_1}\right)^2 - 1\right]\left(\frac{S}{\omega_2} + 1\right)} \times \frac{\left[\left(\frac{S}{\omega_3}\right)^2 + 1\right]\left[\left(\frac{S}{\omega_5}\right)^2 + 1\right]\left[\left(\frac{S}{\omega_7}\right)^2 + 1\right]}{\left[\left(\frac{S}{\omega_4}\right)^2 + 1\right]\left[\left(\frac{S}{\omega_6}\right)^2 + 1\right]\left[\left(\frac{S}{\omega_8}\right)^2 + 1\right]} \quad (8)$$

RADIAL SUSPENSION MODEL

By neglecting gyroscopic effects, a model that is valid at zero shaft speed may be produced analytically.

Figure 13 presents a simplified mechanical drawing of the radial suspension systems. The $x_1 - y_1$ coordinate system is located at the axial position of the upper radial MFG. The forces produced by this bearing in the x and y directions are F_{x1} and F_{y1}, respectively. Similar nomenclature exists for the lower (subscript 2) bearing. The distances d_1 and d_2 refer to the moment arms of the upper and lower bearings about the center of mass of the shaft.

Magnetic loss dynamics in the radial bearings are a much higher-frequency effect than those of their axial counterpart. For this reason, Eq. (3) is an adequate approximation for purposes of analysis.

The net force in the x direction and the net torque about the y axis at the center of mass of the shaft are

$$\Sigma F_x = F_{x1} + F_{x2}$$

$$\Sigma \tau_y = d_1 F_{x1} - d_2 F_{x2} \quad (9)$$

Since there is no axis cross coupling at zero shaft speed, Newton's law and Euler's equation reduce to

$$\Sigma F_x - M_f \ddot{X}_{CM}$$

$$\Sigma \tau_y = I \ddot{\zeta}_1 \quad (10)$$

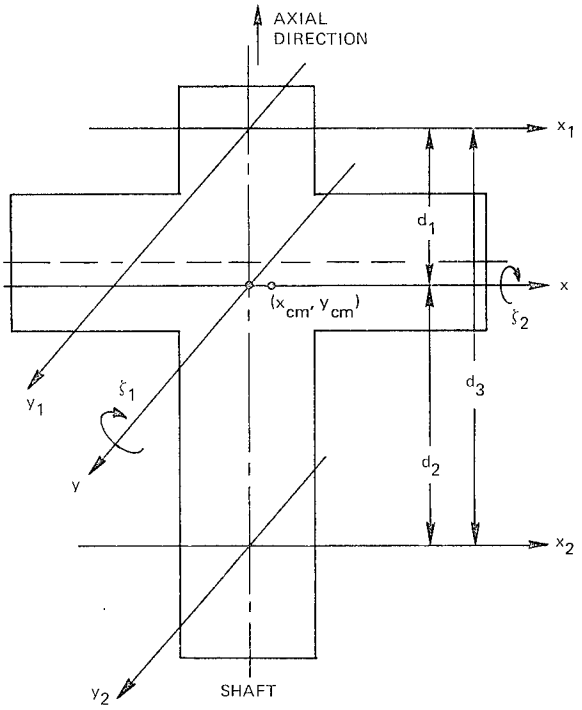

Fig. 13. Simplified radial plant mechanical schematic.

where

I = moment of inertia about x or y axis

ζ = angle of tip

By combining these equations and realizing that

$$x_1 = X_{cm} + d_1\zeta_1$$

$$x_2 = X_{cm} - d_2\zeta_1 \quad (11)$$

transfer functions relating radial control currents and motions may be written

$$\frac{X_1}{I_{cx1}}(S) = \frac{28.1\left[\left(\frac{S}{\omega_{11}}\right)^2 - 1\right]}{\left[\left(\frac{S}{\omega_9}\right)^2 - 1\right]\left[\left(\frac{S}{\omega_{10}}\right)^2 - 1\right]}$$

$$\frac{X_2}{I_{cx2}}(S) = \frac{20.0\left[\left(\frac{S}{\omega_{11}}\right)^2 - 1\right]}{\left[\left(\frac{S}{\omega_9}\right)^2 - 1\right]\left[\left(\frac{S}{\omega_{10}}\right)^2 - 1\right]} \quad (12)$$

The radial suspension system, possessing more degrees of freedom than the axial bearing, had additional minimum/nonminimum phase pole and zero pairs at ω_{10} and ω_{11} (17.7 and 18.0 Hz, 111 and 113 rad/s). This is sufficiently close to a perfect cancellation that it may be ignored for the purposes of compensator design. It does, however, leave a pair of transfer functions in the form of Eq. (4) with a pole frequency of 34.3 Hz, 216 rad/s.

These transfer functions correlate well with actual measurements (Fig. 14) except for the obvious resonance effects. Equations (12) have been made into radial equivalents of Eq. (8) by introduction of vibration spectrum data

$$\frac{X_1}{I_{cx1}}(S) = \frac{2.81}{\left[\left(\frac{S}{\omega_9}\right)^2 + 1\right]} \times \frac{\left[\left(\frac{S}{\omega_{12}}\right)^2 + 1\right]\left[\left(\frac{S}{\omega_{14}}\right)^2 + 1\right]\left[\left(\frac{S}{\omega_{16}}\right)^2 + 1\right]}{\left[\left(\frac{S}{\omega_{13}}\right)^2 + 1\right]\left[\left(\frac{S}{\omega_{15}}\right)^2 + 1\right]\left[\left(\frac{S}{\omega_{17}}\right)^2 + 1\right]}$$

$$\frac{X_2}{I_{cx2}}(S) = \frac{20.0}{\left[\left(\frac{S}{\omega_9}\right)^2 + 1\right]} \frac{\left[\left(\frac{S}{\omega_{18}}\right)^2 + 1\right]}{\left[\left(\frac{S}{\omega_{19}}\right)^2 + 1\right]} \qquad (13)$$

The resonant frequencies of Eq. (13) are presented in Table 1.

Table 1. Resonant radial frequencies. $\left[f_i = \frac{\omega_i}{2}\ (\text{Hz})\right]$.

Upper Bearing		Lower Bearing	
Zeros	Poles	Zeros	Poles
$f_{12} = 140$	$f_{13} = 160$	$f_{18} = 240$	$f_{19} = 600$
$f_{14} = 190$	$f_{15} = 210$		
$f_{16} = 320$	$f_{17} = 340$		

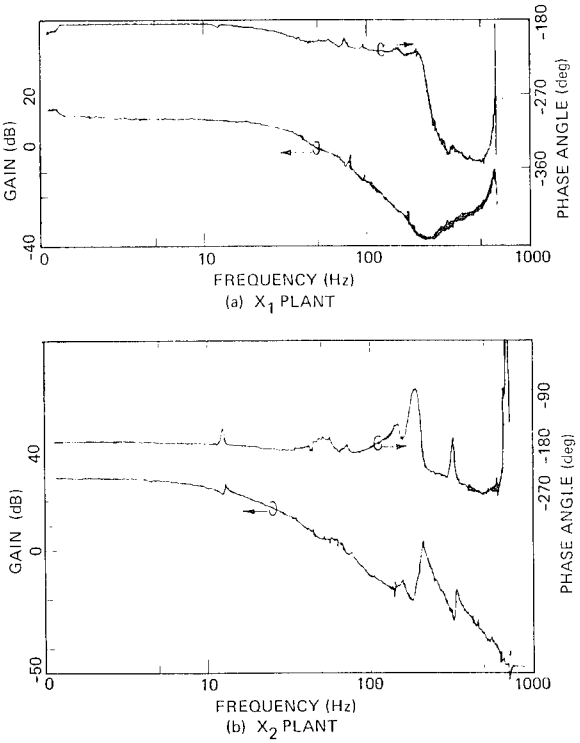

Fig. 14. Radial plant frequency responses.

CONTROL SYSTEM DESIGN CONFIGURATIONS

Compensation of the typical unstable plant (a minimum-phase/nonminimum-phase real pole pair) is most easily illustrated with open-loop Bode plot analysis. Figure 15(a) shows the magnitude and phase response of this unstable plant. A lead must be added to this plant response to achieve closed-loop stability. Figure 15(b) shows the consequence of adding the required lead at frequencies below ω_o (the frequency of the unstable pole). Stability in this case is, at best, marginal. Low-frequency loop gain is also very low. Thus, for good stability and reasonable loop gain, the minimum frequency for introduction of lead is ω_o as shown in Fig. 15(c).

To achieve a closed-loop bandwidth of $10\omega_o$, and therefore improve relative stability and loop gain, 20 dB of gain may be added to the system. Figure 16 illustrates the consequences of adding this gain in the presence of a resonance phenomenon of the type previously discussed. Since the gain at ω_c is greater than unity and the phase shift is less than -180 degrees, the system will oscillate at ω_c.

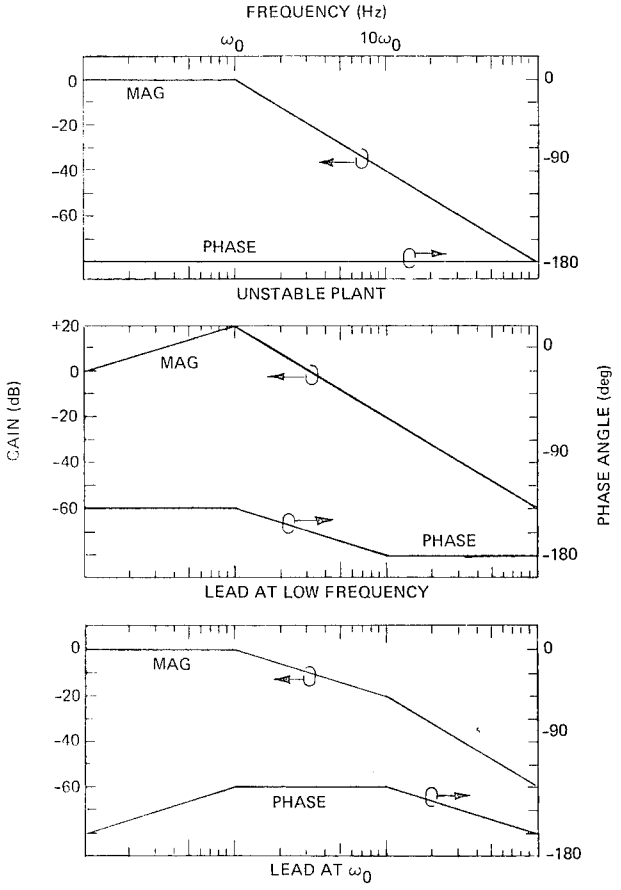

Fig. 15. Bode plot analysis of unstable plant control.

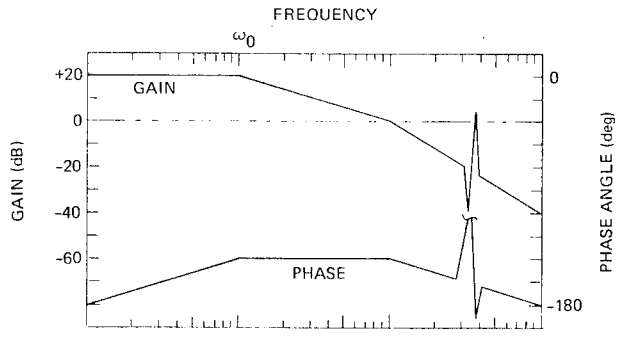

Fig. 16. Oscillation due to increased controller gain.

SYSTEM MODIFICATIONS

Alternatives for the solution of the mechanical resonance problem include mechanical modifications and the utilization of notch (band-reject) filters.

Because of the square-root dependence of frequency on stiffness, a four-fold increase in the stiffness of the flywheel enclosure will move the natural frequency of the spring-mass system by one octave.

In the axial suspension system, such an increase in stiffness may be accomplished by installation of a supporting structure about the flywheel enclosure. An increase in the stiffness of the housing spring was obtained by employing the loading scheme described in Fig. 17. Figure 18 is the frequency spectrum of the output of an accelerometer mounted to the upper housing during free oscillation of the structure. The greatest peaking occurs at a frequency of approximately 380 Hz. This is nearly an octave about the previous fundamental frequency of vibration.

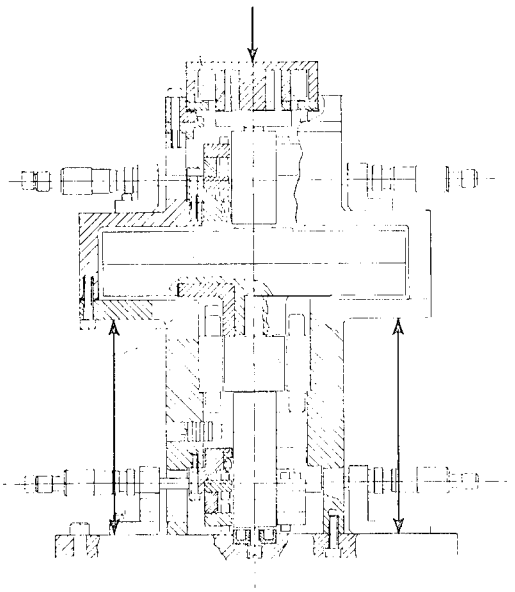

Fig. 17. Loading scheme to alter the flywheel housing stiffness.

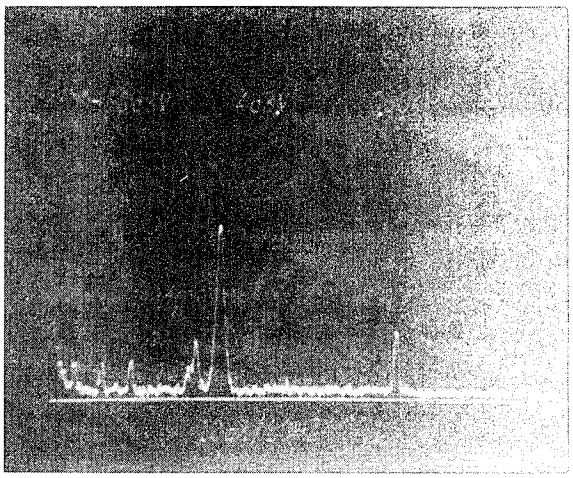

Fig. 18. Vibration spectrum of modified system.

The notch-filter option is best used when the compliant member is not accessible. Such is the case in the lower radial suspension. The resonance phenomenon observed may be traced back to the natural vibration of the flywheel shaft assembly. A notch-filter was required to close the radial loop in the presence of this high Q pole. Since the notch-filter produces approximately 30 dB of attenuation at the resonant frequency of the lower radial suspension, the loop gain may be increased by a factor of 10 to achieve proper stability without causing resonance-induced oscillation.

An active notch filter (Fig. 19) has certain advantages that make it preferable to a passive LC circuit. These include higher Q and less susceptibility to center-frequency drift. The presence of an extra pole at 92 Hz in the axial suspension system is undesirable. By adding one decade of lead (80 to 800 Hz) to the compensation network, the effect of this magnetically induced pole is placed well beyond the bandwidth of the closed-loop system.

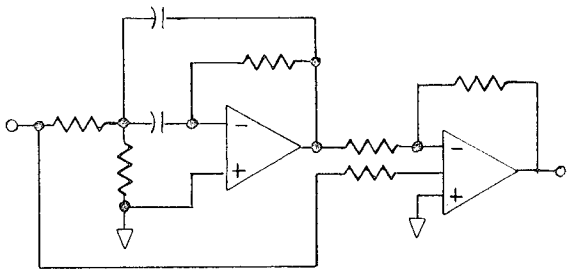

Fig. 19. Active notch filter.

Permanent magnet biased electromagnetic bearings have significant advantages over conventional suspension types in large-scale FESS applications (see Fig. 1). The technical problems that arise due to the nature of these bearings have been shown to be soluable.

REFERENCES

[1]D. Eisenhaure, G. Oberbeck, S. O'Dea, and W. Stanton, Final Report on Research Toward Improved Flywheel Suspension and Energy Conversion Systems, (The Charles Stark Draper Laboratory, Inc., Cambridge, MA, 1977).

[2]D. Eisenhaure and E. Kingsbury, Final Report on the Development of an Advanced Flywheel Bearing Performance Model (The Charles Stark Draper Laboratory, Inc., Cambridge, MA, 1978).

[3]D. Eisenhaure, G. Oberbeck, and J. Downer, "Development of a Low Loss Flywheel Magnetic Bearing," Proc. of 14th Intersociety Energy Conversion Eng. Conf., Vol. 1 (1979), pp. 357-362.

[4]R. Frazier, P. Gilinson, and G. Oberbeck, Magnetic and Electric Suspensions (MIT Press, Cambridge, MA, 1974).

[5]H. Schlicting, Boundary Layer Theory (McGraw-Hill, New York, 1955).

[6]S. Earnshaw, Trans. of the Cambridge Philosophical Society, Vol. 7 (1842), pp. 97-112.

[7]H. Roters, Electromechanic Devices (Wiley, New York, 1941).

[8]J. Downer, Analysis of a Single Axis Magnetic Suspension System (The Charles Stark Draper Laboratory, Inc., Cambridge, MA, 1980).

[9]S. Timoshenko and S. Winowsky-Kreiger, Theory of Plates and Shells (Mc-Graw Hill, New York, 1959), pp. 58-63.

MAGNETIC BEARING SUPPORT OF A 10 KW HR ENERGY STORAGE FLYWHEEL

Martin W. Eusepi
Program Manager, Advanced Technology Department, R&D Division
Mechanical Technology Incorporated
Latham, New York 12110

Donald F. Wilcock
Senior Management Engineering Consultant
Mechanical Technology Incorporated
Latham, New York 12110

ABSTRACT

A 10 KW HR energy storage capacity flywheel, for stationary installations, was taken as a central design point for a range of flywheel sizes from 1 KW HR to 100 KW HR in capacity. Because of the need to minimize frictional losses in order to achieve rational storage lifetime, this study assumed a magnetic bearing construction. In order to avoid both the complexities and the power consumption of servoed types of magnetic bearings, the object of this study was to examine the feasibility of passive magnetic suspension systems for the primary weight-carrying function, combined with small low loss fluid film bearings for the horizontal support function and the stability damping function.

The paper presents the results of this study showing details of both the magnetic suspension and the fluid film bearing support and damping suspension. The total loss function for the flywheel operating in a low vacuum environment to eliminate windage losses was found to be attractive. The end result is a design employing convetional steel for the wheel while retaining practical performance characteristics of cost and efficiency for a stationary installation where size and weight are not critical performance parameters.

The full text of this paper was not available for inclusion in this volume of the Proceedings. It will be published later in a separate volume.

HYDRAULIC ACCUMULATORS AS ENERGY BUFFERS; THERMODYNAMIC MODELING AND THERMAL LOSSES

David R. Otis
University of Wisconsin-Madison
Department of Mechanical Engineering
1513 University Ave.
Madison, WI 53705

ABSTRACT

A review is presented of hydraulic accumulator research related to their employment as energy buffers in vehicles. The need for abandoning the ideal gas assumption is discussed and appropriate literature cited for the treatment of the charge gas process and for the assessment of thermal losses.

INTRODUCTION

The results of many studies have established the hydraulic accumulator as having much too low an energy density (on either a weight or volume basis) to serve as any more than an energy buffer in vehicle propulsion systems, and then only for specialized missions. Yet, even in this limited domain, it appears that hydraulic hybrids are beginning to appear, and this author is surprised to find that the thermodynamic analyses still employ calculation techniques that have long ago been proven to be inadequate and even misleading. This paper will review those developments of which this author is aware, and discuss the modeling of the thermodynamic process experienced by the charge gas.

An accumulator is often used in hydraulic systems for energy storage and pulsation damping. There is an enclosed charge gas volume usually separated from the hydraulic fluid by a piston (as in Fig. 1) or a rubber bladder. As hydraulic fluid is pumped into the accumulator, the charge gas (usually nitrogen) is compressed storing available energy. It is simply a gas spring. The idea of using such a device in urban vehicles undoubtedly arose independently in many minds. An early reference by Benson goes back to 1950[1]. And since 1965 he has developed Stirling cycle engines with an accumulator energy buffer[2,3]. Beale[4] has carried on a parallel development of the Stirling engine and had early recognized the natural coupling with an accumulator energy buffer[5]. The most public attention was probably accorded Dunn and Wojciechowski[6,7,8] who constructed a laboratory simulation with a VW engine and a five gallon accumulator. Tartaglia[9] modified a 1971 Datsun 510 with a 20 hp Wankel engine and an 8 gallon accumulator. Carman[10] has converted a Ford Granada to a hydraulic drive with an accumulator energy buffer and reports 38.4 mpg over an urban course where the same model standard Ford got 16 mpg. There have been a number of other implementations during the 1970's especially as entries in the SCORE competitions[11,12,13].

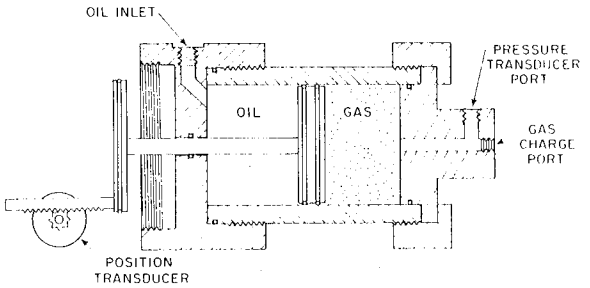

Fig.1. A schematic drawing of the 2-liter piston accumulator used in the tests.

Our first effort at the U.W.-Madison was the construction of a hydraulic bicycle (Fig. 2) for the 1971 U.W. Engineering Exposition[14] which was followed by a stationary prototype of an urban vehicle with a 15 kw Sachs Wankel, six two-liter accumulators, and two 14 kg flywheels. Very little useful data came from our endeavors except to show that it could be done, and to demonstrate that

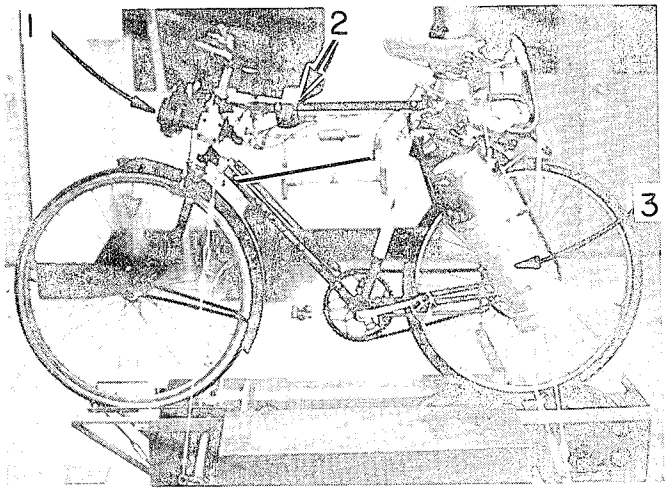

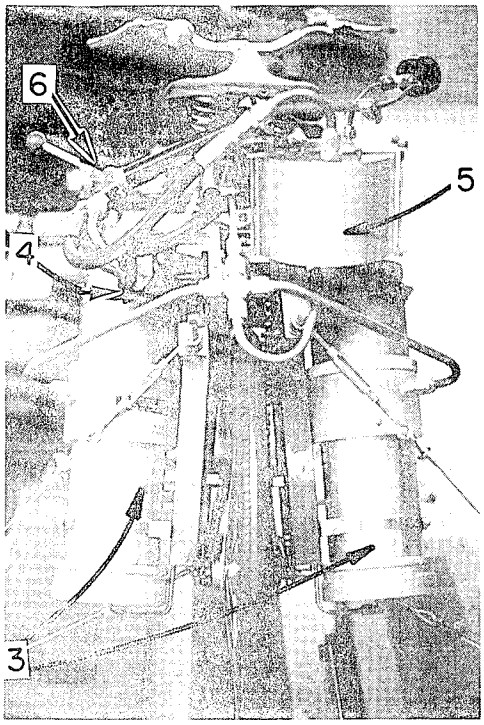

Fig. 2. Hydraulic drive bicycle. A 2-cycle gasoline engine (1) drives an oil pump (2) to fill the hydraulic accumulators (3). A hydraulic motor (4) drives the rear wheel by a chain. For stoppint, the motor acts as a pump pumping oil from the reservoir (5) into the accumulators. Control is accomplished by a 4-way valve (6).

regenerative breaking could be accomplished with reasonable efficiencies. Figure 3 shows the decay of stored energy when cycled between the flywheels and the accumulators, and over the eight cycles an average value of 73% energy recovery per cycle was attained[15].

Based upon our experiences and the best data available from component manufacturers, a computer simulation was carried out for several vehicles to determine their performance on the EPA driving cycle[16,17]. The conclusions of that study were: engine size and fuel consumption can both be reduced by a factor of two with accumulator weight penalty less than 5% of vehicle weight if top speed is limited to 55 mph. These gains were attained in spite of the fact that hydraulic pump and motor efficiencies were quite low at low swash plate angles, and improved designs now overcome some of these earlier difficiencies. Other more recent computer simulations[18,19,20] have reached similar conclusions, and based on one of these a Leyland citybus was to be modified and on trial in the city of Copenhagen by the summer of 1979.

A detailed study at Lawrence Livermore Laboratories[21] explored all types of energy storage systems for automobile propulsion and concluded that mechanical systems do not meet range requirements but are suitable for "buffering". Of the three most promising (see Table 1) the hydraulic accumulator has the lowest energy density being lower than the flywheel by a factor of roughly five. However, as pointed out by Miller and Rasmussen[22] and based upon their experience with a hydraulic hybrid (with 16 hp engine, 500 cu. in. accumulator on a VW chassis yielding 75 mpg), the accumulator size can be much smaller than one might expect if the vehicle driver would anticipate future demand. This work at Honeywell provided the seed for a continuing work on buffering for electric vehicles, and in their recent final report by Buchholz and Mathur[23] they favored the

Table 1. Projected Energy Densities for Mechanical Storage Devices (from Ref. 21 for 75% confidence levels

Storage System	Energy Density - W-h/Lb		
	By year 1982	By year 1990	By year 2000
Flywheel	13.0	17.0	19.0
Compressed air	10.7	17.5	19.5
Hydraulic Accum	1.7	2.0	2.6

hydraulic accumulator (flywheels were excluded by DOE because of extensive work elsewhere) and showed range gains of 19% with conventional technology. In their studies, overall hydraulic system efficiencies were quite low due to frequent operation at small swash plate angles, a problem mentioned earlier, and for which there is hope of improvement. On an optimistic note, a recent study by Benson[24] based on a free piston Stirling engine with an isothermalized accumulator showed 211 mpg for a modified Lewis Research Center urban cycle. Other hybrid engine concepts have been proposed by Heinz[25] and by Ferris[26] both with accumulator energy buffers.

To date, none of these efforts has resulted in a commercially successful vehicle.

In addition to the Copenhagen bus modification, there are several active development vehicle projects. Research at the Technical University of Berlin under Prof. Willumeit[27] has led to the funding of a hydrobus now being developed by M.A.N. of Germany. As reported by Scott[28] (ed. for Auto. Engr.) the 80 passenger double-deck hydrobus prototype is under test in Munich and is expected to be running in Berlin in 1982. A 25% fuel saving is forecast along with benefits of lower emissions, quieter operation, and reduced brake wear. It has a stepless hydrostatic transmission and is propelled by a 100 kw engine. It weighs 16,000 kg, the accumulators weigh 380 kg (but reduced engine weight makes the net increase 200 kg), and will recover braking energy from 50 km/hr with maximum pressure of 330 bar (4785 psi). This amounts to an energy density for the system of about 1 W h/kg (4 kJ/kg).

The M.A.N. effort is also of interest to this conference because of their concurrent development of a flywheel bus (gyrobus) with about five times the energy storage capacity of the hydrobus. As stated by Scott[28], the main gyrobus problem is the demand for an efficient transmission that can handle the inverse relationship between vehicle and flywheel speeds. Beachly and Frank[29] have indicated that this component is the most critical for a flywheel hybrid system accounting for the highest energy loss over a typical driving cycle (about 30%). Accumulators do not have this inverse speed relationship to contend with. But

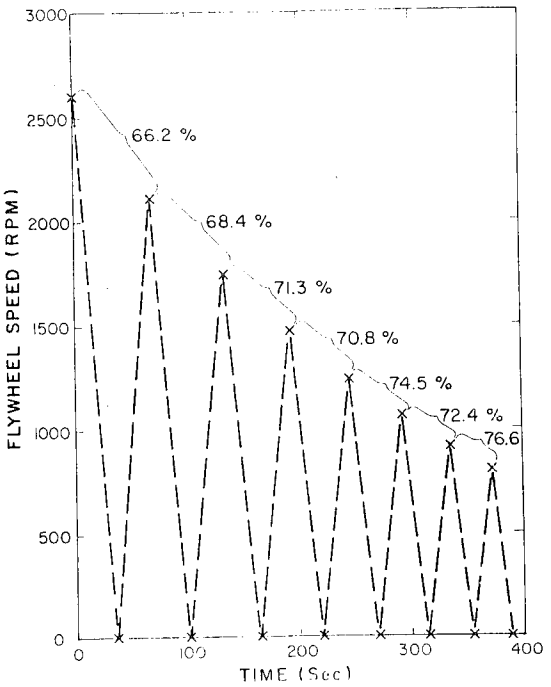

Fig. 3. Flywheel speed versus time as energy is cycled between the flywheels and a bank of three 2-liter accumulators.

they have a problem of their own, namely, hydraulic system pressure usually operates substantially below rated values except when the vehicle is stopped with accumulators fully charged.

In view of the foregoing it appears that hydraulic accumulators will play a limited but not unimportant role in urban transportation even without major new developments.

I would like to turn now from this introductory survey to a topic that has consumed my interest for a number of years: the thermodynamic modeling of the charge gas process, and thermal losses.

THERMODYNAMIC PROCESS MODELING

Most users of hydraulic accumulators ask only the questions "What type and how large?" The work cycle may not be well defined. The charge gas is usually treated as ideal, and the processes are assumed to be adiabatic or isothermal. Many useful papers have been written to guide in the selection of an

accumulator[30-41], but most of these suffer from two important limitations: thermal losses are ignored, and nitrogen is treated as an ideal gas. Important exceptions are: Klein[36] who recognized thermal losses and gave efficiencies for some typical work cycles, Korkmaz and Walz[37] who extended Klein's work, and Beachley[39] who showed the difficiency of the ideal gas assumption.

Even though the design guides generally ignore the thermal loss, most users are aware of it. When the pump stops, system pressure drops as the compression heated charge gas cools; but while perceived as a loss, the user can neither quantify nor control it. I am often asked, "Why not insulate the outside of the accumulator?" But this misses the point! The destruction of available energy[✧] is proportional to the product of the heat flux and the temperature gradient, and this product is maximum in the boundary layer where the charge gas is in contact with the accumulator walls (or the rubber bladder). Insulating the walls on the outside is absolutely to no avail and may result in overheating, since the dissipated energy must be carried away from the system as heat. Insulating the walls on the inside would reduce the loss, but it would be difficult, and the higher gas temperatures could have undesirable effects on the oil and elastomeric materials. One study[23] suggests that if the accumulator is insulated there will be no loss at all; this is incorrect and shows a basic misunderstanding of "thermal loss".

Figure 4 shows a family of pressure-volume histories measured for the charge gas of a two liter piston-type accumulator of the type shown in Fig. 1. The sinusoidal piston motion produces gas volume variations from ±8.6% to ±42%. The enclosed area represents the "energy loss" (or more properly, the available energy destruction), and the fractional loss is indicated in the table insert for each curve. The loss increases

✧The "available energy" (or "availability") of a system is defined as the maximum work that can be produced with heat transport only with the surroundings[42]. Available energy is destroyed in every real process, and "thermal loss" refers to that destruction.

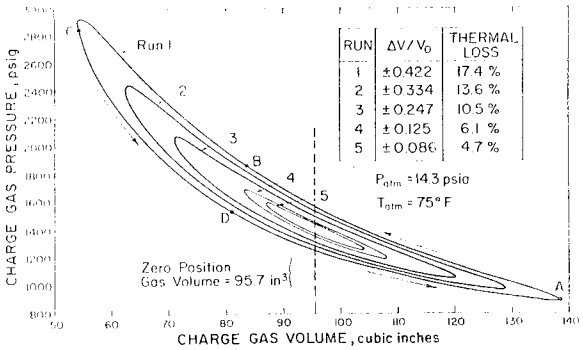

Fig. 4. Pressure-volume measurements for the charge gas of a 2-liter accumulator with sinusoidal volume variation at 0.01 hz. Compression, A-B-C; expansion, C-D-A.

almost linearly with piston stroke, and there is also an increase with precharge pressure (not shown). For this particular accumulator, the maximum loss occurs at 0.01 hz (corresponding to a thermal time constant of $1/2\pi(0.01)$ sec.), and the frequency dependence is shown in Fig. 5 for $\Delta V/V_0$ = 27%. During the cycle, heat is transported from the gas to the accumulator walls during compression, and back into the gas during expansion. The heat capacity of the walls is so large, that wall temperatures vary only a few degrees compared to gas temperature variations of say 100 degrees. Insulating the accumulator on the outside would have virtually no effect on the curves in Fig. 4, except that the average temperature and pressure would creep upward to a level

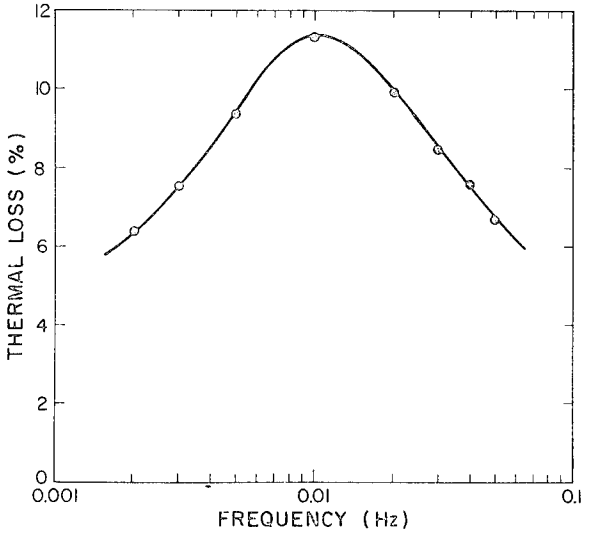

Fig. 5. Thermal loss versus piston frequency for the 2-liter accumulator with a nitrogen precharge pressure of 100 bar (1450 psig) and a volume change of ±27%.

that would permit the dissipated energy to be removed through the insulation. Hence the only effect is to make the system operate hotter, and the loss remains unchanged.

Figure 5 shows that the thermal loss approaches zero in the two extremes of very rapid cycling (adiabatic) and very slow cycling (isothermal), and it is only these two limits that are considered by most of the design guides. But it is the experience of this author that one is seldom near the limits, especially in a vehicle hydraulic hybrid system. Hence, there is a need for a calculation procedure that properly models the thermodynamic behavoir of the charge gas for any process or cycle.

At U.W.-Madison a method was adapted from a thermal damping model which had been used to predict thermal losses in foams during impact[44]. It was first developed for the ideal gas[45], and later

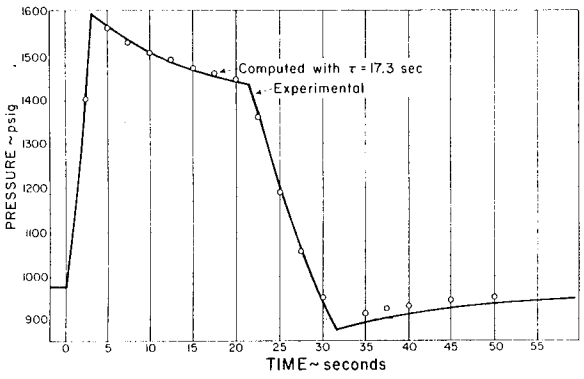

Fig. 6. Comparison of measured and computed pressure history for a 2-liter accumulator.

incorporated real gas properties for nitrogen[17,46,47]. Figure 6 compares predicted and measured pressure histories for a cycle consisting of a compression, a constant volume holding period, an expansion, and a constant volume holding period. The agreement is quite good, and the method allows one to quantify the magnitude of the loss for any combination of processes. By many similar comparisons, it has been found that nitrogen can be treated as an ideal gas only for pressures below 100 bars (1450 psi); fortunately, real gas properties can be introduced into the computer program with little increase in complexity. Many authors persist in assuming ideal gas even up to 200 bars (2900 psi) insisting that

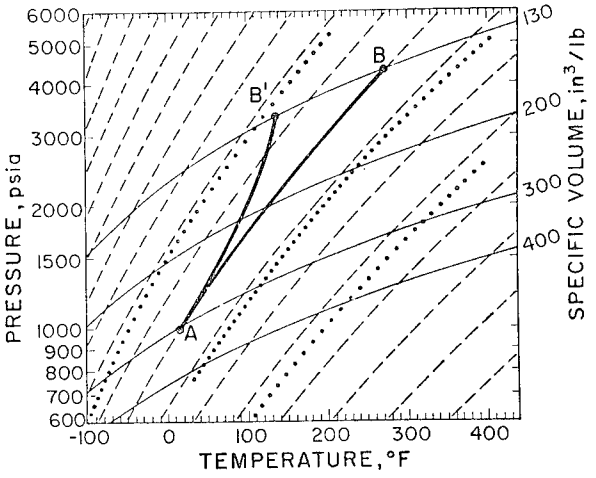

Fig. 7. Plot of Din's nitrogen data showing constant entropy lines (----). Dotted lines (....) are constant entropy lines calculated using the computer program. An isentropic compression process is shown along A-B. If one assumes ideal gas, the isentropic process would be computed as A-B'.

the errors are small. Apparently, they are looking only at the p-v-T relationship and/or isothermal processes where the error is only a few percent. But a larger error lies in the calculation of entropy, and one can see the divergence between ideal and real gas properties for an isentropic process in Fig. 7. Gangrath and White[48], Beachly[39], and Green[49] have also all made this point.

Figure 8 shows the thermal losses predicted using the aforementioned method for a cycle that is more typical of vehicle operation: charging (vehicle decelleration, gas compression), a holding

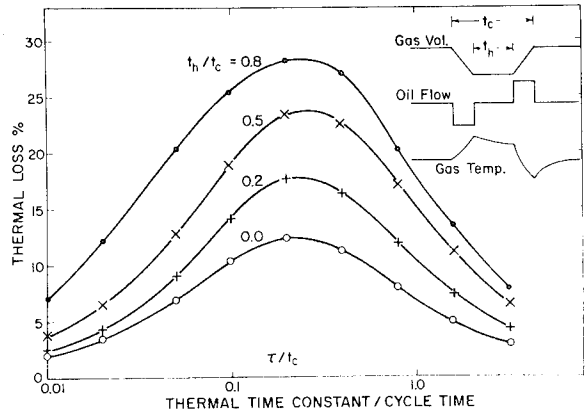

Fig. 8. Thermal loss versus τ/t_c where τ = time constant (about 17 sec. for 2-liter accum.), and t_c is the cycle period.

period (vehicle stopped, constant gas volume), and discharging (vehicle accelerating, gas expansion). For example, for a cycle consisting of a 30 second wait at the traffic light and 10 seconds for both stopping and starting (50 seconds total), and with a 10 gal. accumulator with a time constant of 100 seconds[†], the thermal loss would be 9.3%. The loss can be substantial, attaining a value of about 30% for an infinite holding period for a volume ratio of 0.5 (corresponding to an adiabatic pressure ratio of 3).

By use of this simple model, the designer can accurately predict the performance of an accumulator in a hydraulic hybrid system.

FREE CONVECTION IN THE CHARGE GAS

A model for the thermodynamic processes within the charge gas requires an understanding of the heat transport mechanisms occuring within the charge gas and between the gas and the surrounding walls. For operation typical of a hybrid vehicle (process times of 10 seconds or greater at pressures greater than 70 bar), the thermal transport can be described as unsteady free convection with strong stratification and with transition from laminar to turbulent flow during the cycle. The Rayleigh numbers are greater than $10^{00}10$ so that turbulent flow would ordinarily be expected. But with a cyclical process, the flows must reverse direction, and as the frequency increases there is not enough time for instabilities to develop into turbulence. At these high Rayleigh numbers, one would expect the fluid motions to be confined to boundary layers on the walls, and this is confirmed by our experiments. Heat flux data measured by Levine and Otis[51,52] shown in Fig. 9 for the top, side and bottom of the enclosure show an interesting heat pump effect due to stratification. There is a net heat flow out the top and in at the bottom owing to the formation of hot

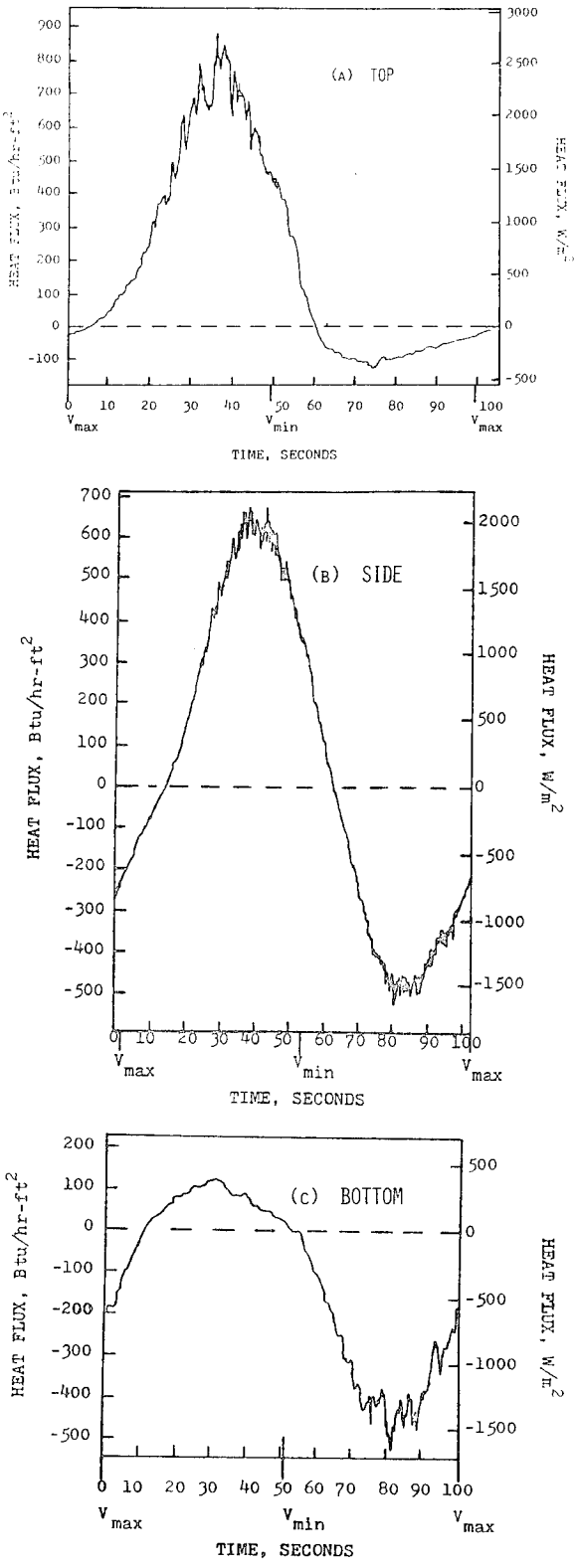

Fig. 9. Heat flux histories at the top, side and bottom surface of the gas enclosure measured for sinusoidal piston motion at 0.01 hz.

[†]Larger calculated values for the time constant reported in the literature[22] are not supported by experiment. Buchwald, et al[19] has reported a measured value of 125 sec. for a 140 liter bladder accumulator, and this author has measured 35 sec. for a 25 liter bladder accumulator.

and cold pools. The process is far more complex than one might have supposed.

Several authors have suggested that accumulators could be operated at constant pressure (isobaric), and this would increase their energy density be a factor of three.[53] This idea was patented in 1871 by Baldwin where he suggested using carbon dioxide and steel wool to maintain a constant pressure of around 850 psi. Unfortunately, there seem to be no gases available with saturation pressures in the 100 to 200 bar range (1450 to 2900 psi), and even if there were, the convection and stratification phenomena just mentioned might cause some difficulties. It is likely that condensation and evaporation may not be reversible (this author has run some experiments with Freon 12 and carbon dioxide that would suggest this) due to the strong gravitational effect on the denser phase. This is an interesting area which should be investigated.

REDUCTION OF THERMAL LOSSES

Thermal losses should never be regarded as a barrier to the practicality of accumulator energy storage, for they can be virtually eliminated. One method is to fill the charge gas volume with an open-celled foamed elastomer which provides an internal insulation as well as additional heat capacity[46,50,54]. Figure 10 illustrates the reduction in the size of the hysteresis loop by using a urethane foam. Amazingly, accumulator manufacturers have shown little interest in this innovation.

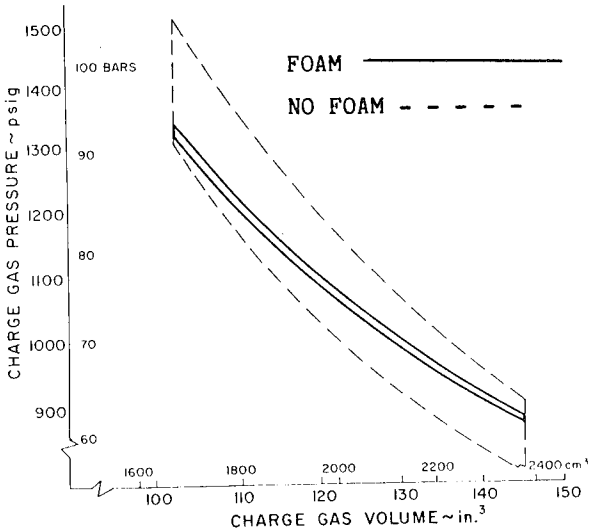

Fig. 10. Pressure-volume measurements traced directly from an X-Y plotter. The dashed line is for the conventional

A novel "isothermalized" accumulator has been developed by Benson[3] and is being used with his Stirling engine hybrid system. The gas charge space is partially filled with a rigid reticulated metal foam, with the remaining space filled with the charge gas and a silicone liquid. When hydraulic fluid displaces the piston, the silicone fluid moves into the metal foam acting as a piston. The gas is then compressed within the metal foam, and the large heat capacity of the foam assures a small temperature rise. In principle this operates the same as the elastomeric foam filler mentioned above. Benson has reported thermal losses of less than 2% with this system.

A method proposed by Sherman and Karlekar[55] involves adding fins to the inside of the accumulator in the form of fine copper wires soldered to the accumulator, but this "hairy wall" would seem to be an expensive solution.

The frequency at which the peak loss occurs is a function of accumulator size, and by replacing one accumulator by several smaller ones, a change in the loss (for better or worse) can be affected. It should also be mentioned that thermal losses are sometimes desirable in situations where damping must be added to the hydraulic system for stability.

CLOSURE

It is hoped that this survey of hydraulic accumulator buffering and the discussion of thermal losses will familiarize the reader with what has been done and indicate sources of more detailed information.

REFERENCES

1. Benson, G. M., "Rotary Engine Hydrostatic Drive System," AAAS Paper, Minn., MN, 1950

2. Benson, G.M., "Thermal Oscillators," Proc. 8th IECEC, Phil., PA, Aug. 1973.

3. Benson, G. M., "Thermal Oscillators," and "Free-Piston Heat Pumps," two papers in Proc. 12th IECEC, Wash.,DC, Aug. 1977.

4. Beale, W. T., "A Stirling-Hydrostatic Drive for Small Vehicles," Proc. 10th IECEC, Aug. 1975, p. 958.

5. Beale, W. T., "Vehicle Drive System," private communication, September 30, 1971

6. Dunn, H. Searl and Wojciechowski, Paul H., "High-Pressure Hydraulic Hybrid With Regenerative Breaking," Proc. of the 7th IECEC, San Diego, Sept. 1972, pp 989-995 (Paper No. 729145)

7. Dunn, H. S. and Wojciechowski, P. H., "Energy Storage and Conversion Efficiency in a Hydraulic/Gas-Turbine Hybrid," Gas Turbine and Products Show, Zurich, Switzerland, March 30, 1974, ASME Paper No. 74-GT-107.

8. Wojciechowski, P.H. and Dunn, H.S., "Energy Regeneration and Conversion Efficiency in a Hydraulic Hybrid Propulsion System," High Speed Ground Transportation, v. 9, no. 1, 1975, p.383.

9. Tartaglia, P. E., "A Low Pollutant, High Energy Efficiency Hybrid Hydraulic Power Plant," Intersociety Conference on Transportation, Denver, Sept. 1973, ASME Paper No. 73-ICT-4.

10. Thoms, Wayne, "A Car That Can Store Power," Mechanix Illustrated, November 1977, p 60.

11. Agnew, P. W., "Regenerative Vehicle Transmission," Department of Mechanical Engineering, The University of Glasgow (private communication); see also "Braking Energy," Machine Design, March 1973, p. 33.

12. Tencer, A., pictures and letter describing the McGill University entry in the SCORE competition, private communication, June 7, 1972.

13. Student Competitions on Relevant Engineering, Inc. (SCORE,Inc.), John H. Sununu, Advisor, 105 Anderson Hall, Tufts University, Mass 02155. In particular see reports for 1972 competition (pub. 1973) and 1979 (in preparation).

14. Sanborn, Steve, "Coast Uphill!", The Wisconsin Engineer, U.W.-Madison, October 1971, p 15-17

15. Dewey, C., Elder, F. T., and Otis, D. R., "Accumulator-charged Hydrostatic Drive for Cars Saves Energy," Hydraulics and Pneumatics, October 1974, p 180-183.

16. Elder, F. T. and Otis, D. R., "Simulation of a Hydraulic Hybrid Vehicle Power Train," Intersociety Conference on Transportation, Denver, Sept. 1973, ASME Paper No. 73-ICT-50.

17. Elder, F. T., "Hydraulic Accumulator Modeling with Applications to Availability Destruction and to a Hybrid Vehicle Simulation," PhD thesis, University of Wisconsin-Madison, 1974.

18. Svoboda, J. V., "Analogue and Digital Modelling in the Design of a Hydraulic Vehicular Transmission," Proc. Instn. Mech. Engrs., v. 193, pp 277-286.

19. Buchwald, P., Christensen, G., Larsen, H., and Pedersen, P. Sunn, "Improvement of Citybus Fuel Economy Using a Hydraulic Hybrid Propulsion System -- A Theoretical and Experimental Study," SAE Paper No. 790305.

20. Heggie, W. S., and Sandri, R., "An Energy-Saving Hydro-Pneumatic Power Plant for the Automobile," ASME Winter Annual Meeting, Dec. 1979, ASME paper no. 79-WA/DSC-15.

21. Behrin, E., et al, "Energy Storage Systems for Automobile Propulsion, vol. 1, Overview and Findings," Univ. of Calif., Lawrence Livermore Lab., UCRL 52303/1, Dec. 1978.

22. Miller, J., and Rasmussen, R., "Hydraulic Accumulators for Hybrid Automobiles and Transport Vehicles," Univ. of Calif. Lawrence Livermore Lab., UCRL 13757, Rep. No. 10017 FR, Ju 26, 1977.

23. Buchholz, R., and Mathur, A., "Assessment and Preliminary Design of an Energy Buffer for Regenerative Braking in Electric Vehicles," DOE/NASA/0048 79/1, NASA CR 159756, Honeywell TSC 10082 FR.

24. Benson, G. M., "Free Piston Stirling Engine Accumulator Buffered Hydrostatic Vehicle Drive," Energy Research and Generation, Inc. report.

25. Heinz, Richard P., "A Free Piston Engine-Pump for a Hybrid Automotive Propulsion System," Private communication, March 1980

26. Ferris, James Jay, "Toward a Hydraulic Prime Mover," Off Highway Vehicle Meeting Expo. MECCA, Milwaukee, Sept. 1978, Paper No. 780748.

27. Willumeit, Prof. Dr.-Ing. H.-P., private communication, June 9, 1975.

28. Scott, David, "Regenerative Breaking Cuts Bus Fuel Needs," Automotive Engineering, October 1979, pp 102-107.

29. Beachley, N.H., and Frank, A.A., "Mechanical Continuously Variable Transmission Degigns for Flywheel Energy Storage Automobiles," Proc. 1979 Mechanical and Magnetic Energy Storage Contractors Review Meeting, CONF 790854, Dec. 1979.

30. Jacobellis, Alphonse A., "Accumulators," Machine Design, March 22, 1962, pp 22-29.

31. Jacobellis, Alphonse A., "Accumulator Size Selection," Machine Design, January 18, 1962, pp 187-190.

32. Dodge, Louis, "Selection Procedure for Hydraulic Accumulators," Product Engineering, August 6, 1962, pp 60-67.

33. Ernst, Walter and Purcell, Howard, "Principles of Fluid Power Storage: Part 1 -- Pressure-Volume Relationships," Hydraulics and Pneumatics, December 1963, pp 97-99 and "Principles of Fluid Power Storage: Part 2 -- Verifying Tests for Pressure-Volume Relationships," Hydraulics and Pneumatics, February 1964, pp 53-58.

34. Hare, R. W., "Selecting a Hydro-Pneumatic Accumulator," Fluid Power International, May 1964, pp 203-206.

35. Russell, John G., "Sizing Accumulators for Pulsation Damping," Hydraulics and Pneumatics, August 1965, pp 71-75.

36. Klein, H. Ch., "Anvendung Hydropneumatischer Energiespeicher in der Olhydraulik,", Konstruction, 16 (1964) Heft 1, S. 12-21.

37. Korkmaz, F. und Walz, L., "Hydrospeicher als Energiespeicher Ideales und Reales Verhalten des Energietragers," Olhydraulik und Pneumatik, 18 (1974) Nr. 2, S. 132-140.

38. Wingate, I., "A Simplified Calculation Method for Hydraulic Accumulator Selection," Power, October 1975, pp 361-365.

39. Beachley, Norman H., "Graphical Determination of Accumulator Characteristics Using Real Gas Data," First Fluid Power Controls and Systems Conference, May 23-25, 1973, Univ. of Wisconsin-Madison.

40. Hydraulic Handbook, Chapter on Accumulators, Trade and Technical Press Ltd., Morden, Surrey, England, 1976.

41. Zahid, Zeke, "Accumulators and Their Applications," Greer Hydraulics, Inc., 1976.

42. Gaggioli, R.A., "Thermodynamics:Second Law Analysis," ACS Sym. Series 122, 1978, pp. 1-13. See also Obert, E.F., Concepts of Thermodynamics, McGraw Hill, 1960, pp. 141-143.

43. Otis, D. R., "Getting Maximum Energy-Savings From Your Accumulator," Hydraulics and Pneumatics, December 1979.

44. Otis, David R., "Thermal Damping in Gas-Filled Composite Materials During Impact Loading," Trans. ASME J. App. Mech., March 1970, pp 38-43.

45. Otis, D. R., "Predicting Performance of Gas Charged Accumulators," First Fluid Power Controls and Systems Conference," May 23-25, 1973, Univ. of Wisconsin, Madison.

46. Otis, D. R., "New Developments in Predicting and Modifying Performance of Hydraulic Accumulators," Proc. of 1974 National Conference on Fluid Power, Philadelphia, Nov. 1974.

47. Elder, F. T. and Otis, D. R., "Accumulators: The Role of Heat Transfer in Fluid Power Losses," Proc. 4th International Fluid Power Symposium, April 16-18, 1975, Sheffield, England, pp D2-27 to D2-37.

48. Gangrath, R. B., and White, W. H., "Optimization of Hydraulic Accumulators for Low Temperature Applications," SAE Paper No. 711B, June 1963.

49. Green, W. L., "The Effects ofDischarge Times on the Selection of Gas Charged Hydraulic Accumulators," Third International Fluid Power Symposium, Turin, May 9-11, 1973.

50. Otis, D. R., "Thermal Losses in Gas-Charged Hydraulic Accumulators," Proc. 8th IECEC, Philadelphia, August 1973, Paper No. 739093.

51. Levine, Andy, "Natural Convection and Availability Losses for Nitrogen Gas in a Piston-Cylinder Enclosure with Sinusoidal Piston Motion," MS Thesis, Dept. of Mech. Engr., Univ. of Wis.-Madison, 1979.

52. Levine, Andy H. and Otis, David R., "Free Convection in a Piston-Cylinder Enclosure with Sinusoidal Piston Motion," to be presented at the 1980 National Heat Transfer Conference, Orlando, July 1980.

53. Baldwin, J.S., "Improvement in Accumulators for Liquids Under Pressure," U.S. Patent No. 121,482, Dec. 5, 1871.

54. Otis, D. R., "Plastic Foams Reduce Heating in Gas-Charged Accumulators," Hydraulics and Pneumatics, February 1975, pp 56-57.

55. Sherman, M. P., and Karlekar, B. V., "Improving the Energy Storage Capacity of Hydraulic Accumulators," Proc. 8th IECEC, Philadelphia, August 1973, Paper No. 739094.

ACKNOWLEDGEMENT

I would like to acknowledge and thank the many contributors to the work at Madison who go unnamed in the reference list: Bob Schasse who constructed the first hydraulic bicycle, John Olsen who prepared all the figures, Mary Stampfli who typed many of the referenced papers (but cannot be blamed for this one which was done by computer), Mark Ganter who helped me with the word processor. The following industrial gifts are acknowledged: a 3 gal. accumulator from Greer Olaer, an 8 hp engine from Briggs Stratton, and a variable displacement pump from Sundstrand.

HIGH PERFORMANCE DUAL MODE CAR

D. W. Rabenhorst
The Johns Hopkins University Applied Physics Laboratory
Johns Hopkins Road
Laurel, MD 20810

ABSTRACT

The extensive use of electric vehicles in place of the present combustion engine vehicles would result in significant improvements in petroleum consumption, urban pollution and noise. However, the electric vehicle is not likely to be widely accepted until its performance can be made more competitive with the vehicles it is intended to replace. The use of flywheel energy storage systems in recent hybrid electric vehicles has resulted in some improvement in range, but not in its acceleration.

In other experiments small engines have been added to otherwise all-electric vehicles to provide improved range capability, but again the use of the all-electric drive components seriously restricts acceleration performance. Some experiments with flywheel/engine hybrid vehicles have resulted in improved fuel consumption, but at the expense of considerable additional complexity in the power train necessitated by the fact that independent control of engine speed, flywheel speed, and vehicle speed is required. Also, this flywheel/engine hybrid vehicle does not offer the advantages of electric vehicle propulsion.

Recently it has been concluded that an attractive vehicle would be one which could be operated either as a true electric vehicle, or as a combustion engine vehicle. Unfortunately, the designs that have been publicized to date are still based essentially on all-electric propulsion trains, resulting from the fact that they utilize electric storage batteries for the electric vehicle mode. When engine use is required, it is used either alone or with the electric power train. In either case the acceleration and passing performance is much less than in a conventional engine vehicle.

The present paper describes a new concept dual mode vehicle which combines the advantages of the electric and engine operating cycles without compromising vehicle acceleration. This vehicle utilizes a relatively large flywheel for the electric driving cycle, instead of batteries. This permits the use of a mechanical

transmission having several times the horsepower than would be practical in an all-electric drive train.

A very small engine is included to provide extended range capability. However, unlike previous dual mode concepts, this engine is only used to overcome rolling losses, and never powers the vehicle directly. Excess power for acceleration, passing and hill climbing is provided by the oversized flywheel and transmission. The large flywheel also eliminates the requirement for a second variable transmission, since the rotational speed range is minimal during engine operation.

The application of this high performance dual mode concept to an existing subcompact production vehicle could result in the following improvements in vehicle performance:

1. Fuel performance at 55 miles an hour would be about 71 miles per gallon. Range per tankful would be 700 miles.

2. Fuel consumption on board the vehicle is zero for the first 25 miles of urban travel.

3. Fuel performance over a range which satisfies more than 90% of all anticipated urban trips (50 miles) is of the order of 140 miles per gallon.

4. Normal acceleration and hill-climbing power is increased as much as 200% over the original vehicle.

5. Size, weight, passenger and cargo space and production cost are expected to be virtually unchanged from the original vehicle.

The full text of this paper was not available for inclusion in this volume of the Proceedings. It will be published later in a separate volume.

INFLUENCE OF CONSTANT POWER START/STOP AND REGENERATIVE BRAKING REGIMES ON EV BATTERIES

E.J. Dowgiallo
U.S. Army Mobility Equipment Research and Development Command
Fort Belvoir, Virginia 22060

S.M. Caulder and A.C. Simon
International Lead-Zinc Research Organization
Naval Research Laboratory
Washington, D.C. 20375

ABSTRACT

Two constant power start/stop drive regimes were developed - one without load leveling including regenerative braking and the other with load leveling. Two lead acid batteries were cycled to these profiles. The duty cycles which are based on a transit bus application with three daily discharges between recharges are described. Data acquired during these runs is presented. Cells were removed at times and a microstructure analysis performed. The effects of temperature, regenerative braking, load leveling and depth of discharging are discussed as they effect capacity (range) and cycle life. The objective is to obtain design data such as effective range and to elucidate the different effects of the two regimes on plate microstructure as a function of cycle life.

INTRODUCTION

The actual costs of operating a battery powered vehicle are strongly dependent on the number of deep discharge cycles that can be obtained from the battery itself. For the lead-acid battery this number is in part dependent on the load profile during discharge; very high discharge rates, even intermittently, reduce the available capacity and shorten life. Other factors such as charge rate and charging regimen, depth of discharge and operating temperature are also important, but this study is directed specifically at the influence of load leveling to avoid the very high discharge rates associated with vehicle acceleration. Since the study involves the comparison of a load leveled battery and one that is not and the testing includes regenerative braking to charge only the battery that is not load leveled, additional information was obtained on the impact of regeneration.

The study takes the form of several series of tests conducted to determine the economic life of the battery as operated over typical driving cycles in a representative operational scenario. Several tests are being conducted to determine the expected improvements in battery cycle life and range resulting from load leveled operation. Plate microstructure and morphology are being examined as cycling progresses to better understand changes and, hopefully, to make possible, reliable prediction of life.

In order to make comparisons with existing data, the baseline battery bus system was chosen to be similar to that of the Maschinenfabrik Augsburg Nurnberg (M.A.N.) Elektrobus which has been deployed in revenue service in Dusseldorf and Monchengladbach and operated 1.5 million miles since October 1974. This battery-powered bus uses a 5,987 kg (13,200 lb) lead-acid battery pack carried on a trailer to provide all propulsion and accessory power. The characteristics of M.A.N. Elektrobus operation which have been used as a basis for comparison are those of the 13 vehicles operating in Benrath (a suburb of Dusseldorf). These vehicles operate in bus service for 21 hours per day using two alternated battery packs per bus. The vehicles are operated for nearly three hours covering about 27 miles between battery changes. Battery changing is accomplished in five minutes at an

automatic battery recharge station. Recharging during peak and midday operations is accomplished in 3 hours with longer charging periods used at night. Regenerative braking is used up to the capacity of the battery to accept charge without causing gassing or overheating. The M.A.N. bus battery pack is made by VARTA Batterie AG and comprises 180-455 ampere hour cells connected in series. Each cell is rated at two volts and the total system voltage is 360 volts. The battery pack is provided with an electrolyte cooling system.

This paper presents the results of a study in which two lead-acid batteries were compared, one was cycled in a regime that simulated the operation of an urban transit bus with a fly-wheel to level the load, the other was cycled without load level assistance. The objective was to obtain design data such as effective range and to elucidate the different effects of the two regimes on plate microstructure as a function of cycle life.

TEST HARDWARE

BATTERY

Lead acid batteries were chosen because DOT needed the information for current transit bus applications and the batteries were immediately available. Gould type 66E-15 cells were purchased since they had a documented history of start/stop use in 350 postal service jeeps. The number of plates was increased from eleven in the jeep cells to fifteen (seven positive and eight negative plates) in this program to approximate the capacity of the Varta five hour rating of 455 Ah used on the M.A.N. bus. Thirty cells were received and cycled to determine their capacities by following the National Electrical Manufacturer's Association (NEMA) methods.[1] Cells were cycled for at least two cycles at the 6 hour (77 ampere) rate in groups of ten cells each to an average voltage of 1.70 volts per cell. The capacities were in the range 374 to 384 Ah for all thirty cells. Cells were then grouped based on capacity. This was accomplished by selecting cells for two nine cell batteries based on nearness to the average capacity of all the cells to assure that cells were matched in both batteries. The low initial capacities which were 82% of rating were not considered abnormal by the manufacturer.

It was anticipated that the capacities would increase during cycling, peaking perhaps after 50 cycles. Capacities had increased to about 90% of that specified after 20 cycles.

Cell interval resistance measurements were performed to make available information for developing a computer model of the battery. The internal resistances of the cells in the station 1 (load leveled) battery were measured before cycling. The cells' specific gravities ranged from 1.275 to 1.285 before the measurements were taken. An osciloscope was used to measure the cell voltage drop upon applying a five amperes current pulse. The internal resistance of each cell was calculated by dividing the voltage change by the current change. The average resistance was 0.58 milliohm with a high of 0.62 milliohm and a low of 0.54 milliohm. Based on polarization curves, these values can increase by a factor of about 1.3 times after a deep discharge.

SIMULATION STATIONS

Two independent test stations were constructed. One, referred to as station 1, simulates the load leveled transit bus profile, while the other, referred to as station 2, simulates the non load leveled profile. These loads were representative of average power and did not simulate the pulse waveforms of a chopper controller. Each station is designed for operation with nine series connected lead-acid cells. A simplified block diagram of the basic components in a test station is shown in Fig. 1.

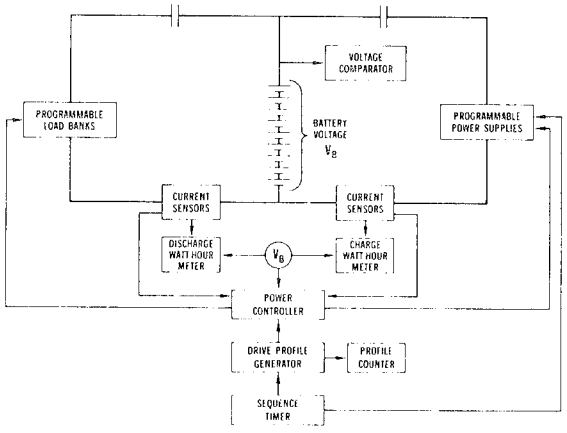

Fig. 1. Block diagram of non load leveled battery test station.

The charger is a programmable power supply (30 volt, 300 amperes) with automatic crossover. Initially the current is limited to a maximum of 25 percent of 462 Ah or 115 amperes crossing over to a modified constant voltage control. In this mode, the initial battery terminal voltage is 2.47 volts per cell which then rises until it reaches 2.56 volts per cell or 7.33 hours have elapsed as controlled by the sequence timer. After this, the charge is continued for 25 minutes before a finishing rate of 15-23 amperes (a maximum of 5 percent of 462 Ah) is applied for 1.25 hours. This is extended for equalization charges.

The regenerative braking charge in station 2 was limited by the power profile envelope, the manufacturer's maximum recommended voltage per cell of 2.60 volts, and the maximum current of two paralleled power supplies of 600 amperes.

The current monitors are Hall effect sensors to the watt-hour units.[2] The percent error of these units is less than $\pm$ 1% of power reading over the current ranges in the bus daily duty cycles. A potential increase in percent error at lower currents such as for equalization charges of long duration was eliminated by using a highly accurate data acquisition system. A $\pm$ 0.25 percent accurate shunt was used for charge currents.

TEST PROGRAM

APPROACH

Charge-discharge tests were made on two identical lead-acid battery cell packs comprising nine cells each using simulated transit loads to ascertain usable energy storage capability, capacity degradation with life and actual (or predicted) deep discharge cycle life. The simulated transit loads were based on operations of a 17,599 kg (38,800 lb) gross vehicle weight transit bus which has an average hotel load including air conditioning or heating of 15 kW. The tests were conducted in a similar manner for both battery packs by operation over predetermined driving cycles which withdrew an equal net energy for each pack.

TRANSIT BUS DUTY CYCLE

The basic driving cycle used for the load leveled and non load leveled tests is the FAKRA cycle which was generated by a European battery bus committee for use in comparative analyses. The FAKRA cycle was slightly modified for use in the DOT program and has been designated as drive cycle A. The characteristics of this drive cycle are shown in Table 1.

Table 1. Drive cycle A characteristics.

Characteristic	Value
Stops/mile	4
Average Acceleration Rate[a]	2.32 km/h/s (1.44 mi/h/s)
Acceleration Time to Cruise Speed[b]	21.6 s
Cruise Speed	48 km/h (31 mi/h)
Cruise Time	11.2 s
Maximum Deceleration Rate	3.5 km/h/s (2.2 mi/h/s)
Deceleration Time from Cruise Speed	14.4 s
Dwell	30 s
Average Speed	18.8 km/h (11.7 mi/h)
Turn Around Time	0
Vehicle Load	15 passengers + driver
Grade	0 percent
Headwind	0 km/h (0 mi/h)

[a]Acceleration to cruise speed may be accomplished by constant torque acceleration at the maximum acceleration rate up to an intermediate speed as limited by propulsion system capability followed by constant horsepower acceleration to cruise speed.

[b]Acceleration time is a performance target. If specified time cannot be realized, maximum vehicle performance shall be used.

The basic daily duty cycle in actual bus service consists of a nine hour charge, a three hour repeat of the drive profile and a three hour recharge, a second three hour drive profile and three hour recharge, and finally, a third three hour drive profile. This duty cycle is repeated with occasional extensions of the nine hour recharge for cell equalization.

POWER PROFILES

The two drive-power profiles corresponding to drive cycle A are shown in the lower section of Fig. 2.

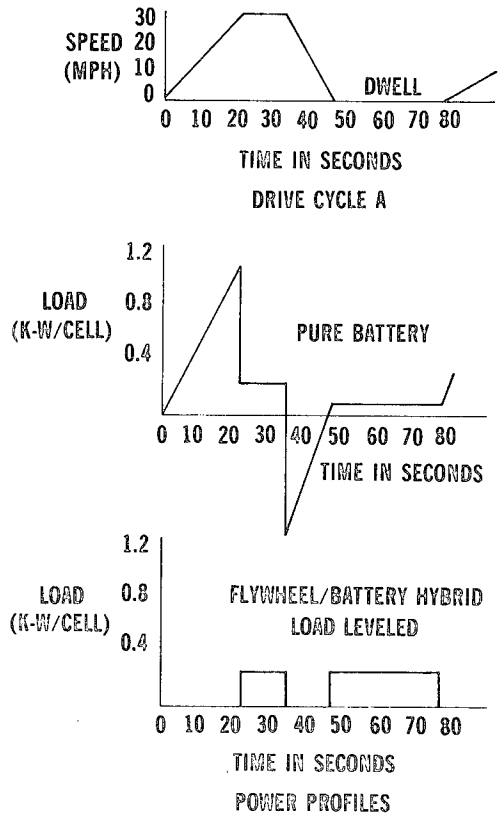

Fig. 2. Drive cycle A and power profiles.

Both driving power profiles were designed to withdraw the same net energy from the battery during the 77 seconds of a driving cycle based on a regenerative braking limit of about 1000 watts per cell. The net energy withdrawn during a drive cycle is about 120 kilowatt-seconds per cell.

In a drive mode, each battery pack is discharged with the driving power profile cycles to a preset minimum voltage or to an elapsed time. A voltage of 1.6 volts per cell was selected for terminating the load leveled driving mode and about one volt per cell for the non load leveled driving mode. These voltages should correspond to about 80 $\pm$ 10% depth of discharge for each condition.

A temperature limit of 54°C (130°F) was recommended by the battery manufacturer. Thermocouple alarms were placed in each cell set within three degrees of this value. When activated, these alarms open circuit the battery pack.

In actual bus service, the battery is subjected to four recharges. The first and second are rapid three hour recharges (initial current of 115 amperes), and the third is a slow nine hour recharge (initial current of 70 amperes). The first and second recharges are spaced between three deep discharge cycles making it possible to alternate between two sets of batteries to maintain continuous bus operation for eighteen hours a day. The fourth recharge is an extended nine hour recharge and is required for cell equalization. This is performed when imbalances are observed in cell voltages or specific gravities.

With Flywheel Assist. The power profile for drive cycle A with load leveling is based on a 17,599 kg (38,800 lb) transit bus with 21 passengers, four stops per mile, and a hotel load of 15 kW. The power is nominally 300 watts per cell. The individual energies for nine series cells are -- cruise: 30,240 watt-seconds (Ws); and stopped (battery energy to increase flywheel energy and to maintain the hotel load): 81,000 Ws. The total energy for each load leveled drive cycle is 111,240 Ws. It is assumed that an electrically paralleled flywheel absorbs the regenerative braking energy and provides acceleration energy. This profile is simulated at station 1 with battery 1.

Without Flywheel Assist. The power profile for drive cycle A without load leveling has a maximum power of 1200 watts per cell during acceleration. The individual energies for nine series cells are -- acceleration: 123,840 Ws; cruise: 25,357 Ws; regenerative braking: 73,350 Ws; and stopped or hotel load: 19,913 Ws. The total energy out of the battery during a drive cycle is, therefore, 169,110 Ws. This is 1.52 times the energy out during the load leveled drive cycle. For comparison of the load leveled and unload leveled

capacities and life cycle effects on a similar energy basis, the net energies in each case should be approximately equal. To achieve this, the regenerative braking contribution to recharging the battery should return about 57,870 Ws (which is the difference between 169,110 Ws for the unload leveled case and 111,240 Ws for the load leveled case). Based on the ideal power profile envelope, the maximum energy that would be available to the battery during regenerative braking is 73,350 Ws. A preset upper voltage limit of 2.60 volts per cell was required by the battery manufacturer. However, this voltage was never reached since the acceleration always preceeds the regenerative brake. Apparently, the amount of energy returned is always accepted since it is significantly less (59%). The total net ideal energy is 95,760 Ws, but due to the battery acceptance capability this should be reduced and approach net energy equality with the load leveled profile. Equality requires a regenerative braking accepted energy return of 57,870 Ws which is 15,480 Ws less than the ideal maximum available of 73,350 Ws. The amount of energy accepted by a battery during recharge generally is about 80% which is in agreement with these figures. This profile (without flywheel assist) is simulated with station 2 and battery 2.

TEST RESULTS

BATTERY 1 (LOAD LEVELED)

Battery 1 was cycled on station 1 which simulated the load leveled power profile. The controls on this station were preset to terminate any discharge when a voltage of 1.6 volts per cell or a time of 5.5 hours was reached. If the low voltage limit was reached first, the battery was open circuited until the 5.5 hours had elapsed. The voltage of 1.6 volts per cell was selected since the depth of discharge should approximate 70% of the capacity of a full discharge at 77 amperes. This was arrived at based on capacity versus discharge rate with voltage as a parameter from the battery manufacturer.[3] Three discharges are performed per duty cycle. The total time for a "daily" duty cycle was increased by the decision to allow enough time to assure reaching the low voltage limit to determine the maximum number of 77 second runs that the battery was capable of. The total time for a daily duty cycle was 31.5 hours (5.5 hours for each of three discharges, plus 3 hours for each of two recharges, and finally 9 hours for the overnight recharge). The 31.5 hour "day" was shortened to 28.5 hours at deep discharge cycle number 74 to eliminate the time lost standing at open circuit since no discharge went the full 5.5 hours. This time was reduced to 4.5 hours thereby eliminating one hour per each of the three daily discharges.

The constant power levels were maintained between 300 and 320 watts for cycles 2 thru 73 and between 307 and 328 watts for cycles 75 thru 88. The overall total energy withdrawn was 469,306 Wh. The watt-hour efficiencies were calculated as the ratio of the watt-hours discharged to the watt-hours of the recharge. The average efficiencies were 82% for the first cycle, 80% for the second cycle, and 67% for the third cycle which is lower since it includes the overnight recharge. These averages are for at least 27 efficiencies for each of the three daily discharges. The overnight recharge used about twice the discharge energy of the first two short recharges which are almost equal.

The original experimental design consisted of three, three hour maximum discharge periods at average currents about equal to the six hour rating of the battery (462 Ah at 77 amperes). However, actual initial capacities were about 80% of this.

The 130°F maximum temperature was exceeded several times. To reduce the temperature, a decision was made to reduce the maximum current during charge from 115 to 70 amperes during the nine hour recharge. This was initiated at cycle 13. This did prevent temperatures from reaching 130°F, but the temperatures were still high; and since it was expected that the non load leveled battery would experience much higher discharge currents, a marginal temperature on the load leveled battery would certainly cause an excessive temperature for the non load leveled battery. Since the intent was to test both batteries under identical circumstances, a decision was made to insert aluminum heat sinks between each grouping of three cells for both batteries. This was accomplished before cycle 40. The center cell temperature never exceeded 120°F on the load leveled battery after this.

Each drive cycle is equivalent to ¼ of a mile. The most drive profiles completed for any single deep discharge were 220 or 55 miles, and the least (under normal charge conditions) were 150 or 37.5 miles. No distinct trends in energy out or number of drive profiles are apparent for these 88 deep discharge cycles which would be equivalent to almost six weeks of bus operation.

BATTERY 2 (NON LOAD LEVELED)

Battery 2 was cycled on station 2 which simulated the non load leveled power profile. The controls on this station were preset for termination of various drive cycles at voltages ranging from 0.91 to 1.40 volts per cell. The 1.60 volts per cell termination voltage for the load leveled station 1 was not applicable since the four times higher peak acceleration power, which produced corresponding currents about seven times higher, would cause premature termination by reaching that voltage during acceleration due to the resultant high internal battery voltage drops. This series of drive cycle tests revealed that the battery voltage dropped sharply at the peak of the constant power acceleration long before the voltage in the following cruise reached 1.6 volts per cell. When this drop first occurred on cycling, the cruise voltage was still as high as 1.95 volts per cell.

EFFECT OF CURRENT LIMITED AND CONTROLLED ACCELERATION AND REGENERATIVE BRAKING

Determination of the effect of variations in peak acceleration power with and without regeneration was considered necessary for the design of future power trains incorporating batteries and flywheels. The power profile in drive cycle A is for a constant acceleration case. Another approach is to use an exponentially decreasing acceleration profile.[4] This is valid if the SAE J227a driving cycle is considered since it only specifies the end points of the acceleration. Power peaks in this mode could be about one third less than the constant acceleration. One assumption is that the area under all acceleration curves is the same since a given velocity must be reached in the same time. Figure 3 includes plots of the constant power drive cycle A (constant power non load leveled with regenerative braking), several constant power drive cycle A profiles with stated current limits, and one constant power exponentially decreasing acceleration version of drive cycle A. All ranges are for ideally matched vehicles and drive line elements which assumes that the flywheel assisted and unassisted cases have the same efficiency.

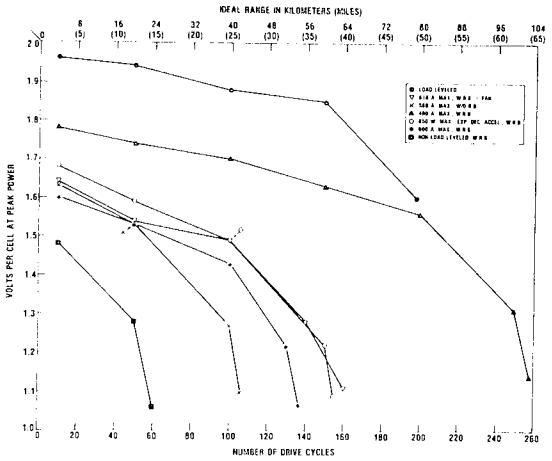

Fig. 3. Volts per cell at peak power versus number of drive cycles and ideal range.

The 400 and 600 amperes limited cases would initially be within power ranges roughly comparable to an exponentially decreasing acceleration profile. The maximum current limitation is a reasonable one in that most electric vehicle controllers are current limited. Referring to Fig. 3, the load leveled case has the maximum range to 1.6 volts per cell, 78 km (49 mi), and the constant acceleration constant power case (non load leveled) has the least, 24 km range (15 mi), to 1.1 volts per cell. The 400 amperes current limited acceleration with regenerative braking has the longest range, 104 km (65 mi) apparently as a result of the regenerative braking recharge. The three profiles, cooled, uncooled, and no regeneration, that are limited at 600 amperes have ranges of 64, 54 and 42 km (40, 34 and 26 mi) respectively. It is interesting to note that the exponentially decreasing acceleration with a constant power envelope with a maximum power of 850 watts per cell follows the 610 amperes fan cooled with regenerative braking range curve.

TEMPERATURE EFFECTS

The relationship of peak power during acceleration to temperature increase is another consideration in load leveling a battery since high temperatures do, in general, decrease cycle life. In order to compare the various modes of operation previously described on a similar basis, the cyclic increase (degrees centigrade per cycle) of the center cell electrolyte temperature as a function of the ratio of peak power to cruise power is plotted in Fig. 4. The differences in temperature are based on the 50th drive cycle and the 100th drive cycle temperatures with the exception of the non load leveled case which did not last beyond the 66th cycle and is based on the 50th and 60th drive cycle temperatures. The peak power is based on the 100th drive cycle.

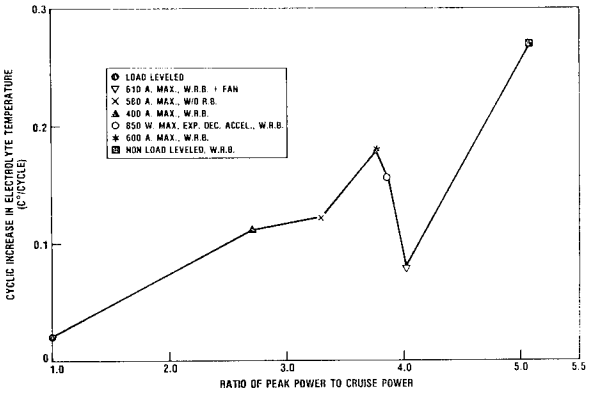

Fig. 4. Ratio of peak to cruise power versus temperature.

Cruise power was used as the reference since it is approximately the same in all cases. The effect of cooling the top of the battery with a fan is significant as evidenced by the relatively small temperature change. The smallest temperature rise is for the load leveled case, and the largest is for the non load leveled case. The temperature change with regenerative braking is larger than without it with approximately the same current limits (600 and 580 amperes respectively). This would be expected since the average absolute current would be higher in the regenerative case. The 600 amperes maximum current with regenerative braking is closer in temperature rise to the exponentially decreasing acceleration case than with fan cooling despite the fact that the fan cooled voltage curve was similar.

CELL EXAMINATION

Comparison of two bus type cells, the first examined before cycling and the second after 74 cycles of load leveled charge-discharge, showed that the firm reticulate structure found throughout the cross section of the positive plate from the first cell is converted to a microstructure of much smaller detail, which is softer and more easily dislodged from the plate after 74 cycles of operation. This change was found at and near the surface of the positive plates in the second cell while the interior of the plate remained with a structure resembling that found in the first cell. This indicated that, at the rates of charge-discharge employed in the load leveled case, the reactions are concentrated in the outer layers of the plate and the entire cross section is not being utilized.

Despite the softening of the outer portion of the active material, the plates of the second cell still looked in good condition and capable of additional cycling. From the amount of sediment in the glass mats and bottom of the cell, however, it did not seem that the use of the glass mats and porous plastic outer sheath was very effective in retaining the active material, once softening had begun.

No major change had taken place in the negative active material after 74 cycles, but there was evidence that in small, isolated areas the plate had become inactive and in these areas only lead sulfate appeared, whether the plate was charged or discharged.

A non load leveled cell examined after 41 cycles did not have as advanced a disintegration of the reticulate structure as in the cell with 74 load leveled cycles. Reticulate structure was still visible at or near the surface but was showing evidence of disintegration. Softening seemed to proceed inwards with the number of cycles in either case.

Expansion of the negative plate began at the surface and proceeded inward. The process of expansion was noticeably more advanced at the bottom of the cell than at the top. The extent of it correlated with the number of cycles.

In general, both positive and negative plates had structural differences that were probably the result of different numbers of cycles rather than differences caused by load leveling or non load leveling.

SUMMARY AND CONCLUSIONS

An ideal flywheel-battery (load leveled) system had a range of 78 km (49 mi) and an unassisted battery only 24 km (15 mi). However, these conclusions are strongly dependent on the chosen drive cycle (particularly the requirement for constant acceleration) and the choice of cut off voltages. The unassisted battery could have a range of 69 km (43 mi) if a constraint is put on maximum current during acceleration to the same final voltage as the flywheel-battery system with some degradation in performance near the end due to decreased acceleration power. However, no degradation in performance would occur with an exponentially decreasing acceleration and an unassisted battery with a range of 62 km (39 mi) to the same final voltage as the constant acceleration profile.

No degradation in performance was observed during the 88 deep discharge cycles carried out with the flywheel assisted battery and the relatively few test cycles conducted to date with the unasisted battery.

Air cooling was essential to keep both batteries below the manufacturer's recommended temperature.

The microstructure of the positive plates of the flywheel assisted battery observed before cycling and after 74 cycles had changed to show finer detail and was found to be relatively soft. This change was found primarily near the surface of the plates indicating non-uniform utilization of the plate. An unassisted battery examined after 41 cycles did not have any structural differences that could be attributed to operation with or without flywheel assist.

ACKNOWLEDGMENTS

The work was performed for the U.S. Department of Transportation, Transportation Systems Center with funding provided by: The U.S. Department of Transportation, Urban Mass Transportation Administration; The U.S. Department of Energy, Transportation Energy Conservation; U.S. Department of Energy, Energy Storage; and Lawrence Livermore Laboratory.

REFERENCES

[1]National Electrical Manufacturers Association, Capacity Determination of Lead-Acid Industrial Storage Batteries for Motive Power Service, Standards Publication No. IB2-1974, 155 East 44th Street, New York, New York 10017.

[2]Ohio Semitronics Inc., Watt-Hour Meter Manual, Model WH7-37U-2X, 1205 Chesapeake Ave., Columbus, Ohio 43212.

[3]Gould Inc., Discharge Characteristics of Gould Type: 66E (TC-107360), Industrial Battery Division, 1601 Rollings Hills Drive, Richmond, Virginia 23288.

[4]Mighdall, P., Hahn, W.F., "State-of-the-Art Power Train Design, "Preliminary Power Train Design for a State-of-the Art Electric Vehicle, DOE/NASA/0595-78/1, NTIS, U.S. Department of Commerce, 5285 Port Royal Road, Springfield, Virginia 22161, Volume 2, Sept. 1978, pp. 69-71.

COMBINED ENERGY STORAGE

(Flywheel/Battery Hybrid)

Edward Kuznetsov
Principal Research Scientist
Battelle's Columbus Laboratories
505 King Avenue
Columbus, Ohio 43201

Gary Kinzel
Assistant Professor
The Ohio State University
Columbus, Ohio 43210

ABSTRACT

In this paper the idea of combining the energy storaging features of a flywheel and a battery is presented. By using a battery as the ballast in a multirimmed flywheel design, the energy density of the flywheel can be dramatically improved. Such a flywheel can store energy even when at rest so that the total flywheel energy density is not as strong a function of speed as in the case of a conventional flywheel. In fact, flywheel speed then becomes a design variable which need not always be maximized for optimum system performance.

INTRODUCTION

Efficient energy storage can result in significant energy conservation in transportation, electric power generation, and other areas. Two of the most widely used and most versatile energy storage systems are electric batteries and flywheels. Although these systems have very little in common, the current state of the art of the two technologies is such that the respective energy densities (amount of energy stored per unit weight) are close in both cases (currently approximately 18 W·h/N).[1,2] Both technologies show a slow but stable trend toward improvement, and this slow trend is likely to continue until and unless a major breakthrough occurs in one or both areas.

The electric battery's efficiency as an energy storage system is modest but acceptable since energy losses due to internal leakage are generally fairly low. Its major disadvantage is a rather low power density, i.e., the rate at which the energy is stored or delivered per unit weight. On the other hand, a flywheel possesses an excellent power density, but dissipates much energy because of drag, friction, and other losses. These losses are inherent because flywheels must operate at very high speeds if the weight is to be kept at a reasonable value. Some improvements are brought about by introducing evacuated chambers, special lubrications, and/or magnetic suspension, etc., but these are costly and in the latter case require energy to operate.

When the two systems are compared, it is apparent that electric batteries and flywheels are complementary in many respects. For this reason, they are sometimes combined to form a more efficient energy storage system, especially for vehicular applications[3-5]. In such a system most of the energy is stored in the batteries while a relatively small flywheel provides peak-shaving capacities (acceleration bursts and regenerative braking).

One of the most advanced flywheel designs is the so-called multirim design, which employs high-strength fiber composites for uniaxially stressed rings. However, only the strength of the outermost ring can be utilized to the fullest extent: hoop stress decreasing proportionally with the radius squared makes the inner rings considerably underloaded. To overcome this disadvantage, some designs introduce additional mass (ballast) at the inner rings as indicated in Fig. 1. When rotating,

the ballast stores kinetic energy and develops centrifugal forces sustained by the structural rings thus inducing additional stress. In this way, the strength of the structural material can be utilized to the fullest extent.

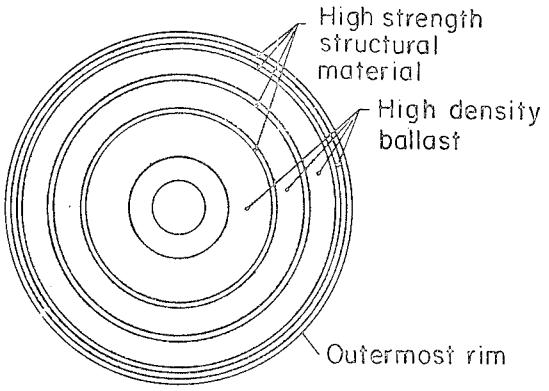

Fig. 1. Conventionally Ballasted Flywheel

It has been found that the greater the mass density of the ballast, the greater the energy density of the flywheel. For this reason, some authors of semi-technical articles have advocated such exotic ballast materials as uranium dust in a lead matrix[6]. However, an analysis shows that even with the best ballast, the added mass increases the kinetic energy of the flywheel slower than it increases the weight. As a result a ballasted multi-irim design has an energy density which is significantly less than that for theoretically ideal single rim design.

The concept described in this paper is the use of a hybrid flywheel with an active ballast which stores electrochemical or other non-mechanical energy. This can be achieved by placing primary (not rechargeable), secondary (rechargeable), or fuel cell elements between the rings (see Fig. 2). In this way, not only the structural material strength is utilized fully, but at the same time, the mass of the battery contributes to the kinetic energy of the rotating flywheel.

Although the concept presented is still in the research stage, it has a number of advantages over separate flywheel and battery systems. The equations illustrating these advantages are presented in the following, together with some observations based on them. At the end of the paper, several possible uses for the hybrid are discussed together with some of the design challenges.

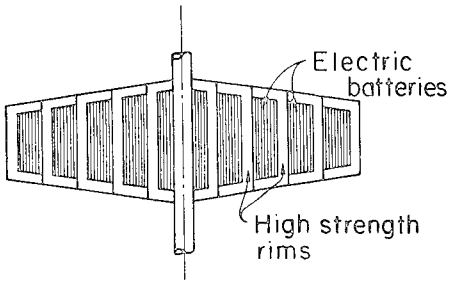

Fig. 2. Cross Section of Proposed Hybrid

BASIC CHARACTERISTICS OF THE HYBRID

In the discussion which follows, it is assumed that the battery members used in the ballast have no mechanical strength and simply rest on the structural rings. This assumption is conservative. Furthermore, it is assumed that each ring and ballast set is structurally independent of the others; this permits the hybrid to be analyzed by considering each set separately. Physically this could be accomplished by bonding a resiliant material to the outside of each interior structural ring.

The actual structure of the hybrid will vary depending on the number of ring and ballast sets. As the rings become thinner, a continuous model is approximated. For the purpose of analysis, a continuous model is assumed such that an elemental section includes both the structural material and battery ballast. It is reasonable to expect that this model is valid as long as the number of the sets is not too small. For this continuous model, each structural ring and ballast set has a total thickness, dr, as show in Fig. 3. For the infinitesimally narrow element at a radius r, the total weight per unit height is

$$dW = [\rho_s t + \rho_b(1-t)]\, r\, dr\, d\theta, \qquad (1)$$

where ρ_s and ρ_b are the weight densities of the structural material and the ballast, respectively; and t is the fraction of the ring thickness, dr, allocated to the structural material. The fraction t will be different for each ring-ballast set in the flywheel, i.e., t will be a function of r.

If the weight density ratio, γ, is defined as

$$\gamma = \frac{\rho_b}{\rho_s}, \qquad (2)$$

Equation (1) can be rewritten as

$$dW = \rho_s[t + \gamma(1-t)]\, r\, dr\, d\theta. \qquad (3)$$

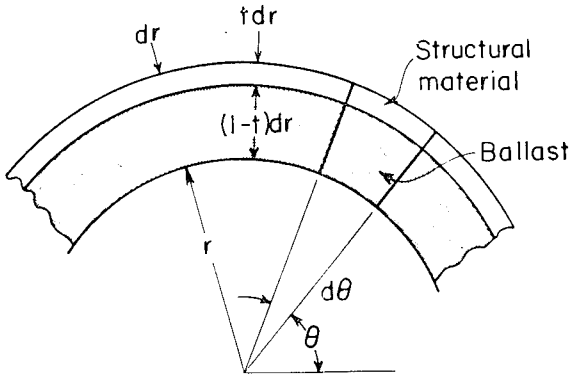

Fig. 3. Differential Element from an Arbitrary Ring of the Battery-Flywheel Hybrid

Now if the flywheel rotates with a constant angular speed, ω, the hoop stress in the structural material is

$$\sigma = \left(\frac{dW\, r\, \omega^2}{g}\right)/(t\, dr\, d\theta)$$

or

$$\sigma = \frac{\rho_s r^2 \omega^2}{gt}[t + \gamma(1-t)]. \qquad (4)$$

The kinetic energy of the element (structural material and ballast) can be written as

$$dK = \frac{dW}{g}\frac{r^2\omega^2}{2}$$

and in terms of stress,

$$dK = \frac{\sigma\, t\, r\, dr\, d\theta}{2}. \qquad (5)$$

The amount of electric energy stored in the ballast (battery) portion of the element is

$$dE = E_b\, dW_b = E_b\, \gamma\, \rho_s\, (1-t)\, r\, dr\, d\theta, \qquad (6)$$

where E_b and W_b are the electrical energy density and weight, respectively, of the battery.

Assuming that the flywheel design is such that all of the structural elements are stressed equally, the stress in Eq. (4) can be treated as a constant. Then solving the equation with respect to t gives a design relationship for the distribution of the structural material along the radius:

$$t(\xi) = \frac{\gamma\, v^2\xi^2}{1 + (\gamma-1)v^2\xi^2}, \qquad (7)$$

where

$$\xi = \frac{r}{R},$$

$$v^2 = \frac{\rho_s}{\sigma}\frac{\omega^2 R}{g}, \qquad (8)$$

and R is the outer radius of the flywheel.

Note that v^2 is a dimensionless parameter incorporating the design stress, density, speed and maximum radius for the structural material in the flywheel. The physical significance of v becomes apparent when the maximum speed of the flywheel is considered. This maximum speed is limited by the allowable stress of the structural material and cannot exceed that for a flywheel with the outermost ring unballasted. For this ring, t is equal to 1 and r is equal to R. Equation (4) then yields

$$\omega_{max}^2 = \frac{\sigma g}{\rho_s R^2}. \qquad (9)$$

When the result is compared with Eq. (8), it is apparent that

$$v = \frac{\omega}{\omega_{max}}, \qquad (10)$$

i.e., v is the ratio of the actual flywheel operational speed to the maximum speed achievable for the structural material.

The weight of the structural material in the hybrid flywheel, W_s, can be evaluated using Eq. (1) and (7). If the hub radius is small enough to be neglected, these equations give

$$W_s = \rho_s R \int_0^1 \int_0^{2\pi} t(\xi)\, \xi\, d\theta\, d\xi = \frac{\pi R^2 \rho_s \gamma}{\gamma-1}\left(1 - \frac{F}{\gamma-1}\right), \qquad (11)$$

where

$$F = \frac{1}{v^2}\ln[1 + v^2(\gamma-1)]. \qquad (12)$$

The weight of the ballast, W_b, occupying the remaining volume of the flywheel is

$$W_b = (\pi R^2 - \frac{W_s}{\rho_s})\gamma\rho_s = \frac{\pi R^2 \gamma \rho_s}{\gamma - 1}(\frac{\gamma F}{\gamma - 1} - 1) \quad . \qquad (13)$$

and the total weight is therefore given by

$$W = W_s + W_b = \frac{\pi R^2 \gamma \rho_s F}{\gamma - 1} \quad . \qquad (14)$$

The kinetic energy of the flywheel is obtained by integrating Eq. (5):

$$K = \frac{\sigma R^2}{2} \int_0^1 \int_0^{2\pi} t\, \xi\, d\theta\, d\xi = \frac{\sigma W_s}{2\rho_s} \quad . \qquad (15)$$

It is known[7] that the value

$$E_s = \frac{\sigma}{2\rho_s} \qquad (16)$$

is the energy density for a thin rotating rim. This therefore represents the theoretically maximum attainable energy density under a uniaxial stress state. Thus Eq. (15) shows that the amount of kinetic energy per unit weight of the structural material in a ballasted multi-rim flywheel is the same as that for the material of a single rim. This is understandable because the elastic energy density of a uniaxially stressed member is

$$E_e = \frac{\sigma\varepsilon}{2\rho_s} = E_s\varepsilon \quad , \qquad (17)$$

where ε is the elastic strain. Hence the kinetic energy of a rotating rim is proportional to its elastic energy with a rather large proportionality factor $(1/\varepsilon)$. In Eq. (15), it should be noted that K is the total kinetic energy of both the structural material and the ballast. Therefore, E_s can be considered as an effective kinetic energy density referred to the structural material.

The true energy density of a ballasted flywheel can be derived by combining Eq. (11), (14), and (15) to give

$$E_k = \frac{K}{W} = E_s \frac{W_s}{W} = E_s w \quad , \qquad (18)$$

where

$$w(v,\gamma) = \frac{E_k}{E_s} = \frac{W_s}{W} = \frac{1}{F} - \frac{1}{\gamma - 1} \quad . \qquad (19)$$

The equation for w is plotted as a function of v and γ in fig. 4. There the curves

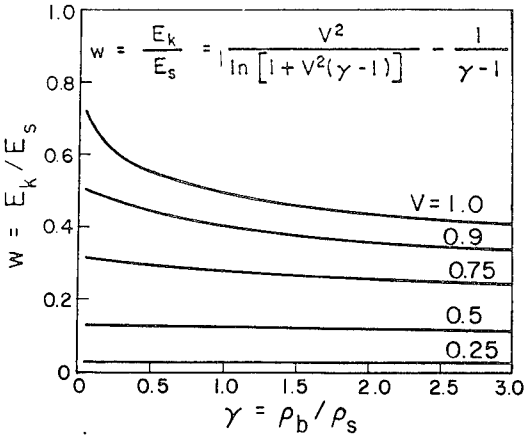

Fig. 4. Effect of Flywheel Speed and Ballast Density on the Kinetic Energy Densities

start with $\gamma = 0$ because as indicated by Eq. (4), at $\gamma \to 0$ the structural rings cannot be equally stressed. Note that for most practical systems, γ is greater than 1. This is because currently used structural materials for high performance flywheels are relatively light synthetics while battery materials tend to be heavy.

The total energy stored in a flywheel with an active ballast is the sum of its kinetic energy given by Eq. (15) and the electric energy of the ballast (electric battery) so that

$$T = E_s W_s + E_b W_b = E_s(W_s + h\, W_b) \quad , \qquad (20)$$

where $h = E_b/E_s$ is a parameter characterizing the relative energy density of the hybrid components or the ballast "quality". Note that h = 0 corresponds to a passive ballast and h large corresponds to a high quality battery relative to the structural material. The hybrid energy density, E_h, can be evaluated using Eqs. (14) and (20):

$$E_h = \frac{T}{W} = E_s \frac{hW + (1-h)W_s}{W} = E_s[h + (1-h)w] \quad . \qquad (21)$$

STUDY OF HYBRID CHARACTERISTICS

The energy density of the hybrid flywheel given by Equation (21) depends on several parameters although the three main parameters are the ballast quality, $h = E_b/E_s$; the relative operational speed, $v = \omega/\omega_{max}$; and the component weight density ratio, $\gamma = \rho_b/\rho_s$. The effect of these three parameters can be established by

a systematic consideration of the equations.

As can be seen from Eq. (18) and Fig. 4, E_k is less than E_s when a ballast is used so that the introduction of a ballast, while providing the utmost utilization of the material's strength, lowers the kinetic energy density. Moreover, because the function w given by Eq. (19) is a decreasing function of γ, the kinetic energy density decreases as the ballast becomes relatively heavier. Therefore, the main advantage of a heavier ballast is an improvement in the volumetric energy density and possibly some cost saving per unit energy stored.

It is of interest to determine the minimal amount of ballast that equalizes the stresses in all of the structural rings when the kinetic energy is a maximum. Obviously this minimum is attained at a maximum rotational speed. Combining Eqs. (13) and (14) and setting v = 1 gives the relaweight of ballast required.

$$\frac{W_b}{W} = \frac{\gamma}{\gamma-1} - \frac{1}{\ln\gamma} . \qquad (22)$$

Because $\gamma = \rho_b/\rho_s$, it follows that the less dense the ballast, i.e., the smaller the value for γ, the smaller the fraction of W which is devoted to ballast. However, as γ decreases, the volume of the ballast and the flywheel as a whole increases for a given total energy stored. As discussed previously, generally γ will be greater than 1. For a ballast of the same weight density as the structural material (γ = 1), Eq. (22) yields* $W_b/W = 0.5$. Using w = 1 - W_b/W, the kinetic energy density of this flywheel is found to be 0.5 E_s, or exactly half of the energy density of a "solid", multirimmed flywheel without any ballast where the inner structural rings are understressed. For such a flywheel, the kinetic energy can be computed directly from Eqs. (9) and (16):

$$E_k = \frac{K}{W} = \frac{I\,\omega^2}{2W} = \frac{1}{2W}\,\frac{W\,R^2}{2g}\,\frac{\sigma g}{\rho_s R^2} = \frac{1}{2}\,E_s \qquad (23)$$

Based on Eq. (18), it is apparent that this value is improved as W_s approaches W, i.e., as the ballast becomes lighter. However, from Figure 4, for reasonable values of γ, e.g., $\gamma \simeq 0.5$, the improvement is only marginal. In addition, the flywheel volume will increase.

* When γ = 1, Eq. (22) can be evaluated using L'Hospital's rule.

For given weight densities of the ballast and structural material, the hybrid flywheel characteristics depend on the ballast quality, h, and the normalized rotational speed, v. As soon as the latter is fixed, the energy density given by Eq. (21) becomes a linear function of h. The straight lines shown in Fig. 5 represent the hybrid flywheel energy densities for several speeds, The most important basic features of the proposed hybrid are revealed by this diagram.

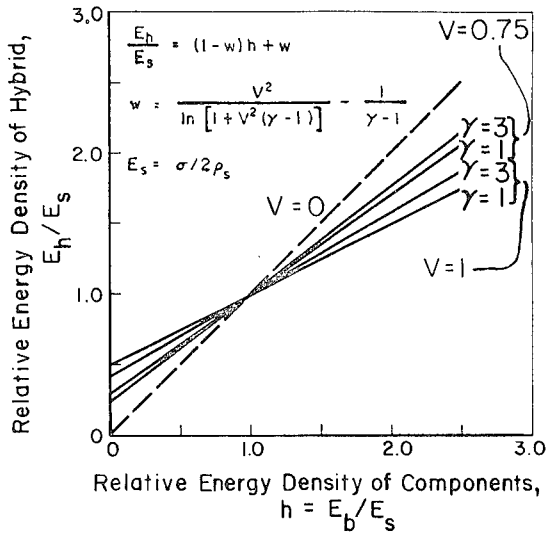

Fig. 5. Energy Density Relationship for Hybrid Flywheel

To the left of the ordinate h = 1 lies the domain of those electric batteries which have a lower energy density than E_s, the effective kinetic energy density referred to the structural material. A hybrid flywheel incorporating such batteries improves its total energy density, E_h, only by increasing the speed or decreasing γ. Here the larger part of the energy stored is kinetic energy. Nevertheless, the contribution of the battery can be considerable, and the total energy density grows rapidly compared to that for the corresponding passively ballasted flywheel. For the latter, the kinetic energy density cannot significantly exceed $E_s/2$ given by Eq. (23). However, for the hybrid, the total energy density E_b can be much higher than E_s as can be seen in Fig. 5.

To the right of the ordinate h = 1 is the domain of those batteries for which E_b is greater than E_s. The lower the operational speed, the higher the hybrid energy density. The explanation lies in the fact that putting a battery into rotation requires the introduction of a structural component whose energy density is in this case worse than that of the battery. Thus,

putting a good battery into rotation is justified only to the extent of obtaining the necessary minimum of kinetic energy for such purposes as power-peak shaving.

By far the most important property of the hybrid flywheel stems from the fact that all the straight lines characterizing its performance intersect at the point (1,1) on the graph of E_h/E_s versus h (Fig. 5). This is especially significant because the current state of the art in electric battery and composite-material flywheel technologies is such that their respective energy densities are rather close. In the vicinity of the point (1,1), the energy density of the hybrid flywheel does not depend on its operational speed. This means that the operational speed, which is increased by all possible means and still represents the most pressing constraint in a conventional design, becomes simply a variable design parameter of a hybrid flywheel. The hybrid therefore provides the designer with more freedom in flywheel design than does the conventional flywheel. In particular, the design need not be based on the highest possible speeds since adding weight to the flywheel ballast can increase the total energy density with no increase in speed.

USES FOR THE HYBRID

The hybrid is a likely candidate wherever high-performance flywheels are required. An obvious use is in small cars which are now designed with independent battery and flywheel systems. A second use is in mass transportation where flywheel energy sources have been used in the past.[8,9]

As conceived, the flywheel-battery hybrid will be heavier than a conventional flywheel alone but lighter than the independent flywheel-and-battery systems currently used because lower speeds permit reduced losses. Therefore, there is a net saving in weight. A theoretical comparison of the proposed hybrid concept with the currently used Garrett concept[3] is shown in Table 1. In both cases, a set of stationary batteries is the primary energy source while the flywheel is used for peak-power shaving. The rotational velocities are selected to give the desired energy stored, and the energy density of the batteries is taken as 3.74 W·h/N, a typical value for lead-acid batteries. This same energy density was assumed for both the moving and the stationary batteries. Because of the lower operating speed, the power losses in the hybrid flywheel are less than half of those for the Garrett system. Under the assumptions given, the entire energy stored in the Garrett system would be dissipated in 12 hours if the speed were maintained by the batteries. In the hybrid system, the energy would not be dissipated until after 27 hours at the assumed operating speed. After 4 hours, about 25% of the energy in the Garrett system would be lost while only about 10% of the hybrid's energy would be lost. Thus, after 4 hours, the energy available in the hybrid system would be about 1.35 times that available in the Garrett system. This means that the hybrid system could propel the vehicle 35% farther than the Garrett system or could be approximately 35% lighter for the same range.

The example in Table 1 illustrates one of the main advantages of the hybrid system; namely, the speed of the flywheel is at the discretion of the designer. To reduce the speed, the mass of the flywheel can be increased by adding battery ballast. Since the battery weight is already a part the system weight, the overall weight of the system increases only if more structural material in the flywheel is required to contain the ballast.

Once the flywheel-battery hybrid is designed, it can be used in much the same fashion as conventional battery-flywheel systems. In particular, regenerative braking can be used; and because of the lower flywheel speeds, regenerative braking can be more efficient.

DISCUSSION AND SUMMARY

The hybrid flywheel concept offers a new way to improve the energy density in a flywheel without increasing the speed of the system and without significantly changing the weight if supplementary batteries are already used. On the other hand, the hybrid presents a number of design problems which are not involved in conventional flywheel design. These include

1. Establishment of the optimum ratio of the structural material and the battery ballast,

2. Development of an efficient means for charging the batteries in the flywheel,

3. Development of an efficient means for extracting the energy of the rotating battery,

4. Establishment of the best ratio (E_k/E_b) for energy storage,

5. Design of containment vessel,

6. Balancing problem due to the introduction of the battery.

energy density, i.e., the former gains as latter loses. This is clearly not the case with the hybrid, which is less sensitive to reducing the stress for the sake of safety.

Because the electrical and kinetic energies are based on physically different

Table 1. Comparison of Hybrid concept with Garrett Flywheel-Battery Combination[a]

	Garrett	Hybrid
Flywheel Weight	267 N	1330 N (1070 N battery)
Operating Speed	25,000 RPM	9000 RPM
Kinetic Energy Stored	1 kW·h	1 kW·h
Flywheel Assembly Weight	667 N	1779 N (approximate)
Stationary Battery Weight	4626 N	3514 N
Total Energy*	18.5 kW·h	18.5 kW·h
Total Weight	5392 N	5293 N
Estimated Losses		
Bearings	0.90 kW	0.37 kW
Seals	0.60 kW	0.075 kW
Air Drag	0.038 kW	0.0075 kW
Total Losses	1.538 kW	0.445 kW
Relative Range for 4 Hour Operation	100%	135%
Total Weight for Same Range as Garrett System	1190 N	881 N

[a]Based on an energy density of E_b = 3.74 w/N

The solutions to these problems will depend on the type of application for the system, and a large amount of research will be required to solve the problems.

In spite of the design problems which must be overcome, the advantages of the proposed hybrid are obvious. Compared to conventional flywheel designs, the hybrid can store and deliver more energy at a lower speed thereby reducing drag and friction losses. An evacuated chamber will still be required; however, a lower vacuum can be tolerated because of the low speeds. The lower speeds also provide an opportunity to improve the factor of safety in the hybrid. Both energy density and maximum stress in a conventional flywheel are proportional to the angular speed squared; so safety factor is an inverse function of the

phenomena, the hybrid is inherently more reliable and safer than a conventional flywheel. If the battery discharges, it will still function as a passive ballast; and if the flywheel itself decelerates due to loss of vacuum, bearing failures, or intentional energy drain, the battery will still function. Improved safety stems from the fact that only part of the total hybrid energy is kinetic and only this part is released in case of catastrophic mechanical failure.

The hybrid also provides operational flexibility in energy storage. By redistributing the energy between the battery and flywheel, it is possible to optimize the charge, storage, and power delivery routines. To some extent, flywheel speed flucuations can be reduced, thereby giving

the hybrid flywheel some of the same beneficial aspects as those of the variable inertia flywheel.[9]

Finally, the hybrid permits the design of well balanced power-to-energy densities and optimum energy-to-volume ratios. The latter benefit is important for applications subject to size restrictions, such as in spacecraft.

REFERENCES

1. Finn, G., "Batteries Move Up the Power Ladder", Product Engineering, Sept. 1978, pp. 81-84.

2. Vaccari, J. A., "Key to New Energy Storage Systems", Product Engineering, Jan. 1979, pp. 46-49.

3. Towgood, D. L., "An Advanced Vehicular Flywheel System for an Electric Powered Passenger Vehicle", 1977 Flywheel Technology Symposium Proceedings, San Francisco, 1978.

4. Latchwill, D. L., "An Advanced Energy Storage Unit for a Postal Service Delivery Vehicle", 1977 Flywheel Technology Symposium Proceedings, San Francisco, 1978.

5. Lawson, L. J., "Flywheel Propulsion for Urban Transit Buses", 1977 Flywheel Technology Symposium Proceedings, San Francisco, 1978.

6. Post, R. F., and Post, S. F., "Flywheels", Scientific American, Dec. 1973, pp. 17-23.

7. Johnson, D. E. and Oplinger, D. W., "Failure Modes of Bi-directionally Reinforced Flywheels", 1977 Flywheel Technology Symposium Proceedings, San Francisco, 1978.

8. Lawson, L. J., "Kinetic Energy Storage: A 'New' Propulsion Alternative for Mass Transportaion", ASME Paper No. 73-ICT-18.

9. Ullam, D. and Velkoff, H., "An Introduction to the Variable Inertia Flywheel (VIF)", ASME Paper No. 79-APM-5, (also published in the Journal of Applied Mechanics, 1979).

NONDESTRUCTIVE EVALUATION OF FIBER REINFORCED FLYWHEELS

B. W. Maxfield, D. M. Boyd, A. J. Schwarber, S. Kulkarni
Lawrence Livermore National Laboratory
P.O. Box 808
Livermore, California 94550

ABSTRACT

It is presently not possible to define a "good" or even "reasonable" procedure for the nondestructive evaluation (NDE) of fiber reinforced plastics (FRP) because failure modes have not been fully established. There is frequently little correlation between measurable internal structural anomalies (discontinuities, inclusions, voids, etc.) and apparent sites of failure initiation in tests taken to failure. Development of reliable NDE techniques on FRP flywheels requires that the structure be characterized as completely as possible. This information can then be used to continue to seek correlations with the flywheel spin test failures.

This report discusses the NDE problems encountered during the inspection of FRP plates and fabricated flywheels. The FRP plates have been evaluated by ultrasonic immersion and radiographic methods in order to assess the manufacturing quality (uniformity). These evaluations help to minimize the use of defective material in the flywheels fabricated from these plates. Assembled flywheels have been evaluated using the same basic methods, with the exception of measurement constraints, to assess for fabricated related (as opposed to material related) anomalies. The type and general usefulness of the information that is obtained depends dramatically upon the details of the flywheel fabrication. It is clear that if NDE methods are going to be used for quality control and performance certification, then the ability to perform reliable NDE must be made part of the design and fabrication processes.

Ultrasonic NDE methods are useful in the search for small volume internal anomalies such as delaminations. Some FRP assemblies are fabricated by laminating many thin layers to achieve the final thickness. It appears that most normal bonding procedures leave a bond line whose acoustic properties are measurably different from the bulk fiber-plastic matrix. This impedes the uniform flow of elastic energy throughout the material giving rise to two problems. First, it can be difficult to distinguish a delamination from a solid interface of different

elastic properties. Second, when energy is reflected from these internal acoustic barriers, the sensitivity to anomalies on the far side is reduced.

Acoustic barriers in laminated structures have been encountered to varying degrees in our evaluations of both plates and flywheels. The most reliable indication of potentially unacceptable anomalies appears to be a large decrease in the back surface reflection. Any anomaly between the front and back surface will reduce the back surface reflection signal. Evaluations on finished flywheels were made using a contract, hand-scanned transducer because water immersion was prohibited. These inspections were also made more difficult by restrictions on mounting and handling the flywheels. The plates were tested in an ultrasonic immersion tank. The results were recorded as an ultrasonic C scan.

Ionizing radiation NDE methods (x-ray, gamma ray, neutrons) are sensitive to the integrated mass per unit area projected by the radiation beam on the detectors (film, imaging screen, counter). For objects of constant thickness, these methods provide a density variation map. Internal voids such as delaminations are imaged as "bright" regions (less energy loss); particle inclusions denser than the host will appear as "dark" regions. Resolution using standard radiographic methods is about one percent of the radiation path length through the material. Some radiation gauging methods can achieve a resolution perhaps two orders of magnitude better but, obviously, care must be taken to correct for thickness variation. In practice, it is difficult to image delaminations unless the radiation path is parallel to the large dimensions of the delamination.

For reasons discussed above it is not practical to radiographically image delaminations in FRP laminated plates larger than a few inches wide. Since the lamination direction is known a priori and radiation path lengths in flywheels are relatively short, radiography is a useful means of imaging delaminations in flywheels. For example, one flywheel made of 15 layers of FRP had a 3 mil delamination that could be imaged radiographically using 100 kV x-rays emanating from a point source located symmetrically on the flywheel axis about four feet from the flywheel. This delamination could also be imaged using collimated radiation incident tangentially on the circular portion of the flywheel.

This report presents results of NDE investigations on 10 RFP plates and 12 finished rotor assemblies covering five different flywheel designs.

The full text of this paper was not available for inclusion in this volume of the Proceedings. It will be published later in a separate volume.

DATA ANALYSIS TECHNIQUES USED AT THE OAK RIDGE Y-12 PLANT FLYWHEEL EVALUATION LABORATORY

R. S. Steele, Jr. and E. F. Babelay, Jr.
Union Carbide Corporation, Nuclear Division
Post Office Box Y, Oak Ridge, Tennessee 37830

ABSTRACT

Since April 1979 the Oak Ridge Flywheel Evaluation Laboratory at the Oak Ridge Y-12 Plant in Oak Ridge, Tennessee, has applied several advanced data analysis techniques to the problem of experimentally evaluating the performance of high-performance composite flywheels. This paper presents some of the more advanced techniques used. Examples are given for each.

Real-time applications include polar plots of runout with interruptions relating to balance and relative motions between parts, radial growth measurements, and temperature of the spinning part. The technique used to measure torque applied to a containment housing during flywheel failure is also presented. The discussion of pre- and post-test analysis techniques includes resonant frequency determination with modal analysis, waterfall charts, and runout signals at failure.

INTRODUCTION

High-performance composite flywheel rotor development is in that very exciting stage when theories are tested in actual hardware. The quantitative evaluation of that hardware is important since the results either verify the theories, point out where they must be amended, or demonstrate their inadequacy. Unfortunately, spin testing of composite flywheels to the degree needed by this program is not an off-the-shelf capability. Further, each flywheel represents considerable investments of time, money, and expertise by the individuals who design and build them. Thus, to make the limited number of rotor spin tests effective, we are obliged to acquire as much information as possible.

The Oak Ridge Y-12 Plant[a] Flywheel Evaluation Laboratory (ORFEL) has been testing composite flywheels since October 1979. Our task in FY 1980 is to test six prototype flywheels submitted by Lawrence Livermore Laboratory. There was a very deliberate effort to incorporate in this new spin-test facility the very latest analysis techniques readily applicable to the study and evaluation of high performance composite flywheels. In this paper we will discuss some of the data analysis techniques used in ORFEL and present examples of their applications.

DATA ANALYSIS TECHNIQUES

EXPERIMENTAL TEST CONFIGURATION

The basic experiment currently conducted at ORFEL consists of suspending the flywheel pendulously from the flexible quill of an air-driven turbine, then rotating with ever-increasing speed until a failure is encountered. All testing is done above the first rigid-body critical speed so that the spin axis will tend to be along a principal axis of the test piece and through the mass center. The spin tank is shown schematically in Fig. 1. Of course, the mechanical aspects of doing the test are not simple. Mechanical parameters such as safety containment, maintenance of a vacuum environment, turbine speed control, and maintenance of dynamic stability in the flexible quill must all be addressed intelligently to produce a successful test. In this paper we will assume that the mechanical aspects are successfully addressed and concentrate on methods of receiving meaningful data from the flywheel.

[a]Operated for the Department of Energy by Union Carbide Corporation, Nuclear Division under Contract W-7405-eng-26.

SENSORS AND SENSOR CHARACTERISTICS

A typical sensor arrangement about a flywheel is shown in Fig. 1 and 2. We generally use proximity probes above and below the flywheel at the hub to detect location and tilt of the shaft. The target for these probes is usually an aluminum ring placed concentric with the flywheel's geometric center. Since the flywheel rims of interest are usually nonmetallic, photo-reflective probes are used to measure axial and radial standoff of the flywheel rim.

The format of the data contained in the signal from these sensors is identical. Since the sensors produce signals proportional to the instantaneous distance between the sensor and the target, and since the targets are rotating in a periodic fashion, the signals will have two components: a steady-state (DC) component which is proportional to the average distance between sensor and target and a periodic (AC) component which fluctuates about the average and is proportional to changes about that average. These components are readily observed if displayed with respect to time on an oscilloscope or captured with a transient recorder as shown in Fig. 3.

One additional piece of information, a phase-reference signal, is needed to correlate the instantaneous standoff with a particular point on the flywheel. This signal is typically generated by a photo-reflective sensor which watches a dark surface for one-half of a revolution and reflective surface for the remainder. The result is a 50% duty-cycle square wave whose leading edge identifies a particular radius on the wheel and is usually defined as zero degrees.

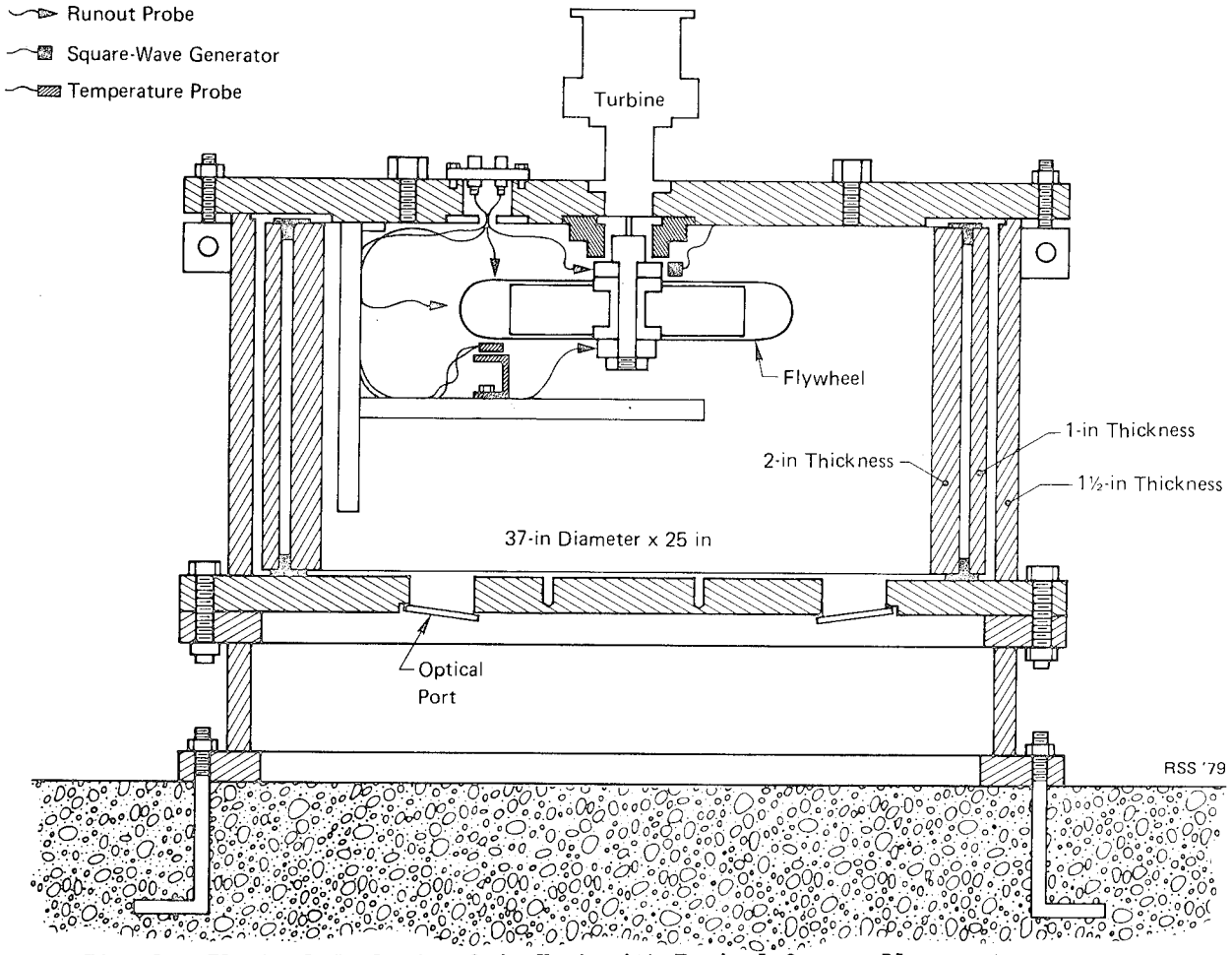

Fig. 1. Flywheel Evalution Spin Tank with Typical Sensor Placement.

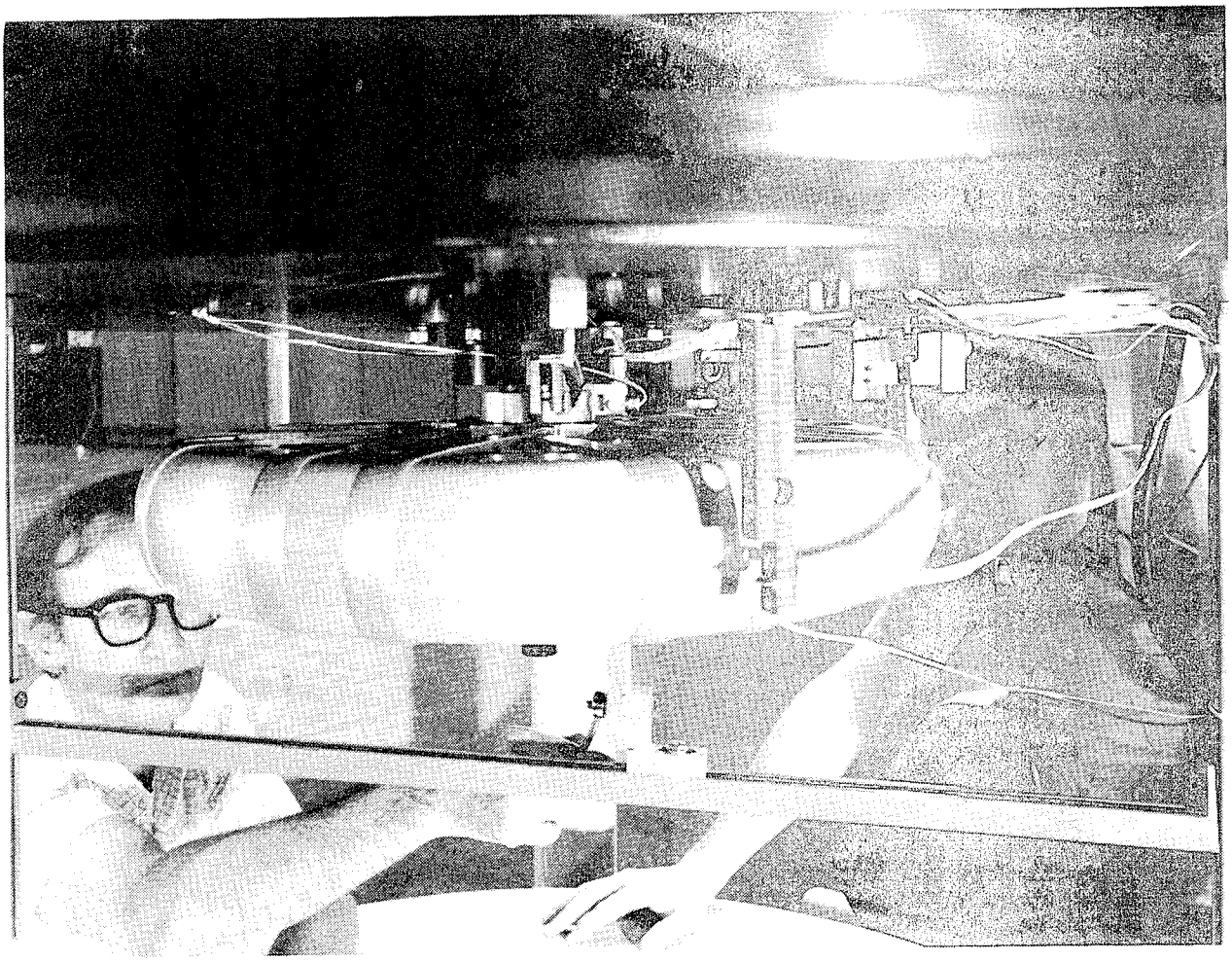

Fig. 2. Flywheel UCCND-2 with Photo-Optical and Electronic Proximity Probes.

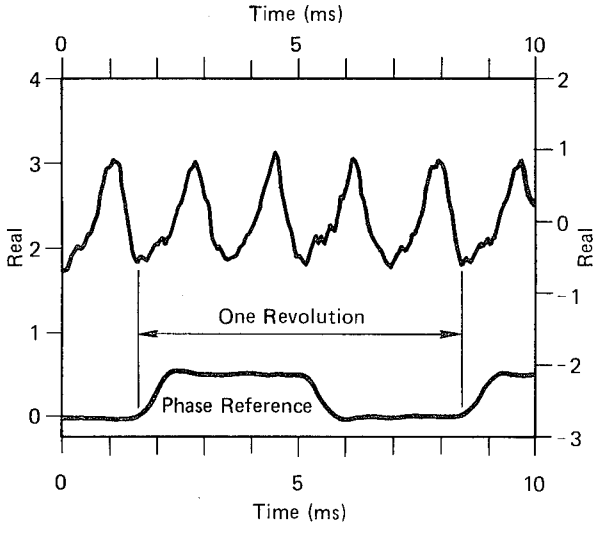

Fig. 3. Time-Domain Plot of a Typical Sensor Output from Garrett AiResearch's Subcircular Flywheel Rim Top with a Phase Reference Signal Bottom. Note the Rims' Four Well-Defined Lobes.

RADIAL GROWTH MEASUREMENTS

The fact that composite flywheels change shape with increasing speed is known but not generally appreciated. A 600-mm (23.62-in.)-diameter flywheel may change 10 mm (0.4 in.) in diameter between its rest and at-speed spin states. Measurement of this property provides an excellent check of an analytical stress model's validity.

The measurement relies on the DC component of the standoff signal from a radial probe. A slow change in the DC component is proportional to a change in the radius of a flywheel and can be monitored using a slow response voltmeter. Fig. 4 is a plot of the radial growth of Flywheel UCCND-2. Note that the scatter in the data decreases as flywheel speed increases. The scatter appears because the response time of the voltmeter was too high and thus was affected by a portion of the AC component at low speeds. Future

measurement will use a low pass filter to reduce that response time.

Flywheel UCCND-2 was a band wrap design in which the spokes wrapped around the outside of the rim. The predicted curve shown is for a rim only--without support bands. The agreement between the two is not particularly good. This may indicate that the bands helped support the rim and thus reduced the radial growth. Other possible reasons for this disagreement include selection of nonrepresentative material properties for the model and incorrect calibration of the measurement sensor. Changes in surface reflectivity will also affect calibration.

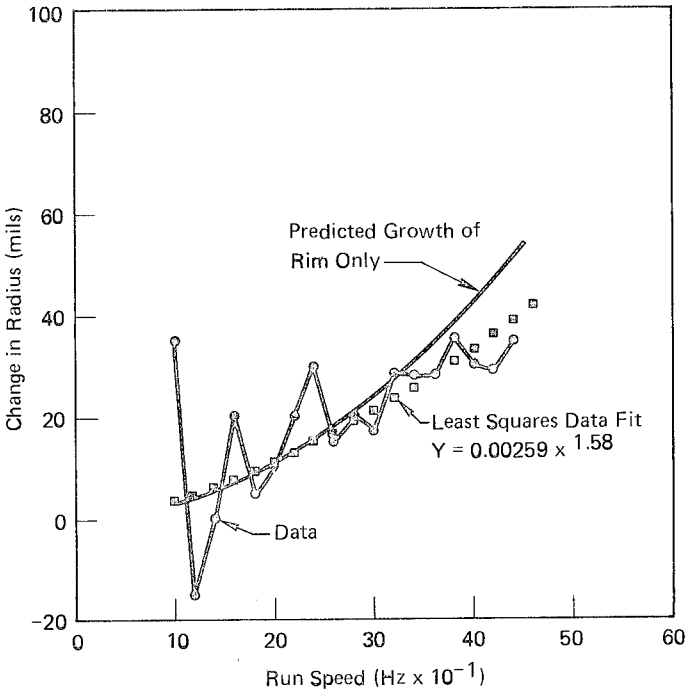

Fig. 4. Rim Radial Growth with Speed, UCCND-2, Test Run 3.

RUNOUT MEASUREMENTS

The AC component of a probe's signal is usually more exciting to analyze since it contains information related directly to the motion of a very rapidly moving object. Rotation of the flywheel at speeds above the rigid body critical frequency dictates that the spin axis must pass through the mass center of the test piece. If the target surface is circular but not concentric with the mass center, the AC component of the sensor will be a sine wave whose frequency is the run speed. The peak-to-peak amplitude of the sine wave is the difference in distance between the points nearest and farthest from the sensor, as is illustrated in Figure 5. That difference is twice the distance from the mass center to the geometric center of the target and is usually called runout. The phase angle or direction of the eccentricity can be determined by triggering an oscilloscope trace as the flywheel passes through a particular angular orientation. Knowing the relative positions of the standoff sensor and the square wave generator, the point on the target closest to the sensor is identified by measuring the percentage of one revolution completed when the highest point on the sine wave occurs. In Fig. 5 the near point is located at 270 degrees, and the far point at 90 degrees relative to the flywheel. Thus, the mass center of the flywheel is located a distance "e" in the direction of 90 degrees from the geometric center.

The eccentricity is easily read directly from the oscilloscope trace but suffers the accuracy, sensitivity, and repeatability limitations of any measurement from an oscilloscope trace. Electronic equipment designed for making this measurement has been used by turbine manufacturers and noise analysts for many years. The heart of such equipment is usually a tracking signal analyzer which measures both amplitude and phase of a data signal with respect to a reference signal. In our system this is equivalent to measuring the x and y distances of the geometric centroid relative to the mass center. An important feature of these analyzers is a tracking notch filter which allows only data occurring at the reference frequency to be measured. This becomes important when target surfaces are not circular and/or contain perturbations such as surface flaws. These filters also eliminate the contribution of whirl modes except when in resonance with the reference signal. Data are usually plotted with increments in speed as presented in Fig. 6.

Initially, the most obvious use for these data is in balancing. In the case of a simple disc, a weight is applied opposite the old mass center such that the new mass center coincides with the geometric center. Thus a minimum load on the bearing and support structure is achieved since most bearing support systems are aligned with the geometric

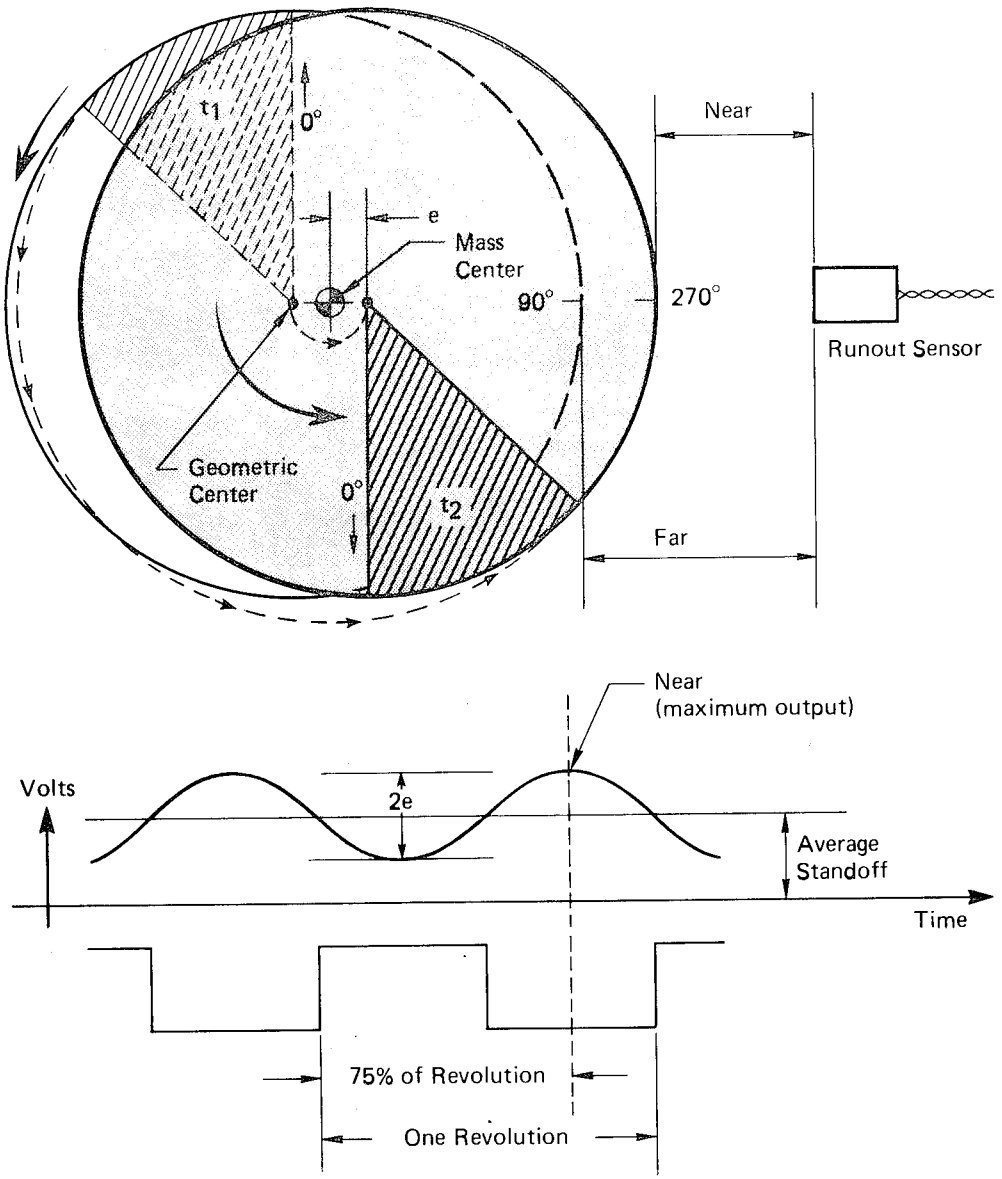

Fig. 5. Development of a Sine Wave Runout Pattern by a Circular Surface Rotating About its Mass Center.

center. In the case of flywheels with significant axial dimensions, a multiplane balancing technique is usually required. Many techniques may be found in advanced technical articles on this subject. Most require runout information of the type described here for runout in several planes during trial runs.

Once balance is achieved, these data become indicators of changes in the position of a target surface's centroid with respect to the spin axis. The location of one centroid with respect to another is one-half the vector difference in their respective runouts. Thus, the movement of one part of a flywheel relative to another is found by observing motions in their respective centroids. This assumes that the motion of the target surface is indicative of movement in the bulk of that part.

The clearest example of this is shown in Fig. 6. These are the runout plots of two sensors observing an aluminum disc assembly with a central steel arbor. The test setup is shown in

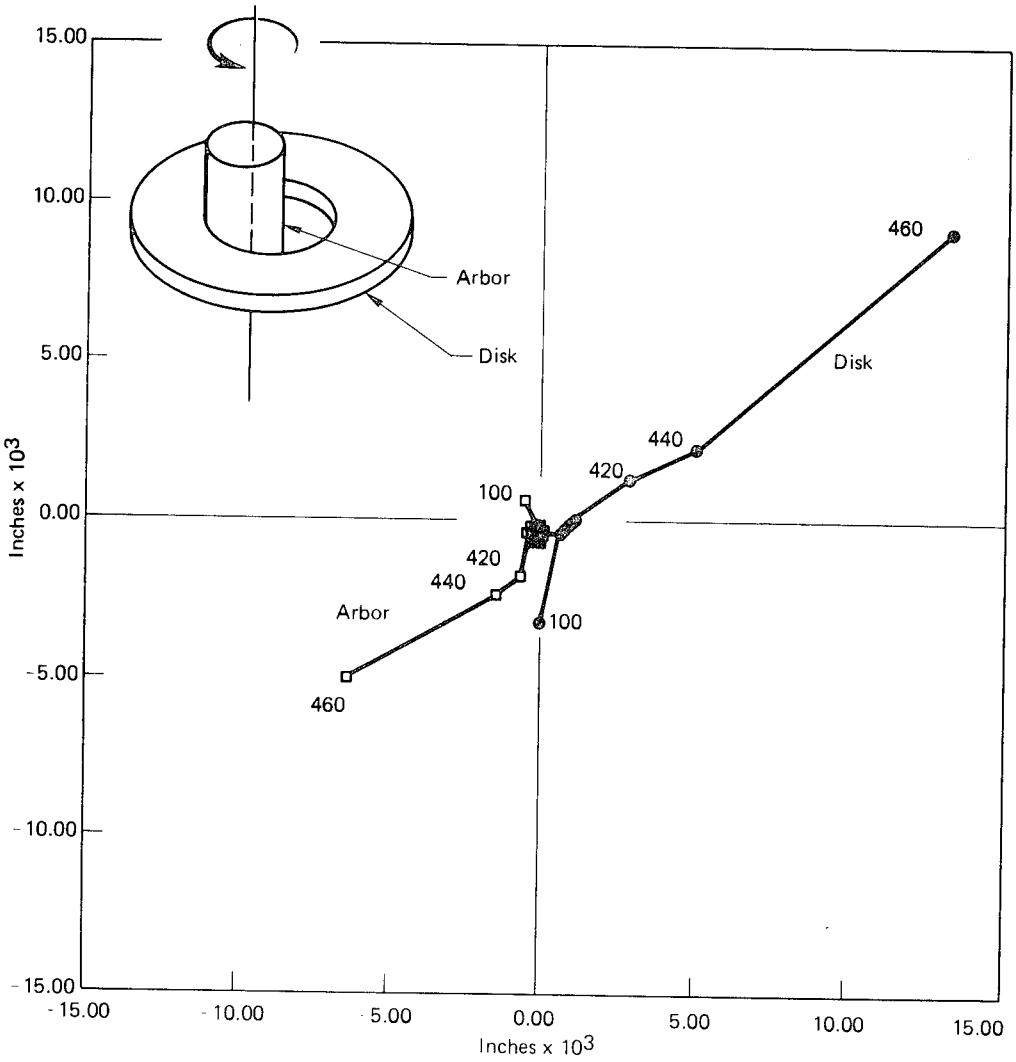

Fig. 6. Disk and Shaft Runout Plots from Dummy -2.

Fig. 7. The data in the runout plot indicate that above 400 rps the disc centroid moved in one direction while the shaft centroid moved in an opposite direction relative to the mass center (the center of the plot). The distance between the two 460-rps speed points is approximately 0.025 inch, which corresponds nicely with the post-test diametrical clearance between the arbor and disc. This plot shows that a clearance first developed between 400 and 420 rps. The arbor chose to rest against the disc hole at about 220 degrees on the disc. As the central hole grew with speed, the eccentricity of both arbor and disc grew since the system mass center must be between these two parts.

So far, we have only considered that portion of the runout signal which is synchronous with the spin frequency. There are at least two other important surface displacements which may appear in these runout signals at a frequency other than the run frequency. They are the result of nonsynchronous whirl and flexural vibration of the flywheel.

Nonsynchronous whirl is a resonant condition of the support system and test piece. It can become destructive when the support system of a spinning, rigid body has insufficient mechanical damping to keep the amplitude of these resonant frequencies insignificantly small. The analytical model of the phenomena has been fairly well described.[1,2] Once the characteristics of the support system are defined these models agree well with experience (see Fig. 8). The occurrence of whirl in a runout signal is shown in Fig. 9. The high frequency

structure is the eccentricity or synchronous runout. The lower frequency component is that contributed by non-synchronous whirl. The frequency of the whirl component can be determined from a trace such as the time domain signal in Fig. 9. A more precise measure is obtained using a spectrum analyzer.

Most readers are familiar with an oscilloscope as an electronic device for displaying a voltage signal with respect to time, i.e., in the time domain. A spectrum analyzer will display the same voltage signal with respect to frequency content, i.e., in the frequency domain. The lower trace in Fig. 9 is the frequency domain display of the upper trace. This clearly shows that the upper trace contains two distinct frequency components. Knowledge of the physical setup allows the operator to identify the lower frequency component as the first-forward whirl mode at 17.2 Hz and the higher frequency component as the run frequency of 177 Hz. Measurements with this accuracy are nearly impossible using a typical time-domain display.

Flexural vibration of a flywheel may also occur and will be observed in the displacement signals. Flexural vibrations are encountered because flywheels are not truly rigid bodies. They bend, twist, and bounce at various natural frequencies, to various degrees depending upon stiffness, geometry, excitation, and damping. Dual-channel spectrum analyzers, capable of measuring and recording both an input forcing function and a structure's response to that forcing function, are capable, with sufficient computer support, of performing modal analyses. A modal analysis is one in which the natural frequencies of a structure are identified and the resonant motion is described. For example, a modal

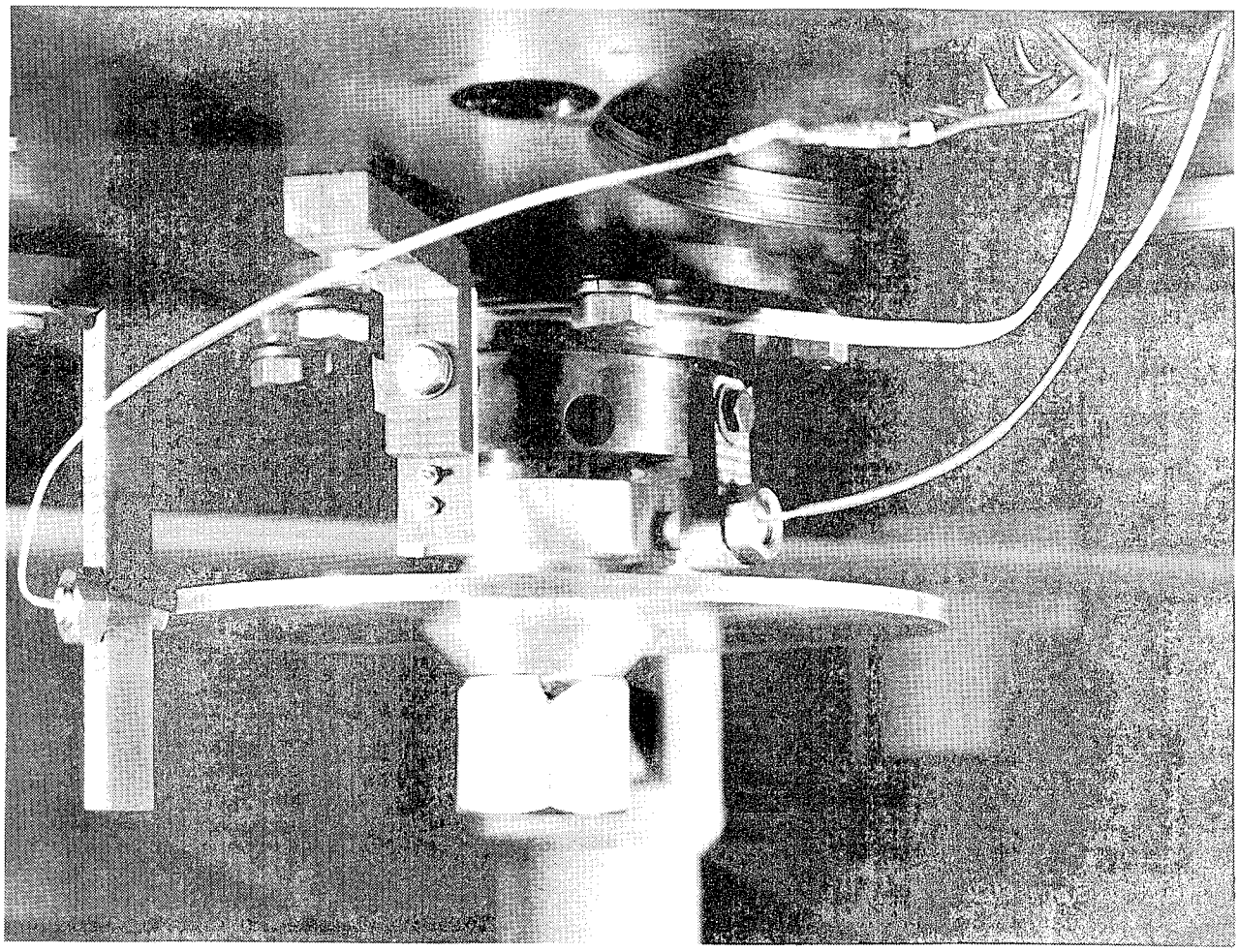

Fig. 7. Sensor Arrangement for Dummy-2 Testing.

analysis of Flywheel UCCND-5 is presented in Fig. 10. These are the six lowest natural frequencies identified for that flywheel when the hub is bolted to the ground. Each figure is a schematic representation of the undeformed and maximum positive and negative displacement configurations of the flywheel vibrating in each particular mode. These modes were excited by tapping the flywheel with a small calibrated hammer with the flywheel at rest. Unfortunately, for ease of analysis, these natural frequencies change with the square of the spin frequency and each could have its own individual scaling factor. This experimental modal analysis is useful because it verifies analytical flywheel models, identifies modal parameters, and indicates which are the predominant frequencies most likely to be of concern during a spin test.

During a run at ORFEL, frequency-domain signals are monitored and recorded. Post-test analysis of each sensor's signal is then performed. Each signal is plotted in the frequency-domain for each 5-rps increment in speed. This produces a so-called waterfall chart, as shown in Fig. 11. The only feature in the plots germane to the present topic is the small ridge line just to the right of the runout ridge between run frequencies 375 and 420 rps. This ridge did not appear on the axial sensor's signal. Absolute identification of this ridge has not been completed because these points match fairly well with both the second-forward whirl frequency and the possible location of the two higher natural vibrational modes. In fact, this may be a resonance of both phenomena.

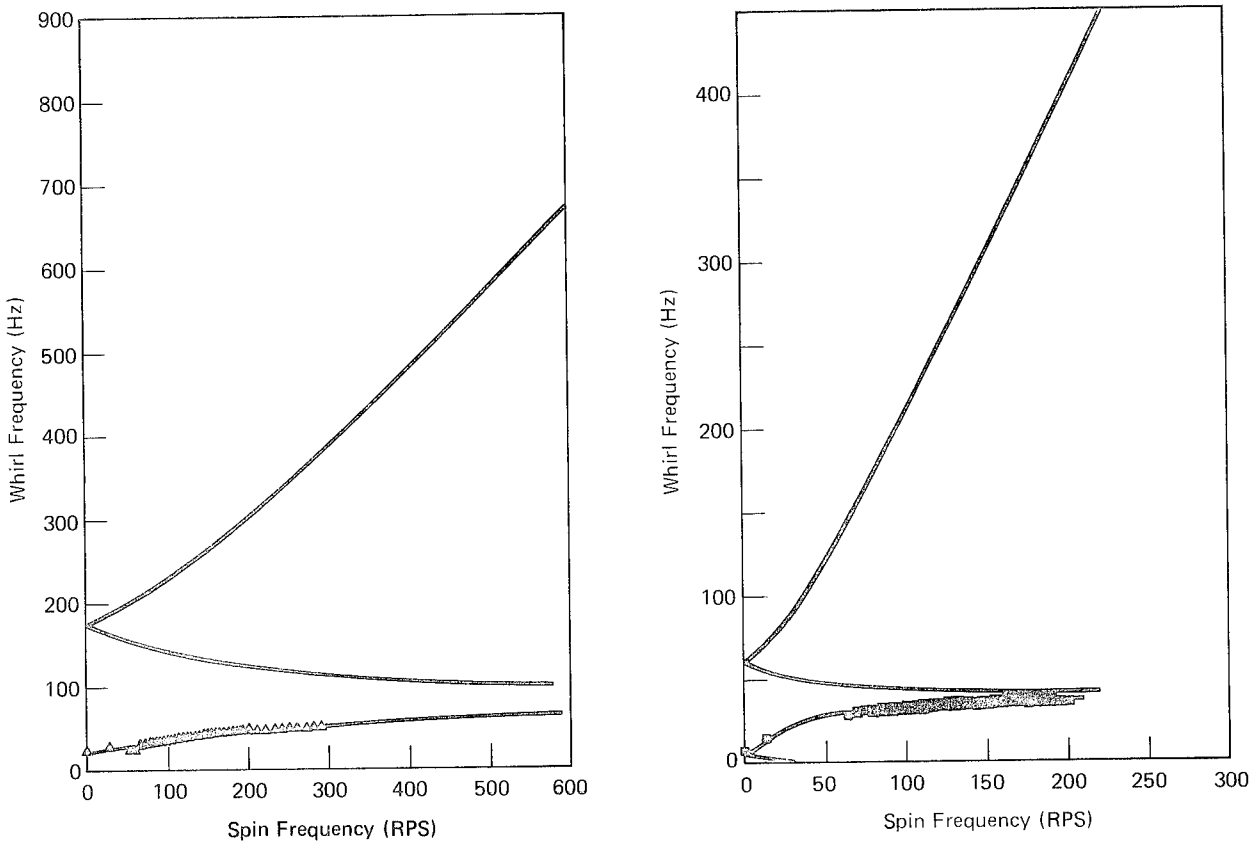

(a) Whirl map for Dummy-3.

(b) SLA wagon wheel.

Fig. 8. Comparison of Experimental Data with Predicted Whirl Maps for Two Different Flywheels Using the Same Suspension System.

MEASUREMENT OF CONTAINMENT TORQUE

In bringing a spinning mass to rest, both linear and angular momentum must be reduced to zero. Thus, to

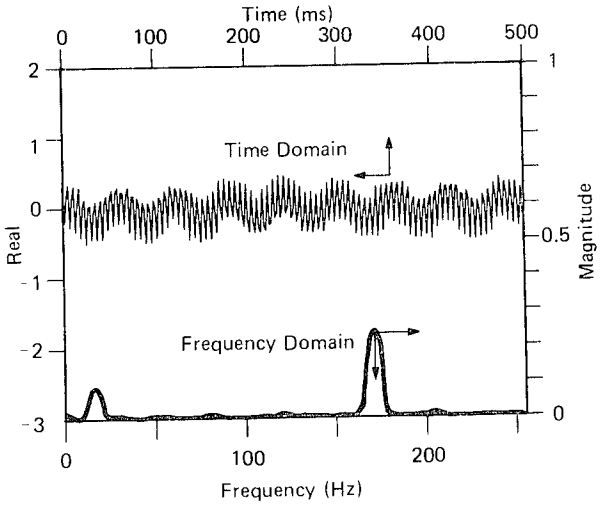

Fig. 9. Time and Frequency Domain Presentation of Flywheel Sensor Data Showing Runout and First-Forward

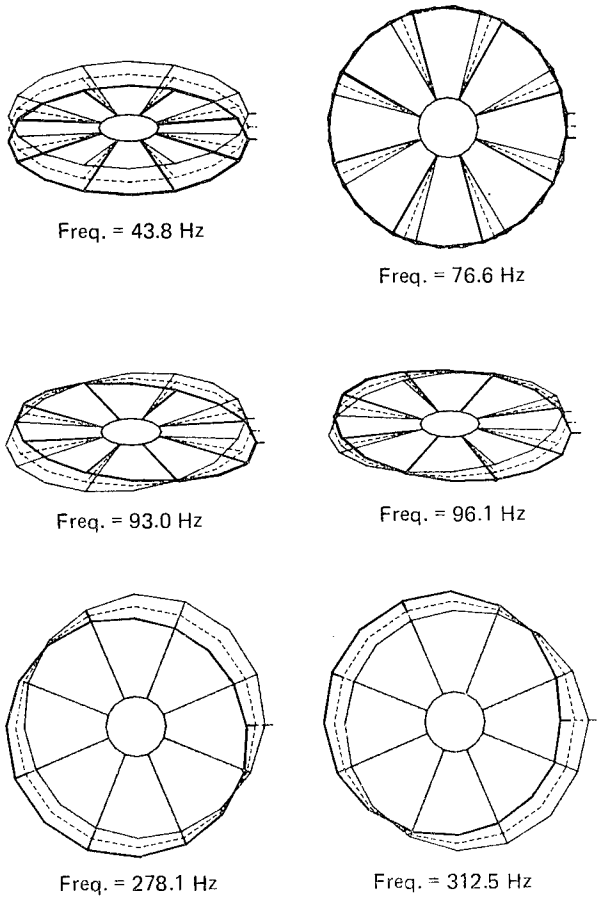

Fig. 10. Six Lowest Vibrational Frequencies of Flywheel UCCND-5 with the Corresponding Resonant Motions.

contain a failing flywheel, the primary containment and its support system must be capable of transmitting the forces required to neutralize both types of momentum. Most fiber-composite flywheels are designed to fail by shredding rather than breaking apart into chunks. Containment of these small fibers is not expected to be a severe problem since each fiber contains only a small amount of linear momentum and the total linear momentum of all particles must add vectorially to zero. In fact, this is one of the very attractive features of composite flywheels.

On the other hand, the total angular momentum contained in a flywheel must be absorbed by the containment and support structures during a failure. The rate at which momentum is absorbed is proportional to the torque opposing it provided by the containment and support system. The key is how the failure mode of a flywheel interacts with the containment.

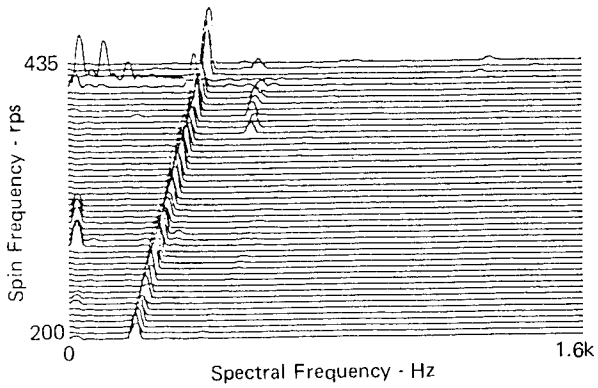

(a) Radial probe, top arbor.

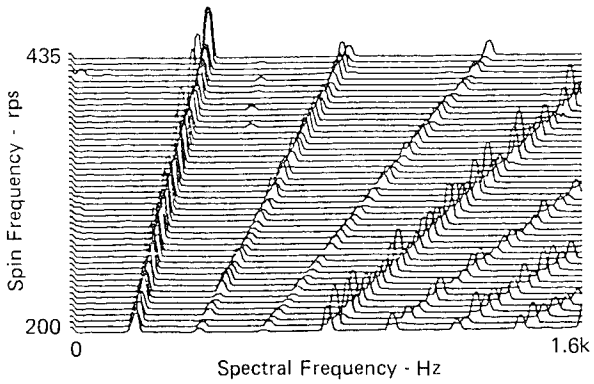

(b) Radial probe, outer rim.

Fig. 11. Waterfall Chart of Radial Sensors Spectral Distributions from UCCND-3, Run 15.

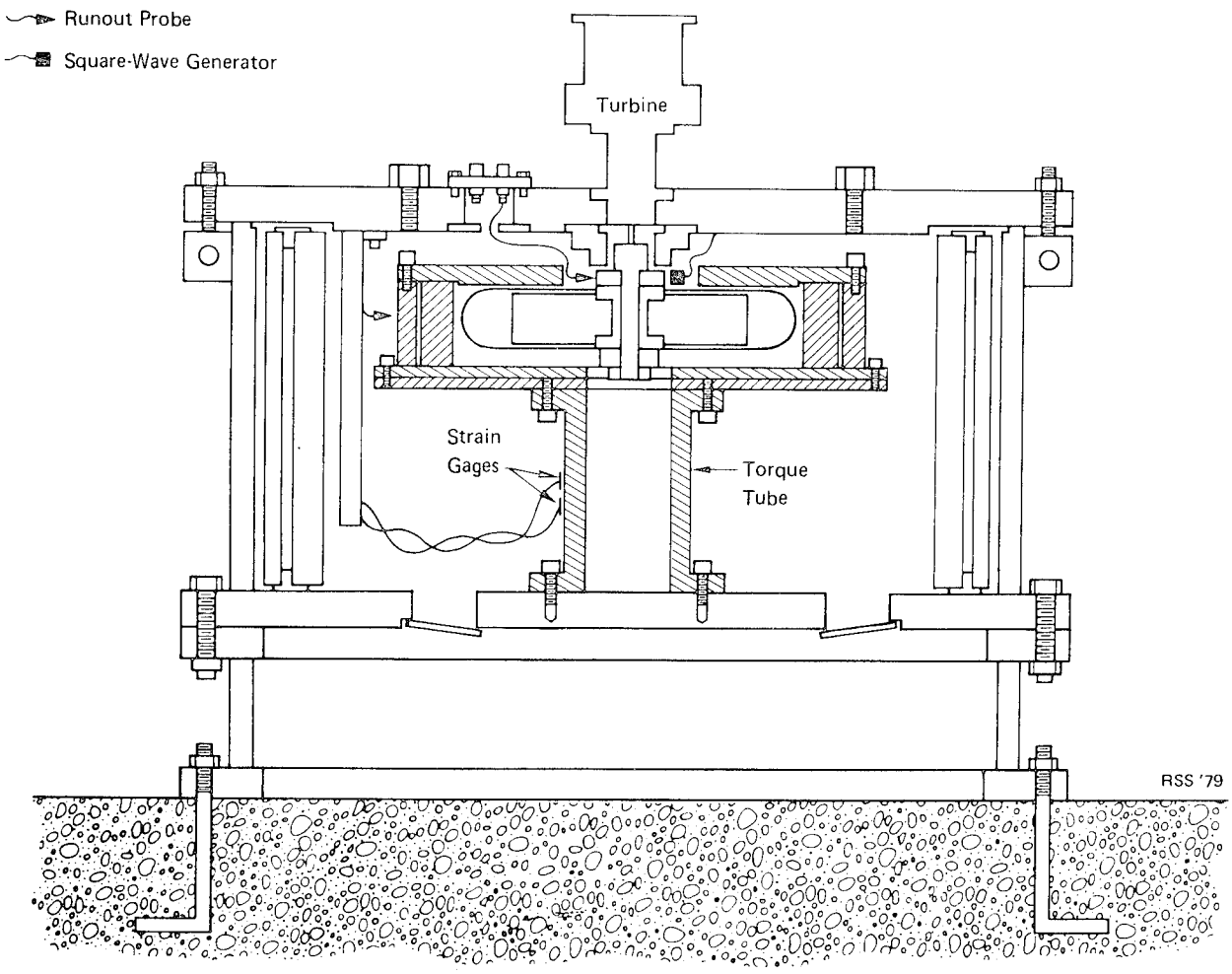

Fig. 12. Torque Tube and Housing Inside the Spin-Test Chamber.

Very little data exist upon which to base containment design specifications. To develop a data base for torque specifications, an apparatus has been built, calibrated, and used in ORFEL. The test apparatus is shown schematically in Fig. 12. This is basically a housing with a clearance between its ID and the flywheel similar to that anticipated in automotive applications. This housing can be customized by simply fabricating new components. Supporting the housing is a steel torque tube 406.4 mm (16 in.) in length with 304.8 mm (12 in.) in diameter flanges on each end. The tube section is 107.2 mm (4.22 in.) in ID and 152.4 mm (6.0 in.) in OD. The central portion of the tube is instrumented with 16 strain gauges. Half are dedicated to torque bridges and half are wired to respond to lateral loads. The torque tube is calibrated to 184,400 N-m (136,000 ft-lb) torque and is expected to be linear to over 271,000 N-m (200,000 ft-lb). Lateral load calibration is to over 88,960 N (20,000 lb) in two orthogonal directions.

The torque measuring system has been used twice, with Flywheels UCCND-4 and UCCND-5. Fig. 13 shows the results with UCCND-4. The flywheel was rotating at 349 rps, stored 0.193 kW-h at 26.9 W-h/kg, and stopped in less than 3.5 ms. The peak measured torque was 515,000 N-m (380,000 ft-lb) with an average of approximately 203,000 N-m (150,000 ft-lb) over the 3.45 ms pulse period. The failure of the UCC-ND series bandwrap flywheels initiates in

the bands. When confined in the torque tube housing the failed band material tends to form a wedge which pushes the rim to the opposite side until it becomes jammed between the side and the wedge. Further rotation simply increases the jamming effect and the rim is brought to a very rapid stop. The result is a high torque for a short duration. The wedge and rim in the jammed position are shown in Fig. 14.

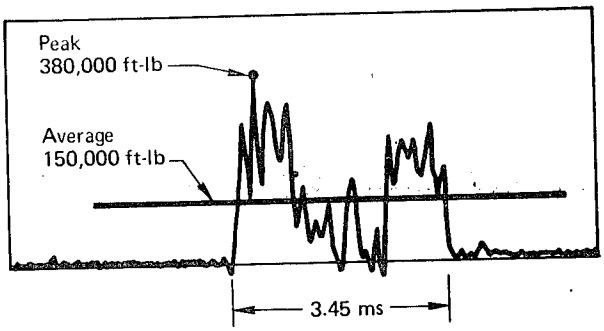

Fig. 13. Torque History in Support Tube During Failure of UCCND-4.

The second flywheel, UCCND-5, failed in a nearly identical fashion but over a much longer time period. Measured torque values were an order of magnitude less. Both tests produced torque values considerably greater than was popularly thought possible.

CLOSING

In this paper we have tried to present the fundamentals of data acquisition and interpretation used in ORFEL. While many of the techniques suffer accuracy limitations and most will benefit from further development, we feel they each currently reveal some piece of information which adds to our understanding of composite flywheel and their characteristics which might otherwise be unnoticed.

REFERENCES

1. J. P. Den Hartog, Mechanical Vibrations, 4th ed., (McGraw-Hill Book Co., New York, 1956, Chap. 6).

2. W. T. Thompson, F. C. Younger, H. S. Gordon, "Whirl Stability of the Pendulously Supported Flywheel System," Transactions of the ASME, Journal of Applied Mechanics, Vol. 44, June 1977, pp 332, 328.

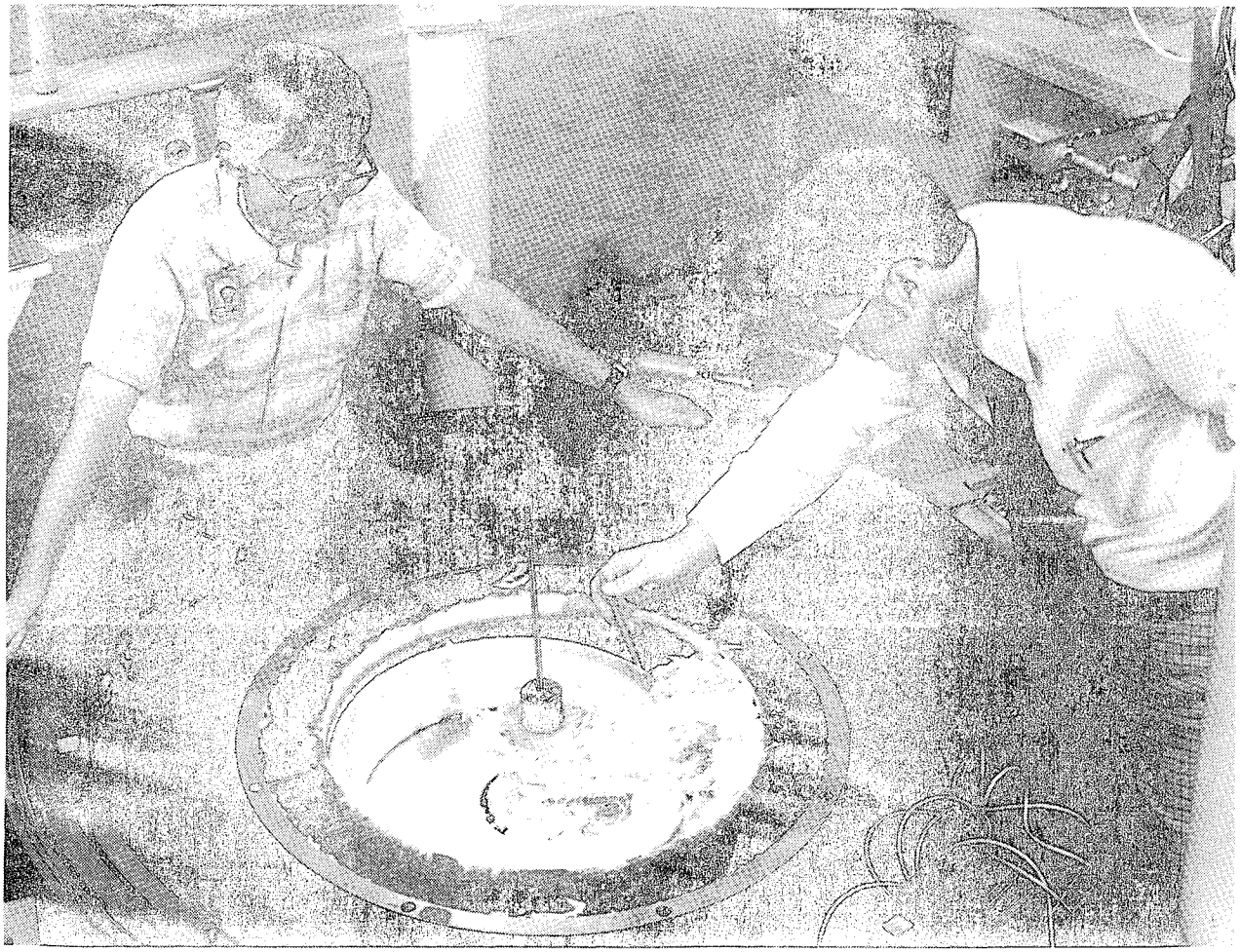

Fig. 14. Flywheel UCCND-4 Debris Inside Torque Tube Housing after Test Run 6.

MOIRE' STRAIN ANALYSIS OF COMPOSITE FLYWHEELS

G. Cuccuru/B. Picasso
Universita Di Cagliari - Facolta Di Ingengeria
Instituto Di Meccanica
09100 Cagliari, Piazza d' Armi
Italy

ABSTRACT

This paper deals with the problem of measuring strains on rotating composite flywheel models by means of moiré technique. Among the classical experimental techniques, strain gages were extensively used by the Authors [1], [2] during a three-years test program on filament wound composite flywheels. The results are briefly discussed in this paper with the object of underlining some of the main drawbacks and limitations of this technique. In particular, the need of an electric transmitter which is in general a noise source in the measuring chain and represents a severe limitation in the number of measuring points available. When tests are performed on filament wound flywheels which are expected to fail with radial delamination, reliability of strain gage data seems to be very poor. Another relevant problem derives from difficulty of heat dissipation in the composite material and consequent errors in strain measurements.

The above mentioned problems were the reason for trying to apply an alternative technique based on the classical moiré method for measuring in plane strains. The model used during the tests was a 500 mm outside diameter single rim flywheel connected to the shaft through a polyamide disc. The rim material was an epoxy resin glass fiber composite with a fiber content of about 65 percent. The model was designed to attain a maximum speed of about 25.000 rpm with a corresponding energy density of 50 whrs/kg. Two different experimental procedures were tried: in the first one moiré grids were bonded on the rim and inner disc; reference grids were stationary and placed at the same radius as the model grids with a gap of about 5 mm. Moiré fringes were observed in stroboscopic light with a commercially available stroboscopic unit. The grids had 500 lines/mm and permitted the observation of fringes only for grid lines disposed in the circumferential direction. In fact with the stroboscopic lamp adopted the flash duration of about 1.2 μS was not short enough to "freeze" the relative motion between the model and reference grids. At a running speed of 9000 rpm at a radius of 200 mm the circumferential displacement corresponding to a time interval of 1μS is about 0,2 mm which is definitely too high for a grid whose pitch was 0,05 mm. For this

reason it was impossible to obtain moiré fringes when grid lines were in the radial direction. Since a high intensity discharge lamp with a flash duration in the range of nanoseconds or a pulse laser were not available, an alternative technique was tried. The reference grid was superimposed on the model grid and bonded to the model material only along a circumferential line. In this way a known strain state of the reference grid was added to that of the model giving a moiré fringe pattern. An initial mismatch was obtained by using moire grids of slightly different pitch. This resulted in an increase of sensitivity which permitted the evaluation of one tenth of a fringe. During the analysis of the experimental results the calculated strains due to rotation of the reference grid were subtracted from those calculated from the fringe pattern to give the actual strain state of the model. Comparison of experimental results with analytical data permitted an initial evaluation of reliability and applicability of the technique.

References

G. A. Cuccuru, F. Ginesu, B. Picasso, P. Priolo - Characterization of Composite Materials for Filament Wound Flywheels. To be published on "Journal of Composite Materials - Technomic Publishing Co. Inc.

F. Ginesu, B. Picasso, P. Priolo - Analisis sperimentale di deformaxioni su volani in vetroresina - CNR - Progetto finalizzato ENERGETICA - Rapporto di avanzamento - Giugno 1977.

The full text of this paper was not available for inclusion in this volume of the Proceedings. It will be published later in a separate volume.

EXPERIMENTAL INVESTIGATION ON THE VIBRATORY BEHAVIOUR OF FILAMENT WOUND COMPOSITE MATERIAL DISCS

G. Cuccuru, B. Picasso, P. Priolo
Department of Mechanics, University of Cagliari,
Piazza d'Armi, 09100 Cagliari, Italy

ABSTRACT

A systematic approach to the static and dynamic non-destructive characterization of filament wound composite material has been attempted for a class of thin annular discs. Five models of various dimensions were subjected to static loading tests and six to vibrating tests, with the main objective of determining the elastic properties. The behaviour of the material, a fiber-glass polyester resin composite, did not allow a quantitative interpretation of the whole set of data, at least with the experimental techniques adopted. Nevertheless, the work could be considered as an initial point of discussion in this field.

INTRODUCTION

Various investigations have been carried out recently concerning the experimental evaluation of the elastic stiffness of composites, by means of resonant analysis of beams under flexural vibration[1,2]. In certain cases[3,4], the resonant condition has been utilized to evaluate structural integrity.

The outstanding qualities of filament wound composite materials for rotating machinery applications such as flywheels or rotors of more general shape, renders the investigation of dynamic characterization techniques particularly attractive.

In this work, the flexural static and dynamic behaviour of a series of glass fiber polyester resin discs has been examined, mainly to clarify some methodological aspects proposed in previous works[5,6]. Besides the classical resonant dwell technique, based on the measurement of the dynamic parameters to detect resonant frequencies, holographic interferometry was extensively used due to its ability to provide visual information of the entire deformation field and modal patterns, as well as to localize delaminations and structural defects.

The first aim of the research was to determine the principal elastic properties for small deformations. In order to obtain static and dynamic values, a static transverse loading test was performed on each disc, followed by a dynamic test with variable excitation frequency.

In principle, it is possible to deduce the elastic static rigidities by analysing the static deformed shape, and the elastic dynamic moduli from the resonant frequency values.

The external disc radius was gradually reduced in order to increase resonant frequency values.

However, it is the authors' opinion that for this type of material transverse loading can produce critical conditions even at very low levels of deformations and stresses. The tendency to delamination typical of filament wound composites, is probably accentuated by the test itself, thus generating highly dispersed data. This fact made it nearly impossible to give a unitary interpretation of the results.

In spite of this the methodology and test results are described in detail in this paper, since they are considered useful for a better comprehension of composite materials. Five static and six dynamic tests were performed on models of various diameters obtained by machining two large discs made of a glass fiber polyester resin composite.

ELASTIC PROPERTIES

The fiber glass polyester resin composite had a fiber volume density of 0.5-0.60 and calculated average elastic para-

meter values[7] of:

$$E_t = 4.15 \cdot 10^{10} \ N/m^2$$
$$E_r = 1.07 \cdot 10^{10} \ N/m^2$$
$$\nu_t = 0.26$$
$$G = 4.2 \cdot 10^{9} \ N/m^2$$

Preliminary tests were conducted on ring-shaped specimens (Fig.1) according to the loading situation a) and b).

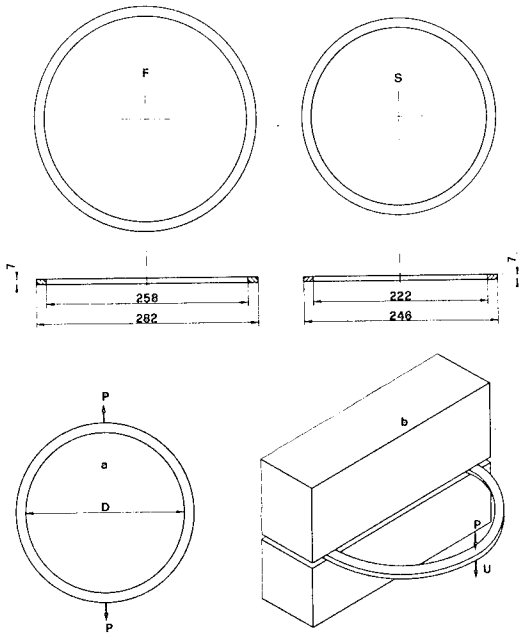

Fig. 1. Rings used for static characterization

By adopting method a), i.e. measuring load P and diameter D variation, it is possible to evaluate the elastic flexural modulus E_t in the plane of the specimen. Using method b), i.e. measuring displacement u and load P, a simple relation between E_t and the tangential modulus G can be obtained. Test results are summarized in Table 1.

Table 1. Static properties of the material

Specimen	E_t (N/m^2)	G (N/m^2)
F	$3.95 \cdot 10^{10}$	$6.78 \cdot 10^{9}$
S	$3.66 \cdot 10^{10}$	$6.87 \cdot 10^{9}$

METHODOLOGY

STATIC CHARACTERIZATION

A disc shaped model is transversely loaded by a force acting on the center of a rigid hub (see Figs. 2b and 3b), to which the internal edge can be considered perfectly clamped. The external edge is simply sustained by a rigid support. By means of double exposure holographic interferometry, the whole disc deformation can be recorded.

If we consider an axisymmetric deflection w(r), the elastic strain energy of an annular orthotropic disc of small thickness h is:

$$V = \int_a^b \{D_r (w'')^2 + 2\frac{D_1}{r} w'w'' + \frac{D_t}{r^2} (w')^2\} \, rdr$$

When the disc is loaded by a force P acting along the inner radius and supported at r = c, the work done by the force is:

$$W = P \{w(a) - w(c)\} \qquad (2)$$

When the internal edge is restrained from rotating no other contributions to the external forces exist, and therefore:

$$V = \frac{W}{2}$$

By measuring w(r), P and thus deriving w' and w'' and assuming that flexural rigidities are independent of the radius, a linear relationship of the rigidities D_r D_l D_t can be written. Treating in this way several independent cases, it becomes possible to write a system of equations capable of determining the elastic properties.

A primary source of error is due to the double differentiation of the measured deflected surface w_s. To reduce this error to within reasonable limits, we operated with high density holographic fringe patterns and preferred to evaluate derivatives by means of the graphical method rather than analytically[8,9].

From careful examination of the fringe pattern noticeable deviations of the real model from the ideal one can be observed: a small relative rotation of the disc edge with respect to the hub; a certain dissymmetry of the deformed surface; the support impedes rotation to a certain extent.

The introduction of corrections for these deviations proves time consuming and burdensome from a computational point of view. However, when non-symmetry plays a secondary role, the same order of accuracy can be achieved by the simpler procedure consisting in starting from the equation of the deflected surface of an orthotropic thin disc transversely loaded[10]:

$$w(r) = A + Br^2 + Cr^{1+k} + Dr^{1-k}$$

where $k = D_t/D_r$ and A to D are constants. If the following boundary conditions are imposed

$r=a \quad N_r = -D_r(w'''+w''/a) + D_t w'/a^2 = -P/2a$

$w'(a)$ = experimental value

$r=c \quad w(c) = 0$

$w'(c)$ = experimental value

the constants A,B,C,D are determined. This solution can be considered dependent on D_r and k; then, varying these parameters, the best fitting for the experimental average curve w_s can be obtained. It must be observed that in practice, for every value of k a value of D_r can be determined which satisfies the above condition.

Both methods here described were applied to the five discs tested; slightly higher values of E_r and E_t were obtained with the first.

DYNAMIC CHARACTERIZATION

Models were tested with clamped inner edge and outer edge free on a piezoelectric shaker driven by an audio oscillator.

Real time holography with initial mismatch in conjunction with time average holography were used for resonant frequency and modal pattern identification. To check the experimental results of the holographic analysis a standard vibration exciter was used, in order to obtain a better understanding of the dynamical behaviour of the models. Amplitude, force and acceleration were measured while forcing frequency was varied over the range of interest.

Experimental frequency values were compared with values obtained by a finite element program, roughly verified in the past[5], corrected to consider rotatory inertia and shear effect. The comparison was made by plotting curves of the analytical frequencies, obtained by varying the elastic constants, and finding the intersection with the corresponding experimental values. Due to the importance of modulus E_r the horizontal axis always refers to this quantity.

STATIC ANALYSIS

Five models were tested with outside diameters ranging from 282 to 179 mm. Figures 2 and 3 show the holographic fringe patterns and displacements along two orthogonal diameters. A check of load-displacement linearity showed in some cases high deviations and non-repeatability of results. A general tendency to an increase of strain with increasing loads in respect of linearity has been observed. Fringe pattern observation led to the following considerations:

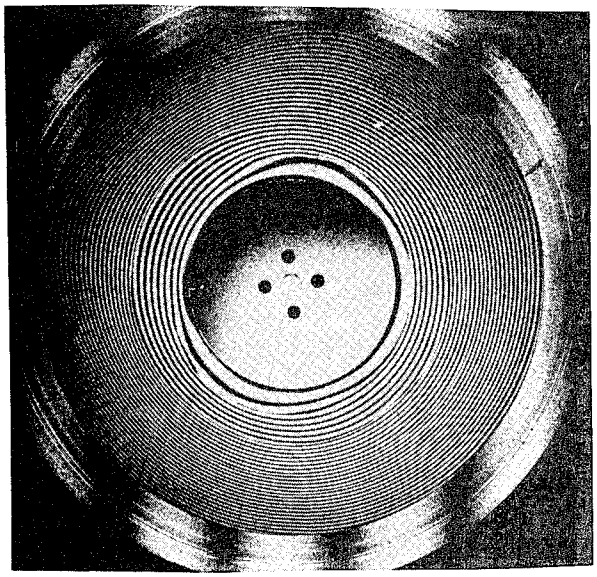

(a)

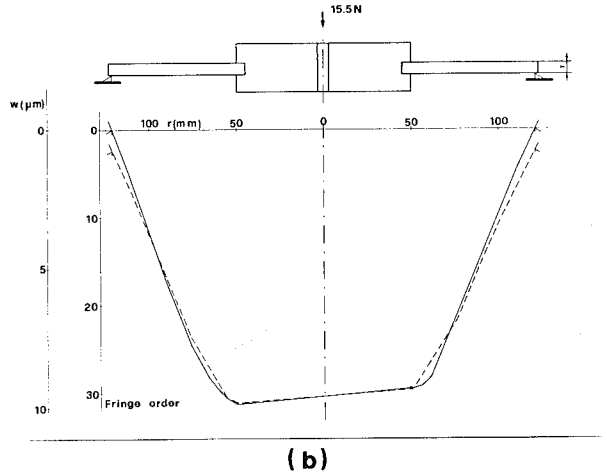

(b)

Fig. 2. Static loading: a) fringe patterns b) deflections along two orthogonal diameters

- presence of partial (Fig.2) or complete delaminations (Fig.3) shown by fringe concentration or superimposition;
- distortion of deflected disc shape (Figs. 2 and 3) shown by fringe ovalization.

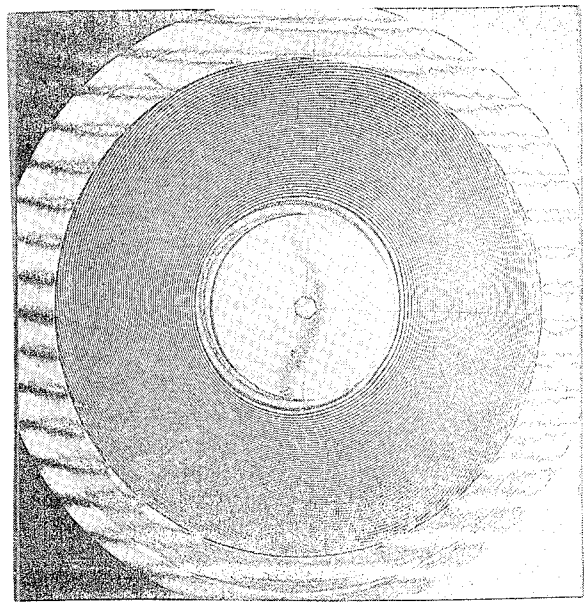

(a)

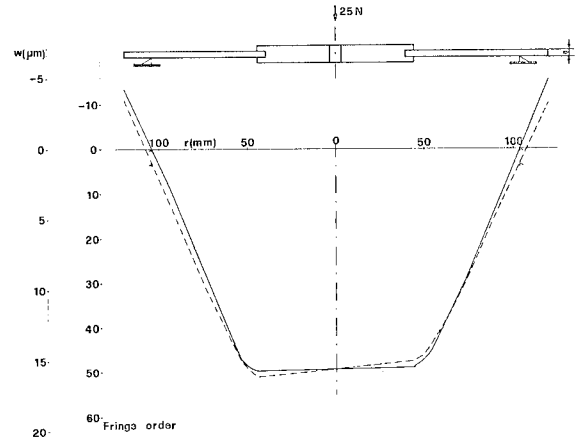

(b)

Fig. 3. Static loading: a) fringe patterns b) deflections along two orthogonal diameters

From examination of the displacement curves the following were established:

- delaminations evidenced by sudden slope variations;
- non-symmetry shown by different displacement behaviour on the two diameters;
- displacement of the external support;
- insufficient constraint against rotation at the connection with the central hub, shown by the slop of the curve at the inner radius.

In spite of the considerable disagreement in some cases with the analytical model, an analysis of the results from the characterization point of view was attempted.

If we fix some value of the elastic parameters to the expected value, i.e. assume for E_t and ν_t $3.92 \cdot 10^{10}$ N/m^2 and 0.26 respectively, we can obtain by the second method described above, for the first two models for E_r $9.12 \cdot 10^9$ and $7.38 \cdot 10^9$ N/m^2 and for the three models cut from the second original disc $3.63 \cdot 10^9$, $3.53 \cdot 10^9$ and $2.45 \cdot 10^9$ N/m^2 respectively. Independently of the real values, indeed considerably lower than the expected values, we observe a certain tendency of radial modulus E_r to decrease with decreasing external diameter.

A tentative hypothesis could be made to explain this fact, that is, the static-dynamic cycle test itself generates defects in the material. Then the decreasing of E_r observed would now be dependent on this progressive damage rather than on initial imperfections.

DYNAMIC ANALYSIS

In describing the results of dynamic tests performed mainly by means of holographic interferometry, it should be pointed out that the principal aim of the experimental and theoretical work was to obtain reliable values of material elastic radial modulus.

If it is considered that resonant frequencies depend on the square root of an elastic modulus, it follows that small uncertainties in frequency values determination lead to considerable errors in elastic modulus evaluation. From the considerable amount of experimental data collected during the tests it seems evident that dispersion and lack of repeatability of measured frequency values were a substantial obstacle for elastic moduli evaluation. Resonant frequencies measured with real time holographic interferometry were sometimes different from the values measured with other techniques such as sand patterns or mechanical impedance measurement. In these last cases, an increase of resonant frequencies with time was observed, especially when large amplitude excitation was used over long time intervals. Modal patterns observed with holographic interferometry and sand patterns were sometimes confused and distorted,

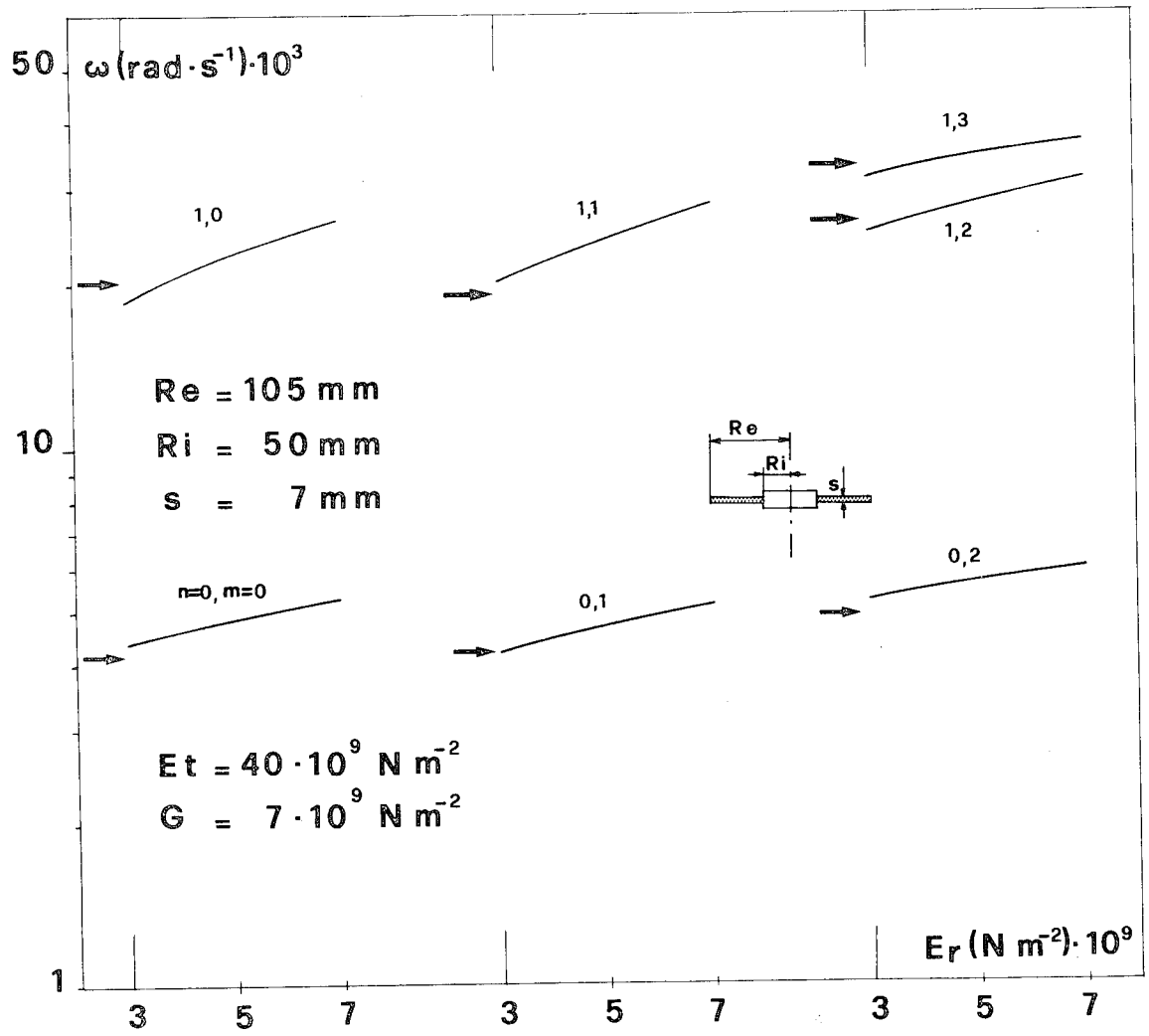

Fig. 4. Finite element curves relating natural frequency and radial modulus. Arrows indicate experimental results

and presented, in many cases, great irregularities. Material delaminations and dishomogeneities were probably the main reason of a similar behaviour which prevented the achievement of reliable elastic moduli values.

Figure 4 shows the experimental results obtained for one of the models tested. The experimental data are plotted on the curves that represent the frequency dependence on the modulus E_r, taking into account the effect of shear and rotary inertia.

Though there is a general agreement between experimental and theoretical values, the objective of sharp determination of radial modulus was not achieved as is evidently seen by the different modulus values that correspond to the various resonant frequencies. However, it was possible to determine a range of variation which in this case runs from $22 \cdot 10^9$ N/m^2 to $39 \cdot 10^9$ N/m^2.

In a first stage of the experimental activity holographic interferometry was only used to detect resonant frequencies by modal pattern identification. The results were quite unsatisfactory due to the large scattering of data and lack of repeatability. A marked improvement was obtained by using other techniques in conjunction with holographic interferometry. In particular Lissajous patterns obtained by sending displacement and acceleration signals to an oscilloscope and mechanical impedance measurement greatly reduced scattering of experimental values with a consequent reduction of a main source of error in modulus calculation.

TABLE 2. VALUES OF $E_r (N/m^2) 10^9$ DERIVING FROM STATIC AND DYNAMIC TESTS

MODEL	STATIC VALUES	DYNAMIC VALUES m = 0 n=0	m = 0 n=1	m = 0 n=2	m = 1 n=0	m = 1 n=1	m = 1 n=2	m = 2 n=0	m = 2 n=1	m = 2 n=2	m = 3 n=0	m = 3 n=1	m = 3 n=2
R_i=44 R_e=121	9.3	9.9	9.2	5.6	3.6	4.8							
R_i=44 R_e=104		8.1		8.3	6.6	11.0	11.0						
R_i=44 R_e= 89	7.5	10.3	<2.0	10.0	6.8	10.0							
s=6mm													
R_i=50 R_e=141	3.7	<2.0	3.5					<2.0	4.4			4.5	3.2
R_i=50 R_e=123	3.6	3.4	3.0					<2.0					
R_i=50 R_e=105	2.5	2.2	3.6		3.2	2.7		2.2	3.6			3.9	
s=7mm													

$E_t = 40 \cdot 10^9 \ N/m^{-2}$

$G = 7.10^9 \ N/m^{-2}$

$\nu_t = 0.26$

The last case (Fig.4 and the last row of Table 2) treated in this way clearly confirms this fact.

Table 2 shows the results of static and dynamic tests: dispersion of E_r values is considerable in spite of the large number of data. At this stage it is impossible to assess a reliable value for the elastic radial modulus.

An improvement of the experimental techniques, aimed at the precise determination of resonant frequencies and the further investigation on the influence of internal defects on dynamical behaviour, could probably lead to the evaluation of the usefulness and reliability of the technique proposed.

CONCLUSIONS

A quantitative interpretation of the whole set of experimental data referring to out of plane static loading and vibratory tests, over a class of thin discs of filament wound composite material, is rendered rather difficult because of the scattering of results.

Scattering seems to depend mainly on the nature of material used - in fact it has been dramatically reduced in similar tests performed on discs of practically homogeneous material, such as polycarbonate.

In relation to the experimental procedures adopted, double exposure holographic interferometry seems to be sufficiently accurate for static characterization as well as for defects visualization. The dynamic

characterization, based on the flexural resonance technique proved critical especially at the lowest frequencies, mainly because of the difficulty in identifying without ambiguity the resonant vibrating mode and frequency. The use of various experimental techniques at low and high amplitude, i.e. holographic interferometry and methods based on observing the Lissajous pattern and measuring the mechanical impedence, can be useful in avoiding some uncertainty. However, at the present time, scattering although reduced if compared with the first analyses, is still so great as to compromise in practice a reliable evaluation of the elastic dynamic properties.

Furthermore, the analysis was complicated by a tendency of the radial modulus E_r to undergo alteration by the test cycle itself.

However, it seems that all the difficulties encountered in the analysis could be overcome with appropriate refinements of the experimental equipment and methodology. Future work on this subject will be aimed at attaining this goal.

LIST OF SYMBOLS

a = internal radius of the disc. In the diagrams this was indicated by R_i
b = external radius of the disc. In the diagrams this was indicated by R_e
c = radius where the disc is supported
D_r = flexural rigidity = $E_r h^3/12(1-\nu_t\nu_r)$
D_t = flexural rigidity = $E_t h^3/12(1-\nu_t\nu_r)$
D_1 = flexural rigidity = $\nu_t D_r$
E_r = Young's modulus in radial direction
E_t = Young's modulus in tangential direction
G = tangential modulus = G_{rt}
h = thickness of the disc. In the diagrams this was indicated by s
n = number of nodal circles of a natural vibrating mode
m = number of nodal diameters
P = force acting at the center of the hub
r = current radius
V = total strain energy
W = work done by the external load
w, w', w'', w''' = deflection of the disc and its first to third derivatives with respect to radius r
w_s = experimental value of w
ν_r, ν_t = Poisson's ratios
ω = circular natural frequency

REFERENCES

1. R.F. Gibson, R. Plunkett: Dynamic stiffness and damping of fiber-reinforced composite materials. "The Shock and Vibration Digest", 9, no.2, February 1977.

2. B.E. Read, G.D. Dean: "The determination of dynamic properties of polymers and composites". Adam Hilger Ltd., Bristol, 1978.

3. G.D. Sims, G.D. Dean, B.E. Read, B.C. Western: Assessment of damage in GRP laminates by stress wave emission and dynamic mechanical measurements. Journal of Materials Science, 12, 2329-2342, 1977.

4. P. Cawley, R.D. Adams: A vibration technique for non-destructive testing of fibre composite structures. Journal of Composite Materials, 13, pg.161, April 1979.

5. F. Ginesu, B. Picasso, P. Priolo: Vibration analysis of polar orthotropic annular discs. Journal of Sound and Vibration, 65 (1), 97-105, 1979.

6. G.A. Cuccuru, F. Ginesu, B. Picasso, P. Priolo: Characterization of composite materials for filament wound flywheels. Journal of Composite Materials, 14, pg.31, January 1980.

7. I. Crivelli Visconti:"Materiali compositi - tecnologie e progettazione". Ed. Tamburini, 1975.

8. D.G. Berghaus, J.P. Cannon: Obtaining derivatives from experimental data using smoothed-spline functions. Experimental Mechanics, January 1973.

9. R.E. Rowlands, T. Liber, I.M. Daniel, P.G. Rose: Higher-order numerical differentiation of experimental information. Experimental Mechanics, March 1973.

10. S.G. Lekhnitskii: "Anisotropic Plates", Gordon & Breach, New York, 1968.

ACKNOWLEDGEMENTS

This paper presents some results of a research sponsored by the CNR, Italian Research Council under grants Nos. 79.2273.07 and 79.1729.07.

FROM VEHICLES TO SATELLITES: THE TECHNOLOGY REVOLUTION OF HIGH PERFORMANCE FLYWHEELS

D. Davis, PhD; A. Csomar and B. Ginsburg
Rockwell International/Rocketdyne Division
Canoga Park, California

ABSTRACT

During the past ten years, dramatic technological advances in rotating machinery, materials and fabrication techniques have resulted in flywheel systems, which do merit the designation "Super Flywheel". Within this time period, the rotating energy storage density of operational systems has increased over 500% and the new composite material configurations show promise of boosting this number above 1000% within the next few years.

This paper provides some insights into this rapidly maturing high energy storage system and specifically describes pertinent programs through which Rockwell International has infused aerospace technology into the efforts.

The full text of this paper was not available for inclusion in this volume of the Proceedings. It will be published later in a separate volume.

LAMINATED, COMPOSITE FLYWHEEL FAILURE ANALYSIS

R. P. Nimmer
General Electric Company
Corporate Research and Development
Schenectady, New York 12301

ABSTRACT

The author presents spin test data, nondestructive ultrasound data, and supporting failure analysis in an effort to more completely characterize the performance and failure of the laminated S2-glass disc used as the core of the General Electric Company's hybrid flywheel. Based upon previous test results and the assumption that the laminated disc would fail as a result of fiber breakage in the individual laminae, an energy density of 53 Wh/kg was expected from the new laminated discs. However, burst tests of these laminated discs resulted in considerably smaller energy density values ranging from 33.0 to 40.5 Wh/kg. Classical laminated plate analysis suggests a partial explanation for these lower performance levels since it predicts that matrix damage would initiate at relatively low rotational speeds and spread rapidly over the disc. Furthermore, ultrasonic examination of both graphite and S2-glass, laminated discs provides experimental corroboration of this analytical prediction. Although no ultrasonic property variations were observed in a laminated graphite disc which was accelerated to a rotational speed below the speed predicted to cause initial matrix damage, significant differences were observed in a laminated S2-glass wheel which exceeded the "matrix-damage-speed" in a spin test. Acoustic signal attenuation, wave speed velocities, and noise levels were all measured on wheels before and after spin tests. Although both the attenuation and wave speed measurements are in agreement with analytical predictions, the increased noise level observed in the outside region of the disc has not been fully explained.

INTRODUCTION

Although various organizations have pursued many different designs for composite flywheels,[1] the General Electric Company has developed and begun to optimize a concept reported by Lustenader and Zorzi[2] based upon a laminated disc and a filament-wound outer ring assembled with an interference fit between these two components. Figure 1 illustrates a flywheel based upon this design concept. The central disc is made of S2-glass-epoxy, and the outer ring is filament-wound graphite-epoxy. The laminated S2-glass disc is fabricated by laying up unidirectional, preimpregnated material with an angle α between adjacent laminae. The objective of the lamination process is to obtain isotropy in material properties - both strengths and stiffnesses. The rationale for this laminated design, as well as results of spin tests, are described by Hatch in Ref. 3.

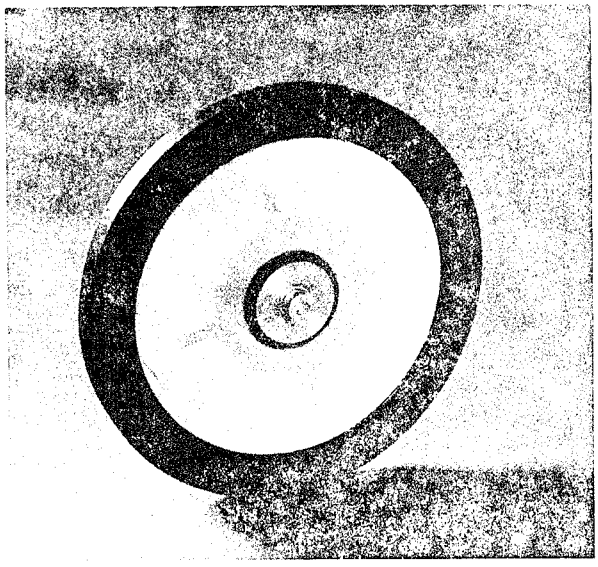

Fig. 1. General Electric Co. hybrid composite flywheel; laminated S2-glass central disc with filament wound graphite outer ring.

The development of this design concept and characterization of its performance and ultimate failure have been pursued through analysis, spin tests, and nondestructive examination via ultrasonics. Tests conducted to date have focused upon the behavior of the laminated central disc. Although originally fiber rupture was considered to be the controlling failure mechanism in the laminated disc, spin tests carried out to date, as well as supporting analysis and acoustic examination, indicate that the failure is actually more closely related to the failure of the epoxy which makes up the matrix of the laminated disc. The work presented here summarizes all of the results, both analytical and experimental, leading to this suggested failure mechanism. This study emphasizes nondestructive, acoustic testing techniques which have seen widespread use for quality control and identification of damage in metal parts and are now being applied to composites.[4] Although some of the results are anomalous when viewed from traditional metals methodology, such acoustic testing provides very important information with respect to the establishment of the failure mechanism.

FAILURE MECHANISMS AND TEST RESULTS

Lustenader and Zorzi[2] associated failure of the laminated disc with the ultimate, uniaxial strength of an individual lamina of the disc in the direction of the fibers of that lamina. Thus the disc's failure was associated with fiber breakage in the area of maximum stress around the bolt holes used for hub attachment in their design. Although the S2-glass laminated discs manufactured and tested during the current program were elastomerically bonded to their hubs, thus eliminating stress concentrations around bolt holes, a similar failure mechanism based upon fiber breakage was assumed for original performance estimates. This definition of disc failure led to the expectation of about 53 Wh/kg at failure for an S2-glass disc without any outer ring and almost 85 Wh/kg for an optimized design using a graphite outer ring.[5]

It should be pointed out that damage to a laminated composite is incurred well before stresses become large enough to break fibers. For example, it is well-known that in uniaxial tensile tests, a measurable reduction in laminate stiffness occurs at strains substantially lower than those associated with ultimate failure. This reduction in stiffness is generally associated with epoxy failures in laminae perpendicular to the direction of load application. In a laminated flywheel disc, the stress state is maximum and hydrostatic in nature at the center of the wheel. Therefor, some matrix damage will occur at this point at rotational speeds which are much less than those required to break fibers. Although this had been recognized, it was initially considered to be a damage which could be tolerated.

In order to study the behavior and systematically assess the performance expected of a composite flywheel similar to the one shown in Fig. 1, the laminated central disc was first studied without any exterior ring. Hatch[3] as well as Lustenader and Zorzi[2] discuss test results of laminated E-glass discs attached to aluminum hubs with bolted attachments. Nimmer, et al.[6] present test results for laminated S2-glass discs without bolt holes. In this latter case, the wheels tested were elastomerically bonded to aluminum hubs. Using a failure criterion based upon fiber failure near the center of the laminated disc, tip speeds in the vicinity of 885 m/s (2900 f/s) and energy density values approaching 53 Wh/kg (24 Wh/lb.) were expected from these S2-glass flywheels. However, the test results were substantially less than those predicted. Table 1 summarizes the important information with respect to five S2-glass laminated disc tests as well as three tests of laminated graphite flywheels. The last four tests reported in Table 1 were performed for the Lawrence Livermore Laboratories.

The fact that these test results were below initial expectations suggested that more extensive consideration of possible failure mechanisms was necessary. Both analytical techniques, as well as nondestructive testing with ultrasound, were utilized in this effort. The results of both efforts seem to reinforce one another and provide new insight into the failure of laminated composite flywheels.

ANALYTICAL PROCEDURE

In order to study these hypotheses in more detail, an analytical effort was launched to study the possible effects of matrix failure in the laminated discs. The first step in the analytical procedure was to solve the plane stress equilibrium

Table 1

TEST DATA SUMMARY

Test Number	Material	Stacking Sequence	Outside Diam. cm (in.)	Thickness cm (in.)	Weight kg (lb.)	RPM at Burst	Tip Speed at Burst m/s (f/s)	Energy Den. at Burst Wh/kg (Wh/lb.)	Stress at Center at Burst MPa (ksi)	Comments
1	S2-Glass -Epoxy	(0/-45/45/90)	22.54 (8.8)	2.41 (0.95)	1.79 (3.94)	65,000	760 (2495)	40.1 (18.2)	427 (62)	Drop in turbine RPM at failure; fibrous debris. (General Electric Co. flywheel.)
2	S2-Glass -Epoxy	(0/-45/45/90)	22.54 (8.8)	2.54 (1.0)	1.81 (4.02)	37,500	439 (1440)	13.4 (6.07)	144 (21)	Large orbit and increase in vacuum pressure occurred simultaneously prior to failure. (General Electric Co. flywheel.)
3	S2-Glass -Epoxy	±-9	22.54 (8.8)	2.14 (0.842)	1.58 (3.49)	58,000	679 (2230)	31.9 (14.5)	345 (50)	Drop in turbine RPM at failure; fibrous debris. (General Electric Co. flywheel.)
4	S2-Glass -Epoxy	±-9	28.58 (11.25)	2.69 (1.06)	3.2 (7.05)	49,000	733 (2405)	37.22 (16.9)	397 (57.6)	Large shaft orbit just prior to failure. (General Electric Co. flywheel.)
5	S2-Glass	(0/90/30/-60/60/-30)	40.32 (15.78)	1.07 (0.42)	2.88 (6.35)	30,100*	638* (2094)	28.24* (12.82)	306.8* (44.5)	Nondestructive test; wheel run to 30,100 RPM and acoustically tested before and after spin. Differences observed. (Lawrence Livermore Lab flywheel.)
6	Graphite -Epoxy	(0/90/45/-45)	31.1 (12.25)	0.635 (0.25)	0.924 (2.04)	44,500	725 (2378)	36.3 (16.5)	344 (50)	(Lawrence Livermore Lab flywheel.)
7	Graphite -Epoxy	(0/90/45/-45)	34.3 (13.5)	0.635 (0.25)	1.106 (2.46)	35,000*	628* (2061)	27.4* (12.42)	252* (36.6)	Nondestructive test; wheel run to 35,000 RPM and acoustically tested before and after spin. No difference observed. (Lawrence Livermore Lab flywheel.)
8	Graphite -Epoxy	(0/90/45/-45)	34.3 (13.5)	0.625 (0.25)	1.106 (2.46)	48,200	862 (2827)	51.5 (23.4)	474 (68.8)	(Lawrence Livermore Lab flywheel.)

*Nondestructive test.

equation for a rotating disc given in Ref. 7 as

$$\frac{d}{dr}(r\,\sigma_r) - \sigma_\theta + \rho\,\omega^2\,r^2 = 0 \qquad (1a)$$

For an isotropic disc, the solution of this equation in terms of the radial displacement leads to the following stress distributions:

$$\sigma_r = \frac{3+\nu}{8}\,\rho\,\omega^2(b^2 - r^2) \qquad (1b)$$

$$\sigma_\theta = \frac{3+\nu}{8}\,\rho\,\omega^2\,b^2 - \frac{1+3\nu}{8}\,\rho\,\omega^2\,r^2 \qquad (1c)$$

In using this equation, the laminated disc is assumed to be isotropic in nature and the stresses σ_r and σ_θ must be interpreted as average stresses over the thickness of the disc. The state of stress in the individual laminae of the disc will be quite different than the average stress and can then be calculated with the use of classical laminated plate theory described in Refs. 8 and 9. For the sake of completeness, this technique is briefly summarized here. The plane stress constitutive equations which relate stress to strain in the "material coordinate system" of an individual lamina can be expressed as

$$\begin{Bmatrix}\sigma_L\\ \sigma_T\\ \tau_S\end{Bmatrix} = \begin{bmatrix}Q_{LL} & Q_{LT} & 0\\ Q_{LT} & Q_{TT} & 0\\ 0 & 0 & Q_{SS}\end{bmatrix}\begin{Bmatrix}\varepsilon_L\\ \varepsilon_T\\ \gamma_S\end{Bmatrix} \qquad (2)$$

where the subscripts L and T denote longitudinal and transverse "material directions" and

$$Q_{LL} = E_L/\lambda \qquad (3a)$$

$$Q_{TT} = E_T/\lambda \qquad (3b)$$

$$Q_{LT} = Q_{TL} = \nu_{LT}\,Q_{TT} \qquad (3c)$$

$$Q_{SS} = G_S \qquad (3d)$$

$$\lambda = 1 - \nu_{LT}\,\nu_{TL} \qquad (3e)$$

The stress or strain in the material coordinate system (L-T) of any lamina K of an n-layered laminate can be calculated from the knowledge of lamina stress or strain in the reference coordinate system (X-Y) with the use of the coordinate transformation matrix $[T]_k$ and Eqs. (4a) and (4b).

$$\{\sigma_{LT}\}_k = [T]_k\,\{\sigma_{XY}\}_k \qquad (4a)$$

$$\{\varepsilon_{LT}\}_k = [T]_k\,\{\varepsilon_{XY}\}_k \qquad (4b)$$

Using Eqs. (2) and (4), it can be shown that

$$\{\sigma_{XY}\}_K = [T]_K^{-1}\,[Q_{LT}]_K\,[T_K]\{\varepsilon_{XY}\}_K \qquad (5)$$

If a state of plane stress is assumed, then an average stress state can be defined as

$$\{\sigma_{XY}\}_{Avg} = \frac{1}{t} \sum_{K=1}^{n} h_K \{\sigma_{XY}\}_K \qquad (6)$$

where t is the thickness of the total laminate and h_K is the thickness of lamina K. Since it follows from the assumption of plane stress that

$$\{\varepsilon_{XY}\}_k \equiv \{\varepsilon_{XY}\}_{Avg} \qquad (7)$$

for each layer K, the expression relating average stress and strain takes the form

$$\{\sigma_{XY}\}_{Avg} = [a]\{\varepsilon_{XY}\}_{Avg} \qquad (8)$$

where

$$[a] \triangleq \frac{1}{t} \sum_{K=1}^{n} h_K [T]^{-1} [Q_{LT}][T] \qquad (9)$$

Now with the use of Eqs. (2), (4b) and (8), it can be shown that the stresses in the material coordinates of each layer k can be calculated from the average stress state by using the following relation:

$$\{\sigma_{LT}\} = [Q_{LT}][T][a]^{-1} \{\sigma_{XY}\}_{Avg} \qquad (10)$$

Thus, the stress state in any given layer of the laminated disc can be calculated with Eq. (10) and the average state of stress defined by the solution of Eq. (1).

Once the state of stress in the laminae have been determined, lamina failure can be defined with an appropriate failure criterion. The criterion applied in this study is Hill's generalization of the von Mises' failure criterion which has been applied to fiber reinforced composites by Azzi and Tsai[10] and can be defined as

$$\frac{\sigma_L^2}{F_L^2} - \frac{\sigma_L \sigma_T}{F_L^2} + \frac{\sigma_T^2}{F_T^2} + \frac{\tau_S^2}{F_S^2} = 1 \qquad (11)$$

where F_L, F_T and F_S are the characteristic longitudinal, transverse and shear strengths of a lamina. Although the Tsai-Wu failure criterion may be more generally accepted, the strictly tensile nature of stresses in this problem, as well as the lack of data with respect to the interactive material strength terms of the Tsai-Wu criterion, seem to make the Tsai-Hill criterion acceptable with respect to the goals of this analysis. Failure is predicted at a given point in a structure when the left hand side of Eq. (11) reaches 1.0. It should be noted however, that "failure" of a given lamina as defined by Eq. (11) certainly is not synonymous with ultimate failure. Substantial strength can remain in a composite structure even though matrix failure occurs in one or more laminae as is certainly the case in a laminated flywheel. Since the average stress state at the center of the disc is hydrostatic, the lamina stresses calculated from Eq. (10) will be identical for each and every layer and will therefore undergo matrix failure simultaneously. Physically, this probably has very little effect on the total strength of the disc since no fibers are broken and the matrix in the rest of the disc is still intact. However, one possible failure mechanism for a rotating laminated disc is that failure occurs when matrix damage in all of the laminae has spread to the outer radius of the disc, or at least far enough that the discs integrity is significantly affected. In such a case there could be little or no undamaged resin remaining, and even though no fibers have been broken, the binder may no longer be able to hold the fibers together.

As previously mentioned, "first ply" or matrix failure is associated with a change in the stiffness of the laminate. In order to obtain fundamental information with respect to this failure mechanism, two simple bounding analyses were performed. In the first analysis, the original moduli of the material (E_L, E_T, G_S) are used throughout the analysis with respect to Eq. (10). Thus, the decrease in the laminate modulus due to matrix failure is ignored and the results will form an upper bound for the proposed failure mechanism. The average state of stress at a radial distance is calculated from the solution of the equilibrium Eq. (1) and laminae stresses are then calculated from Eq. (10). Use of the failure criterion defined in Eq. (11) then defines the flywheel rotational speed which is associated with matrix damage within the given radius r_D. For the second analysis, the so-called method of mode limited discount[11] is used to account for the damage in material moduli as individual plies fail. In this method, the transverse and shear moduli (E_T, G_S) of a lamina which has undergone matrix failure are set to zero while the longitudinal modulus remains intact. Once this discount has been accomplished, the average constitutive constants associated with the damaged disc areas can be recalculated from Eq. (9). Equation (1) is then resolved - this time in two zones.

In the zone inside the radius r_D which defines the boundary of the matrix damaged region the discounted moduli are used; in the region outside r_D, the original moduli are used. The average stress state defined by this solution is then used with a laminate stress analysis to calculate the rotational speed consistent with a damage boundary r_D. This approach is more realistic in that it takes the reduced modulus in the interior regions into account; a reduction which results in the inner material putting additional load on the undamaged outer material, thereby accelerating failure. However, it does overestimate the average strain in the damaged inner areas (as shown in Fig. 2).

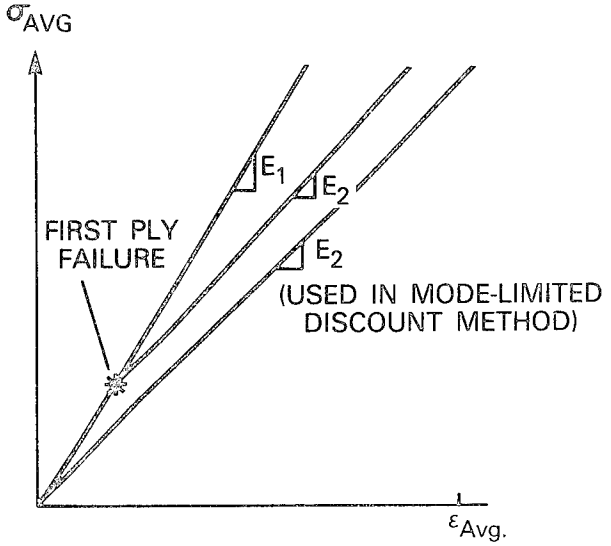

Fig. 2. Average uniaxial stress-strain relations bounding actual failure mechanism.

Figure 3 illustrates the progressive matrix damage predicted by these two bounding analyses for the flywheels similar to discs 1 and 2 whose test results are presented in Table 1. The stacking sequence in these wheels is described as [0/+45°/-45°/90°]. The material properties used in this analysis are listed in Table 2. In Fig. 3, the tip speed at which the disc's matrix has been damaged throughout its entire thickness is plotted on the ordinate versus the nondimensional radial coordinate $\bar{r}_D = r_D/b$, where b is the disc outside radius. Thus, $\bar{r}_D$ marks the boundary of a circular region within which matrix damage has been sustained through the entire thickness. As shown, matrix damage is incurred at the center of the disc at a relatively modest tip speed of about 390 m/s (1270 f/s) when the average biaxial stress at the center of the disc reaches about 135 MPa (19 ksi). As presented in Eqs. (1b) and (1c), the average stresses in a spinning disc are highest at the center of the disc. In addition, it follows from the previously outlined analysis that the state of stress in each and every laminae is the same at the center of the disc as a result of the biaxial state of average stress. Theoretically, all the plies at the disc center fail transversely at the same time. However, this simultaneous failure is not the rule as the failure moves out radially; in such a case the state of stress becomes increasingly uniaxial as you move out radially. Hence, the state of stress in the plies is entirely different, and failure occurs at different levels of average stress.

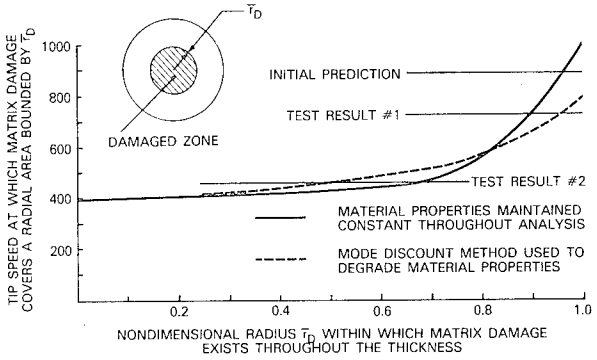

Fig. 3. Progressive matrix failure of a laminated S2-glass epoxy disc with (0/-45°/45°/90°) stacking sequence.

Two additional points need to be made with respect to the damage curve in Fig. 3. Since the state of stress in the center of the disc is balanced biaxially, the laminate strength at this point is independent of both stacking sequence and stress orientation. However, for radial positions approaching the outside radius of the disc, the stress state becomes increasingly uniaxial. This, in turn, means that there are "strong" and "weak" directions of stress application with respect to laminae fiber orientation. It has been shown[12] that the uniaxial tensile strength of a laminate is higher if the stress is applied in a fiber direction than if the stress is applied in a direction bisecting the angle between two adjacent fiber orientations (off-axis strength). For the analysis described in Fig. 3, the "worst case" stress orientation

Table 2. Material properties assumed for S2-glass laminate.

$E_L^{(1)}$ = 48.95 GPa (7.1 × 10^6 psi)	$F_L^{(1)}$ = 1500.0 MPa (218 ksi)
$E_T^{(1)}$ = 10.0 GPA (1.45 × 10^6 psi)	$F_T^{(1)}$ = 54.1 MPa (7.85 ksi)
$G_S^{(2)}$ = 5.58 GPa (0.81 × 10^6 psi)	$F_S^{(2)}$ = 64.1 MPa (9.3 ksi)
$\nu^{(2)}$ = 0.3	

(1) Vendor data.

(2) Average data inferred from literature.

was always assumed for damage prediction. In addition, consideration of the relative sizes of the terms in the failure criterion indicates that although the transverse strength is a dominant factor in the center of the disc where the stress is balanced biaxial, the shear strength becomes a very important factor in determining the off-axis, uniaxial laminate strength near the outside diameter of the disc. Although the laminate shear strengths become increasingly important in characterizing laminate failure for large values of $\bar{r}_D$, accurate data of this sort are often harder to find. Sometimes, as in the case of the S2-glass properties listed in Table 2, shear strengths are not even reported by vendors. In addition, laminate failure analyses similar to those carried out here do not always predict experimental results accurately. For example, using the properties in Table 2 the uniaxial strength of a $[0/-45°/45°/90°]_S$ S2-glass laminate loaded at 22-1/2" to the fiber direction is projected to be 214 MPa (31 ksi) through laminate analysis. Tests carried out at the Virginia Polytechnic Institute[12] result in strengths of 300 MPa (43.5 ksi). Thus, the analysis considerably underestimated laminate strength for the S2-glass. In order to properly account for this material strength in the analysis, the experimental test results with respect to off-axis laminate strength reported in Ref. 12 are used to correct the failure curves in the outer area of the S2-glass disc.

In addition to the relatively low tip speed at which initial matrix damage is predicted, there are several other observations of note. First of all, in both analyses illustrated in Fig. 3, the damage which initiates at the center of the disc spreads quite rapidly. For example, by the time the tip speed of the disc has reached 420 - 450 m/s, matrix damage has initiated in an area within 50% of the disc's outside radius. As the damaged zone continues to grow, it takes increasingly higher increments in tip speed growth to increase the radius of the damaged zone by equal amounts. This is because the radial stress drops off very rapidly near the outside radius and larger values of uniaxial average stresses are required to induce matrix damage throughout the laminate thickness than are required in a biaxial state of stress. Finally, it is apparent that when the mode discount method is used to account for degrading material properties during matrix failure, the tip speed curve rises more gradually with respect to the radial location and the predicted tip speed associated with damage all the way to the disc's outside diameter is less than that predicted without modal discount. Both of these effects are associated with the fact that the interior material actually shifts load to the exterior material as a result of the modulus of the material decreasing when the matrix is damaged.

Also indicated in Fig. 3 are the tip speeds at failure of the two S2-glass flywheels with $[0/-45/+45/90]_S$ stacking sequence which were tested. The bounding analyses in Fig. 3 indicate that for the higher of the two failure speeds, the damaged area of the disc had extended to between 90% and 95% of the disc's outside radius when failure occurred. If the lower bound analysis is used, the tip speed at which matrix damage covers the entire disc radius is only about 10% higher than the tip speed observed at failure. Figure 3 may also provide some insight into the failures at lower tip speeds like the second experimental point in the figure. With reference to this failure, it must be

noted that even though the failure speed was much lower, the bounding curves indicate that 50% to 60% of the disc's diameter would have sustained matrix damage throughout the thickness.

Figure 4 is a similar plot which illustrates the progressive matrix failure associated with a graphite epoxy wheel. The material properties used in this analysis are listed in Table 3. The general character of the curves is quite similar to the S2-glass curves of Fig. 3. However, it should be noted that the initiation of matrix damage takes place at a much higher tip speed than for the S2-glass disc in spite of the fact that the transverse strengths of the S2-glass and graphite laminae reported in Tables 2 and 3 are quite similar. This significant delay in the onset of matrix damage is a result of the substantially stiffer longitudinal modulus of the graphite epoxy laminate in comparison to the S2-glass (see Tables 2 and 3). The increased fiber stiffness prevents transverse laminate strains from exceeding limiting values until much higher disc tip speeds. In addition, comparison of Figs. 3 and 4 reveals that although there is a significant difference in the two bounding analyses presented for S2-glass, there is very little difference between these two analyses with respect to the graphite. Again, this can be understood in terms of the higher fiber stiffness of the graphite. As a result, matrix failure in the graphite epoxy laminae has a much smaller effect upon the overall average composite properties than it does in the S2-glass laminae. As in the case of Fig. 3, experimental off-axis test results[13] were used to correct the curves as $\bar{r}_D \to 1.0$.

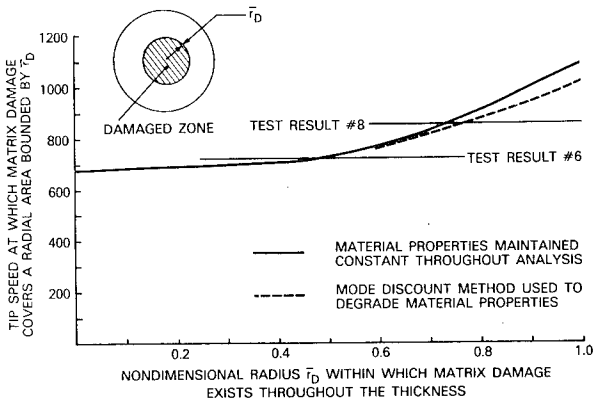

Fig. 4. Progressive matrix failure of a laminated graphite-epoxy disc with (0/-45°/45°/90°) stacking sequence.

Test results for laminated graphite flywheels with a $[0/-45/45/90]_s$ stacking sequence are also exhibited in Fig. 4. For the higher of the two failures, the damaged area is predicted to have reached a radius between 73 and 78% of the outside radius at burst, and the lower bound analysis predicts a maximum tip speed which is only about 18.5% higher than the observed failure speed. Again, in the case of the lower failure, the analysis indicates that the full thickness damage area extends over a very substantial 45% of the wheel's diameter.

EXPERIMENTAL DEFINITION OF PROGRESSIVE DISC DAMAGE

In order to experimentally detect the damage predicted by analysis, a program was undertaken using nondestructive, ultrasonic tests of laminated discs. Two flywheels were tested during this program. One of the wheels was laminated graphite epoxy, the other a laminated S2-glass epoxy. Both were designed and built by the Lawrence Livermore Laboratory. Although a variety of measurements was taken, the common approach for all the tests was to compare measurements taken on wheels that had been spin-tested with identical measurements on wheels which had never been tested. Whenever possible, this comparison was made on the same wheel, before and after a test. When this was not possible, an identical, sister wheel was employed for comparison.

The first acoustic tests were carried out on a 34.3 cm (13.5 in.) graphite epoxy disc, 0.64 cm (0.25 in.) thick with a stacking sequence described as $[0/-45°/45°/90°]_{3s}$. The wheel is illustrated in Fig. 5. As can be seen, the hub of the flywheel was attached with an elastomeric bond. C-scans of this wheel were conducted before and after a spin test in which the tip speed of the wheel reached 625 m/s (2060 f/s). During a C-scan, the wheel is immersed in a tank of water, which acts as a transfer medium. An acoustic transducer continuously traverses the surface of the piece being inspected, sending and receiving signals as it goes. These signals are in turn processed and can be reported in a variety of ways. The reflected, backwall signal can be monitored, and a recording device used to indicate the locations where the backwall signal falls below a preassigned level, indicating interference with the signal and possible damage. Alternately, a particular portion

Table 3. Material properties assumed for graphite laminate.

E_L = 144.8 GPa (21 × 10^6 psi)	F_L = 1786.0 MPa (259 ksi)
E_T = 9.65 GPa (1.4 10^6 psi)	F_T = 48.3 MPa (7.0 ksi)
G_S = 4.83 GPa (0.7 × 10^6 psi)	F_S = 71.7 MPa (10.4 ksi)
ν = 0.3	

All properties from vendor supplied data.

of the piece's interior can be monitored and the recording device can be used to indicate areas of the piece where reflected signals (noise) above a preassigned level are being received from the monitored interior area. Because of the irregularity of the graphite disc's surface, the acoustic signal was focused beyond the back surface of the wheel, and the signal was gated to identify irregularities (noise) in the lower half thickness of the wheel. With this procedure, the recording device indicates "black" wherever the signal level of the noise received from the gated area exceeds a preassigned level. Although a 15.0 MHz focused transducer was used in this test, the laminated material acted as an acoustic filter which would not pass frequencies greater than 5 MHz. Noise level data were collected for the wheel prior to and following the spin test. The gain setting for the noise level cut-off was chosen so that most of the response associated with fiber orientation is no longer visible, as can be seen in Fig. 6a. After completion of this test, a second C-scan was performed; these results are also displayed for comparison in Fig. 6b. Note that there is no new damage indicated by comparison of the scan performed after the test with the scan performed prior to the test. This is predictable, since Fig. 4 indicates that a tip speed of 626 m/s is not enough to cause any matrix damage to the graphite disc.

However, the situation is entirely different for the second wheel which was nondestructively examined. This wheel was made of laminated S2-glass with a [0/90°/30°/-60°/60°/-30°] stacking sequence. The outside diameter measured 40.6 cm (16 in.) and the wheel was 1.1 cm (0.44 in.) thick, similar to the wheel shown in Fig. 7. Again, the subject wheel was ultrasonically tested before and after the spin test with the same immersed system previously described. As in the graphite wheel, a long wave technique was selected with the instrument gain set to an arbitrary level which eliminated most of the interior noise response indicative of fiber orientation. The focal point was varied from the backwall to the midwall in an effort to optimize the system. Since the S2-glass flywheel's surface was much smoother than the graphite's the final selection was to focus on the backwall. As in the previous test, it was decided to monitor the inherent noise (hash) of this composite and look to abnormal conditions above a preassigned level.

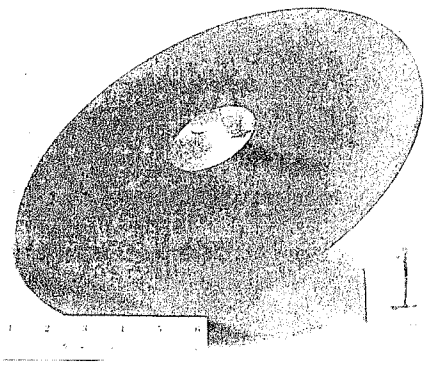

Fig. 5. Lawrence Livermore Laboratory laminated graphite flywheel subjected to ultrasound tests.

With the test parameters set, a partial "C" scan was recorded before the spin test. As shown in Fig. 8a, the wheel before the spin test appears to be fairly uniform over the areas tested. After completing the pretest "C" scan, the laminated disc was spun to a tip speed of 638 m/s (2094 f/s). As can be seen from Fig. 3, the analyses indicate that at this tip speed matrix damage should exist within a

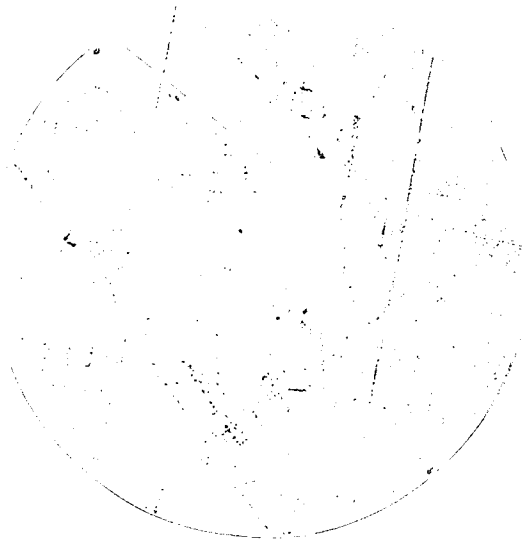

Fig. 6a. C-scan of graphite epoxy flywheel before spin test.

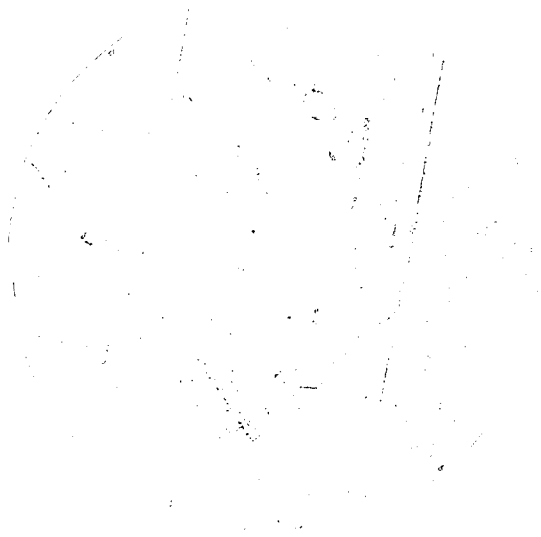

Fig. 6b. C-scan of graphite epoxy flywheel after spin test to v_T = 626 m/s.

boundary of from 84 to 88% of the outside radius. The wheel speed is within about 11% of the previously measured failure speed for an S2-glass disc of this stacking sequence shown in Table 1. When the flywheel was "C" scanned after the spin test, the results were markedly different from the pretest scan as can be seen from a comparison of Figs. 8a and 8b. Although the center portion appears to be very similar to pretest results, the outer 4.45 cm (1.75 in.) of the periphery is quite different. The noise level in this region increased by about 8 dB. Not only did the noise level increase, but the backwall reflection also increased by about 8 dB. As a result, if the backwall had been monitored and the recorder keyed to a reduction in backwall signal, the "C" scans before and after the spin test would have been comparable. There was no visible damage to the circumference of the wheel, and the region of large noise extends rather far from the outside radius for it to be interpreted as edge-effect delamination associated with free edges of laminated composites. In contrast, when the attenuation of the acoustic signal during repeated reflections between the front and back flywheel surfaces was measured after the spin test, it was discovered that there was more signal attenuation in the central portion of the disc and less in the outer 4.45 cm. This is quite the reverse of the behavior observed in metals where an increase in noise is usually accompanied by an increase in signal attenuation. For a composite, increase in attenuation is generally associated with microcracks in the matrix,[14] and this is what was expected in the center of the disc. However, the increased noise level in the outside regions remains unexplained. It has been suggested that it may be associated with residual stresses in the disc as a result of the modulus change in the damaged material, but conclusive evidence is lacking.

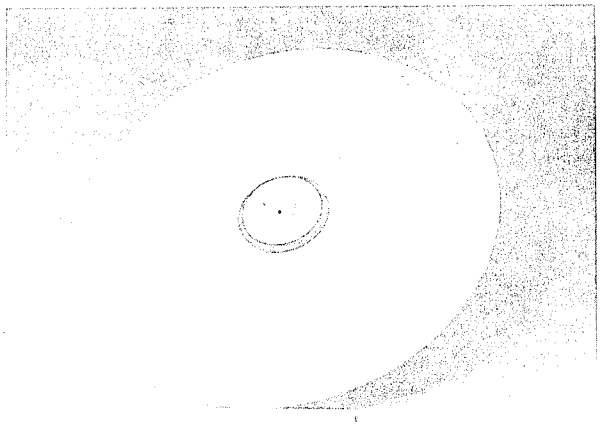

Fig. 7. Lawrence Livermore Laboratory laminated S2-glass flywheel subjected to ultrasound tests.

In order to gain a more quantitative measure of the material state in the disc after spinning, velocities of waves propagating through the disc thickness were also measured. As previously mentioned, the matrix cracking predicted by the

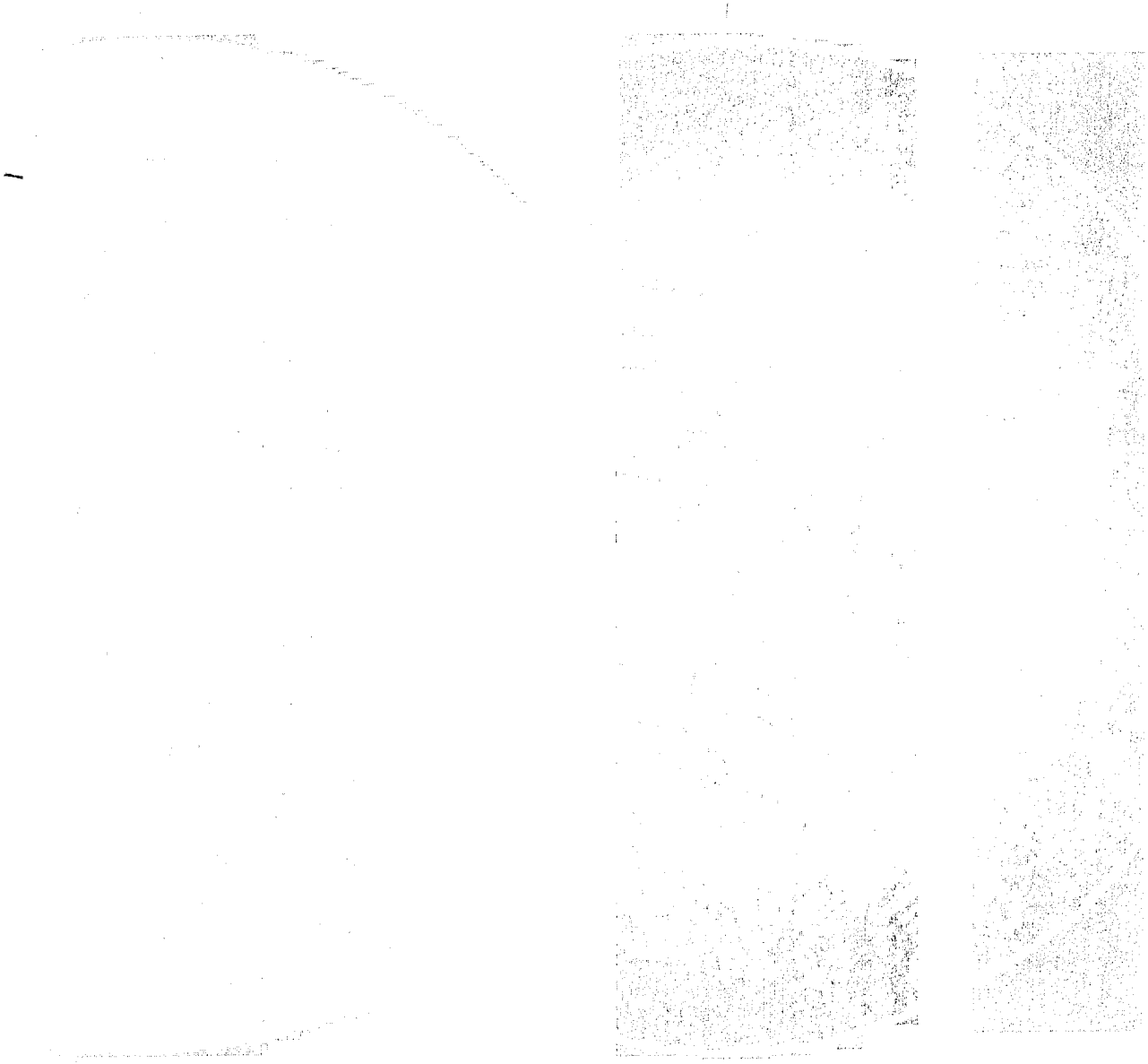

Fig. 8a. C-scan of S2-glass flywheel before spin test.

Fig. 8b. C-scan of S2-glass flywheel after spin test to v_T = 638 m/s.

analyses results in a reduction in stiffness of the composite. This stiffness reduction would then appear as a decreased speed of sound in the damaged material as compared with undamaged material. To measure these velocities, the time counter of the 7603 Tektronix scope was used to measure transit time between the first and second backwall reflections. These acoustic velocities were measured at a number of locations along a wheel radius in order to determine how they varied in space over the wheel. Both longitudinal and shear wave speeds were measured. In order to obtain an indication of what these wave speeds are in a wheel before spinning, similar tests were also made on another laminated S2-glass wheel. This wheel was made of the same material and was processed identically; its outside diameter was 38.1 cm (15 in.).

The results of these acoustic velocity studies are presented in Figs. 9a and 9b. There are several interesting things to note: first, both the longitudinal and the shear velocities are higher at all locations in the unspun disc than they are in the disc spun to a tip speed of 638 m/s. Second, although the longitudinal wave speeds are constant over the entire radius

of the unspun laminated disc, there is a visible variation in both the longitudinal and the shear wave speeds with respect to radial location in the disc after spinning. In both cases, the wave speeds are slower in the interior regions of the disc with gradually increasing values as the outside radius of the disc is approached. In the case of the longitudinal wave, the velocity near the outside radius approaches the velocity measured in the unspun wheel. This behavior seems to agree quite well with the analytical prediction of progressive matrix failure which moves outward radially as the rotational speed of the wheel is increased. The gradual increase in the shear wave speed for the unspun disc is not presently understood.

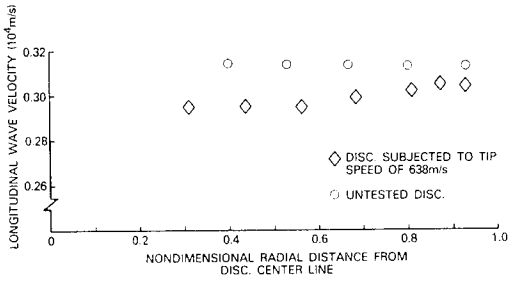

Fig. 9a. Comparison of longitudinal wave speeds through the thickness of S2-glass disc before and after spin tests.

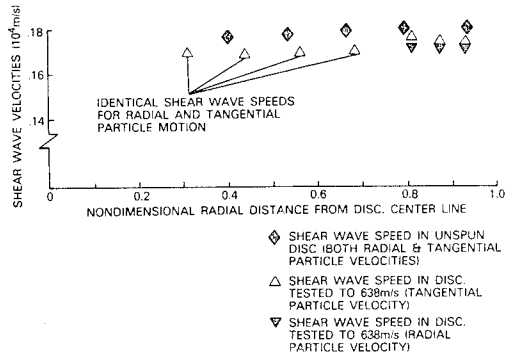

Fig. 9b. Comparison of shear wave speeds in S2-glass discs before and after spin tests.

Another rather interesting phenomenon is visible in the speeds of shear waves propagating through the disc thickness. The particular motion of these waves is perpendicular to the direction of wave propagation and the direction of particle motion can be varied by rotating the acoustic transducer. As part of this investigation, wave speeds were measured for particle motion in both the radial and the tangential directions. As expected, these wave speeds are the same in the unspun disc as well as in the interior regions of the disc which was spun; however, in the outer 3 to 5 cm of the spun disc, the wave speed associated with radial particle motion is higher than the speed associated with tangential motion. This indicates an anisotropy in material properties which is not present in the original disc. The difference in these wave speeds seems to be maximum near the radius where the longitudinal wave speed begins to increase, perhaps indicative of the onset of matrix damage. Since the stress field in this area is increasingly uniaxial, the damage occurring in the laminates no longer occurs in all laminae simultaneously. Rather, transverse microcracks will occur in the more radially oriented laminae first. Although these microcracks would lower shear moduli and wave speeds associated with tangential particle motion, the shear waves associated with radial particle motion would not be substantially affected since the fibers in these layers would be the major contributor to shear modulus and they remain damaged. This explanation, however, does not account for the reduction in radial-particle motion, shear wave speed in the outer 3 to 4 cm of the disc.

In spite of the fact that the author cannot completely explain all the experimental data, the general trend seems to corroborate the analytical expectation of matrix microcracks which cover a substantial portion of the flywheel disc at speeds below ultimate failure. Although this damage can clearly accumulate without causing the failure of the wheel, as can be seen from the S2-glass test, its presence and continued growth probably contribute to the ultimate failure. With respect to this contention, it should be pointed out again that the acoustic tests on the S2-glass wheel were carried out after that wheel reached a speed within 11% of previously encountered failures.

CONCLUSIONS

Bounding analyses have been presented which predict microcracking in the epoxy-resin matrix throughout the thickness of laminated discs, initiating at the center of the disc at rotational speeds substantially below predicted failure speeds. As the wheel speed increases, this matrix

damage propagates outward in the disc quite rapidly. In the outer regions of the disc, the average stress field becomes increasingly tangential and the matrix damage appears first in laminae oriented in more radial directions - the more tangential laminae remaining undamaged. The character of the failure is predominately transverse tension in the interior regions of the disc where average stress states are nearly hydrostatic. In the outer regions of the disc, where the stress field approaches a strictly tangential nature, the shear strength of the composite laminae become increasingly important. The higher fiber stiffness of graphite with respect to S2-glass serves to raise the tip speeds at which this matrix damage appears as well as the predictions of ultimate failure from this damage mechanism.

To support these analytical predictions, nondestructive ultrasound tests were carried out both on graphite and S2-glass wheels. The ultrasound tests on a graphite wheel before and after spin test to 626 m/s revealed no difference in measured response. This agrees with the analyses since no matrix damage was expected until approximately 680 m/s. Similar tests were conducted on an S2-glass disc before and after spinning to a tip speed of 638 m/s. In this case, the tip speed was within 10 to 15% of expected failure speeds and well above the level necessary for matrix damage to accumulate in the disc interior. Measurements of signal attenuation and longitudinal wave speed indicated higher attenuation values and lower wave speeds over the area bounded by a radius approximately 75% of the outside wheel radius. These observations support the analytical predictions since matrix microcracking increases signal attenuation in a composite as it decreases moduli and hence wave speeds. In the same area of the disc where a decreased attenuation was observed, a corresponding increase in noise also appeared in "C" scans. This is counter to past experience with metals where attenuation and noise trends are generally in the same direction. Although this effect may be associated with residual stresses in the disc due to moduli degradation in the interior regions, a complete understanding of this behavior is not in hand. A difference in shear wave speed for radial and tangential particle motion was also observed in a limited area of the spun S2-glass disc reaching a maximum near the inner boundary of the high noise area observed in the "C" scan and progressively decreasing toward the outer radius. This phenomenon may be associated with the selective damage to laminae oriented in radial directions near the outside periphery of the disc where the average stress field is predominately tangential. This explanation does not account for the observed decrease in the shear wave speed associated with radial particle motion.

The results of this study are important in that they provide substantial insight into the failure mechanisms of laminated flywheel discs and reduce the discrepancies between previous performance predictions and experiments. It appears that fiber breakage may not be necessary to cause flywheel failure. Substantial matrix damage may occur at much lower speeds, resulting in flywheel failure. From the point of view of material development, stiffer fibers and resins capable of sustaining larger strains before cracking would improve the behavior of these laminated discs. The results also suggest that the initiation of this type of damage, although not immediately catastrophic, must be considered carefully within the context of fatigue design.

REFERENCES

1. Proceedings of the 1977 Flywheel Technology Symposium, Oct. 5-7, 1977, San Francisco, CA, Dept. of Energy Publication CONF-771053, March 1978.

2. Lustenader, E. L. and Zorzi, E. S., "A Status of the 'Alpha Ply' Composite Flywheel Concept Development," presented at SAMPE Meeting, Anaheim, CA, May 3, 1978.

3. Hatch, B. D., "Alpha-Cross-Ply Composite Flywheel Development," presented at the 1977 Flywheel Technology Symposium, Oct. 5-7, 1977, San Francisco, CA.

4. Rose, J. L. and Shelton, W., "Damage Analysis in Composite Materials," Composite Reliability, ASTM Special Technical Publication 580, 1975, p. 215.

5. Nimmer, R. P., Torossian, K. A., Hickey, J. S., and Wilkinson, J. P. D., "Laminated Composite Disc Flywheel Development," First Semiannual Report to the Lawrence Livermore Laboratories, Subcontract No. 2479309, General Electric Corporate Research and Development Report No. SRD-79-016, Jan. 31, 1979.

6. Nimmer, R. P., Hickey, J. S., and Torossian, K. A., "Laminated Disc Flywheel Development," Second Semiannual Report to Lawrence Livermore Laboratories, Subcontract No. 2479309, General Electric Corporate Research and Development Center Report (to be published).

7. Timoshenko, S. P. and Goodier, J. N., Theory of Elasticity, McGraw-Hill, 3rd Edition, 1970, p. 80.

8. Pagano, N. J., "Exact Moduli of Anisotropic Laminates," Composite Materials, Vol. 2; Mechanics of Composite Materials, edited by G. P. Sendeckyj, Academic Press, New York and London, 1974.

9. Vicario, A. A., Jr., Toland, R. H., and Bert, C. W., Composite Materials, Vol. 7; Structural Design and Analysis, Part I, edited by C. C. Chamis, Academic Press, New York, 1975, pp. 51-97, pp. 149-206.

10. Azzi, V. D. and Tsai, S. W., Experimental Mechanics, Vol. 5, p. 283, 1965.

11. Tsai, S. W. and Hahn, H. T., Composite Materials Workbook, Air Force Material Laboratory Report No. AFML-TR-78-33, March 1978, p. 195.

12. Duke, J. C., "Investigation of the Strength of Fiber-Reinforced Composite Laminate Specimens," Virginia Polytechnic Institute, College of Engineering Report No. VPI-79.26, Aug. 29, 1979.

13. Kulkarni, S. V., Stone, R. G., and Toland, R. H., "Prototype Development of an Optimized, Tapered-Thickness, Graphite/Epoxy Composite Flywheel," Lawrence Livermore Laboratory Report UCRL-52623, Nov. 1978.

14. Hayford, D. T. and Henneke, E. G., "A Model for Correlation Damage and Ultrasonic Attenuation in Composites," Composite Materials: Testing and Design (Fifth Conference), ASTM Special Technical Publication 674, S. W. Tsai, Ed., 1979, pp. 184-200.

ACKNOWLEDGMENTS

A portion of the work reported here was conducted for the Lawrence Livermore Laboratories under subcontract number 2479309 and with the program direction of Dr. Satish Kulkarni who first suggested ultrasonically testing both the graphite and the S2-glass wheels supplied by Lawrence Livermore Laboratory. The author would also like to acknowledge the efforts of L. B. Burnett who performed the ultrasonic tests and Dr. Robert Gilmore who provided advice with respect to technique and interpretation. The S2-glass discs spun to destruction were fabricated by Kevoric Torossian, and his efforts in optimizing process parameters must be recognized. All of the spin tests were carried out by John Hickey and Jim Retersdorf, whose patience and steady work was indispensable.

ROTOR TESTING AND DIAGNOSTICS

Alan D. Sapowith
AVCO Systems Division
201 Lowell Street
Wilmington, MA 01887

ABSTRACT

Report on flywheel burst test conducted on 9 July 1979 under U.S. Army Mobility Equipment Research and Development Command Contract DAAG53-75-C-0269. Data includes 11 strain gage channels vs. speed and a comparison of measured vs. predicted radial stiffness to circumferential stiffness at several radial positions. These data corroborated Avco's constant stress design concept, which is described. Report also includes burst speed data at a specific energy level of 32.3 watt-hrs/lb (.6 kw-hrs) and a failure mode evaluation (benign) applicable to containment requirements.

The full text of this paper was not available for inclusion in this volume of the Proceedings. It will be published later in a separate volume.

EVALUATION OF FLYWHEEL CONTAINMENT

D. L. Kerr/J. Hickey
Corporate Research & Development
General Electric Company
P.O. Box 43
Schenectady, New York

ABSTRACT

This paper summarizes a program which was undertaken to provide a sound basis for defining the material, configuration, and dimensions of the containment structure to be used in the Flywheel Energy Storage System being developed for a transit bus by the General Electric Company under Contract with the Department of Transportation.

The paper includes a brief description of the full size system, which consists of 8 flywheel discs, 40 inches in diameter, rotating at 10,500 RPM and having more than 11 kw-hr of useful stored kinetic energy at that speed. It describes the failure modes of concern, the procedure used to obtain a preliminary definition of the containment structure required to contain a flywheel rotor failure, and the rationale for deciding to implement a small scale containment test program to give more definitive answers to the containment design problem.

The small scale test program facilities and equipment are described as well as the test program and results to date.

Two basic types of containment have been investigated. One is all-steel; the other is Kevlar cloth wrapped on a metal liner. Results to date indicate that the kevlar approach may be lighter, but suffers from requiring significantly more volume, which is a serious disadvantage in the transit bus application. An all-steel containment, though not necessarily optimum, gives promise of providing a satisfactory design which will weigh less than had been anticipated.

The full text of this paper was not available for inclusion in this volume of the Proceedings. It will be published later in a separate volume.

☆U.S. Government Printing Office: 1980/10—689-102/5510